The mysterious aftereffects of COVID-19 infection p. 614

Discharging Fukushima's legacy p. 621

New tools for neuromodulation win *Science* & PINS prize p. 637

Science

$15
7 AUGUST 2020
sciencemag.org

AAAS

BUBBLE RUPTURE

Surface tension drives the wrinkling and collapse in viscous fluids p. 685



CONTENTS

7 AUGUST 2020 • VOLUME 369 • ISSUE 6504



612

NEWS

IN BRIEF

604 News at a glance

IN DEPTH

606 **Why infection poses a special risk to pregnant women**
Cardiovascular and immune system changes in moms-to-be make them more vulnerable to serious disease *By M. Wadman*

607 **COVID-19 unlikely to cause birth defects, but doctors await fall births**
By M. Wadman
PODCAST

608 **Fast, cheap tests could enable safer reopening**
Models show test accuracy matters less than speed and frequency for curbing outbreaks *By R. F. Service*

609 **Pandemic hits scientist parents hard**
New data quantify lost work hours and productivity *By K. Langin*

610 **Abortion opponents dominate Trump's fetal tissue review board**
Ethics advisory board will rule on federal funding for research that uses fetal organs and cells *By M. Wadman and J. Kaiser*

611 **Trump directive on state counts said to threaten rigor of census**
Experts decry order to exclude undocumented residents *By J. Mervis*

612 **Siberia's 'gateway to the underworld' hit by heat wave**
Thawing Batagay permafrost holds deep climate history *By R. Stone*

613 **Deforestation in the Brazilian Amazon is still rising sharply**
Satellite images suggest clearings are up by at least 28% *By H. Escobar*
LETTERS pp. 634 & 635

FEATURES

614 **The long haul**
Some COVID-19 survivors are still sick months later. Doctors want to learn why and what they can do *By J. Couzin-Frankel*

INSIGHTS

PERSPECTIVES

618 **Chimeric plants—the best of both worlds**
Overcoming graft incompatibility between species could protect future crop yields *By M. C. McCann*
REPORT p. 698

620 **Specificity in legume nodule symbiosis**
Structural variation in recognition molecules shapes symbiotic partnerships *By T. Bisseling and R. Geurts*
RESEARCH ARTICLE p. 663

621 **Opening the floodgates at Fukushima**
Tritium is not the only radioisotope of concern for stored contaminated water *By K. O. Buesseler*

623 **Unifying the synthesis of nucleoside analogs**
A short, versatile synthetic pathway transforms achiral reactants into nucleoside analogs *By G. J. Miller*
REPORT p. 725

624 **COVID-19 in Africa: Dampening the storm?**
The dampened course of COVID-19 in Africa might reveal innovative solutions *By M. Mbow* et al.

626 **Interferon responses in viral pneumonias**
Are interferon-mediated antiviral immune responses beneficial or detrimental in COVID-19? *By G. E. Grajales-Reyes and M. Colonna*
REPORTS pp. 706, 712, & 718

628 **John D. Gearhart (1943–2020)**
Pioneer of human pluripotent stem cell research *By P. J. Donovan and K. S. Zaret*

PHOTO: KATIE ORLINSKY/NAT GEO IMAGE COLLECTION

Published by AAAS

POLICY FORUM

629 Engage with animal welfare in conservation
Conservation could better promote not just the quantity of species but the quality of animal life
By N. Sekar and D. Shiller

BOOKS *ET AL.*

632 The unlikely role of dinosaurs in the diversity discourse
Western civilization's appreciation of variety may be related to the discovery of sudden extinction events *By J. M. Determann*

633 Saving species, one roll at a time
Players collaborate to rescue endangered animals in a new conservation-themed game
By A. Chuang

LETTERS

634 The Amazon's road to deforestation
By L. Ferrante and P. M. Fearnside
NEWS STORY p. 613

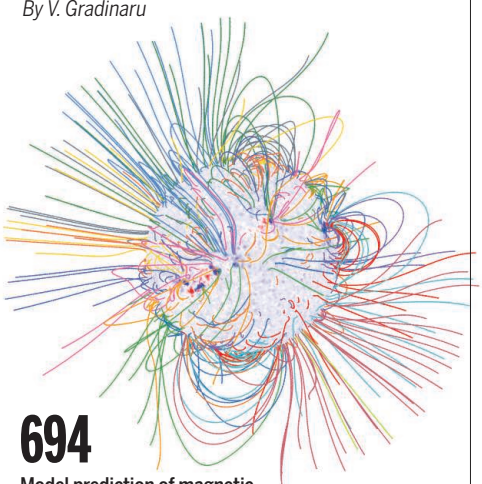
634 Smoke pollution's impacts in Amazonia
By G. de Oliveira et al.
NEWS STORY p. 613

635 Investors can help rein in Amazon deforestation
By A. G. Nazareno and W. F. Laurance
NEWS STORY p. 613

636 Technical Comment abstracts

PRIZE ESSAY

637 Expanding the brain researcher's toolkit
Better delivery vectors and opsins enable precise, minimally invasive neuromodulation
By V. Gradinaru



694
Model prediction of magnetic field lines in the Sun's corona

IMAGE: Z. YANG *ET AL.*

RESEARCH

IN BRIEF

639 From *Science* and other journals

RESEARCH ARTICLES

642 Cell biology
The proteasome controls ESCRT-III–mediated cell division in an archaeon *G. Tarrason Risa* et al.
RESEARCH ARTICLE SUMMARY; FOR FULL TEXT: DX.DOI.ORG/10.1126/SCIENCE.AAZ2532

Coronavirus
643 Potent neutralizing antibodies from COVID-19 patients define multiple targets of vulnerability *P. J. M. Brouwer* et al.

650 A neutralizing human antibody binds to the N-terminal domain of the Spike protein of SARS-CoV-2 *X. Chi* et al.

656 Structural biology
Structural insight into precursor ribosomal RNA processing by ribonuclease MRP *P. Lan* et al.

663 Plant science
Ligand-recognizing motifs in plant LysM receptors are major determinants of specificity *Z. Bozsoki* et al.
PERSPECTIVE p. 620

REPORTS

670 Nanomaterials
Chemical vapor deposition of layered two-dimensional $MoSi_2N_4$ materials
Y.-L. Hong et al.

674 Framework materials
Sequencing of metals in multivariate metal-organic frameworks *Z. Ji* et al.

680 Ferroelectrics
Emergent helical texture of electric dipoles
D. D. Khalyavin et al.

685 Fluid mechanics
A new wrinkle on liquid sheets: Turning the mechanism of viscous bubble collapse upside down *A. T. Oratis* et al.

689 Metallurgy
How hair deforms steel *G. Roscioli* et al.
PODCAST; VIDEO

694 Solar physics
Global maps of the magnetic field in the solar corona *Z. Yang* et al.

698 Plant science
Cell-cell adhesion in plant grafting is facilitated by β-1,4-glucanases *M. Notaguchi* et al.
PERSPECTIVE p. 618

702 Coronavirus
Unexpected air pollution with marked emission reductions during the COVID-19 outbreak in China *T. Le* et al.

Coronavirus
706 Type III interferons disrupt the lung epithelial barrier upon viral recognition *A. Broggi* et al.

712 Type I and III interferons disrupt lung epithelial repair during recovery from viral infection *J. Major* et al.

718 Impaired type I interferon activity and inflammatory responses in severe COVID-19 patients *J. Hadjadj* et al.
PERSPECTIVE p. 626

725 Organic chemistry
A short de novo synthesis of nucleoside analogs *M. Meanwell* et al.
PERSPECTIVE p. 623

731 Coronavirus
Broad neutralization of SARS-related viruses by human monoclonal antibodies
A. Z. Wec et al.

DEPARTMENTS

603 Editorial
Productivity in a pandemic *By Caitlyn Collins*

738 Working Life
Building bridges *By Ruofan Yu*

ON THE COVER



Thirty-six wrinkles develop during the sudden collapse of a centimeter-sized bubble of silicone oil, 100 times as viscous as honey. The black hole (center) is the opening of the bubble as it pops. Surface tension, not gravity, drives bubble collapse and initiates a rapid compression that dynamically buckles the film. This event highlights how physical intuition around gravity may prove erroneous when applied to interfacial phenomena. See page 685.
Photo: Oliver McRae/Boston University

Science Staff 602
Science Careers 737

SCIENCE (ISSN 0036-8075) is published weekly on Friday, except last week in December, by the American Association for the Advancement of Science, 1200 New York Avenue, NW, Washington, DC 20005. Periodicals mail postage (publication No. 484460) paid at Washington, DC, and additional mailing offices.

Copyright © 2020 by the American Association for the Advancement of Science. The title SCIENCE is a registered trademark of the AAAS.

Domestic individual membership, including subscription (12 months): $165 ($74 allocated to subscription). Domestic institutional subscription (51 issues): $2148; Foreign postage extra: Air assist delivery: $98. First class, airmail, student, and emeritus rates on request. Canadian rates with GST available upon request, GST #125488122. Publications Mail Agreement Number 1069624. **Printed in the U.S.A.**
Change of address: Allow 4 weeks, giving old and new addresses and 8-digit account number. **Postmaster:** Send change of address to AAAS, P.O. Box 96178, Washington, DC 20090–6178. **Single-copy sales:** $15 each plus shipping and handling available from backissues.sciencemag.org; bulk rate on request. **Authorization to reproduce** material for internal or personal use under circumstances not falling within the fair use provisions of the Copyright Act can be obtained through the Copyright Clearance Center (CCC), www.copyright.com. The identification code for *Science* is 0036-8075. *Science* is indexed in the *Reader's Guide to Periodical Literature* and in several specialized indexes.

Published by AAAS

Science AAAS

Editor-in-Chief Holden Thorp, hthorp@aaas.org

Executive Editor Monica M. Bradford

Editors, Research Valda Vinson, Jake S. Yeston **Editor, Insights** Lisa D. Chong

DEPUTY EDITORS Julia Fahrenkamp-Uppenbrink (UK), Stella M. Hurtley (UK), Phillip D. Szuromi, Sacha Vignieri **SR. EDITORIAL FELLOW** Andrew M. Sugden (UK) **SR. EDITORS** Gemma Alderton (UK), Caroline Ash (UK), Brent Grocholski, Pamela J. Hines, Di Jiang, Marc S. Lavine (Canada), Ian S. Osborne (UK), Beverly A. Purnell, L. Bryan Ray, H. Jesse Smith, Keith T. Smith (UK), Jelena Stajic, Peter Stern (UK), Valerie B. Thompson, Brad Wible, Laura M. Zahn **ASSOCIATE EDITORS** Michael A. Funk, Priscilla N. Kelly, Tage S. Rai, Seth Thomas Scanlon (UK), Yury V. Suleymanov **LETTERS EDITOR** Jennifer Sills **LEAD CONTENT PRODUCTION EDITORS** Harry Jach, Lauren Kmec **CONTENT PRODUCTION EDITORS** Amelia Beyna, Jeffrey E. Cook, Chris Filiatreau, Julia Katris, Nida Masiulis, Suzanne M. White **SR. EDITORIAL COORDINATORS** Carolyn Kyle, Beverly Shields **EDITORIAL COORDINATORS** Aneera Dobbins, Joi S. Granger, Jeffrey Hearn, Lisa Johnson, Maryrose Madrid, Ope Martins, Shannon McMahon, Jerry Richardson, Hilary Stewart (UK), Alana Warnke, Alice Whaley (UK), Anita Wynn **PUBLICATIONS ASSISTANTS** Jeremy Dow, Alexander Kief, Ronmel Navas, Brian White **EXECUTIVE ASSISTANT** Jessica Slater **ASI DIRECTOR, OPERATIONS** Janet Clements (UK) **ASI SR. OFFICE ADMINISTRATOR** Jessica Waldock (UK)

News Editor Tim Appenzeller

NEWS MANAGING EDITOR John Travis **INTERNATIONAL EDITOR** Martin Enserink **DEPUTY NEWS EDITORS** Elizabeth Culotta, Lila Guterman, David Grimm, Eric Hand (Europe), David Malakoff **SR. CORRESPONDENTS** Daniel Clery (UK), Jon Cohen, Jeffrey Mervis, Elizabeth Pennisi **ASSOCIATE EDITORS** Jeffrey Brainard, Catherine Matacic **NEWS REPORTERS** Adrian Cho, Jennifer Couzin-Frankel, Jocelyn Kaiser, Kelly Servick, Robert F. Service, Erik Stokstad, Paul Voosen, Meredith Wadman **INTERNS** Eva Frederick, Rodrigo Perez Ortega **CONTRIBUTING CORRESPONDENTS** Warren Cornwall, Ann Gibbons, Mara Hvistendahl, Sam Kean, Eli Kintisch, Kai Kupferschmidt (Berlin), Andrew Lawler, Mitch Leslie, Eliot Marshall, Virginia Morell, Dennis Normile (Shanghai), Elisabeth Pain (Careers), Charles Piller, Michael Price, Tania Rabesandratana (Barcelona), Emily Underwood, Gretchen Vogel (Berlin), Lizzie Wade (Mexico City) **CAREERS** Donisha Adams, Rachel Bernstein (Editor), Katie Langin (Acting Editor) **COPY EDITORS** Julia Cole (Senior Copy Editor), Cyra Master (Copy Chief) **ADMINISTRATIVE SUPPORT** Meagan Weiland

Creative Director Beth Rakouskas

DESIGN MANAGING EDITOR Marcy Atarod **GRAPHICS MANAGING EDITOR** Alberto Cuadra **PHOTOGRAPHY MANAGING EDITOR** William Douthitt **WEB CONTENT STRATEGY MANAGER** Kara Estelle-Powers **DESIGN EDITOR** Chrystal Smith **DESIGNER** Christina Aycock **GRAPHICS EDITOR** Nirja Desai **INTERACTIVE GRAPHICS EDITOR** Xing Liu **SENIOR SCIENTIFIC ILLUSTRATORS** Valerie Altounian, Chris Bickel **SCIENTIFIC ILLUSTRATOR** Alice Kitterman **SENIOR GRAPHICS SPECIALISTS** Holly Bishop, Nathalie Cary **SENIOR PHOTO EDITOR** Emily Petersen **PHOTO EDITOR** Kaitlyn Dolan

Chief Executive Officer and Executive Publisher Sudip Parikh

Publisher, Science Family of Journals Bill Moran

DIRECTOR, BUSINESS SYSTEMS AND FINANCIAL ANALYSIS Randy Yi **DIRECTOR, BUSINESS OPERATIONS & ANALYSIS** Eric Knott **DIRECTOR OF ANALYTICS** Enrique Gonzales **MANAGER, BUSINESS OPERATIONS** Jessica Tierney **SENIOR BUSINESS ANALYST** Cory Lipman, Meron Kebede **FINANCIAL ANALYST** Alexander Lee **ADVERTISING SYSTEM ADMINISTRATOR** Tina Burks **SENIOR SALES COORDINATOR** Shirley Young **DIGITAL/PRINT STRATEGY MANAGER** Jason Hillman **QUALITY TECHNICAL MANAGER** Marcus Spiegler **ASSISTANT MANAGER DIGITAL/PRINT** Rebecca Doshi **SENIOR CONTENT SPECIALISTS** Steve Forrester, Jacob Hedrick, Antoinette Hodal, Lori Murphy **PRODUCTION SPECIALIST** Kristin Wowk **DIGITAL PRODUCTION MANAGER** Lisa Stanford **CONTENT SPECIALIST** Kimberley Oster **ADVERTISING PRODUCTION OPERATIONS MANAGER** Deborah Tompkins **DESIGNER, CUSTOM PUBLISHING** Jeremy Huntsinger **SR. TRAFFIC ASSOCIATE** Christine Hall **SPECIAL PROJECTS ASSOCIATE** Sarah Dhere

ASSOCIATE DIRECTOR, BUSINESS DEVELOPMENT Justin Sawyers **GLOBAL MARKETING MANAGER** Allison Pritchard **DIGITAL MARKETING MANAGER** Aimee Aponte **JOURNALS MARKETING MANAGER** Shawana Arnold **MARKETING ASSOCIATES** Tori Velasquez, Mike Romano, Ashley Hylton **DIGITAL MARKETING SPECIALIST** Asleigh Rojanavongse **SENIOR DESIGNER** Kim Huynh

DIRECTOR AND SENIOR EDITOR, CUSTOM PUBLISHING Sean Sanders **ASSISTANT EDITOR, CUSTOM PUBLISHING** Jackie Oberst

DIRECTOR, PRODUCT & PUBLISHING DEVELOPMENT Chris Reid **DIRECTOR, BUSINESS STRATEGY AND PORTFOLIO MANAGEMENT** Sarah Whalen **ASSOCIATE DIRECTOR, PRODUCT MANAGMENT** Kris Bishop **SR. PRODUCT ASSOCIATE** Robert Koepke **DIGITAL PRODUCT STRATEGIST** Michael Hardesty **SPJ ASSOCIATE** Samantha Bruno Fuller

DIRECTOR, INSTITUTIONAL LICENSING Iquo Edim **ASSOCIATE DIRECTOR, RESEARCH & DEVELOPMENT** Elisabeth Leonard **MARKETING MANAGER** Kess Knight **SENIOR INSTITUTIONAL LICENSING MANAGER** Ryan Rexroth **INSTITUTIONAL LICENSING MANAGER** Marco Castellan **MANAGER, AGENT RELATIONS & CUSTOMER SUCCESS** Judy Lillibridge **SENIOR OPERATIONS ANALYST** Lana Guz **FULFILLMENT COORDINATOR** Melody Stringer **SALES COORDINATOR** Josh Haverlock

DIRECTOR, GLOBAL SALES Tracy Holmes **US EAST COAST AND MID WEST SALES** Stephanie O'Connor **US WEST COAST SALES** Lynne Stickrod **US SALES MANAGER, SCIENCE CAREERS** Claudia Paulsen-Young **US SALES REP, SCIENCE CAREERS** Tracy Anderson **ASSOCIATE DIRECTOR, ROW** Roger Goncalves **SALES REP, ROW** Sarah Lelarge **SALES ADMIN ASSISTANT, ROW** Bryony Cousins **DIRECTOR OF GLOBAL COLLABORATION AND ACADEMIC PUBLISHING RELATIONS, ASIA** Xiaoying Chu **ASSOCIATE DIRECTOR, INTERNATIONAL COLLABORATION** Grace Yao **SALES MANAGER** Danny Zhao **MARKETING MANAGER** Kilo Lan **ASCA CORPORATION, JAPAN** Kaoru Sasaki (Tokyo), Miyuki Tani (Osaka) **COLLABORATION/CUSTOM PUBLICATIONS/JAPAN** Adarsh Sandhu

DIRECTOR, COPYRIGHT, LICENSING AND SPECIAL PROJECTS Emilie David **RIGHTS AND LICENSING COORDINATOR** Jessica Adams **RIGHTS AND PERMISSIONS ASSOCIATE** Elizabeth Sandler **CONTRACTS AND LICENSING ASSOCIATE** Lili Catlett

MAIN HEADQUARTERS
Science/AAAS
1200 New York Ave. NW
Washington, DC 20005

SCIENCE INTERNATIONAL
Clarendon House
Clarendon Road
Cambridge, CB2 8FH, UK

SCIENCE CHINA
Room 1004, Culture Square
No. 59 Zhongguancun St.
Haidian District, Beijing, 100872

SCIENCE JAPAN
ASCA Corporation
Sibaura TY Bldg. 4F, 1-14-5
Shibaura Minato-ku
Tokyo, 108-0073 Japan

EDITORIAL
science_editors@aaas.org

NEWS
science_news@aaas.org

INFORMATION FOR AUTHORS
sciencemag.org/authors/science-information-authors

REPRINTS AND PERMISSIONS
sciencemag.org/help/reprints-and-permissions

MEDIA CONTACTS
scipak@aaas.org

MULTIMEDIA CONTACTS
SciencePodcast@aaas.org
ScienceVideo@aaas.org

INSTITUTIONAL SALES AND SITE LICENSES
sciencemag.org/librarian

PRODUCT ADVERTISING & CUSTOM PUBLISHING
advertising.sciencemag.org/products-services
science_advertising@aaas.org

CLASSIFIED ADVERTISING
advertising.sciencemag.org/science-careers
advertise@sciencecareers.org

JOB POSTING CUSTOMER SERVICE
employers.sciencecareers.org
support@sciencecareers.org

MEMBERSHIP AND INDIVIDUAL SUBSCRIPTIONS
sciencemag.org/subscriptions

MEMBER BENEFITS
aaas.org/membercentral

AAAS BOARD OF DIRECTORS
CHAIR Steven Chu
PRESIDENT Claire M. Fraser
PRESIDENT-ELECT Susan G. Amara
TREASURER Carolyn N. Ainslie
CHIEF EXECUTIVE OFFICER Sudip Parikh
BOARD Cynthia M. Beall, Rosina M. Bierbaum, Ann Bostrom, Stephen P.A. Fodor, S. James Gates, Jr., Laura H. Greene, Kaye Husbands Fealing, Maria M. Klawe, Robert B. Millard, Alondra Nelson, William D. Provine

BOARD OF REVIEWING EDITORS (Statistics board members indicated with **(S)**)

Adriano Aguzzi, *U. Hospital Zürich*
Takuzo Aida, *U. of Tokyo*
Leslie Aiello, *Wenner-Gren Foundation*
Judith Allen, *U. of Manchester*
Sebastian Amigorena, *Institut Curie*
James Analytis, *U. of California, Berkeley*
Trevor Archer, *NIEHS, NIH*
Paola Arlotta, *Harvard U.*
Johan Auwerx, *EPFL*
David Awschalom, *U. of Chicago*
Clare Baker, *U. of Cambridge*
Nenad Ban, *ETH Zürich*
Franz Bauer, *Pontificia U. Católica de Chile*
Ray H. Baughman, *U. of Texas at Dallas*
Peter Bearman, *Columbia U.*
Carlo Beenakker, *Leiden U.*
Yasmine Belkaid, *NIAID, NIH*
Philip Benfey, *Duke U.*
Gabriele Bergers, *VIB*
Bradley Bernstein, *Mass. General Hospital*
Alessandra Biffi, *Harvard Med. School*
Peer Bork, *EMBL*
Chris Bowler, *École Normale Supérieure*
Ian Boyd, *U. of St. Andrews*
Emily Brodsky, *U. of California, Santa Cruz*
Ron Brookmeyer, *U. of California, Los Angeles* **(S)**
Christian Büchel, *UKE Hamburg*
Dennis Burton, *Scripps Res.*
Carter Tribley Butts, *U. of California, Irvine*
György Buzsáki, *New York U. School of Med.*
Blanche Capel, *Duke U.*
Annmarie Carlton, *U. of California, Irvine*
Nick Chater, *U. of Warwick*
Zhijian Chen, *UT Southwestern Med. Ctr.*
Ib Chorkendorff, *Denmark TU*
James J. Collins, *MIT*
Robert Cook-Deegan, *Arizona State U.*
Alan Cowman, *Walter & Eliza Hall Inst.*
Carolyn Coyne, *U. of Pittsburgh*
Roberta Croce, *VU Amsterdam*
Ismaila Dabo, *Penn State U.*
Jeff L. Dangl, *U. of North Carolina*
Tom Daniel, *U. of Washington*
Chiara Daraio, *Caltech*
Nicolas Dauphas, *U. of Chicago*
Frans de Waal, *Emory U.*
Claude Desplan, *New York U.*
Sandra Díaz, *U. Nacional de Córdoba*
Ulrike Diebold, *TU Wien*
Hong Ding, *Inst. of Physics, CAS*
Jennifer Dionne, *Stanford U.*
Dennis Discher, *U. of Penn.*
Gerald Dorn, *Washington U. in St. Louis*
Jennifer A. Doudna, *U. of California, Berkeley*
Bruce Dunn, *U. of California, Los Angeles*
William Dunphy, *Caltech*
Christopher Dye, *U. of Oxford*
Todd Ehlers, *U. of Tübingen*
Jennifer Elisseeff, *Johns Hopkins U.*
Tim Elston, *U. of North Carolina*
Andrea Encalada, *U. San Francisco de Quito*
Nader Engheta, *U. of Penn.*
Karen Ersche, *U. of Cambridge*
Barry Everitt, *U. of Cambridge*
Vanessa Ezenwa, *U. of Georgia*
Michael Feuer, *The George Washington U.*
Toren Finkel, *U. of Pittsburgh Med. Ctr.*
Gwenn Flowers, *Simon Fraser U.*
Peter Fratzl, *Max Planck Inst. Potsdam*
Elaine Fuchs, *Rockefeller U.*
Eileen Furlong, *EMBL*
Jay Gallagher, *U. of Wisconsin*
Daniel Geschwind, *U. of California, Los Angeles*
Karl-Heinz Glassmeier, *TU Braunschweig*
Ramon Gonzalez, *U. of South Florida*
Elizabeth Grove, *U. of Chicago*
Nicolas Gruber, *ETH Zürich*
Hua Guo, *U. of New Mexico*
Kip Guy, *U. of Kentucky College of Pharmacy*
Taekjip Ha, *Johns Hopkins U.*
Christian Haass, *Ludwig Maximilians U.*
Sharon Hammes-Schiffer, *Yale U.*
Wolf-Dietrich Hardt, *ETH Zürich*
Louise Harra, *U. College London*
Jian He, *Clemson U.*
Carl-Philipp Heisenberg, *IST Austria*
Ykä Helariutta, *U. of Cambridge*
Janet G. Hering, *Eawag*
Hans Hilgenkamp, *U. of Twente*
Kai-Uwe Hinrichs, *U. of Bremen*
Lora Hooper, *UT Southwestern Med. Ctr.*
Fred Hughson, *Princeton U.*
Randall Hulet, *Rice U.*
Auke Ijspeert, *EPFL*
Akiko Iwasaki, *Yale U.*
Stephen Jackson, *USGS and U. of Arizona*
Kai Johnsson, *EPFL*
Peter Jonas, *IST Austria*
Matt Kaeberlein, *U. of Washington*
William Kaelin Jr., *Dana-Farber Cancer Inst.*
Daniel Kammen, *U. of California, Berkeley*
V. Narry Kim, *Seoul Nat. U.*
Robert Kingston, *Harvard Med. School*
Nancy Knowlton, *Smithsonian Institution*
Etienne Koechlin, *École Normale Supérieure*
Alex L. Kolodkin, *Johns Hopkins U.*
Julija Krupic, *U. of Cambridge*
Thomas Langer, *Max Planck Inst. Cologne*
Mitchell A. Lazar, *U. of Penn.*
Wendell Lim, *U. of California, San Francisco*
Jianguo Liu, *Michigan State U.*
Luis Liz-Marzán, *CIC biomaGUNE*
Jonathan Losos, *Washington U. in St. Louis*
Ke Lu, *Chinese Acad. of Sciences*
Christian Lüscher, *U. of Geneva*
Jean Lynch-Stieglitz, *Georgia Inst. of Tech.*
Fabienne Mackay, *QIMR Berghofer*
Anne Magurran, *U. of St. Andrews*
Oscar Marín, *King's College London*
Charles Marshall, *U. of California, Berkeley*
Christopher Marx, *U. of Idaho*
Geraldine Masson, *CNRS*
C. Robertson McClung, *Dartmouth College*
Rodrigo Medellín, *U. Nacional Autónoma de México*
Graham Medley, *LSHTM*
Jane Memmott, *U. of Bristol*
Baoxia Mi, *U. of California, Berkeley*
Edward Miguel, *U. of California, Berkeley*
Tom Misteli, *NCI, NIH*
Yasushi Miyashita, *U. of Tokyo*
Alison Motsinger-Reif, *NIEHS, NIH* **(S)**
Daniel Nettle, *Newcastle U.*
Daniel Neumark, *U. of California, Berkeley*
Beatriz Noheda, *U. of Groningen*
Helga Nowotny, *Vienna Sci., Res. & Tech. Fund*
Rachel O'Reilly, *U. of Birmingham*
Harry Orr, *U. of Minnesota*
Pilar Ossorio, *U. of Wisconsin*
Andrew Oswald, *U. of Warwick*
Isabella Pagano, *Istituto Nazionale di Astrofisica*
Margaret Palmer, *U. of Maryland*
Elizabeth Levy Paluck, *Princeton U.*
Jane Parker, *Max Planck Inst. Cologne*
Giovanni Parmigiani, *Dana-Farber Cancer Inst.* **(S)**
Daniel Pauly, *U. of British Columbia*
Samuel Pfaff, *Salk Inst. for Biological Studies*
Julie Pfeiffer, *UT Southwestern Med. Ctr.*
Matthieu Piel, *Institut Curie*
Kathrin Plath, *U. of California, Los Angeles*
Martin Plenio, *Ulm U.*
Katherine Pollard, *U. of California, San Francisco*
Elvira Poloczanska, *Alfred-Wegener-Inst.*
Julia Pongratz, *Ludwig Maximilians U.*
Philippe Poulin, *CNRS*
Jonathan Pritchard, *Stanford U.*
Félix A. Rey, *Institut Pasteur*
Trevor Robbins, *U. of Cambridge*
Joeri Rogelj, *Imperial College London*
Amy Rosenzweig, *Northwestern U.*
Mike Ryan, *U. of Texas at Austin*
Shimon Sakaguchi, *Osaka U.*
Miquel Salmeron, *Lawrence Berkeley Nat. Lab*
Nitin Samarth, *Penn. State U.*
Jürgen Sandkühler, *Med. U. of Vienna*
Erica Ollmann Saphire, *La Jolla Inst.*
Alexander Schier, *Harvard U.*
Wolfram Schlenker, *Columbia U.*
Susannah Scott, *U. of California, Santa Barbara*
Rebecca Sear, *LSHTM*
Vladimir Shalaev, *Purdue U.*
Jie Shan, *Cornell U.*
Beth Shapiro, *U. of California, Santa Cruz*
Jay Shendure, *U. of Washington*
Steve Sherwood, *U. of New South Wales*
Brian Shoichet, *U. of California, San Francisco*
Robert Siliciano, *Johns Hopkins U. School of Med.*
Lucia Sivilotti, *U. College London*
Alison Smith, *John Innes Centre*
Richard Smith, *U. of North Carolina* **(S)**
Mark Smyth, *QIMR Berghofer*
Pam Soltis, *U. of Florida*
John Speakman, *U. of Aberdeen*
Tara Spires-Jones, *U. of Edinburgh*
Allan C. Spradling, *Carnegie Institution for Sci.*
V. S. Subrahmanian, *Dartmouth College*
Ira Tabas, *Columbia U.*
Sarah Teichmann, *Wellcome Sanger Inst.*
Rocio Titiunik, *Princeton U.*
Shubha Tole, *Tata Inst. of Fundamental Res.*
Wim van der Putten, *Netherlands Inst. of Ecology*
Reinhilde Veugelers, *KU Leuven*
Bert Vogelstein, *Johns Hopkins U.*
Kathleen Vohs, *U. of Minnesota*
David Wallach, *Weizmann Inst. of Sci.*
Jane-Ling Wang, *U. of California, Davis* **(S)**
David Waxman, *Fudan U.*
Jonathan Weissman, *U. of California, San Francisco*
Chris Wikle, *U. of Missouri* **(S)**
Terrie Williams, *U. of California, Santa Cruz*
Ian A. Wilson, *Scripps Res.* **(S)**
Yu Xie, *Princeton U.*
Jan Zaanen, *Leiden U.*
Kenneth Zaret, *U. of Penn. School of Med.*
Jonathan Zehr, *U. of California, Santa Cruz*
Xiaowei Zhuang, *Harvard U.*
Maria Zuber, *MIT*

Science serves as a forum for discussion of important issues related to the advancement of science by publishing material on which a consensus has been reached as well as including the presentation of minority or conflicting points of view. Accordingly, all articles published in *Science*—including editorials, news and comment, and book reviews—are signed and reflect the individual views of the authors and not official points of view adopted by AAAS or the institutions with which the authors are affiliated.

Published by AAAS

EDITORIAL

Productivity in a pandemic

Almost overnight, coronavirus disease 2019 (COVID-19) has upended daily life, including the work of scientific research. But scientists have not experienced these new disruptions equally. You may have heard that women scientists seem to be submitting fewer papers for publication (including preprints), whereas men are submitting more. If this imbalance is correct, then the effects could include fewer women being granted tenure and promotion, a larger gender pay gap, and even some women being pushed out of science.

Why might women scientists be publishing less than men during the pandemic? To answer this question, let's examine what's happening in the wider world of work—and, crucially, at home. In the United States, most workers have children: A 2013 Gallup poll showed that 86% of people become parents during their working-age lives. Many adults juggle paid work with unpaid caregiving (for children, parents, partners, and other loved ones). But in most households, women perform the bulk of childcare and housework. This is true for women scientists at home, as reported in 2010 by the American Association of University Professors. In academia, this makes it tough for women to publish as much as their male colleagues, even in the best of times.

Now add a global pandemic to this scenario.

Researchers who have managed to stay employed are trying to work from home just as schools and daycare centers have closed. Those with young children, in particular, are struggling to stay afloat. One study during the early stage of the pandemic showed that women scientists with young children, more so than similar men, are scaling back their research time to meet these heightened demands. And because women faculty do more service work than men in "normal" times—the less-prestigious student advising, program supervision, and committee tasks that keep academic institutions afloat—my guess is that these duties are consuming more of women's time as universities coordinate pandemic responses.

This gender gap matters because in academia, publishing is the primary criterion for tenure, promotion, and raises. Publishing less during the pandemic could undermine the careers of an entire generation of women scholars. Women are already underrepresented in science, and their representation declines at every career stage. This disparity is pronounced for women of color. And because a diverse workforce can boost scientific creativity and productivity, the pandemic's lasting impacts on women could harm scientific innovation.

The window of opportunity for advancement in academia is narrow. The time requiring the most devotion—tenure track—often coincides with the early years of parenthood. For parents in science, especially mothers, this timing does not bode well.

This hard truth helps explain why the upper echelons of academia have long been occupied by white men with stay-at-home wives and, though rarely, by women who decided to forgo motherhood altogether. The success that men achieve in their careers is due in no small part to the support of women. Yes, today's dads spend more time caring for their kids than did fathers of previous generations, yet both men and women report finding it tough to reconcile family commitments with the demands of science.

> "Why might women scientists be publishing less than men during the pandemic?"

The bottom line is that science is simply not welcoming to parents. After having children, an astounding 43% of mothers and 23% of fathers leave full-time employment in science, technology, engineering, and mathematics fields in the United States. In response, some universities have instituted policies such as paid parental leave and temporary tenure clock suspension. But research finds that men in academia often use this time as a sabbatical to submit and publish more, whereas women do not—presumably, they use it to care for newborns.

Nothing is likely to change until there are policies to support parents, not just in academia but in all walks of life. Among developed nations, the United States is a laggard on every dimension of federal work-family policy. Correcting this would benefit children, families, universities—indeed, the entire scientific enterprise. But until society's beliefs change about who can and should care for children, such efforts will fall short.

As the pandemic grinds on and uncertainty prevails about reopening schools and childcare centers, the effects on research productivity, especially for women, will only get worse. Gender equity in scientific publishing will elude us until we address gender equity at home.

–Caitlyn Collins



PHOTO: ELIE HONEIN

Caitlyn Collins
is an assistant professor of sociology at Washington University in St. Louis, Missouri, USA.
c.collins@wustl.edu

10.1126/science.abe1163

Published by AAAS

> “Since when has this virus operated on our schedule?”
>
> **Jeff Gregorich,** a local school superintendent in Arizona, in *The Washington Post*, on the state's requirement that schools reopen on 17 August. He fears that date is too soon to keep students, staff members, and the community safe from COVID-19.

IN BRIEF

Edited by **Jeffrey Brainard**

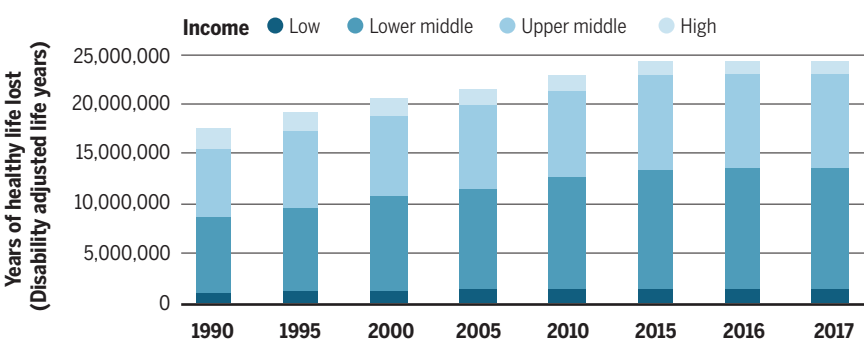
PUBLIC HEALTH

One in three children poisoned by lead

One in three of the world's 2.4 billion children and adolescents under age 20 has a blood lead level that exceeds what would trigger public health alarms in the United States, a report says. The majority live in lower and middle-income countries, mostly in Asia and the Pacific, according to an analysis by UNICEF and the advocacy group Pure Earth published last week. The potent neurotoxin can reduce a child's intelligence test score and cause other health problems; lead poisoning is blamed for nearly $1 trillion of lost lifetime earnings. Most lead enters the environment through poorly regulated smelters that recycle car batteries. Lead poisoning has worsened considerably during the past 2 decades because car sales in those countries have tripled, the report says. Scientists consider no amount of lead exposure safe, but the U.S. Centers for Disease Control and Prevention has set the threshold for action at 5 milligrams per deciliter—the level met or exceeded in 800 million children worldwide. The report recommends more blood-level testing, prevention, and environmental cleanup.

The risky middle

Lead pollution burdens children and adults by reducing years of healthy life (shown here for all ages), especially in middle-income countries where exposures have grown.



House backs spending increases

FUNDING | The U.S. House of Representatives last week approved windfalls for three federal research agencies as part of a $1.3 trillion package of appropriations for fiscal year 2021 that would give modest increases to several other science agencies. The $5 billion added to the National Institutes of Health would raise its budget to $47 billion, science programs at the Department of Energy would receive $6.25 billion on top of their regular $7.05 billion allocation, and DOE's Advanced Research Projects Agency-Energy would get an extra $250 million above its $435 million budget. The Democrat-led House avoided a tight cap on domestic spending for 2021 by labeling these and other boosts as “emergency” infrastructure investments. The Republican-led Senate has yet to adopt its version of the 2021 budget, meaning federal agencies will likely face a spending freeze starting on 1 October followed by months of budget uncertainty. No Republicans voted for the House bill.

MeTooSTEM head admits hoax

COMMUNITY | MeTooSTEM founder and former Vanderbilt University neuroscientist BethAnn McLaughlin has admitted to fabricating the Twitter persona of a nonexistent female Native American anthropologist at Arizona State University, *The New York Times* reported on 4 August. “My actions are inexcusable,” said the statement, issued by her lawyer. “I apologize without reservation to all the people I hurt.” McLaughlin announced on 31 July that Alepo, the woman supposedly behind the account @Sciencing_Bi, had died of COVID-19. Suspicions arose after Twitter users could not find evidence that the professor existed. By 2 August, Twitter had suspended McLaughlin's and the @Sciencing_Bi accounts. Followers of @Sciencing_Bi reacted angrily to the deception, noting how hurtful it was that the account purported to be an Indigenous female scientist who was then said to have died. McLaughlin achieved prominence 2 years ago as an advocate for survivors of sexual harassment in science and by founding a nonprofit advocacy group, MeTooSTEM. But colleagues and volunteers there began to resign after many, including women of color, accused McLaughlin of bullying them.

Reprint fees linked to conflicts

PUBLISHING | Journals that charge for reprints of their articles tend to publish more papers in which authors report financial conflicts of interest, a study has found. Many pharmaceutical companies pay journals—including the *Science* family of journals—for reprints, which are paper or electronic copies of a published paper. Companies often use these to share favorable research findings about their treatments with physicians and others. Articles in journals that accept reprint fees are nearly three times as likely as those

CREDITS: (GRAPHIC) X. LIU/*SCIENCE*; (DATA) UNICEF AND PURE EARTH; INSTITUTE FOR HEALTH METRICS AND EVALUATION, GBD 2017 RESULTS TOOL; GLOBAL HEALTH DATA EXCHANGE (2018)

Published by AAAS

in other journals to have an author who disclosed payment from industry, a study published on 24 July in *PLOS ONE* found. Ad revenues have received more attention than reprint fees as potentially biasing decisions by journal editors about which papers to publish. But journals that collect revenue from industry ads did not publish more articles with disclosed conflicts of interest, according to the study, which examined 128,721 papers in 159 biomedical journals.

Snake River dams staying put

CONSERVATION | The Trump administration announced last week that it will not remove four large dams on the Snake River to restore habitat for endangered salmon in the Pacific Northwest. The announcement was the culmination of a 3-year environmental review by a trio of federal agencies responsible for balancing the needs of endangered animals with business, recreation, and transportation interests. According to the agencies' final environmental impact statement, removing the dams would increase regional greenhouse gas emissions and raise the risk of regional power outages. The decision marked a defeat for environmentalists, who have fought for decades to remove what they consider as the most harmful dams in a network of 14 barriers on the Columbia and Snake rivers that have contributed to a 98% decline in salmon populations compared with historic numbers. Twenty-eight populations in the region are now listed as threatened or endangered.

Dinosaur leg shows tumor

PALEONTOLOGY | A deformed bone uncovered in Canada's Alberta province offers the first clear example of a malignant tumor diagnosed in a dinosaur. The partial fibula—a bone from the lower leg—belonged to a *Centrosaurus*, a horned plant-eating dinosaur, that lived roughly 76 million years ago. Paleontologists initially thought the bone's strange shape was caused by a fracture that hadn't healed cleanly. But a study published on 3 August in *The Lancet Oncology* compared the fossil's internal structure with a bone tumor from a human patient and concluded that the dinosaur suffered from osteosarcoma, a cancer of immature bone tissue that primarily attacks teens and young adults. A similar case in a human, left untreated, would likely be fatal, the team wrote. But researchers found evidence that the dinosaur likely died in a flood.



PHOTO: AARON LOJEWSKI/WWW.FAIRBANKSAURORATOURS.COM

GEOPHYSICS

Earthquake sensors detect aurorae

Researchers have successfully repurposed an array of seismometers, which typically measure Earth's shaking, to detect the aurora borealis high above. The approach supplements aurora monitoring that relies on high-sensitivity magnetometers, which measure magnetic fields and are difficult and expensive to maintain in remote regions. The colorful glowing lights appear in the night sky when charged particles ejected by the Sun penetrate Earth's magnetic field and collide with atmospheric gases, creating electromagnetic disturbances. Seismometers are usually equipped with shielding to protect their sensors, which have magnetic components, from resulting interference. But by using an array of largely unshielded seismometers deployed several years ago across Alaska (*Science*, 6 October 2017, p. 22), researchers captured the magnetic fluctuations caused by three aurorae, they reported last week in *Seismological Research Letters*. Future observations could help fill gaps in data about the incidence and intensity of aurorae.

Published by AAAS



IN DEPTH

Obstetrician Yalda Afshar is probing COVID-19's impact in pregnancy. Her own baby is due in October.

PHOTO: APARNA SRIDHAR

COVID-19

Why infection poses a special risk to pregnant women

Cardiovascular and immune system changes in moms-to-be make them more vulnerable to serious disease

By **Meredith Wadman**

Yalda Afshar hears the worries every day from her patients: Will COVID-19 hit me harder because I'm pregnant? If I'm infected, will the virus damage my baby? Afshar, a high-risk obstetrician at Ronald Reagan University of California (UC), Los Angeles, Medical Center, understands the women's concerns better than most: Her first child is due in October.

Data on pregnancy and COVID-19 are woefully incomplete. But they offer some reassurance: Fetal infections later in pregnancy appear to be rare, and experts are cautiously optimistic that the coronavirus won't warp early fetal development (see sidebar, p. 607). But emerging data suggest some substance to the other worry of Afshar's patients: Pregnancy does appear to make women's bodies more vulnerable to severe COVID-19, the disease caused by SARS-CoV-2. That's partly because of pregnant women's uniquely adjusted immune systems, and partly because the coronavirus' points of attack—the lungs and the cardiovascular system—are already stressed in pregnancy.

The prescription for caregivers is simple, says David Baud, an expert on emerging infectious diseases and pregnancy at Lausanne University Hospital: "Protect your pregnant patients. The first ones who need the masks are pregnant women. The first to avoid social contact should be pregnant women."

Science's COVID-19 reporting is supported by the Pulitzer Center and the Heising-Simons Foundation.

The best U.S. data available so far were published by the Centers for Disease Control and Prevention (CDC) late in June. Among 91,412 women of reproductive age with coronavirus infections, the 8207 who were pregnant were 50% more likely to end up in intensive care units (ICUs) than their nonpregnant peers. Pregnant women were also 70% more likely to need ventilators, although they were no more likely to die.

CDC's data only offer a partial view, however. Pregnancy status was only available for 28% of the 326,000 U.S. women of reproductive age whose coronavirus infections had been reported to CDC by early June.

A second paper, published by the Public Health Agency of Sweden last month in *Acta Obstetricia et Gynecologica Scandinavica*, used a more complete data set. Using data for all of Sweden during 4 weeks in March and April, researchers calculated infected pregnant women's rate of ICU admission compared with that of infected nonpregnant women of reproductive age. The study was small: Only 13 coronavirus-infected pregnant women and 40 nonpregnant infected women were admitted to Swedish ICUs in that time frame. But, Baud says, "From my point of view, it is the most robust data."

The results were sobering: The researchers found that pregnant or immediately postpartum women with COVID-19 were nearly six times as likely to land in ICUs as their nonpregnant, COVID-19–infected peers.

It's well known that pregnancy boosts the risk of serious disease from respiratory viral infections. During the H1N1 flu epidemic of 2009, pregnant women accounted for 5% of U.S. deaths, although they constituted about 1% of the population. One study found pregnant women with severe acute respiratory syndrome (SARS), which is caused by a virus that's a close cousin of SARS-CoV-2, were significantly more likely to be admitted to the ICU and to die than nonpregnant peers.

Viral infections can be more severe in pregnant women in part because "the entire immune system is geared toward making sure not to create any antifetal immune response," says Akiko Iwasaki, an immunologist at the Yale School of Medicine. "The mother has to compromise her own immune defense in order to preserve the baby's health."

At the same time, the immune system is far from inactive in pregnancy, and "the really significant immune response to the infection certainly has the potential to cause complications," says Carolyn Coyne, a virologist at the University of Pittsburgh.

In addition, SARS-CoV-2 strikes the lungs and the cardiovascular system, which in pregnancy are already strained. "As the uterus grows there is less and less room for the lungs. That's why pregnant women often feel short of breath. And that affects your pulmonary function," says Denise

Published by AAAS

Corrected 6 August 2020. See full text.

Jamieson, chair of obstetrics and gynecology at Emory University School of Medicine.

To supply the fetus, pregnant women also need extra oxygen and blood to ferry it: up to 50% more by late pregnancy. This may multiply the stress that COVID-19 has been shown to put on the cardiovascular system (*Science*, 24 April, p. 356). "The heart is already working for two," Baud says. "And if you are a virus known to induce vessel change, inflammation, this will increase the workload of the heart even more."

Malavika Prabhu, a maternal and fetal medicine specialist at Weill Cornell Medicine, adds that later in pregnancy, "with so much blood going around and the organs more metabolically active, all that extra fluid can go in places it shouldn't go—including filling your lungs with fluid."

Finally, pregnant women's blood has an increased tendency to clot, thought to be due to their need to quickly staunch bleeding after delivering a baby. But the coronavirus itself can have a similar effect (*Science*, 5 June, p. 1039). "COVID is thought to increase your likelihood of clotting, and then pregnancy further increases your likelihood of clotting," Jamieson says.

Elevated dangers to the mother don't end with delivery, according to work by Prabhu and colleagues in the journal *BJOG* last month. They followed all 675 pregnant women admitted for delivery at three New York hospitals during 4 weeks in late March and April. After giving birth, nine of 70 infected women, or about 13%, had at least one of three complications that doctors watch for after delivery: fever, low blood oxygen, and hospital readmission. Among 605 noninfected women, 27, or 4.5%, had one of these problems. "Many diseases are unmasked in the postpartum period. We learned that COVID-19 is one of those," Prabhu says. She noted that 79% of the pregnant women who tested positive when admitted were asymptomatic.

Experts all say better data are desperately needed to understand and address the risks to pregnant, coronavirus-infected women. Jamieson notes that registries gathering data on pregnant women infected with H1N1 influenza in 2009 and with Zika in 2015 and 2016 were abandoned after those epidemics passed. "We really need investment in a long-term, well-funded surveillance system that captures pregnancy outcomes."

With a colleague at UC San Francisco, Afshar is co–principal investigator of the Pregnancy Coronavirus Outcomes Registry now collecting data from more than 1100 U.S. pregnant women. She hopes it will begin to answer urgent questions such as the impact on mother and fetus of drugs being given to fight COVID-19; how infection influences a mother's immune status; and whether and how anticlotting drugs ought to be used in pregnant women with COVID-19.

"It has been very strange to counsel women and their families, and witness their stress, and not be able to give them evidence-based recommendations," Afshar says. "I lose sleep for every woman I take care of, to make sure I am doing the right thing for her. And it's just the same, I would say, for myself." ■

COVID-19 unlikely to cause birth defects, but doctors await fall births

When a pregnant woman gets sick, her doctors have two patients: the woman and her fetus. While obstetricians work to understand COVID-19's impact on mothers-to-be (see main story, p. 606), they are also carefully tracking the virus' impact on the fetus, acutely aware that other viruses, including Zika, cytomegalovirus (CMV), and rubella, can cause serious birth defects. Researchers are cautiously optimistic the same will not prove true with the new coronavirus.

A case study published last month demonstrated conclusively that fetuses can be infected late in pregnancy. But such infections appear to be "extremely rare," says lead author Daniele De Luca, a critical care neonatologist at Paris Saclay University Hospitals AP-HP. Stanley Plotkin, a physician-scientist who invented the widely used rubella vaccine, notes: "This is not rubella." The 1964 epidemic of that disease led to the births of tens of thousands of damaged babies in the United States.

It's still too soon to be certain that fetuses won't be damaged if they are infected during the sensitive first trimester, when tissues and organs take shape. But Carolyn Coyne, a virologist who studies placental infections at the University of Pittsburgh, is optimistic. "If [the virus] was a devastating pathogen causing fetal malformations early in pregnancy, we would have very clear cases from China," which had the earliest surge of COVID-19 cases. Senior Chinese obstetricians contacted by *Science* said they had seen no cases of congenital anomalies but warned that numbers were too small to draw firm conclusions.

Plotkin notes rubella and CMV are commonly blood-borne, allowing those viruses to reach the placenta during the first trimester, before it is a fully formed barrier to viral invasion. "Although SARS-CoV-2 virus does occasionally get into the blood, it is not basically a [blood-borne] infection," he says. "That's important."

In one study of nearly 700 pregnant women admitted to three New York hospitals for delivery, 71 babies born to infected moms were uninfected themselves. Another study published this month in *eLife* suggests the virus is unlikely to easily invade placental cells. Scientists led by Roberto Romero at the National Institute of Child Health and Human Development and Wayne State University found placental cells rarely simultaneously express a pair of molecules that the virus relies on to invade cells: ACE2, a membrane-bound receptor, and TMPRSS-2, an enzyme that activates the virus after it has bound ACE2. By contrast, they found that receptors for Zika and CMV are abundant on placental cells.

Still, a mother's SARS-CoV-2 infection could affect her fetus' growth. Researchers in the New York study also examined placentas from a subset of women and found clots in blood vessels on the fetal side of the placenta in nearly half—14 of 29—of COVID-19–infected mothers. Only 11% of placentas—12 out of 106—from uninfected moms had similar clots. Another study, by researchers at Northwestern University, found significantly more blood vessel injury and clots on the maternal side of the placenta in 15 of 16 infected women than in controls.

Blood clots could limit the oxygen and nutrients delivered to the fetus. These studies suggest the need to closely monitor fetal growth during the second half of a COVID-19–affected pregnancy, says Malavika Prabhu, a maternal and fetal medicine specialist at Weill Cornell Medicine and first author on the New York study.

Meanwhile, she and others await a wave of babies conceived early in the pandemic and due in the fall. "If you have COVID-19 at 8 weeks during embryonic development, what is the outcome for that baby? That's data that needs time to gestate," says Yalda Afshar, a high-risk obstetrician at Ronald Reagan University of California, Los Angeles, Medical Center. —*M.W.*

Published by AAAS

COVID-19

Fast, cheap tests could enable safer reopening

Models show test accuracy matters less than speed and frequency for curbing outbreaks

By **Robert F. Service**

Even as the United States ramped up coronavirus testing from about 100,000 per week in mid-March to more than 5 million per week in late July, the country fell further behind in stemming the spread of the virus. Now, diagnostics experts, public health officials, and epidemiologists are calling for a radical shift in testing strategy: away from diagnosing people who have symptoms or were exposed and toward screening whole populations using faster, cheaper, sometimes less accurate tests. By making it possible to identify and isolate infected individuals more quickly, proponents say, the shift would slow the virus' spread, key to safely reopening schools, factories, and offices.

"America faces an impending disaster," says Rajiv Shah, president of the Rockefeller Foundation. Testing, he says, needs to focus on "massively increasing availability of fast, inexpensive screening tests to identify asymptomatic Americans who carry the virus. Today, we are conducting too few of these types of tests."

Rebecca Smith, an epidemiologist at the University of Illinois, Urbana-Champaign (UIUC), agrees. To stop outbreaks from overwhelming communities, she says, "we need fast, frequent testing," which could mean faster versions of existing RNA tests or new kinds of tests aimed at detecting viral proteins. But researchers say the federal government will need to provide major financial backing for the push.

Today, COVID-19 testing relies primarily on the polymerase chain reaction (PCR), a technique to amplify the virus' genetic material, making it easy to detect. If administered properly, such tests are highly accurate, spotting positive cases nearly 100% of the time. That accuracy is vital for decisions about treating individual patients. But PCR tests cost about $100 each, require specialized machinery and reagents, and typically take at least 1 to 2 days to return results.

The recent increase in coronavirus cases across the United States has added to the delay, pushing wait times to 2 weeks in some places. While they wait, people who are infected but don't yet know it may continue to interact with others and spread the virus.

And if their infective period ends before they get their results, isolating them won't help. "It's like calling the fire department after your house burns to the ground," says A. David Paltiel, an operations research expert at the Yale School of Public Health. "You can't play catch up with this virus."

A 24 July preprint on medRxiv underscored the downsides of slow tests. Shixiong Hu, a researcher with the Hunan Provincial Center for Disease Control and Prevention, and his colleagues followed 1178 people who tested positive for SARS-CoV-2 from January to April and tested their 15,648 contacts, defined as people who had been within 1 meter of a positive person between 2 days before and 14 days after the person's symptoms began. Based on which contacts were infected and when, the researchers estimated that people were most likely to spread the virus 1.8 days before the onset of symptoms. The finding suggests testing people only when they show symptoms and giving them test results days to weeks later does little to slow viral spread, says Daniel Larremore, an applied mathematician at the University of Colorado, Boulder.

Larremore and his colleagues have modeled the benefits of more frequent tests, including ones that are less accurate than today's. Fast tests repeated every 3 days, with isolation of people who test positive, prevent 88% of viral transmission compared with no tests; a more sensitive test used every 2 weeks is less than half as effective at cutting transmission, they report in a 27 June preprint on medRxiv.

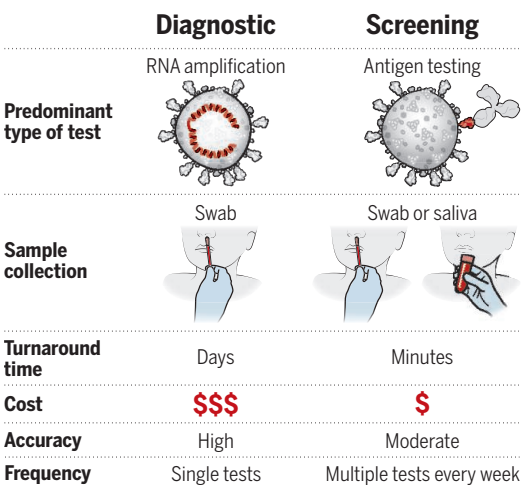
Paltiel and his colleagues reached much the same conclusion when they modeled a variety of testing regimes aimed at safely reopening a 5000-student university. In a 31 July paper in *JAMA Network Open*, they found that, with 10 students infected at the start of the semester, a test that identified only 70% of positive cases, given to every student every 2 days, could limit the number of infections to 28 by the end of the semester. Screening every 7 days allowed greater viral spread, with the model predicting 108 infections. "A higher frequency of testing makes up for poor sensitivity," Paltiel says.

Smith says these and related studies have prompted UIUC to set up tests for all 60,000 students and faculty multiple times per week when the students return to campus this fall. The approach relies on an experimental fast PCR setup described in an 18 June preprint that bypasses some of the usual slow procedures for isolating viral RNA and tests saliva rather than nasal swabs, says Martin Burke, a UIUC chemist who was one of the test's developers. Smith says her team predicts that if the university tests everyone every 3 to 4 days, on average, it will detect positive cases half a day before those people reach peak infectivity.

Antigen tests, which immobilize antibodies on a test strip, promise an even greater speedup. Those antibodies detect viral proteins in saliva or a nasal swab. Such tests cost as little as $1 to $2 each, give a yes/no readout within minutes, much like a pregnancy test, and are already used to detect influenza, HIV, and other viruses. Two companies—Quidel Corporation and Becton, Dickinson and Company (BD)—have received emergency use authorization from the U.S. Food and Drug Administration to sell antigen tests for SARS-CoV-2. Other companies have similar tests in the works.

Speed counts

Standard COVID-19 tests sacrifice speed and low cost for accurate diagnosis. Faster, cheaper screening tests could catch and isolate infected people more quickly.



GRAPHIC: N. DESAI/*SCIENCE*

Published by AAAS

Because antigen tests don't amplify viral material but simply detect what is present in the sample, they are less accurate than PCR. Some antigen tests correctly detect only one-half to three-quarters of infections. But they could still be a valuable health tool if performed often enough; few infected people would be missed in multiple rounds of tests. And people who receive a positive antigen test could be isolated and retested with a PCR test to confirm the result.

Among the hurdles facing widespread, repeat screening is the scarcity of such tests. Quidel and BD together manufacture about 3 million antigen tests per week. But a national screening strategy would likely require 25 million fast tests or more, says Jonathan Quick, who heads pandemic response for the Rockefeller Foundation. On 16 July, the foundation released a national COVID-19 testing plan calling on the federal government to spend $75 billion on providing 30 million screening and diagnostic tests per week.

Quick says companies are reluctant to ramp up production dramatically if they are unsure of the market for the products. One solution, he adds, could be a promise by the federal government to buy tens of millions of tests, much as it has done with vaccine doses. In one such effort, the governors of six U.S. states announced this week they are banding together to ask Quidel and BD for a total of 3 million tests.

Or the Trump administration could take over test production using the Defense Production Act, which allows the federal government to direct private companies to meet national defense needs. "I don't think it's either/or," Quick says. "It's and/both. We don't have time to wait."

Help could also come from a National Institutes of Health test development program, which last week announced nearly $250 million in awards to seven companies for scaling up production of novel rapid SARS-CoV-2 tests, with a goal of reaching some 42 million tests per week by the end of this year.

Even with federal help, broad screening programs are likely to be costly. Paltiel's study estimated that testing 5000 students every 3 days for an abbreviated 80-day semester would cost about $1.5 million, which may be beyond the reach of many universities, let alone high schools and small businesses.

But if organizations won't or can't make the investment, Paltiel asserts, "they have to ask themselves if they have any business reopening." Quick adds: "Investing will be far less costly for the nation than another economic shutdown, which will happen if we don't contain the outbreaks." ■



PHOTO: ISTOCK.COM/MOYO STUDIO

With working parents and children stuck at home, interruptions are the new normal.

COVID-19

Pandemic hits scientist parents hard

New data quantify lost work hours and productivity

By **Katie Langin**

When COVID-19 hit the United Kingdom, Michele Veldsman—a postdoc at the University of Oxford—took her 2-year-old daughter out of day care. She and her husband split child care responsibilities so they could each work half days. However, by the time the cognitive neuroscientist responded to urgent emails, she had little time left to dive into the data analyses and writing she'd hoped to make progress on. Nor did she have time for things such as virtual conferences, journal clubs, or collaborations. "I really need to be going to the stage of independence," says Veldsman, who hopes to land a faculty position. "Collaborations … show that independence, which I don't have time to do now."

For months, stories such as Veldsman's have flooded social media. "All it takes is 5 minutes on Twitter to see how much people are struggling right now," says Michelle Cardel, an assistant professor at the University of Florida College of Medicine. Parents in all professions are under strain as the pandemic keeps children home from day care or school. But scientists who have young children often face maximum professional pressure at the same time, as they apply for jobs and bid for tenure. And data quantifying the scale of their struggles are starting to emerge.

In the early weeks of the pandemic, scientists who had children 5 years of age or younger reported working 38% fewer research hours than normal, and those with children between ages 6 and 11 worked 32% fewer hours. That's compared with a 16% drop for all other scientists, according to a survey of about 4500 U.S. and European principal investigators published last month in *Nature Human Behaviour*. A survey of about 3300 Brazilian academics, posted as a preprint last month on bioRxiv, found that parents—especially mothers of young children—struggled to submit manuscripts as planned. A study that Cardel co-authored on U.S. faculty members, now in review, found similar results, she says.

"It's just been a constant juggling act," says Larry Snyder, a professor of industrial and systems engineering at Lehigh University and the father of 8- and 12-year-old girls. In May, he and his wife—an English professor at Lehigh—found that their children needed assistance 15 times per hour. Interruptions take "your attention away, and it takes a while to get your attention back," Snyder says. (While speaking with *Science*, one of his daughters interrupted to ask to use his iPad for her math exercises. "I didn't stage that," he joked.)

Published by AAAS

Many academics are pushing for policies that will ease the burden. At Stanford University, postdocs and faculty members sent letters to administrators in June asking that campus day care centers be reopened as soon as possible. In July, the group 500 Women Scientists released a policy statement for supervisors and administrators, recommending flexible deadlines, contract extensions, and other workplace adjustments.

Some institutions have given all junior faculty tenure clock extensions. But it's not clear whether such policies will ultimately benefit parents, says Dashun Wang, director of the Center for Science of Science and Innovation at Northwestern University and a co-author of the *Nature Human Behaviour* study. Gender neutral policies that extend tenure clocks after the birth of a child are a cautionary tale, he says. Research indicates that such policies "actually ended up exacerbating [gender] differences" in tenure rates because men took advantage of the extra time to publish more.

Scientists at different career stages and in different disciplines may require different forms of support, notes Mary Sue Coleman, president of the Association of American Universities. "What I would hope is that universities would really sit down and have serious discussions with those who are affected and try to jointly come up with some solutions."

She adds that university administrators are in a difficult position. "The financial consequences [of COVID-19] are devastating," says Coleman, who is a former university president. "A lot of the issues that people are talking about are ones that require money to make happen, and that's going to be in short supply—so it's going to be very tough."

Universities may want to consider redistributing teaching loads away from professors who have small children, says Fernanda Staniscuaski, an associate professor of molecular biology at the Federal University of Rio Grande do Sul and lead author of the study on Brazilian academics. "It doesn't sound fair … because it's my choice to have children," she told *Science* while breastfeeding her third child. "But maybe [it can] be voluntary."

Rebecca Calisi Rodríguez—an associate professor of neurobiology at the University of California, Davis—says that's precisely what's been happening at her university. She isn't able to help junior colleagues because she's barely surviving herself with 4- and 8-year-old children at home. "I feel exhausted," she says. "By the end of the day I feel more behind in my work than when I started." But some senior faculty members have volunteered to take on extra classes. "I hope I see more of [that] across the country and the globe." ■

SCIENCE AND POLITICS

Abortion opponents dominate Trump's fetal tissue review board

Ethics advisory board will rule on federal funding for research that uses fetal organs and cells

By **Meredith Wadman** *and* **Jocelyn Kaiser**

Fourteen months ago, the Trump administration clamped down on federally funded fetal tissue research by requiring that such projects go through an ethics review by a new advisory board. Research advocates were eager to learn whom Health and Human Services (HHS) Secretary Alex Azar would appoint to the board and to see its ideological makeup. Last week, they got their first look as it gathered online for a one-time meeting run by the National Institutes of Health (NIH).

Although the 1-hour public portion of the meeting was perfunctory—limited to introductions and public comments—it offered a glimpse of the opposition that may greet researchers who have asked NIH to fund work with fetal tissue donated after elective abortions. According to an analysis by *Science*, at least 10 of the 15 members of the NIH Human Fetal Tissue Research Ethics Advisory Board oppose abortion, and several have publicly stated positions against the funding of fetal tissue research.

> **"The board is stacked with people who are known to oppose use of tissue from induced abortions."**
>
> **R. Alta Charo**, University of Wisconsin, Madison

"The board is stacked with people who are known to oppose use of tissue from induced abortions, regardless of the scientific necessity and regardless of the fact that using such tissue does not in any way affect whether an abortion will take place," says R. Alta Charo, a lawyer and bioethicist at the University of Wisconsin, Madison. The board includes "real scientists who understand the research importance of this tissue," Charo says. But because the panel does not need to reach unanimity in order to reject a proposal, their presence "will not stand in the way of a majority dismissing it out of hand."

But Mallory Quigley, vice president of communications for the Susan B. Anthony List, which opposes abortion, says previous expert panels examining similar topics have leaned heavily toward people in favor of the research. "We are pleased and encouraged to see this board is more properly balanced."

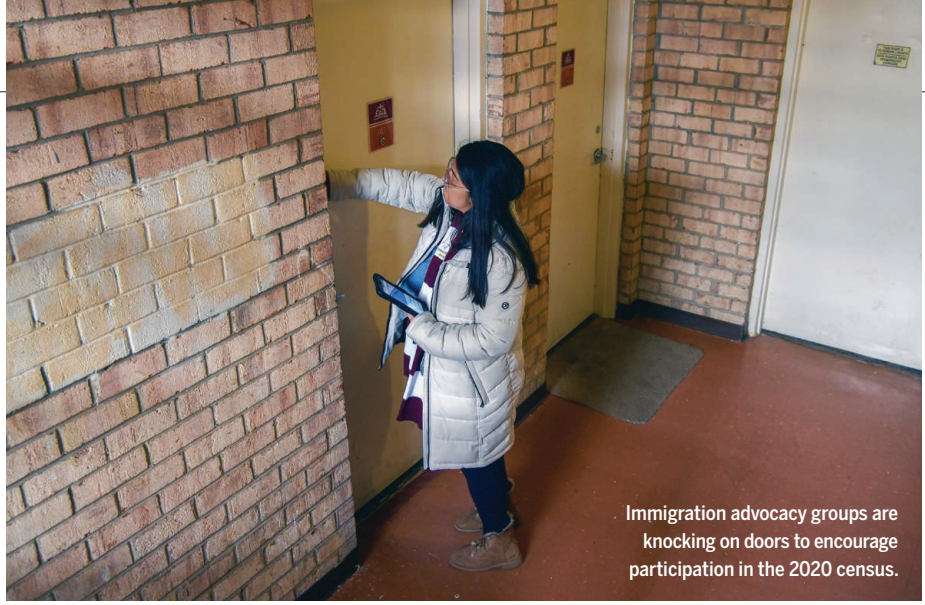
Scientists use human fetal tissue for research on conditions from HIV to Alzheimer's disease. More recently, at least one scientist has been prevented from studying the new coronavirus by his lack of access to the tissue, his colleagues told *The Washington Post*. A 2018 NIH workshop attended by HHS leaders concluded that human fetal tissue remains the "gold standard" for certain studies.

The majority of the new board's members do not agree. For example, the board's chair, Paige Comstock Cunningham, an attorney, ethicist, and interim president of Taylor University, a Christian university in Upland, Indiana, has testified before Congress in opposition to federally funded fetal tissue studies. Cunningham noted her "appreciation to Secretary Azar and the leadership" for "what I believe to be the first time there has been this kind of independent ethics advisory board reviewing these proposals." (Further details of the board's makeup are available at scim.ag/FetalTissueBoard.)

NIH officials and board members did not reveal how many proposals the board reviewed in the closed session of last week's meeting. But NIH Principal Deputy Director Lawrence Tabak told panelists that some are responses to a $20 million NIH program funding research on alternatives to fetal tissue. NIH Director Francis Collins has said that proposals under the program cannot be carried out without using fetal tissue as a comparator.

Tabak noted that the proposals being reviewed had already been recommended for funding after two stages of scientific review. The board's task, he said, was to "address whether the [HHS] secretary should or should not withhold funds for a proposed project because of ethical considerations." The board will disclose its decisions in a report to Azar and to two congressional committees by 18 August. Azar will have the final word on each project. ■

Published by AAAS



Immigration advocacy groups are knocking on doors to encourage participation in the 2020 census.

PHOTO: MARVIN JOSEPH/*THE WASHINGTON POST* VIA GETTY IMAGES

STATISTICAL SCIENCE

Trump directive on state counts said to threaten rigor of census

Experts decry order to exclude undocumented residents

By **Jeffrey Mervis**

President Donald Trump wants the U.S. Census Bureau to help him wage war against what he calls "illegal" immigration. But census advocates and demography experts are worried that the nation's largest statistical agency would have to compromise its high standards if it is compelled to join the fight.

On 21 July, Trump told the Census Bureau to exclude undocumented residents from its tally of each state's population. Those numbers, which are gleaned from the overall 2020 census now underway, are used to decide how many seats each state gets in the 435-member U.S. House of Representatives.

Democrats in Congress and civil rights groups have decried Trump's directive, saying it violates the U.S. Constitution's requirement to count every resident, and several groups have sued to block it. But Republicans generally back the president's argument that only citizens should count in apportionment. In the meantime, the statistics community is warning it may be technically impossible for the agency to satisfy Trump's request, which would require using information already in government files to try to identify undocumented residents.

In June 2019, the U.S. Supreme Court rejected the administration's controversial attempt to add a citizenship question to the 2020 census, which began on 1 April. Two weeks later, Trump sought an end run by ordering the bureau to use Social Security records, immigration documents, driver's license data, and other information already on file to calculate how many residents are U.S. citizens. His new memo goes further, telling census officials to divide the population into three groups: citizens, documented immigrants, and undocumented residents.

"I don't know what set of data sources the bureau could identify for that purpose," says economist Amy O'Hara of Georgetown University, who until 2017 oversaw Census Bureau efforts to use such "administrative records" to improve the quality of its many surveys. "And for the ones they have, it's not clear how they would operationalize them."

Census officials have tried to remain upbeat. The Census Bureau's chief scientist, John Abowd, "has said he can count the number of citizens," notes Rob Santos, incoming president of the American Statistical Association and chief methodologist at the Urban Institute. "But he's never said that he can count the number of undocumented residents. And he'd be crazy to promise that."

Among the problems, experts say, is that available information on a person's citizenship status is often not up to date, or is not linked to a specific address, a key census data point. Obeying the president's memo could put the agency's core principles to the test, says former Census Bureau Director Kenneth Prewitt. "The bureau will struggle with the enormous burden of whether to release substandard results [from the census]," he testified last week before a congressional panel reviewing Trump's memo. "The bureau will not want to inflict that damage. It is too honorable, too scientific, too proud of its professional standards, too faithful to its constitutional duties."

In every census, the agency conducts a massive follow-up effort to reach those who don't reply to multiple requests to fill out the survey. That door-knocking campaign costs billions of dollars and requires an army of enumerators. But Prewitt and other former directors believe the new directive boosts the chances of an unprecedentedly large undercount in the 2020 census.

"I am very concerned that [Trump's directive] will increase the fear of many in the hard-to-count community that their data … will be given over to immigration enforcement," John Thompson, who stepped down as census director shortly after Trump took office, told the congressional panel. "The end result will most likely be increased undercounts of these populations."

The pandemic, meanwhile, forced the agency to suspend most door-to-door visits in mid-March. In a coronavirus relief bill that the Democrat-led House approved in May, it gave the census an additional 4 months to prepare the state population totals, which are due 31 December. In keeping with that revised schedule, census officials last month said they would resume full field operations by 11 August and finish by the end of October. But the extension was absent from the Republican-led Senate's version of the bill released last week. Media have reported that the White House now wants the state tallies by the original deadline. To meet that goal, the Census Bureau now plans to conclude field operations by the end of September. But that compressed schedule leaves census officials with little time to figure out how to generate the numbers that Trump wants.

At the hearing, the current census director, Steven Dillingham, declined to wade into the partisan debate over Trump's directive. "I am not in a position in which I can express my opinions with regard to the policy, the history, and certainly not the legal analysis [behind the directive]," he told Representative Carolyn Maloney (D–NY), who chairs the House oversight panel that held the hearing. "My job is to execute the 2020 census, and our goal is a complete and accurate count."

But when Representative James Comer (R–KY) asked whether Dillingham was "confident we can get an accurate count of legal citizens, for purposes of apportionment," Dillingham dodged the question. "I am confident that we will analyze the data we have," Dillingham replied, "and look at methodologies that might be employed for that purpose." ■

Published by AAAS



Global warming has widened the Batagay megaslump from a gully to a pit more than 900 meters across.

CLIMATE CHANGE

Siberia's 'gateway to the underworld' hit by heat wave

Thawing Batagay permafrost holds deep climate history

By **Richard Stone**

On a spring day in 2019, Alexander Kizyakov rappelled down the 60-meter headwall of the Batagay megaslump in eastern Siberia, pausing to chisel out chunks of ice-rich soil that had been frozen for eons. "One of my hobbies is rock climbing," says Kizyakov, a permafrost scientist at Lomonosov Moscow State University. Colleagues below sampled the most ancient soil along the base of the cliff. Such work is too dangerous in summertime, when the constant crackling of melting ice is punctuated by groans as slabs of permafrost, some as big as cars, shear off the headwall.

Known to locals as the "gateway to the underworld," Batagay is the largest thaw slump on the planet. Once just a gully on a slope logged in the 1960s, the scar has expanded year by year, as the permafrost thaws and meltwater carries off the sediment. Now more than 900 meters wide, it epitomizes the vulnerability of permafrost in the Arctic, where temperatures have shot up twice as fast as the global average over the past 30 years.

But it is also a time capsule that is seducing scientists with its snapshots of ancient climates and ecosystems. "It's a mind-blowing place," says Thomas Opel, a paleoclimatologist at the Alfred Wegener Institute. Dates from ice and soil gathered at Batagay show it holds the oldest exposed permafrost in Eurasia, spanning the past 650,000 years, Opel and colleagues reported in May at the online general assembly of the European Geosciences Union. That record could reveal how permafrost and surface vegetation responded to past warm climates. "It gives us a window into times when permafrost was stable, and times when it was eroding," Opel says.



Researchers rappel down a frozen, 60-meter-tall headwall to gather ever more ancient soil.

Global warming is inflicting wounds across Siberia. Outbursts of pent-up methane gas in thawing permafrost have pocked Russia's desolate Yamal and Gydan peninsulas with holes tens of meters across. Apartment buildings are listing and collapsing on the unsteady ground, causing about $2 billion of damage per year to the Russian economy. Forest fires during the past three summers have torched millions of hectares across Siberia, blanketing the land with dark soot and charcoal that absorb heat and accelerate melting.

Intensifying this year's fires was a heat wave that baked Siberia for the first half of 2020. On 20 June, the town of Verkhoyansk, just 75 kilometers from Batagay and one of the coldest inhabited places on Earth, reached 38°C, the hottest temperature ever recorded in the Arctic. The record heat "would have been effectively impossible without human-induced climate change," said the authors of a 15 July study by World Weather Attribution, a collaboration of meteorologists who analyze the influence of climate change on extreme weather events.

A pressing question is how much carbon the thawing soil will release to the atmosphere, and whether the lusher growth of Arctic plants in the warming climate will absorb enough carbon to offset the release. The Arctic may already have reached a tipping point: Based on observations at 100 field sites, northern permafrost released on average about 600 million tons more carbon than vegetation absorbed each year from 2003 to 2017, scientists estimated in October 2019.

Scientists are venturing to Batagay in annual campaigns to learn what it can say on the matter. Visits, organized by the Institute of Applied Ecology of the North in Yakutsk, are not for the faint of heart. In 2014, Kseniia Ashastina slogged through 3 kilometers of mosquito-infested forest to reach the headwall's edge. "You hear a lot of cracking noises as you get closer, and all of a sudden there are no trees and you're standing on an overhang," says Ashastina, a paleobotanist at the Max Planck Institute for the Science of Human History. She and colleagues from the Senckenberg Research Institute and Natural History Museum lodged with Indigenous Siberians—Evens and Sakha—some of whom fear the megaslump. "They say it's eating their land, swallowing up the trees and their sacred places," she says.

PHOTOS: (TOP TO BOTTOM) KATIE ORLINSKY/NAT GEO IMAGE COLLECTION; THOMAS OPEL

Published by AAAS

To learn the age of the permafrost, Opel's team relies on luminescence dating, which reveals the last time minerals in the soil saw daylight, and a new Russian technique for dating chlorine in the ice. The dates allow them to match soil layers to the known climate record, while abundances of two isotopes trapped in ice wedges, oxygen-18 and deuterium, are proxies for local temperatures. Assaying the soil composition should yield insights into how much carbon the permafrost sequestered over the millennia, as the climate warmed and cooled.

The permafrost also holds glimpses of ancient Arctic ecosystems. Sampling trapped plant remains, the team learned that during the last ice age, when winter temperatures plunged even lower than in modern times, the vegetation was surprisingly lush, supporting woolly mammoths, woolly rhinos, and other now-vanished herbivores in a meadow steppe ecosystem. "It was a paradise for the foraging animals," Ashastina says.

Sometimes, the remains of these lost creatures tumble out of the headwall in exquisite condition. In 2018, scientists recovered a young ginger-colored Lena horse (*Equus lenensis*), an extinct relative of the Yakutian horse, with intact soft tissue. The superb preservation of the 42,000-year-old foal has inspired an attempt to clone it. Some of its muscle cells are particularly promising, says P. Olof Olsson, a molecular biologist with the Abu Dhabi Biotech Research Foundation, which is teaming up on the effort with North-Eastern Federal University in Yakutsk. "I'm skeptically optimistic," Olsson says. "At least, it's not impossible."

As the elements carve up more of the Batagay megaslump, it could transport scientists deeper into time. Glaciers scour away soil as they advance, but they largely bypassed Siberia during recent ice ages, leaving the permafrost hundreds of meters thick in some areas. For decades, as hot summers liquefied its ice-rich soil, Batagay's headwall advanced about 10 meters per year, says Frank Guenther, a permafrost researcher at the University of Potsdam. Since 2016, he says, that rate has surged to 12 to 14 meters per year. It's harder to peg how fast the slump is deepening, and thus how much farther back in time the thaw is penetrating.

The oldest permafrost ever dated, from Canada's Yukon territory, is 740,000 years old. Climate watchers may cringe at the thought, but several more roasting Siberian summers could push the Batagay megaslump to claim another record. ■

Richard Stone is senior science editor at the Howard Hughes Medical Institute's Tangled Bank Studios.

ENVIRONMENT

Deforestation in the Brazilian Amazon is still rising sharply

Satellite images suggest clearings are up by at least 28%

By **Herton Escobar**

Deforestation in the Brazilian Amazon has risen sharply in the past year—again. Estimates set to be released this week by Brazil's National Institute for Space Research (INPE) will show clearings have increased by at least 28% during the current monitoring year, which runs from August through July, compared with the previous year. It is the second steep hike under Brazilian President Jair Bolsonaro, who has made good on his campaign promise to loosen environmental law enforcement and step up development in the Amazon.

The numbers come from Brazil's Real-time Deforestation Detection System (DETER), which uses low-resolution satellite images to quickly identify new forest clearings and alert authorities to possible illegal deforestation. More than 8700 square kilometers (km^2) of primary forest cover has already disappeared from the images since August 2019, according to data updated through 23 July, compared with 6800 km^2 in the previous 12 months. (Data for the final week will be released on 7 August.) Although the system doesn't identify the causes of deforestation, other studies show the vast majority is illegal, carried out by ranchers, loggers, miners, and land grabbers who seek to profit from public forest lands.

> **"We need clear messages and decisive actions against these illegal activities."**
> **Luiz Aragão**, National Institute for Space Research

Deforestation has been slowly rising in Brazil since 2013, but Bolsonaro's actions and words have given it a big boost. "Deforestation is a high-risk enterprise, profoundly connected to political decisions and rhetoric that influence the perception of that risk," says Raoni Rajão, an environmental policy researcher at the Federal University of Minas Gerais, Belo Horizonte. Developers now feel a sense of impunity, Rajão says. Clearings are even on the rise within legally protected areas and Indigenous lands, where criminals rarely ventured in the past. Meanwhile, law enforcement operations are down, and field agents who combat illegal miners have been publicly reprimanded and subjected to internal investigations by their own agencies.

Last year, Bolsonaro called similarly worrisome estimates from DETER "a lie" and fired INPE's director, Ricardo Galvão. But numbers released later by the Amazon Deforestation Satellite Monitoring Project, a higher resolution system also operated by INPE that produces Brazil's official deforestation data, were even worse. They showed that 10,100 km^2 of forest were cleared between August 2018 and July 2019—a 34% increase from the previous year.

Pressured by public opinion and investors concerned about sustainability, Bolsonaro has taken some steps to protect the forest. Earlier this year he re-created the Amazon Council—composed largely of military officers—to oversee sustainable development of the region, and in May he authorized the deployment of the armed forces to combat environmental crimes there. Another decree on 15 July made the use of fire in the Amazon illegal for the next 4 months.

The latter measure may indeed help reduce deforestation, if properly enforced. After trees are felled, developers must burn the downed vegetation to clear the land for pastures or cropland, Rajão says. He also sees hope in the fact that the amount of forest felled in the first 3 weeks of July was considerably lower than in July 2019, although still much higher than in the same month of previous years. "That may be a positive sign," he says. "But we have to wait and see."

The resurgence of deforestation—Brazil's largest source of greenhouse gas emissions—is "a disaster for Brazil's international reputation," says Luiz Aragão, head of INPE's Remote Sensing Division. "We need clear messages and decisive actions against these illegal activities," Aragão says (see Letters, pp. 634, 635). "Brazil needs to re-establish its environmental order if we have ambitions to grow economically and participate as a leader in the discussion of global issues." ■

Herton Escobar is a science and environment journalist in São Paulo.

Published by AAAS



THE LONG HAUL

Some COVID-19 survivors are still sick months later. Doctors want to learn why and what they can do

By **Jennifer Couzin-Frankel**

Athena Akrami's neuroscience lab reopened in June without her. Life for the 38-year-old is a pale shadow of what it was before 17 March, the day she first experienced symptoms of the novel coronavirus. At University College London (UCL), Akrami's students probe how the brain organizes memories to support learning, but at home, she struggles to think clearly and battles joint and muscle pain. "I used to go to the gym three times a week," Akrami says. Now, "My physical activity is bed to couch, maybe couch to kitchen."

Science's COVID-19 reporting is supported by the Pulitzer Center and the Heising-Simons Foundation.

Her early symptoms were textbook for COVID-19: a fever and cough, followed by shortness of breath, chest pain, and extreme fatigue. For weeks, she struggled to heal at home. But rather than ebb with time, Akrami's symptoms waxed and waned without ever going away. She's had just 3 weeks since March when her body temperature was normal.

PHOTO: RYAN LOW

Published by AAAS

Neuroscientist Athena Akrami has had debilitating symptoms since her coronavirus infection more than 4 months ago.

"Everybody talks about a binary situation, you either get it mild and recover quickly, or you get really sick and wind up in the ICU," says Akrami, who falls into neither category. Thousands echo her story in online COVID-19 support groups. Outpatient clinics for survivors are springing up, and some are already overburdened. Akrami has been waiting more than 4 weeks to be seen at one of them, despite a referral from her general practitioner.

The list of lingering maladies from COVID-19 is longer and more varied than most doctors could have imagined. Ongoing problems include fatigue, a racing heartbeat, shortness of breath, achy joints, foggy thinking, a persistent loss of sense of smell, and damage to the heart, lungs, kidneys, and brain.

The likelihood of a patient developing persistent symptoms is hard to pin down because different studies track different outcomes and follow survivors for different lengths of time. One group in Italy found that 87% of a patient cohort hospitalized for acute COVID-19 was still struggling 2 months later. Data from the COVID Symptom Study, which uses an app into which millions of people in the United States, United Kingdom, and Sweden have tapped their symptoms, suggest 10% to 15% of people—including some "mild" cases—don't quickly recover. But with the crisis just months old, no one knows how far into the future symptoms will endure, and whether COVID-19 will prompt the onset of chronic diseases.

Researchers are now facing a familiar COVID-19 narrative: trying to make sense of a mystifying illness. Distinct features of the virus, including its propensity to cause widespread inflammation and blood clotting, could play a role in the assortment of concerns now surfacing. "We're seeing a really complex group of ongoing symptoms," says Rachael Evans, a pulmonologist at the University of Leicester.

Survivor studies are starting to probe them. Last month, researchers across the United Kingdom including Evans launched a study that will follow 10,000 survivors for 1 year to start, and up to 25 years. Ultimately, researchers hope not just to understand the disease's long shadow, but also to predict who's at highest risk of lingering symptoms and learn whether treatments in the acute phase of illness can head them off.

For Götz Martin Richter, a radiologist at the Klinikum Stuttgart in Germany, what's especially striking is that just as the illness' acute symptoms vary unpredictably, so, too, do those that linger. Richter thinks of two patients he has treated: a middle-aged man who experienced mild pneumonia from COVID-19, and an elderly woman already suffering from chronic leukemia and arterial disease, who almost died from the virus and had to be resuscitated. Three months later, the man with the mild case "falls asleep all day long and cannot work," Richter says. The woman has minimal lung damage and feels fine.

EARLY IN THE PANDEMIC, doctors learned that SARS-CoV-2, the virus that causes COVID-19, can disrupt a breathtaking array of tissues in the body (*Science*, 24 April, p. 356). Like a key fitting neatly into a lock, SARS-CoV-2 uses a spike protein on its surface to latch onto cells' ACE2 receptors. The lungs, heart, gut, kidneys, blood vessels, and nervous system, among other tissues, carry ACE2 on their cells' surfaces—and thus are vulnerable to COVID-19. The virus can also induce a dramatic inflammatory reaction, including in the brain. Often, "The danger comes when the body responds out of proportion to the infection," says Adrija Hajra, a physician at Albert Einstein College of Medicine in New York City. She continues to care for those who were infected in the spring and are still recovering.

> **"I used to go to the gym three times a week. [Now,] my physical activity is bed to couch, maybe couch to kitchen."**
>
> **Athena Akrami**, University College London

Despite the novelty of SARS-CoV-2, its long-term effects have precedents: Infections with other pathogens are associated with lasting impacts ranging from heart problems to chronic fatigue. "Medicine has been used to dealing with this problem" of acute viral illness followed by ongoing symptoms, says Michael Zandi, a neurologist at UCL. Even common illnesses such as pneumonia can mean a monthslong recovery. "I see a lot of people who had [the brain inflammation] encephalitis 3, 4 years ago, and still can't think, or are tired," Zandi says. Infections with certain bacteria and Zika virus, among others, are linked to Guillain-Barre syndrome, in which the immune system attacks nerve tissue, causing tingling, weakness, and paralysis. (Some cases of Guillain-Barre after COVID-19 have been reported, but "it's not definite [there's] a spike," says Rachel Brown, a UCL neurologist who works with Zandi.)

Based on experience with other viruses, doctors can "extrapolate and anticipate" potential long-term effects of COVID-19, says Jeffrey Goldberger, chief of cardiology at the University of Miami. Like SARS-CoV-2, some other viruses, such as Epstein-Barr, can damage heart tissue, for example. In those infections, the organ sometimes heals completely. Sometimes, scarring is mild. "Or," Goldberger says, "it could be severe and lead to heart failure."

Michael Marks, an infectious disease specialist at the London School of Hygiene & Tropical Medicine who's helping lead the U.K. survivor study, says he's not too surprised at emerging aftereffects. "What we're experiencing is an epidemic of severe illness," he says. "So therefore, there is an epidemic" of chronic illness that follows it.

But outcomes following SARS-CoV-2 also appear distinct in ways both hopeful and dispiriting. Early this year, many doctors feared the virus would induce extensive, permanent lung damage in many survivors because two other coronaviruses, the viruses that cause the first severe acute respiratory syndrome (SARS) and Middle East respiratory syndrome, can devastate the lungs. One study of health care workers with SARS in 2003 found that those with lung lesions 1 year after infection still had them after 15 years.

"We expected to see a lot of long-term damage from COVID-19: scarring, decreased lung function, decreased exercise capacity," says Ali Gholamrezanezhad, a radiologist at the Keck School of Medicine at the University of Southern California who in mid-January began to review lung scans from COVID-19 patients in Asia. Hundreds of scans later, he has concluded that COVID-19 ravages the lungs less consistently and aggressively than SARS did, when about 20% of patients sustained lasting lung damage. "COVID-19 is in general a milder disease," he says.

At the same time, the sheer breadth of complications linked to COVID-19 is mind-boggling. In late April, Akrami collaborated with Body Politic, a group of COVID-19 survivors, to survey more than 600 who still had symptoms after 2 weeks. She logged 62 different symptoms and is now readying the findings for publication and developing a second survey to capture longer term ailments. "Even though it's one virus, it can cause all different kinds of diseases in people," says Akiko Iwasaki, an immunologist at Yale University who is studying lingering effects on the immune system.

BY NOW IT'S CLEAR that many people with COVID-19 severe enough to put them in a hospital face a long recovery (*Science*, 24 April, p. 359). The virus ravages the

Published by AAAS

heart, for example, in multiple ways. Direct invasion of heart cells can damage or destroy them. Massive inflammation can affect cardiac function. The virus can blunt the function of ACE2 receptors, which normally help protect heart cells and degrade angiotensin II, a hormone that increases blood pressure. Stress on the body from fighting the virus can prompt release of adrenaline and epinephrine, which can also "have a deleterious effect on the heart," says Raul Mitrani, a cardiac electrophysiologist at the University of Miami who collaborates with Goldberger.

Mitrani and Goldberger, who co-authored a June paper in *Heart Rhythm* urging follow-up of patients who might have heart damage, worry in particular about the enzyme troponin, which is elevated in 20% to 30% of hospitalized COVID-19 patients and signifies cardiac damage. (Troponin is sky-high during a heart attack, for example.) How the heart heals following COVID-19 might determine whether an irregular heartbeat develops or persists, Goldberger believes. "We have one guy in the hospital right now who had COVID 2 months ago and had all sorts of arrhythmia problems" then, Goldberger says. "He's recovered from his COVID, but still has the arrhythmia." For some patients with coronavirus-induced heart problems, treatments as simple as cholesterol-lowering drugs, aspirin, or beta blockers could help, Goldberger says.

Many people the pair has seen with heart complications post–COVID-19 had preexisting conditions, most commonly diabetes and hypertension. COVID-19, Goldberger suspects, tips them into more hazardous terrain or accelerates the onset of heart problems that, absent the coronavirus, might have developed later.

But other patients are affected without apparent risk factors: A paper in July in *JAMA Cardiology* found that 78 of 100 people diagnosed with COVID-19 had cardiac abnormalities when their heart was imaged on average 10 weeks later, most often inflammation in heart muscle. Many of the participants in the study were previously healthy, and some even caught the virus while on ski trips, according to the authors.

Severe lung scarring appears less common than feared—Gholamrezanezhad knows of only one recovered patient who still needs oxygen at rest. Scarring seems most likely to accompany underlying lung disease, hypertension, obesity, and other conditions. Lung damage is also seen in people who spend weeks on a ventilator. Gholamrezanezhad suspects that, as with harm to the heart, previously healthy people are not exempt from the virus' long-term effects on the lungs, though their risk is likely lower.

Then there's the nervous system, a worrying target. Severe complications seem relatively rare but aren't limited to those whom the virus renders critically ill. Brown, Zandi, and colleagues described 43 people with neurologic complications last month in *Brain*; many had been hospitalized during their acute infection, but not always for long—and for some, neurologic problems were their most debilitating symptom and the reason for hospital admission. Several were struggling to recover from encephalitis. Others had inflammation in their brain's white matter, which helps transmit electrical signals.

Separately, doctors are starting to see a class of patients who, like Akrami, struggle to think clearly—another outcome physicians have come upon in the past. After some severe viral infections, there are "those people who still don't feel quite right afterward, but have normal brain scans," Brown says. Some neurologists and patients describe the phenomenon as "brain fog." It's largely a mystery, though one theory suggests it's similar to a "postviral fatigue related to inflammation in the body," Brown says.

Could that be happening here? "Who knows, really?" Brown says. "These patients need to be followed."

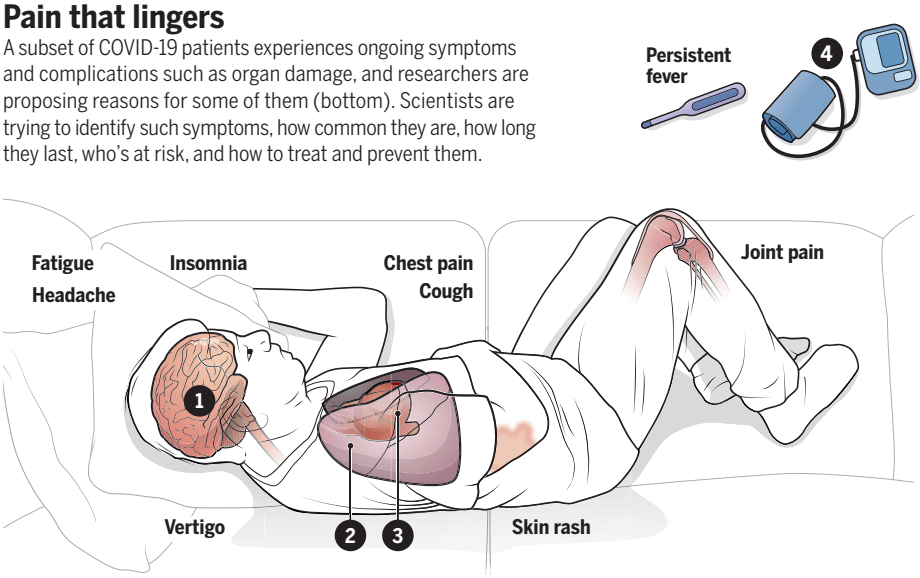
PEOPLE LIKE THESE pose a growing concern (though they are also often dismissed by physicians). Collectively, these "long-haulers" describe dozens of symptoms, including many that could have multiple causes, such as fatigue, joint pain, and fever. "It's time to give some voice to this huge population of patients," Akrami says.

The most bedeviling and common lingering symptom seems to be fatigue, but researchers caution against calling it chronic fatigue syndrome. That's "a specific diagnosis," Marks says. "You might have fibrosis in the lungs, and that will make you feel fatigued; you might have impaired heart function, and that will make you feel fatigued." Trying to trace symptoms to their source is critical to understanding and ultimately managing them, he says.

Iwasaki agrees. Doctors would treat symptoms differently depending on whether they result from a lingering infection or are rooted in autoimmune abnormalities. She has begun to recruit people who weren't hospitalized when they had COVID-19 and will sift through her volunteers' immune cells, examining whether they're primed to attack, and measuring whether the balance among different cell types is as it should be. She'll also hunt for virus in saliva. "We're pretty

Pain that lingers

A subset of COVID-19 patients experiences ongoing symptoms and complications such as organ damage, and researchers are proposing reasons for some of them (bottom). Scientists are trying to identify such symptoms, how common they are, how long they last, who's at risk, and how to treat and prevent them.



1 Brain fog
Difficulty thinking can occur after acute COVID-19 infection. The virus may damage brain cells, and inflammation in the brain or body may also cause neurologic complications. Other viral infections can also lead to brain fog.

2 Shortness of breath
Doctors are eyeing lung and heart complications including scarring. Patients who become critically ill with COVID-19 seem more likely to have lingering shortness of breath, but those with mild cases are also at risk.

3 Heart arrhythmia
The virus can harm the heart, and doctors are concerned about long-term damage. How the heart heals after COVID-19 could help determine whether a patient develops an irregular heartbeat.

4 Hypertension
Some patients have high blood pressure after an acute infection, even when cases were relatively mild and people were previously healthy, possibly because the virus targets blood vessels and heart cells.

GRAPHIC: V. ALTOUNIAN/*SCIENCE*

Published by AAAS



Doctors and nurses inspect a patient's scans in Istanbul. Concern is growing that the lungs and other organs can struggle to heal after a COVID-19 infection.

PHOTO: CHRIS MCGRATH/GETTY IMAGES

much searching for anything," she says.

Iwasaki is especially struck by the number of young, healthy, active people—people like Akrami—who fall into the long-hauler category. As she and others struggle to find ways to help them, she wonders what might head off their symptoms. One possibility, she says, is monoclonal antibodies, which are now being tested as a treatment for acute infection and might also forestall lasting immune problems.

Hers is one of several survivor studies now underway. While Goldberger's hometown of Miami faces a surge of acutely ill patients, he is looking ahead, applying for funding to image the heart and map its electrical activity in COVID-19 patients after they leave the hospital. Gholamrezanezhad is recruiting 100 patients after hospital discharge to follow for up to 2 years for lung assessments. Like many physicians, he fears the societal impact of even uncommon complications, including in the millions of people never hospitalized. "When you consider how many people are getting the disease, it's a big problem," he says.

Across the Atlantic Ocean, Richter has recruited 300 volunteers in Germany for long-term follow-up, including lung scans. In the United Kingdom, patients will soon be able to sign up for that country's survivor study, with many giving blood samples and being examined by specialists. The researchers will probe patients' DNA and examine other characteristics such as age and health history to learn what might protect them from, or make them susceptible to, a range of COVID-19 induced health problems. Knowing who's at risk of, say, kidney failure or cardiac arrhythmia could mean more targeted follow-up. The U.K. researchers are also keen to see whether patients who received certain treatments in the acute phase of illness, such as steroids or blood thinners, are less prone to later complications.

For her part, Akrami is one of 2 million people infected weeks or months ago participating in the COVID Symptom Study. The study welcomes anyone infected, and with 10% to 15% of people who use the app reporting ongoing symptoms, it has already yielded a welter of data, says Andrew Chan, an epidemiologist and physician at Harvard Medical School.

> **"Even though it's one virus, it can cause all different kinds of diseases in people."**
>
> **Akiko Iwasaki**, Yale University

As he and his colleagues parse the data, they are identifying distinct "types" of acute illness, based on clusters of symptoms. Chan wonders whether certain early symptoms correlate with specific ones that linger. He acknowledges the risk that the app's data could be skewed, because people who aren't feeling well may be more likely to participate than those who have smooth recoveries. "We're trying to develop data analysis tools" to account for that tilt, he says, "similar to methods used in polling. You have to weigh the biases."

One of the few systematic, long-term studies of COVID-19 patients with mild acute symptoms is underway in San Francisco, where researchers are recruiting 300 adults from local doctors and hospitals, for 2 years of follow-up. "We don't have a broad idea of what's happening" after the initial illness, says Steven Deeks, an HIV researcher at the University of California, San Francisco, who is leading the study, modeled on HIV cohorts he has followed for decades. What does "ongoing symptoms" even mean, Deeks asks. "Is that weeks, months? We don't know that it's years."

More than 100 people ranging in age from 18 to 80 have signed up so far. Cardiologists, neurologists, pulmonologists, and others are assessing the volunteers, and blood, saliva, and other biological specimens are being banked and analyzed.

Although scientists hope they'll learn how to avert chronic symptoms and help patients currently suffering, this latest chapter in the COVID-19 chronicle has been sobering. The message many researchers want to impart: Don't underestimate the force of this virus. "Even if the story comes out a little scary, we need a bit of that right now," Iwasaki says, because the world needs to know how high the stakes are. "Once the disease is established, it's really hard to go backward." ■

Published by AAAS



INSIGHTS

PERSPECTIVES

PLANT BIOLOGY

Chimeric plants—the best of both worlds

Overcoming graft incompatibility between species could protect future crop yields

By **Maureen C. McCann**

The cutting of the shoot of one plant (the scion) and joining, or grafting, to another (the rootstock) has been a practice of growers for millennia. The resulting chimeric organisms have enabled propagation of fruits and vegetables with desired characteristics, control of tree size to facilitate fruit harvests, and preservation of elite wine cultivar scions on rootstocks resistant to phylloxera, a destructive insect. Most plant species will graft to themselves, some to closely related species, but rarely will plants successfully graft to more distant relatives (*1*). On page 698 of this issue, Notaguchi *et al.* (*2*) identify a key enzymatic activity that promotes establishment of grafts between the tobacco plant *Nicotiana benthamiana* and a broad range of species. They demonstrate that two incompatible species can be grafted using tissue from *N. benthamiana* as an interscion. This could substantially expand the combinations of species with which it is possible to generate chimeras.

Compatibility between two species depends on establishment of a successful graft union at the cut boundaries and the extended survival of the composite, grafted plant. In contrast to other compatible-incompatible interactions, such as recognition of pollen as self or not-self by female floral organs, there is as yet no evidence for a specific recognition mechanism between graft components. It is critical, though, that the cells at the cut surfaces begin to adhere to each other, that cells at the boundary divide and grow, and that the vasculature, required for transport of water, nutrients, and long-distance signaling molecules from the roots to the aerial parts of the plant, is

Chimeric Egg & Chips (left photo) and TomTato (right photo) plants are grafts involving closely related species. Other chimeras may be possible if grafting can be applied more generally.

PHOTO: THOMPSON & MORGAN

Published by AAAS

reconnected (*1*). Notaguchi *et al.* implicate a specific cellulase in promoting cell-cell adhesion. How cellulase might facilitate this physiological process is a remaining question.

Cellulases act to digest cellulose, the main scaffolding component of plant cell walls (*3*), and this might enable remodeling and fusion of cellulose microfibrils between cell walls of the vasculature or other cell types between the scion and rootstock. Another possibility is that cellulose degradation triggers surveillance mechanisms for cell wall integrity, thereby promoting cell wall biosynthesis (*3*). Although cell walls of different plant species can have very different compositions (*3*), cellulose is always a component, which might account for why an enzyme activity targeting cellulose as its substrate appears to facilitate compatibility between taxonomically distant species.

The ability to make grafts between plants of the same species opened up the field of long-distance signaling in plant research, because mobile proteins, messenger RNAs (mRNAs), and small RNAs were identified as signaling molecules (*1*). Originating in rootstocks, the plant hormone florigen was identified as a factor that promotes flowering and strigolactone as a plant hormone that promotes branching. The mechanism by which RNA silencing spreads systemically was elucidated with grafts (*1*). Grafts also enable the study of lifelong interactions between genomes of different plant species, how the architecture of root systems can affect plant vigor and health, and the design of new crop species. Examples of commercial success from grafts include the TomTato, a plant producing both potatoes from the root and tomatoes above ground, and Egg & Chips, an eggplant scion on a potato rootstock (*4*) (see the photos). Tomatoes, eggplants, and potatoes, together with tobacco, belong to the same family, Solanaceae, and thus they are naturally amenable to grafting.

Notaguchi *et al.* demonstrate that *N. benthamiana* scions or rootstocks can graft to phylogenetically distant soybeans and chrysanthemums, as well as representatives from 38 flowering plant (angiosperm) families. By expanding the combinations of species that can be used as scions and rootstocks, grafting technology could produce chimeras between distant relatives that contribute to a more sustainable agricultural footprint and help to preserve biodiversity.

Multiple biotic and abiotic stressors are increasing with climate change, which exacerbates the yield gap, the difference between theoretical and actual yield, for many agronomic and vegetable crops. Drought- or pathogen-resistant or salt-tolerant rootstocks, either naturally so or genetically engineered, could expand the growing range of desired cultivars. The ability to graft across a broad range of eudicots (one of the two classes of flowering plants) provides a tool to compile tolerance traits across species: Such traits are multigenic and therefore not easily addressed by engineering one or a few transgenes. Genetic differences in the resilience of tree species to water or temperature stress will make some species particularly vulnerable on the anticipated time scale of climate change (*5*). Sturdy rootstocks could be used to preserve at-risk species within a shorter time frame than breeding programs could achieve.

Familiarity and ease, together with automation of the process for compatible species, has made grower acceptance of grafting technology an attractive strategy to increase yields and product quality, and to grow fruits and vegetables in new environments. Grafting is also an asexual, vegetative propagation technique that might circumvent current restrictions for genetically modified organisms (GMOs) (*6*). For example, grafting on genetically modified rootstocks to overcome soilborne disease susceptibility of a scion cultivar might overcome regulatory hurdles because the disease-resistant fruits have not themselves been genetically modified (*7*). The rootstock could be modified to produce small RNAs that spread systemically to silence gene expression in the scion, thereby indirectly modifying characteristics of the aerial parts of the plant (*6*). Similarly, genetically engineered scions could enhance the productivity of conventional cultivars of root or tuber crops such as potato and cassava. Such transgrafted plants have the potential to address concerns about transgene flow or escape of transgenic products (*8*).

A key remaining technical problem is the failure of grafting for monocotyledonous species (the other class of flowering plants besides eudicots). Wheat, rice, and maize provide two-thirds of global human calories (*9*). The vasculature of these and other monocots differs from those of all other flowering plants, and grafts between monocots and eudicots may fail because of anatomical incompatibilities in reconnecting phloem and xylem vasculature. The parasitic plant *Striga* is a eudicot that successfully invades and connects to the vasculature of rice. Therefore, elucidating natural mechanisms of parasitism may provide useful insights (*1*). However, monocot scions also fail to graft successfully to monocot rootstocks. Understanding and overcoming this limitation is important to protect future global food security.

Plants straddle two worlds, with their roots in a world of earth and water and their aerial parts in a world of air and light. In the current Anthropocene, an ancient technique, informed by new mechanistic understanding, may help plants and humans to make the best of both worlds. ■



PHOTO: THOMPSON & MORGAN

Department of Biological Sciences, Purdue University, West Lafayette, IN, USA. Email: mmccann@purdue.edu

REFERENCES AND NOTES

1. C. W. Melnyk, *Regeneration* **4**, 3 (2016).
2. M. Notaguchi *et al.*, *Science* **369**, 698 (2020).
3. N. C. Carpita *et al.*, in *Biochemistry and Molecular Biology of Plants*, B. B. Buchanan *et al.*, Eds. (Wiley, ed. 2, 2015).
4. Thompson & Morgan, "2-in-1 cropping vegetables"; https://blog.thompson-morgan.com/2-in-1-cropping-vegetables/.
5. S. M. Scheiner, M. Barfield, R. D. Holt, *Evol. Appl.* **13**, 388 (2019).
6. M. Lusser, C. Parisi, D. Plan, E. Rodríguez-Cerezo, *Nat. Biotechnol.* **30**, 231 (2012).
7. V. M. Haroldsen *et al.*, *Front Plant Sci.* **3**, 39 (2012).
8. G. Song, A. E. Walworth, W. H. Loescher, *J. Am. Soc. Hortic. Sci.* **140**, 203 (2015).
9. C. Zhao *et al.*, *Proc. Natl. Acad. Sci. U.S.A.* **114**, 9326 (2017).

10.1126/science.abd1641

Published by AAAS

PLANT BIOLOGY

Specificity in legume nodule symbiosis

Structural variation in recognition molecules shapes symbiotic partnerships

By **Ton Bisseling**[1,2] and **Rene Geurts**[2]

Some plant species establish mutualistic cooperation with nitrogen-fixing bacteria to overcome nitrogen shortage. The interaction between legume plants and rhizobial bacteria is the canonical example of such mutualism. It leads to the formation of root nodules, which provide the environment for the bacteria to convert atmospheric dinitrogen into ammonia. Nodule formation is initiated by rhizobium-secreted compounds called nodulation (Nod) factors. Perception of Nod factors by receptors in the plant root cells initiates nodule organogenesis and is essential for bacterial infection (*1*). Several legumes evolved a narrow host range such that only one or a few rhizobium species can initiate nodulation (*2*). This specificity is largely determined by the Nod factor receptors. On page 663 of this issue, Bozsoki *et al.* (*3*) provide structural characterization of the binding site of a Nod factor receptor in legumes. The structural basis of rhizobial Nod factor recognition is a key to understanding the evolution of specificity in symbioses.

Rhizobial Nod factors are structural variants of acylated chitin oligomers. Chitin oligomers (COs), as well as acylated COs, also function as important symbiotic signals when released by nutrient-scavenging mutualistic arbuscular mycorrhizal (AM) fungi (*4*, *5*). Perception of COs and/or acylated COs by the root enables the fungus to establish intracellular infection in roots of a wide range of plant species. In addition to rhizobia and AM fungi, acylated COs are also produced by other mutualistic microbes, such as some nutrient-scavenging mutualistic ectomycorrhizal fungi that colonize roots of some tree species and probably some nodulating nitrogen-fixing *Frankia* bacteria (*6*–*8*). COs can also trigger innate immune responses in plants as a defense response to pathogenic fungi. The lysine motif (LysM)–type chitin receptor kinase CHITIN ELICITOR RECEPTOR KINASE (CERK) was found to be essential for AM symbiosis as well as innate immunity (*1*).

Genetic and biochemical studies in the model legumes *Lotus japonicus* (lotus) and *Medicago truncatula* (medicago) uncovered a heterodimer of LysM-type receptor kinases that function as specific high-affinity rhizobium Nod factor receptors. This receptor pair is called NOD FACTOR RECEPTOR 1 (LjNFR1) and LjNFR5 in lotus and LYSM DOMAIN–CONTAINING RECEPTOR-LIKE KINASE 3 (MtLYK3) and NOD FACTOR PERCEPTION (MtNFP) in medicago (*1*). The medicago receptor pair recognizes sulfated Nod factors, whereas the lotus receptor pair binds to fucosylated Nod factors (*1*). LjNFR1 and MtLYK3 are close homologs of the CERK-type receptors LjCERK6 and MtCERK1. They evolved through a series of duplications in a legume ancestor and lost the ability to recognize COs but gained specificity toward Nod factors (*9*–*13*). This raises questions about which structural changes in the receptor had to occur to make it Nod factor specific.

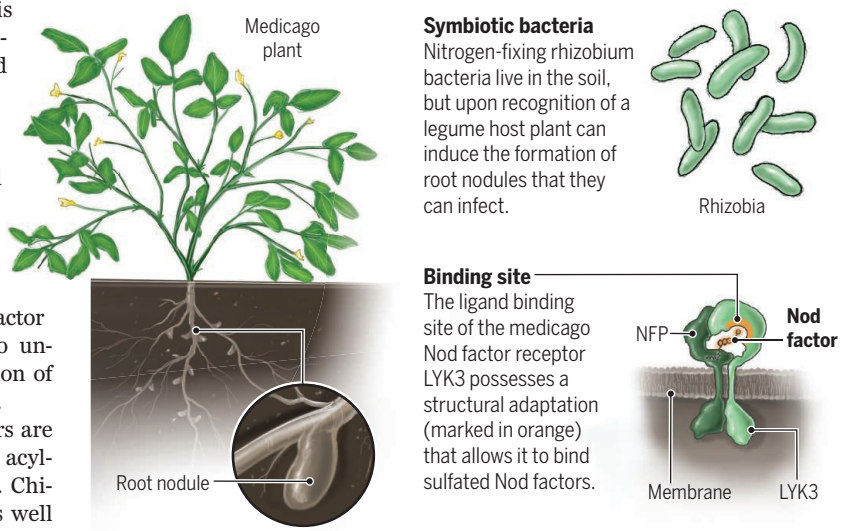
Bozsoki *et al.* show how the structural adaptations in LjNFR1 and MtLYK3 make them specific for Nod factors. The crystal structures of the ligand-binding sites of LjNFR1, MtLYK3, and the CERK receptors are highly similar. The main structural difference is in a small region of the first LysM domain of the Nod factor receptors, which determines ligand specificity (see the figure). In Nod factor receptors of different legume species, this region is variable, suggesting adaptations to recognize specific Nod factor structures. By contrast, in CERK receptors, this region is highly conserved. Using these molecular fingerprints, Bozsoki *et al.* constructed ligand recognition motifs specific for fucosylated or sulfated Nod factors, which allows engineering of rhizobium specificity.

The structural characterization of rhizobium Nod factor–binding motifs in receptors is an essential advance in understanding their evolution. Furthermore, it may provide a basis for engineering specific Nod factor receptors that can be used to improve the nodulation trait, or even to transfer it to nonlegume crops, which would allow these crops to grow without addition of nitrogen fertilizer. Nevertheless, the study of Bozsoki *et al.* also raises several questions.

Additional regions contribute to the functionality of LjNFR1 and MtLYK3 in symbiotic signaling. This suggests that lineage-specific adaptations have occurred in these Nod factor receptors that go beyond ligand specificity. This divergence could be the result of coevolution with the interacting LysM-type

The nodulation recognition system in legumes

Medicago plant (left) is shown with nitrogen-fixing root nodules and rhizobium bacteria that produce nodulation (Nod) factors. On the right is the heterodimeric complex of two lysine motif (LysM)–type receptors [NOD FACTOR PERCEPTION (NFP) and LYSM DOMAIN–CONTAINING RECEPTOR-LIKE KINASE 3 (LYK3)] binding a Nod factor.



GRAPHIC: C. BICKEL/*SCIENCE*

[1]Beijing Advanced Innovation Center for Tree Breeding by Molecular Design, Beijing University of Agriculture, 102206 Beijing, China. [2]Wageningen University, Cluster Plant Developmental Biology, Laboratory of Molecular Biology, Droevendaalsesteeg 1, 6708PB Wageningen, Netherlands. Email: ton.bisseling@wur.nl; rene.geurts@wur.nl

Published by AAAS

receptor with which they form a heterodimer, but data are currently lacking.

Lotus and medicago have a narrow rhizobial host range, which, at least in part, can be explained by the occurrence of specific ligand recognition motifs in LjNFR1 and MtLYK3. However, several legumes are more promiscuous and can establish root nodules with a wide range of rhizobium species that produce Nod factors with different structures. It should be feasible to model the corresponding Nod factor receptors and identify the structural characteristics of such promiscuity.

An important issue is the evolutionary origin of Nod factor perception in nodulation. Nodulation is not specific to legumes, but occurs in 10 plant lineages in four taxonomic orders. It has been proposed that nodulation has a single evolutionary origin (~110 million years ago), driven by an acylated CO-producing, nitrogen-fixing *Frankia* bacterium (*14*). Among nodulating nonlegumes, *Parasponia* (Cannabaceae) is the only lineage that is nodulated by Nod factor–producing rhizobia, and the corresponding receptors have recently been identified (*13*). Notably, *Parasponia* did not experience a duplication of the *CERK* gene. Instead, a single LysM-type receptor fulfills multiple functions, including CO-induced innate immunity, AM symbiosis, and rhizobium Nod factor–induced nodulation (*13*). These observations suggest that the ancestral gene from which the legume Nod factor receptors evolved already encoded a LysM-type receptor that could perceive COs as well as acylated COs. In legumes, the duplication of this gene may have allowed the evolution of highly specific Nod factor receptors. Subsequent coevolution of Nod factor structure and the receptor ligand–binding site could have resulted in host specificity through a key-lock system, which is considered an important driver in the evolution of efficient symbiotic systems (*2*). ■

REFERENCES AND NOTES

1. C. Zipfel, G. E. D. Oldroyd, *Nature* **543**, 328 (2017).
2. P. Remigi, J. Zhu, J. P. W. Young, C. Masson-Boivin, *Trends Microbiol.* **24**, 63 (2016).
3. Z. Bozsoki *et al.*, *Science* **369**, 663 (2020).
4. F. Maillet *et al.*, *Nature* **469**, 58 (2011).
5. A. Genre *et al.*, *New Phytol.* **198**, 190 (2013).
6. P. Lerouge *et al.*, *Nature* **344**, 781 (1990).
7. T. V. Nguyen *et al.*, *BMC Genomics* **17**, 796 (2016).
8. K. R. Cope *et al.*, *Plant Cell* **31**, 2386 (2019).
9. S. De Mita, A. Streng, T. Bisseling, R. Geurts, *New Phytol.* **201**, 961 (2014).
10. Z. Bozsoki *et al.*, *Proc. Natl. Acad. Sci. U.S.A.* **114**, E8118 (2017).
11. C. Gibelin-Viala *et al.*, *New Phytol.* **223**, 1516 (2019).
12. F. Feng *et al.*, *Nat. Commun.* **10**, 5047 (2019).
13. L. Rutten *et al.*, *Plant Physiol.* 10.1104/pp.19.01420 (2020),
14. R. van Velzen, J. J. Doyle, R. Geurts, *Trends Plant Sci.* **24**, 49 (2019).

10.1126/science.abd3857

NUCLEAR WASTE

Opening the floodgates at Fukushima

Tritium is not the only radioisotope of concern for stored contaminated water

By **Ken O. Buesseler**

In the time since Japan's triple earthquake, tsunami, and nuclear disaster in 2011, much has improved in the ocean offshore from the Fukushima Daiichi Nuclear Power Plant (FDNPP). Concentrations of cesium isotopes, some of the most abundant and long-lived contaminants released, are hundreds of thousands of times lower than at their peak in April 2011. Since mid-2015, none of the fish caught nearby exceed Japan's strict limit for cesium of 100 Bq/kg (*1, 2*). Yet, enormous challenges remain in decommissioning the reactors and clean-up on land. Small, and sometimes unexpected, sources of contaminants still continue to enter the ocean to this day (*3*). Two of the biggest unresolved issues are what to do with the more than 1000 tanks at the site that contain contaminated water and the impact of releasing more than 1 million tons of this water into the ocean.

The tank water is a combination of recovered groundwater and deliberately injected cooling waters, both of which became contaminated when interacting with the highly radioactive nuclear reactor cores. From the first months after the earthquake and tsunami, these waters were contained in tanks to prevent further radioisotope releases and remediated by using several systems, most notably the Advanced Liquid Processing System (ALPS). ALPS was designed to efficiently remove more than 62 different contaminants. The installation in an ice dam and other groundwater barriers, as well as the diversion of groundwater flow around the site, also assisted in reducing the daily accumulation of water from more than 400 to less than 200 metric tons per day.

Despite this effort, no decontamination system can remove 100% of all radioactive contaminants. Tritium, ^{3}H, is notoriously difficult to remove because it is a radioactive form of hydrogen that is part of the water molecule itself. Fortunately, tritium is relatively harmless because it emits a low-energy β particle that does little damage to living cells. As a result, tritium has the lowest dose coefficient for those radioactive isotopes reported in the tanks (*4*) and higher allowable release limits (see the table). These properties do not detract from the potential for large amounts of tritium to have harmful health effects.

The total amount of tritium contained in the tanks also matters, which is reported to be around 1 PBq (PBq = 10^{15} Bq) (*5*). That total is far less than the 8000 PBq of tritium still remaining from global atmospheric nuclear testing in the 1960s or the 2000 PBq from natural interactions between cosmogenic particles and nitrogen that form tritium in the atmosphere. In addition, all nuclear power facilities emit tritium that, depending on plant design, can be several PBq per year, or even higher, as in the case of nuclear fuel reprocessing plans such as at Cap de La Hague (*6*).

However, this story is not only about tritium but what else is in the tanks. It was not until mid-2018 when TEPCO, the operator at FDNPP, released data detailing the amounts of more dangerous isotopes, such

Release limits and risk

Different isotopes pose different environmental and health challenges.

ISOTOPE	MAX RELEASE (BQ/LITER)[1]	FOOD LIMIT (BQ/KG)[2]	HALF-LIFE (YEARS)[3]
^{3}H	60,000	10,000	12.35
^{14}C	2000	10,000	5730
^{99}Tc	1000	10,000	211,000
^{125}Sb	800	1000	2.77
^{60}Co	200	1000	5.27
^{106}Ru	100	100	1.01
^{137}Cs	90	100	30.0
^{134}Cs	60	100	2.06
^{90}Sr	30	100	29.1
^{129}I	9	100	16,000,000

[1]Maximum levels allowed in Japan for waters released from nuclear reactor operations. [2]Limits allowed for food safety (CODEX standard based upon adult consumer and annual consumption limit). [3]Half-life is a physical property indicating the time it takes for 50% of an isotope to decay. A shorter value means a quicker loss.

Woods Hole Oceanographic Institution, Woods Hole, MA, USA. Email: kbuesseler@whoi.edu

Published by AAAS

as ruthenium-106, cobalt-60, and strontium-90 (*7*). The concentrations of these radioactive isotopes are orders of magnitude lower than tritium but highly variable from tank to tank (see the figure). By TEPCO's own assessments, more than 70% of the tanks would need secondary treatment to reduce concentrations below that required by law for their release (*7*).

However, there are other important factors to consider. These radioactive isotopes behave differently than tritium in the ocean and are more readily incorporated into marine biota or seafloor sediments (see the figure). For example, the biological concentration factors in fish are up to 50,000 higher for carbon-14 than tritium (*8*). Also, isotopes such as cobalt-60 are up to 300,000 times more likely to end up associated with seafloor sediments (*8*). As a result, models of the behavior of tritium in the ocean, with tritium's rapid dispersion and dilution, cannot be used to assess the fate of these other potential contaminants.

To assess the consequences of the tank releases, a full accounting after any secondary treatments of what isotopes are left in each tank is needed. This includes the volume, not just for the nine isotopes currently reported but for a larger suite of possible contaminants, such as plutonium. Plutonium may be present in FDNPP cooling waters but was not released in large amounts to the atmosphere in 2011.

The public has been told that there are few options other than ocean discharge. However, given the short half-lives of the isotopes known in the tanks, time would help. With a 12.3-year half-life, in 60 years, 97% of all of the tritium would decay, along with several of the other shorter lived isotopes. In those intervening years of cleanup on site, about four times the current volume would be generated. The risk of tank leaks—even if stored in earthquake-resistant tanks, similar to what Japan already does for petroleum or liquefied natural gas—needs to be weighed against the greatly reduced amount of radioactivity after decay. The lack of space, the reason for the urgency in ocean release, could be alleviated if tanks were stored just outside the boundaries of the current FDNPP.

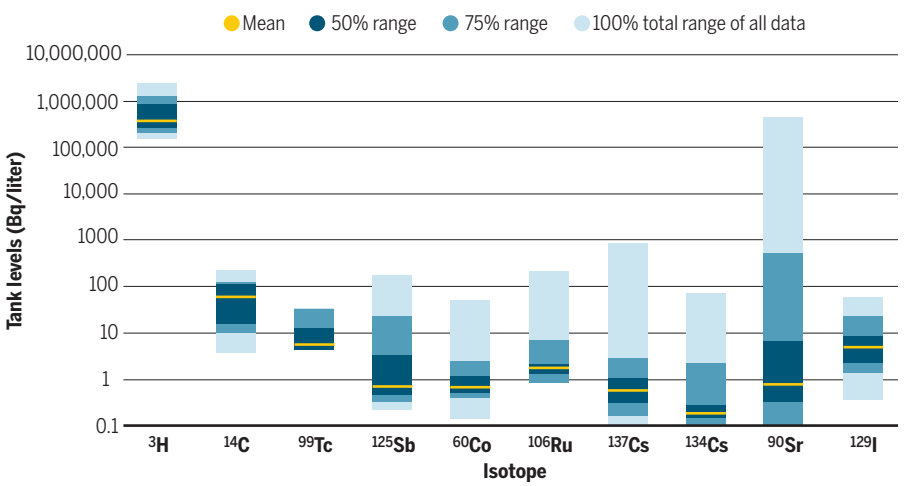
Last, public fears should not be dismissed because these decisions may have negative impacts on local fisheries that are just now rebuilding. Making data available is a good start (*9*) but not enough. Seafood and ocean monitoring should continue to involve local fisherman, and studies that involve public participation in sampling would be an effective tool to improve public education and build confidence in the results (*10*).

The current focus on tritium in the wastewater holding tanks ignores the other radioactive isotopes but presents a solvable issue. A solution includes reducing the concentrations of non-tritium contaminants, reporting after secondary treatment independently verifies concentrations for all contaminants in each tank, and reconsidering other storage options. If there is a release, supporting independent ocean study of multiple contaminants in seawater, marine biota, and seafloor sediments should occur before, during, and after. Although the operators have promised some of this, actions will matter more than words. What needs to be added to the discussion is that the non-tritium isotopes in those tanks have vastly different toxicities and fates in the ocean. ■

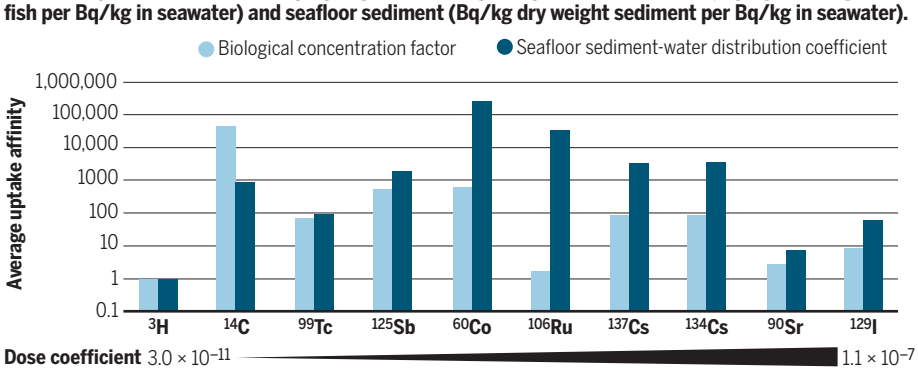
Sorting out what is in the tanks

One legacy of the Fukushima Daiichi nuclear disaster after the 2011 Tohoku-oki earthquake and tsunami is the accumulation of water with a variety of radioisotopes in tanks. Assessing the risk of discharging water from these tanks back into the ocean requires knowing radioisotope amounts and their ability to concentrate in seafloor sediments and biological tissues.

Radioisotope concentration ranges for more than 200 tanks reported on 31 Dec 2019 by TEPCO (*9*) organized by their effective dose (dose coefficient).



Radioisotopes concentrate to varying degrees in biological systems such as fish (Bq/kg wet weight fish per Bq/kg in seawater) and seafloor sediment (Bq/kg dry weight sediment per Bq/kg in seawater).



GRAPHIC: N. CARY/*SCIENCE*

REFERENCES AND NOTES

1. K. Buesseler *et al.*, *Annu. Rev. Mar. Sci.* **9**, 173 (2017).
2. Radioactivity levels are measured in becquerels (Bq) per unit volume or mass, with 1 Bq = one decay event per second.
3. V. Sanial, K. O. Buesseler, M. A. Charette, S. Nagao, *Proc. Natl. Acad. Sci. U.S.A.* **114**, 11092 (2017).
4. International Commission on Radiological Protection (ICRP) publication 119, "Compendium of dose coefficients based upon ICRP publication 60" (ICRP, 2010).
5. TEPCO, Draft study responding to the subcommittee report on handling ALPS treated water, 24 March 2020.
6. P.-E. Oms *et al.*, *Sci. Total Environ.* **656**, 1289 (2019).
7. T. E. P. C. O. Treated Water Portal Site, www4.tepco.co.jp/en/decommission/progress/watertreatment/index-e.html.
8. International Atomic Energy Agency (IAEA), Technical report series No. 422, "Sediment distribution coefficients and concentration factors for biota in the marine environment" (IAEA, 2004).
9. TEPCO, "Radiation concentration estimates for each tank area (as of March 31, 2020)" (TEPCO 31 December 2019); www4.tepco.co.jp/en/decommission/progress/watertreatment/images/tankarea_en.pdf.
10. Our Radioactive Ocean, https://ourradioactiveocean.org.

ACKNOWLEDGMENTS

This work was supported by the Deerbrook Charitable Trust and the Center for Marine and Environmental Radioactivity. Writing assistance by K. Kostel is also appreciated.

10.1126/science.abc1507

Published by AAAS

DRUG DEVELOPMENT

Unifying the synthesis of nucleoside analogs

A short, versatile synthetic pathway transforms achiral reactants into nucleoside analogs

By **Gavin J. Miller**

Nucleosides, the building blocks of DNA and RNA, typically contain a ribose sugar attached to a nucleobase. Structurally modified nucleoside analogs can disrupt the biological processes that mediate nucleoside assembly into DNA and RNA. Nucleoside analogs that target viral and cell replication have delivered generations of drugs combatting cancer, herpes simplex virus, human immunodeficiency virus, and hepatitis C virus (*1*–*4*). Despite these successes, considerable challenges remain in chemically synthesizing nucleoside analogs, especially the development of short and general synthetic routes. On page 725 of this issue, Meanwell *et al.* (*5*) report a rapid and scalable de novo synthesis of a diverse range of nucleoside analogs from simple achiral starting materials. Their approach builds on previous work by Peifer *et al.* (*6*), who introduced a facile and enantioselective synthetic approach to pentose sugars.

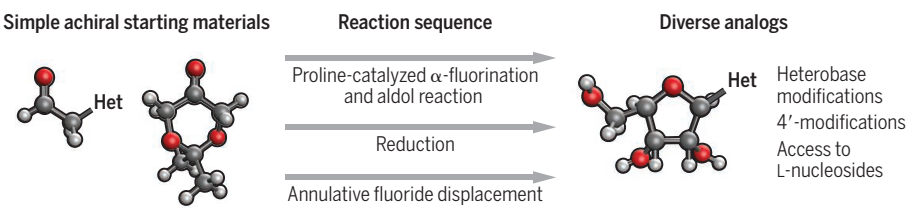
The molecular assembly of nucleosides requires consideration of the complex stereochemical environment within the sugar ring and must also enable any modification from the native metabolite to be included in the final analog structure. In many cases, a "chiral pool" of available carbohydrate starting materials has been used effectively, because the majority of the stereochemical information required is already in place. However, this strategy often requires lengthy and costly synthetic processes and is not usually amenable to rapid diversification, that is, accessing many different structures within one synthetic pathway. Asserting control of stereochemistry at the position where the nucleobase (or an unnatural variant thereof) is incorporated is crucial to avoid difficult and inefficient separation of diastereomeric mixtures. Finally, stereochemically defined modifications must be installed at key positions around the sugar ring. For example, the antiviral drug sofosbuvir has modifications at the 2′-position carbon atom of the ribose ring where the native hydrogen and hydroxyl groups are replaced with methyl and fluoride, respectively.

Lennard-Jones Laboratory, School of Chemical and Physical Sciences, Keele University, Keele, Staffordshire ST5 5BG, UK. Email: g.j.miller@keele.ac.uk

Starting from a simple ketone and heteroaryl aldehyde, Meanwell *et al.* used a proline-mediated organocatalytic α-fluorination, followed by an aldol reaction, to furnish a fluorohydrin intermediate. This material was converted through to the nucleoside analog scaffold by using an annulative fluoride displacement strategy that enabled formation of the sugar ring product (see the figure). The process used simple, commercially available chemicals, and the reaction sequence installed the correct spatial orientation of atoms at all ring positions in high yield and with excellent stereochemical purity.

Versatile nucleoside synthesis

Nucleosides are often synthesized by modifying natural chiral compounds. Meanwell *et al.* present a scalable three-step synthesis from simple achiral molecules. Het, heteroaromatic group.



Having established this method to access the nucleoside core structure, the utility of this short synthetic approach was explored and shown to be amenable in accessing an exciting range of derivatives, including nucleosides containing different nucleobases (endogenous and exogenous), partially protected species, enantiomeric L-nucleosides, locked nucleosides, and iminonucleosides. The protocol also enabled products from these reactions to undergo further functionalization—for example, to 2′-modified analogs—drastically improving their ease of synthetic access. The pivotal annulative fluoride displacement method was also adapted to enable direct access to 4′-position–modified derivatives of α-linked D- and L-nucleosides, providing a contemporary structural motif for future exploration in nucleoside-analog medicinal chemistry. Finally, in an examination of scalability, the α-fluorination-aldol reaction was completed on a 380-g scale with a 72% yield and afforded a rapid, two-step entry to a precursor of MK-3682 (uprifosbuvir), a hepatitis C RNA polymerase inhibitor developed by Merck (*7*).

Nucleoside analogs are a historically accomplished class of drug with highly diversified scaffolds and proven potential to treat a wide range of diseases (*1*–*4*). Their complexity requires that efficient and adaptable synthetic methodologies are developed to enable entry to new classes of analogs and to support current requirements to produce quantities that can satisfy pharmaceutical demand. In this context, the de novo synthetic approach developed by Meanwell *et al.* has unified access to a wide range of nucleosides and will serve as a blueprint for future developments, such as rapidly accessing 4′-modified–β-D-linked analogs.

Alongside this new synthetic methodology, examples describing the enzymatic synthesis of nucleoside derivatives are increasing (*8*). Combining these two powerful synthetic approaches is an exciting prospect for the field, yet challenges lie ahead. For example, allied to these achievements is the requirement for phosphorylated forms of nucleosides (*9*) and broadening scaffold access to include sugar-heterocycle substitution (*10*). Finally, the repurposing of the nucleoside analog remdesivir to target the viral replication machinery of severe acute respiratory syndrome coronavirus 2 (SARS-CoV-2) (*11*) further highlights the critical need for nucleoside-analog therapeutic development and the underpinning importance of synthetic organic chemistry. ■

REFERENCES AND NOTES

1. L. P. Jordheim *et al.*, *Nat. Rev. Drug Discov.* **12**, 447 (2013).
2. M. Guinan *et al.*, *Molecules* **25**, 2050 (2020).
3. K. L. Seley-Radtke, M. K. Yates, *Antiviral Res.* **154**, 66 (2018).
4. M. K. Yates, K. L. Seley-Radtke, *Antiviral Res.* **162**, 5 (2019).
5. M. Meanwell *et al.*, *Science* **369**, 725 (2020).
6. M. Peifer *et al.*, *J. Am. Chem. Soc.* **136**, 5900 (2014).
7. E. De Clercq, *J. Med. Chem.* **59**, 2301 (2015).
8. C. C. Nawrat *et al.*, *Org. Lett.* **22**, 2167 (2020).
9. B. Roy *et al.*, *Chem. Rev.* **116**, 7854 (2016).
10. G. Romeo *et al.*, *Chem. Rev.* **110**, 3337 (2010).
11. R. T. Eastman *et al.*, *ACS Cent. Sci.* **6**, 672 (2020).

10.1126/science.abd1283

GRAPHIC: A. KITTERMAN/*SCIENCE*

Published by AAAS

VIEWPOINT: COVID-19

COVID-19 in Africa: Dampening the storm?

The dampened course of COVID-19 in Africa might reveal innovative solutions

By **Moustapha Mbow[1], Bertrand Lell[2,3], Simon P. Jochems[4], Badara Cisse[5], Souleymane Mboup[6], Benjamin G. Dewals[7], Assan Jaye[8], Alioune Dieye[1], Maria Yazdanbakhsh[4]**

Coronavirus disease 2019 (COVID-19) has spread rapidly and extensively to most countries in the world, resulting in considerable mortality in Europe and the United States, as well as in numerous upper-middle-income countries in South America and Asia. Experts predicted millions of COVID-19 deaths in Africa because many countries in the continent rank poorly on the United Nations Development Programme's Human Development Index. However, more than 4 months after the first cases in Africa were detected, prevalence and mortality are still low. It remains unclear if Africa is really spared from substantial cases and deaths. However, differences between Africa and the most affected countries in reliable reporting and death registration, lockdown stringency, demography, sociocultural aspects, environmental exposures, genetics, and the immune system could help to explain the experience of COVID-19 in Africa.

Africa faces major health and socioeconomic challenges that should have allowed rapid transmission of COVID-19. These include a weak health system (per capita health expenditure of <$50 in most West African countries compared with >$2500 in Europe and the United States), population crowding, poverty, and unhygienic conditions (*1*). Population densities are very high in most African capital cities such as Dakar (12,617 persons/km^2), Abidjan (11,155 persons/km^2), or Lagos (13,909 persons/km^2), whereas New York City has 7101 persons/km^2. However, although community transmission was reported in many major African cities months ago, the predicted number of cases and deaths has not yet been observed (see the figure). Low case numbers are often attributed to insufficient testing. However, many African countries implemented testing early on, and, based on the Our World in Data database (*2*), more tests per the number of cases were carried out than in other countries at similar phases of the epidemic (see the figure). Regarding the number of deaths, few functional civil registration services and thus statistics exist on the continent, raising questions about the reliability of mortality data. Potential underreporting of COVID-19–associated deaths would not be specific to Africa, but the margin of error could be wider. To date, African countries have not indicated acute health emergencies; however, reliable age-stratified data are needed to fully grasp the COVID-19 situation in Africa to allow appropriate measures to be taken.

Measures such as travel restrictions, curfews, and school closures were implemented early in Africa compared with other continents, often before an African country had detected a case (fig. S1). These early responses might have resulted in fewer imported cases and reduced intracountry transmission, allowing sufficient time to prepare the constrained health systems for diagnosis and to prepare strategies for quarantine, contact tracing, and social distancing on a continent that already has experience in such practices to control epidemics such as Lassa fever and Ebola. Although it is likely that the early lockdown in Africa contributed to the slow spread, containment measures are not fully respected in many countries. Most people work in the informal business sector, such as in traditional markets, making strict lockdown measures impossible to implement. Recently, some African governments have been pressured to relax lockdown measures, for example, to carry out congregational prayers in mosques in Senegal. It remains unknown whether relaxation of containment measures will result in increased cases or if other factors are at play.

The majority of COVID-19–associated deaths occur in older people. Africa has a comparatively young population, with a median population age of 19.7 years for the continent versus 38.6 years for the United States. Africa's youthful population is reflected in the structure of age-stratified cases (fig. S2). Based on global age-specific case fatality rates for COVID-19 and the age demographics of Africa, COVID-19 deaths would be expected to be only four times (*3*), rather than the observed 40 times, lower than in Europe or the United States. However, no aggregated data on age-specific case or death rates are available for the continent. There is substantial intergenerational mixing in Africa, and, with more cases of subclinical infections in the young, it could be a matter of time before expansive numbers of cases and deaths are recorded. Alternatively, a more rapid development of herd immunity among the youthful population might lead to fewer severe cases. Data from antibody tests (serosurveys) should clarify if transmission was more widespread with a high rate of asymptomatic and mild cases in African countries than in other countries.

The genetic characteristics of the severe acute respiratory syndrome coronavirus 2 (SARS-CoV-2) and human genetics may be among the reasons for low incidence of severe COVID-19 in Africa. Although the relative contribution from Africa to the SARS-CoV-2 GISAID (Global Initiative on Sharing All Influenza Data) sequence database is small, the isolates found in Africa are representative of the different clades of SARS-CoV-2 found on other continents (fig. S3). Thus, it is unlikely that strains of SARS-CoV-2 in Africa have reduced virulence. Moreover, African-Americans constitute a disproportionate burden of deaths in the United States, so it seems unlikely that the lower mortality from COVID-19 in Africa is due to genetic factors. Nonetheless, the COVID Human Genetic Effort consortium aims to elucidate whether genetics can play a role in the patterns of disease worldwide.

SARS-CoV-2 infection leads to a heterogeneous outcome. About 80% of symptomatic cases are mild to moderate, whereas ~20% can develop severe respiratory disease and display high rates of mortality (*4*). The development of an effective adaptive immune response can limit viral infection, whereas uncontrolled activation of innate immune cells leads to a "cytokine storm" and hyperinflammation in the lungs, ultimately leading to acute respiratory distress syndrome (ARDS) and multiorgan failure (*4*, *5*). Being able to suppress viral infection early or to temper excessive inflammatory responses are likely complementary mechanisms to prevent severe disease.

[1]Department of Immunology, Faculty of Medicine, Pharmacy, and Odontology, Cheikh Anta Diop University of Dakar, Dakar, Senegal. [2]Department of Medicine I, Division of Infectious Diseases and Tropical Medicine, Medical University of Vienna, Vienna, Austria. [3]Centre de Recherches Médicales de Lambaréné, Lambaréné, Gabon. [4]Leiden University Center of Infectious Diseases, Leiden, Netherlands. [5]London School of Hygiene and Tropical Medicine, London, UK. [6]Institute of Health Research, Epidemiological Surveillance and Training, Dakar, Senegal. [7]Laboratory of Immunology-Vaccinology, FARAH, University of Liège, Liège, Belgium. [8]Medical Research Council at the London School of Hygiene and Tropical Medicine, Banjul, The Gambia.
Email: moustapha2.mbow@ucad.edu.sn; m.yazdanbakhsh@lumc.nl

Published by AAAS

Most convalescent symptomatic COVID-19 patients develop virus-specific neutralizing antibodies as well as specific $CD4^+$ and $CD8^+$ T cell responses (*5*). The efficiency and adequacy of these adaptive responses to clear viral infections depends on multiple factors, including past or concurrent infections with other pathogens. For example, antibodies directed to the four human coronaviruses that cause "common colds" could cross-react and neutralize SARS-CoV-2 in humans (*6*), and preexisting cross-reactive T cells can be found in individuals that have not been exposed to SARS-CoV-2 (*7*), suggesting previous exposure to related human coronaviruses could generate immunological cross-reactivity (*7*).

There are considerable differences in environmental exposures in Africa, compared with Europe or the United States. Noncommunicable diseases (NCDs)—such as cardiovascular diseases, obesity, and type 2 diabetes—are risk factors for severe COVID-19. These environmentally and behaviorally driven conditions are increasingly recognized in urban centers in Africa, and most COVID-19 deaths in Africa have been in older people with NCDs. However, infectious diseases such as HIV, tuberculosis, malaria, and other respiratory infections or those caused by helminths (parasitic worms) are prevalent in Africa, but there is currently little information on whether, or how, these infections affect COVID-19 disease progression.

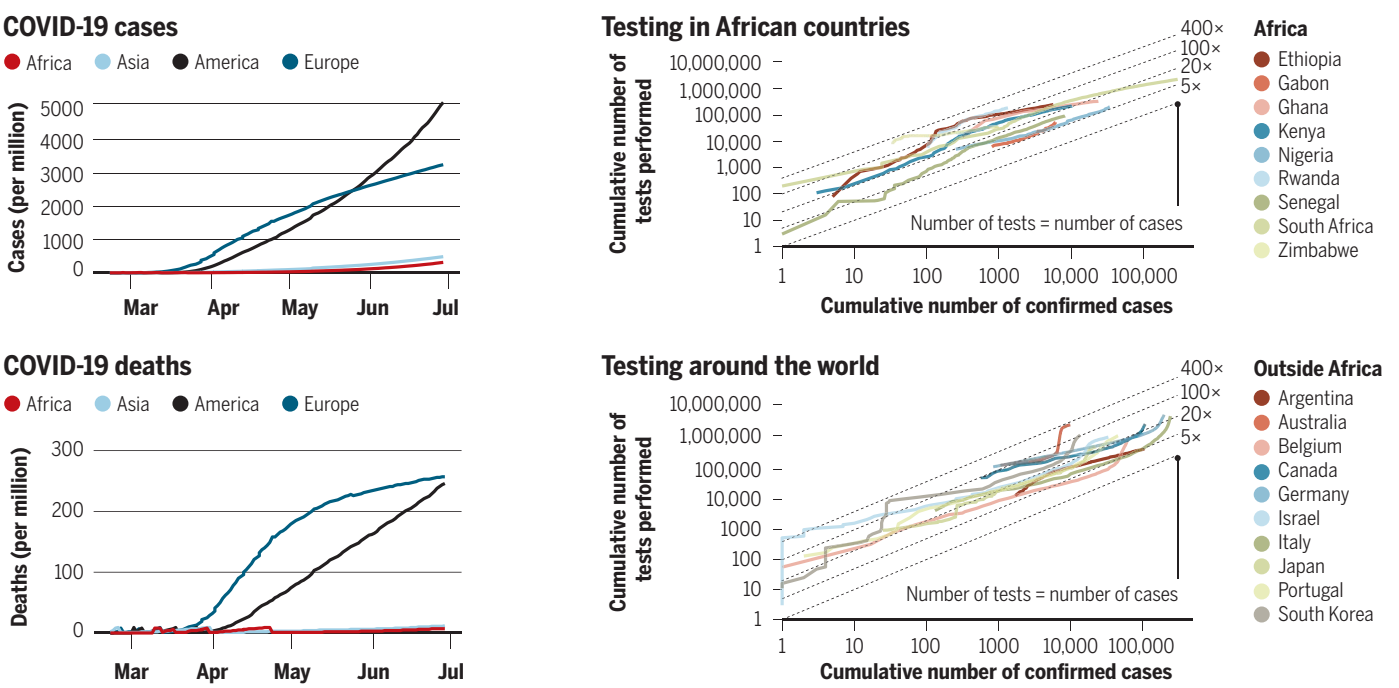
It is increasingly recognized that the immune system is shaped not only by genetics but also by environmental factors, such as exposure to microorganisms and parasites. This educates the immune system to protect against invading pathogens not only specifically but also nonspecifically through, for example, "trained immunity," which involves the reprogramming of innate cells that, on secondary encounter with a pathogen, can show a stronger response (*8*) or "virtual memory" (*9*). Virtual memory T cells (T_{VM} cells) expand in response to cytokines such as helminth-induced interleukin-4 (IL-4), rather than through pathogen-specific antigens, leading to enhanced antiviral effector functions (*9*). Thus, it can be envisaged that T_{VM} cells are more prevalent in people in Africa owing to the higher exposure to such pathogens. This could contribute to the control of SARS-CoV-2. Additionally, as postulated by the "hygiene hypothesis," early and chronic exposure to pathogens leading to relentless immune cell activation in harsh environments induces a strong regulatory immune response to counteract excessive inflammation (*10*).

The ability to prevent excessive inflammation could be a critical parameter that is associated with COVID-19 outcome. Recent data suggest that inflammatory alveolar macrophages (AMs), which can arise from differentiation of recruited monocytes upon infection, are increased in the lungs of patients with severe COVID-19 (*11*). It is unclear whether these monocyte-derived AMs are an important source of the cytokine-release syndrome observed during SARS-CoV-2 infection or whether they are involved in the pathogenesis of ARDS. However, monocyte and macrophage inflammatory cytokines, such as IL-6, have been repeatedly observed to be a marker of severe COVID-19, and myeloid cells are thus likely to be associated with the hyperinflammation. Monocytes from African individuals with high exposure to pathogens can be less proinflammatory (*12*). Thus, their recruitment into the lungs might prevent high cytokine production and therefore lead to better outcomes of COVID-19. Moreover, the airway microbiota, as well as more distal gut microbiota, could play important roles in preventing or potentiating respiratory tract infections and modulating virus-induced inflammation, as has been shown for several respiratory viruses (*13*). The known variations in microbiota across geographical areas could thus also participate in modulating disease severity and should be studied.

Africa should be part of the roadmap for COVID-19 research. Although there are no available data on the immune responses in African COVID-19 patients, studies show

COVID-19 distribution and cases versus testing

The distribution of coronavirus disease 2019 (COVID-19) cases and deaths per 1 million inhabitants per continent reveals surprisingly low rates in Africa (left). This is despite comparable levels of testing per confirmed cases across continents (right). The dotted lines show the number of tests performed per number of detected cases. Data are from European Centre for Disease Prevention and Control COVID-19 situation updates, United Nations World Population Prospects 2019, and Our World in Data (*2*).



GRAPHIC: X. LIU/*SCIENCE*

Published by AAAS

clear differences in the activation, proinflammatory, and memory profiles of the immune cells not only in Africans versus Europeans but also among Africans with high and low exposure to microorganisms and parasites (*14*) (fig. S4). Does the difference in immunological profiles matter for the outcome of COVID-19 in Africa? This needs further investigation, and the pattern of COVID-19 in urban and rural Africa could be informative.

There are differences in opinion about whether the pattern of SARS-CoV-2 spread is different in Africa compared with that in the United States and Europe. So far, despite a paucity of data, it appears that the virus is spreading differently and potentially with an attenuated outcome in Africa. There has been limited testing of asymptomatic cases or of antibody titers. Therefore, it is unknown whether early interventions were successful in preventing transmission or whether there are differences in susceptibility between populations of different regions. Perhaps the COVID-19 pandemic can emphasize the need for widespread implementation of public health tools, such as high-quality data, accurate diagnostics for track and trace, good communication, and an effective vaccine. Early testing of vaccines in different regions of Africa is essential because the high degree of exposure to pathogens can limit some vaccine responses (*15*). The first COVID-19 vaccine testing is starting in South Africa (Ox1Cov-19 Vaccine VIDA-Trial), and others are planned. Hopefully, this will stimulate the full participation of Africa in research into the critical factors that hold the key to innovative solutions in the fight against the pandemic. ■

REFERENCES AND NOTES

1. M. Martinez-Alvarez *et al.*, *Lancet Glob. Health* **8**, 631 (2020).
2. Our World in Data, Statistics and research: Coronavirus pandemic (COVID-19); https://ourworldindata.org/coronavirus.
3. F. Mougeni *et al.*, *MedRxiv* 10.1101/2020.05.19.20106914 (2020).
4. X. Cao, *Nat. Rev. Immunol.* **20**, 269 (2020).
5. N. Vabret *et al.*, *Immunity* **52**, 910 (2020).
6. K. Ng *et al.*, *bioRxiv* 10.1101/2020.05.14.095414 (2020).
7. A. Grifoni *et al.*, *Cell* **181**, 1489 (2020).
8. R. J. W. Arts *et al.*, *Cell Host Microbe* **23**, 89 (2018).
9. M. Rolot *et al.*, *Nat. Commun.* **9**, 4516 (2018).
10. M. Yazdanbakhsh, P. G. Kremsner, R. van Ree, *Science* **296**, 490 (2002).
11. M. Liao *et al.*, *Nat. Med.* **26**, 842 (2020).
12. K. K. Smolen *et al.*, *J. Immunol.* **193**, 3003 (2014).
13. N. Li, W.-T. Ma, M. Pang, Q.-L. Fan, J.-L. Hua, *Front. Immunol.* **10**, 1551 (2019).
14. M. Mbow *et al.*, *Immunology* **143**, 569 (2014).
15. E. Muyanja *et al.*, *J. Clin. Invest.* **124**, 3147 (2014).

ACKNOWLEDGMENTS

We thank all the researchers who have kindly deposited and shared genome data on GISAID (www.gisaid.org) and K. Stam and F. Mougeni for graphs.

SUPPLEMENTARY MATERIALS

science.sciencemag.org/content/369/6504/624/suppl/DC1

10.1126/science.abd3902

CORONAVIRUS

Interferon responses in viral pneumonias

Are interferon-mediated antiviral immune responses beneficial or detrimental in COVID-19?

By **Gary E. Grajales-Reyes** *and* **Marco Colonna**

The severe acute respiratory syndrome coronavirus 2 (SARS-CoV-2) outbreak quickly developed into a pandemic in March 2020. To date, no vaccines or antiviral medications are available, and given the urgency, many clinical trials have started screening existing antiviral drugs for efficacy against SARS-CoV-2 infection. Among a variety of therapeutic approaches, the use of different types of interferon (IFN) as antiviral agents is under investigation owing to promising outcomes in other coronavirus-induced pathologies (*1*). Through different mechanisms and effector proteins, IFNs play an important role in the inhibition of viral replication (*2*). On pages 712 and 706 of this issue, Major *et al.* (*3*) and Broggi *et al.* (*4*), respectively, describe the mechanisms by which IFN-λ responses contribute to pathogenesis in viral pneumonias. Conversely, on page ZZZ, Hadjadj *et al.* (*5*) studied peripheral blood responses from a cohort of 50 patients with coronavirus disease 2019 (COVID-19), demonstrating that critically ill patients have reduced IFN responses paired with a proinflammatory response.

IFNs are important cytokines of the innate and adaptive immune system and are classified into three main types: I (α or β), II (γ), and III (λ). During viral infections, pattern-recognition receptors detect viral nucleic acids, inducing the production of IFNs. The expression of type I, II, and III IFNs is not redundant among all the IFN-producing cells. In particular, expression of IFN-λ is tissue specific and is mainly produced by dendritic cells, epithelial cells, and hepatocytes. In humans, IFN-λ includes four members (IFNL1 to -4), all of which bind and induce signaling through the heterodimeric IFN-λ receptor (IFNLR) (*6*), which is mostly restricted to epithelial cells, dendritic cells, and neutrophils (*7*, *8*). Signaling through the IFNLR triggers an intracellular signaling pathway, which in turn induces expression of a group of IFN-stimulated genes (ISGs) (*9*). IFNLR signaling also induces expression of the tumor suppressor p53, which limits viral replication by enhancing IFN signaling and causing cell cycle arrest of infected cells (*10*, *11*).

Although IFN-λ has antiviral effects, it has been shown that in mice, IFN-λ produced in response to influenza virus infection increased susceptibility to pneumonia caused by subsequent infection with methicillin-resistant *Staphylococcus aureus* (called superinfection) (*12*). IFN-λ caused expansion and restructuring of the nasal microbiota, as well as impaired epithelial barrier function, which allow bacteria to invade and colonize the tissue. Consistent with this observation, Broggi *et al.* showed that amounts of IFN-λ messenger RNA (mRNA) from bronchoalveolar lavage fluid and naso-oropharyngeal samples correlated with disease morbidity in SARS-CoV-2–positive patients. They found that the association between morbidity and IFN-λ observed in humans was reproduced in mice treated with intratracheal polyinosinic:polycytidylic acid [poly(I:C)], a synthetic double-stranded RNA that mimics viral RNA and induces innate immune responses. Intratracheal poly(I:C) administration was also associated with impaired lung epithelial barrier function.

SARS-CoV and influenza virus infect lung alveolar epithelial cells. As viral replication proceeds, lung epithelial cells die because of cytopathic effects as well as immune-mediated damage. Recovery is then achieved through epithelial cell proliferation and differentiation. Both Major *et al.* and Broggi *et al.* show that after influenza virus infection or intratracheal poly(I:C) challenge, respectively, IFN-λ impairs lung epithelial cell proliferation during recovery. Major *et al.* further found that IFN-λ impairs differentiation of alveolar epithelial progenitor cells into secretory and multiciliated cell subtypes. In accordance, both groups identified that the impaired epithelial proliferation is dependent on expression of IFNLR. Mice in which the *Ifnlr1* gene is deleted (*Ifnlr1*$^{-/-}$) had improved epithelial proliferation after an influenza virus or poly(I:C) challenge. This phenotype was mediated by lung stromal cells because

Department of Pathology and Immunology, Washington University School of Medicine, St Louis, MO 63110, USA. Email: garygrajalesreyes@wustl.edu; mcolonna@wustl.edu

Published by AAAS

chimeric mice with wild-type bone marrow and *Ifnlr1*$^{-/-}$ lung stroma display the same enhancement in epithelial proliferation as that of *Ifnlr1*$^{-/-}$ mice. As a consequence of enhanced epithelial recovery, *Ifnlr1*$^{-/-}$ mice had better survival in models of *S. aureus* and *Streptococcus pneumoniae* superinfections. Mechanistically, gene expression analyses by Major *et al.* and Broggi *et al.* demonstrated that IFN-λ signaling in lung epithelial cells induces expression of ISGs and the p53 pathway (see the figure).

Given the intrinsic antiviral effects of IFN-λ and expression of IFNLR in the airway epithelium, IFN-λ is being investigated as a therapeutic agent for COVID-19. However, data from both Major *et al.* and Broggi *et al.* caution against the unintended consequences of appropriate antiviral responses in pneumonias, as caused by SARS-CoV-2. In other tissues, inhibition of cell division and death of the infected cells would be the appropriate response to prevent spreading of the virus to live cells. By contrast, in the context of viral pneumonias and alveolar epithelial cells, failure to proliferate results in destruction of the gas exchange barrier and susceptibility to bacterial superinfections.

These findings will certainly impose a challenge on the ongoing clinical trials and future treatment regimen design. These trials are investigating the effects of subcutaneous pegylated IFNL1a in different cohorts of patients with COVID-19. Despite its physiological role in epithelial antiviral immunity, clinical trials have mainly evaluated the effects of IFN-λ in viral hepatitis rather than viral pneumonia. It is unclear whether short pulses rather than sustained administration of IFN-λ can have the desired antiviral effects without affecting lung epithelial proliferation. A potential alternative approach considering these data is IFNLR blockade. As Major *et al.* and Broggi *et al.* showed in mice, it is possible that the enhanced proliferative response observed after blocking IFN-λ signaling would outweigh the benefit of a deficient epithelial IFN-λ response in the lungs for SARS-CoV-2 infection.

The study by Hadjadj *et al.* focused on type I IFN responses in human SARS-CoV-2 infection. Like IFN-λ, type I IFNs induce expression of ISGs and p53. However, their antiviral action is broader because the type I IFN receptor is ubiquitously expressed. Hadjadj *et al.* discovered a profound suppression of type I IFN signatures in peripheral blood from critically ill COVID-19 patients. Plasma concentrations of IFN-α in these patients were lower than in mild to moderate patients, suggesting that systemic type I IFN responses may be beneficial. Multiplex gene analysis revealed that critically ill patients had down-regulation of ISG expression. Irrespective of disease severity, SARS-CoV-2–positive patients had reduced numbers of plasmacytoid dendritic cells, which are an important cellular source of type I IFNs. Severe and critically ill patients had increased plasma viral load when compared with that of mild to moderate patients. These patients also displayed a proinflammatory response driven by the transcription factor nuclear factor κB (NF-κB), which was characterized by increased interleukin-6 (IL-6) and tumor necrosis factor–α (TNF-α).

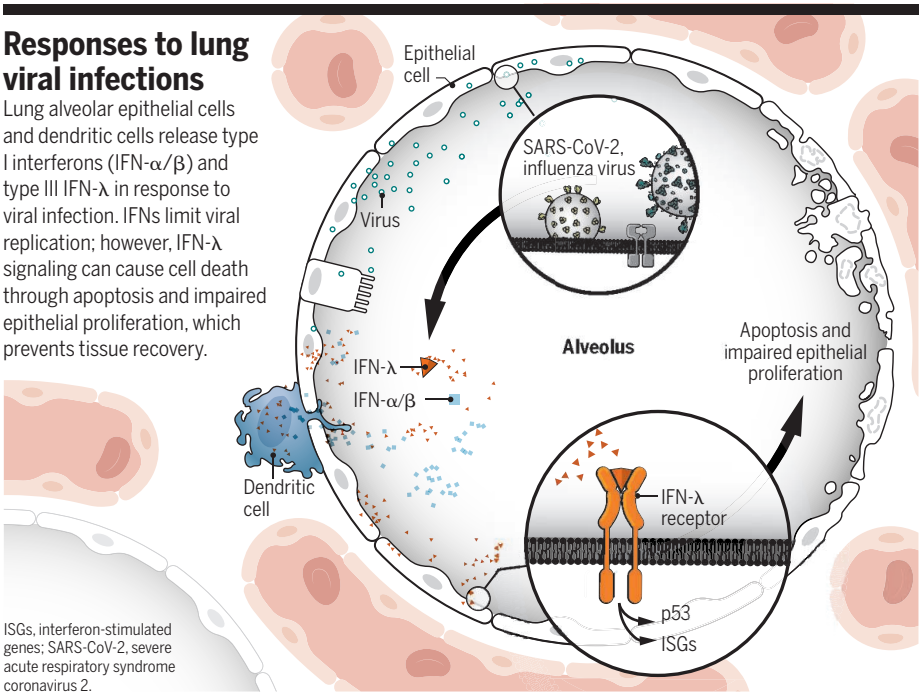
In seeming contrast with the peripheral blood data by Hadjadj *et al.*, Broggi *et al.* showed that SARS-CoV-2–positive patients had increased amounts of type I IFN mRNA in naso-oropharyngeal and bronchoalveolar lavage fluid. Major *et al.* also tested whether type I IFNs damage airway epithelium in a mouse influenza model. Blockade of endogenous type I IFN signaling did not augment epithelial cell proliferation, suggesting that type I IFNs may not be as detrimental to lung epithelia as IFN-λ.

Given the complexity of IFN responses in SARS-CoV-2 infection, further insight into their impact on the disease is of the utmost importance for continued development of drugs targeting the IFN pathways. Research is needed to establish whether IFN-λ and type I IFNs have similar effects or whether one is more beneficial or detrimental than the other. It should be conclusively established whether type I IFN responses are augmented in lungs of COVID-19 patients in contrast to the suppressed type I IFN responses observed in the blood. Further research will be necessary to determine whether suppression of blood type I IFN in critically ill COVID-19 patients is due to the ability of SARS-CoV-2 proteins to interfere with IFN signaling. This possibility is supported by the observation of Hadjadj *et al.* that down-regulated expression of type I IFNs and ISG signatures in peripheral blood are paired with up-regulated expression of genes promoting type I IFN signaling, suggesting a compensatory response to blockade of IFN signaling. Alternatively, low type I IFN may be the consequence rather than the cause of a generalized immunosuppression induced by high viral titers.

Although mouse influenza virus infection is a prototypic model of viral pneumonia, it may not precisely recapitulate the cytopathic and proinflammatory effects of SARS-CoV-2. Thus, additional experimental models should be tested to evaluate lung pathogenicity of IFNs in SARS-CoV-2 infection and to test IFNs or IFN blockade as potential therapeutic options. ■

Responses to lung viral infections

Lung alveolar epithelial cells and dendritic cells release type I interferons (IFN-α/β) and type III IFN-λ in response to viral infection. IFNs limit viral replication; however, IFN-λ signaling can cause cell death through apoptosis and impaired epithelial proliferation, which prevents tissue recovery.



ISGs, interferon-stimulated genes; SARS-CoV-2, severe acute respiratory syndrome coronavirus 2.

GRAPHIC: V. ALTOUNIAN/*SCIENCE*

REFERENCES AND NOTES

1. S. Bimonte *et al.*, *In Vivo* **34** (suppl.), 1597 (2020).
2. J. W. Schoggins, *Annu. Rev. Virol.* **6**, 567 (2019).
3. J. Major *et al.*, *Science* **369**, 712 (2020).
4. A. Broggi *et al.*, *Science* **369**, 706 (2020).
5. J. Hadjadj *et al.*, *Science* **369**, ZZZ (2020).
6. E. Andreakos, I. Zanoni, I. E. Galani, *Curr. Opin. Immunol.* **56**, 67 (2019).
7. K. Blazek *et al.*, *J. Exp. Med.* **212**, 845 (2015).
8. E. A. Hemann *et al.*, *Nat. Immunol.* **20**, 1035 (2019).
9. S. V. Kotenko *et al.*, *Nat. Immunol.* **4**, 69 (2003).
10. C. Porta *et al.*, *Oncogene* **24**, 605 (2005).
11. A. Takaoka *et al.*, *Nature* **424**, 516 (2003).
12. P. J. Planet *et al.*, *mBio* **7**, e01939 (2016).

10.1126/science.abd2208

Published by AAAS

RETROSPECTIVE

John D. Gearhart (1943–2020)

Pioneer of human pluripotent stem cell research

By **Peter J. Donovan**[1] *and* **Kenneth S. Zaret**[2]

John Gearhart, the developmental biologist who first derived human pluripotent stem cells from primordial germ cells, died on 27 May. He was 77. The discovery of one type of human pluripotent stem cell, along with the contemporaneous discovery of another type of human pluripotent stem cell by James Thomson, made it possible to grow human stem cells in a petri dish that could, in principle, develop into any body tissue. The implications for stem cell–based therapeutics were profound, as were concerns that biologists were going a step too far. John tackled the issues head on, speaking with the public, politicians, and the press with patience and determination.

John spent his early years on a family farm in Pennsylvania's Allegheny Mountains. After his father passed away when John was 6, he was sent to a boarding school for orphans in Philadelphia. He obtained a B.S. in biology in 1964 from Pennsylvania State University and studied lilacs at the University of New Hampshire, earning an M.S. in genetics in 1966. He expanded his repertoire by studying *Drosophila* genetics at Cornell University in Ithaca, New York, earning his Ph.D. in 1970. As a postdoc in the lab of embryologist Beatrice Mintz, a pioneer in the development of mouse chimeras and transgenics, John began his work in the field of study that he would continue for the rest of his life. He took a professor position at the University of Maryland School of Medicine and then at Johns Hopkins University in Baltimore, Maryland, where he later became director of multiple research programs. John was a founding member of the International Society for Stem Cell Research. In 2008, he became a professor at the University of Pennsylvania School of Medicine and director of the school's Institute for Regenerative Medicine.

The 1960s, when John began his career, were a golden time for mammalian embryology. Studies of odd testicular tumors (teratomas and teratocarcinomas) and their pluripotent stem cells, known as embryonal carcinoma cells, provided models for embryogenesis. The development of monoclonal antibodies to embryonal carcinoma cells allowed characterization and isolation of specific cell types. As a newly minted assistant professor, John initially focused on mouse genetic models of intellectual disability, but he later realized the need to generate human cells to better understand the condition.

John's research was among many studies that led to the push for developing normal pluripotent stem cell lines. Biologists Martin Evans and Gail Martin made strides toward the goal when they independently succeeded in deriving the cells from peri-implantation mouse embryos. Biologist Brigid Hogan and I (P.J.D.) then demonstrated that pluripotent stem cells, called embryonic germ cells, could be formed from primordial germ cells in mice, suggesting a different way to make human stem cells. John, along with others attempting to develop human stem cells, had to obtain access to elusive human material and overcome the fear that developing such cells could evoke negative reactions. Motivated by the potential for such a discovery to shed light on conditions such as Down syndrome, John had no hesitation in moving forward. In 1998, he led the team that successfully developed human embryonic germ cells.

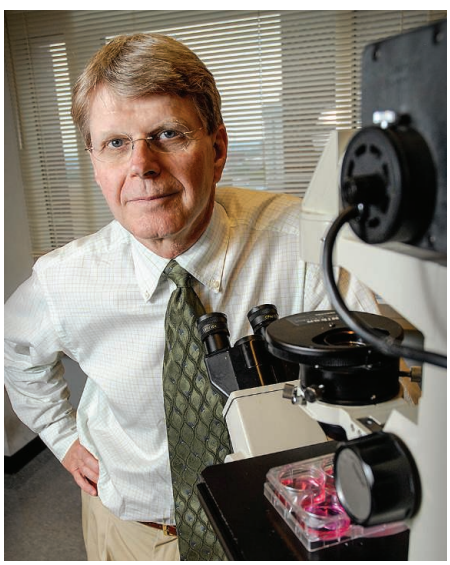


PHOTO: CANDACE DICARLO

With an intuitive understanding of the implications of stem cell research, John began asking questions about the ethical and moral issues involved even before his groundbreaking discovery. Once his landmark paper was published, he made the momentous career decision to step out of the lab and into the public sphere to talk to the world about the power and potential of stem cells. The remarkable span of topics John studied during his training was reflected in his ability to explain, discuss, and debate the issues from multiple perspectives. For years, he devoted himself to educating the public about what stem cells could and could not do. He made more than 100 trips to Washington, D.C., to lobby elected officials to fund their ethical use.

John served as an important and rare example of a scientist dedicating his life to public service. He inspired many others in the stem cell field to do the same, arguing that it is our responsibility as scientists to explain the work to the public who funds it and to inform and educate those tasked with regulating it. John was guided by the classic medical dictum "first, do no harm." His highest priority was making sure that potential clinical applications of pluripotent stem cells would be safe for patients. Yet his advocacy came at a personal risk. He received death threats and needed police protection during some of his first trips to the Capitol.

John had a warm and welcoming presence and was generous in sharing research credit. He had a mischievous sense of humor and would roar with laughter as he told stories of pranks he pulled on fellow students in his university days. John and I (P.J.D.) collaborated prior to, and as colleagues at, Johns Hopkins. A friend and mentor, he was always excited to discuss research, and he encouraged me to join him in engaging the public and their representatives. I (K.S.Z.) worked most closely with John when I began at the Institute for Regenerative Medicine in 2009. I was humbled by his relentless advocacy for the stem cell field. He never missed a chance to strengthen it and expand its reach.

John Gearhart was a generous, thoughtful person who left an indelible mark both on the stem cell field and on how science is communicated to the public. John was also a devoted father who would light up when talking about his two daughters. Despite his monumental contributions to research and science advocacy, we think he would like to be remembered as a man who cared about his treasured children. John showed that no matter what your scientific accomplishments, some things in life are more important. ■

10.1126/science.abd6915

[1]Sue and Bill Gross Stem Cell Research Center and Departments of Developmental and Cell Biology and Biological Chemistry, University of California, Irvine, CA 92697, USA. [2]Institute for Regenerative Medicine and Department of Cell and Developmental Biology, Perelman School of Medicine, University of Pennsylvania, Philadelphia, PA 19104, USA. Email: pdonovan@uci.edu; zaret@pennmedicine.upenn.edu

Published by AAAS



POLICY FORUM

CONSERVATION

Engage with animal welfare in conservation

Conservation could better promote not just the quantity of species but the quality of animal life

By **Nitin Sekar** [1] *and* **Derek Shiller** [2]

Leading conservationists have emphasized that conservation's priority is the protection of species and populations, not the welfare of individual nonhuman animals (hereafter "animals") (*1*–*3*). Although individual conservationists often harbor concern for animal welfare, conservation organizations and scientists frequently downplay or ignore the ethical implications of actions they promote that harm individual animals, from culling and sport hunting to the discontinuation of wildlife rescue from oil spills (*3*–*5*). A growing body of scientific evidence should prompt conservation organizations to reconsider their inattention to animal welfare. A wide variety of vertebrate species (and perhaps some invertebrates) are capable of experiencing physical and emotional pain, engaging in substantive relationships, and executing cognitively complex tasks (*6*–*8*), bolstering claims that animal well-being is morally significant and policy-relevant. Addressing animal welfare in conservation would be politically challenging, and given the central role of predation and competition in ecosystems, conservation science cannot altogether avoid difficult decisions; harming animals can be a necessary step toward a worthwhile goal. Despite these trade-offs, conservation organizations face a singular opportunity to reshape conservation into a discipline that promotes both the quantity of species and the quality of animal life.

Although humans are exceptional in many ways, the once-popular belief that it is unscientific to ascribe emotions or thoughts to animals is now regarded as inconsistent with evolutionary theory, experimental evidence, and any reasonable burden of proof (*9*, *10*). Commonalities in basic neural functioning across vertebrate species, ranging from fish to mammals, suggest similarities in experiential capacities (*9*, *11*). Evidence indicates that the thalamocingulate division of the limbic system and the anterior cingulate cortex evolved prior to the radiation of mammals, with all studied mammals sharing seven basic emotional systems including joy, fear, grief, parental nurturance, and playfulness. Deep neurological similarities underpin the extensive use of mammalian models in medical research, including for depression and anxiety. Further, research indicates that convergent evolution of the mammalian cortex and avian pallium has led to similar neural architecture between birds and mammals (*12*), with birds exhibiting similar forms of some affective states, consciousness, and attachment-oriented behaviors.

[1]Wildlife and Habitats Division, WWF-India, New Delhi, India. [2]The Humane League, New York, NY, USA.
Email: nitin.sekar@gmail.com

PHOTO: SYLVAIN CORDIER/MINDEN PICTURES

Free-ranging (non-native) horses in Monument Valley Tribal Park, USA. Management of free-ranging horses in North America has included creative efforts that try to reconcile conservation and animal welfare values.

Recent research has also demonstrated that various animal species are cognitively sophisticated, with findings including tool use in diverse taxa; spontaneous insight and innovative behavior; self-recognition and metacognition; collaboration to solve unfamiliar tasks; planning for future events; political strategy; empathetic concern; and the ability to recognize hundreds of human words (see supplementary materials).

TRADE-OFFS

The accumulating scientific evidence that animals have vibrant inner lives was anticipated by modern philosophers, the field of animal welfare science, and numerous world cultures that have accorded moral relevance to the quality of animal life. Yet with limited exceptions, the most prominent international conservation organizations do not attempt to promote animal welfare in their mission or vision statements or to safeguard animal welfare in their readily available public policies. This contrasts with often robust ethics policies on a range of other social and environmental issues.

From one perspective, the omission of animal welfare is befuddling. Conservationists must believe that animals deserve protection from human-induced harm; by combating habitat destruction and poaching, conservation often already promotes wild animal welfare. Officially recognizing the imperative of protecting animals as individuals could broaden conservation's constituency. Whereas the public often finds the value of biodiversity to be abstract and unrelatable, many people are concerned when human actions unnecessarily violate the freedom and well-being of wild animals. Conservation organizations have realized this, often using stories of human-induced suffering of individual animals to generate empathy and raise funds.

Yet, owing to the pervasiveness of activities that compromise animal welfare, many conservation organizations could face a variety of political risks and programmatic complications if they were to officially endorse the legitimacy of animal welfare concerns. Conservation organizations often depend on a diverse coalition of political interests, including groups that habitually harm animals. For instance, the U.S. government is one of the largest bilateral sources of funding for international conservation largely because the U.S. Congress's International Conservation Caucus is among the largest bipartisan caucuses in the legislature, with

Published by AAAS

many participants being vocal supporters of recreational hunting and fishing. For conservation organizations to acknowledge that killing animals for recreation might have moral implications (*4*) could complicate these politically important relationships in both halls of power and remote settings globally. There are well-evidenced concerns for how wild animals, especially wide-ranging species like elephants, some cetaceans, and carnivores, fare in captivity, but zoos can also inspire considerable support for wildlife conservation. Finally, conservation organizations and conservationists themselves (like other environmentalists) often regularly purchase factory farm products even though factory farms pose serious concerns about human-induced animal suffering. For conservation organizations, officially acknowledging the moral significance of animal welfare could complicate how many conservationists see themselves and generally cause discontent within their communities.

Furthermore, conservation programming takes place in complex socioecological systems that pose practical trade-offs between animal welfare and biodiversity conservation or even human rights. At its extreme, efforts to curtail hunting and fishing in the world's poor rural areas could unjustly harm communities that rely on bushmeat or wild fish for their nutrition and livelihoods. Conservation groups can be seen as elitist, out-of-touch, or culturally oppressive where they oppose the killing of dangerous animals like elephants or traditional practices like subsistence whaling—such conflicts could become more common if conservation organizations consistently prioritize the interests of individual animals. In settings where wildlife tourism is not profitable, prohibiting sport hunting could deprive organizations of funding to protect wildlife from poaching, perversely leading to an increase in the killing of wildlife. Additionally, there are many examples of direct trade-offs between animal welfare and traditional conservation objectives like preventing extinction and maintaining ecosystem function. Invasive mammals—like goats on the Galapagos or feral cats on remote islands—suffer during eradication campaigns, but there may be no other way to secure the future for endangered native species. Programs to cull white-tailed deer similarly might be necessary to ensure the regeneration of forests in the eastern United States. Ecological research and reintroduction programs can also involve duress for the animals involved.

A PRAGMATIC BALANCE

Despite challenges posed by these trade-offs, conservation science should adjust its priorities in response to the overwhelming evidence that animals think and feel. Only explicit consideration of animal welfare in decision-making can ensure that conservation organizations do not unnecessarily compromise the well-being of individual animals. As a community, conservation organizations should set in motion three processes to (i) develop consensus principles, (ii) build the evidence base to identify best practices, and (iii) develop advisory institutions that can advance best practices. Each of these should engage diverse voices, including representatives from different cultures, countries with diverse political realities, and researchers and practitioners from both animal welfare science and conservation.

The process of developing consensus principles to bring animal welfare concerns into conservation science has already begun, with ideas coming from national regulatory bodies, nongovernmental organizations concerned with wild animal welfare, the World Association of Zoos and Aquariums (*13*), animal welfare experts (*14*, *15*), and the burgeoning compassionate conservation movement (*3*, *4*). Conservation and animal welfare organizations should collaborate to systematically refine and select practically applicable ethical principles. Given the diverse cultural practices and economic systems that involve harm to animals, prohibitions on animal captivity, killing animals, and eating meat are unlikely to gain consensus support—but that need not prevent constructive discussions on minimizing human-induced suffering of animals, general agreement to minimize suffering during killing, and principles guiding the circumstances when killing animals might be acceptable. Animal welfare principles can alert conservationists to when the harm an activity causes to individual animals outweighs the benefits to biodiversity.

Second, international conservation and animal welfare organizations should fund the development of an evidence base for how best to engage with wildlife in a way that minimizes avoidable suffering. Again, scientists have begun this process (*4*, *13*, *14*)—but the evidence compiled must come from more diverse settings and situations and reflect practical limitations and trade-offs faced by conservation organizations in places where even human rights are not adequately realized. In addition to improving conservation practice, such evidence would help animal welfare organizations recognize where the protection of biodiversity, ecological function, and local communities might necessitate harming individual animals. This evidence review process would also highlight areas of research that could help resolve ethical dilemmas posed by conservation programming.

International conservation bodies should also work with animal welfare scientists to establish advisory committees that review (voluntarily submitted) conservation project proposals to assess whether they satisfy principles of animal welfare. The process could be modeled as a voluntary version of the Institutional Animal Care and Use Committee that reviews animal research in the United States, working to promote best practices, build precedent, and collect real-life cases that can improve the evidence base. The committees' recommendations should provide a basis for informed debate about the trade-offs between wildlife conservation and animal welfare, helping better define whether the suffering of individual animals might be commensurate with conservation benefits (*14*). Over time, the cumulative experience of these committees should allow conservation organizations to recommend evidence-based animal welfare safeguards that can fit into the broader category of social and environmental safeguards, much like policies striving to minimize carbon emissions or protect human rights in conservation and development.

Inevitably, these processes will take time. In the meanwhile, conservation organizations can take two steps toward building a better world for all animals: publicly commit to considering animal welfare in their decisions, and adopt policies against the purchase of factory farm meat where less harmful alternatives are available. Given the implications of factory farming not just for animal welfare but also for climate change and biodiversity, such action would further demonstrate the sincerity of conservation organizations' pursuit of a more just and sustainable planet. ■

REFERENCES AND NOTES

1. M. E. Soule, *Bioscience* **35**, 727 (1985).
2. P. Kareiva, M. Marvier, *Bioscience* **62**, 962 (2012).
3. D. Ramp, M. Bekoff, *Bioscience* **65**, 323 (2015).
4. A. D. Wallach *et al.*, *Conserv. Biol.* **32**, 1255 (2018).
5. J. A. Estes, M. T. Tinker, in *Effective Conservation Science: Data Not Dogma*, P. Kareiva, M. Marvier, B. Silliman, Eds. (Oxford Univ. Press, 2017), pp. 128–134.
6. V. A. Braithwaite, P. Boulcott, *Dis. Aquat. Organ.* **75**, 131 (2007).
7. I. B.-A. Bartal *et al.*, *Science* **334**, 1427 (2011).
8. N. S. Clayton, A. Dickinson, *Nature* **395**, 272 (1998).
9. J. Panksepp, *PLOS ONE* **6**, e21236 (2011).
10. G. A. Mashour, M. T. Alkire, *Proc. Natl. Acad. Sci. U.S.A.* **110** (suppl. 2), 10357 (2013).
11. T. E. Feinberg, J. Mallatt, *Front. Psychol.* **4**, 667 (2013).
12. A. B. Butler, R. M. J. Cotterill, *Biol. Bull.* **211**, 106 (2006).
13. D. J. Mellor *et al.*, Caring for Wildlife: The World Zoo and Aquarium Animal Welfare Strategy (WAZA Executive Office, 2015).
14. S. Dubois *et al.*, *Conserv. Biol.* **31**, 753 (2017).
15. J. O. Hampton *et al.*, *Conserv. Biol.* **33**, 751 (2019).

ACKNOWLEDGMENTS

We thank H. Telkänranta, N. Shah, S. Sekar, N. Mohapatra, D. Mistree, M. Malik, A. Lerner, K. Kolappa, S. Kishore, P. Hannam, G. Fricchione, M. Doshi, P. Chanchani, and four anonymous reviewers. This piece reflects the views of the authors and not the official positions of their organizations.

SUPPLEMENTARY MATERIALS

science.sciencemag.org/content/369/6504/629/suppl/DC1

10.1126/science.aba7271

Published by AAAS



Mass extinctions, such as the one that killed the *Quetzalcoatlus northropi*, emphasize the importance of biodiversity.

SCIENCE AND SOCIETY

The unlikely role of dinosaurs in the diversity discourse

Western civilization's appreciation of variety may be related to the discovery of sudden extinction events

By **Jörg Matthias Determann**

Who would disagree that diversity is a good thing? The United Nations has promoted biological and cultural diversity as ideals for decades. *Scientific American* has asserted that diversity is essential for excellence (*1*). Countries such as Qatar, where I live, have put much effort into diversifying their economies. McKinsey and Company, a firm hardly known for being at the forefront of social justice, has found that businesses with more diverse workforces perform better financially (*2*). To be sure, promoters of equity and inclusion have also been described by critics as forming part of a diversity "machine" (*3*) or "industry" (*4*). However, most of us probably value plurality and variety.

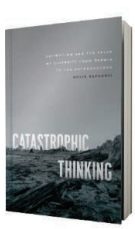
Where does our appreciation of diversity come from? In his new book, *Catastrophic Thinking*, historian of paleontology David Sepkoski answers this question by delving into our collective imagination of the deep past. He quotes from archival documents and scientific reports and considers apocalyptic fiction in his analysis. While the tone of the narrative remains as serious as the topic, references to popular culture make it accessible.

Sepkoski argues that the increase in diversity discourse that began in the 1980s was linked to the discovery that sudden extinction events, such as the one at the Cretaceous–Tertiary boundary more than 60 million years ago, could drastically reduce the number of species on Earth. In such a scenario, the normal rules of natural selection do not apply. Entire taxa could disappear within a short period of time through no fault of their own. Paleontologists thus reimagined life on Earth as precarious, and they recognized mass extinctions in the fossil record as the cause of sudden drops in diversity.

This "new catastrophism" of the late 20th century was different from the Darwinian understanding of extinction as a gradual and inevitable process in which natural competition slowly weeded out the unfit. In the struggle for life, Charles Darwin and his successors thought that declines in some populations were simply making way for those that were better adapted to particular habitats. As new species replaced older ones, nature was perceived to be in balance, if not on a path of improvement. Conservation efforts during this period were thus confined to charismatic animals, with little consideration to broader biological diversity.

Sepkoski draws on distinctive personal insights into the research on extinction events to frame his narrative. The son of Jack Sepkoski, a University of Chicago paleontologist who was a central figure in extinction research in the 1970s and 1980s, he writes with deep familiarity tempered by professional distance. His father, we learn, combined a fascination for fossils with a knack for mathematical methods and a dedication to long-term data collection. Over the course of a decade, the elder Sepkoski built the first computerized record of marine fossils. Published in 1982, this database revealed larger patterns of diversification and extinction.

Sepkoski acknowledges that "new catastrophism" is not the only explanation for the rise in popularity of the concept of diversity. Contemporary debates about equity and inclusion, for example, are rooted in longer political, economic, and legal histories that fall outside the purview of this book. Nevertheless, he convincingly demonstrates that an ecological perspective has profoundly shaped our views of biological and social communities. From the 1980s onward, global conservation efforts aimed at biodiversity, and cultural diversity soon gained traction.



Catastrophic Thinking
David Sepkoski
University of Chicago Press, 2020. 360 pp.

Sepkoski's magisterial work will hopefully serve as an inspiration for more comprehensive histories of the concept of diversity. While very detailed, his narrative focuses on Western voices. Undoubtedly, those on the receiving end of European imperialism had visions of catastrophic collapse long before the specter of mass extinction became part of broader science and culture. This shortcoming aside, *Catastrophic Thinking* is essential reading for those seeking to understand the origin of one of the most powerful concepts under consideration today. ■

The reviewer is at the Department of Liberal Arts and Sciences, Virginia Commonwealth University School of the Arts in Qatar, Doha, Qatar. Email: jmdetermann@vcu.edu

REFERENCES AND NOTES

1. F. Guterl, *Scientific American*, 1 October 2014.
2. V. Hunt, D. Layton, S. Prince, "Why diversity matters," McKinsey and Company, 1 January 2015.
3. F. R. Lynch, *Society* **34**, 32 (1997).
4. A. Gardner, *Areo*, 10 September 2019.

10.1126/science.abd0109

IMAGE: STOCKTREK IMAGES/NATGEO IMAGE COLLECTION

Published by AAAS

CONSERVATION

Saving species, one roll at a time

Players collaborate to rescue endangered animals in a new conservation-themed game

By **Angela Chuang**

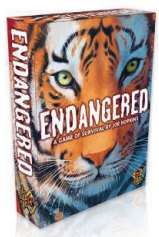
Species conservation evokes visions of khaki-clad antipoaching teams, zoo breeding programs, and volunteer-led beach cleanups. Certain furred, fanged, and feathered creatures may also spring to mind, as do the many fundraising pleas made on their behalf. *Endangered* is a new board game that brings together these elements of conservation and more as players cooperatively work to convince an international panel of ambassadors to vote "yes" on passing a resolution to save a target species.

This is no simple task, because each ambassador represents a different country with individual demands. They may refuse to support the resolution if the initiative lacks sufficient funds, if habitat destruction is not addressed, or if a large enough population of the species under consideration exists in the wild. However, the need to influence ambassadors often fades to the background as players are immersed in mitigating immediate threats such as oil spills and forest clear-cutting.

Conservation is a highly multidisciplinary and cooperative enterprise. *Endangered* acknowledges these characteristics by placing all players on the same team, with each person assuming a specific role, such as zoologist, environmental lawyer, or philanthropist. Each role brings special abilities into play, from lobbying power to knowledge of a species' migration behaviors.

The base game has a two-sided board that allows players to mount conservation efforts for either tigers or sea otters, with each module incorporating species-specific gameplay. (In three upcoming expansions, players will be able to save California condors, sea turtles, tapirs, polar bears, and more.)

In the tiger module, the board simulates a forest habitat, with wooden tiger figurines occupying various spaces on a grid. Deforestation tiles fragment the landscape, multiplying over the course of the game, which limits the creatures' movement. Tigers caught in deforested regions become collateral damage, which creates incentives for players to strategically move them away from at-risk areas. Players can encourage population growth by moving two tiger pieces to the same square, although mating success is not guaranteed. The game even incorporates some basic tiger biology. For example, because tigers are solitary creatures, pairs must separate after reproductive events and occupy their own spaces on the board. Offspring similarly require their own spaces within the shrinking habitat, which creates spatial puzzles for players to solve.



Endangered
Joe Hopkins
Grand Gamers Guild, 2020.



As in real life, strategic planning and chance combine to determine a species' fate.

Player actions, animal reproductive success, and habitat destruction are all determined by dice rolls, an agonizing reminder that the best-laid plans can only bring one so far. Adding to the uncertainty, a random "impact" card is revealed after each player's turn. One such card, the "clear-cutting" card, hastens the rate of deforestation. The "poachers" card, meanwhile, instantly removes tigers from the board. In a darkly humorous imitation of life, the mundanely named "bureaucracy" card packs one of the stronger punches in the game: It continuously slows the pace of actions that players can take.

Facts printed on the impact cards educate and provide fodder for discussing conservation. The "government upheaval" card, for example, describes how strict antipoaching controls of Siberian tigers loosened after the collapse of the Soviet Union in 1991. Players who scoff at the seemingly random "shark attack" card in the otter module learn that human fishing activities can deplete otter prey sources, leading them to expand their range into more dangerous territories. As they do in real life, indirect human activities can act as the final nail in the coffin for species imperiled on multiple fronts.

It is tempting to pour one's efforts into addressing the most visible issues, such as widening swaths of ocean pollution in the otter module, but the all-important vote by the international panel determines whether the players ultimately win or lose the game. As the game makes clear, in the end, influencing international policy is just as critical for saving species as local efforts.

Despite its cooperative nature, *Endangered* sets a high bar when it comes to strategy. The trade-offs that players are forced to make between staving off imminent species extinction and working toward more sustainable long-term goals create tough but satisfying team decisions. The game is by no means easy, but it feels accessible and would likely be enjoyable to board gamers of all experience levels. Its obvious educational component also makes it a promising candidate for classrooms and appropriate to pair with discussions on conservation challenges.

The take-home messages from this game are clear: Long-term conservation cannot be carried out by a few lone actors, habitat restoration cannot be maintained without funding, and nothing is sustainable without long-term solutions. ■

The reviewer is at the University of Florida Institute of Food and Agricultural Sciences Citrus Research and Education Center and the Department of Entomology and Nematology, University of Florida, Lake Alfred, FL 33850, USA.
Email: angelachuang@utk.edu

10.1126/science.abc7387

PHOTO: MARC SPECTER/GRAND GAMERS GUILD

Published by AAAS



Reopening Brazil's Highway BR-319 puts Amazon ecosystems and Indigenous peoples at risk.

PHOTO: UESLEI MARCELINO/REUTERS/NEWSCOM

Edited by **Jennifer Sills**

The Amazon's road to deforestation

Brazil's Amazon region is undergoing a period of environmental setback, during which large infrastructure projects are being pushed forward and environmental protection is being reduced (*1*). One of these projects is the reopening of Highway BR-319, which was built in 1973 but abandoned in 1988. The road connects Porto Velho, located in an area of abundant deforestation, to Manaus in the heart of the Amazon rainforest (*2*, *3*). With BR-319 and its planned side roads open to traffic, the deforested area would likely increase to more than 1200% of the 2011 level by 2100 (*2*). The road and related deforestation would affect 63 official Indigenous lands, which are home to 18,000 Indigenous people (*3*). The huge block of forest opened to deforestation by these roads contains a carbon stock that, if released, would greatly increase the chances that global mitigation efforts will fail to contain climate change (*4*).

A judicial decision that is no longer subject to appeal ruled that environmental studies must be carried out before paving a part of the highway designated as "lot C" (*5*). However, on 24 June, the federal government opened bidding for paving this stretch of road (*6*). Brazil's Federal Public Ministry characterized this breach of a judicial decision as "bad faith" and an "affront" to the judiciary (*7*). The justification by a representative of the executive branch was that the paving would not cause an increase in the traffic on the highway (*8*), an opinion without any technical basis. Paving highways in the Amazonian interior has been shown to increase the number and size of vehicles and to result in increased migration, land speculation, and deforestation (*9*–*11*).

The failure of the government to abide by the judicial decision will set a dangerous precedent for other mega-developments in the Amazon, including hydroelectric dams and the Barão do Rio Branco project, which would build a road through a series of areas protected for traditional peoples and for biodiversity (*12*). If Highway BR-319 is paved before the required environmental studies have been conducted, it will be a decisive indicator of Brazil's reluctance to comply with its commitments under the climate and biodiversity conventions, and it will likely accelerate anthropogenic climate change.

Lucas Ferrante[1]* and Philip Martin Fearnside[2]
[1]Ecology Graduate Program, National Institute for Research in Amazonia (INPA), Manaus, Amazonas, Brazil. [2]Department of Environmental Dynamics, INPA, Manaus, Amazonas, Brazil.
*Corresponding author.
E-mail: lucasferrante@hotmail.com

REFERENCES AND NOTES

1. L. Ferrante, P. M. Fearnside, *Environ. Conserv.* **46**, 261 (2019).
2. M. dos Santos Júnior *et al.*, "BR-319 Como Propulsora de Desmatamento: Simulando o Impacto da Rodovia Manaus-Porto Velho" (Instituto do Desenvolvimento Sustentável da Amazônia, 2018); https://idesam.org/publicacao/simula-desmatamento-br319.pdf [in Portuguese].
3. L. Ferrante *et al.*, *Land Use Pol.* **94**, 104598 (2020).
4. E. M. Nogueira *et al.*, *Glob. Change Biol.* **21**, 1271 (2015).
5. Tribunal Regional Federal da Primeira Região, "Numeração Única 0005716.70.2005.4.01.3200" (2019); http://philip.inpa.gov.br/publ_livres/Dossie/BR-319/Documentos%20Oficiais/25.EMENTA%20E%20AC%C3%93RD%C3%83O%20(EMBARGOS%20DE%20DECLARA%C3%87%C3%83O).pdf [Portuguese]
6. Departamento Nacional de Infraestrutura de Transportes, "Aviso de Licitação, RDC Eletrônico nº 216/2020," *Diário Oficial da União* (2020); www.in.gov.br/web/dou/-/aviso-de-licitacao-263222480 [in Portuguese].
7. Justiça Federal da 1ª Região, "Processo Judicial Eletrônico Número: 1016749-49.2019.4.01.3200" (2020); www.fatoamazonico.com/wp-content/uploads/2020/07/Impugnacao-protocolada.pdf.pdf [in Portuguese].
8. R. Hofmann, "Texts sent on June 24, 2020 to the 'Fórum de Sustentabilidade da Rodovia BR-319' WhatsApp group organized by the Federal Public Ministry" (2020); http://philip.inpa.gov.br/publ_livres/Dossie/BR-319/Outros%20documentos/Rose_hofmann_textos_Grupo_Forum_BR-319.pdf [in Portuguese].
9. W. F. Laurance *et al.*, *J. Biogeogr.* **29**, 737 (2002).
10. D. C. Nepstad *et al.*, *For. Ecol. Manag.* **154**, 395 (2001).
11. A. S. P. Pfaff *et al.*, *J. Reg. Sci.* **47**, 109 (2007).
12. F. Wenzel, "Asfaltando a Amazônia," *Piauí* (2020); https://piaui.folha.uol.com.br/asfaltando-a-amazonia/ [in Portuguese].

10.1126/science.abd6977

Smoke pollution's impacts in Amazonia

The combination of increasing Amazon deforestation and the specter of drought now threatens widespread fire and respiratory health risks that could worsen the coronavirus disease 2019 (COVID-19) pandemic, endangering all Amazonians, but particularly vulnerable traditional and rural peoples (*1*, *2*).

Deforestation in the Brazilian Amazon between January and June (3070 km^2) was 25% higher than it was during the same period in 2019 (2446 km^2) and 46% higher than the 4-year average of January through June from 2016 to 2019 (2108 km^2) (*3*). Within Indigenous lands, which make up 23% of the Brazilian Amazon (*4*),

Published by AAAS

deforestation quadrupled in the past 4 years (from 105 km^2 in 2016 to 497 km^2 in 2019) (*5*). Fire is intrinsic to the deforestation process—forest is left to dry after cutting and then burned to prepare for agriculture. The majority of deforested land in 2020, and 45% of the trees cut in 2019, has remained unburned (*4*). Between July and December this year, under dry conditions, most of this land will be set ablaze (*6*).

Current indices predict a severe western Amazon drought in mid- to late 2020 (*2*). In drought years, deforestation fires often escape into surrounding forest understories. The smoke arising in large quantities from both deforestation and understory fires is extremely toxic, causing shortness of breath, coughing, and lung damage. Fires in the Amazon are responsible for 80% of increases in fine particulate pollution ($PM_{2.5}$) regionally, affecting 24 million Amazonians (*7*). The likely relationship between air pollutants linked to fire, such as $PM_{2.5}$, and COVID-19 infection (*8*, *9*) suggests that fire could aggravate the current COVID-19 crisis in Amazonia, where infection rates are already high (1 in 100 in June) (*10*). Indigenous peoples are at particular risk, given that they are currently suffering COVID-19 mortality rates that are 1.5 times the Brazil-wide average (*11*).

To avoid a combination of smoke and COVID-19 that could be catastrophic, Brazil must repeat in 2020 its past successes as an international leader curbing deforestation and fire (*12*). A moratorium on deforestation and associated burning in at-risk areas and strong enforcement from current infrastructure are urgently needed.

Gabriel de Oliveira[1]*, Jing M. Chen[1], Scott C. Stark[2], Erika Berenguer[3,4], Paulo Moutinho[5,6], Paulo Artaxo[7], Liana O. Anderson[8], Luiz E. O. C. Aragão[9,10]

[1]Department of Geography and Planning, University of Toronto, Toronto, ON, Canada. [2]Department of Forestry, Michigan State University, East Lansing, MI 48824, USA. [3]Environmental Change Institute, University of Oxford, Oxford, UK. [4]Lancaster Environment Centre, Lancaster University, Lancaster, UK. [5]Amazon Environmental Research Institute (IPAM), Brasília, DF, Brazil. [6]Woods Hole Research Center, Falmouth, MA 02540, USA. [7]Institute of Physics, University of São Paulo, São Paulo, SP, Brazil. [8]National Center for Monitoring and Early Warning of Natural Disasters (CEMADEN), São José dos Campos, SP, Brazil. [9]National Institute for Space Research (INPE), São José dos Campos, SP, Brazil. [10]Department of Geography, College of Life and Environmental Sciences, University of Exeter, Exeter, UK.
*Corresponding author.
Email: gabriel.deoliveira@utoronto.ca

REFERENCES AND NOTES

1. J. Barlow, E. Berenguer, R. Carmenta, F. França, *Glob. Chang. Biol.* **26**, 319 (2020).
2. L. E. O. C. Aragão, C. H. L. Silva Junior, L. O. Anderson, "Brazil's challenge to restrain deforestation and fires in the Amazon during COVID-19 pandemic in 2020: Environmental, social implications and their governance" (Tech. Rep. National Institute for Space Research, 2020).
3. TerraBrasilis, DETER (Notices), Analyses—Legal Amazon (2020); http://terrabrasilis.dpi.inpe.br/app/dashboard/alerts/legal/amazon/aggregated/#. To find total deforestation, select "Civil Year" above the "Monthly variation of DETER project area" line graph, then select the green box below the graph for each month to include. Scroll down to the "Areas by Years" bar graph to see the totals for those months in each year.
4. W. S. Walker, *Proc. Natl. Acad. Sci. U.S.A.* 10.1073/pnas.1913321117 (2020).
5. TerraBrasilis, PRODES (Deforestation), Analyses—Legal Amazon, (2020); http://terrabrasilis.dpi.inpe.br/app/dashboard/deforestation/biomes/legal_amazon/increments. At the top, select "Indigenous Areas." Total deforestation by year can be found in the "Deforestation increments—Legal Amazon—Indigenous Areas" bar graph.
6. P. Moutinho *et al.*, "The Amazon in flames: Deforestation and fire during the COVID-19 pandemic" (Tech. Rep. Amazon Environmental Research Institute, 2020).
7. C. L. Reddington *et al.*, *Nat. Geosci.* **8**, 768 (2015).
8. Z. Yongjian, X. Jingu, H. Fengming, C. Liqing, *Sci. Total Environ.* **727**, 138704 (2020).
9. D. Fattorini, F. Regoli, *Environ. Pollut.* **264**, 114732 (2020).
10. Ministry of Health of Brazil, "Coronavírus Brasil" (2020); https://covid.saude.gov.br/ [in Portuguese].
11. M. Fellows *et al.*, "They are not numbers: They are lives! COVID-19 threatens Indigenous peoples in the Brazilian Amazon" (Tech. Rep. Amazon Environmental Research Institute, 2020).
12. P. Brando *et al.*, *Flora* **268**, 1 (2020).

10.1126/science.abd5942

Investors can help rein in Amazon deforestation

The Brazilian Amazon—the largest tropical rainforest in the world—has reached its highest level of deforestation since 2008 (*1*). In 2019, 10,897 km^2 of land were deforested, a 50.7% jump over the previous year (*1*). A combination of threats, including tens of thousands of forest fires (*2*), expanding road networks (*3*, *4*), weakened environmental laws (*5*, *6*), and a failure to enforce environmental laws and regulations (*6*), is responsible. Given the staunchly pro-development policies of Brazil's current government, a coalition of key actors in the financial sector is needed to help protect the embattled Amazon rainforest.

Efforts of corporations and investors to slow Amazon deforestation are gaining momentum. On 7 July, executives of nearly 40 Brazilian corporations urged the Brazilian government to combat illegal deforestation and warned that Brazil's image and business abroad were suffering as a result (*7*). This plea comes on the heels of a call by 29 global investors, managing $3.7 trillion in assets, to protect the Amazon rainforest and its Indigenous peoples (*8*). Global efforts to slow forest loss are also targeting corporations operating in Amazonia. In October 2019, almost 250 international investors, with $17.2 trillion in assets, called on firms to urgently slow deforestation within their Brazilian operations and supply chains (*9*). Moreover, some international partners of Brazil's agribusiness, such as the European Union, are adopting measures to limit imports of commodities from Brazil that promote illegal deforestation (*10*).

NEXTGEN VOICES: SUBMIT NOW

Funding quandary

Add your voice to *Science*! In this NextGen Voices survey, a reader asks for your advice! Have you been in this situation or one like it? Do you have any tips that you would like to share? Become a NextGen Voices peer mentor by contributing your thoughts!

Dear NextGen Voices peer mentors,

I am a young researcher with several research proposals in hand. However, I have no funding, and my grant applications are still pending. My contract requires me to publish several papers a year, but I can't conduct experiments or produce reliable results without funding. With restrictions in place for coronavirus disease 2019 (COVID-19), I also do not have as much access to my lab as I would under normal circumstances. How can I use this time most effectively to ensure that I can stay in academia long-term?

Sincerely,

Funding Fix

To submit, go to www.sciencemag.org/nextgen-voices
Deadline for submissions is 21 August. A selection of the best responses will be published in the 2 October issue of *Science*. Submissions should be 150 words or less. Anonymous submissions will not be considered.

Published by AAAS

These corporations and investors have called for the Brazilian government to demonstrate a clear commitment to eliminating deforestation and protecting the rights of Indigenous peoples. However, the government's principal response so far—banning fires in the Amazon for 120 days (*11*)—will not halt or reverse the deforestation crisis. Instead, Brazil should follow the lead of investors (*9*) and scientists (*10*) who have urged the government to improve the systems that monitor Amazon land use and agricultural commodity production. Beyond this, Brazil needs to follow the scientific guidelines for conservation and sustainable use produced by the Science Panel for the Amazon—a program funded by the United Nations Sustainable Development Solutions Network that encompasses 150 authorities, including scientists, political planners, and Indigenous leaders (*12*).

Alison G. Nazareno[1]* and William F. Laurance[2]
[1]Department of Genetics, Ecology and Evolution, Federal University of Minas Gerais, Belo Horizonte, Minas Gerais, Brazil. [2]Centre for Tropical Environmental and Sustainability Science, College of Science and Engineering, James Cook University, Cairns, QLD 4878, Australia.
*Corresponding author: E-mail: alisongn@ufmg.br

REFERENCES AND NOTES

1. TerraBrasilis, PRODES (Deforestation), Analyses—Legal Amazon, "Deforestation increments – Legal Amazon – States" (2020); http://terrabrasilis.dpi.inpe.br/app/dashboard/deforestation/biomes/legal_amazon/increments.
2. H. Escobar, *Science* **365**, 853 (2019).
3. T. Vilela *et al.*, *PNAS* **117**, 7095 (2020).
4. W. F. Laurance *et al.*, *Science* **291**, 438 (2001).
5. L. Ferrante, P. M. Fearnside, *Science* **368**, 481 (2020).
6. E. J. A. L. Pereira *et al.*, *Land Use Pol.* **17**, 122 (2020).
7. M. de Sousa, "Brazil corporations urge action on illegal logging in Amazon," *ABC News* (2020).
8. T. Phillips, "Trillion-dollar investors warn Brazil over 'dismantling' of environmental policies," *The Guardian* (2020).
9. "Investor statement on deforestation and forest fires in the Amazon" (2019); www.ceres.org/sites/default/files/Investor%20statement%20on%20deforestation%20and%20forest%20fires%20in%20the%20Amazon_1%20Oct%202019.pdf.
10. R. Rajão *et al.*, *Science* **369**, 246 (2020).
11. J. Gonzales, "Brazil bows to pressure from business, decrees 120-day Amazon fire ban," *Mongabay* (2020).
12. S. Hanbury, "Scientists launch ambitious conservation project to save the Amazon," *Mongabay* (2020).

10.1126/science.abd7578

TECHNICAL COMMENT ABSTRACTS

Response to Comment on "Activation of methane to CH_3^+: A selective industrial route to methanesulfonic acid"

Christian Díaz-Urrutia and Timo Ott

Roytman and Singleton argue that our proposed electrophilic mechanism for the sulfonation of methane in superacid conditions is "not plausible." We clarify certain terms that might have caused misinterpretation of our proposed mechanism and supplement the discussion. We reaffirm that an electrophilic mechanism may be operative under our reaction conditions.

Full text: dx.doi.org/10.1126/science.aax9966

Where Science Gets Social.

AAAS.ORG/COMMUNITY






AAAS' Member Community is a one-stop destination for scientists and STEM enthusiasts alike. It's "Where Science Gets Social": a community where facts matter, ideas are big and there's always a reason to come hang out, share, discuss and explore.

Member COMMUNITY AAAS

AMERICAN ASSOCIATION FOR THE ADVANCEMENT OF SCIENCE

Published by AAAS

Cite as: C. Díaz-Urrutia, T. Ott, *Science* 10.1126/science.aax9966 (2020).

Response to Comment on "Activation of methane to CH_3^+: A selective industrial route to methanesulfonic acid"

Christian Díaz-Urrutia and Timo Ott

R&D Department, Chemical Division, Grillo-Werke AG, 47169 Duisburg, Germany.

***Corresponding author. Email: t.ott@grillo.de**

Roytman and Singleton argue that our proposed electrophilic mechanism for the sulfonation of methane in superacid conditions is "not plausible." We clarify certain terms that might have caused misinterpretation of our proposed mechanism and supplement the discussion. We reaffirm that an electrophilic mechanism may be operative under our reaction conditions.

The main theme of the initial communication of our results as an industrial chemistry report in *Science* (*1*) was the evolution of our process for the direct sulfonation of methane to value-added methanesulfonic acid (MSA) from the bench scale to an industrial pilot plant setting. This scalable process is a one-step reaction that uses standard industrial high-pressure and distillation materials and constitutes a milestone in the search for methods to use natural gas beyond heating and flaring (*2*). In addition to the experimental observations presented within our report, the long-term reproducibility and selectivity observed at the pilot plant scale led us to propose that an electrophilic mechanism might be operative, rather than a free radical pathway.

Indirect evidence for transient $[CH_3]^+$ formation has been widely discussed in the literature in the context of several transformations such as alkylations and decomposition of the nonclassical carbocation $[CH_5]^+$, leading to H_2 and $[CH_3]^+$ in superacid media (*3*, *4*). Precedent for the first step of our proposed electrophilic mechanism can be found in the work of Olah *et al.* in which HOOH is protonated in highly acidic conditions to form $HOOH_2^+$ (*3*, *5*). In the presence of methane, $HOOH_2^+$ formally inserts into one of the C-H bonds to exclusively form protonated methanol. More recently, an in-depth density functional theory (DFT) study of this reaction showed the low energy barrier for the hydroxylation of alkanes to alcohol by $HOOH_2^+$ (*6*). The high reactivity associated with superelectrophilic $HOOH_2^+$ is due to the low energy of the σ* orbital of the peroxo bond (−9.18 eV), which is the same as, or even lower than, that of the highest occupied molecular orbital (HOMO) energy of alkanes (−10.8 to −8.0 eV). This enables the nucleophilic transfer of σ electrons of the alkane C-H bond to the σ* orbital of the peroxo bond. According to calculations (*6*), this step results in the formation of a transient carbenium ion and the formation of two water molecules from $HOOH_2^+$. Under these conditions, the resulting carbenium ion is hydrated to form protonated methanol (*6*). This example aims to show the role of the carbenium ion in these transformations. To expand on the idea presented in our report, we proposed the formation of a transient, reactive, heavily solvated species with carbenium ion character based on the reaction between methane and sulfonyl peroxide (e.g., MMSP, DMSP) or any other peroxide in this respect (e.g., H_2O_2), in an analogous fashion to the reactivity described above. We do not propose that a discrete $[CH_3]^+$ species would exist at appreciable concentrations or would have a lifespan that would be observable by any spectroscopic means. The previous literature typically depicts $[CH_3]^+$ when referring to reactive intermediates of the same nature (*4*).

There are three important points to address in terms of the reactivity of the posited superelectrophilic species and solvent:

1. The solvent system used is 33 to 36% oleum, and the reactions are run with CH_4 at high pressure. At 50°C, the major component of the reaction medium is expected to be $H_2S_2O_7$ (*7*).

2. The Hammett acidity values (H_0) of oleum solutions increase drastically with changes in the concentration of SO_3. For example, 5% and 50% oleum solutions have H_0 values of −12.73 and −14.44, respectively, indicating that the reaction medium acidity strongly depends on the SO_3 content (*3*). Our unpublished results as well as previous reports (*8*) have shown that increases in yields and conversions to MSA are obtained when Lewis acids (e.g., $AlCl_3$) or strong superacids (e.g., magic acid FSO_3H-SbF_5, triflic acid) are used (see below).

3. The reaction conditions have a substantial influence on product distribution, irrespective of the catalyst or initia-

tor used. For instance, at higher temperatures or higher SO_3 concentrations, MSA is dehydrated to its anhydride [$CH_3S(O_2)OS(O_2)CH_3$], which is subsequently converted to methyl bisulfate (MBS) (*9*, *10*). We have observed the conversion of MSA anhydride into MBS in hot oleum solutions.

We agree that at this point there is not conclusive evidence to describe with certainty the proposed electrophilic species under our reaction conditions, but this argument does not necessarily discard the involvement of these so-called species in the sulfonation of methane. The cationic chain reaction as proposed in our original publication might not directly involve a transient $[CH_3]^+$.

Roytman and Singleton stated that MBS is "an unreactive thermodynamic sink in these reactions," but they provided no context or reaction conditions to which they were referring (*11*). Similar systems using ethane have shown that ethylbisulfate, $CH_3CH_2OSO_3H$, is an intermediate or kinetic product in sulfonation reactions under varying conditions (*12*, *13*). For example, ethylbisulfate is proposed to be in equilibrium with $CH_3CH_2^+$ and $^-OSO_3H$ under acidic conditions (H_2SO_4 98%, 150° to 180°C), affording $HO_3SCH_2CH_2OSO_3H$ as the thermodynamic product (Fig. 1). Interestingly, this compound ($HO_3SCH_2CH_2OSO_3H$) is the dominant product, although in small yields, in the reaction of ethane in ~30% oleum at 90°C in the absence of any initiator or catalyst (*10*). It is important to note that ^{13}C labeling experiments indicated that scrambling occurred through the intermediacy of ethyl cation (via rapid 1,2-H shift), ethylene, or both (*14*). The mechanism of the organic reaction depicted in Fig. 1 remains unknown.

We admit that oversimplification of our original report and proposed mechanism led to a miscommunication of our ideas (*1*). The transition or intermediate state depicted in the publication was not drawn properly and should show an initial C-O bond formation between $[CH_3]^+$ and SO_3: $[H_3C–OSO_2]^+$. The depiction of the transition or intermediate state was simplified during the peer review process, but originally it explicitly showed C-O bond formation. A formal correction to the paper has been made. This could be followed by rearrangement that precludes formation of a sulfite intermediate. The most likely pathway could be an electrophilic concerted mechanism to afford the C-S bond in MSA. We do not yet have additional insights into the specific steps that follow; this remains unknown. Roytman and Singleton incorrectly stated that "[the authors] noted that bond formation at the oxygen atom could not account for the formation of MSA…" (*11*). In fact, we did not discard a C-O bond formation pathway to produce MSA; we only emphasized that a sulfite intermediate might not be the preferred route (*1*). The energy argument outlined by Roytman and Singleton is based on "…energies derived from heat of formation…" (*11*) in the gas phase, which does not account for the proposed intermediacy of oxenium ions reported by Olah *et al.* in electrophilic substitution reactions with $HOOH_2^+$ and HO_3^+ (*3*, *5*). We recognize that our proposed mechanism at this point leaves some questions unanswered, especially the stabilization of certain components and structures under real oleum conditions, but we believe that some of the concepts presented are very important to consider in future studies of this work. The counterargument based on a radical pathway, which is favored by Roytman and Singleton, is not supported by enough experimental evidence to disprove an alternative electrophilic pathway. At this point, both pathways might be valid to explain this transformation, although we strongly believe that the superacidic electrophilic activation might be more representative of our experimental results.

We will not address the computational results presented by Roytman and Singleton (*11*) because these were performed after we published our original work; perhaps they merit a full paper elsewhere. Without getting into specific details, their calculations used implicit solvent corrections that have led to inaccuracies in polar systems, especially in very polar acid solvents (*13*), and the authors did not consider the complex and variable structure of oleum where free SO_3 is not observed in the range of concentrations used in our experiments (*3*).

Roytman and Singleton correctly stated (*11*) that previous studies have proposed a free radical mechanism for the synthesis of MSA (*8*, *10*). However, these experiments differ in many ways from our experimental conditions. Physical parameters (e.g., temperature, pressure, concentration, type and size of reactor) as well as chemical conditions (e.g., metal peroxide salts and metal promoters) were different, and they were run on small scales (e.g., 3 ml of fuming H_2SO_4). The reaction mechanism in those cases is not well understood (*8*, *10*). In our publication, we proposed an alternative electrophilic pathway that might be operative within a very limited set of reaction conditions (*1*). Under strictly oxygen- and peroxide-free conditions, we performed the sulfonation reaction with catalytic amounts of magic acid (FSO_3H-SbF_5) under the same reaction conditions (90 bar CH_4, 50°C) affording small amounts of MSA (0.06 to 0.1% yield). Control experiments under the same conditions without initiator showed zero formation of MSA after several weeks. The formation of MSA using magic acid might indicate the potential involvement of electrophilic species; a radical-mediated pathway seems less likely because a radical-like initiator is absent.

From an industrial perspective, it is important to gain a further understanding of the role the sulfonyl peroxide plays in this process in order to expand this development to the industrial-scale synthesis of other value-added products (*15*). There is still much to learn about this process at the molec-

ular level, and we appreciate the opportunity to expand the discussion of this complex topic presented in our initial communication through this scholarly channel.

REFERENCES AND NOTES

1. C. Díaz-Urrutia, T. Ott, Activation of methane to CH_3^+: A selective industrial route to methanesulfonic acid. *Science* **363**, 1326–1329 (2019). doi:10.1126/science.aav0177 Medline
2. F. Schüth, Making more from methane. *Science* **363**, 1282–1283 (2019). doi:10.1126/science.aaw7738 Medline
3. G. A. Olah, G. K. S. Prakash, A. Molnar, S. Sommer, *Superacid Chemistry* (Wiley, ed. 2, 2009). For the composition of oleum of sulfuric acid, see Chapter 2.2.2.1; for the nonclassical carbocation CH_5^+ and its reactivity, see Chapter 3.5; for oxonium ions, see Chapter 4.2.1; for oxenium ions, see Chapter 4.3.4.1.
4. N. J. Gunsalus, A. Koppaka, S. H. Park, S. M. Bischof, B. G. Hashiguchi, R. A. Periana, Homogeneous functionalization of methane. *Chem. Rev.* **117**, 8521–8573 (2017). doi:10.1021/acs.chemrev.6b00739 Medline
5. G. A. Olah, N. Yoneda, D. G. Parker, Oxyfunctionalization of hydrocarbons. 4. Fluorosulfuric acid-antimony pentafluoride, fluorosulfuric acid, sulfuric acid, and hydrofluoric acid induced electrophilic oxygenation of alkanes with hydrogen peroxide. *J. Am. Chem. Soc.* **99**, 483–488 (1977). doi:10.1021/ja00444a027
6. H. Shi, Y. Wang, Z. Zhang, Hydroxylation of alkanes by hydrogen peroxide in superacid: A superelectrophilic active intermediate and an ionization-hydration process. *J. Mol. Catal. Chem.* **258**, 35–45 (2006). doi:10.1016/j.molcata.2006.05.017
7. G. E. Walrafen, T. F. Young, The structures of oleums. *Trans. Faraday Soc.* **56**, 1419–1425 (1960). doi:10.1039/tf9605601419
8. S. Mukhopadhyay, A. T. Bell, Direct sulfonation of methane at low pressure to methanesulfonic acid in the presence of potassium peroxydiphosphate as the initiator. *Org. Process Res. Dev.* **7**, 161–163 (2003). doi:10.1021/op020079n
9. E. A. Robinson, V. Silberberg, The reaction of methanesulfonic acid with sulfur trioxide. *Can. J. Chem.* **44**, 1437–1444 (1965). doi:10.1139/v66-212
10. N. Basickes, T. E. Hogan, A. Sen, Radical-initiated functionalization of methane and ethane in fuming sulfuric acid. *J. Am. Chem. Soc.* **118**, 13111–13112 (1996). doi:10.1021/ja9632365
11. V. A. Roytman, D. A. Singleton, Comment on "Activation of methane to CH_3^+: A selective industrial route to methanesulfonic acid". *Science* **364**, eaax7083 (2019). doi:10.1126/science.aax7083 Medline
12. M. M. Konnick, S. M. Bischof, M. Yousufuddin, B. G. Hashiguchi, D. H. Ess, R. A. Periana, A mechanistic change results in 100 times faster CH functionalization for ethane versus methane by a homogeneous Pt catalyst. *J. Am. Chem. Soc.* **136**, 10085–10094 (2014). doi:10.1021/ja504368r Medline
13. J. T. Fuller III, S. Butler, D. Devarajan, A. Jacobs, B. G. Hashiguchi, M. M. Konnick, W. A. Goddard III, J. Gonzales, R. A. Periana, D. H. Ess, Catalytic mechanism and efficiency of methane oxidation by Hg(II) in sulfuric acid and comparison to radical initiated conditions. *ACS Catal.* **6**, 4312–4322 (2016). doi:10.1021/acscatal.6b00226
14. A. Sen, M. A. Benvenuto, M. Lin, A. C. Hutson, N. Basickes, Activation of methane and ethane and their selective oxidation to the alcohols in protic media. *J. Am. Chem. Soc.* **116**, 998–1003 (1994). doi:10.1021/ja00082a022
15. After publication of the original paper, BASF acquired Grillo-Werke's (Duisburg, Germany) intellectual property (IP) and know-how for the production of methanesulfonic acid (MSA) from methane.

ACKNOWLEDGMENTS

We thank I. Biertümpel and C. Réthoré for helpful discussions, and N. Bloch, J. Stölzel, N. Kirschner, and B. Röhricht for technical support. **Funding:** This work was solely supported by Grillo-Werke AG. **Competing interests:** The authors declare no other conflicts of interests. **Data and materials availability:** All results are reported in the main text and supplementary materials.

11 May 2019; accepted 20 July 2020
Published online 7 August 2020
10.1126/science.aax9966

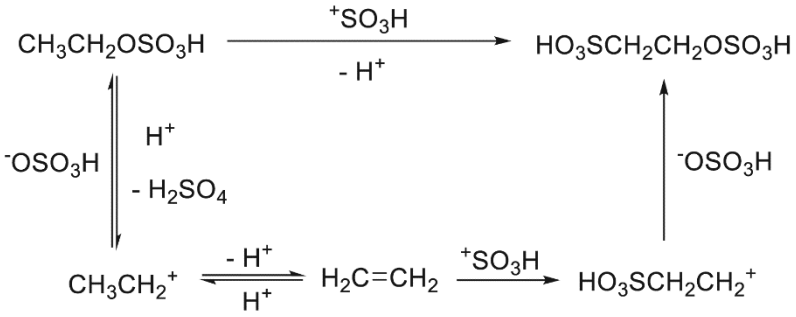


Fig. 1. Reaction of ethylbisulfate to $HO_3SCH_2CH_2OSO_3H$ in sulfuric acid, from (*14*).

PRIZE ESSAY

NEUROMODULATION

Expanding the brain researcher's toolkit

Better delivery vectors and opsins enable precise, minimally invasive neuromodulation

By **Viviana Gradinaru**

Despite the wealth and quality of basic neuroscience research, there is still little we can do to treat or prevent most brain disorders. Industry efforts, meanwhile, have shied away from this field, particularly after a series of major drug candidates for the treatment of Alzheimer's disease failed to meet expectations (*1*).

My previous research, which entailed developing and using optogenetics (*2*, *3*) to understand how deep brain stimulation works in Parkinson's disease (PD) (*4*, *5*), resulted in two key insights: We need to look and intervene earlier in brain disease progression, and we need to be able to access relevant cell populations with noninvasive yet precise tools to investigate, prevent, contain, or even reverse the course of disease. Accumulating evidence has highlighted a third insight: We may need to look beyond the brain to fully understand brain disorders (*6*, *7*).

My goal has been to develop an effective toolkit for neuromodulation so we can start to bridge the gap between what we know and what we can do to treat the brain. To achieve minimally invasive optogenetic-mediated modulation, we need to be able to penetrate the blood–brain barrier (BBB) so that vectors can be delivered systemically rather than through intracranial injections and address the poor reach of visible light through tissue so that large tissue volumes can be recruited without implantation of optical fibers. For early intervention, we need to get past the neuronal and brain-centric view of neurological disease.

PENETRATING THE BLOOD–BRAIN BARRIER

The adult brain is protected from compounds circulating in the blood by the BBB. Gene delivery to the brain requires surgery that is not only invasive but also results in limited tissue coverage and nonuniform gene expression. To achieve sufficient coverage for conditions characterized by broad dysfunction, such as neurodegeneration, multiple injections are needed, each of which creates local inflammation and damage. Systemic delivery would therefore be preferable to focal delivery because it does not require surgery and achieves broader tissue coverage.

We have pioneered a powerful strategy that allows for the generation and selection of adeno-associated viral (AAV) vectors with optimized properties through Cre-recombination-dependent AAV-targeted evolution (CREATE) (*8*). My lab has used CREATE to synthesize AAVs that cross the BBB and transduce most cells in the adult mouse brain (see the first figure). These systemically delivered AAVs enable noninvasive brainwide transduction of specific cell types and regions in rodents when used with gene regulatory elements (*9*).

DEVELOPING OPSINS FOR MINIMALLY INVASIVE RECRUITMENT OF LARGE TISSUE VOLUMES

During our quest to achieve systemic delivery of AAVs with opsin cargoes, we learned that the lower per-cell transgene copy number produced by systemic delivery led to ineffective overall opsin conductance. We needed better, high-performance opsins to make this method viable. To achieve such opsins, we built diversity into channelrhodopsin (ChR) using structure-guided SCHEMA (*10*) protein recombination from distinct opsin parents and then measured membrane localization and photocurrents. However, the dominant method for testing opsin properties—whole-cell patch clamping—has low throughput, so we used machine learning with limited training data to efficiently explore the vast sequence space and restrict the number of opsins to be tested.

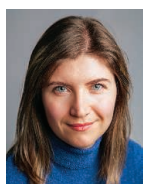
With Gaussian-process models trained on a limited experimental set of 102 functionally characterized ChRs, we selected ChR sequences that the models predicted would express, localize, and function. The result was a panel of high-photocurrent ChRs with exceptional light sensitivity (ChRgers) (*11*).

These high-fluxing opsins not only overcome the low-copy number limitation of systemic delivery but also allow the light source to be placed at a distance from the transduced cells (for example, on a thinned mouse skull rather than implanted directly in the brain).

The net effect of these advances is more effective coverage by both light and transgenes.

Division of Biology and Biological Engineering, California Institute of Technology, Pasadena, CA 91125, USA.
Email: viviana@caltech.edu

PHOTOS: (TOP TO BOTTOM) JIM CORNFIELD; COURTESY OF GUOSONG HONG



GRAND PRIZE WINNER

Viviana Gradinaru

Viviana Gradinaru received her B.S. from the California Institute of Technology (CalTech) and a Ph.D. in neuroscience from Stanford Medical School. After a year in industry, Gradinaru started her lab in the Division of Biology and Biological Engineering at Caltech in 2012, where she is now a professor of neuroscience and biological engineering. Gradinaru's research group specializes in developing neuroscience tools and methods, including engineering of microbial opsins and viral vectors with optimized brain tropism with systemic delivery. Her research uses mouse models of neurodevelopmental and neurodegenerative disorders combined with electrophysiology and optogenetics to understand the cellular basis of dysfunction with the goal of developing new strategies for intervention.



FINALIST

Guosong Hong

Guosong Hong received his undergraduate degree from Peking University and a Ph.D. from Stanford University. After completing his postdoctoral fellowship at Harvard University, Guosong started his lab in the Department of Materials Science and Engineering at Stanford University in 2018. His research aims to develop new materials-enabled neurotechnologies to interrogate and manipulate the brain with high spatiotemporal resolution, minimal invasiveness, and targeted neural specificity. **www.sciencemag.org/content/369/6504/638**

Published by AAAS

This may be particularly useful for advancing optogenetic studies in nonhuman primates (NHPs), a key model relevant to human health. Optogenetics has had a relatively limited impact in NHP research, compared to its impact in smaller model organisms, predominantly owing to coverage problems stemming from the delivery limitations for genes and photons. Using systemic delivery of high-performance opsins to transduce and recruit large brain regions in NHPs could enable better neuromodulation in these important animal models.

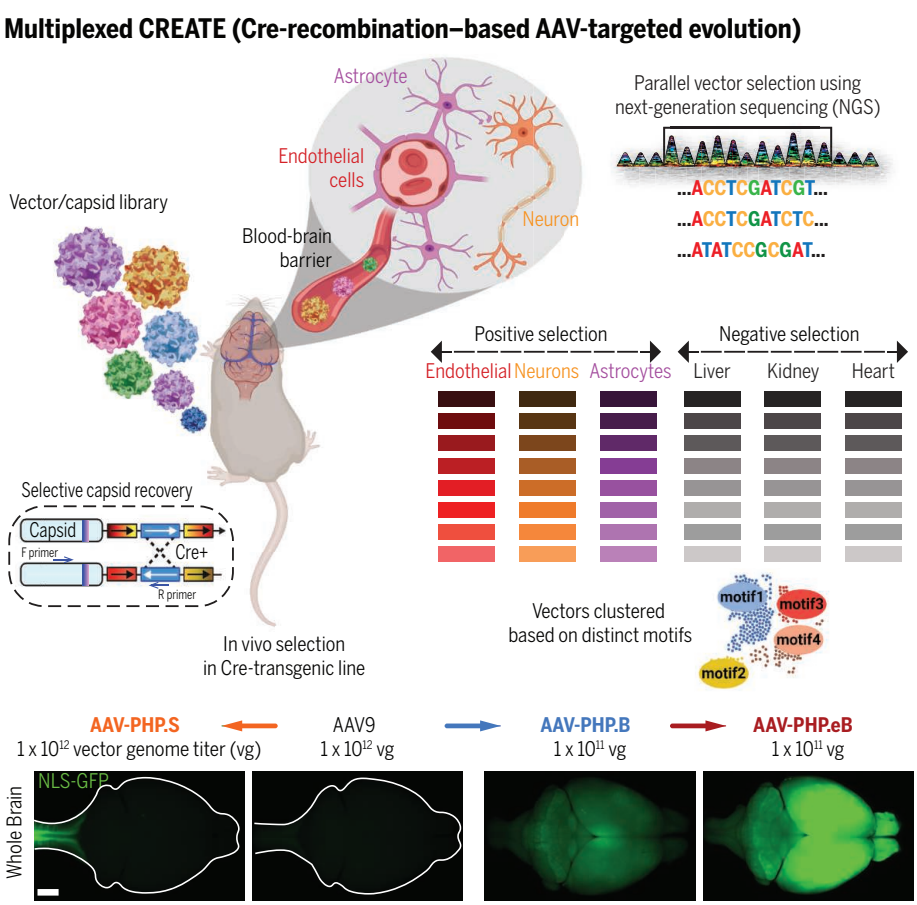
OVERCOMING THE NEURONAL AND BRAIN-CENTRIC VIEW OF NEUROLOGICAL DISEASE

Neurodegeneration research has focused mainly on compromised neurons and circuits in the brain. Nevertheless, evidence points to roles for inflammation mediated by non-neuronal brain cells and body-to-brain connections (by way of the peripheral nervous system and/or a compromised BBB) (*6*, *7*).

Engineering gene-delivery tools that specifically target non-neuronal brain cells relevant to neurodegeneration, such as the brain endothelial cells that constitute the vasculature and the BBB, may be paradigm shifting because an impaired BBB can initiate and/or precipitate neurodegeneration. The ability to perform both positive and negative selection is key to yielding vectors with desired organ, cell type, and cell region tropisms.

To enable this, we transformed our CREATE platform into multiplexed M-CREATE (*12*), an in vivo screening strategy that incorporates next-generation sequencing, synthetic library generation, and a dedicated analysis pipeline. Using M-CREATE, we identified capsid variants that exhibited bias toward vascular cells or that targeted neurons with greater specificity, as well as capsids that transduced the central nervous system broadly or crossed the BBB in diverse murine strains.

As a weak BBB can allow pathological factors into the brain (*13*, *14*), functionally targeting BBB permeability by means of engineered AAVs can affect body-to-brain access through the circulation. Modulating permeability affords the opportunity to study and/or repair a barrier that can be weakened in disease or to deliver therapies to the brain by way of the bloodstream.



Engineered systemic AAV capsids with improved tropism for peripheral sensory neurons (AAV-PHP.S, left) or the central nervous system (AAV-PHP.B and AAV-PHP.eB, right) upon systemic delivery in adult mice. Panels show native eGFP (enchanced green fluorescent protein) in the intact brain. Scale bar represents 1 mm.

MODULATING THE PERIPHERAL NERVOUS SYSTEM TO ADDRESS CENTRAL DYSFUNCTION

Synucleinopathies are neurodegenerative diseases characterized by the aggregation of insoluble amyloid α-synuclein (αSyn) fibrils. PD is a synucleinopathy characterized by death of selected midbrain and brainstem neuronal populations and motor dysfunction. Roughly 90% of Parkinson's cases arise sporadically, making the study of its etiology difficult. Emerging findings suggest that nonmotor features such as loss of smell and gastrointestinal deficits may precede clinical diagnosis (*15*, *16*).

Postmortem biopsies from asymptomatic PD-diagnosed individuals have revealed the presence of pathologic αSyn assemblies in gastrointestinal tissue, leading Braak and colleagues to suggest that αSyn aggregation may originate in peripheral tissues such as the gut and progress to the brain by way of autonomic fibers (*17*, *18*). Understanding the role of the peripheral nervous system in propagating pathology may therefore aid our understanding of neurodegeneration and help prevent it.

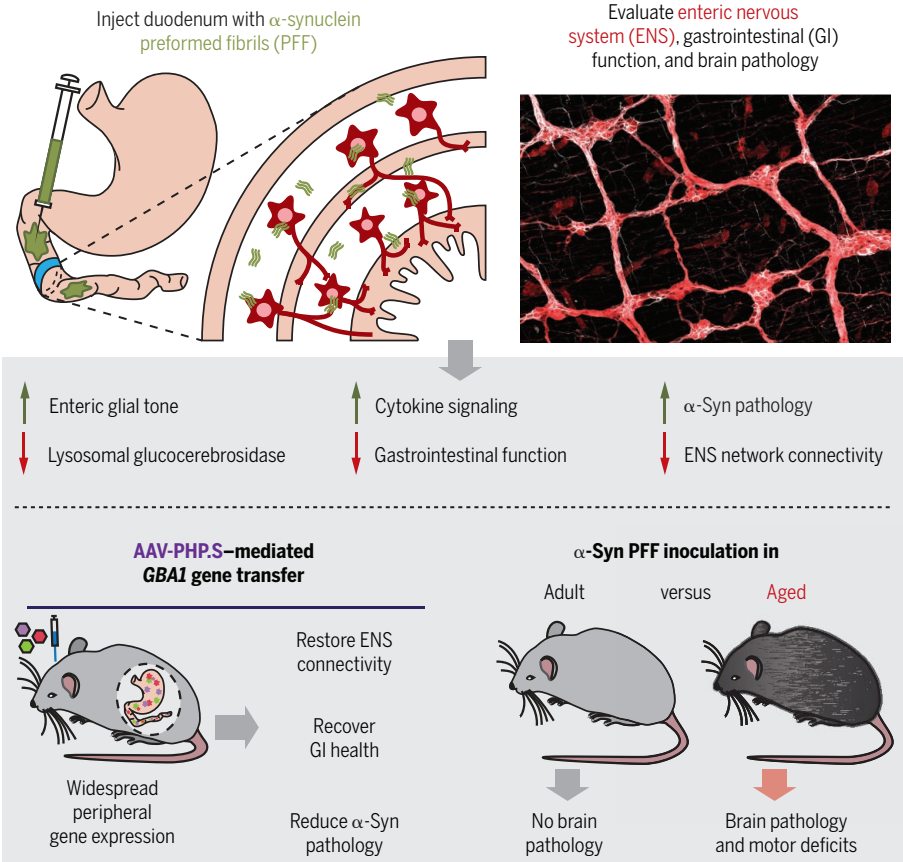
Recognizing the lack of tools and methods available to study peripheral nervous systems, we developed whole-body tissue clearing and a tunable and rapid vector expression system that we used to evaluate network connectivity in the enteric nervous system (ENS) (*19*, *20*). We injected a modest amount of αSyn preformed fibrils into the gut lining of mice (specifically the highly innervated duodenal wall) and observed subsequent gastrointestinal inflammation and physiological changes to the ENS (measured by optogenetics, calcium imaging, and changes in fecal production) (*21*). ENS pathology was also associated with a severe deficit in the lysosomal enzyme glucocerebrosidase, encoded by the gene *GBA1*, known to be involved in Gaucher disease and PD.

We therefore delivered *GBA1* by means of the AAV-PHP.S capsid, which efficiently transduces the peripheral nervous system, to noninvasively restore glucocerebrosidase in the periphery. This led to a reduction in αSyn pathology and hints at a possible therapeutic target for early PD.

Lastly, we demonstrated that inoculation of αSyn fibrils in aged mice, but not younger mice, resulted in progression of αSyn histopathology to the midbrain and decreased dopamine in the striatum, and subsequent motor defects. Taken together, this work (summarized in the second figure) shifts the focus of neurodegenerative disease etiology to the peripheral nervous system and expands our understanding of the role played by the ENS in prodromal synucleinopathy.

GRAPHIC: ADAPTED FROM CHAN *ET AL.* (*9*) BY N. DESAI/*SCIENCE*

Published by AAAS



αSyn fibrils can disrupt the enteric nervous system and aging increases susceptibility to the progression of αSyn pathology from the gut to the brain, leading to motor dysfunction. These deleterious effects were mitigated by peripheral gene transfer of *GBA1*, through the systemic administration of specially engineered AAVs.

SUMMARY OF FINDINGS

We aim to bridge the gap between what is currently feasible in neuromodulation and what is needed to meaningfully improve the lives of those with neuropathologies. We have used protein engineering principles to noninvasively, effectively, and specifically deliver effector genomes to nervous tissues and associated cell types (*22*). We have made advances in the creation of systemic viruses that cross the BBB, which open up the potential for noninvasive modulation of targets deep in the brain. In addition, we have used our gene delivery and optogenetic tools to modulate the peripheral nervous system in a mouse model of PD, demonstrating the potential utility of neuromodulation beyond the brain for the treatment of brain disorders. A number of relevant barriers remain, including the need to expand the AAV modest packaging limit, to penetrate the BBB in a variety of species, and to carefully consider and mitigate AAV side effects with better vectors, delivery methods, and immune avoidance strategies. Nevertheless, the findings and resources generated by this work represent a step forward with implications for neurological disorders and will be generalizable across neurological and psychiatric indications. ■

REFERENCES AND NOTES

1. K. Servick, *Science* 10.1126/science.aax4236 (2019).
2. V. Gradinaru *et al.*, *Cell* **141**, 154 (2010).
3. V. Gradinaru *et al.*, *J. Neurosci.* **27**, 14231 (2007).
4. V. Gradinaru, M. Mogri, K. R. Thompson, J. M. Henderson, K. Deisseroth, *Science* **324**, 354 (2009).
5. C. Xiao *et al.*, *Neuron* **90**, 333 (2016).
6. C. Godinho-Silva, F. Cardoso, H. Veiga-Fernandes, *Annu. Rev. Immunol.* **37**, 19 (2019).
7. P. Borghammer, N. Van Den Berge, *J. Parkinsons Dis.* **9** (s2), S281 (2019).
8. B. E. Deverman *et al.*, Nat. Biotechnol. 34, 204 (2016).
9. K. Y. Chan *et al.*, *Nat. Neurosci.* **20**, 1172 (2017).
10. C. N. Bedbrook *et al.*, *Proc. Natl. Acad. Sci. U.S.A.* **114**, E2624 (2017).
11. C. N. Bedbrook *et al.*, *Nat. Methods* **16**, 1176 (2019).
12. S. R. Kumar *et al.*, *Nat. Methods* **17**, 541 (2020).
13. A. Montagne, Z. Zhao, B. V. Zlokovic, *J. Exp. Med.* **214**, 3151 (2017).
14. A. R. Nelson, M. D. Sweeney, A. P. Sagare, B. V. Zlokovic, *Biochim. Biophys. Acta* **1862**, 887 (2016).
15. C. H. Hawkes, K. Del Tredici, H. Braak, *Parkinsonism Relat. Disord.* **16**, 79 (2010).
16. H.-Y. Sung, J.-W. Park, J.-S. Kim, *J. Mov. Disord.* **7**, 7 (2014).
17. H. Braak *et al.*, *Neurobiol. Aging* **24**, 197 (2003).
18. H. Braak, U. Rüb, W. P. Gai, K. Del Tredici, *J. Neural Transm.* **110**, 517 (2003).
19. V. Gradinaru, J. Treweek, K. Overton, K. Deisseroth, *Annu. Rev. Biophys.* **47**, 355 (2018).
20. B. Yang *et al.*, *Cell* **158**, 945 (2014).
21. C. Challis *et al.*, *Nat. Neurosci.* **23**, 327 (2020).
22. C. N. Bedbrook, B. E. Deverman, V. Gradinaru, *Annu. Rev. Neurosci.* **41**, 323 (2018).

ACKNOWLEDGMENTS

Research described in this essay was funded mainly by the NIH Director's New Innovator and Pioneer Awards and NIH BRAIN Grants to V.G. The author is a cofounder and board member of Capsida Biotherapeutics.

10.1126/science.abd2660

GRAPHIC: ADAPTED FROM CHALLIS *ET AL.* (*21*) AND CHAN *ET AL.* (*9*) BY N. DESAI/*SCIENCE*

Published by AAAS

PRIZE ESSAY



FINALIST
Guosong Hong
Guosong Hong received his undergraduate degree from Peking University and a Ph.D. from Stanford University. After completing his postdoctoral fellowship at Harvard University, Guosong started his lab in the Department of Materials Science and Engineering and the Wu Tsai Neurosciences Institute at Stanford University in 2018. His research aims to develop new materials-enabled neurotechnologies to interrogate and manipulate the brain with high spatiotemporal resolution, minimal invasiveness, and targeted neural specificity. **www.sciencemag.org/content/369/6504/638**

NEUROMODULATION

Seeing the sound

An ultrasound-mediated deep-tissue light source for noninvasive optogenetics

By **Guosong Hong**

Optogenetics, which uses light to control genetically modified neurons, is revolutionizing neuroscience research by allowing for the precise deconstruction of neural circuits with neuron type specificity (*1*, *2*). However, due to limited tissue penetration of visible light, invasive craniotomy and intracranial implantation of obtrusive optical fibers or light-emitting diodes (LEDs) are usually required for in vivo optogenetic neural modulation in the brains of rodents and other mammalian subjects (*3*). Perturbation of the endogenous neural and glial activity has been reported as a consequence of chronic gliosis at the implant/neural interface, as has permanent damage to neural tissue (*4*–*7*).



THE CHALLENGE OF INVASIVE OPTOGENETICS

The need for invasive delivery of a light source represents a long-standing challenge for in vivo optogenetics. This need is because visible photons can only achieve limited penetration in brain tissue (*8*). The conventional optogenetic toolbox comprises opsins with activation spectra in the range of 430 to 610 nm that have limited tissue penetration due to scattering and absorption of photons by the brain tissue (*9*). Several strategies have been employed to increase penetration, including the use of opsins with red-shifted activation spectra (*10*, *11*), two-photon stimulation of opsins (*12*), and conversion of brain-penetrant near-infrared light into visible photons via intracortically injected upconversion nanoparticles (*13*, *14*).

Despite these advances, such approaches are still invasive, requiring either partial removal of the scalp and skull (*10*, *12*) or intracranial delivery of nanomaterials into deep brain tissue (*13*, *14*).

CONVERTING SOUND INTO LIGHT

Our approach (*15*) to address this challenge has been to replace direct light illumination with focused ultrasound (FUS), which affords much deeper penetration (~5 cm for FUS versus 100 μm for visible photons) in biological tissues, including the brain (*16*–*19*). However, ultrasound does not activate opsins directly. Thus, a local transducer that converts sound into light in the brain is required.

I am a materials scientist with extensive training in neurobiology (*7*), and am therefore aware of the types of materials that can absorb sound waves and emit light in return. Such substances, known as mechanoluminescent materials, have previously been used primarily in dynamic stress mapping of structures (*20*), displays (*21*, *22*), and photonic skins (*23*). If these materials could be delivered to a deep brain region, they could become a light source that can be turned on and off by FUS from outside the brain.

In our study, we made zinc sulfide (ZnS) nanoparticles co-doped with trace amounts of silver (Ag) and cobalt (Co) to afford the mechanoluminescence property. Unlike pristine, dopant-free ZnS, which is a photoluminescent material with a submicrosecond lifetime after 400-nm photoexcitation, Co dopant ions trap the excited electrons and store the photoexcitation energy until being triggered by FUS. Ag dopant ions tune the emission color to 470-nm blue light for activation of channelrhodopsin-2 (ChR2) (Fig. 1A).

AN ENDOGENOUS MECHANISM TO DELIVER AND RECHARGE THE NANOSCOPIC LIGHT SOURCE

This method, however, has a substantial drawback: Because 400-nm photoexcitation is required to "precharge" the nanoparticles and FUS simply controls when light should be emitted by releasing the trapped energy (Fig. 1A), the material must be charged with 400-nm irradiation outside the brain before delivery into deep tissue and can only be triggered once by FUS.

Our solution to this problem is made possible by the pervasive nature of the blood circulation inside the body. Not only do blood vessels penetrate the entire brain, allowing delivery of ZnS nanoparticles to any region; blood also passes through superficial vessels near the skin, providing accessible locations shallow enough for 400-nm light to penetrate and recharge these na-

Department of Materials Science and Engineering, Wu Tsai Neurosciences Institute, Stanford University, Stanford, CA, USA. Email: guosongh@stanford.edu

PHOTO: COURTESY OF GUOSONG HONG

Published by AAAS

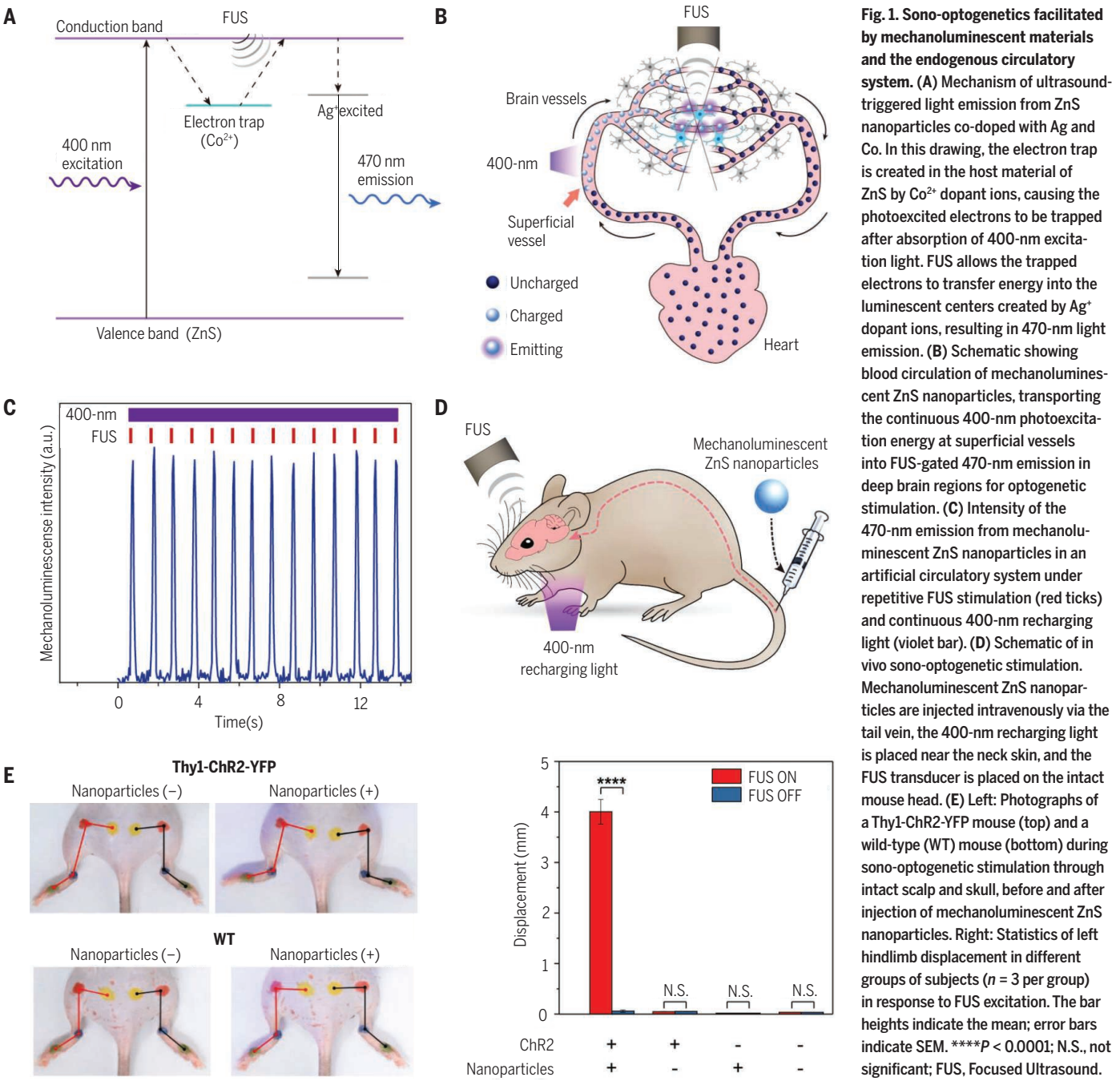


Fig. 1. Sono-optogenetics facilitated by mechanoluminescent materials and the endogenous circulatory system. (A) Mechanism of ultrasound-triggered light emission from ZnS nanoparticles co-doped with Ag and Co. In this drawing, the electron trap is created in the host material of ZnS by Co^{2+} dopant ions, causing the photoexcited electrons to be trapped after absorption of 400-nm excitation light. FUS allows the trapped electrons to transfer energy into the luminescent centers created by Ag^{+} dopant ions, resulting in 470-nm light emission. **(B)** Schematic showing blood circulation of mechanoluminescent ZnS nanoparticles, transporting the continuous 400-nm photoexcitation energy at superficial vessels into FUS-gated 470-nm emission in deep brain regions for optogenetic stimulation. **(C)** Intensity of the 470-nm emission from mechanoluminescent ZnS nanoparticles in an artificial circulatory system under repetitive FUS stimulation (red ticks) and continuous 400-nm recharging light (violet bar). **(D)** Schematic of in vivo sono-optogenetic stimulation. Mechanoluminescent ZnS nanoparticles are injected intravenously via the tail vein, the 400-nm recharging light is placed near the neck skin, and the FUS transducer is placed on the intact mouse head. **(E)** Left: Photographs of a Thy1-ChR2-YFP mouse (top) and a wild-type (WT) mouse (bottom) during sono-optogenetic stimulation through intact scalp and skull, before and after injection of mechanoluminescent ZnS nanoparticles. Right: Statistics of left hindlimb displacement in different groups of subjects (n = 3 per group) in response to FUS excitation. The bar heights indicate the mean; error bars indicate SEM. ****P < 0.0001; N.S., not significant; FUS, Focused Ultrasound.

noscopic light sources as they circulate in the body. After the ZnS nanoparticles are injected intravenously, they can be charged by 400-nm light when passing through superficial vessels, pumped by the heart into cerebral vessels, and then gated by FUS to release the stored energy locally, all without exiting the blood circulation (Fig. 1B).

SONO-OPTOGENETICS: A RECHARGEABLE LIGHT SOURCE INSIDE THE BODY

We investigated the feasibility of such an approach first in an artificial circulatory system, where we were able to confirm that the nanoparticles light up, recharge, and light up again without losing intensity (Fig. 1C). The average intensity of FUS-triggered light emission is ~1 mW/mm², an amount sufficient to activate ChR2 (*24*).

We then carried out in vivo experiments, injecting the nanoparticles into the tail vein of mice that expressed ChR2 in the motor cortex. We positioned the shaved mouse head underneath a transducer that aimed ultrasound at the motor cortex of the brain (Fig. 1D). Then—without any surgery to the scalp, skull, or brain, and without any implantation of optical fiber or LED devices—we were able to evoke hindlimb motion in the animal, which was synchronized with the FUS pulses. The same animal did not exhibit any hindlimb motion before nanoparticle injection under the same stimulation protocol, nor did wild-type mice demonstrate any hindlimb motion, regardless of nanoparticle injection (Fig. 1E).

In our approach, which we refer to as "sono-optogenetics," the focal size of FUS in the mouse brain is ~700 μm. The localized light source thus has a similar cross-sectional diameter in the brain. Additionally, FUS can be turned on and off with submillisecond precision, with a latency time of 10 ms before light emission. These features have made the virtual light source in our work

GRAPHIC: ADAPTED FROM G. HONG BY N. DESAI/*SCIENCE*

Published by AAAS

similar to conventional fiber optics in both spatial and temporal resolution (*3*).

Sono-optogenetics provides a tool for rapidly screening different target regions in the brain for optogenetic neural modulation, because one can easily change the location of ultrasound focus. We envisage that this approach will also be able to be used in other organs that are usually refractory to fiber implantation (e.g., spinal cord, heart, and lungs) and for any application in which a light source is needed deep in the body. ■

REFERENCES AND NOTES

1. K. Deisseroth, *Nat. Neurosci.* **18**, 1213 (2015).
2. R. D. Airan, K. R. Thompson, L. E. Fenno, H. Bernstein, K. Deisseroth, *Nature* **458**, 1025 (2009).
3. F. Zhang *et al.*, *Nat. Protoc.* **5**, 439 (2010).
4. J. W. Salatino, K. A. Ludwig, T. D. Y. Kozai, E. K. Purcell, *Nat. Biomed. Eng.* **1**, 862 (2017).
5. G. Hong, C. M. Lieber, *Nat. Rev. Neurosci.* **20**, 330 (2019).
6. T. I. Kim *et al.*, *Science* **340**, 211 (2013).
7. G. Hong *et al.*, *Science* **360**, 1447 (2018).
8. G. S. Hong, A. L. Antaris, H. J. Dai, *Nat. Biomed. Eng.* **1**, 0010 (2017).
9. K. M. Tye, K. Deisseroth, *Nat. Rev. Neurosci.* **13**, 251 (2012).
10. J. H. Marshel *et al.*, *Science* **365**, eaaw5202 (2019).
11. J. Y. Lin, P. M. Knutsen, A. Muller, D. Kleinfeld, R. Y. Tsien, *Nat. Neurosci.* **16**, 1499 (2013).
12. R. Prakash *et al.*, *Nat. Methods* **9**, 1171 (2012).
13. S. Chen *et al.*, *Science* **359**, 679 (2018).
14. S. Chen, *Science* **365**, 456 (2019).
15. X. Wu *et al.*, *Proc. Natl. Acad. Sci. U.S.A.* **116**, 26332 (2019).
16. J. B. Wang, M. Aryal, Q. Zhong, D. B. Vyas, R. D. Airan, *Neuron* **100**, 728 (2018).
17. W. Legon *et al.*, *Nat. Neurosci.* **17**, 322 (2014).
18. R. Airan, *Science* **357**, 6350 (2017).
19. J. A. Zagzebski, *Essentials of Ultrasound Physics* (Mosby, 1996).
20. L. S. Liu *et al.*, *Adv. Mater. Technol.* **4**, 1800336 (2019).
21. S. M. Jeong, S. Song, S. K. Lee, N. Y. Ha, *Adv. Mater.* **25**, 6194 (2013).
22. X. Wang *et al.*, *Adv. Mater.* **27**, 2324 (2015).
23. X. Qian *et al.*, *Adv. Mater.* **30**, 1800291 (2018).
24. N. C. Klapoetke *et al.*, *Nat. Methods* **11**, 338 (2014).

10.1126/science.abd3636

Published by AAAS

RESEARCH

IN *SCIENCE* JOURNALS

Edited by **Michael Funk**



A single human hair viewed by scanning electron microscopy during cutting with a razor.

PHOTO: GIANLUCA ROSCIOLI, PH.D. STUDENT IN TASAN GROUP AT MIT

METALLURGY

A hair-splitting way to get dull

Razors eventually become dull after shaving even though the blade is about 50 times harder than the hair. Whereas edge rounding and brittle cracking of a blade's hard coating were thought to be responsible, a detailed microstructural investigation by Roscioli *et al*. shows a different mechanism. A combination of out-of-plane bending, microstructural heterogeneity, and asperities—microscopic chips along the smooth edge—sometimes caused fracture to occur if the conditions lined up. This fracture originated at the hair-edge asperity interface and created chipping that dulled a blade faster than other processes. —BG *Science*, this issue p. 689

STRUCTURAL BIOLOGY

Adapted to the task at hand

RNA-based catalysts perform fundamental tasks in cellular RNA metabolism, especially in eukaryotes, where RNAs are cut by specialized ribonucleoproteins (RNPs) as part of ribosome assembly or messenger RNA regulation or splicing. Both RNA and protein components play a role in shaping how these large catalytic complexes interact with their RNA substrates. Lan *et al*. determined the cryo–electron microscopy structures of a yeast RNP called ribonuclease MRP both alone and bound to a small RNA substrate. Comparison with the related ribonuclease P revealed differences in both protein and RNA components that enable ribonuclease MRP to recognize substrates with a specific sequence motif, rather than purely recognizing RNA structure as ribonuclease P does. These structures aid in considering how RNPs evolved and why they remain central to eukaryotic RNA processing. —MAF

Science, this issue p. 656

FERROELECTRICS

A helix of dipoles

In magnetic materials, magnetic dipoles typically line up parallel or antiparallel to each other. However, more complex orderings, such as helical, can also occur. Khalyavin *et al.* found that in the material $BiCu_{0.1}Mn_{6.9}O_{12}$, a helical order can be formed out of electric rather than magnetic dipoles. The material also harbors an associated structural helical order, which symmetry analysis suggests might be switchable with an applied electric field. —JS

Science, this issue p. 680

CORONAVIRUS

Air pollution epidemic

The lockdown enforced in most cities in China in response to the outbreak of severe acute respiratory syndrome coronavirus 2 (SARS-CoV-2) resulted in the virtual absence of motor vehicle traffic and sharply reduced manufacturing activity for several weeks. Le *et al*. report some of the anticipated and unanticipated effects that this had on air pollution there, including unexpectedly high levels of particulate matter abundances and severe haze formation in some areas. This natural experiment will help in the assessment of air pollution mitigation strategies. —HJS

Science, this issue p. 702

PLANT SCIENCE

Switching perception of friend and foe

Lysine motif receptors in plants perceive glycans that signal the presence of pathogenic or symbiotic nitrogen-fixing microbes. Bozsoki *et al*. now define the portions of these receptors that create the discriminatory binding pocket (see the Perspective by Bisseling and

Published by AAAS

Geurts). The motifs were conserved in receptors that initiate immune responses, reflecting the invariable nature of the chitin fragments that they sense. Conversely, the motifs in receptors that respond to symbiotic signals were more varied, reflecting the greater diversity of the lipochitooligosaccharides (Nod factors) that they sense. With domain swapping, the authors switched the Nod factor specificity of receptors from two legume species and also enabled a chitin receptor that was otherwise dedicated to the detection of pathogenic microbes to instead recognize Nod factors. —PJH

Science, this issue p. 663; see also p. 620



Plants use related systems to sense pathogens and beneficial nitrogen-fixing bacteria, which inhabit root nodules.

FLUID MECHANICS

Slower-motion bubble collapse

The collapse of viscous bubbles is of practical interest to geophysics, glass manufacturing, and food processing. Previous studies have suggested that gravity or small punctures may play a role in the wrinkling and collapse of viscous bubbles. By studying bubbles with a range of viscosity and by tilting them both sideways and upside down, Oratis *et al*. conclude that gravity is not a factor. Instead, surface tension and dynamic stress of the compressed liquid seem to be the main driving mechanisms for the behavior of the bubbles and the wrinkling instability. —MSL

Science, this issue p. 685

CANCER

Panning for diagnostic gold

Accurate and timely diagnosis and categorization of cancer is not always simple even under optimal conditions. It can be nearly impossible in the developing world, where the required specialists and equipment may not be available and biopsy results can take months to return. To address this diagnostic bottleneck, Min *et al*. devised an automated image cytometry system named CytoPAN that can correctly detect breast cancer and identify its subtype in 1 hour using samples obtained by fine-needle aspiration, a less invasive technique than core biopsy. The system is relatively affordable and requires minimal training, which should decrease the barriers to access in low-resource areas. —YN

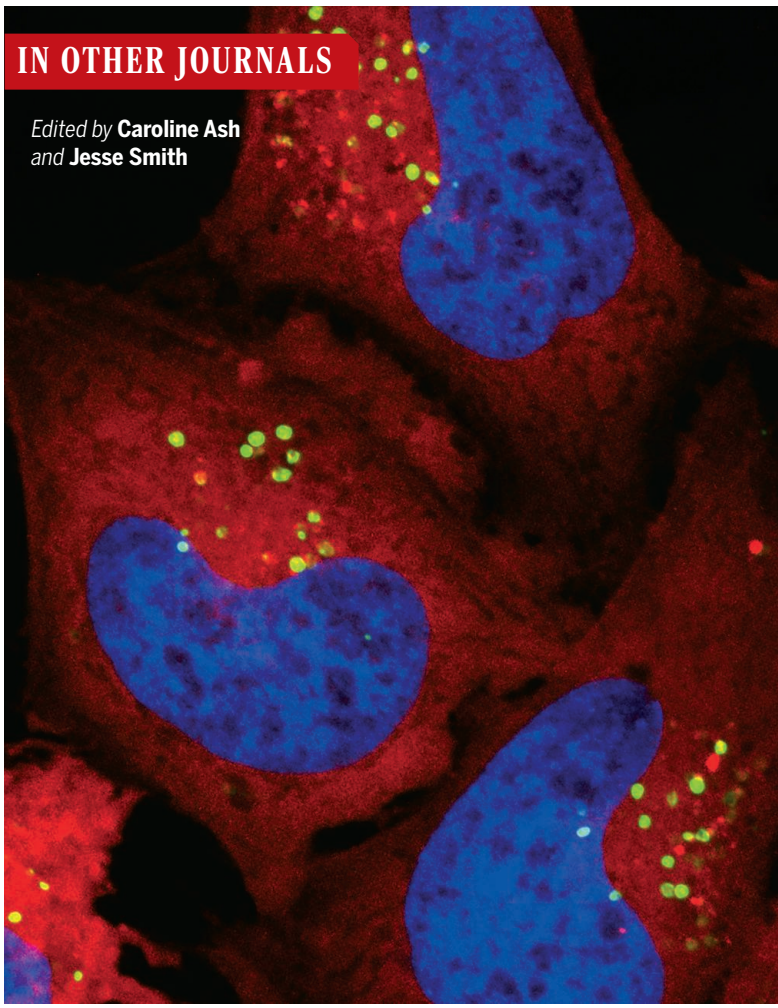
Sci. Transl. Med. **12**, eaaz9746 (2020).

DEEP BIOSPHERE

Lower power limit to subseafloor life

Microorganisms in sediment in the subseafloor have survived under extreme energy constraints for millions of years. Using a global bioenergetic ecosystem model, Bradley *et al.* calculated the rate of microbial energy use in marine sediment deposited in the past ~2.6 million years, as well as the rate and thermodynamic properties of organic matter degradation. The total power use of the subseafloor biosphere was found to be <0.1% of the power produced by photosynthesis in the overlying ocean. The majority of subseafloor microbes subsist at energy fluxes two orders of magnitude lower than previous estimates for cell maintenance power. Extraordinarily low energy fluxes are likely for almost all sediment-hosted life beneath the ocean. —FI

Sci. Adv. 10.1126/sciadv.aba0697 (2020).



IN OTHER JOURNALS

Edited by **Caroline Ash** *and* **Jesse Smith**

CORONAVIRUS

Modeling coronavirus infection

Initially, severe acute respiratory syndrome coronavirus 2 (SARS-CoV-2) infection was largely associated with respiratory issues. However, we now know that clinical presentation is complex and varied, with complications also seen in the cardiac, neurological, and gastrointestinal systems. Stem cell and organoid systems provide useful model systems with which to better understand the mechanisms of action. Yang *et al.* developed a human pluripotent stem cell–based platform for modeling virus infection and coronavirus disease 2019 (COVID-19). Adult human pancreatic α and β cells and liver hepatocyte and cholangiocyte organoids are permissive to SARS-CoV-2 infection with resultant strong chemokine induction. These model systems should show clinical relevance (for example, by providing an understanding of the correlation between COVID-19 and diabetes) and potentially identify drug treatment. —BAP

Cell Stem Cell **27**, 125 (2020).

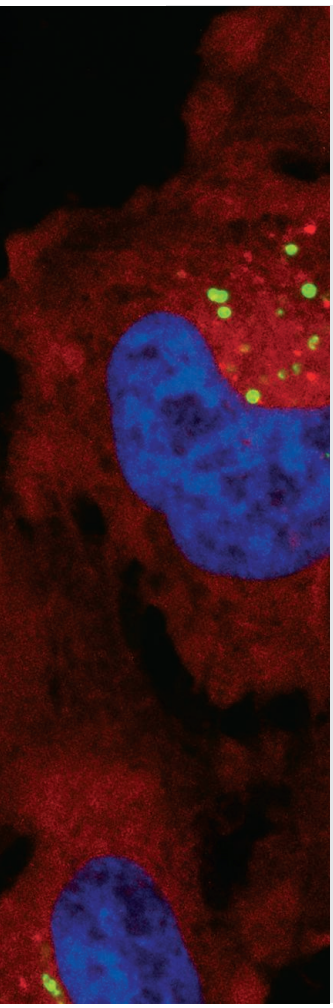
STRUCTURAL BIOLOGY

Folding for self-protection

Small interfering RNAs play an important role in regulating protein expression. In human cells, they guide Argonaute2 (AGO2), a protein that cleaves RNA, to its target site on messenger RNA (mRNA). Ruijtenberg *et al.* used live-cell imaging to observe mRNA cleavage in human cells and show that dynamic mRNA interactions can shield the target sites. In the

CREDITS (LEFT TO RIGHT): NINJATACOSHELL/WIKICOMMONS CC BY; C.J. ELLISON *ET AL.*, *CURR. BIOL.* **30**, 2974 (2020)

Published by AAAS



CELL BIOLOGY

Breaking and exiting

Some bacteria, including *Salmonella* and *Shigella* spp., can take up residence within vacuoles inside mammalian host cells. To gain access to the nutrient-rich host cytosol, the internalized bacteria must break out from their vacuole, but how? Ellison *et al.* used super-resolution live-cell imaging and correlative light and electron microscopy to characterize this process. They developed a reporter for the host lipid sphingomyelin, which is normally found on extracellular-facing membranes. The authors found that sphingomyelin became exposed to the cytosol on bacteria-containing vacuoles. This exposure occurred just before the vacuoles ruptured, releasing the bacteria into the cytosol. Sphingomyelin exposure can thus be used as an early indicator of bacterial invasion and potentially more widely as an indicator of membrane damage that threatens the integrity of the cytosol. —SMH

Curr. Biol. **30**, 2974 (2020).

Live-cell imaging using a sphingomyelin marker shows spots of membrane damage.

PHOTO: NATURE PICTURE LIBRARY/ALAMY STOCK PHOTO

absence of translation, target sites remain masked for several minutes and cleavage is slow. A translating ribosome can stimulate cleavage. Comparing computed and experimental cleavage curves under different conditions showed that the ribosome unfolds the RNA, providing access to the target site. Although other factors will affect cleavage efficiency, mRNA dynamics appear to play an important role in regulating protein-RNA interactions. —VV

Nat. Struct. Biol. 10.1038/s41594-020-0461-1 (2020).

ECOTOXICOLOGY

Down the line

Human activities release countless chemicals into the environment, many of which have shown negative impacts on both aquatic and terrestrial species. One notable class of damaging compounds are the endocrine disrupters, which have been shown to influence physiology and function across systems in vertebrates. Major *et al.* show that such compounds can influence multiple generations of fishes, including those that have experienced no exposure, through epigenetic methylation. Specifically, they exposed inland silversides (*Menidia beryllina*) to a suite of these compounds at environmentally relevant levels early in life and found that methylation altered both gene body and promoter regions. These alterations persisted across both the F_1 and F_2 generations and had the potential to affect many functions, including growth, immune function, stress, pigmentation, and repair. These results suggest that our waste effluents may continue to affect other species indefinitely. —SNV

Front. Mar. Sci. **7**, 471 (2020).



Endocrine-disrupting pollutants have a persistent, harmful intergenerational effect on *Menidia beryllina*, shown here.

POLITICAL SCIENCE

Union membership reduces racism

Historical research has suggested that the advent of unions created social ties that may have reduced white workers' racism toward their African American co-workers. Frymer and Grumbach used national survey data in the United States to show that union membership is associated with reduced negative racial attitudes among white workers toward African Americans. They then used longitudinal data to show that gaining union membership predicts reductions in negative racial attitudes. Compared with nonunionized workers, unionized workers also support more policies that would benefit African Americans. These data have implications for understanding the interplay of declining union membership and racism in the United States. —TSR

Am. J. Pol. Sci. 10.1111/ajps.12537 (2020).

EDUCATION

Depression as a lab mate

The impact of mental health, including depression, has become a prominent concern in STEM graduate education. As more and more science- and medical-based graduate programs require undergraduate applicants to have research experience, Cooper *et al.* sought to understand how undergraduates' symptoms of depression affect their research experiences and vice versa. The team interviewed 35 undergraduate life sciences majors that identified with having depression and show that students' depression affected their motivation and productivity, creativity and risk-taking, engagement and concentration, and self-perception and socializing during research experiences. Additionally, the demands of research affected students' depression. An initial set of evidence-based recommendations for mentors to consider in promoting an inclusive research experience for students with depression is provided. —MM

CBE Life Sci. Educ. **19**, ar19 (2020).

NANOMATERIALS

Polarized perovskite luminescence

Optical elements can generate circularly polarized luminescence (CPL), but sources that directly emit CPL are desirable for many applications. Kim *et al.* synthesized formamidinium lead bromide nanocrystals (NCs) with mixtures of longer achiral ligands and shorter chiral (*R*)-2-octylamine. Lower fractions of the chiral ligand formed smaller NCs that had stronger CPL at room temperature, apparently because these NCs have a higher fraction of chiral ligands that also have stronger electronic interactions with their perovskite cores. The perovskite NCs exhibited a luminescence dissymmetry *g*-factor of ~0.06 at wavelengths between 520 and 540 nanometers. Although purification steps removed some of the chiral ligand, CPL could be restored in thin films with the addition of (*R*)- or (*S*)-methylbenzylammonium bromide. —PDS

ACS Nano **14**, 8816 (2020).

Published by AAAS

ALSO IN *SCIENCE* JOURNALS

Edited by **Michael Funk**

CORONAVIRUS

A different picture in Africa

With the spread of the coronavirus disease 2019 (COVID-19) pandemic across the globe, experts predicted that Africa would suffer an overwhelming number of cases and deaths, but this seems not to be the case. Despite potential issues with reporting, there may be distinct factors in the African nations that are contributing to reduced mortality from COVID-19. In a Perspective, Mbow *et al.* discuss how the younger age of the population of Africa could limit severe disease. Other factors might also be involved, particularly exposure to other infectious diseases and parasites that could train the immune systems of Africans to better cope with infection. Further research is needed, but the course of COVID-19 in Africa could improve our understanding of the disease's risk factors and potentially identify innovative solutions to prevent and treat it. —GKA

Science, this issue p. 624

CELL BIOLOGY

Proteasomal control of division in Archaea

In eukaryotes, proteasome-mediated degradation of cell cycle factors triggers mitotic exit, DNA segregation, and cytokinesis, a process that culminates in abscission dependent on the protein ESCRT-III. By studying cell division in an archaeal relative of eukaryotes, Tarrason Risa *et al*. identified a role for the proteasome in triggering cytokinesis by an archaeal ESCRT-III homolog. Cell division in this archaeon was driven by stepwise remodeling of a composite ESCRT-III–based division ring, where rapid proteasome-mediated degradation of one ESCRT-III subunit triggered the constriction of the remaining ESCRT-III–based copolymer. These data strengthen the case for the eukaryotic cell division machinery having its origins in Archaea. —SMH

Science, this issue p. 642

CORONAVIRUS

Sites of vulnerability in SARS-CoV-2

Antibodies that neutralize severe acute respiratory syndrome coronavirus 2 (SARS-CoV-2) could be an important tool in treating coronavirus disease 2019 (COVID-19). Brouwer *et al*. isolated 403 monoclonal antibodies from three convalescent COVID-19 patients. They show that the patients had strong immune responses against the viral spike protein, a complex that binds to receptors on the host cell. A subset of antibodies was able to neutralize the virus. Competition and electron microscopy studies showed that these antibodies target diverse epitopes on the spike, with the two most potent targeting the domain that binds the host receptor. —VV

Science, this issue p. 643

CORONAVIRUS

Hitting SARS-CoV-2 in a new spot

A key target for therapeutic antibodies against severe acute respiratory syndrome coronavirus 2 (SARS-CoV-2) is the spike protein, a trimeric protein complex with each monomer comprising an S1 and an S2 domain that mediate binding to host cells and membrane fusion, respectively. In addition to the receptor binding domain (RBD), S1 has an N-terminal domain (NTD). In searching for neutralizing antibodies, there has been a focus on the RBD. Chi *et al*. isolated antibodies from 10 convalescent patients and identified an antibody that potently neutralizes the virus but does not bind the RBD. Cryo–electron microscopy revealed the epitope as the NTD. This NTD-targeting antibody may be useful to combine with RBD-targeting antibodies in therapeutic cocktails. —VV

Science, this issue p. 650

CORONAVIRUS

Seeking broad protection

As scientists develop therapeutic antibodies and vaccines against severe acute respiratory syndrome coronavirus 2 (SARS-CoV-2), the risk of emergent coronaviruses makes it important to also identify broadly protective antibodies. Wec *et al*. isolated and characterized hundreds of antibodies against the viral spike protein of SARS-CoV-2 from the memory B cells of a survivor of the 2003 outbreak caused by the related coronavirus, SARS-CoV. In both of these viruses, the spike protein facilitated viral entry by binding to the angiotensin-converting enzyme 2 (ACE2) receptor on human cells. The antibodies targeted multiple sites on the spike protein, but of nine antibodies that showed strong cross-neutralization, eight targeted the domain that binds to ACE2. These eight antibodies also neutralized a bat SARS-related virus. Illuminating the epitopes on the viral spike protein that bind cross-neutralizing antibodies could guide the design of broadly protective vaccines. —VV

Science, this issue p. 731

PLANT SCIENCE

Grafting success by cell wall remodeling

Plants that produce great fruit may not always have great roots. Grafting of a productive scion onto a resilient rootstock has provided agriculturalists with solutions to this and other challenges. Notaguchi *et al*. have now studied why some plant grafts work better than others (see the Perspective by McCann). The tobacco relative *Nicotiana benthamiana* (*Nb*) turns out to be the superhero of grafting, able to form grafts with plants from a wide range of evolutionary families. A bit of *Nb*, set as a middleman between a tomato scion and an *Arabidopsis* rootstock, negotiated a successful junction between these two otherwise nonconversant plant species. The expression of β-1,4-glucanases secreted into the extracellular region turns out to be key in facilitating cell wall reconstruction. —PJH

Science, this issue p. 698; see also p. 618

NANOMATERIALS

Stabilizing monolayer nitrides with silicon

Transition metal carbides and nitrides are nonlayered materials that in monolayer form have potentially useful electronic and chemical properties. These monolayers are usually made by chemical etching that produces flakes with surface defects that have poor air and water stability. Hong *et al*. report that introducing silicon during chemical vapor deposition growth of molybdenum nitride passivates the surface and prevents island formation. Centimeter-scale monolayer films of the semiconductor $MoSi_2N_4$ form as a MoN_2 layer sandwiched by two Si-N bilayers. These layers possess high mechanical strength and ambient stability. —PDS

Science, this issue p. 670

FRAMEWORK MATERIALS

Mapping metal sequences in MOFs

Most metal-organic frameworks (MOFs) contain just one type of metal in the nodes connecting the organic linkers. Multivariate MOFs containing multiple metals can offer greater selectivity in

Published by AAAS

sorption and catalytic properties, but determining the arrangement of metals in these materials is challenging. Ji *et al*. found that atom-probe tomography can reveal sequences of metals for MOF-74 single crystals containing combinations of cobalt, cadmium, lead, and manganese ions. In this MOF, the metals form oxide rods that are connected by the organic linker into a honeycomb lattice. The obtained sequences, which were tuned by varying the proportion of metals and synthesis temperature, could be random, short and long duplicates, and single metal insertions. —PDS

Science, this issue p. 674

SOLAR PHYSICS

The magnetic field in the Sun's corona

The solar corona is the outermost layer of the Sun's atmosphere, consisting of hot, diffuse, and highly ionized plasma. The magnetic field in this region is expected to drive many of its physical properties but has been difficult to measure with observations. Yang *et al*. used near-infrared imaging spectroscopy to determine the electron density and magnetohydrodynamic wave speed in the corona. By combining these measurements, they derived maps of the magnetic field throughout the entire observable corona. The method could potentially be used to produce routine magnetic field maps for the corona that are similar to those already available for the Sun's surface. —KTS

Science, this issue p. 694

CORONAVIRUS

Interferons interfere with lung repair

Interferons (IFNs) are central to antiviral immunity. Viral recognition elicits IFN production, which in turn triggers the transcription of IFN-stimulated genes (ISGs), which engage in various antiviral functions. Type I IFNs (IFN-α and IFN-β) are widely expressed and can result in immunopathology during viral infections. By contrast, type III IFN (IFN-λ) responses are primarily restricted to mucosal surfaces and are thought to confer antiviral protection without driving damaging proinflammatory responses. Accordingly, IFN-λ has been proposed as a therapeutic in coronavirus disease 2019 (COVID-19) and other such viral respiratory diseases (see the Perspective by Grajales-Reyes and Colonna). Broggi *et al*. report that COVID-19 patient morbidity correlates with the high expression of type I and III IFNs in the lung. Furthermore, IFN-λ secreted by dendritic cells in the lungs of mice exposed to synthetic viral RNA causes damage to the lung epithelium, which increases susceptibility to lethal bacterial superinfections. Similarly, using a mouse model of influenza infection, Major *et al*. found that IFN signaling (especially IFN-λ) hampers lung repair by inducing p53 and inhibiting epithelial proliferation and differentiation. Complicating this picture, Hadjadj *et al*. observed that peripheral blood immune cells from severe and critical COVID-19 patients have diminished type I IFN and enhanced proinflammatory interleukin-6– and tumor necrosis factor-α–fueled responses. This suggests that in contrast to local production, systemic production of IFNs may be beneficial. The results of this trio of studies suggest that the location, timing, and duration of IFN exposure are critical parameters underlying the success or failure of therapeutics for viral respiratory infections. —STS

Science, this issue p. 706, p. 712, p. 718; see also p. 626

ORGANIC CHEMISTRY

Short path to a complex ring

Nucleotide analogs are valuable tools and therapeutics because of their ability to interfere with processes such as DNA synthesis, which are vital to rapidly dividing cells and replicating viruses. These molecules are challenging to synthesize chemically. Meanwell *et al*. developed a "ribose last" synthetic strategy in which a fluorinated acyclic nucleic acid is formed by an L- or D-proline–catalyzed aldol reaction (see the Perspective by Miller). This intermediate can then be cyclized to yield the nucleic acid analog in one pot with control of anomeric conformation based on cyclization conditions. Nucleotide analogs accessible by this strategy include those with modifications at C2′ and C4′, purines and pyrimidines, and locked and protected products. —MAF

Science, this issue p. 725; see also p. 623

MUCOSAL IMMUNOLOGY

The second way to anticommensal IgA

Mammals rely on secretory immunoglobulin A (SIgA) at the intestinal surface to maintain a homeostatic relationship with the commensal gut microbiota. B lymphocytes differentiate into IgA-producing plasma cells through a thymus-dependent pathway that depends on the B cell protein CD40 transducing a signal from CD40 ligand on T cells. Grasset *et al*. investigated the contribution of a receptor called TACI found predominantly on B cells to an alternative, thymus-independent pathway of plasma cell differentiation. The mucosal immune system was found to use parallel pathways dependent on either CD40 or TACI to provide B cells the help needed to generate SIgA capable of binding commensal bacteria. —IRW

Sci. Immunol. **5**, eaat7117 (2020).

SYSTEMS BIOLOGY

Drug targets found in translation

Translating findings from preclinical animal models to human subjects is challenging, and it is even more so when different types of data are compared. Brubaker *et al*. developed a method to compare transcriptomic data from inflammatory bowel disease patients with proteomics data from a mouse model of the disease. Their analysis suggested that integrin signaling contributed to resistance to the antitumor necrosis factor antibody infliximab. Experimentally, inhibiting α_1 integrin subunit signaling enhanced the ability of infliximab to suppress proinflammatory cytokine release from immune cells. —JFF

Sci. Signal. **13**, eaay3258 (2020).

Published by AAAS

RESEARCH ARTICLE SUMMARY

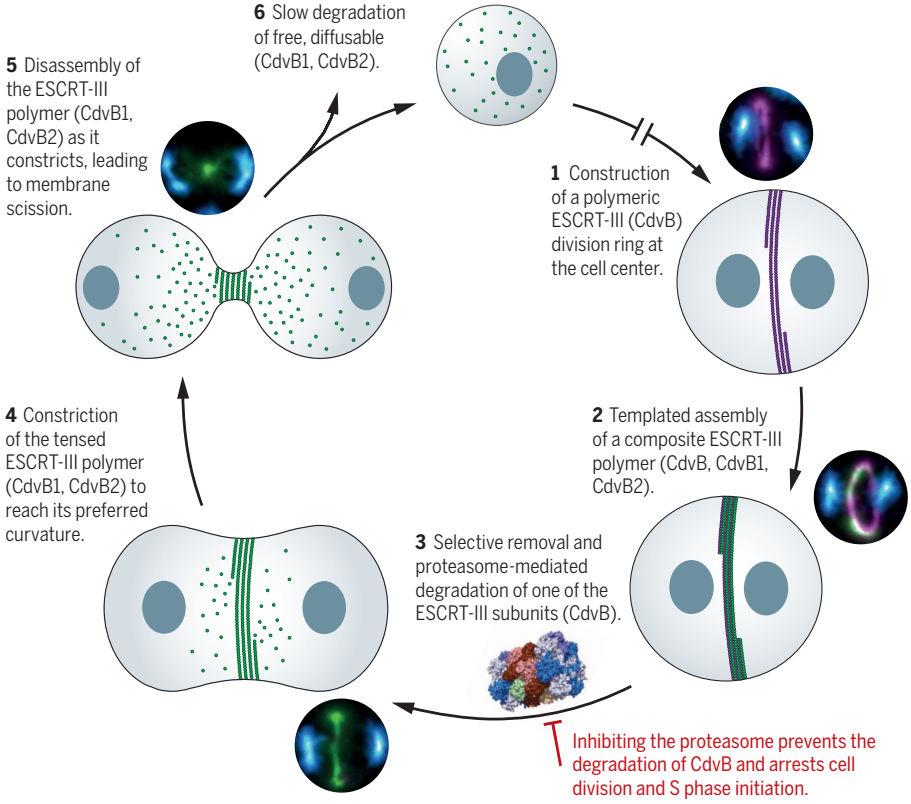
CELL BIOLOGY

The proteasome controls ESCRT-III–mediated cell division in an archaeon

Gabriel Tarrason Risa*, Fredrik Hurtig*, Sian Bray, Anne E. Hafner, Lena Harker-Kirschneck, Peter Faull, Colin Davis, Dimitra Papatziamou, Delyan R. Mutavchiev, Catherine Fan, Leticia Meneguello, Andre Arashiro Pulschen, Gautam Dey, Siân Culley, Mairi Kilkenny, Diorge P. Souza, Luca Pellegrini, Robertus A. M. de Bruin, Ricardo Henriques, Ambrosius P. Snijders, Anđela Šarić, Ann-Christin Lindås, Nicholas P. Robinson†, Buzz Baum†

INTRODUCTION: Eukaryotes likely arose from a symbiotic partnership between an archaeal host and an alpha-proteobacterium, giving rise to the cell body and the mitochondria, respectively. Because of this, a number of proteins controlling key events in the eukaryotic cell division cycle have their origins in archaea. These include ESCRT-III proteins, which catalyze the final step of cytokinesis in many eukaryotes and in the archaeon *Sulfolobus acidocaldarius*. However, to date, no archaeon has been found that harbors homologs of cell cycle regulators, like cyclin-dependent kinases and cyclins, which order events in the cell cycle across all eukaryotes. Thus, it remains uncertain how key events in the archaeal cell cycle, including division, are regulated.

RATIONALE: An exception to this is the 20*S* proteasome, which is conserved between archaea and eukaryotes and which regulates the eukaryotic cell cycle through the degradation of cyclins. To explore the function of the 20*S* proteasome in the archaeon *S. acidocaldarius*, we determined its structure by crystallography and carried out in vitro biochemical analyses of its activity with and without inhibition. The impact of proteasome inhibition on cell division and cell cycle progression was examined in vivo by flow cytometry and super-resolution microscopy. Following up with mass spectrometry, we identified proteins degraded by the proteasome during division. Finally, we used molecular dynamics simulations to model the mechanics of this process.



Model of ESCRT-III–mediated cell division in the archaeon *S. acidocaldarius*. The model shows the sequential stages of the division process in *S. acidocaldarius* (labeled 1 to 6), together with the corresponding stage-specific images. DNA is in blue, CdvB in purple, and CdvB1 and CdvB2 in green. The broken arrow represents an extended period where cells progress through G_1, S, and G_2. Note that Vps4 (not shown) is likely required for ESCRT-III polymer disassembly.

RESULTS: Here, we present a structure of the 20*S* proteasome of *S. acidocaldarius* to a resolution of 3.7 Å, which we used to model its sensitivity to the eukaryotic inhibitor bortezomib. When this inhibitor was added to synchronous cultures, it was found to arrest cells mid-division, with a stable ESCRT-III division ring positioned at the cell center between the two separated and prereplicative nucleoids. Proteomics was then used to identify a single archaeal ESCRT-III homolog, CdvB, as a key target of the proteasome that must be degraded to enable division to proceed.

Examining the localization patterns of CdvB and two other archaeal ESCRT-III homologs, CdvB1 and CdvB2, by flow cytometry and super-resolution microscopy revealed the sequence of events that leads to division. First, a CdvB ring is assembled. This CdvB ring then templates the assembly of the contractile ESCRT-III homologs, CdvB1 and CdvB2, to form a composite division ring. Cell division is then triggered by proteasome-mediated degradation of CdvB, which allows the CdvB1:CdvB2 copolymer to constrict, pulling the membrane with it. During constriction, the CdvB1:CdvB2 copolymer is disassembled, thus vacating the membrane neck to drive abscission, yielding two daughter cells with diffuse CdvB1 and CdvB2.

CONCLUSION: This study reveals a role for the proteasome in driving structural changes in a composite ESCRT-III copolymer, enabling the stepwise assembly, disassembly, and contraction of an ESCRT-III–based division ring. Although it is not yet clear how proteasomal inhibition prevents *S. acidocaldarius* cells from resetting the cell cycle to initiate the next S phase, these data strengthen the case for the eukaryotic cell cycle regulation having its origins in archaea. ■

The list of author affiliations is available in the full article online.
*These authors contributed equally to this work.
†Corresponding author. Email: b.baum@ucl.ac.uk (B.B.); n.robinson2@lancaster.ac.uk (N.P.R.)
Cite this article as G. Tarrason Risa *et al.*, *Science* **369**, eaaz2532 (2020). DOI: 10.1126/science.aaz2532

READ THE FULL ARTICLE AT
https://doi.org/10.1126/science.aaz2532

RESEARCH ARTICLE

CELL BIOLOGY

The proteasome controls ESCRT-III–mediated cell division in an archaeon

Gabriel Tarrason Risa[1]*, Fredrik Hurtig[2]*, Sian Bray[3], Anne E. Hafner[1,4,5], Lena Harker-Kirschneck[1,4,5], Peter Faull[6], Colin Davis[6], Dimitra Papatziamou[7], Delyan R. Mutavchiev[1], Catherine Fan[1], Leticia Meneguello[1], Andre Arashiro Pulschen[1], Gautam Dey[1], Siân Culley[1], Mairi Kilkenny[3], Diorge P. Souza[1], Luca Pellegrini[3], Robertus A. M. de Bruin[1], Ricardo Henriques[1], Ambrosius P. Snijders[6], Anđela Šarić[1,4,5], Ann-Christin Lindås[2], Nicholas P. Robinson[7]†, Buzz Baum[1,4]†

Sulfolobus acidocaldarius is the closest experimentally tractable archaeal relative of eukaryotes and, despite lacking obvious cyclin-dependent kinase and cyclin homologs, has an ordered eukaryote-like cell cycle with distinct phases of DNA replication and division. Here, in exploring the mechanism of cell division in *S. acidocaldarius*, we identify a role for the archaeal proteasome in regulating the transition from the end of one cell cycle to the beginning of the next. Further, we identify the archaeal ESCRT-III homolog, CdvB, as a key target of the proteasome and show that its degradation triggers division by allowing constriction of the CdvB1:CdvB2 ESCRT-III division ring. These findings offer a minimal mechanism for ESCRT-III–mediated membrane remodeling and point to a conserved role for the proteasome in eukaryotic and archaeal cell cycle control.

The eukaryotic cell cycle is ordered by oscillations in the activity of a conserved set of cyclin-dependent kinases. Although both cyclins and cyclin-dependent kinases have yet to be identified outside of eukaryotes, *Sulfolobus acidocaldarius*, a member of the TACK (Thaumarchaeota, Aigarchaeota, Crenarchaeota, and Korarchaeota) superphylum of Archaea, possesses an ordered cell cycle with distinct phases of DNA replication and division, similar in structure to the cell cycle observed in many eukaryotes (*1*). Several of the enzymes used to drive key events in the cell cycle are also conserved from archaea to eukaryotes. For example, archaeal homologs of eukaryotic Cdc6, Orc, MCM, and GINS proteins initiate DNA replication at multiple origins in *S. acidocaldarius*, just as they do in eukaryotes (*2*, *3*). Additionally, previous work shows that homologs of ESCRT-III and the AAA+ adenosine triphosphatase (ATPase) Vps4, proteins that mediate abscission and other membrane remodeling processes in eukaryotes, play an important role in TACK archaeal cell division (*4*). These observations beg the question: Are any of these common events regulated by conserved elements of the cell cycle control machinery that are shared across archaea and eukaryotes?

[1]MRC-Laboratory for Molecular Cell Biology, University College London (UCL), London, UK. [2]Department of Molecular Biosciences, The Wenner-Gren Institute, Stockholm University, Stockholm, Sweden. [3]Biochemistry Department, University of Cambridge, Cambridge, UK. [4]Institute for the Physics of Living Systems, UCL, London, UK. [5]Department of Physics and Astronomy, UCL, London, UK. [6]Proteomics Platform, The Francis Crick Institute, London, UK. [7]Faculty of Health and Medicine, Division of Biomedical and Life Sciences, Lancaster University, Lancaster, UK.
*These authors contributed equally to this work.
†Corresponding author. Email: b.baum@ucl.ac.uk (B.B.); n.robinson2@lancaster.ac.uk (N.P.R.)

Although archaea lack clear homologs of both cyclins and cyclin-dependent kinases, archaeal homologs of the 20*S* core eukaryotic proteasome are readily identifiable (*5*–*8*). In eukaryotes, cell division is initiated by activation of the ubiquitin-E3 ligase, APC, which triggers proteasome-mediated degradation of cyclin B and securin and likely a host of other proteins (*9*), leading to irreversible mitotic exit (*10*), chromosome segregation, and cytokinesis (*11*, *12*). This led us to test whether proteasome-mediated degradation also plays a role in regulating the cell cycle reset in TACK archaea (*1*).

Here, we report that proteasomal activity is required for *S. acidocaldarius* cell division, using inhibitors of the 20*S* proteasome. Proteomics analyses identified a single archaeal ESCRT-III homolog, CdvB (Saci_1373), as a key target for proteasome-mediated degradation during the final stages of the cell division cycle. CdvB is part of the CdvABC operon (Saci_1374, Saci_1373, and Saci_1372) and has previously been implicated in *S. acidocaldarius* cell division (*13*–*15*). A combination of microscopy and flow cytometry data further suggest that CdvB both templates the assembly of a contractile ESCRT-III copolymer, composed of the paralogs CdvB1 (Saci_0451) and CdvB2 (Saci_1416), and prevents their constriction. As a consequence, proteasome-mediated degradation of CdvB triggers cell division.

Results

Bortezomib inhibits the S. acidocaldarius proteasome

To determine a detailed structure of the *S. acidocaldarius* proteasome, building on previous work (*16*), we coexpressed the α subunit and N-terminally truncated β subunit of the proteasome (Saci_0613 and Saci_0662ΔN). This enabled us to produce diffracting crystals of the catalytically inactive, 28-subunit 20*S* proteasome, allowing us to determine its structure to a resolution of 3.7 Å [Fig. 1A; figs. S1, A to C, and S2, A to C; and table S1; Protein Data Bank (PDB) ID 6Z46]. Structures of the equivalent complexes from the euryarchaeon *Archaeoglobus fulgidus* (PDB ID 1J2Q) and *Saccharomyces cerevisiae* (PDB ID 4NNN) were then used to generate a homology model of an N-terminally truncated catalytically active β subunit (Saci_0909ΔN), which was docked into the structure of the *S. acidocaldarius* proteasome in place of one inactive β subunit (Saci_0662 ΔN) (see methods) (*17*). It was then possible to dock bortezomib (PS-341, Velcade), an established small-molecule inhibitor of the proteasomes of euryarchaeota and eukaryotes (*18*–*20*), into the model's active site (Fig. 1B and fig. S1, D and E). Here, the boronic acid moiety of bortezomib forms a bond with the nucleophilic hydroxyl group of the active site threonine, indicating that the small molecule is likely able to inhibit the proteolytic activity of the *S. acidocaldarius* 20*S* proteasome as it does in eukaryotes and in the euryarchaeon *Haloferax volcanii* (*20*, *21*).

To determine whether bortezomib can inhibit the *S. acidocaldarius* proteasome in vitro, as suggested by this structural analysis, we examined the ability of the active complex [consisting of α subunits, together with N-terminally truncated structural and catalytically active β subunits (Saci_0613/Saci_0662ΔN/Saci_0909ΔN)] to degrade a Urm1-tagged green fluorescent protein (GFP) substrate, using a biochemical setup we described previously (see methods) (*16*). When this assay was carried out with different concentrations of inhibitor, the rate of substrate degradation was diminished (Fig. 1C and fig. S3, A to D). We then mutated a conserved valine residue (V49) that mediates critical contacts between the active site and the inhibitor (*22*) to a threonine (V49T). As expected, this led to a reduction in the sensitivity of the purified *S. acidocaldarius* 20*S* proteasome to bortezomib (fig. S3, E and F), validating the mode of inhibitor action.

Proteasomal inhibition arrests the cell cycle of S. acidocaldarius

Having demonstrated that bortezomib inhibits the *S. acidocaldarius* 20*S* proteasome activity in vitro, bortezomib was added to *S. acidocaldarius* cultures to look for a possible role for the 20*S* proteasome in cell cycle control. For this experiment, cells were synchronized to G_2 using acetic acid, released, and observed by flow cytometry as they reentered the cell cycle and divided (see methods) (*23*). Notably, when bortezomib was added to cultures 80 min after release from the acetic acid arrest, the cells failed to divide (Fig. 1D and fig. S4, A and B). Furthermore, this bortezomib-

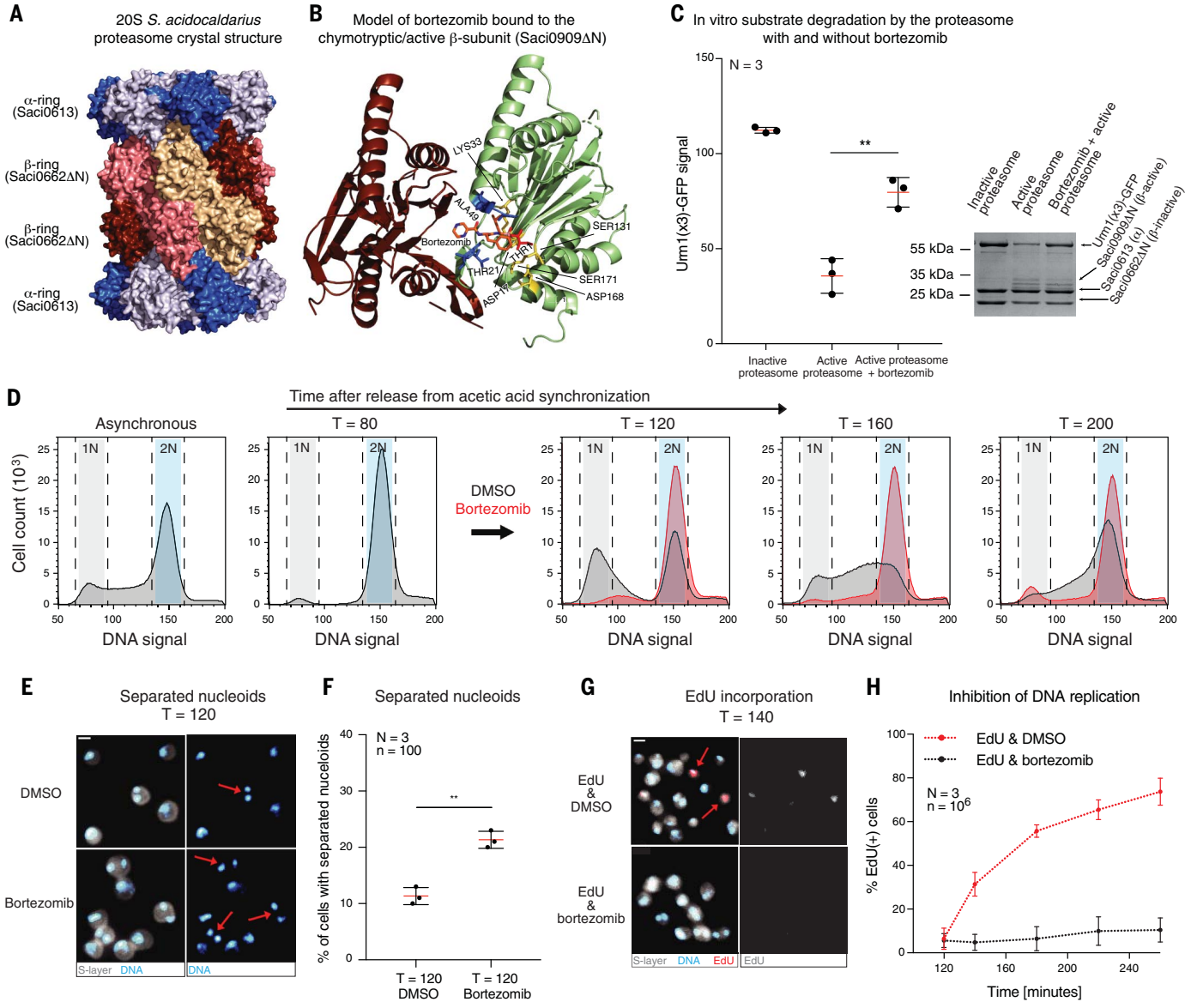


Fig. 1. *S. acidocaldarius* cell division is arrested after inhibition of the proteasome. (**A**) Side view of the *S. acidocaldarius* 28-subunit Saci_0613/Saci_0662ΔN 20S proteasome assembly. Saci_0613 α subunits are indicated by blue and purple hues; Saci_0662ΔN β subunits are indicated by red, pink, and beige hues. (**B**) Modeled binding of the reversible inhibitor bortezomib to the active β subunit (Saci_0909ΔN) chymotryptic site in the *S. acidocaldarius* 20S proteasome using the CovDock software. The catalytic threonine (Thr^{1}) is shown as a red stick covalently bound to the boronic acid group of the bortezomib molecule. The Asp^{17}, Lys^{33}, Ser^{129}, Asp^{166}, and Thr^{169} involved in catalysis are shown as yellow sticks. The two loops (blue) harboring the conserved residues Ala^{20}, Ser^{21}, and Gly^{47} to Val^{49} mediate binding of the inhibitor. (**C**) Quantified degradation assay of GFP control or Urm1(x3)-GFP substrate by the Saci_0613/Saci_0662ΔN/Saci_0909ΔN 20S proteasome. Error bars represent means ± SD from $N = 3$. Data were analyzed using Welch's t test; $^{**}p = 0.0034$. (**D**) Flow cytometry histograms showing 1N and 2N DNA signals in cells in an asynchronous and a synchronized population treated with bortezomib or DMSO 80 min after release (before division). $N = 3$, and $n = 10^5$. Representative histograms are shown. T, time after release. (**E**) Wide-field microscopy images of synchronized cells treated with DMSO or bortezomib for 40 min, 80 min after release from acetic acid. Fixed cells were stained with Hoechst to visualize DNA and concanavalin A to visualize the S-layer. Red arrows indicate cells with separated nucleoids. Representative images are shown. Scale bar, 1 μm. (**F**) Quantification of the percentage of cells in synchronized populations harboring separated nucleoids after treatment with DMSO or bortezomib. Error bars represent means ± SD from $N = 3$ and $n = 100$. Data were analyzed using a ratio paired t test; $^{**}p = 0.0069$. (**G**) Wide-field microscopy images of synchronized STK cells treated for 40 min with DMSO or bortezomib, 100 min after release from acetic acid. Cells were stained with Hoechst to visualize DNA and concanavalin A to visualize the S-layer, and "click" chemistry was used to visualize EdU. Red arrows indicate the cells with EdU incorporated into newly synthesized DNA. Scale bar, 1 μm. (**H**) Quantification of the percentage of synchronized cells with incorporated EdU after DMSO or bortezomib treatment. Error bars represent means ± SD from $N = 3$ and $n = 10^6$.

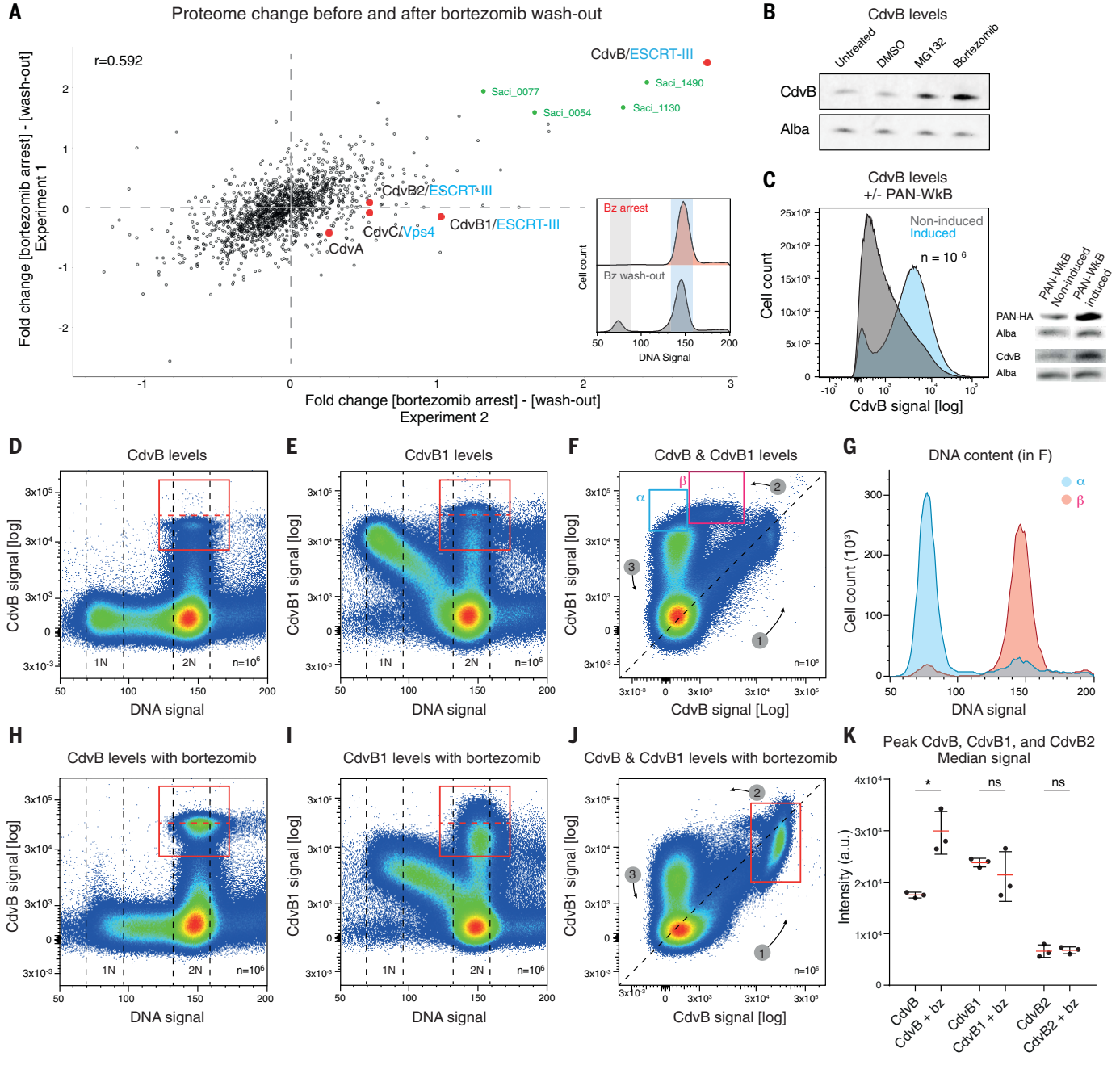


Fig. 2. CdvB is targeted by the *S. acidocaldarius* proteasome during cell division. (**A**) Mass spectrometry scatterplot correlating two independent replicates of proteome changes in predivision synchronized cells treated with bortezomib for 40 min versus the population 15 min after bortezomib had been washed out (after division). The top five hits are in green (apart from CdvB). See table S6 for the complete data. The inset shows two representative histograms of the bortezomib-treated and wash-out samples. (**B**) Western blots of CdvB and Alba (loading control) for synchronized cells which, 80 min after release from acetic acid, were left untreated or treated for 40 min with DMSO, MG132, or bortezomib. (**C**) (Left) Flow cytometry histogram comparing the CdvB signal under noninduced and induced conditions for a PAN-WkB-HA dominant negative overexpression strain and (right) Western blots showing the change in PAN-WkB-HA and CdvB protein levels. (**D** and **E**) Flow cytometry scatterplots of DNA versus CdvB (D) and CdvB1 (E) protein signals of cells in an asynchronous culture. The red boxes highlight the "mitotic" cells with high CdvB and CdvB1 signals in (D) and (E), respectively. Each blue spot represents a single cell, with the density gradient going from blue to red. Representative plots are shown; $N = 3$, and $n = 10^6$. (**F**) Flow cytometry scatterplot of the CdvB versus CdvB1 signal of an asynchronous culture showing the alternating accumulation and loss of the proteins. $N = 3$, and $n = 10^6$. (**G**) Flow cytometry histogram of the DNA distribution of cells in the boxes shown in (F), showing the shift from 2N to 1N taking place only after complete CdvB degradation. (**H** and **I**) Flow cytometry scatterplots of DNA versus CdvB and CdvB1 signals for an asynchronous culture treated with bortezomib. Representative plots are shown; $N = 3$, and $n = 10^6$. (**J**) Flow cytometry scatterplot of CdvB versus CdvB1 levels in an asynchronous culture treated with bortezomib showing an accumulation of cells expressing CdvB and CdvB1 and the selective increase in CdvB levels. Representative plot is shown; $N = 3$, and $n = 10^6$. (**K**) Quantification of median CdvB, CdvB1, and CdvB2 signals in the mitotic populations. Data were analyzed using a ratio paired two-tailed *t* test for CdvB with and without bortezomib (bz); $*p = 0.0245$. Error bars represent means ± SD from $N = 3$. ns, not significant; a.u., arbitrary units.

induced cell cycle arrest was accompanied by a twofold enrichment in the number of cells harboring compact and separated nucleoids [relative to those treated with the dimethyl sulfoxide (DMSO) solvent; Fig. 1, E and F]. Although a similar arrest was observed in cells treated with MG132, a second proteasome inhibitor, this arrest proved more readily reversible, as expected given the inhibitory constant (K_i) values of bortezomib and MG132 (0.6 and 4 nM, respectively) (fig. S5A).

To test whether predivision cells treated with bortezomib were inhibited from undergoing DNA replication as well as cell division, as is the case for a proteasome inhibition–induced mitotic arrest in eukaryotes, we made use of a *S. acidocaldarius* mutant strain expressing thymidine kinase (STK). STK cells incorporate the thymidine analog 5-ethynyl-2′-deoxyuridine (EdU) into newly synthesized DNA, which can be visualized with click-it chemistry (see methods) (*24*). Using this assay, the majority of synchronized STK cells divided and incorporated EdU into their DNA as they entered S phase [note that EdU prevents the completion of S phase in *S. acidocaldarius* (*24*)]. By contrast, there was no evidence of EdU incorporation, and therefore DNA synthesis, in cells treated with bortezomib before division (Fig. 1, G and H, and fig. S4, C and D). When bortezomib was added to synchronous cultures at a later stage to inhibit the proteasome in newly divided cells, however, these G_1 cells continued unimpeded into S phase and G_2 (fig. S4E). These data indicate that inhibiting proteasome activity specifically prohibits cells from dividing and also, directly or indirectly, from initiating the next round of DNA replication.

CdvB is targeted by the proteasome during cell division

Having observed cell cycle arrest after proteasome inhibition (with bortezomib and MG132), we set out to identify proteins that are subject to proteasome-mediated degradation during cell division using tandem mass tag (TMT) labeling and quantitative mass spectrometry. Hits were identified by comparing the proteomes of bortezomib-treated synchronized cultures enriched for cells arrested before division with those of cultures 15 min after inhibitor washout, at which point most arrested cells had divided (see methods). Notably, among the large set of proteins sampled by mass spectrometry, the protein concentration that decreased the most after release from the arrest was CdvB, an ESCRT-III homolog previously identified as a component of the archaeal division machinery (*13*–*15*, *25*) (Fig. 2A and table S6). As expected, CdvB was also identified among the top hits when the proteomes of MG132-treated predivision cultures were compared with the proteomes of DMSO-treated controls (fig. S5B and table S7). These results were confirmed by Western blotting using antibodies validated against cell extracts and purified proteins (Fig. 2B and figs. S6, A and B, and S7B; see methods). Furthermore, CdvB levels increased markedly in cells after induced expression of a Walker B dominant-negative PAN AAA+ ATPase (Saci_0656), a protein known to cap the 20*S* proteasome, which aids protein degradation by threading proteins into its core (*8*) (Fig. 2C). Notably, CdvB was the only division protein consistently enriched in these experiments (Fig. 2A and figs. S5A and S7B). CdvA (Saci_1374, an archaea-specific ESCRT-III recruitment protein), CdvC (Saci_1372, a Vps4 homolog), and CdvB1 and CdvB2 (Saci_0451 and Saci_1416, ESCRT-III homologs), were largely unaffected by proteasome inhibition. This selectivity was not due to differences in Cdv gene transcription, because all of these components of the cell division machinery are transcribed as part of the same predivision wave (*13*, *14*), which we confirmed remains active during a bortezomib-induced predivision arrest (fig. S7A). Taken together, these observations imply a role for selective proteasome-mediated degradation of CdvB at division.

We observed a similar sudden loss of CdvB protein from cells when we used flow cytometry to assess the levels of different ESCRT-III proteins in a population of unperturbed cells as they underwent division (see methods). Again, CdvB was found accumulating to high levels in predivision cells but was absent from newly divided G_1 cells (Fig. 2D and fig. S8C). By contrast, CdvB1 and CdvB2 were maintained at high levels throughout the division process and then partitioned between newly divided daughter cells (Fig. 2E and fig. S8, A, D, and F). In examining the dynamics of CdvB and CdvB1 levels during cell division, it also became clear that CdvB was degraded in cells with 2N DNA content, i.e., before cell division (Fig. 2, F and G, and figs. S8E and S10C). As expected, a flow cytometry analysis of CdvB revealed increased levels in cells arrested before division by bortezomib (Fig. 2H), whereas median levels of CdvB1 and CdvB2 remained unaltered (Fig. 2, I to K, and fig. S8B). Taken together, these observations show that CdvB is selectively targeted for proteasome-mediated degradation partway through the division process.

CdvB degradation triggers constriction of the CdvB1:CdvB2 ring

Previous studies have suggested that CdvB, an essential gene in *S. acidocaldarius*, is actively required for division (*13*–*15*, *25*, *26*). By contrast, our data suggest that the protein is degraded during division. To reconcile these data and understand the role of CdvB and its degradation in cell division, we used super-resolution radial fluctuations (SRRF) super-resolution microscopy to image the archaeal ESCRT-III division rings at different stages in the division process (see methods) (*27*, *28*). This revealed three distinct categories of ESCRT-III division rings: (i) CdvB rings that lack CdvB1, (ii) rings with colocalized CdvB and CdvB1, and (iii) CdvB1 rings that lack CdvB (Fig. 3A). Conspicuously, cells harboring a CdvB1 ring, but lacking CdvB signal, were the only ones seen in a state of constriction. These data support a role for the selective proteasome-mediated degradation of CdvB from preassembled CdvB:CdvB1 rings. This is consistent with the fact that CdvB rings had a mean diameter of 1.23 μm (n = 496, SD = 0.15) (Fig. 3B) and CdvB1 rings co-staining for CdvB had a near-identical mean diameter of 1.24 μm (n = 285, SD = 0.17), whereas CdvB1 rings that lacked CdvB tended to be variable in size and smaller (mean = 0.62 μm, n = 61, SD = 0.35) (Fig. 3C). Moreover, as expected for a division ring, the diameter of the CdvB1 ring was nearly perfectly correlated with the diameter of the division neck, as measured by concanavalin A staining of the archaeal S-layer (fig. S8G). Finally, the diameters of CdvB1 and CdvB2 rings were near perfectly correlated in all images, suggesting that the two ESCRT-III homologs work together during the ring constriction stage of the division process [N = 399, correlation coefficient (r) = 0.98, $p = 2.2 \times 10^{-16}$] (fig. S8H). Taken together, these data suggest that constriction is triggered by the selective and rapid degradation of CdvB by the proteasome. In line with this thinking, we were unable to detect CdvB1 rings lacking CdvB (or CdvB2 rings lacking CdvB) in cells after treatment with the proteasome inhibitor bortezomib. Moreover, all of the rings in bortezomib-treated cells had a mean diameter equivalent to the uniform width of CdvB rings that span the longest axis of the cell, highlighting the role of the proteasome-mediated degradation of CdvB in triggering cell constriction (mean = 1.23 μm, N = 346, SD = 0.32) (Fig. 3D).

The flow cytometry profiles of exponentially growing asynchronous populations co-stained for CdvB and CdvB1 could also be used to generate an approximate timeline of cell division events. This revealed populations of cells in three distinct phases of the division process: (i) 2N cells with peak levels of CdvB but low CdvB1, (ii) 2N cells with peak levels of both CdvB and CdvB1, and (iii) 2N cells with falling levels of CdvB that retain peak levels of CdvB1 (fig. S9A). Because the doubling time of these *S. acidocaldarius* cultures was about 2 hours and 45 min, the relative sizes of these subpopulations could be used to calculate the time spent by a typical cell in each stage of the division process. Notably, this requires taking the exponential age distribution resulting from binary division into account (fig. S9B) (*29*). Thus, the entire process of ESCRT-III–mediated cell division was estimated to have a duration of ~6.2 min (fig. S9, B and C) (*29*). The division process was further resolved on the basis of

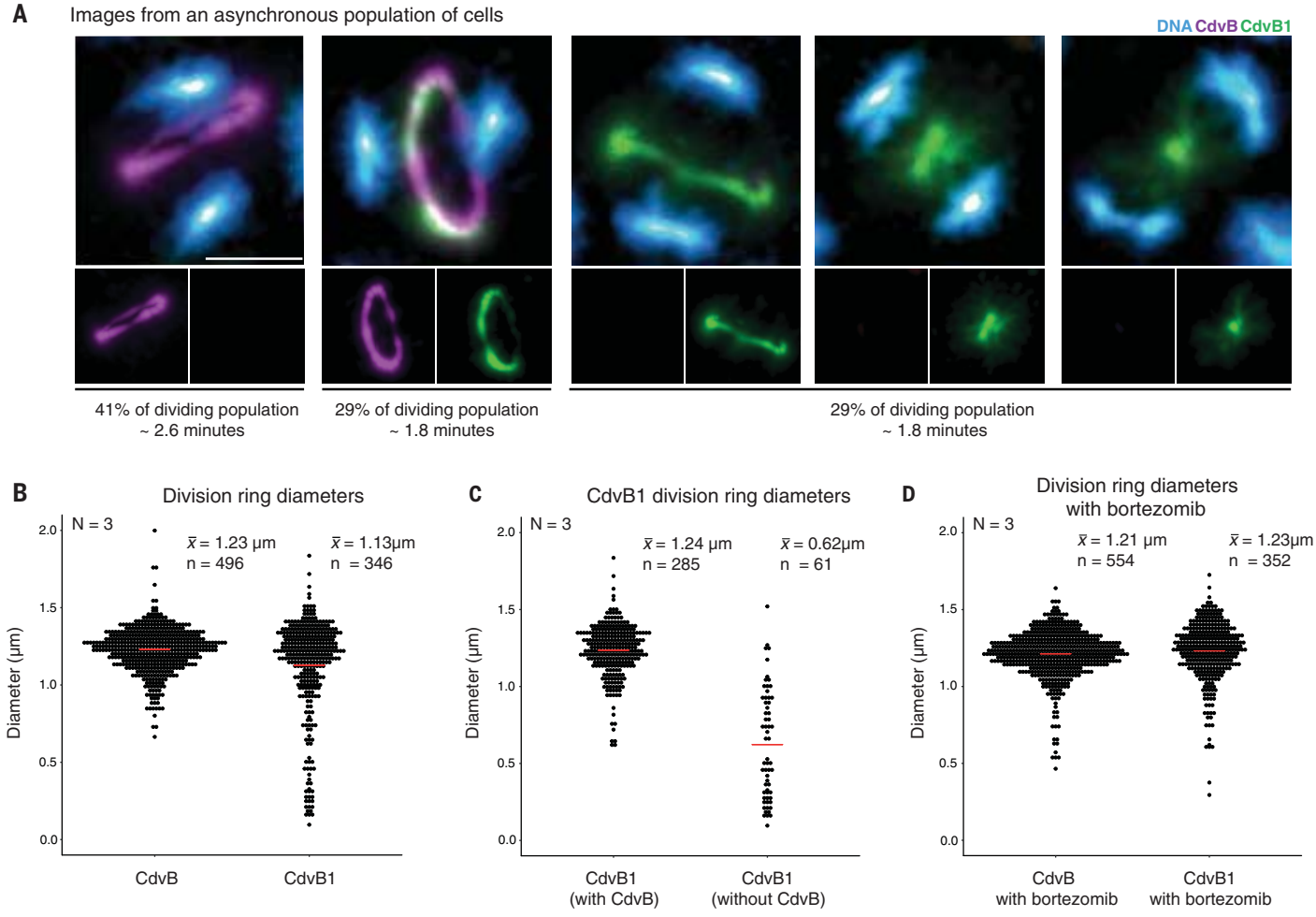


Fig. 3. Targeted degradation of CdvB triggers constriction of CdvB1. (**A**) Representative SRRF super-resolution images of ring structures observed in exponentially growing asynchronous cell cultures. Cells were stained for DNA with Hoechst (blue), CdvB (purple), and CdvB1 (green); the images below the composites represent the CdvB (left) and CdvB1 (right) channels. Percentages refer to the total ring-bearing population. Minutes of the total cell cycle are adjusted for the exponential (binary fission) age distribution. Scale bar, 0.5 µm. (**B**) Quantification of CdvB and CdvB1 ring diameters in an asynchronous culture. $\bar{x}$, mean ring diameters. (**C**) Quantification of ring diameters of CdvB and CdvB1 in the presence and absence of a CdvB ring, showing how the removal of CdvB leads to constriction of CdvB1. (**D**) Quantification of ring diameters of CdvB and CdvB1 in the presence of the proteasomal inhibitor bortezomib. The data in (B) to (D) all stem from more than six fields of view and three biological replicates. Red bars represent the mean values.

these data to reveal the following sequence of events: (i) CdvB rings had an average lifetime of ~2.6 min, before the assembly of CdvB1, (ii) CdvB:CdvB1 rings then persisted for ~1.8 min, before CdvB was degraded by the proteasome, (iii) causing CdvB1 rings to constrict within a period of ~1.8 min. Although we observed minor variations in the percentage of cells in the other two stages of division, the percentage of cells in the contractile phase of the division process (as CdvB is being degraded) appeared highly reproducible (fig. S9C).

Physical model of ESCRT-III–mediated cell division in Archaea

To better monitor changes in both the levels and localization of the CdvB1 ring during the final stages of the division process, we imaged fixed cells using linear structured illumination microscopy (iSIM) [see methods]. This revealed that constriction of the CdvB1 division ring was accompanied by both an increase in the intensity of the fluorescent signal at the neck and a concomitant increase in the level of the diffuse cytoplasmic signal (Fig. 4A and fig. S10A). Throughout division, the sum intensity of CdvB1 remained constant (fig. S10B). As a result, newly divided cells had high levels of diffuse CdvB1 (something we never observed imaging CdvB), in line with the flow cytometric data (Fig. 2F and fig. S8, C and D). The absence of large polymeric CdvB1:CdvB2 structures in these early G_1 cells implies that CdvB1 and CdvB2 do not form de novo ESCRT-III filaments without a CdvB template. In keeping with this conclusion, CdvB2 appeared diffuse when it was ectopically expressed in cells arrested in G_2 with acetic acid, a treatment that inhibits the expression of endogenous Cdv proteins (fig. S11, A to C). Taken together, these observations suggest that the division machinery follows a fixed sequence in which CdvB initially forms an ESCRT-III ring [in a process that likely depends on CdvA (*25*, *30*)], which then templates the assembly of CdvB1:CdvB2 rings. This CdvB1:CdvB2 ring constricts after the sudden removal and degradation of CdvB and is then disassembled during the division process.

To test whether these findings provide a plausible physical mechanism for *S. acidocaldarius* cell division, we used these data as the basis for a coarse-grained molecular dynamics model of ESCRT-III–mediated cell division, based on a recently developed physical model of ESCRT-III–dependent membrane scission (*31*) (see methods). In these simulations, a modeled filament, representing the division ring, was allowed to associate with the plasma membrane of a cell modeled in three dimensions

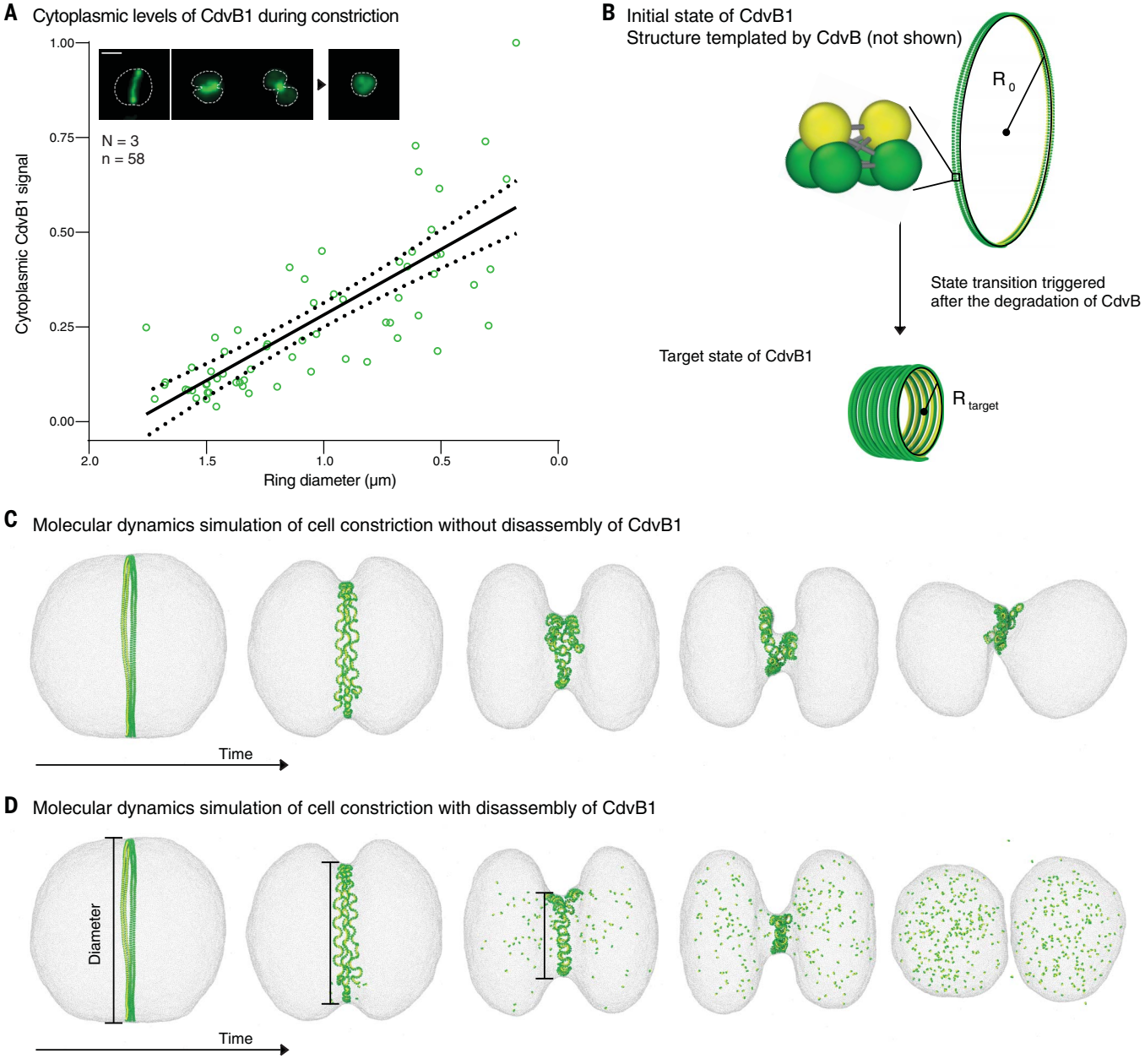
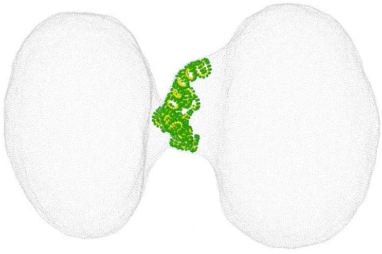
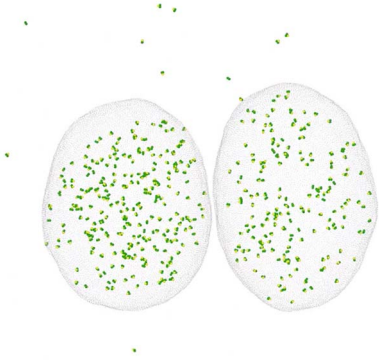


Fig. 4. Physical model of ESCRT-III–mediated cell division in Archaea. (**A**) Quantification of cytoplasmic CdvB1 signal plotted against the CdvB1 ring diameter from a linear iSIM microscopy dataset, with linear regression with 95% confidence interval shown in black. The inset shows representative linear iSIM microscopy images of CdvB1 at various stages of constriction and a cell in G_1 after division. The outline of each cell is highlighted with a white dashed line. Scale bar, 1 μm. (**B**) The molecular dynamics simulation of the ESCRT-III filament is built with three-beaded subunits, which are connected by harmonic springs to form a helix. Only the green beads are attracted by the modeled cell membrane. The helix undergoes a geometrical change from a state with low curvature $1/R_0$, corresponding to CdvB1 with CdvB, to a state with high curvature $1/R_{target}$, corresponding to CdvB1 without CdvB. This change occurs after the proteasomal degradation of CdvB. (**C**) Simulation snapshots as a function of time showing that cell division is not achieved by constriction of the ESCRT-III filament alone; see Movie 1. (**D**) Simulation snapshots showing that disassembly of the ESCRT-III filament is necessary for cell division; see Movie 2.

through its membrane-binding interface. To model the division process, we defined two different preferred filament conformations: a CdvB1 (CdvB+) state with low curvature (defined by a large preferred radius R_0) and a CdvB1 (CdvB–) state with high curvature (defined by the small target radius R_{target}) (Fig. 4B). In this model, the transition between the initial CdvB1 (CdvB+) state and the CdvB1 (CdvB–) state represents the rapid loss of CdvB, which was modeled by an instantaneous shortening of the bonds connecting neighboring elements in the filament. Although the constriction of the CdvB1 ESCRT-III filament was able to rapidly reduce the cell circumference in these simulations, it was not sufficient to induce division because of the steric hindrance at the neck (Fig. 4C and Movie 1, where R_{target}/R_0 = 5%). This is a generic problem faced by molecular machines that cut membrane tubes from the inside. Thus, it was only when CdvB1 filaments were allowed to disassemble as they constricted, as observed in cells (Fig. 4A), that division occurred (Fig. 4D). This was modeled as a gradual loss of individual subunits from both ends of the helix at a specified rate, such that the filament length



Movie 1. Constriction simulation without filament disassembly.



Movie 2. Constriction simulation with filament disassembly.

decreases linearly in time (Movie 2, where R_{target}/R_0 = 5%). In sum, these data and simulations highlight the importance of disassembling the CdvB1:CdvB2 copolymer during constriction, so that the ESCRT-III filament does not crowd the neck and prevent scission.

Discussion

These findings demonstrate how proteasome-mediated degradation of CdvB, a component of the ESCRT-III ring, plays a key role in ordering the changes in ESCRT-III copolymer structure to drive cell division and suggest an elegant mechanism by which *S. acidocaldarius* cells divide. First, cells assemble a structural noncontractile CdvB ring at the center of the cell. This ESCRT-III filament acts as a template for the assembly of CdvB1 and CdvB2 ESCRT-III proteins, which have a smaller preferred radius of curvature. The tension stored in this CdvB1:CdvB2 polymer is then released once the CdvB template is removed and degraded by the proteasome, driving membrane constriction. During constriction, this copolymer is disassembled gradually to enable scission of the membrane bridge connecting the two nascent daughter cells.

Although we were able to demonstrate that the proteasome is able to directly degrade CdvB in vitro (fig. S12), the process is likely more complicated in vivo. This is supported by the observation that a defective PAN proteasome cap leads to an accumulation of CdvB (Fig. 2C). Moreover, previous studies have implicated the ESCRT-III–associated protein Vps4 (CdvC) in the division process (*14*, *32*). In eukaryotes, Vps4 plays a role in the stepwise disassembly of composite ESCRT-III filaments and in membrane deformation (*31*, *33*, *34*). Because the role of Vps4 appears to be conserved, these data suggest that CdvC might be required to selectively extract CdvB from the composite CdvB, CdvB1:CdvB2 copolymer. This soluble pool of CdvB might then be rapidly targeted to the proteasome via PAN, and possibly other proteins, leading to its degradation before it can be reincorporated back into the ring. Although this remains speculation, under this model, the degradation of CdvB would make this change in ESCRT-III polymer structure functionally irreversible. CdvC might then also catalyze the disassembly of the CdvB1:CdvB2 polymer, which is required to vacate the division neck, thus aiding the final process of membrane scission. In line with this idea, previous studies have found that truncating the CdvC-interacting domain in CdvB, CdvB1, or CdvB2 leads to an arrest at various points during the constriction process (*15*), implying that CdvC plays one or more essential roles in archaeal cell division.

This study reveals that ESCRT-III–mediated cell division in *S. acidocaldarius* is regulated by the selective proteasome-mediated degradation of CdvB. It also reveals parallels between cell cycle control in archaea and eukaryotes, implying that proteasome-mediated regulation predates cyclins and cyclin-dependent kinases. Further work will be required (i) to identify all the relevant targets of the proteasome during this final cell cycle transition in Archaea, (ii) to determine whether the proteasome plays an analogous role in driving ESCRT-III–dependent cell division in eukaryotes, (iii) to determine whether the degradation of any of these proteins plays a role in resetting the archaeal cell cycle in a manner analogous the role played by cyclin degradation in eukaryotes, and (iv) to determine if there are other shared design features governing cell cycle progression across the archaeal-eukaryotic divide. However, this study emphasizes the utility of using archaea as a simple model to explore fundamental features of eukaryotic molecular cell biology that have been conserved over 2 billion years of evolution.

Materials and methods summary

Cell culturing, synchronization, and drug treatments

S. acidocaldarius strains were grown at 75°C and pH 3.0 to 3.5 in Brock medium supplemented with NZ-amine and sucrose, with the exception of the STK and MW001 strains that were also supplemented with uracil. Synchronization was achieved with acetic acid treatment and proteasome inhibition by supplementing bortezomib or MG132.

Biochemistry and mass spectrometry

Biochemical analyses were carried out on extracted protein by Western blotting and mass spectrometry and on RNA by quantitative polymerase chain reaction (qPCR). In vitro assays of proteasome activity were studied in the context of active and inactive proteasome assemblies supplemented with a 3xUrm1-GFP reporter. Proteins of interest were expressed in *Escherichia coli*. The antibody specificities for CdvB, CdvB1, and CdvB2 were tested by enzyme-linked immunosorbent assay (ELISA) and whole Western blots.

S. acidocaldarius *genetics*

Two overexpression strains were generated: (i) a dominant negative PAN-WalkerB-HA (HA, hemagglutinin) and (ii) a wild-type CdvB2. Both proteins were subject to arabinose induction and maintained on a plasmid complementing the strains' uracil auxotrophy.

Microscopy and flow cytometry

All microscopy and flow cytometry studies were done on ethanol-fixed cells, staining for DNA and the S-layer and with antibodies against ESCRT-III homologs. For super-resolution, SRRF and linear iSIM were used.

Crystallography

The inactive proteasome subunits were overexpressed in and purified from *E. coli*. Subsequently, crystals were grown in CZ buffer (see methods), and a 3.7-Å dataset was collected from a single crystal at SOLEIL, France.

Molecular dynamics simulations

A fluid spherical membrane consisting of 48,000 particles was modeled together with a chiral ESCRT-III filament modeled with three-beaded subunits (*31*). Simulations for the constriction and disassembly of the ESCRT-III filament were run with the LAMMPS molecular dynamics package.

REFERENCES AND NOTES

1. R. Bernander, The cell cycle of *Sulfolobus*. *Mol. Microbiol.* **66**, 557–562 (2007). doi: 10.1111/j.1365-2958.2007.05917.x; pmid: 17877709
2. D. Ausiannikava, T. Allers, Diversity of DNA replication in the Archaea. *Genes* **8**, 56 (2017). doi: 10.3390/genes8020056; pmid: 28146124
3. S. Lang, L. Huang, The *Sulfolobus solfataricus* GINS complex stimulates DNA binding and processive DNA unwinding by minichromosome maintenance helicase. *J. Bacteriol.* **197**, 3409–3420 (2015). doi: 10.1128/JB.00496-15; pmid: 26283767
4. Y. Caspi, C. Dekker, Dividing the archaeal way: The ancient Cdv cell-division machinery. *Front. Microbiol.* **9**, 174 (2018). doi: 10.3389/fmicb.2018.00174; pmid: 29551994
5. M. Groll, H. Brandstetter, H. Bartunik, G. Bourenkow, R. Huber, Investigations on the maturation and regulation of

archaebacterial proteasomes. *J. Mol. Biol.* **327**, 75–83 (2003). doi: 10.1016/S0022-2836(03)00080-9; pmid: 12614609
6. J. Löwe *et al*., Crystal structure of the 20S proteasome from the archaeon *T. acidophilum* at 3.4 Å resolution. *Science* **268**, 533–539 (1995). doi: 10.1126/science.7725097; pmid: 7725097
7. F. Zhang *et al*., Structural insights into the regulatory particle of the proteasome from *Methanocaldococcus jannaschii*. *Mol. Cell* **34**, 473–484 (2009). doi: 10.1016/j.molcel.2009.04.021; pmid: 19481527
8. J. Maupin-Furlow, Proteasomes and protein conjugation across domains of life. *Nat. Rev. Microbiol.* **10**, 100–111 (2011). doi: 10.1038/nrmicro2696; pmid: 22183254
9. J. F. Giménez-Abián, L. A. Díaz-Martínez, K. G. Wirth, C. De la Torre, D. J. Clarke, Proteasome activity is required for centromere separation independently of securin degradation in human cells. *Cell Cycle* **4**, 1558–1560 (2005). doi: 10.4161/cc.4.11.2145; pmid: 16205121
10. S. López-Avilés, O. Kapuy, B. Novák, F. Uhlmann, Irreversibility of mitotic exit is the consequence of systems-level feedback. *Nature* **459**, 592–595 (2009). doi: 10.1038/nature07984; pmid: 19387440
11. M. Glotzer, A. W. Murray, M. W. Kirschner, Cyclin is degraded by the ubiquitin pathway. *Nature* **349**, 132–138 (1991). doi: 10.1038/349132a0; pmid: 1846030
12. K. Wickliffe, A. Williamson, L. Jin, M. Rape, The multiple layers of ubiquitin-dependent cell cycle control. *Chem. Rev.* **109**, 1537–1548 (2009). doi: 10.1021/cr800414e; pmid: 19146381
13. A.-C. Lindås, E. A. Karlsson, M. T. Lindgren, T. J. G. Ettema, R. Bernander, A unique cell division machinery in the Archaea. *Proc. Natl. Acad. Sci. U.S.A.* **105**, 18942–18946 (2008). doi: 10.1073/pnas.0809467105; pmid: 18987308
14. R. Y. Samson, T. Obita, S. M. Freund, R. L. Williams, S. D. Bell, A role for the ESCRT system in cell division in Archaea. *Science* **322**, 1710–1713 (2008). doi: 10.1126/science.1165322; pmid: 19008417
15. J. Liu *et al*., Functional assignment of multiple ESCRT-III homologs in cell division and budding in *Sulfolobus islandicus*. *Mol. Microbiol.* **105**, 540–553 (2017). doi: 10.1111/mmi.13716; pmid: 28557139
16. R. S. Anjum *et al*., Involvement of a eukaryotic-like ubiquitin-related modifier in the proteasome pathway of the archaeon *Sulfolobus acidocaldarius*. *Nat. Commun.* **6**, 8163 (2015). doi: 10.1038/ncomms9163; pmid: 26348592
17. A. Šali, T. L. Blundell, Comparative protein modelling by satisfaction of spatial restraints. *J. Mol. Biol.* **234**, 779–815 (1993). doi: 10.1006/jmbi.1993.1626; pmid: 8254673
18. J. Adams *et al*., Proteasome inhibitors: A novel class of potent and effective antitumor agents. *Cancer Res.* **59**, 2615–2622 (1999). pmid: 10363983
19. D. Chen, M. Frezza, S. Schmitt, J. Kanwar, Q. P. Dou, Bortezomib as the first proteasome inhibitor anticancer drug: Current status and future perspectives. *Curr. Cancer Drug Targets* **11**, 239–253 (2011). doi: 10.2174/156800911794519752; pmid: 21247388
20. X. Fu *et al*., Ubiquitin-like proteasome system represents a eukaryotic-like pathway for targeted proteolysis in Archaea. *mBio* **7**, e00379–e16 (2016). doi: 10.1128/mBio.00379-16; pmid: 27190215
21. N. L. Hepowit, J. A. Maupin-Furlow, Rhodanese-like domain protein UbaC and its role in ubiquitin-like protein modification and sulfur mobilization in Archaea. *J. Bacteriol.* **201**, e00254-19 (2019). doi: 10.1128/JB.00254-19; pmid: 31085691
22. R. Oerlemans *et al*., Molecular basis of bortezomib resistance: Proteasome subunit β5 (*PSMB5*) gene mutation and overexpression of PSMB5 protein. *Blood* **112**, 2489–2499 (2008). doi: 10.1182/blood-2007-08-104950; pmid: 18565852
23. M. Lundgren, A. Andersson, L. Chen, P. Nilsson, R. Bernander, Three replication origins in *Sulfolobus* species: Synchronous initiation of chromosome replication and asynchronous termination. *Proc. Natl. Acad. Sci. U.S.A.* **101**, 7046–7051 (2004). doi: 10.1073/pnas.0400656101; pmid: 15107501
24. T. Gristwood, I. G. Duggin, M. Wagner, S. V. Albers, S. D. Bell, The sub-cellular localization of *Sulfolobus* DNA replication. *Nucleic Acids Res.* **40**, 5487–5496 (2012). doi: 10.1093/nar/gks217; pmid: 22402489
25. R. Y. Samson *et al*., Molecular and structural basis of ESCRT-III recruitment to membranes during archaeal cell division. *Mol. Cell* **41**, 186–196 (2011). doi: 10.1016/j.molcel.2010.12.018; pmid: 21255729
26. N. Yang, A. J. M. Driessen, Deletion of cdvB paralogous genes of *Sulfolobus acidocaldarius* impairs cell division. *Extremophiles* **18**, 331–339 (2014). doi: 10.1007/s00792-013-0618-5; pmid: 24399085
27. N. Gustafsson *et al*., Fast live-cell conventional fluorophore nanoscopy with ImageJ through super-resolution radial fluctuations. *Nat. Commun.* **7**, 12471 (2016). doi: 10.1038/ncomms12471; pmid: 27514992
28. R. F. Laine *et al*., NanoJ: a high-performance open-source super-resolution microscopy toolbox. bioRxiv 432674 [Preprint]. 6 October 2018; .doi: 10.1101/432674
29. S. Wold, K. Skarstad, H. B. Steen, T. Stokke, E. Boye, The initiation mass for DNA replication in *Escherichia coli* K-12 is dependent on growth rate. *EMBO J.* **13**, 2097–2102 (1994). doi: 10.1002/j.1460-2075.1994.tb06485.x; pmid: 8187762
30. M. J. Dobro *et al*., Electron cryotomography of ESCRT assemblies and dividing *Sulfolobus* cells suggests that spiraling filaments are involved in membrane scission. *Mol. Biol. Cell* **24**, 2319–2327 (2013). doi: 10.1091/mbc.e12-11-0785; pmid: 23761076
31. L. Harker-Kirschneck, B. Baum, A. E. Šarić, Changes in ESCRT-III filament geometry drive membrane remodelling and fission in silico. *BMC Biol.* **17**, 82 (2019). doi: 10.1186/s12915-019-0700-2; pmid: 31640700
32. B. E. Mierzwa *et al*., Dynamic subunit turnover in ESCRT-III assemblies is regulated by Vps4 to mediate membrane remodelling during cytokinesis. *Nat. Cell Biol.* **19**, 787–798 (2017). doi: 10.1038/ncb3559; pmid: 28604678
33. A.-K. Pfitzner, V. Mercier, A. Roux, Vps4 triggers sequential subunit exchange in ESCRT-III polymers that drives membrane constriction and fission. bioRxiv 718080 [Preprint]. 29 July 2019; https://doi.org/10.1101/718080.doi: 10.1101/718080
34. C. Caillat, S. Maity, N. Miguet, W. H. Roos, W. Weissenhorn, The role of VPS4 in ESCRT-III polymer remodeling. *Biochem. Soc. Trans.* **47**, 441–448 (2019). doi: 10.1042/BST20180026; pmid: 30783012

ACKNOWLEDGMENTS

We thank the MRC LMCB at UCL for their support; the flow cytometry STP at the Francis Crick Institute for assistance, with special thanks to S. Purewal and D. Davis; C. Bertoli for mentorship and advice; J. M. Garcia-Arcos for help early on in this project; the entire Baum lab for their input throughout the project; the Albers lab for advice and reagents, with special thanks to M. Van Wolferen and S. Albers; the members of the Wellcome consortium for archaeal cytoskeleton studies for advice and comments; and J. Löwe, S. Oliferenko, M. Balasubramanian, and D. Gerlich for discussions and advice on the manuscript. N.P.R. and S.B. would like to thank N. Rzechorzek, A. Simon, and S. Anjum for discussion and advice. **Funding:** The Baum, Henriques, and de Bruin labs received support from the MRC (MC_CF12266). G.T.R. was supported by MRC (1621658). F.H. was supported by Vetenskapsrådet (621-2013-4685) and A.A.P. by the HFSP (LT001027/2019 fellowship). A collaborative grant from the Wellcome Trust supported A.A.P., D.P.S., G.D., S.C., and the Baum, Lindas, and Henriques labs (203276/Z/16/Z). D.R.M. was supported by a BBSRC grant awarded to B.B. (BB/K009001/1). L.M. and R.A.M.d.B. were supported by Cancer Research UK (C33246/A20147). P.F., C.D., and A.P.S. were supported by the Francis Crick Institute, which receives its core funding from Cancer Research UK (FC001999), the UK Medical Research Council (FC001999), and the Wellcome Trust (FC001999). L.H.-K. was supported by the Biotechnology and Biological Sciences Research Council (BB/M009513/1). A.Š. and A.E.H. were supported by the European Research Council (802960) and the Engineering and Physical Sciences Research Council (EP/R011818/1). N.P.R. was supported by the Isaac Newton Trust Research Grant (Trinity College and Department of Biochemistry, Cambridge) and start-up funds from the Division of Biomedical and Life Sciences (Lancaster University) and received a BBSRC Doctoral Training Grant (RG53842) for S.B. **Author contributions:** B.B. and G.T.R. conceived the study. Initial observations were made by F.H. and G.T.R. Structural work was planned and carried out by S.B. and N.P.R., with assistance from M.K. and L.P. In vitro proteasome assays were planned and performed by D.P. and N.P.R. Cell biology methods and experiments were developed by G.T.R., F.H., G.D., D.R.M., and S.C. with guidance from B.B., R.H., and A.-C.L. Molecular genetics were done by F.H., D.R.M., A.A.P., and G.T.R. Biochemical analysis was carried out by F.H., G.T.R., L.M., A.A.P., and D.P.S. RNA analysis was carried out by C.F., with guidance from B.B. and R.A.M.d.B. Mass spectrometry preparation and analysis was carried out by P.F., C.D., and G.T.R., with guidance from A.P.S. The physical model was built by A.E.H. and L.H.-K., with guidance from A.Š. and B.B. The paper was written by G.T.R., F.H., and B.B., with input from all other authors. **Competing interests:** The authors declare no competing interests. **Data and materials availability:** All data are available in the manuscript or the supplementary materials. The crystal structure of the *S. acidocaldarius* 20S proteasome is available at PDB, with the ID 6Z46. All materials are available from B.B. or N.P.R. on request.

SUPPLEMENTARY MATERIALS

science.sciencemag.org/content/369/6504/eaaz2532/suppl/DC1
Materials and Methods
Figs. S1 to S14
Tables S1 to S7
References (*35*–*53*)

View/request a protocol for this paper from *Bio-protocol*.

27 August 2019; resubmitted 30 March 2020
Accepted 11 June 2020
10.1126/science.aaz2532

RESEARCH ARTICLE

CORONAVIRUS

Potent neutralizing antibodies from COVID-19 patients define multiple targets of vulnerability

Philip J. M. Brouwer[1]*, Tom G. Caniels[1]*, Karlijn van der Straten[1,2]*, Jonne L. Snitselaar[1], Yoann Aldon[1], Sandhya Bangaru[3], Jonathan L. Torres[3], Nisreen M. A. Okba[4], Mathieu Claireaux[1], Gius Kerster[1], Arthur E. H. Bentlage[5], Marlies M. van Haaren[1], Denise Guerra[1], Judith A. Burger[1], Edith E. Schermer[1], Kirsten D. Verheul[1], Niels van der Velde[6], Alex van der Kooi[6], Jelle van Schooten[1], Mariëlle J. van Breemen[1], Tom P. L. Bijl[1], Kwinten Sliepen[1], Aafke Aartse[1,7], Ronald Derking[1], Ilja Bontjer[1], Neeltje A. Kootstra[8], W. Joost Wiersinga[2], Gestur Vidarsson[5], Bart L. Haagmans[4], Andrew B. Ward[3], Godelieve J. de Bree[2]†, Rogier W. Sanders[1,9]†, Marit J. van Gils[1]†

The rapid spread of severe acute respiratory syndrome coronavirus 2 (SARS-CoV-2) has had a large impact on global health, travel, and economy. Therefore, preventative and therapeutic measures are urgently needed. Here, we isolated monoclonal antibodies from three convalescent coronavirus disease 2019 (COVID-19) patients using a SARS-CoV-2 stabilized prefusion spike protein. These antibodies had low levels of somatic hypermutation and showed a strong enrichment in VH1-69, VH3-30-3, and VH1-24 gene usage. A subset of the antibodies was able to potently inhibit authentic SARS-CoV-2 infection at a concentration as low as 0.007 micrograms per milliliter. Competition and electron microscopy studies illustrate that the SARS-CoV-2 spike protein contains multiple distinct antigenic sites, including several receptor-binding domain (RBD) epitopes as well as non-RBD epitopes. In addition to providing guidance for vaccine design, the antibodies described here are promising candidates for COVID-19 treatment and prevention.

The rapid emergence of three novel pathogenic human coronaviruses in the past two decades has caused major concerns. The latest, severe acute respiratory syndrome coronavirus 2 (SARS-CoV-2), is responsible for >3 million infections and 230,000 deaths worldwide as of 1 May 2020 (*1*). Coronavirus disease 2019 (COVID-19), caused by SARS-CoV-2, is characterized by mild, flu-like symptoms in most patients. However, severe cases can present with bilateral pneumonia that may rapidly deteriorate into acute respiratory distress syndrome (*2*). With high transmission rates and no proven curative treatment available, health care systems are severely overwhelmed, and stringent public health measures are in place to prevent infection. Safe and effective treatment and prevention measures for COVID-19 are urgently needed.

During the outbreak of the first severe acute respiratory syndrome coronavirus (SARS-CoV) and Middle Eastern respiratory syndrome coronavirus (MERS-CoV), plasma of recovered patients containing neutralizing antibodies (NAbs) was used as a safe and effective treatment option to decrease viral load and to reduce mortality in severe cases (*3*, *4*). Recently, a small number of COVID-19 patients treated with convalescent plasma showed clinical improvement and a decrease in viral load (*5*). An alternative treatment strategy would be to administer purified monoclonal antibodies (mAbs) with neutralizing capacity. mAbs can be thoroughly characterized in vitro and expressed in large quantities. In addition, because of the ability to control dosing and composition, mAb therapy has improved efficacy over convalescent plasma treatment and prevents the potential risks of antibody-dependent enhancement (ADE) from non-neutralizing or poorly neutralizing Abs present in plasma that consists of a polyclonal mixture (*6*). Recent studies with patients infected with the Ebola virus highlight the superiority of mAb treatment over convalescent plasma treatment (*7*, *8*). Moreover, mAb therapy has been proven safe and effective against influenza virus, rabies virus, and respiratory syncytial virus (RSV) (*9*–*11*).

The main target for NAbs on coronaviruses is the spike (S) protein, a homotrimeric glycoprotein that is anchored in the viral membrane. Recent studies have shown that the S protein of SARS-CoV-2 bears considerable structural homology to that of SARS-CoV, consisting of two subdomains: the N-terminal S1 domain, which contains the N-terminal domain (NTD) and the RBD for the host cell receptor angiotensin-converting enzyme-2 (ACE2), and the S2 domain, which contains the fusion peptide (*12*, *13*). Similar to other viruses containing class 1 fusion proteins (e.g., HIV-1, RSV, and Lassa virus), the S protein undergoes a conformational change and proteolytic cleavage upon host cell receptor binding from a prefusion to a postfusion state, enabling merging of viral and target cell membranes (*14*, *15*). When expressed as recombinant soluble proteins, class 1 fusion proteins generally have the propensity to switch to a postfusion state. However, most NAb epitopes present in the prefusion conformation (*16*–*18*). The recent successes of isolating potent NAbs against HIV-1 and RSV using stabilized prefusion glycoproteins reflect the importance of using the prefusion conformation for isolating and mapping mAbs against SARS-CoV-2 (*19*, *20*).

Early efforts at obtaining NAbs focused on reevaluating SARS-CoV–specific mAbs isolated after the 2003 outbreak that might cross-neutralize SARS-CoV-2 (*21*, *22*). Although two mAbs were described to cross-neutralize SARS-CoV-2, most SARS-CoV NAbs did not bind SARS-CoV-2 S protein or neutralize SARS-CoV-2 virus (*12*, *21*–*23*). More recently, the focus has shifted from cross-neutralizing SARS-CoV NAbs to the isolation of new SARS-CoV-2 NAbs from recovered COVID-19 patients (*24*–*28*). S protein fragments containing the RBD have yielded multiple NAbs that can neutralize SARS-CoV-2 by targeting different RBD epitopes (*24*–*28*). In light of the rapid emergence of escape mutants in the RBD of SARS-CoV and MERS, monoclonal NAbs targeting epitopes other than the RBD are a valuable component of any therapeutic antibody cocktail (*29*, *30*). Indeed, therapeutic antibody cocktails with a variety of specificities have been used successfully against Ebola virus disease (*7*) and are being tested widely in clinical trials for HIV-1 (*31*). NAbs targeting non-RBD epitopes have been identified for SARS-CoV and MERS, supporting the rationale for sorting mAbs using the entire ectodomain of the SARS-CoV-2 S protein (*32*). In addition, considering the high sequence identity between the S2 subdomains of SARS-CoV-2 and SARS-CoV, using the complete S protein ectodomain instead of only the RBD may allow the isolation of mAbs that cross-neutralize different β-coronaviruses (*33*). In an attempt to obtain mAbs that target both RBD and non-RBD epitopes, we set out to isolate mAbs using the complete prefusion S protein ectodomain of SARS-CoV-2.

[1]Department of Medical Microbiology, Amsterdam UMC, University of Amsterdam, Amsterdam Institute for Infection and Immunity, 1105AZ Amsterdam, Netherlands. [2]Department of Internal Medicine, Amsterdam UMC, University of Amsterdam, Amsterdam Institute for Infection and Immunity, 1105AZ Amsterdam, Netherlands. [3]Department of Integrative Structural and Computational Biology, The Scripps Research Institute, La Jolla, CA 92037, USA. [4]Department of Viroscience, Erasmus Medical Center, Rotterdam, 3015GD, Netherlands. [5]Sanquin Research, Department of Experimental Immunohematology, Amsterdam, Netherlands and Landsteiner Laboratory, Amsterdam UMC, University of Amsterdam, 1006AD Amsterdam, Netherlands. [6]IBIS Technologies BV, 7521PR Enschede, Netherlands. [7]Department of Virology, Biomedical Primate Research Centre, 2288GJ Rijswijk, Netherlands. [8]Department of Experimental Immunology, Amsterdam UMC, University of Amsterdam, Amsterdam Institute for Infection and Immunity, 1105AZ Amsterdam, Netherlands. [9]Department of Microbiology and Immunology, Weill Medical College of Cornell University, New York, NY 10021, USA.
*These authors contributed equally to this work.
†Corresponding author. Email: m.j.vangils@amsterdamumc.nl (M.J.v.G.); r.w.sanders@amsterdamumc.nl (R.W.S.); g.j.debree@amsterdamumc.nl (G.J.d.B.)

Phenotyping SARS-CoV-2–specific B cell subsets

We collected a single blood sample from three polymerase chain reaction–confirmed SARS-CoV-2–infected individuals (COSCA1, COSCA2, and COSCA3) ~4 weeks after symptom onset. COSCA1 (a 47-year-old male) and COSCA2 (a 44-year-old female) showed symptoms of an upper respiratory tract infection and mild pneumonia, respectively (Table 1). Both remained in home isolation during the course of COVID-19 symptoms. COSCA3, a 69-year-old male, developed a severe pneumonia and became respiratory insufficient 1.5 weeks after symptom onset, requiring admission to the intensive

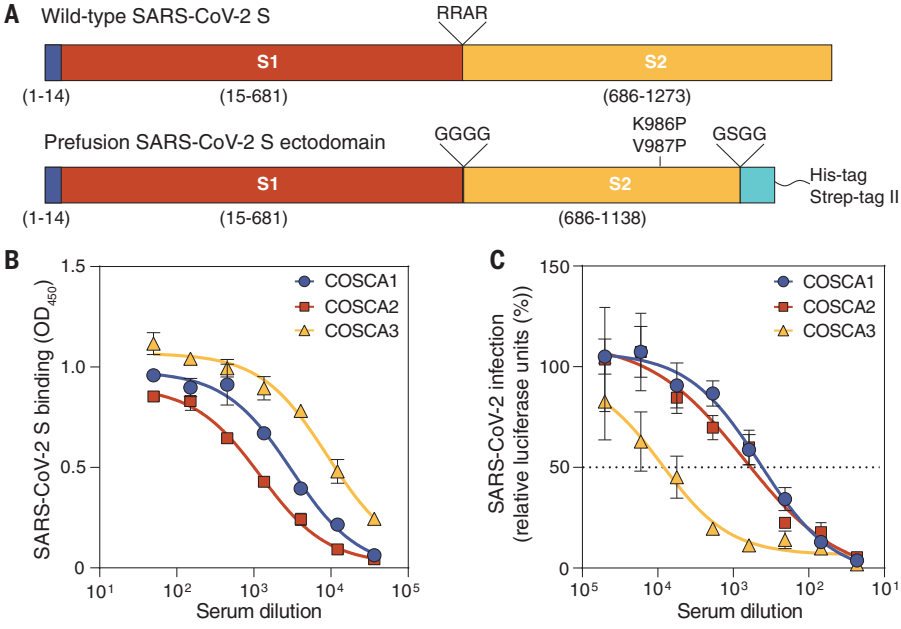


Fig. 1. Design of SARS-CoV-2 S protein and serology of COSCA1, COSCA2, and COSCA3. (**A**) (Top) Schematic overview of the authentic SARS-CoV-2 S protein with the signal peptide shown in blue and the S1 (red) and S2 (yellow) domains separated by a furin-cleavage site (RRAR; top). (Bottom) Schematic overview of the stabilized prefusion SARS-CoV-2 S ectodomain, where the furin cleavage site is replaced with a glycine linker (GGGG), two proline mutations are introduced (K986P and V987P), and a trimerization domain (cyan) preceded by a linker (GSGG) is attached. (**B**) Binding of sera from COSCA1, COSCA2, and COSCA3 to prefusion SARS-CoV-2 S protein as determined by ELISA. The mean values and SDs of two technical replicates are shown. (**C**) Neutralization of SARS-CoV-2 pseudovirus by heat-inactivated sera from COSCA1, COSCA2, and COSCA3. The mean and SEM of at least three technical replicates are shown. The dotted line indicates 50% neutralization.

Table 1. Patient characteristics, symptoms of COVID-19, treatment modalities, and sampling time points of three SARS-CoV-2–infected patients.

	COSCA1	COSCA2	COSCA3
Patient characteristics			
Age (years)	47	44	69
Gender	Male	Female	Male
Comorbidities	None	None	None
Symptoms, from onset to relief, days			
Fever (>38°C)	4–10	1–4	6–18
Coughing	2–35	3–17	1–20
Sputum production	2–35	No	1–20
Dyspnea	4–24	No	No
Sore throat	1–5	5–17	No
Rhinorrhea	2–34	5–17	No
Anosmia	No	5–17	No
Myalgia	No	1–4	6–18
Headache	No	No	1–18
Other	No	No	Delirium
Treatment modalities, treatment period, days			
Hospital admission	No	No	8–24
ICU admission	No	No	11–18
Oxygen therapy	No	No	8–24
Intubation	No	No	11–16
Dialysis	No	No	No
Drug therapy			
Antiviral	No	No	No
Antibiotic	No	No	Cefotaxime, 8–12 Ciprofloxacin, 8–11
Immunomodulatory	No	No	No
NSAIDs	No	No	No
Sampling time point, days after symptom onset	27	28	23

care unit for mechanical ventilation. To identify S protein–specific antibodies in the sera obtained from all three patients, we generated soluble, prefusion-stabilized S proteins of SARS-CoV-2 using stabilization strategies previously described for S proteins of SARS-CoV-2 and other β-coronaviruses (Fig. 1A) (*12*, *34*). As demonstrated by the size-exclusion chromatography trace, SDS–polyacrylamide gel electrophoresis (PAGE), and blue native PAGE, the resulting trimeric SARS-CoV-2 S proteins were of high purity (fig. S1, A and B). Sera from all patients showed strong binding to the S protein of SARS-CoV-2 in an enzyme-linked immunosorbent assay (ELISA), with end-point titers of 13,637, 6133, and 48,120 for COSCA1, COSCA2, and COSCA3, respectively (Fig. 1B), and showed cross-reactivity to the S protein of SARS-CoV (fig. S1C). COSCA1, COSCA2, and COSCA3 had varying neutralizing potencies against SARS-CoV-2 pseudovirus, with 50% inhibition of virus infection (ID_{50}) values of 383, 626, and 7645, respectively (Fig. 1C), and similar activities against authentic virus (fig. S1D). In addition, all sera showed cross-neutralization of SARS-CoV pseudovirus and authentic SARS-CoV virus, albeit with low potency (fig. S1, E and F). The potent S protein–binding and -neutralizing responses observed for COSCA3 are consistent with earlier findings showing that severe disease is associated with a strong humoral response (*35*). On the basis of these strong serum binding and neutralization titers, we sorted SARS-CoV-2 S protein–specific B cells for mAb isolation from COSCA1, COSCA2, and COSCA3.

Peripheral blood mononuclear cells were stained dually with fluorescently labeled prefusion SARS-CoV-2 S proteins and analyzed for the frequency and phenotype of specific B cells by flow cytometry (Fig. 2A and fig S2). The analysis revealed a frequency ranging from 0.68 to 1.74% of S protein–specific B cells ($S\text{-}AF647^+$, $S\text{-}BV421^+$) among the total pool of B cells ($CD19^+Via\text{-}CD3^-CD14^-CD16^-$), (Fig. 2B). These SARS-CoV-2 S protein–specific B cells showed a predominant memory ($CD20^+CD27^+$) and plasmablasts/plasma cells (PBs/PCs) ($CD20^-CD27^+CD38^+$) phenotype. We observed a threefold higher percentage of PBs/PCs for SARS-CoV-2 S protein–specific B cells compared with total B cells ($P = 0.034$), indicating an enrichment of specific B cells in this subpopulation (Fig. 2C). COSCA3, who experienced severe symptoms, showed the highest frequency of PBs/PCs in both total (34%) and specific (60%) B cells (Fig. 2C and fig. S2). As expected, the SARS-CoV-2 S protein–specific B cells were enriched in the immunoglobulin G–positive (IgG^+) and IgM^-/IgG^- (most likely representing IgA^+) B cell populations, although a substantial portion of the specific B cells were IgM^+, particularly for COSCA3 (Fig. 2D).

Genotypic signatures of the SARS-CoV-2–specific antibody response

SARS-CoV-2 S protein–specific B cells were subsequently single-cell sorted for sequencing and mAb isolation. In total, 409 heavy chain (HC) and light chain (LC) pairs were obtained from the sorted B cells of the three patients (137, 165, and 107 from COSCA1, COSCA2, and COSCA3, respectively), of which 323 were unique clonotypes. Clonal expansion occurred in all three patients (Fig. 3A) but was strongest in COSCA3, where it was dominated by HC variable (VH) regions VH3-7 and VH4-39 (34 and 32% of SARS-CoV-2 S protein–specific sequences, respectively). Even though substantial clonal expansion occurred in COSCA3, the median somatic hypermutation (SHM) was 1.4%, with similar SHM in COSCA1 and COSCA2 (2.1 and 1.4%, respectively) (Fig. 3B). These SHM levels are similar

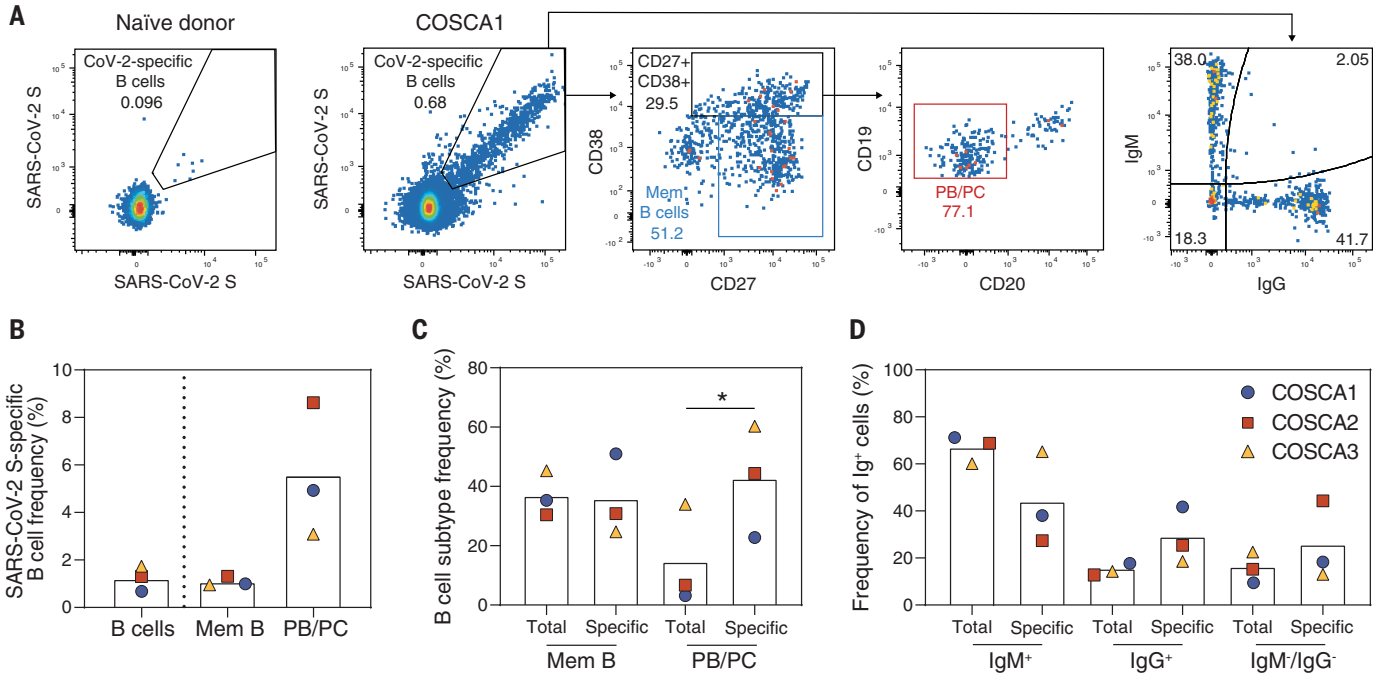


Fig. 2. Characterization of SARS-CoV-2 S protein–specific B cells derived from COSCA1, COSCA2, and COSCA3. (**A**) Representative gates of SARS-CoV-2 S protein–specific B cells shown for a naïve donor (left panel) or COSCA1 (middle left panel). Each dot represents a B cell. The gating strategy to identify B cells is shown in fig. S2. From the total pool of SARS-CoV-2 S protein–specific B cells, $CD27^+CD38^-$ memory B cells (Mem B cells; blue gate) and $CD27^+CD38^+$ B cells were identified (middle panel). From the latter gate, PBs/PCs ($CD20^-$; red gate) could be identified (middle right panel). SARS-CoV-2 S protein–specific B cells were also analyzed for their IgG or IgM isotype (right panel). (**B**) Frequency of SARS-CoV-2 S protein–specific B cells in total B cells, Mem B cells, and PBs/PCs. Symbols represent individual patients, as shown in (D). (**C**) Comparison of the frequency of Mem B cells ($CD27^+CD38^-$) and PB/PC cells ($CD27^+CD38^+CD20^-$) between the specific (SARS-CoV2 S^{++}) and nonspecific B cells (gating strategy is shown in fig. S2). Symbols represent individual patients, as shown in (D). Statistical differences between two groups were determined using paired *t* test (*$P = 0.034$). (**D**) Comparison of the frequency of IgM^+, IgG^+, and IgM^-IgG^- B cells in specific and nonspecific compartments. Bars represent means; symbols represent individual patients.

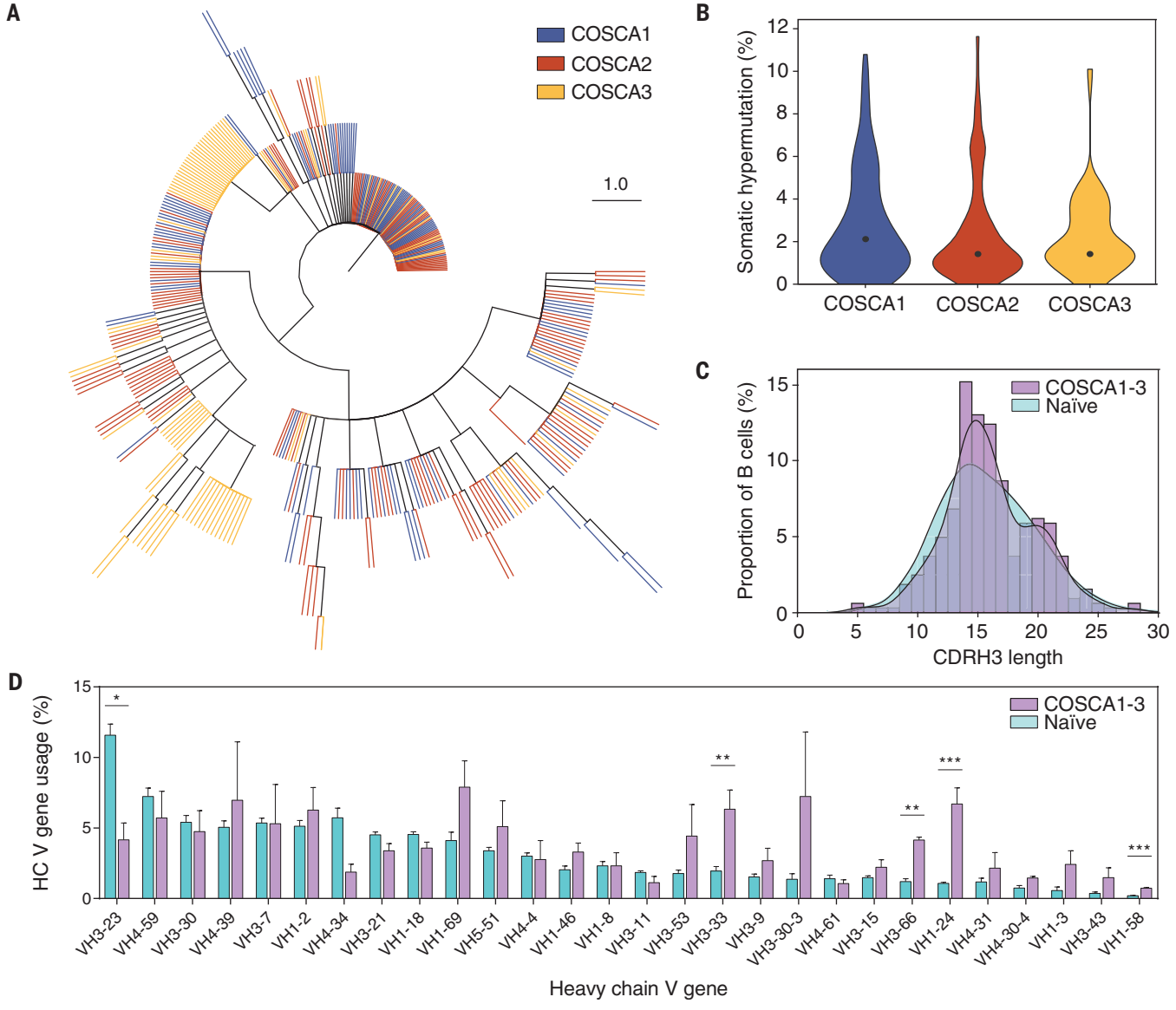
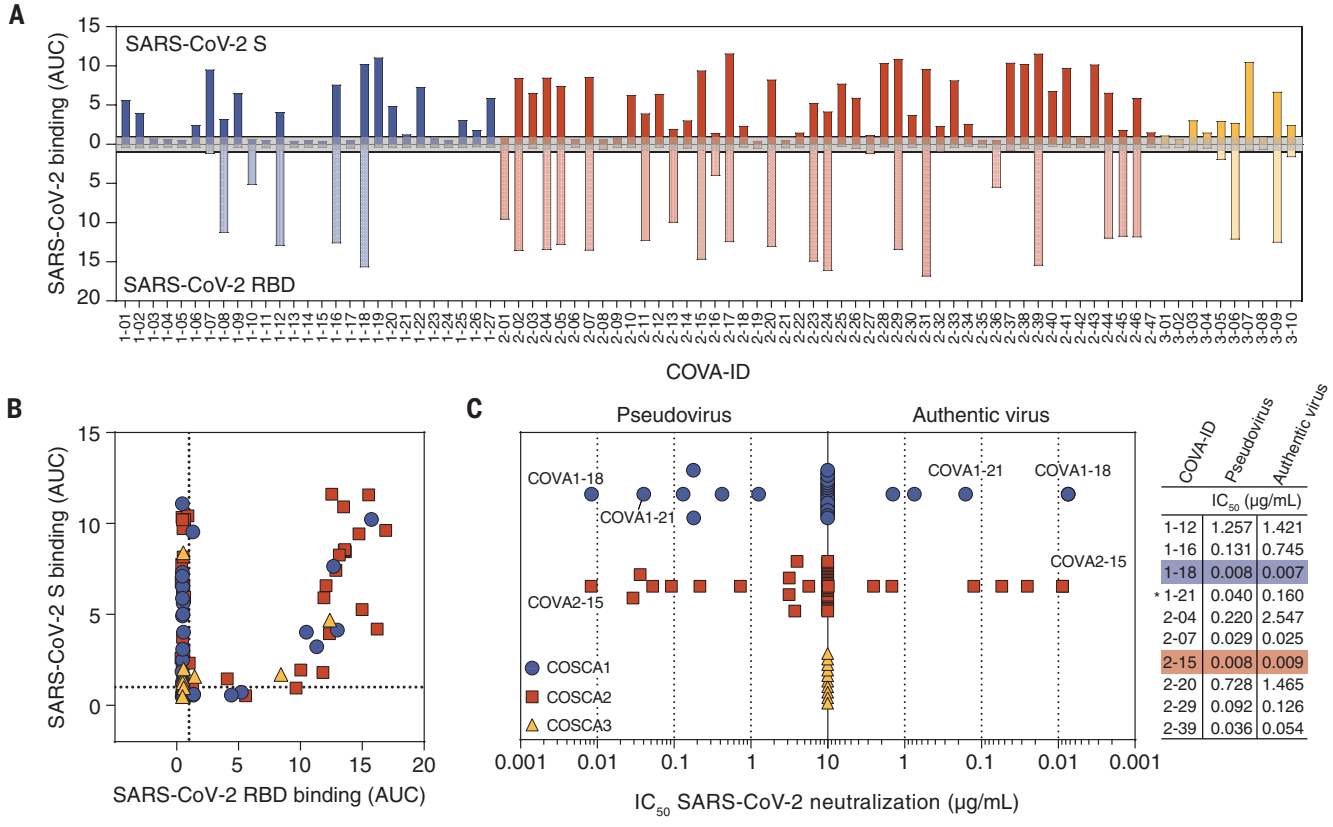


Fig. 3. Genotypic characterization of SARS-CoV-2 S protein–specific B cell receptors. (**A**) Maximum-likelihood phylogenetic tree of 409 isolated paired B cell receptor HCs. Each color represents sequences isolated from different patients (COSCA1, COSCA2, and COSCA3). (**B**) Violin plot showing SHM levels (%; nucleotides) per patient. The dot represents the median SHM percentage. (**C**) Distribution of CDRH3 lengths in B cells from COSCA1, COSCA2, and COSCA3 (purple, *n* = 323) versus a representative naïve population from three donors (cyan, *n* = 9.791.115) (*37*). (**D**) Bar graphs showing the mean (± SEM) VH gene usage (%) in COSCA1, COSCA2, and COSCA3 (purple, *n* = 323) versus a representative naïve population (cyan, *n* = 363,506,788). The error bars represent the variation between different patients (COSCA1, COSCA2, and COSCA3) or naïve donors (*37*). Statistical differences between two groups were determined using unpaired *t* tests (with Holm–Sidak correction for multiple comparisons, adjusted *P* values: *$P < 0.05$; **$P < 0.01$; ***$P < 0.001$).

to those observed in response to infection with other respiratory viruses (*36*).

A hallmark of antibody diversity is the heavy chain complementarity-determining region 3 (CDRH3). Because the CDRH3 is composed of V, D, and J gene segments, it is the most variable region of an antibody in terms of both amino acid composition and length. The average length of CDRH3 in the naïve human repertoire is 15 amino acids (*37*), but for a subset of influenza virus and HIV-1 broadly neutralizing antibodies, long CDRH3 regions of 20 to 35 amino acids are crucial for high-affinity antigen–antibody interactions (*38*, *39*). Even though the mean CDRH3 length of isolated SARS-CoV-2 S protein–specific B cells did not differ substantially from that of a naïve population (*37*), we observed a significant difference in the distribution of CDRH3 length (two-sample Kolmogorov–Smirnov test, $P = 0.006$) (Fig. 3C). This difference in CDRH3 distribution can largely be attributed to an enrichment of longer (~20 amino acid) CDRH3s, leading to a bimodal distribution as opposed to the bell-shaped distribution that was observed in the naïve repertoire (Fig. 3C and fig. S3).

Next, to determine SARS-CoV-2–specific signatures in B cell receptor repertoire usage, we compared ImmunoGenetics (IMGT) database–assigned unique germline V regions from the sorted SARS-CoV-2 S protein–specific B cells with the well-defined extensive germline repertoire in the naïve population (Fig. 3D) (*37*). Multiple VH genes were enriched in COSCA1, COSCA2, and COSCA3 compared with the naïve repertoire, including VH3-33 ($P = 0.009$) and VH1-24 ($P < 0.001$) (Fig. 3D). Even though the enrichment of VH1-69 was not significant ($P > 0.05$), it should be noted



COVA-ID	Pseudovirus IC50 (μg/mL)	Authentic virus IC50 (μg/mL)
1-12	1.257	1.421
1-16	0.131	0.745
1-18	0.008	0.007
*1-21	0.040	0.160
2-04	0.220	2.547
2-07	0.029	0.025
2-15	0.008	0.009
2-20	0.728	1.465
2-29	0.092	0.126
2-39	0.036	0.054

Fig. 4. Phenotypic characterization of SARS-CoV-2 S protein–specific mAbs. (**A**) Bar graph depicting the binding of mAbs from COSCA1 (blue), COSCA2 (red), and COSCA3 (yellow) to SARS-CoV-2 S protein (dark shading) and SARS-CoV-2 RBD (light shading) as determined by ELISA. Each bar indicates the representative area under the curve (AUC) of the mAb indicated below from two experiments. The gray area represents the cutoff for binding (AUC = 1). The maximum concentration of mAb tested was 10 μg/ml. (**B**) Scatter plot depicting the binding of mAbs from COSCA1, COSCA2, and COSCA3 [see (C) for color coding] to SARS-CoV-2 S protein and SARS-CoV-2 RBD as determined by ELISA. Each dot indicates the representative AUC of a mAb from two experiments. (**C**) Midpoint neutralization concentrations (IC_{50}) of SARS-CoV-2 pseudovirus (left) or authentic SARS-CoV-2 virus (right). Each symbol represents the IC_{50} of a single mAb. For comparability, the highest concentration was set to 10 μg/ml, although the actual start concentration for the authentic virus neutralization assay was 20 μg/ml. The IC_{50}s for pseudotyped and authentic SARS-CoV-2 virus of a selection of potently neutralizing RBD and non-RBD–specific mAbs (with asterisk) are shown in the adjacent table. Colored shading indicates the most potent mAbs from COSCA1, COSCA2, and COSCA3.

that an enrichment of VH1-69 has been shown in response to a number of other viral infections, including influenza virus, hepatitis C virus, and rotavirus (*40*), and an enrichment of VH3-33 was observed in response to malaria vaccination, whereas the enrichment of VH1-24 appears to be specific for COVID-19 (Fig. 3D) (*41*). By contrast, VH4-34 ($P > 0.05$) and VH3-23 ($P = 0.018$) were substantially underrepresented in SARS-CoV-2–specific sequences compared with the naïve population. Although usage of most VH genes was consistent between COVID-19 patients, VH3-30-3 and VH4-39 in particular showed considerable variability. Thus, upon SARS-CoV-2 infection, the S protein recruits a subset of B cells from the naïve repertoire enriched in specific VH segments and CDRH3 domains.

Identification of unusually potent SARS-CoV-2–neutralizing antibodies

Subsequently, all HC and LC pairs were transiently expressed in human embryonic kidney (HEK) 293T cells and screened for binding to SARS-CoV-2 S protein by ELISA. A total of 84 mAbs that showed high-affinity binding were selected for small-scale expression in HEK 293F cells and purified (table S1). We obtained few S protein–reactive mAbs from COSCA3, possibly because most B cells from this individual were IgM^+, whereas cloning into an IgG backbone nullified avidity contributions to binding and neutralization present in the serum. To gain insight in the immunodominance of the RBD as well as its ability to cross-react with SARS-CoV, we assessed the binding capacity of these mAbs to the prefusion S proteins and the RBDs of SARS-CoV-2 and SARS-CoV using ELISA. Of the 84 mAbs tested, 32 (38%) bound to the SARS-CoV-2 RBD (Fig. 4, A and B), with seven mAbs (22%) showing cross-binding to SARS-CoV RBD (fig. S4A). We also observed 33 mAbs (39%) that bound strongly to SARS-CoV-2 S but did not bind the RBD, of which 10 mAbs (30%) also bound to the S protein of SARS-CoV (Fig. 4, A and B). Notably, some mAbs that bound very weakly to soluble SARS-CoV-2 S protein in ELISA showed strong binding to membrane-bound S protein, implying that their epitopes are presented poorly on the stabilized soluble S protein or that avidity is important for their binding (table S1). Surface plasmon resonance (SPR) assays confirmed binding of 77 mAbs to S protein and 21 mAbs to the RBD with binding affinities in the nanomolar to picomolar range (table S1).

All 84 mAbs were subsequently tested for their ability to block infection. A total of 19 mAbs (23%) inhibited SARS-CoV-2 pseudovirus infection with varying potencies (Fig. 4C) and, of these, 14 (74%) bound the RBD. Seven of the 19 mAbs could be categorized as potent neutralizers [median inhibitory concentration (IC_{50}) < 0.1 μg/ml], six as moderate neutralizers (IC_{50} = 0.1 to 1 μg/mL), and six as weak neutralizers (IC_{50} = 1 to 10 μg/ml). With an IC_{50} of 0.008 μg/ml, the RBD-targeting antibodies COVA1-18 and COVA2-15 in particular were unusually potent. However, they were

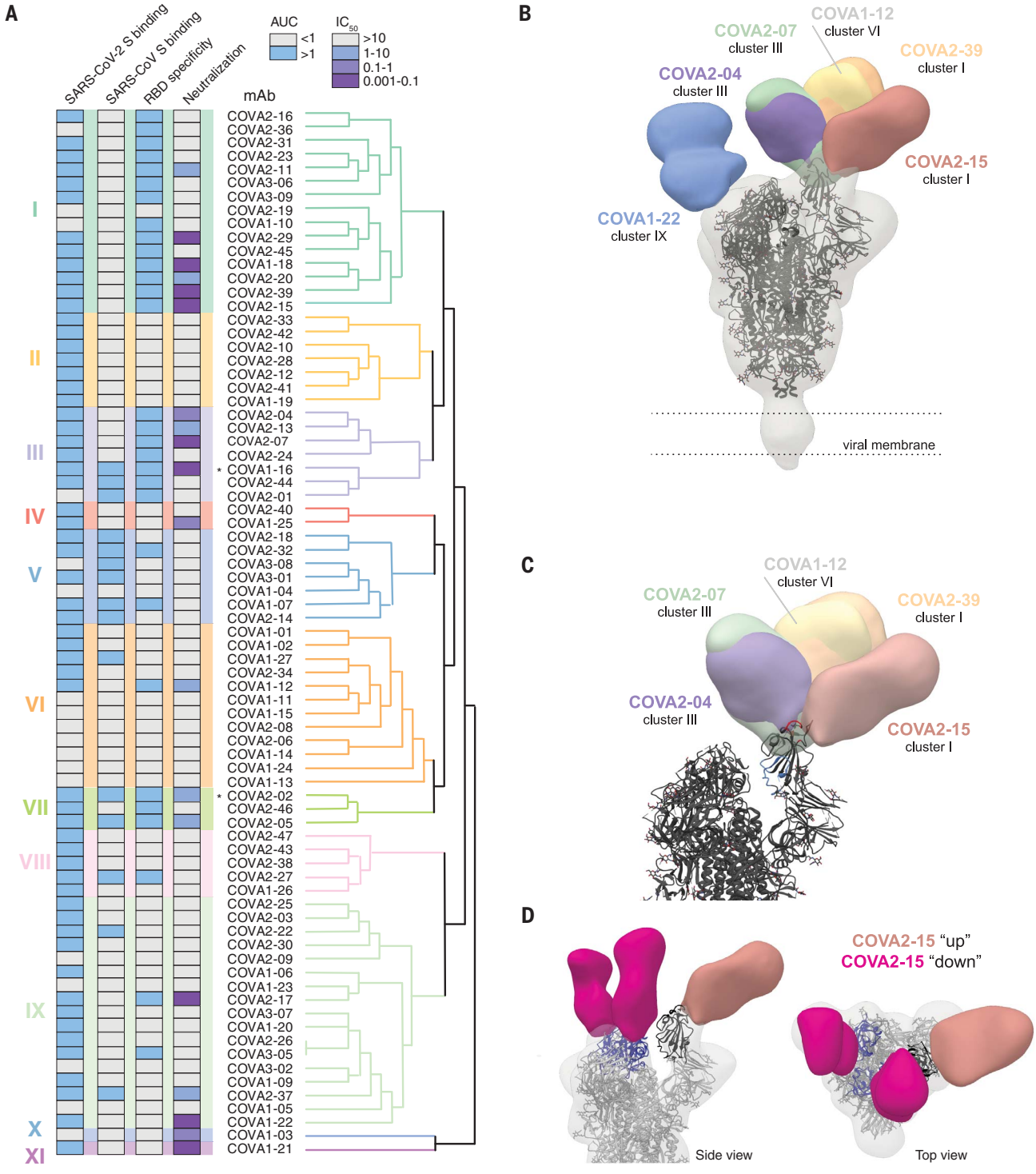


Fig. 5. Antigenic clustering of SARS-CoV-2 S protein–specific mAbs. (**A**) Dendrogram showing hierarchical clustering of the SPR-based cross-competition heat map (table S2). Clusters are numbered I to XI and are depicted with color shading. ELISA binding to SARS-CoV-2 S protein, SARS-CoV S protein, and SARS-CoV-2 RBD as presented by AUC and neutralization IC_{50} (μg/ml) of SARS-CoV-2 is shown in the columns on the left. ELISA AUCs are shown in gray (AUC < 1) or blue (AUC > 1), and neutralization IC_{50} is shown in gray (>10 μg/ml), blue (1 to 10 μg/ml), violet (0.1 to 1 μg/ml), or purple (0.001 to 0.1 μg/ml). Asterisks indicate antibodies that cross-neutralize SARS-CoV pseudovirus. (**B**) Composite figure demonstrating binding of NTD-mAb COVA1-22 (blue) and RBD mAbs COVA2-07 (green), COVA2-39 (orange), COVA1-12 (yellow), COVA2-15 (salmon), and COVA2-04 (purple) to SARS-CoV-2 spike (gray). The spike model (PDB 6VYB) is fit into the density. (**C**) Magnification of SARS-CoV-2 spike comparing epitopes of RBD mAbs with the ACE2-binding site (red) and the epitope of mAb CR3022 (blue). (**D**) Side (left) and top (right) views of the 3D reconstruction of COVA2-15 bound to SARS-CoV-2 S protein. COVA2-15 binds to both the down (magenta) and up (salmon) conformations of the RBD. The RBDs are colored blue in the down conformation and black in the up conformation. The angle of approach for COVA2-15 enables this broader recognition of the RBD while also partially overlapping with the ACE2-binding site and therefore blocking receptor engagement.

quite different in other aspects, such as their HC V gene usage (VH3-66 versus VH3-23), LC usage (VL7-46 versus VK2-30), HC sequence identity (77%), and CDRH3 length (12 versus 22 amino acids). Seventeen of the mAbs also interacted with the SARS-CoV S and RBD proteins and two of these cross-neutralized the SARS-CoV pseudovirus (IC_{50} = 2.5 μg/ml for COVA1-16 and 0.61 μg/ml for COVA2-02; fig. S4B), with COVA2-02 being more potent against SARS-CoV than against SARS-CoV-2. Next, we assessed the ability of the 19 mAbs to block infection of authentic SARS-CoV-2 virus (Fig. 4C and fig. S4C). Although previous reports suggested a decrease in neutralization sensitivity of primary SARS-CoV-2 compared with pseudovirus (*25*, *27*, *28*), we observed very similar potencies for seven of the 19 NAbs, including the most potent NAbs (IC_{50} = 0.007 and 0.009 μg/ml for COVA1-18 and COVA2-15, respectively; Fig. 4C). NAbs COVA1-18, COVA2-04, COVA2-07, COVA2-15, and COVA2-39 also showed strong competition with ACE2 binding, illustrating that blocking ACE2 binding is their likely mechanism of neutralization (fig. S4D). The RBD-targeting mAb COVA2-17, however, showed incomplete competition with ACE2. This corroborates previous observations that the RBD encompasses multiple distinct antigenic sites, some of which do not involve blocking of ACE2 binding (*23*, *25*, *26*). The non-RBD NAbs all bear substantially longer CDRH3s compared with RBD NAbs (fig. S4E), suggesting a convergent, CDRH3-dependent contact between antibody and epitope.

Multiple targets of vulnerability on the SARS-CoV-2 S protein

To identify and characterize the antigenic sites on the S protein and their interrelationships, we performed SPR-based cross-competition assays using S protein, followed by clustering analysis. We note that competition clusters do not necessarily equal epitope clusters but the analysis can provide clues as to the relationship between mAb epitopes. We identified 11 competition clusters, of which nine contained more than one mAb and two contained only one mAb (clusters X and XI; Fig. 5A and fig. S5). All nine multiple-mAb clusters included mAbs from at least two of the three patients, emphasizing that these clusters represent common epitopes targeted by the human humoral immune response during SARS-CoV-2 infection. Three clusters included predominantly RBD-binding mAbs (clusters I, III, and VII), with cluster I forming two subclusters. These three clusters were confirmed by performing cross-competition experiments with soluble RBD instead of complete S protein (fig. S5B). Four clusters (V, VI, XIII, and IX) included predominantly mAbs that did not interact with RBD, and clusters II, IV, X, and XI consisted exclusively of non-RBD mAbs. mAbs with diverse phenotypes (e.g., RBD and non-RBD–binding mAbs) merged together in multiple clusters, suggesting that these mAbs might target epitopes bridging the RBD and non-RBD sites or that they sterically interfere with each other's binding as opposed to binding to overlapping epitopes. Although clusters II, V, and VIII contained only mAbs incapable of neutralizing SARS-CoV-2, clusters I, III, IV, VI, and VII included both non-NAbs and NAbs. Cluster V was formed mostly by non-RBD–targeting mAbs that also bound to SARS-CoV. However, these mAbs were not able to neutralize either SARS-CoV-2 or SARS-CoV, suggesting that these mAbs target a conserved non-neutralizing epitope on the S protein. Finally, the two non-RBD mAbs COVA1-03 and COVA1-21 formed single-mAb competition clusters (clusters X and XI, respectively) and showed an unusual competition pattern, because binding of either mAb blocked binding by most of the other mAbs, but not vice versa (figs. S5 and S6 and table S2). We hypothesize that these two mAbs allosterically interfere with mAb binding by causing conformational changes in the S protein that shield or impair most other mAb epitopes. COVA1-21 also efficiently blocked virus infection without blocking ACE2, suggesting an alternative mechanism of neutralization than blocking ACE2 engagement (fig. S4C). The SPR-based clustering was corroborated using biolayer interferometry competition assays on a subset of NAbs (fig. S6). Overall, our data are consistent with the previous identification of multiple antigenic RBD sites for SARS-CoV-2 and additional non-RBD sites on the S protein, as described for SARS-CoV and MERS-CoV (*32*, *42*).

To visualize how selected NAbs bound to their respective epitopes, we generated Fab–SARS-CoV-2 S complexes that were imaged by single-particle negative-stain electron microscopy (EM; Fig. 5, B and C, and fig. S7). We obtained low-resolution reconstruction with six Fabs, including five RBD-binding Fabs from three different competition clusters. COVA1-12 overlapped highly with the epitope of COVA2-39, whereas COVA2-04 approached the RBD at a different angle somewhat similar to that of the cross-binding SARS-CoV–specific mAb CR3022 (*42*). The EM reconstructions confirmed the RBD as the target of these NAbs but revealed a diversity in approach angles (Fig. 5B). Furthermore, whereas four RBD NAbs interacted with a stoichiometry of one Fab per trimer, consistent with one RBD being exposed in the "up state" and two in the less accessible "down state" (*13*, *43*), COVA2-15 bound with a stoichiometry of three per trimer (fig. S7). COVA2-15 was able to bind RBD domains in both the up and down state (Fig. 5D). In either conformation, the COVA2-15 epitope partially overlapped with the ACE2-binding site, and therefore the mAb blocks receptor engagement. The higher stoichiometry of this mAb may explain its unusually strong neutralization potency. None of the epitopes of the five RBD Fabs overlapped with that of CR3022, which is unable to neutralize SARS-CoV-2 (*42*), although COVA2-04 does approach the RBD from a similar angle as CR3022. The sixth Fab for which we generated a three-dimensional (3D) reconstruction was from the non-RBD mAb COVA1-22 placed in competition cluster IX. EM demonstrated that this mAb bound to the NTD of S1. Such NTD NAbs have also been found for MERS-CoV (*44*).

Conclusions

Convalescent COVID-19 patients showed strong anti–SARS-CoV-2 S protein–specific B cell responses and developed memory and antibody-producing B cells that may have participated in the control of infection and the establishment of humoral immunity. We isolated 19 NAbs that targeted a diverse range of antigenic sites on the S protein, of which two showed picomolar neutralizing activities (IC_{50} = 0.007 and 0.009 μg/ml or 47 and 60 pM, respectively) against authentic SARS-CoV-2 virus. This illustrates that SARS-CoV-2 infection elicits high-affinity and cross-reactive mAbs targeting the RBD as well as other sites on the S protein. Several of the potent NAbs had VH segments virtually identical to their germline origin, which holds promise for the induction of similar NAbs by vaccination because extensive affinity maturation does not appear to be a requirement for potent neutralization. The most potent NAbs both targeted the RBD on the S protein and fell within the same competition cluster, but were isolated from two different individuals and bore little resemblance genotypically. Although direct comparisons are difficult, the neutralization potency of these and several other mAbs exceeds the potencies of the most advanced HIV-1 and Ebola mAbs under clinical evaluation, as well as the approved anti-RSV mAb palivizumab (*45*). Through large-scale SPR-based competition assays, we defined NAbs that targeted multiple sites of vulnerability on the RBD and the additional previously undefined non-RBD epitopes on SARS-CoV-2. This is consistent with the identification of multiple antigenic RBD sites for SARS-CoV-2 and the presence of additional non-RBD sites on the S protein of SARS-CoV and MERS-CoV (*32*). Subsequent structural characterization of these potent NAbs will guide vaccine design, and simultaneous targeting of multiple non-RBD and RBD epitopes with mAb cocktails paves the way for safe and effective COVID-19 prevention and treatment.

REFERENCES AND NOTES

1. E. Dong, H. Du, L. Gardner, *Lancet Infect. Dis.* **20**, 533–534 (2020).
2. N. Chen *et al.*, *Lancet* **395**, 507–513 (2020).
3. J. Mair-Jenkins *et al.*, *J. Infect. Dis.* **211**, 80–90 (2015).
4. J. H. Ko *et al.*, *Antivir. Ther.* **23**, 617–622 (2018).

5. C. Shen *et al*., *JAMA* **323**, 1582 (2020).
6. R. Kulkarni, in *Dynamics of Immune Activation in Viral Diseases*, P. V. Bramhachari, Ed. (Springer, 2020), pp. 9–41.
7. S. Mulangu *et al*., *N. Engl. J. Med.* **381**, 2293–2303 (2019).
8. J. van Griensven *et al*., *N. Engl. J. Med.* **374**, 33–42 (2016).
9. E. Hershberger *et al*., *EBioMedicine* **40**, 574–582 (2019).
10. N. J. Gogtay *et al*., *Clin. Infect. Dis.* **66**, 387–395 (2018).
11. T. Sandritter, *J. Pediatr. Health Care* **13**, 191–195, quiz 196–197 (1999).
12. D. Wrapp *et al*., *Science* **367**, 1260–1263 (2020).
13. A. C. Walls *et al*., *Cell* **181**, 281–292.e6 (2020).
14. F. Li, *Annu. Rev. Virol.* **3**, 237–261 (2016).
15. J. Shang *et al*., *Nature* **581**, 221–224 (2020).
16. R. W. Sanders *et al*., *PLOS Pathog.* **9**, e1003618 (2013).
17. J. E. Robinson *et al*., *Nat. Commun.* **7**, 11544 (2016).
18. S. Jiang, C. Hillyer, L. Du, *Trends Immunol.* **41**, 355–359 (2020).
19. J. S. McLellan, W. C. Ray, M. E. Peeples, *Curr. Top. Microbiol. Immunol.* **372**, 83–104 (2013).
20. D. Sok *et al*., *Proc. Natl. Acad. Sci. U.S.A.* **111**, 17624–17629 (2014).
21. X. Tian *et al*., *Emerg. Microbes Infect.* **9**, 382–385 (2020).
22. C. Wang *et al*., *Nat. Commun.* **11**, 2251 (2020).
23. D. Pinto *et al*., Structural and functional analysis of a potent Sarbecovirus neutralizing antibody. bioRxiv 2020.04.07.023903 [Preprint]. 10 April 2020); https://doi.org/10.1101/2020.04.07.023903.
24. X. Chen *et al*., *Cell. Mol. Immunol.* **17**, 647–649 (2020).
25. S. J. Zost, P. Gilchuk *et al*., Potently neutralizing human antibodies that block SARS-CoV-2 receptor binding and protect animals. bioRxiv 2020.05.22.111005 [Preprint]. 22 May 2020; https://doi.org/10.1101/2020.05.22.111005.
26. D. F. Robbiani *et al*., Convergent antibody responses to SARS-CoV-2 infection in convalescent individuals. bioRxiv 2020.05.13.092619 [Preprint]. 22 May 2020; https://doi.org/10.1101/2020.05.13.092619.
27. B. Ju *et al*., *Nature* 10.1038/s41586-020-2380-z (2020).
28. T. F. Rogers *et al*., Rapid isolation of potent SARS-CoV-2 neutralizing antibodies and protection in a small animal model. bioRxiv 2020.05.11.088674 [Preprint]. 15 May 2020; https://doi.org/10.1101/2020.05.11.088674.
29. X. C. Tang *et al*., *Proc. Natl. Acad. Sci. U.S.A.* **111**, E2018–E2026 (2014).
30. J. ter Meulen *et al*., *PLOS Med.* **3**, e237 (2006).
31. M. Grobben, R. A. Stuart, M. J. van Gils, *Curr. Opin. Virol.* **38**, 70–80 (2019).
32. B. Shanmugaraj, K. Siriwattananon, K. Wangkanont, W. Phoolcharoen, *Asian Pac. J. Allergy Immunol.* **38**, 10–18 (2020).
33. S. F. Ahmed, A. A. Quadeer, M. R. McKay, *Viruses* **12**, 254 (2020).
34. J. Pallesen *et al*., *Proc. Natl. Acad. Sci. U.S.A.* **114**, E7348–E7357 (2017).
35. J. Zhao *et al*., *Clin. Infect. Dis.* ciaa344 (2020).
36. E. Goodwin *et al*., *Immunity* **48**, 339–349.e5 (2018).
37. B. Briney, A. Inderbitzin, C. Joyce, D. R. Burton, *Nature* **566**, 393–397 (2019).
38. N. C. Wu *et al*., *Nat. Commun.* **8**, 15371 (2017).
39. L. Yu, Y. Guan, *Front. Immunol.* **5**, 250 (2014).
40. F. Chen, N. Tzarum, I. A. Wilson, M. Law, *Curr. Opin. Virol.* **34**, 149–159 (2019).
41. J. Tan *et al*., *Nat. Med.* **24**, 401–407 (2018).
42. M. Yuan *et al*., *Science* **368**, 630–633 (2020).
43. Q. Wang *et al*., *Cell* **181**, 894–904.e9 (2020).
44. N. Wang *et al*., *Cell Rep.* **28**, 3395–3405.e6 (2019).
45. K. E. Pascal *et al*., *J. Infect. Dis.* **218** (suppl. 5), S612–S626 (2018).

ACKNOWLEDGMENTS

We thank C. Russell and A. Han for helpful comments on the manuscript; J. Koopsen for help with the phylogenetic analyses; and H. Turner, B. Anderson, and C. Bowman for assistance with the EM studies. **Funding:** This work was supported by a Netherlands Organization for Scientific Research (NWO) Vici grant (to R.W.S.); by the Bill & Melinda Gates Foundation through the Collaboration for AIDS Vaccine Discovery (CAVD) grants OPP1111923, OPP1132237, and INV-002022 to R.W.S. and grant OPP1170236 to A.B.W.; by the Fondation Dormeur, Vaduz (to R.W.S. and to M.J.v.G.) and Health Holland PPS-allowance LSHM20040 (to M.J.v.G.); and by the Netherlands Organisation for Health Research and Development (ZONMW to B.L.H). M.J.v.G. is a recipient of an AMC Fellowship from Amsterdam UMC and a COVID-19 grant from the Amsterdam Institute for Infection and Immunity. R.W.S and M.J.v.G. are recipients of support from the University of Amsterdam Proof of Concept fund (contract no. 200421) as managed by Innovation Exchange Amsterdam (IXA). The funders had no role in study design, data collection, data analysis, data interpretation, or data reporting. **Author contributions:** P.J.M.B., T.G.C., K.v.d.S., G.V., B.H., A.B.W., G.J.d.B., R.W.S., and M.J.v.G. conceived and designed experiments. K.v.d.S., W.J.W., N.K., and G.d.B arranged medical ethical approval, recruitment of study participants, and collection of study material. P.J.M.B., T.G.C., J.L.S., Y.A., S.B., J.L.T., N.M.A.O., G.K., A.E.H.B., M.M.v.H., D.G., J.A.B., E.E.S., K.D.V., J.v.S., M.J.v.B., T.P.L.B., K.S., R.D., and I.B. performed the experiments. P.J.M.B., T.G.C., M.C., and A.A. set up experimental assays. P.J.M.B., T.G.C., K.v.d.S., N.v.d.V., A.v.d.K., R.W.S., and M.J.v.G. analyzed and interpreted data. P.J.M.B., T.G.C., K.v.d.S., G.J.d.B., R.W.S., and M.J.v.G. wrote the manuscript with input from all listed authors. **Competing interests:** Amsterdam UMC has filed a patent application concerning the SARS-CoV-2 mAbs described here. **Data and materials availability:** Reagents and materials presented in this study are available from the corresponding authors under a materials transfer agreement with the Amsterdam UMC. Variable domain sequences of HC and LCs are available in table S1 and were uploaded on GenBank under accession numbers MT599820 to MT599987. The coordinates of the negative stain electron microscopy reconstructions were deposited in the Electron Microscopy Data Bank under accession numbers EMD-22061 to EMD-22066. This work is licensed under a Creative Commons Attribution 4.0 International (CC BY 4.0) license, which permits unrestricted use, distribution, and reproduction in any medium, provided the original work is properly cited. To view a copy of this license, visit https://creativecommons.org/licenses/by/4.0/. This license does not apply to figures/photos/artwork or other content included in the article that is credited to a third party; obtain authorization from the rights holder before using such material.

SUPPLEMENTARY MATERIALS

science.sciencemag.org/content/369/6504/643/suppl/DC1
Materials and Methods
Figs. S1 to S5
References (*46*–*56*)
Tables S1 and S2
MDAR Reproducibility Checklist

View/request a protocol for this paper from *Bio-protocol*.

4 May 2020; accepted 10 June 2020
Published online 15 June 2020
10.1126/science.abc5902

CORONAVIRUS

A neutralizing human antibody binds to the N-terminal domain of the Spike protein of SARS-CoV-2

Xiangyang Chi[1]*, Renhong Yan[2]*, Jun Zhang[1]*, Guanying Zhang[1], Yuanyuan Zhang[2], Meng Hao[1], Zhe Zhang[1], Pengfei Fan[1], Yunzhu Dong[1], Yilong Yang[1], Zhengshan Chen[1], Yingying Guo[2], Jinlong Zhang[1], Yaning Li[3], Xiaohong Song[1], Yi Chen[1], Lu Xia[2], Ling Fu[1], Lihua Hou[1], Junjie Xu[1], Changming Yu[1], Jianmin Li[1]†, Qiang Zhou[2]†, Wei Chen[1]†

Developing therapeutics against severe acute respiratory syndrome coronavirus 2 (SARS-CoV-2) could be guided by the distribution of epitopes, not only on the receptor binding domain (RBD) of the Spike (S) protein but also across the full Spike (S) protein. We isolated and characterized monoclonal antibodies (mAbs) from 10 convalescent COVID-19 patients. Three mAbs showed neutralizing activities against authentic SARS-CoV-2. One mAb, named 4A8, exhibits high neutralization potency against both authentic and pseudotyped SARS-CoV-2 but does not bind the RBD. We defined the epitope of 4A8 as the N-terminal domain (NTD) of the S protein by determining with cryo–eletron microscopy its structure in complex with the S protein to an overall resolution of 3.1 angstroms and local resolution of 3.3 angstroms for the 4A8-NTD interface. This points to the NTD as a promising target for therapeutic mAbs against COVID-19.

The global outbreak of COVID-19 has emerged as a severe threat to human health (*1*–*3*). COVID-19 is caused by a novel coronavirus, the severe acute respiratory syndrome coronavirus 2 (SARS-CoV-2), which is an enveloped, positive-strand RNA virus that causes symptoms such as cough, headache, dyspnea, myalgia, fever, and severe pneumonia in humans (*1*, *3*–*5*).

SARS-CoV-2 is a member of the β coronavirus genus, which also contains SARS-CoV and MERS-CoV, which caused epidemics in 2002 and 2012, respectively (*6*, *7*). SARS-CoV-2 shares about 80% sequence identity to SARS-CoV and uses the same cellular receptor, angiotensin-converting enzyme 2 (ACE2) (*8*–*16*).

The trimeric S protein decorates the surface of coronavirus and plays a pivotal role during viral entry (*17*, *18*). During infection, the S protein is cleaved into the N-terminal S1 subunit and C-terminal S2 subunit by host proteases such as TMPRSS2 (*18*, *19*) and changes conformation from the prefusion to the postfusion state (*20*). S1 and S2 comprise the extracellular domain (ECD; 1 to 1208 amino acids) and a single transmembrane helix and mediate receptor binding and membrane fusion, respectively (*16*). S1, which consists of the N-terminal domain (NTD) and the receptor binding domain (RBD), is critical in determining tissue tropism and host ranges (*21*, *22*). The RBD is responsible for binding to ACE2, whereas the function of NTD is not well understood. In some coronaviruses, the NTD may recognize specific sugar moieties upon initial attachment and might play an important role in the prefusion-to-postfusion transition of the S protein (*23*–*26*). The NTD of the MERS-CoV S protein can serve as a critical epitope for neutralizing antibodies (*26*).

The SARS-CoV-2 S protein–targeting monoclonal antibodies (mAbs) with potent neutralizing activity are a focus in the development of therapeutic interventions for COVID-19 (*27*–*29*). Many studies reported the functions and structures of SARS-CoV-2–neutralizing antibodies that target the RBD and inhibit the association between the S protein and ACE2 (*28*–*34*). The RBD-targeting antibodies, applied individually, might induce resistance mutations in the virus (*26*). Antibodies that target non-RBD epitopes might be added to antibody cocktail therapeutics for SARS-CoV-2. We thus sought to identify antibodies to different regions of the S protein and to the Nucleocapsid (N) protein.

[1]Beijing Institute of Biotechnology, Academy of Military Medical Sciences (AMMS), Beijing 100071, China. [2]Key Laboratory of Structural Biology of Zhejiang Province, Institute of Biology, Westlake Institute for Advanced Study, School of Life Sciences, Westlake University, Hangzhou 310024, Zhejiang Province, China. [3]Beijing Advanced Innovation Center for Structural Biology, Tsinghua-Peking Joint Center for Life Sciences, School of Life Sciences, Tsinghua University, Beijing 100084, China.
*These authors contributed equally to this work.
†Corresponding author. Email: cw0226@foxmail.com (W.C.); zhouqiang@westlake.edu.cn (Q.Z.); lijmqz@126.com (J.L.)

Results

Isolation of human mAbs from memory B cells and plasma B cells

To isolate mAbs and analyze the humoral antibody responses to SARS-CoV-2, we collected plasma and peripheral blood mononuclear cells (PBMCs) from 10 Chinese patients who had recovered from SARS-CoV-2 infection. The age of donors ranges from 25 to 53 years. The interval from disease confirmation date to blood collection date ranged from 23 to 29 days for patients 1 to 5 and 10 to 15 days for patients 6 to 10 (table S1). We evaluated the titers of binding antibodies in plasma to different fragments of the SARS-CoV-2 S protein—including the full ECD, S1, S2, and the RBD—and to the N protein. Plasma from all the patients except donor 2 bound to all five SARS-CoV-2 protein segments, whereas that from donor 2 recognized S-ECD and S2 only (Fig. 1A). The neutralizing capacities of plasma against authentic SARS-CoV-2 and HIV-vectored pseudotyped SARS-CoV-2 are correlated [correlation coefficient (r) = 0.6868, $P < 0.05$] (Fig. 1B). These results indicate that humoral immune responses were specifically elicited for all 10 patients during their natural infection with SARS-CoV-2.

To isolate S protein–specific mAbs, we first sorted the immunoglobulin G–positive (IgG^+) memory B cells from PBMCs of convalescent patients 1 to 5 with flow cytometry, using S-ECD as the probe (Fig. 1C). The percentage of S-ECD–reactive IgG^+ B cells ranges from 0.56 to 11%, as revealed with fluorescence activating cell sorting (FACS). To avoid losing B cells with low copies of S-ECD–specific receptors on cell surfaces, we sorted plasma B cells from mixed PBMCs derived from another five convalescent patients (patients 6 to 10) without using S-ECD protein as the probe in flow cytometry. The percentage of plasma B cells in CD3-$CD19^+$ B cells was 12.8%, which is higher than the percentage of memory B cells in CD3-$CD19^+$ B cells (Fig. 1C).

From the sorted B cells, we identified 9, 286, 43, 12, and 26 clones of single B cell from patients 1 to 5, respectively, and 23 clones of single B cell from the mixed PBMCs of patients 6 to 10 (Fig. 1D). The distribution of the sequenced heavy (IgH) gene families was comparable among the 10 donors, with *VH3* being the most commonly used VH gene, whereas different donors displayed variable preferences for the light chain (IgL) gene families (Fig. 1D). The combination of V3 and J4, V3 and D3, and D3 and J4 were the most common usage for the IgH gene family (fig. S1). The average mutations of amino acids per mAb from memory B cells ranged from 17.50 to 48.04 for donors 1 to 5, respectively, whereas mAbs from plasma B cells possessed an average of 13.99 amino acid mutations for donors 6 to 10 (Fig. 1E). Human antibodies elicited through repeated exposures to different antigens confer an average of 26.46 amino acid mutations per Ab, as previously reported (*35*). These results indicate that natural SARS-CoV-2 infection elicited high levels of somatic hypermutation (SHM) in memory B cells. The lengths of complementarity-determining region 3 (CDR3) for antibodies were similar among the donors, with average lengths of these CDR3 ranging from 13.9 to 17.7 for VH and 9.3 to 10.1 for VL (Fig. 1F). The CDR3 lengths of these mAbs were longer than that in antigen-specific immune receptors (means of 12.7 for VH and 6.5 for VL, respectively) reported previously (*36*).

Binding profiles of SARS-CoV-2 S protein–specific human mAbs

To screen for S protein–specific antibodies, we determined the binding specificity using enzyme-

linked immunosorbent assay (ELISA) for the 399 human mAbs sorted above. From donors 1 to 5, respectively, 1, 16, 1, 3, and 9 S-ECD–specific mAbs were identified. A total of 35 S-ECD–specific mAbs were identified from donors 6 to 10 (Fig. 2A). We further characterized domain specificities of the 35 mAbs with different fragments of the S protein, including S1, S2, and RBD (Fig. 2A). The S-reactive mAbs are classified into four major groups on the basis of their medium effective concentration (EC_{50}) values (Fig. 2A). Group 1 recognizes only S-ECD. Group 2 recognizes S-ECD and S1, with subgroup 2A binding S-ECD and S1 and subgroup 2B binding S-ECD, S1, and RBD. Group 3 interacts with both S1 and S2, where subgroup 3A targets the RBD and subgroup 3B fails to bind the RBD. Group 4 recognizes S-ECD and S2. Only four mAbs recognize the RBD among the 35 S-specific mAbs (Fig. 2, A and B).

We performed a competition-binding assay using ELISA for several representative mAbs to determine whether there are overlapping antigenic sites between different mAbs, with CR3022 being used as a positive control mAb that reported to bind the SARS-CoV-2 RBD (Fig. 2C) (*37*). Among these mAbs, 4A8 in group 2A competed with 1M-1D2 in group 2B. Another RBD-reactive mAb, 2M-10B11 in group 2B, competed with CR3022, suggesting overlapped epitopes on RBD for these two mAbs. These results indicate that antibody responses elicited by natural SARS-CoV-2 infection were diverse in epitope recognition of S proteins.

To characterize the diversity in gene usage and affinity maturation, the phylogenetic trees of these S-ECD–specific mAbs were analyzed on the basis of the amino acid sequences of VHDJH and VLJL by using a neighbor-joining method in MEGA7 Software (*38*). Results indicate that the VH gene usage is very diverse among the 35 mAbs from 10 donors, with *VH3-30* being the most frequently used germline gene. There was no particularly favored VH gene identified among S1, S2, or RBD-reactive mAbs (Fig. 2D). The percentages of heavy chain variable gene sequence identity ranged from 40.9 to 97.6% in the 35 S-ECD–specific mAbs (fig. S2 and table S2).

Neutralizing activities of SARS-CoV-2 S–specific human mAbs

We first performed in vitro neutralization studies of the 35 S-ECD–specific mAbs using authentic SARS-CoV-2 in Vero-E6 cells (Fig. 3A). Of the 35 S-ECD–specific mAbs, only three mAbs neutralized authentic SARS-CoV-2. MAb 1M-1D2, 4A8, and 0304-3H3 exhibited medium to high neutralizing capacity with EC_{50} of 28, 0.61, and 0.04 μg/ml, respectively. As expected, the RBD-targeting control mAb, CR3022, failed to neutralize authentic SARS-CoV-2 (*37*). Moreover, although the CR3022-competing mAb, 2M-10B11, bound to the SARS-CoV-2 RBD with an EC_{50} of 5 ng/ml (Fig. 2A), it also failed to neutralize authentic SARS-CoV-2. These results suggest that binding affinities of mAbs against RBD do not correlate fully with the neutralizing abilities of mAbs. To further investigate the inhibitory activity of the three authentic SARS-CoV-2–neutralizing

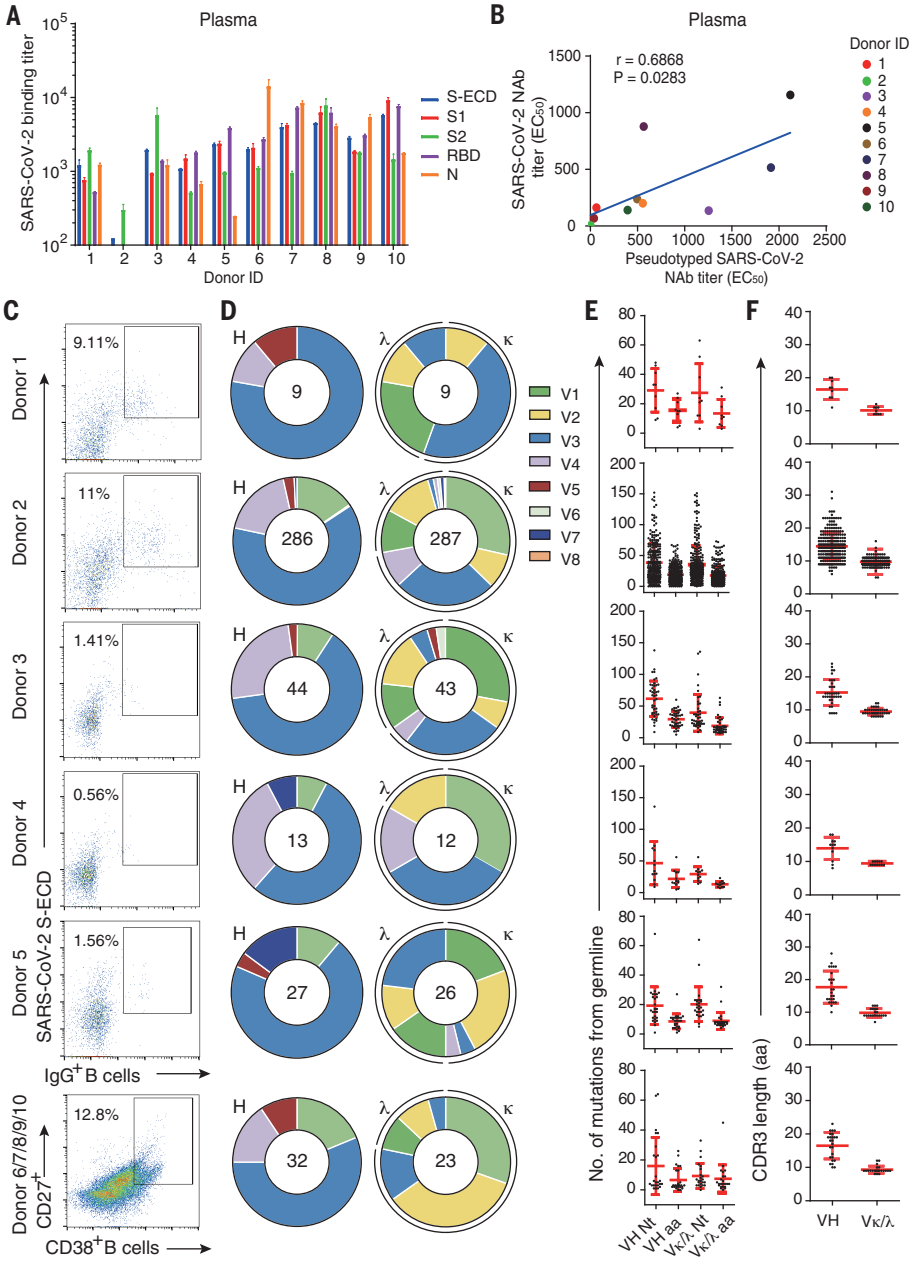
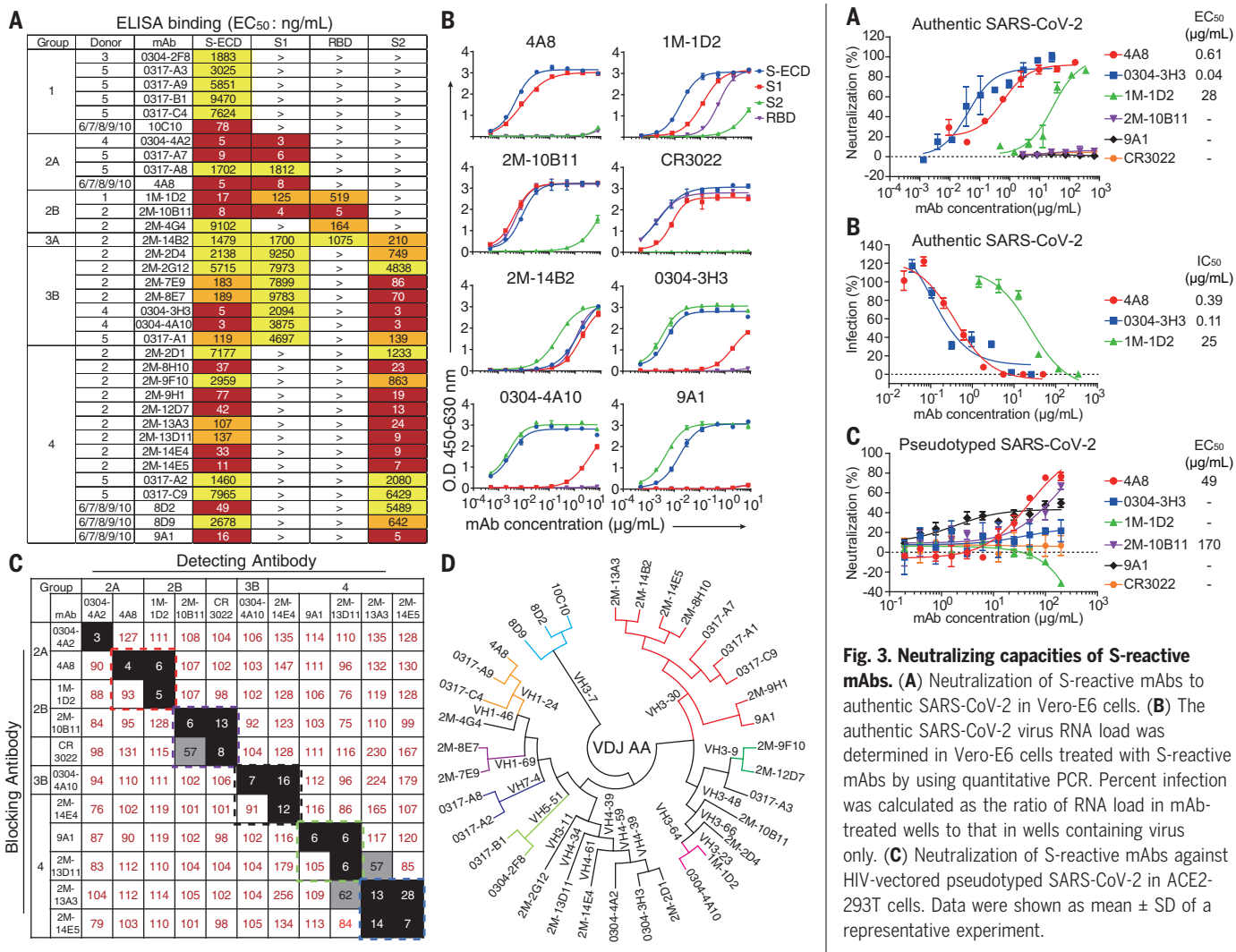


Fig. 1. Isolation of antigen-specific mAbs from convalescent patients of SARS-CoV-2. (**A**) Reactions of plasma to SARS-CoV-2 proteins. S-ECD (extracellular domain of S protein), S1, S2, RBD (receptor binding domain), and N protein were used in ELISA to test the binding of plasma. Plasma of heathy donors were used as control, and cut-off values were calculated as optical density (OD) 450 of control × 2.1. Data were shown with mean and SD of a representative experiment. (**B**) The correlations between the authentic SARS-CoV-2 neutralizing antibody (NAb) titers and the pseudotyped SARS-CoV-2 NAb titers in plasma. Neutralizing assays of plasma against authentic SARS-CoV-2 were performed by using Vero E6 cells, and neutralization against pseudotyped SARS-CoV-2 were determined by using ACE2-293T cells. The correlations were calculated by means of Pearson correlation test in Graphpad 7.0. (**C**) Flow cytometry sorting from PBMCs of 10 convalescent patients. (**D**) Distribution of V gene families in heavy and light chains of all distinct clones (the total number is shown in the center of the pie charts) for each donor. (**E**) The number of amino acid (AA) and total nucleotide (Nt) mutations from the germline of all clonal sequences identified in (D) is shown. (**F**) CDR3 amino acid lengths of VH and VL of all clonal sequences identified in (D).



Group	Donor	mAb	S-ECD	S1	RBD	S2
1	3	0304-2F8	1883	>	>	>
	5	0317-A3	3025	>	>	>
	5	0317-A9	5851	>	>	>
	5	0317-B1	9470	>	>	>
	5	0317-C4	7624	>	>	>
	6/7/8/9/10	10C10	78	>	>	>
2A	4	0304-4A2	5	3	>	>
	5	0317-A7	9	6	>	>
	5	0317-A8	1702	1812	>	>
	6/7/8/9/10	4A8	5	8	>	>
2B	1	1M-1D2	17	125	519	>
	2	2M-10B11	8	4	5	>
	2	2M-4G4	9102	>	164	>
3A	2	2M-14B2	1479	1700	1075	210
3B	2	2M-2D4	2138	9250	>	749
	2	2M-2G12	5715	7973	>	4838
	2	2M-7E9	183	7899	>	86
	2	2M-8E7	189	9783	>	70
	4	0304-3H3	5	2094	>	3
	4	0304-4A10	3	3875	>	3
	5	0317-A1	119	4697	>	139
4	2	2M-2D1	7177	>	>	1233
	2	2M-8H10	37	>	>	23
	2	2M-9F10	2959	>	>	863
	2	2M-9H1	77	>	>	19
	2	2M-12D7	42	>	>	13
	2	2M-13A3	107	>	>	24
	2	2M-13D11	137	>	>	9
	2	2M-14E4	33	>	>	9
	2	2M-14E5	11	>	>	7
	5	0317-A2	1460	>	>	2080
	5	0317-C9	7965	>	>	6429
	6/7/8/9/10	8D2	49	>	>	5489
	6/7/8/9/10	8D9	2678	>	>	642
	6/7/8/9/10	9A1	16	>	>	5

Group		2A		2B			3B	4				
	mAb	0304-4A2	4A8	1M-1D2	2M-10B11	CR 3022	0304-4A10	2M-14E4	9A1	2M-13D11	2M-13A3	2M-14E5
2A	0304-4A2	3	127	111	108	104	106	135	114	110	135	128
	4A8	90	4	6	107	102	103	147	111	96	132	130
2B	1M-1D2	88	93	5	107	98	102	128	106	76	119	128
	2M-10B11	84	95	128	6	13	92	123	103	75	110	99
	CR 3022	98	131	115	57	8	104	128	111	116	230	167
3B	0304-4A10	94	110	111	102	106	7	16	112	96	224	179
4	2M-14E4	76	102	119	101	101	91	12	116	86	165	107
	9A1	87	90	119	102	98	102	116	6	6	117	120
	2M-13D11	83	112	110	104	104	104	179	105	6	57	85
	2M-13A3	104	112	114	105	102	104	256	109	62	13	28
	2M-14E5	79	103	110	101	98	105	134	113	84	14	7

Fig. 2. Binding profiles of Spike protein–specific mAbs. (**A**) Heatmap showing the binding of mAbs to different types of spike proteins determined by using ELISA. The EC_{50} value for each S-mAb combination is shown, with dark red, orange, yellow, or white shading indicating high, intermediate, low, or no detectable binding, respectively. EC_{50} values greater than 10,000 ng/ml are indicated (>). (**B**) Binding curves of representative mAbs. CR3022 is a control that was reported to bind SARS-CoV and SARS-CoV-2 RBD. Data were shown with mean and SD of a representative experiment. (**C**) Heatmap showing the competing binding of some representative S-reactive mAbs assayed in ELISA. Numbers in the box indicate the percentage binding of detecting mAb in the presence of the blocking antibody compared with the binding of detecting mAb in the absence of the blocking antibody. The mAbs were considered competing if the inhibiting percentage is <30% (black boxes with white numbers). The mAbs were judged to noncompete for the same site if the percentage is >70% (white boxes with red numbers). Gray boxes with black numbers indicate an intermediate phenotype (30 to ~70%). (**D**) Phylogenetic trees of all the S-specific mAbs.

Fig. 3. Neutralizing capacities of S-reactive mAbs. (**A**) Neutralization of S-reactive mAbs to authentic SARS-CoV-2 in Vero-E6 cells. (**B**) The authentic SARS-CoV-2 virus RNA load was determined in Vero-E6 cells treated with S-reactive mAbs by using quantitative PCR. Percent infection was calculated as the ratio of RNA load in mAb-treated wells to that in wells containing virus only. (**C**) Neutralization of S-reactive mAbs against HIV-vectored pseudotyped SARS-CoV-2 in ACE2-293T cells. Data were shown as mean ± SD of a representative experiment.

mAbs—4A8, 0304-3H3, and 1M-1D2—we tested the RNA load of authentic SARS-CoV-2 in Vero-E6 cells treated with each mAb using real-time quantitative polymerase chain reaction (PCR) (Fig. 3B). Consistent with the cytopathic effect (CPE) assay results (Fig. 3A), mAbs 0304-3H3 and 4A8 displayed higher inhibitory capacities than did 1M-1D2 (Fig. 3B).

We next performed luciferase reporter gene assays for all 35 S-binding mAbs using HIV-vectored pseudotyped SARS-CoV-2 (*39*), among which three mAbs exhibited neutralizing activity against the pseudotyped virus (Fig. 3C). 4A8 protected ACE2-293T cells with an EC_{50} of 49 μg/ml. Although mAb 2M-10B11 and 9A1 did not neutralize authentic SARS-CoV-2, 2M-10B11 protected against pseudotyped virus with an EC_{50} of 170 μg/ml, and 9A1 provided weak protection. To our surprise, neutralization by 0304-3H3 and 1M-1D2 was not observed (Fig. 3C). The inconsistency between the results for pseudotyped SARS-CoV-2 compared with authentic SARS-CoV-2 were also observed for mAbs against MERS-CoV (*40*, *41*) and may be caused by the different presentation of S protein resulted from the different environmental factors the viruses underwent, such as the cells used for the neutralizing assays or for the production of the pseudotyped or authentic virions (*42*). On the basis of these results, 4A8 is a potential candidate for the treatment of SARS-CoV-2 because it displayed strong neutralizing capacities against both authentic and pseudotyped SARS-CoV-2.

Binding characterization of candidate mAbs

To determine the possible neutralizing mechanism of the mAbs, we determined the binding affinities of the five mAbs with potential neutralizing activity against different segments of the S protein—including the full S-ECD and domains S1, S2, and RBD—using biolayer interferometry (BLI). All five tested mAbs bound to S-ECD with high affinity; equilibrium dissociation constants (K_d) were less than 2.14 nM (Fig. 4A). 4A8 and 1M-1D2 bound to S1 with K_d of 92.7 and 108 nM, respectively, whereas 0304-3H3 and 9A1 targeted S2 with K_d of 4.52 and <0.001 nM, respectively

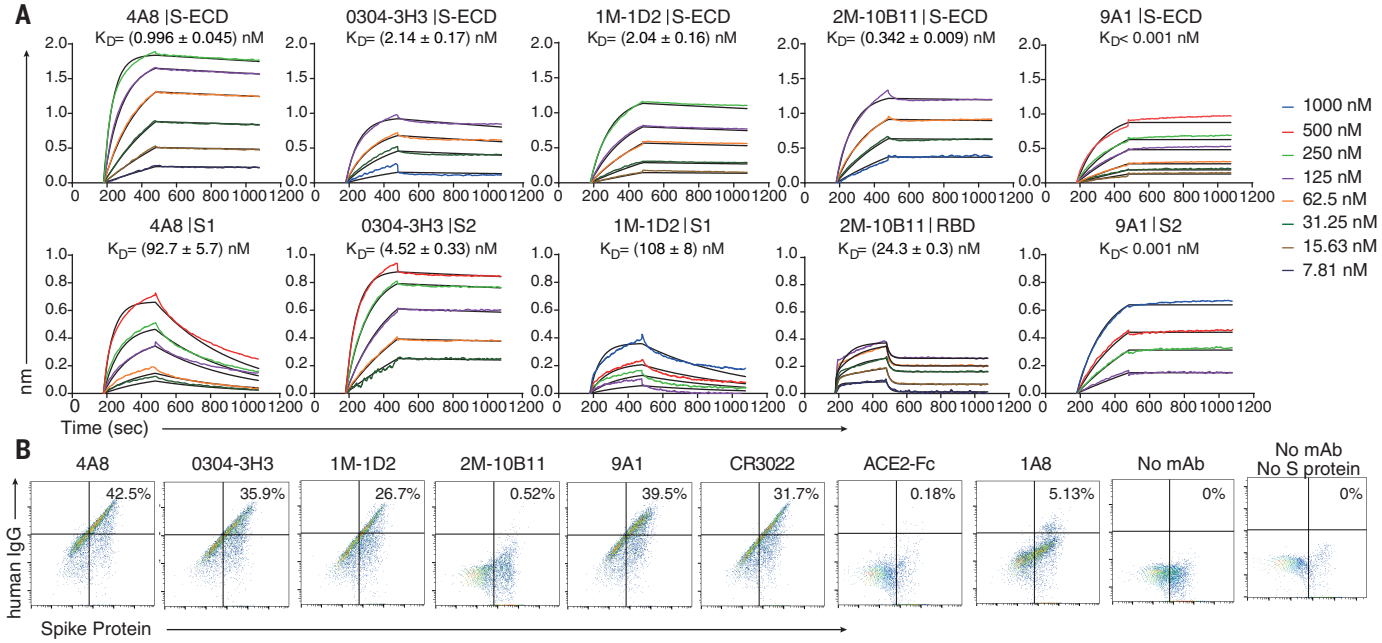


Fig. 4. 4A8 did not block the binding of Spike protein to ACE2 receptor. (**A**) BLI sensorgrams and kinetics of mAbs binding to S proteins. Global fitting curves are shown as black lines. The K_d were calculated by using a 1:1 binding model in Data Analysis Software 9.0, except for 2M-10B11, which used a heterogeneous ligand model owing to avidity effect. (**B**) The binding of S protein to human ACE2-overexpressing 293T cells were determined by means of flow cytometry. After the preincubation of S protein with each indicated mAb, the mAb-S mixtures were added to the ACE2-expressing cells. Cells were stained with anti-human IgG fluorescein isothiocyanate (mAb binding, *x* axis) and anti-His (S binding, *y* axis). Percentages of double-positive cells are shown. Control mAb CR3022 and 1A8 were previously reported to bind SARS-CoV RBD and Marburg glycoprotein, respectively, and ACE2-Fc protein was a human ACE2 protein conjugated with human Fc.

(Fig. 4A, bottom). Moreover, 2M-10B11 bound the RBD with K_d of 24.3 nM, which was obtained by using heterogeneous ligand model owing to the avidity effects (Fig. 4A, bottom).

To investigate whether these mAbs block the binding of S protein to ACE2, we performed flow cytometry using human embryonic kidney (HEK) 293T cells expressing human ACE2. As expected, only 2M-10B11 among the five mAbs and ACE2-Fc prevented S protein from binding to ACE2. In the presence of 2M-10B11, only 0.52% of cells were double positive for IgG and S protein (Fig. 4B). CR3022, which competes with 2M-10B11, did not block the binding of S to ACE2. The control mAb 1A8, targeting the Marburg glycoprotein, did not interfere with the binding either, and the 5.13% of double positives may be due to the nonspecific binding of 1A8 to S protein. 4A8 also failed to interfere with the binding of the S protein to ACE2.

Cryo-EM structure of the complex between 4A8 and S-ECD

The mAb 4A8 was overexpressed and purified by Protein A resin, and the S-ECD of SARS-CoV-2 was purified through M2 affinity resin and size exclusion chromatography (SEC). 4A8 and S-ECD protein were mixed and incubated at a stoichiometric ratio of ~1.2 to 1 for 1 hour and applied to SEC to remove excess proteins (fig. S3A). The fraction containing the complex was concentrated for cryo–electron microscopy (cryo-EM) sample preparation.

To investigate the interactions between 4A8 and the S protein, we solved the cryo-EM structure of the complex at an overall resolution of 3.1 Å (Fig. 5 and movie S1). Details of cryo-EM sample preparation, data collection and processing, and model building can be found in in the supplementary materials, materials and methods (figs. S3 to S5). The S protein exhibits asymmetric conformations similar to the previously reported structures (*21*, *22*), with one of three RBDs in "up" conformation and the other two RBDs in "down" conformation (Fig. 5).

Recognition of the NTD by 4A8

In the S protein–4A8 complex, each trimeric S protein is bound with three solved 4A8 Fabs, each of which interacts with one NTD of the S protein. Despite the different conformations of the three S protein protomers, the interface between 4A8 and each NTD is identical (Fig. 5 and fig. S3I). The map quality at the NTD-4A8 region was improved through focused refinement to a local resolution of 3.3 Å, enabling reliable analysis of the interactions between the NTD and 4A8.

Association with 4A8 appears to stabilize the NTD epitope, which is invisible in the reported S protein structure alone (*21*, *22*). Supported by the high resolution of NTD, we were able to build the structural model for five new loops for NTD, designated N1 (residues 14 to 26), N2 (residues 67 to 79), N3 (residues 141 to 156), N4 (residues 177 to 186), and N5 (residues 246 to 260), among which the N3 and N5 loops mediate the interaction with 4A8 (fig. S5A). Besides, three new glycosylation sites (Asn^{17}, Asn^{61}, and Asn^{149}) on the NTD are identified in this structure (fig. S6).

The heavy chain of 4A8 mainly participates in binding to the NTD mainly through three complementarity-determining regions (CDRs), named CDR1 (residues 25 to 32), CDR2 (residues 51 to 58), and CDR3 (residues 100 to 116) (Fig. 6A and fig. S5B). The interface is constituted by an extensive hydrophilic interaction network, and the buried surface area at the 4A8-NTD interface is 832 $Å^2$. Arg^{246} on the N5 loop of the NTD represents one docking site, which is stabilized by Trp^{258}, simultaneously interacting with Tyr^{27} and Glu^{31} of 4A8 on CDR1 (Fig. 6B). On the N3 loop of the NTD, Lys^{150} and Lys^{147} respectively form salt bridges with Glu^{54} and Glu^{72} of 4A8 (Fig. 6C). Lys^{150} is also hydrogen (H)–bonded with 4A8-Tyr^{111}, while His^{146} forms a H-bond with 4A8-Thr^{30} (Fig. 6C). In addition to the hydrophilic interactions, Trp^{152} and Tyr^{145} on the N3 loop of the NTD also interact with Val^{102}, Pro^{106}, and Phe^{109} on the CDR3 of 4A8 through hydrophobic and/or π-π interactions (Fig. 6D). Additionally, the glycosylation site of Asn^{149} on

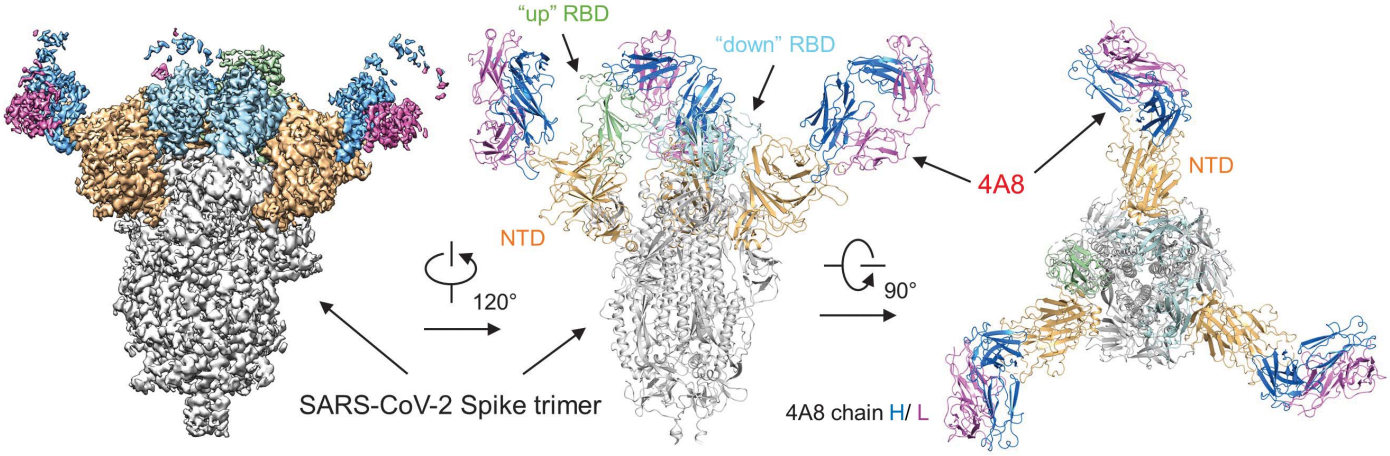


Fig. 5. Cryo-EM structure of the 4A8 and S-ECD complex. The domain-colored cryo-EM map of the complex is shown on the left, and two perpendicular views of the overall structure are shown on the right. The heavy and light chains of 4A8 are colored blue and magenta, respectively. The NTDs of the trimeric S protein are colored orange. The one "up" RBD and two "down" RBDs of trimeric S protein are colored green and cyan, respectively.

the NTD is close to the 4A8-NTD interface, of which N-glycans might participate in the interactions on the interface (Fig. 6A and fig. S6).

Discussion

There is an urgent need for prophylactic and therapeutic interventions for SARS-CoV-2 infections given the ongoing COVID-19 pandemic. Our work reveals that naturally occurring human SARS-CoV-2 mAbs isolated from the B cells of 10 recovered donors are diverse in gene usage and epitope recognition of S protein. The majority of the isolated mAbs did not recognize the RBD, and all the mAbs that neutralize authentic SARS-CoV-2 failed to inhibit the binding of S protein to ACE2. These unexpected results suggest the presence of other important mechanisms for SARS-CoV-2 neutralization in addition to suppressing the viral interaction with the receptor.

The S1-targeting mAb 4A8 does not block the interaction between ACE2 and S protein but exhibits high levels of neutralization against both authentic and pseudotyped SARS-CoV-2 in vitro. Many neutralizing antibodies against SARS-CoV-2 were reported to target the RBD of the S protein and block the binding between RBD and ACE2 (*28*–*30*, *32*–*34*). Our results show that 4A8 binds to the NTD of S protein with potent neutralizing activity. Previous study has shown that mAb 7D10 could bind to the NTD of S protein of MERS-CoV probably by inhibiting the RBD-DPP4 binding and the prefusion-to-postfusion conformational change of S protein (*26*). We aligned the crystal structure of 7D10 in complex with the NTD of S protein of MERS-CoV with our complex structure and found that the interfaces between the mAb and the NTDs are partially overlapped (fig. S7). 7D10 may inhibit the interaction between MERS-CoV and DPP4 through its light chain, which is close to the RBD. In our complex, the light chain of 4A8 is away from the RBD (fig. S7). Therefore, we speculate that 4A8 may neutralize SARS-CoV-2 by restraining the conformational changes of the S protein. Furthermore, sequence alignment of the S proteins from SARS-CoV-2, SARS-CoV, and MERS-CoV revealed varied NTD surface sequences that are respectively recognized by different mAbs (fig. S8).

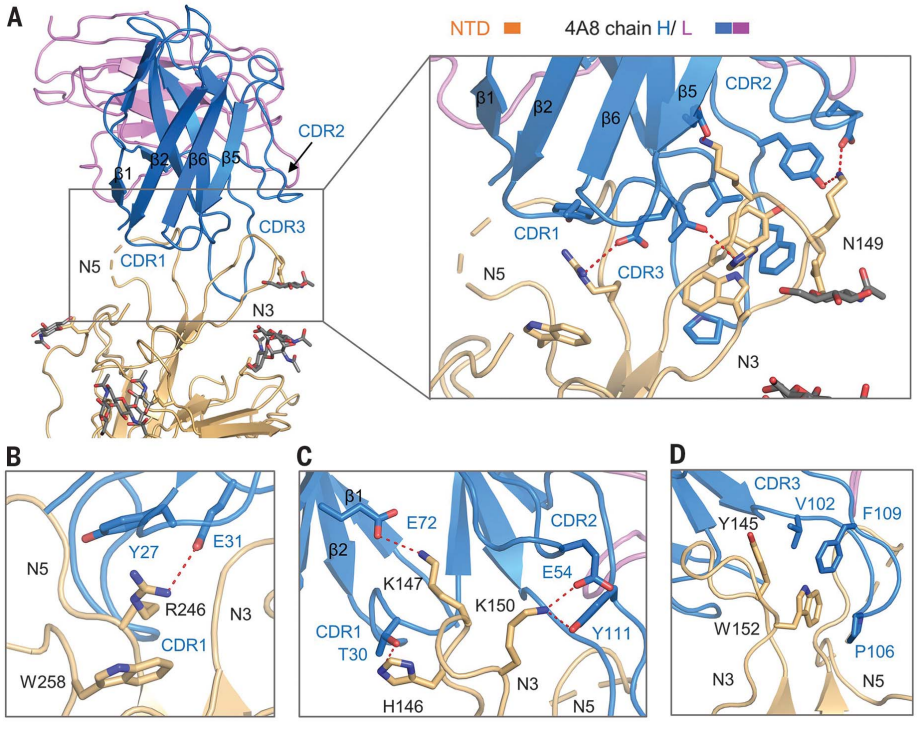


Fig. 6. Interactions between the NTD and 4A8. (**A**) Extensive hydrophilic interactions on the interface between NTD and 4A8. Only one NTD-4A8 is shown. (**B** to **D**) Detailed analysis of the interface between NTD and 4A8. Polar interactions are indicated by red dashed lines. The residues involved in hydrophobic interactions are presented as spheres.

This work reports a fully human neutralizing mAb recognizing a vulnerable epitope of NTD on S protein of SARS-CoV-2, functioning with a mechanism that is independent of receptor binding inhibition. Combination of 4A8 with RBD-targeting antibodies may avoid the escaping mutations of the virus and serve as promising "cocktail" therapeutics. The information obtained from these studies can be

used for development of the structure-based vaccine design against SARS-CoV-2.

REFERENCES AND NOTES

1. N. Zhu *et al*., *N. Engl. J. Med.* **382**, 727–733 (2020).
2. F. Wu *et al*., *Nature* **579**, 265–269 (2020).
3. C. Huang *et al*., *Lancet* **395**, 497–506 (2020).
4. P. Zhou *et al*., *Nature* **579**, 270–273 (2020).
5. C. C. Lai, T. P. Shih, W. C. Ko, H. J. Tang, P. R. Hsueh, *Int. J. Antimicrob. Agents* **55**, 105924 (2020).
6. T. G. Ksiazek *et al*., *N. Engl. J. Med.* **348**, 1953–1966 (2003).
7. A. M. Zaki, S. van Boheemen, T. M. Bestebroer, A. D. Osterhaus, R. A. Fouchier, *N. Engl. J. Med.* **367**, 1814–1820 (2012).
8. W. Li *et al*., *Nature* **426**, 450–454 (2003).
9. J. H. Kuhn, W. Li, H. Choe, M. Farzan, *Cell. Mol. Life Sci.* **61**, 2738–2743 (2004).
10. K. Kuba *et al*., *Nat. Med.* **11**, 875–879 (2005).
11. D. S. Dimitrov, *Cell* **115**, 652–653 (2003).
12. J. Lan *et al*., *Nature* **581**, 215–220 (2020).
13. Q. Wang *et al*., *Cell* **181**, 894–904.e9 (2020).
14. R. Yan *et al*., *Science* **367**, 1444–1448 (2020).
15. J. Shang *et al*., *Nature* **581**, 221–224 (2020).
16. M. Hoffmann *et al*., *Cell* **181**, 271–280.e8 (2020).
17. T. M. Gallagher, M. J. Buchmeier, *Virology* **279**, 371–374 (2001).
18. G. Simmons, P. Zmora, S. Gierer, A. Heurich, S. Pöhlmann, *Antiviral Res.* **100**, 605–614 (2013).
19. S. Belouzard, V. C. Chu, G. R. Whittaker, *Proc. Natl. Acad. Sci. U.S.A.* **106**, 5871–5876 (2009).
20. W. Song, M. Gui, X. Wang, Y. Xiang, *PLOS Pathog.* **14**, e1007236 (2018).
21. D. Wrapp *et al*., *Science* **367**, 1260–1263 (2020).
22. A. C. Walls *et al*., *Cell* **181**, 281–292.e6 (2020).
23. C. Krempl, B. Schultze, H. Laude, G. Herrler, *J. Virol.* **71**, 3285–3287 (1997).
24. F. Künkel, G. Herrler, *Virology* **195**, 195–202 (1993).
25. G. Lu, Q. Wang, G. F. Gao, *Trends Microbiol.* **23**, 468–478 (2015).
26. H. Zhou *et al*., *Nat. Commun.* **10**, 3068 (2019).
27. B. Ju *et al*., Potent human neutralizing antibodies elicited by SARS-CoV-2 infection. *bioRxiv* 2020.03.21.990770 [Preprint] 26 March 2020. https://doi.org/10.1101/2020.03.21.990770.
28. C. Wang *et al*., *Nat. Commun.* **11**, 2251 (2020).
29. D. Wrapp *et al*., *Cell* **181**, 1004–1015.e15 (2020).
30. X. Chen *et al*., *Cell. Mol. Immunol.* **17**, 647–649 (2020).
31. M. Yuan *et al*., *Science* **368**, 630–633 (2020).
32. Y. Wu *et al*., *Science* **368**, 1274–1278 (2020).
33. B. Ju *et al*., *Nature* 10.1038/s41586-020-2380-z (2020).
34. Y. Cao *et al*., *Cell* 10.1016/j.cell.2020.05.025 (2020).
35. A. Burkovitz, I. Sela-Culang, Y. Ofran, *FEBS J.* **281**, 306–319 (2014).
36. E. P. Rock, P. R. Sibbald, M. M. Davis, Y. H. Chien, *J. Exp. Med.* **179**, 323–328 (1994).
37. C. G. Price, P. W. Abrahams, *Environ. Geochem. Health* **16**, 27–30 (1994).
38. S. Kumar, G. Stecher, K. Tamura, *Mol. Biol. Evol.* **33**, 1870–1874 (2016).
39. Q. Li *et al*., *Vaccine* **35**, 5172–5178 (2017).
40. J. Xu *et al*., *Emerg. Microbes Infect.* **8**, 841–856 (2019).
41. L. Wang *et al*., *J. Virol.* **92**, e02002-17 (2018).
42. J. Shang *et al*., *Proc. Natl. Acad. Sci. U.S.A.* **117**, 11727–11734 (2020).

ACKNOWLEDGMENTS

We thank the Cryo-EM Facility and Supercomputer Center of Westlake University for providing cryo-EM and computation support, respectively. We thank the Beijing Institute of Microbiology and Epidemiology, Academy of Military Medical Sciences, China, for providing the SARS-CoV-2. We also thank T. Fang, T. Yu, P. Lv, and E. Ma for providing technical support. **Funding:** This work was funded by the National Key R&D Program of China (2020YFC0841400), the National Natural Science Foundation of China (projects 31971123, 81803429, 81703048, 31900671, 81920108015, and 31930059), the Key R&D Program of Zhejiang Province (2020C04001), the SARS-CoV-2 emergency project of the Science and Technology Department of Zhejiang Province (2020C03129), the Leading Innovative and Entrepreneur Team Introduction Program of Hangzhou, the National Science and Technology Major Project of the Ministry of Science and Technology of China, (2018ZX10101003-005-007), and the Special Research Program of Novel Coronavirus Pneumonia of Westlake University. **Author contributions:** W.C., Q.Z., and J.L. conceived the project. X.C., R.Y., Ju.Z., G.Z., Y.Z., Y.G., Y.L., L.X., M.H., Z.Z., P.F., Y.D., Z.C., Ji.Z., X.S., Y.C., L.F., L.H., J.X., and C.Y. did the experiments. All authors contributed to data analysis. X.C., R.Y., J.L., Q.Z., and W.C. wrote the manuscript. **Competing interests:** W.C., J.L., X.C., Ju.Z., L.F., C.Y., J.X., L.H., G.Z., P.F., M.H., Y.D., X.S., Y.C., and Ji.Z. are listed as inventors on a pending patent application for mAb 4A8. The other authors declare that they have no competing interests. **Data and materials availability:** Atomic coordinates and cryo-EM density maps of the S protein of SARS-CoV-2 in complex bound with 4A8 (PDB: 7C2L; whole map: EMD-30276, antibody-epitope interface-focused refined map: EMD-30277) have been deposited to the Protein Data Bank (www.rcsb.org) and the Electron Microscopy Data Bank (www.ebi.ac.uk/pdbe/emdb), respectively. Antibody sequences have been deposited at GenBank (MTA 622682 to 622751). This work is licensed under a Creative Commons Attribution 4.0 International (CC BY 4.0) license, which permits unrestricted use, distribution, and reproduction in any medium, provided the original work is properly cited. To view a copy of this license, visit https://creativecommons.org/licenses/by/4.0. This license does not apply to figures/photos/artwork or other content included in the article that is credited to a third party; obtain authorization from the rights holder before using such material.

SUPPLEMENTARY MATERIALS

science.sciencemag.org/content/369/6504/650/suppl/DC1
Materials and Methods
Figs. S1 to S7
Tables S1 to S4
References (*43*–*66*)
Movie S1
MDAR Reproducibility Checklist

8 May 2020; accepted 17 June 2020
Published online 22 June 2020
10.1126/science.abc6952

STRUCTURAL BIOLOGY

Structural insight into precursor ribosomal RNA processing by ribonuclease MRP

Pengfei Lan[1,2], Bin Zhou[1,2], Ming Tan[1,2], Shaobai Li[1,2], Mi Cao[1,2], Jian Wu[1,2]*, Ming Lei[1,2,3]*

Ribonuclease (RNase) MRP is a conserved eukaryotic ribonucleoprotein complex that plays essential roles in precursor ribosomal RNA (pre-rRNA) processing and cell cycle regulation. In contrast to RNase P, which selectively cleaves transfer RNA–like substrates, it has remained a mystery how RNase MRP recognizes its diverse substrates. To address this question, we determined cryo–electron microscopy structures of *Saccharomyces cerevisiae* RNase MRP alone and in complex with a fragment of pre-rRNA. These structures and the results of biochemical studies reveal that coevolution of both protein and RNA subunits has transformed RNase MRP into a distinct ribonuclease that processes single-stranded RNAs by recognizing a short, loosely defined consensus sequence. This broad substrate specificity suggests that RNase MRP may have myriad yet unrecognized substrates that could play important roles in various cellular contexts.

Ribonuclease mitochondrial RNA processing (RNase MRP) is an essential eukaryotic ribonucleoprotein (RNP) that cleaves RNA substrates in a site-specific manner and plays pivotal roles in RNA metabolism (*1*–*3*). Its importance is manifested by the fact that a proteinaceous endoribonuclease that can cleave RNAs with sequence specificity has not been found in nature (*4*). RNase MRP is structurally and evolutionarily closely related to RNase P, another essential RNase that catalyzes the maturation of the 5′-end of precursor transfer RNA (pre-tRNA) (*3*, *5*–*8*). In contrast to RNase P, RNase MRP processes much more diversified substrates. *Saccharomyces cerevisiae* RNase MRP is predominantly localized in the nucleolus, where it is responsible for precursor ribosomal RNA (pre-rRNA) processing at a specific A3 site in the internal transcribed spacer region 1 (ITS1) to release the mature 5.8*S* rRNA (*9*–*12*). *S. cerevisiae* RNase MRP also asymmetrically and temporally exists in a single discrete cytoplasmic spot in daughter cells, where it regulates the cell cycle by cleaving the 5′-untranslated region (UTR) of the cyclin B2 (CLB2) mRNA (*13*, *14*). Similar roles of human RNase MRP in ribosome assembly and cyclin-dependent cell cycle regulation have also been established (*15*, *16*). Several protein subunits of human RNase MRP have been considered immunological targets in autoimmune diseases (*17*–*19*), and mutations in the RNA subunit of human RNase MRP (RMRP) cause a spectrum of severely debilitating human diseases, including cartilage-hair hypoplasia (CHH) (*20*, *21*), underscoring RNase MRP's essential role in human health.

[1]State Key Laboratory of Oncogenes and Related Genes, Ninth People's Hospital, Shanghai Jiao Tong University School of Medicine, Shanghai 200011, China. [2]Shanghai Institute of Precision Medicine, Shanghai 200125, China. [3]Key Laboratory of Cell Differentiation and Apoptosis of Chinese Ministry of Education, Shanghai Jiao Tong University School of Medicine, Shanghai 200025, China.
*Corresponding author. Email: leim@shsmu.edu.cn (M.L.); wujian@shsmu.edu.cn (J.W.)

The RNase MRP holoenzyme contains a large catalytic RNA and multiple essential proteins (*22*, *23*). Except for one or two species-specific proteins, the catalytic RNA and most of the protein subunits of RNase MRP are conserved from yeast to humans (*3*). In *S. cerevisiae* RNase MRP, the majority of the protein components are shared with *S. cerevisiae* nuclear RNase P with the exception of Rmp1 and Snm1 (*3*, *22*). Previous secondary structure analyses predicted that the RNA component of *S. cerevisiae* RNase MRP (Nme1) has a similar RNase P-type catalytic (C) domain (*24*–*26*). In particular, key nucleotides in the predicted active center highly resemble those in RNase P RNA, which suggests that both ribozymes likely share the same catalytic mechanism (*3*, *27*). In sharp contrast to the C domain, the rest of the Nme1 RNA is completely different from the specificity (S) domain of RNase P RNA (*3*). Indeed, it is not even clear whether this part of Nme1 is involved in the specific recognition of substrates. It has been speculated that this diversified RNA region and specific protein components of RNase MRP have coevolved during evolution, giving rise to altered substrate specificity (*28*, *29*). Despite extensive biochemical and genetic studies, the lack of a high-resolution structure of RNase MRP severely hinders our understanding of how this essential RNP could process such diversified substrates as pre-rRNA and CLB2 mRNA.

Here, we present the cryo–electron microscopy (cryo-EM) structures of *S. cerevisiae* RNase MRP holoenzyme alone and in complex with an ITS1 fragment containing the A3 cleavage site. These structures reveal that although the catalytic center of RNase MRP is nearly identical to that in RNase P, a striking local refolding of key protein subunits transforms RNase MRP into a distinct ribonuclease to process single-stranded RNAs by recognizing a short consensus sequence.

Characterization of the *S. cerevisiae* RNase MRP holoenzyme

We purified the endogenous RNase MRP holoenzyme from *S. cerevisiae* using a two-step affinity purification scheme with a protein A tag on subunit Pop4 and a triple-Flag tag on the RNase MRP–specific subunit Rmp1, the latter of which effectively prevented the contamination from RNase P (fig. S1A) (*30*, *31*). The purified RNase MRP complex was subjected to mass spectrometry analysis, confirming the presence of all previously identified protein components in *S. cerevisiae* RNase MRP (fig. S1, A and B, table S1, and supplementary materials).

The purified RNase MRP holoenzyme was fully active to process a 123-nucleotide (nt) ITS1 fragment of yeast pre-rRNA containing the A3 site with no detectable activity to pre-tRNA (Fig. 1A and fig. S1C) (*10*, *32*). Sequence and phylogenetic analysis of ITS1 regions from multiple species in Saccharomycetaceae revealed a highly conserved 12-nt fragment containing the A3 cleavage site with a GC-rich stem and a long stretch of AU-rich sequence at its 5′ and 3′ termini, respectively (Fig. 1B and fig. S2). Notably, neither the stem nor the AU-rich sequence is required for the substrate recognition by RNase MRP (Fig. 1A and fig. S3). Further experiments showed that a 21-nt fragment with the A3 site at the center can be efficiently processed by RNase MRP (Fig. 1A and fig. S3). This finding suggests that whereas RNase P recognizes the three-dimensional structural feature of pre-tRNA, RNase MRP processes short, single-stranded substrates with a distinct sequence specificity (Fig. 1A and fig. S3). This is consistent with a previous in vitro selection of *S. cerevisiae* RNase MRP substrates (*32*). Hereafter, we refer to this 21-nt fragment as $ITS1_{A3}$ (Fig. 1A). For simplicity, we define the nucleotide 3′ to the cleavage site as the "center" (position 1) of $ITS1_{A3}$ (Fig. 1A).

Structures of RNase MRP and its complex with the $ITS1_{A3}$ substrate

To gain insights into the architecture of RNase MRP and the molecular basis of substrate recognition by RNase MRP, we determined the cryo-EM structures of *S. cerevisiae* RNase MRP holoenzyme alone and its complex with the $ITS1_{A3}$ substrate at resolutions of 2.5 Å and 2.8 Å, respectively (Fig. 1, C and D, fig. S4, and table S2). The cryo-EM density maps were of sufficient quality to enable us to build the atomic model of RNase MRP (Fig. 1, C and D, and fig. S5, A to C). Nucleotides A(−2) to A5 in the $ITS1_{A3}$ substrate were clearly discernable in the density map (fig. S5D). In addition, the EM map also revealed a stacking of the bases of A6 and A7 with A5, which allowed us to generate a model of $ITS1_{A3}$ containing nine continuous nucleotides, A(−2) to A7 (Fig. 1D and fig. S5D). The structure of apo RNase MRP

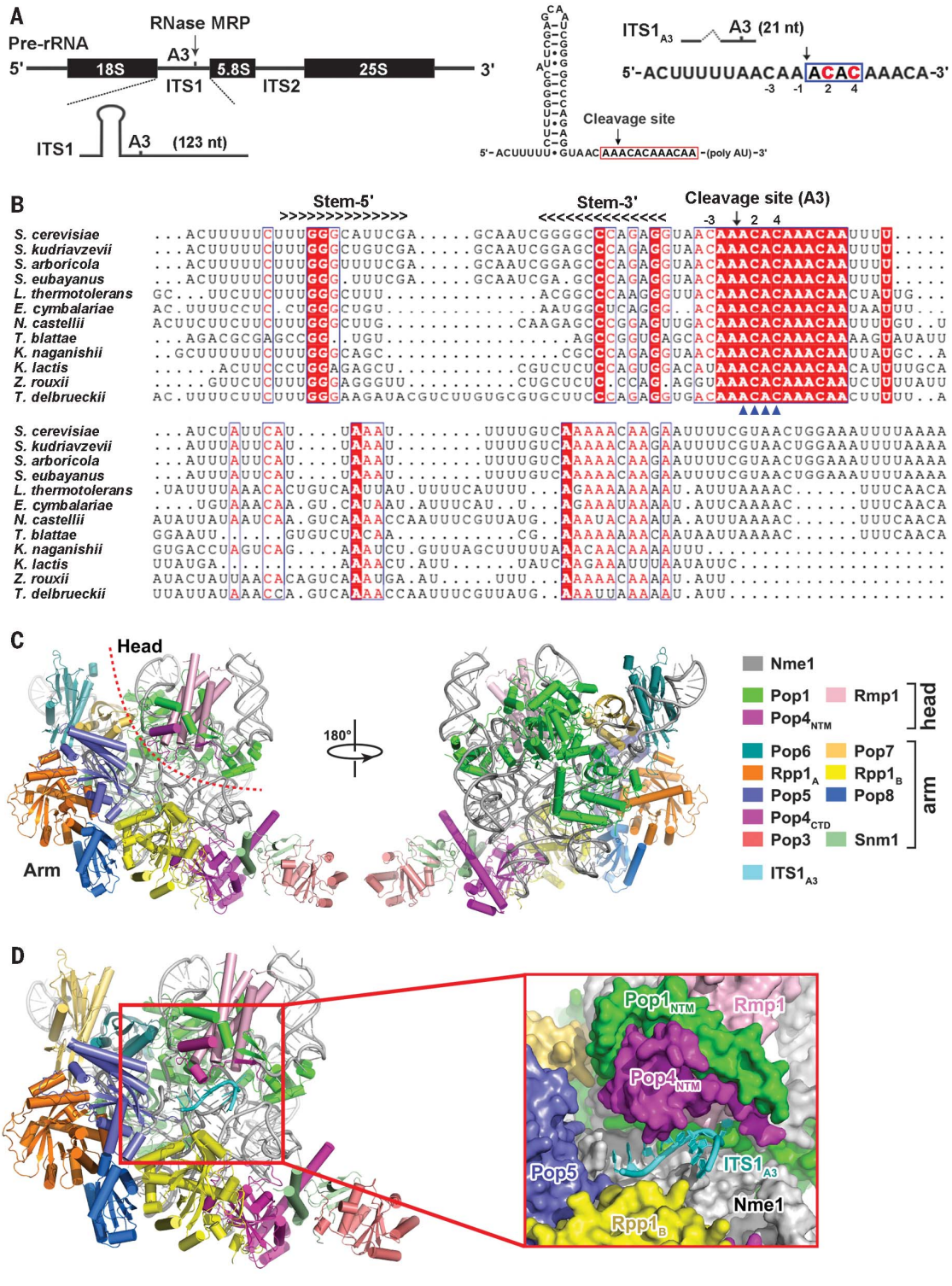


Fig. 1. Overall structures of the *S. cerevisiae* RNase MRP holoenzyme alone and in complex with the $ITS1_{A3}$ substrate. (**A**) Schematic diagram of the *S. cerevisiae* 35*S* pre-rRNA transcript. Mature rRNAs and spacers are shown as black boxes and lines, respectively, along with predicted secondary structure of the 5′-stem in ITS1. The numbering scheme of the A3 cleavage site is shown under the sequence of $ITS1_{A3}$; the consensus recognition sequence is boxed with C2 and C4 colored in red. (**B**) Multiple sequence alignment of the ITS1 region from representative species (*Saccharomyces cerevisiae*, *S. kudriavzevii*, *S. arboricola*, *S. eubayanus*, *Lachancea thermotolerans*, *Eremothecium cymbalariae*, *Naumovozyma castellii*, *Tetrapisispora blattae*, *Kazachstania naganishii*, *Kluyveromyces lactis*, *Zygosaccharomyces rouxii*, *Torulaspora delbrueckii*) in Saccharomycetaceae. Nucleotides important for substrate recognition are highlighted by blue triangles. (**C**) Front and back views of the overall structure of the *S. cerevisiae* RNase MRP complex. The protein and RNA subunits of RNase MRP are shown in cartoon representation and colored according to the scheme shown at the right. The boundary between the head and arm modules in the protein hook is denoted by a red dashed line. (**D**) Overall structure of the *S. cerevisiae* RNase MRP in complex with the single-stranded $ITS1_{A3}$ substrate. The RNase MRP complex and the $ITS1_{A3}$ substrate are shown as cartoons and colored as in (C). A close-up view of the substrate-binding pocket is shown in surface representation at the right. $Pop1_{NTM}$ and $Pop4_{NTM}$ are the N-terminal motifs of Pop1 and Pop4.

can be superimposed onto that of the RNase MRP–$ITS1_{A3}$ complex with a root mean square deviation (RMSD) value of ~0.5 Å (fig. S6A), which suggests that RNase MRP adopts a rigid conformation before substrate binding. Below we focus on the RNase MRP–$ITS1_{A3}$ complex structure, unless stated otherwise.

In the RNase MRP holoenzyme, the Nme1 RNA forms a compact structure occupying the central region of the complex (Fig. 1C). Eleven protein subunits sequentially contact one another and interlink together to form a hook-shaped architecture, with Pop1, Rmp1, and part of Pop4 as the head, and Pop6-Pop7, Pop5-$(Rpp1)_2$-Pop8, and Pop4-Snm1-Pop3 subcomplexes as

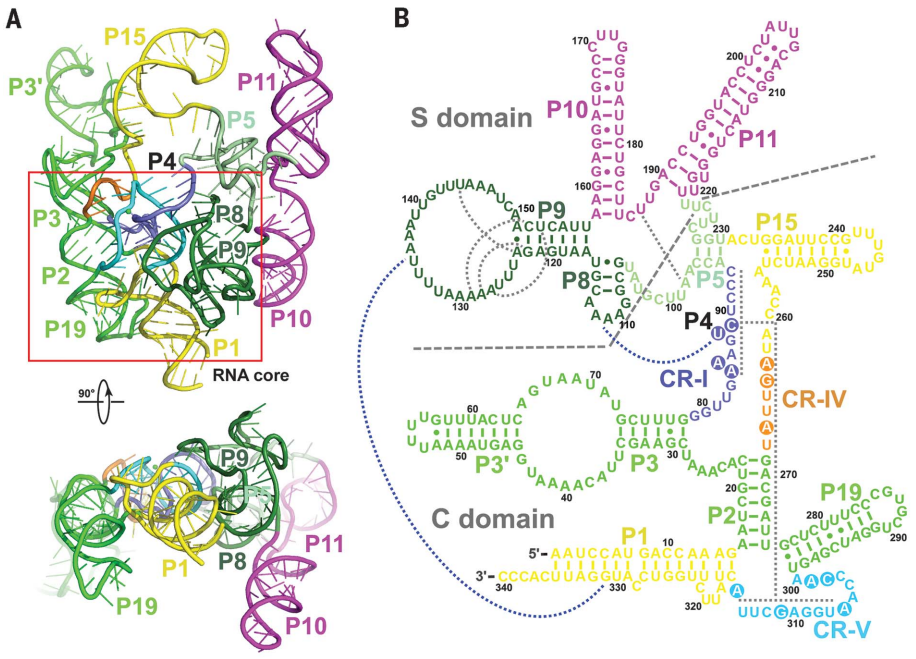


Fig. 2. Structure of the Nme1 RNA. (**A**) Two orthogonal views of the overall structure of the Nme1 RNA. CR-I, CR-IV, and CR-V are colored in slate, orange, and cyan, respectively. The helical RNA core is highlighted by a red box. (**B**) Secondary structure diagram of the Nme1 RNA. The canonical Watson-Crick and noncanonical base-pairing interactions are shown as solid lines and dots, respectively. The long-range base-pairing and tertiary interactions are denoted as gray and blue dotted lines, respectively. The gray dashed line denotes the boundary between the C and S domains. Nucleotides that are universally conserved in all known MRP RNAs are highlighted with shaded circles.

the arm (Fig. 1C). This protein hook tightly wraps around and stabilizes Nme1, involving intricate interactions between Nme1 and the protein head module at one side and an extended, flat interface between Nme1 and the arm module at the other (Fig. 1C). Together, these RNA-protein interactions shape the holoenzyme into a configuration with a deep, narrow groove at the catalytic center, in which the single-stranded $ITS1_{A3}$ substrate lies snugly (Fig. 1D). The Pop1-Pop4-Rmp1 ternary motif in the head module mediates specific interactions with the substrate (Fig. 1D). The EM density map of this ternary motif is well ordered in the complex, but it is of poor quality in the apo structure, which suggests a local induced-fit mechanism for substrate recognition by RNase MRP (fig. S6B). It is noteworthy that the $ITS1_{A3}$-binding surface on the Pop1-Pop4-Rmp1 motif is highly conserved in Saccharomycetaceae, underscoring the important function of this ternary motif in substrate recognition (fig. S7, A to C).

Structure of the Nme1 RNA

The Nme1 RNA adopts an extended single-layered configuration with a compact core from which four stems—P3′, P10, P11, and P15—extend in different directions (Fig. 2, A and B). The RNA core is characterized by three helices packed in parallel, which are composed of coaxially stacked stems P19-P2-P3, P1-P4, and P9-P8, respectively (Fig. 2, A and B). Except for the tip of P19, helices P19-P2-P3 and P1-P4 highly resemble their counterparts in the RNase P structure (fig. S8, A and B) (*30*, *33*). In particular, three conserved regions (CR-I, CR-IV, and CR-V) in the core of Nme1 fold into a pseudoknot motif, which is identical to the structure observed in the catalytic center of RNase P (fig. S8, A and B) (*30*, *34*–*37*).

Previous sequence analyses predicted a long stem, ymP5, in the Nme1 RNA, but failed to assign it as the P9 stem because the predicted ymP5 contains a much longer duplex than P9 normally has in RNase P (*3*, *25*, *26*). Therefore, we did not anticipate that stems P8 and P9 in the S domain of Nme1 could coaxially stack together to form a continuous helix in the RNA core with a duplex region that resembles helix P9-P8 in the RNase P structure (fig. S8, B and C). In fact, the P9 stem in Nme1 contains a very large loop, part of which (U132–A136) is disordered while the rest folds back to its own minor groove and mediates non–Watson-Crick interactions with three consecutive base pairs: A121-U153, G122-C152, and A123-A151 (fig. S8, C and D), allowing P9 to contact P1 in the same fashion as in RNase P (fig. S8, B and C). Similarly, on the other end of the P9-P8 helix, the pentaloop of stem P8 ($_{109}$GAAAA$_{113}$) that corresponds to the previously identified consensus sequence GARAR (R = purine) in RNase MRP RNAs interacts with the minor groove of stem P4, closely resembling the P8-P4 interface in RNase P RNA (fig. S8, B and C) (*30*). From these findings, we conclude that the compact RNA core with three helices packed in parallel is conserved in both RNase MRP and RNase P RNAs (Fig. 2A and fig. S8, A and B) (*30*). In addition to stem P9, the structure of Nme1 also reveals a 3–base pair stem, P5, immediately adjacent to P4, which was not predicted by previous analyses but is very likely conserved in all RNase MRPs (Fig. 2, A and B) (*3*, *25*–*27*).

Except for the P9-P8 helix, the rest of the S domain in Nme1 (stems P10 and P11, previously named ymP6 and ymP7) is markedly different from the S domain in RNase P RNA (fig. S8E) and only makes very limited contacts with protein subunits in RNase MRP (Fig. 1C). Both P10 and P11 can be considerably reduced in size with marginal effects on viability or pre-rRNA processing in vivo, indicating that these stems are not critical for RNase MRP function (*38*). This is in sharp contrast to the P10/11-P12 branch of the RNase P RNA, in which conserved regions CR-II and CR-III fold into a T-loop structure and play an important role in pre-tRNA substrate binding (fig. S8, A and B) (*30*, *39*, *40*). Collectively, we conclude that the S domain of Nme1 is distinct from its counterpart in RNase P RNA both structurally and functionally.

Protein subunits and their interactions with Nme1

The overall architecture of the protein hook in RNase MRP resembles that of RNase P (fig. S9A). In particular, the Pop6-Pop7 heterodimer, the Pop5-$(Rpp1)_2$-Pop8 heterotetramer, and the Pop4-Snm1-Pop3 heterotrimer are identical to their counterparts in RNase P (fig. S9, A to D) (*30*, *33*, *41*). These three protein subcomplexes together form an elongated arm and cover the surface of one side of the Nme1 RNA (Fig. 1C and fig. S9A). The protein head module contains Pop1, Rmp1, and the N-terminal motif of Pop4 ($Pop4_{NTM}$) (Fig. 3A). Pop1, the largest protein subunit in both RNase MRP and RNase P, is composed of three motifs: an N-terminal motif (NTM), an internal motif (INM), and a large C-terminal globular domain (CTD) (Fig. 3A). $Pop1_{CTD}$ is separated from the rest of the head module, covering the RNA core in the same fashion as in RNase P from the other side of the RNA opposite to the arm module (Fig. 3A and fig. S9E).

Notwithstanding these similarities, marked structural differences do exist in both the RNA and protein subunits in the vicinity of the substrate-binding site. In RNase P, $Pop1_{NTM}$ adopts a helical structure enriched with positively charged residues to stabilize the open junction between CR-IV and stems P4, P7, and

P15 of the Rpr1 RNA, thereby serving as an anchor for pre-tRNA substrate recognition (Fig. 3B and fig. S10, A and B) (*30*). $Pop4_{NTM}$, by contrast, folds into a small compact motif and binds the Rpr1 RNA from the opposite side of $Pop1_{NTM}$ (Fig. 3B and fig. S10, A and C) (*30*). Strikingly, in RNase MRP, both $Pop1_{NTM}$ and $Pop4_{NTM}$ completely refold themselves and adopt extended conformations, wrapping around one end of the helix bundle of Rmp1 (Fig. 3B and fig. S11, A to D). This intricate ternary subcomplex sits atop stem P5 and mediates intimate interactions with the pseudoknot of Nme1, forming part of the substrate-binding groove and playing an important role in specific recognition of single-stranded substrates (Fig. 3B). Note that although $Pop1_{NTM}$ adopts completely different conformations in RNase MRP and RNase P, a short stretch of arginine residues (Arg^{94}, Arg^{97}, Arg^{98}, and Arg^{99}) occupies exactly the same location and mediates similar stacking and electrostatic interactions with the RNA pseudoknot, underscoring the crucial function of these residues in stabilizing the catalytic center in both RNPs (fig. S12, A and B) (*30*). In addition to $Pop1_{NTM}$, $Pop1_{INM}$ in RNase MRP also reorganizes itself with a distinct fold, sitting in a deep cleft formed by the junction among stems P5 and P8 to P11 (Fig. 3B and fig. S11B). In comparison, $Pop1_{INM}$ in RNase P forms a different topology and associates with the P7-P8′-P8-P9-P10/11 junction from the opposite direction (Fig. 3B and fig. S10B) (*30*).

Another distinct structural feature of RNase MRP occurs at the interface between stem P9 of Nme1 and the Pop4-Snm1-Pop3 heterotrimer. In both RNase P and RNase MRP, a long helix of Pop4 simultaneously associates with the termini of stems P1 and P9, enhancing the long-range RNA-RNA interactions (Fig. 3C). In RNase MRP, Pop4 Tyr^{78} in the helix mediates a stacking interaction with nucleotide U125 of Nme1, stabilizing the loop of stem P9 in a folded conformation (Fig. 3C). This in turn allows the Pop4 helix to maintain its direction so that it can be connected to $Pop4_{NTM}$ in the head module for substrate recognition (Fig. 3C). By contrast, in RNase P the local structure of Rpr2 and the bulge in stem P9 change the direction of the Pop4 helix with a sharp turn of ~90°, which otherwise would have a severe collision with the T-loop of the RNA if the helix adopted the same continuous conformation as in RNase MRP (Fig. 3D). Furthermore, the folded loop in stem P9 in RNase MRP occupies the location of the TψC loop of pre-tRNA in the RNase P complex, indicating that pre-tRNA could not fit into the substrate-binding site in RNase MRP (Fig. 3E). We conclude that although RNase MRP shares the same overall structural organization as RNase P, several key structural differences in both protein and RNA subunits define RNase MRP as a distinct ribozyme to process non–pre-tRNA substrates.

The RNase MRP–$ITS1_{A3}$ interface

Although $ITS1_{A3}$ is a single-stranded substrate, it adopts a helical-like conformation, resembling the 5′ strand of the pre-tRNA acceptor stem in the RNase P complex (fig. S13, A and B). $ITS1_{A3}$ is accommodated deep within the substrate-binding site, sitting on the minor groove of stem P4 in the Nme1 pseudoknot with its backbone partially or completely buried in a solvent-excluded contact area of ~1200 $Å^2$ (Fig. 4A). The overall conformation of the $ITS1_{A3}$ substrate is mainly governed by two sets of the π-π stacking interactions among bases: A(−2) stacks with A(−1), A1, and C2, and A3 stacks with A5, A6, and A7 (Fig. 4, A and B). The A(−2)-A(−1)-A1-C2 stack is further extended into the Nme1 RNA by the base of U266 in CR-IV of Nme1 (Fig. 4, A to C). Notably, this intermolecular continuous base stack highly resembles the stacking between the 5′-leader of pre-tRNA and nucleotide A314 in CR-IV of the Rpr1 RNA in the RNase P–pre-tRNA complex structure (Fig. 4C and fig. S13, C and D) (*30*). In addition to the stacking, the sugar ring and the phosphate backbone of A(−1) in $ITS1_{A3}$ mediate two electrostatic interactions with the main chain of Pop5 N-terminal residue Val^2 (Fig. 4C and fig. S13C), which are also conserved in the RNase P–pre-tRNA interactions (fig. S13D) (*30*). Together, these observations indicate that both RNase MRP and RNase P use the same molecular mechanism to nonspecifically bind nucleotides of the substrates 5′ to the cleavage site (fig. S13, A to D) (*30*).

The most prominent features of the $ITS1_{A3}$ substrate are the two cytosines, C2 and C4, that define the sequence-specific recognition of $ITS1_{A3}$ by RNase MRP. The side chain of Pop4 Arg^{28} points to the $ITS1_{A3}$ substrate and coordinates two electrostatic interactions with the Watson-Crick donor and acceptor groups of C2 in $ITS1_{A3}$ (Fig. 4, B and D, and fig. S13E). When the RNase MRP–$ITS1_{A3}$ structure is

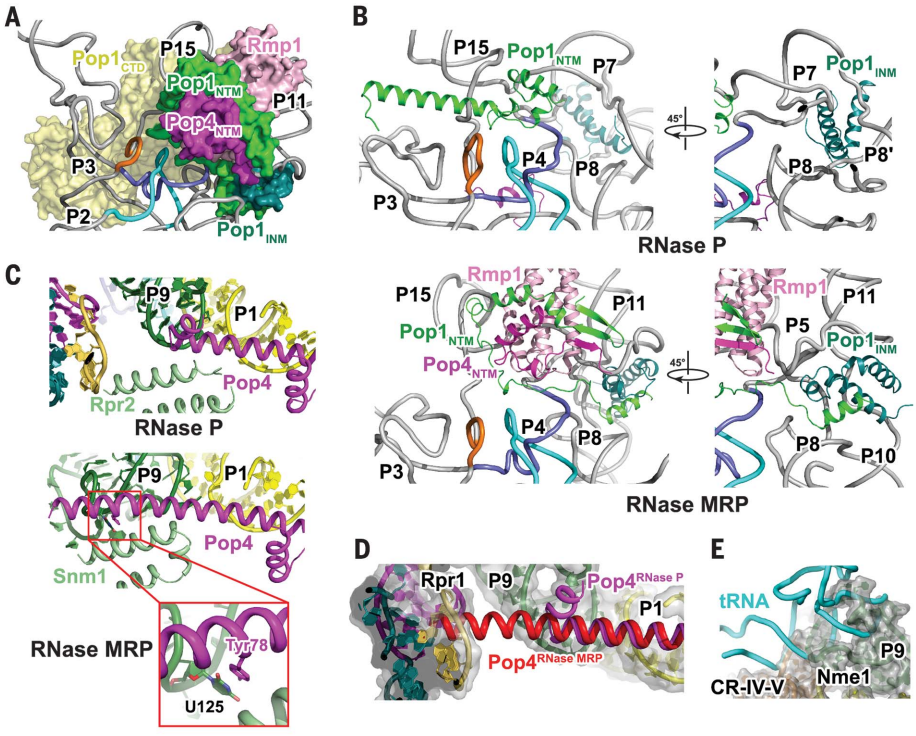


Fig. 3. Protein subunits and their interaction with Nme1. (**A**) Interface between the protein head module and the Nme1 RNA. $Pop1_{INM}$, internal motif of Pop1; $Pop1_{CTD}$, C-terminal domain of Pop1. (**B**) Structural comparison of the protein head modules in *S. cerevisiae* RNase P (top) and RNase MRP (bottom), in two related views, reveals the refolding of $Pop1_{NTM}$, $Pop1_{INM}$, and $Pop4_{NTM}$ in the two complexes. (**C**) Close-up view of the Pop4 helix in RNase P (top) and RNase MRP (bottom) bound to its corresponding RNA subunits Rpr1 and Nme1, respectively. Inset: Close-up view of the stacking interaction between Pop4 Tyr^{78} and U125 of Nme1. (**D**) The Pop4 helix in RNase MRP (red) would have a collision with the CR-II-III T loop structure when RNase MRP is superposed onto RNase P, based on their RNA components. For clarity, only the Pop4 helix in RNase P (in magenta) and in RNase MRP (red) as well as the RNase P Rpr1 RNA are shown. (**E**) Structural superposition analysis of RNase P and RNase MRP reveals that the pre-tRNA substrate in RNase P has a collision with stem P9 of Nme1 in RNase MRP. For clarity, only the Nme1 RNA of RNase MRP and the pre-tRNA substrate are shown.

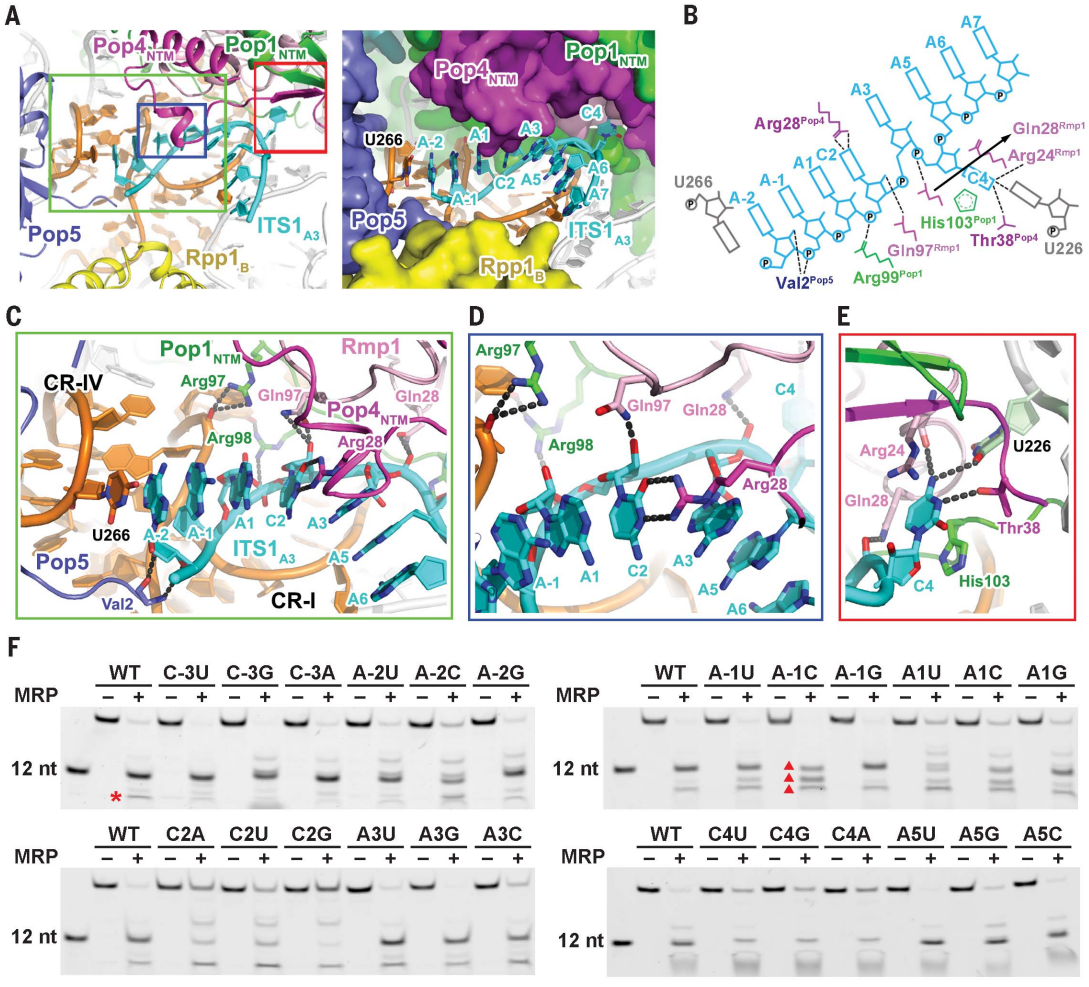


Fig. 4. Substrate recognition by RNase MRP. (**A**) The $ITS1_{A3}$ substrate adopts a deformed helical conformation and is accommodated deep within the substrate-binding groove. The $ITS1_{A3}$-binding groove is shown in ribbon (left) and surface (right) representation, colored as in Fig. 1C. The $ITS1_{A3}$ substrate is shown as a cartoon and colored in cyan. Base-stacking interaction recognitions of C2 and C4 are highlighted in green, blue, and red boxes, respectively [enlarged in (C) to (E)]. (**B**) Schematic diagram of the RNase MRP–$ITS1_{A3}$ interaction. Nucleotides in $ITS1_{A3}$ and Nme1 are shown in cyan and gray, respectively. Residues in Pop1, Pop4, Rmp1, and Pop5 are colored as in Fig. 1C. Hydrogen bonds and electrostatic interactions are denoted as black dashed lines. (**C**) Close-up view of the stacking interactions among the nucleotide bases in $ITS1_{A3}$ and between $ITS1_{A3}$ and U266 in CR-IV of Nme1. (**D**) Detailed interactions of $ITS1_{A3}$ C2 with Pop4 Arg^{28} and Rmp1 Gln^{97}. (**E**) $ITS1_{A3}$ C4 flips into a pocket formed by $Pop1_{NTM}$, $Pop4_{NTM}$, Rmp1, and the Nme1 RNA. (**F**) In vitro cleavage activity assay of wild-type (WT) and single nucleotide–substituted $ITS1_{A3}$ substrates. A 12-nucleotide oligo was used as a marker for the product correctly processed by RNase MRP. A minor cleavage between A(−5) and A(−4) is denoted by a red star. Three equal-amount cleavage products due to the A-to-C substitution at position −1 are denoted by red triangles.

overlaid onto that of the RNase P–pre-tRNA complex, the short helix in $Pop4_{NTM}$ occupies the equivalent position of pre-tRNA G71-C72 in the RNase P–pre-tRNA complex and the C2–Pop4 Arg^{28} interaction strikingly mimics the C2-G71 base pairing in pre-tRNA, stabilizing the single-stranded $ITS1_{A3}$ in the helical conformation (fig. S13, E and F) (*30*). This Pop4 Arg^{28}–mediated "pseudo–Watson-Crick" interaction, together with a hydrogen bond between the sugar-ring hydroxyl group of C2 and the side chain of Rmp1 Gln^{97}, prefers a cytosine at position 2 in the $ITS1_{A3}$ substrate (Fig. 4, B and D). In addition to the interaction with C2, the guanidino group of Pop4 Arg^{28} also makes a stacking interaction with the base of A3, serving as a stabilizing connector between C2 and A3 (Fig. 4, B and D).

In contrast to C2, C4 flips out from the helical position and points into a pocket formed by the protein head module and the Nme1 RNA (Fig. 4, B and E, and fig. S13G). The base of C4 is sandwiched by the side chains of Rmp1 Arg^{24} and Pop1 His^{103} through stacking interactions in the center of the pocket (Fig. 4, B and E). The structure shows that the cavity of the pocket is not optimal to accommodate bulky purine nucleotides (Fig. 4E). Notably, the edge of the base of C4 is surrounded with three hydrogen-bonding interactions with Nme1 U226, Rmp1 Arg^{24}, and Pop4 Thr^{38}, providing a strong preference for cytosine at this position (Fig. 4E). In addition to these sequence-specific interactions, the backbone phosphate group of C4 accepts one hydrogen bond from Rmp1 Gln^{28}, further stabilizing the base of C4 in the pocket (Fig. 4E). Collectively, the RNase MRP–$ITS1_{A3}$ complex structure demonstrates that RNase MRP recognizes a short single-stranded region of $ITS1_{A3}$ and that two nucleotides, C2 and C4, make sequence-specific interactions with RNase MRP.

Consensus substrate sequence

To further define the consensus substrate sequence for RNase MRP, we mutated each nucleotide from C(−3) to A5 in $ITS1_{A3}$ and evaluated their effects using the in vitro activity assay. Consistent with the structure, substitution of C4 with any other nucleotides all led to reduced activity, confirming that position 4 relative to the cleavage site prefers a cytosine (Fig. 4F) (*32*). In contrast to C4, mutational analysis of C2 resulted in a hierarchical ranking of C>U>A>G, from the most to the least preferred nucleotide for position 2 in $ITS1_{A3}$ (Fig. 4F). Notably, this nucleotide ranking is in perfect agreement with the RNase MRP–$ITS1_{A3}$ interface at C2. First, despite the shape of uracil resembling that of cytosine, its imino group does not provide compatible hydrogen bond acceptors to the guanidino group of Pop4 Arg^{28} (Fig. 4D). Second, because of the small size of the pocket, a pyrimidine is preferred at position 2 (Fig. 4D). Third, if a purine could be fit into position 2 by some local structural adjustment, adenine is more favorable than guanine because of the same consideration of hydrogen

bond compatibility with the side chain of Pop4 Arg^{28} (Fig. 4D).

In accordance with the observation that nucleotides other than C2 and C4 in $ITS1_{A3}$ make no sequence-specific interactions with RNase MRP, single-nucleotide replacement at positions –3, –2, –1, or 5 in $ITS1_{A3}$ had marginal effect on the processing activity of RNase MRP (Fig. 4F). Surprisingly, substitution of A1 or A3 with a uracil or cytosine led to a detectable reduction in activity (Fig. 4F). Close examination of complex structure suggested that the stacking interaction between A3 and the guanidino group of Pop4 Arg^{28} would likely be weakened by a pyrimidine replacement of A3 (Fig. 4F). Similarly, a pyrimidine at position 1 would also attenuate the stacking interaction with C2 (Fig. 4F). Therefore, the mutational data are consistent with the structural information, which suggests a preference for purines for positions 1 and 3 in the substrate. In aggregate, our structural and biochemical data define a short consensus sequence for the RNase MRP substrate as 5′-*RCRC-3′ (where * denotes the cleavage site). Notably, an A-to-C substitution at position –1 would generate two additional optimal cleavage sites between positions –5 and –4 and between –3 and –2 (Fig. 1A). Indeed, the activity assay of this mutant $ITS1_{A3}$ substrate generated three equal-amount products with the expected sizes (Fig. 4F), providing an independent validation of the consensus sequence for RNase MRP substrates.

A minor band appeared below the consensus product in the in vitro assay, indicating a cleavage event between A(–5) and A(–4) in $ITS1_{A3}$ using 5′-*ACAA-3′ as the substrate recognition sequence (Fig. 4F). This is in agreement with the mutational data indicating that the majority of the single-nucleotide substitutions in $ITS1_{A3}$ are not deleterious and can still be cleaved by RNase MRP (Fig. 4F). In addition to $ITS1_{A3}$, several substrates of yeast RNase MRP have been identified, and among them the cleavage regions in the 5′-UTRs of CLB2 mRNA and chitinase CTS1 mRNA have been biochemically characterized (*13*, *42*). In light of the RNase MRP–$ITS1_{A3}$ structure, we performed multiple sequence alignment of these cleavage regions. The resulting cleavage sequences of this alignment largely abide by the 5′-*RCRC-3′ rule derived from the structural and mutational analysis of the RNase MRP–$ITS1_{A3}$ interaction with some exceptions (fig. S14), which suggests that despite the preferred 5′-*RCRC-3′ substrate sequence, RNase MRP can still process a broader spectrum of single-stranded RNA substrates.

Active site

The cryo-EM density map unveils three putative metal ions (M1, M2, and M3) in the vicinity of the scissile phosphate, which would stabilize the $ITS1_{A3}$ substrate at the catalytic center of RNase MRP (fig. S15, A and B). The EM density map is of sufficient quality to allow us to define the locations of the putative M1 and M3 ions (fig. S15B). M1 corresponds to one of the putative catalytic magnesium ions (Mg^{2+}) in the RNase P–pre-tRNA structure (Fig. 5, A and B) (*30*) and is coordinated by inner-sphere contacts with the scissile phosphate of $ITS1_{A3}$ and the nonbridging phosphoryl oxygens of Nme1 A86 and G87 (Fig. 5A). Although the local density map for M2 is not discrete, we could model a putative Mg^{2+} ion in the density (fig. S15B) so that it is stabilized by A86, A305, and A306 of Nme1 as well as by the O3′ leaving group of A(–1) in the $ITS1_{A3}$ substrate (Fig. 5A), occupying the equivalent position of the other catalytic ion in the RNase P–pre-tRNA structure (Fig. 5, A and B) (*30*). In contrast to catalytic M1 and M2 ions, the third putative metal ion M3 may play a structural role by mediating contacts with the backbone of Nme1 G87 and the scissile phosphate of $ITS1_{A3}$, thereby helping to stabilize the local substrate geometry at the active site (Fig. 5A).

The configuration of this RNA-based catalytic center of RNase MRP is identical to that in the RNase P–pre-tRNA complex, except for the conformation of the conserved uridine in stem P4 of the RNA subunits (Fig. 5, A and B) (*30*). Upon pre-tRNA binding in RNase P, U93 in Rpr1 rotates through a large angle to point into the P4 stem and interacts with the putative M1 Mg^{2+} ion, transforming the ribozyme into a fully active state (Fig. 5B) (*30*). In contrast, the corresponding uridine U88 of Nme1 in the RNase MRP–$ITS1_{A3}$ complex structure still maintains a flipped-out conformation (Fig. 5A). We propose that the snapshot captured in the RNase MRP–$ITS1_{A3}$ complex structure represents a state of initial substrate binding to RNase MRP, in which U88 is still in an inactive conformation (Fig. 5A). Given that fewer than half of the nucleotides in $ITS1_{A3}$ can be observed in the EM density map, it is possible that the rest of $ITS1_{A3}$, although disordered in the structure, may help to induce the conformational change of U88 to fully activate the ribozyme. How RNase MRP is fully activated by $ITS1_{A3}$ warrants future investigation. Thus, although the biochemistry and cryo-EM structure of the RNase MRP–$ITS1_{A3}$ complex reveal clear substrate recognition differences relative to RNase P–pre-tRNA interactions, both essential RNase P and MRP ribonucleoprotein complexes appear to share a common two–metal ion S_N2-type catalytic mechanism (Fig. 5C) (*30*, *37*).

Discussion

In sharp contrast to RNase P, which has a penchant for the tRNA-like fold, it has remained a mystery how RNase MRP recognizes its substrates. So far, only a few RNase MRP substrates have been identified, severely impeding our understanding of RNase MRP function. The short consensus sequence derived from our structural and biochemical studies implies that RNase MRP may have myriad substrates that have not been identified but could play important roles in various cellular contexts. Future work is required to identify and characterize these novel RNase MRP substrates.

Mutations in the RNA component of human RNase MRP causing the highly pleiotropic disease CHH exemplify RNase MRP's essential and irreplaceable role in humans (*20*, *21*). Comparative analysis of the RNA components of yeast and human RNase MRP shows that, except for peripheral stems P10, P11, and P15, most of the structural elements in yeast Nme1 RNA are conserved in human RMRP (Fig. 2B and figs. S16 and S17A) (*21*). Three-dimensional mapping of disease-derived mutations onto the corresponding positions in Nme1 structure unveils that, although these incapacitating mutations are found in a wide range of locations in *RMRP*, most of them are spatially clustered in the helical core near the catalytic center of the RNA (fig. S17B). In particular, A70 > G is the most prevalent mutation, found in more than 90% of the CHH patients (*21*). This adenine nucleotide is conserved in all RNase P and MRP RNAs and forms a key Hoogsteen base pair with a uracil or cytosine (C250 in human RMRP) in the center of the catalytic pseudoknot (fig. S17C). Structure-based analysis suggests that although these positions are not directly involved in substrate binding and processing, their mutations very likely induce conformational changes of the RNA, leading to defective substrate binding and processing. Further structural and functional studies of the human RNase MRP holoenzyme will be required to fully understand the effects of these disease mutations.

The structure of yeast RNase MRP explains why RNase MRP is observed in eukaryotes but not in bacteria and archaea (*2*, *6*, *43*). It has long been appreciated that the RNase P and MRP family of ribonucleases share a common ancestor from the "RNA world," presumably a ribozyme that can catalyze the 5′-end maturation of pre-tRNA (*44*). The overall architecture of this ribozyme has been faithfully succeeded by bacterial and archaeal RNase Ps, in particular the two RNA-based anchors (the A-anchor and the T-loop anchor) that can specifically recognize the three-dimensional structure of pre-tRNA through the double-anchor mechanism (Fig. 5D) (*30*, *37*, *45*). It is noteworthy that this high specificity endowed by the RNA anchors, on the other hand, also constrains the ability of bacterial and archaeal RNase Ps to process non–pre-tRNA–like substrates. Although bacteria and archaea had acquired additional protein subunits during evolution

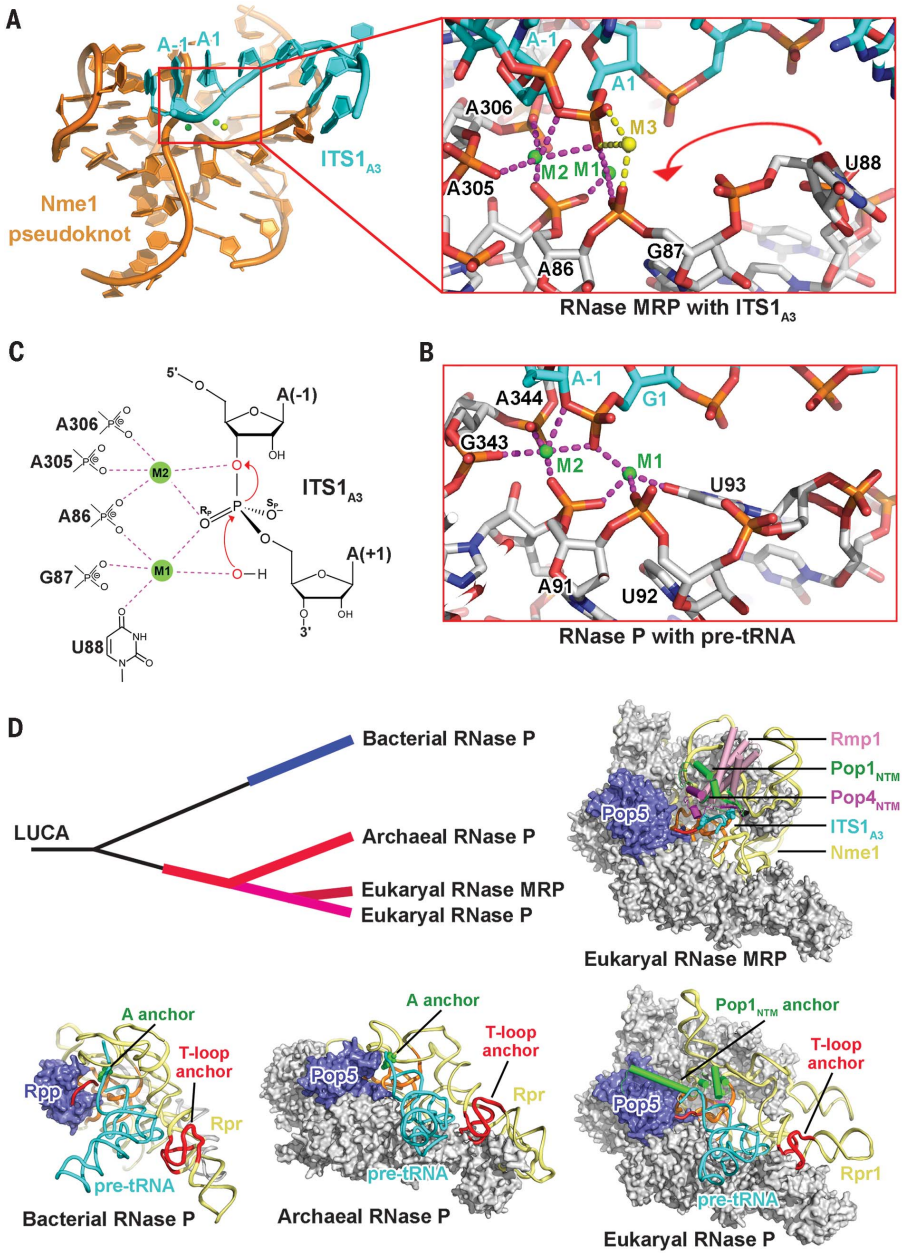


Fig. 5. Implications for catalysis and evolution of RNase MRP. (**A**) Left: Overview of the catalytic center in yeast RNase MRP. The pseudoknot of Nme1 and the $ITS1_{A3}$ substrate are colored in orange and cyan, respectively. Right: Close-up view of the catalytic center. The coordination of modeled ions M1 and M2 is highlighted by magenta dashed lines and that of M3 in yellow dashed lines. The conserved nucleotide U88 of Nme1 flips out and points away from the catalytic center in the complex structure. (**B**) Close-up view of the catalytic center in yeast RNase P (PDB: 6AH3) (*30*). The coordination of modeled ions M1 and M2 is essentially identical to that in RNase MRP except for nucleotide U93. In the presence of the pre-tRNA substrate, the corresponding conserved nucleotide U93 points into the catalytic center to coordinate the M1 metal ion. (**C**) Proposed reaction mechanism for the processing of $ITS1_{A3}$ by yeast RNase MRP. The reactive oxygens are colored in red, the $ITS1_{A3}$ scissile phosphate is depicted in a pre-attack state, and the interactions between catalytically important nucleotides and reactive oxygens mediated by modeled ions M1 and M2 are shown as magenta dashed lines. M1 coordinates an attacking hydroxyl nucleophile during the cleavage reaction. (**D**) The schematic cladogram at upper left depicts the possible evolutionary pathway of RNase P and RNase MRP (LUCA, last universal common ancestor). Proteins that mainly function to stabilize the catalytic RNA subunit and adopt similar architectures in both RNase P and RNase MRP are shown in gray surface. Single-stranded regions 5′ to the cleavage site in pre-tRNA and $ITS1_{A3}$ are colored in red; the remaining substrates are in cyan.

[Rpp for bacteria; $(Pop5\text{-}Rpp30)_2$ and Rpp29-Rpp21-Rpp38 for archaea], these proteins did not replace the essential function of RNA-based anchors for pre-tRNA recognition (Fig. 5D) (*45*–*47*). The evolution of protein subunits Pop1 and Pop4 in eukaryotic RNase P and MRP released this limitation; Pop1 is a new addition in eukaryotes, whereas Pop4 has evolved from its archaeal ancestor Rpp29 with a new N-terminal motif (*48*, *49*). In eukaryotic nuclear RNase P, whereas the T-loop anchor has been retained, the A-anchor was replaced by the NTM of Pop1, which folds into a compact module and locks the cleavage site of pre-tRNA in the catalytic center (Fig. 5D) (*30*). In contrast, RNase MRP had abandoned both RNA-based anchors during evolution, and the NTMs of Pop1 and Pop4 adopt extended conformations that are completely different from those in RNase P (Fig. 5D). Consequently, these refolded motifs, together with RNase MRP specific subunit Rmp1, specifically recognize single-stranded substrates with a short consensus sequence (Fig. 4, A to F, and Fig. 5D). Therefore, the replacement of the rigid RNA-based apparatus by malleable protein subunits Pop1 and Pop4 in eukaryotic RNase P and MRP not only allows eukaryotes to maintain the activity to accurately process pre-tRNA and pre-tRNA–like substrates, but also endows them with the capability of processing much more diversified single-stranded substrates using the same two–metal ion catalysis mechanism (Fig. 5, C and D).

RNase MRP is one of the two remaining RNA-based RNP catalysts that are found only in eukaryotic cells. The other is the spliceosome, which assembles with nuclear pre-mRNAs and splices out the major class of introns (*50*). But why is RNase MRP specifically needed, given that there are many proteinaceous endoribonucleases in eukaryotic cells? The known RNA endonucleases either cleave their targets through recognition of specific structures or have very limited or no sequence specificity (*51*–*55*). On the other hand, some molecular machineries have sequence-specific RNA cleavage activities but require a guide RNA for target recognition (*54*). A proteinaceous endoribonuclease that can cleave only RNA in a sequence-specific manner has not yet been found. Therefore, the evolution of RNase MRP likely reflects the need to process single-stranded RNAs with sequence specificity in eukaryotes, which contain many more RNA transcripts than bacteria and archaea. The identification and characterization of these RNase MRP substrates will help to unveil the in vivo function of this abundant essential RNP.

REFERENCES AND NOTES

1. R. Karwan, J. L. Bennett, D. A. Clayton, *Genes Dev.* **5**, 1264–1276 (1991).
2. M. C. Marvin, D. R. Engelke, *J. Cell. Biochem.* **108**, 1244–1251 (2009).

3. O. Esakova, A. S. Krasilnikov, *RNA* **16**, 1725–1747 (2010).
4. W. Yang, *Q. Rev. Biophys.* **44**, 1–93 (2011).
5. N. Jarrous, V. Gopalan, *Nucleic Acids Res.* **38**, 7885–7894 (2010).
6. A. Hernandez-Cid, S. Aguirre-Sampieri, A. Diaz-Vilchis, A. Torres-Larios, *IUBMB Life* **64**, 521–528 (2012).
7. D. Evans, S. M. Marquez, N. R. Pace, *Trends Biochem. Sci.* **31**, 333–341 (2006).
8. S. Altman, L. A. Kirsebom, in *The RNA World*, R. Gesteland, T. Cech, J. Atkins, Eds. (Cold Spring Harbor Laboratory Press, 1999), pp. 351–380.
9. S. Chu, R. H. Archer, J. M. Zengel, L. Lindahl, *Proc. Natl. Acad. Sci. U.S.A.* **91**, 659–663 (1994).
10. Z. Lygerou, C. Allmang, D. Tollervey, B. Séraphin, *Science* **272**, 268–270 (1996).
11. L. Lindahl *et al*., *RNA* **15**, 1407–1416 (2009).
12. M. E. Schmitt, D. A. Clayton, *Mol. Cell. Biol.* **13**, 7935–7941 (1993).
13. T. Gill, T. Cai, J. Aulds, S. Wierzbicki, M. E. Schmitt, *Mol. Cell. Biol.* **24**, 945–953 (2004).
14. T. Gill, J. Aulds, M. E. Schmitt, *J. Cell Biol.* **173**, 35–45 (2006).
15. K. C. Goldfarb, T. R. Cech, *Genes Dev.* **31**, 59–71 (2017).
16. C. T. Thiel *et al*., *Am. J. Hum. Genet.* **77**, 795–806 (2005).
17. N. Jarrous, P. S. Eder, C. Guerrier-Takada, C. Hoog, S. Altman, *RNA* **4**, 407–417 (1998).
18. H. Van Eenennaam *et al*., *Arthritis Rheum.* **46**, 3266–3272 (2002).
19. H. A. Gold, J. N. Topper, D. A. Clayton, J. Craft, *Science* **245**, 1377–1380 (1989).
20. M. Ridanpää *et al*., *Cell* **104**, 195–203 (2001).
21. S. Mattijssen, T. J. Welting, G. J. Pruijn, *Wiley Interdiscip. Rev. RNA* **1**, 102–116 (2010).
22. J. R. Chamberlain, Y. Lee, W. S. Lane, D. R. Engelke, *Genes Dev.* **12**, 1678–1690 (1998).
23. T. J. Welting, B. J. Kikkert, W. J. van Venrooij, G. J. Pruijn, *RNA* **12**, 1373–1382 (2006).
24. M. Dávila López, M. A. Rosenblad, T. Samuelsson, *RNA Biol.* **6**, 208–220 (2009).
25. O. Esakova, A. Perederina, C. Quan, M. E. Schmitt, A. S. Krasilnikov, *RNA* **14**, 1558–1567 (2008).
26. X. Li, D. N. Frank, N. Pace, J. M. Zengel, L. Lindahl, *RNA* **8**, 740–751 (2002).
27. Y. Zhu, V. Stribinskis, K. S. Ramos, Y. Li, *RNA* **12**, 699–706 (2006).
28. S. C. Walker, D. R. Engelke, *Crit. Rev. Biochem. Mol. Biol.* **41**, 77–102 (2006).
29. O. Esakova, A. Perederina, I. Berezin, A. S. Krasilnikov, *Nucleic Acids Res.* **41**, 7084–7091 (2013).
30. P. Lan *et al*., *Science* **362**, eaat6678 (2018).
31. K. Salinas, S. Wierzbicki, L. Zhou, M. E. Schmitt, *J. Biol. Chem.* **280**, 11352–11360 (2005).
32. O. Esakova, A. Perederina, C. Quan, I. Berezin, A. S. Krasilnikov, *RNA* **17**, 356–364 (2011).
33. A. Perederina, O. Esakova, C. Quan, E. Khanova, A. S. Krasilnikov, *EMBO J.* **29**, 761–769 (2010).
34. J. Wu *et al*., *Cell* **175**, 1393–1404.e11 (2018).
35. A. V. Kazantsev *et al*., *Proc. Natl. Acad. Sci. U.S.A.* **102**, 13392–13397 (2005).
36. A. Torres-Larios, K. K. Swinger, A. S. Krasilnikov, T. Pan, A. Mondragón, *Nature* **437**, 584–587 (2005).
37. N. J. Reiter *et al*., *Nature* **468**, 784–789 (2010).
38. X. Li, S. Zaman, Y. Langdon, J. M. Zengel, L. Lindahl, *Nucleic Acids Res.* **32**, 3703–3711 (2004).
39. A. S. Krasilnikov, X. Yang, T. Pan, A. Mondragón, *Nature* **421**, 760–764 (2003).
40. A. S. Krasilnikov, Y. Xiao, T. Pan, A. Mondragón, *Science* **306**, 104–107 (2004).
41. A. Perederina *et al*., *RNA* **17**, 1922–1931 (2011).
42. J. Aulds, S. Wierzbicki, A. McNairn, M. E. Schmitt, *J. Biol. Chem.* **287**, 37089–37097 (2012).
43. V. Gopalan, N. Jarrous, A. S. Krasilnikov, *RNA* **24**, 1–5 (2018).
44. L. B. Lai, A. Vioque, L. A. Kirsebom, V. Gopalan, *FEBS Lett.* **584**, 287–296 (2010).
45. F. Wan *et al*., *Nat. Commun.* **10**, 2617 (2019).
46. W. Y. Chen, D. K. Pulukkunat, I. M. Cho, H. Y. Tsai, V. Gopalan, *Nucleic Acids Res.* **38**, 8316–8327 (2010).
47. M. Kimura, *Biosci. Biotechnol. Biochem.* **81**, 1670–1680 (2017).
48. E. Hartmann, R. K. Hartmann, *Trends Genet.* **19**, 561–569 (2003).
49. M. A. Rosenblad, M. D. López, P. Piccinelli, T. Samuelsson, *Nucleic Acids Res.* **34**, 5145–5156 (2006).
50. J. A. Doudna, T. R. Cech, *Nature* **418**, 222–228 (2002).
51. J. Houseley, D. Tollervey, *Cell* **136**, 763–776 (2009).
52. K. Januszyk, C. D. Lima, *Curr. Opin. Struct. Biol.* **24**, 132–140 (2014).
53. D. L. Court *et al*., *Annu. Rev. Genet.* **47**, 405–431 (2013).
54. R. C. Wilson, J. A. Doudna, *Annu. Rev. Biophys.* **42**, 217–239 (2013).
55. D. L. Makino, F. Halbach, E. Conti, *Nat. Rev. Mol. Cell Biol.* **14**, 654–660 (2013).

ACKNOWLEDGMENTS

We thank the staff members of the Electron Microscopy System and Mass Spectrometry System at Shanghai Institute of Precision Medicine for providing technical support and assistance in data collection. **Funding:** Supported by grants from the National Natural Science Foundation of China (31525007 and 31930063 to M.L., 31900929 and U1932114 to P.L.), Shanghai Municipal Education Commission Gaofeng Clinical Medicine Grant Support (20181711 to J.W.), the Shanghai Sailing Program (19YF1425400 to P.L.), and the Young Elite Scientist Sponsorship Program of China Association for Science and Technology (2018QNRC001 to P.L.). **Author contributions:** P.L. and B.Z. purified the RNase MRP complex; P.L., M.T., M.C., B.Z., and S.L. prepared cryo-EM specimens, collected data sets, and determined the structure; J.W. carried out model building and refinement; P.L. and B.Z. carried out biochemical analysis; all authors contributed to data interpretation and writing of the manuscript; M.L. and P.L. wrote the manuscript; and M.L., P.L., and J.W. initiated and orchestrated the project. **Competing interests:** The authors declare no competing interests. **Data and materials availability:** The cryo-EM 3D maps of yeast RNase MRP alone and in complex with $ITS1_{A3}$ were deposited in the EMDB database with accession codes EMD-30296 and EMD-30297, respectively. The atomic models of yeast RNase MRP alone and in complex with $ITS1_{A3}$ were deposited in the PDB database with accession codes 7C79 and 7C7A, respectively. All other data needed to evaluate the conclusions in the paper are found in the main text or supplementary materials.

SUPPLEMENTARY MATERIALS

science.sciencemag.org/content/369/6504/656/suppl/DC1
Materials and Methods
Figs. S1 to S17
Tables S1 and S2
References (*56*–*67*)
MDAR Reproducibility Checklist

1 April 2020; accepted 11 June 2020
Published online 25 June 2020
10.1126/science.abc0149

PLANT SCIENCE

Ligand-recognizing motifs in plant LysM receptors are major determinants of specificity

Zoltan Bozsoki[1]*, Kira Gysel[1]*, Simon B. Hansen[1]*, Damiano Lironi[1], Christina Krönauer[1], Feng Feng[2], Noor de Jong[1], Maria Vinther[1], Manoj Kamble[1], Mikkel B. Thygesen[3], Ebbe Engholm[3], Christian Kofoed[3]†, Sébastien Fort[4], John T. Sullivan[5], Clive W. Ronson[5], Knud J. Jensen[3], Mickaël Blaise[1]‡, Giles Oldroyd[2], Jens Stougaard[1], Kasper R. Andersen[1]§¶, Simona Radutoiu[1]§¶

Plants evolved lysine motif (LysM) receptors to recognize and parse microbial elicitors and drive intracellular signaling to limit or facilitate microbial colonization. We investigated how chitin and nodulation (Nod) factor receptors of *Lotus japonicus* initiate differential signaling of immunity or root nodule symbiosis. Two motifs in the LysM1 domains of these receptors determine specific recognition of ligands and discriminate between their in planta functions. These motifs define the ligand-binding site and make up the most structurally divergent regions in cognate Nod factor receptors. An adjacent motif modulates the specificity for Nod factor recognition and determines the selection of compatible rhizobial symbionts in legumes. We also identified how binding specificities in LysM receptors can be altered to facilitate Nod factor recognition and signaling from a chitin receptor, advancing the prospects of engineering rhizobial symbiosis into nonlegumes.

Glycan elicitors produced by bacteria and fungi are specifically recognized in plants and trigger the establishment of mutualistic or pathogenic associations (*1*–*3*). Receptors with extracellular lysine motif (LysM) domains and intracellular kinases or pseudokinases present in all land plants often act in complexes (*4*–*7*) to perceive glycans and initiate specific signaling (*8*–*13*). Phylogenetic studies have revealed receptor relatedness but have failed to elucidate receptor function or ligand selectivity (*14*–*16*). Chitin hexamers (CO6) or larger oligomers released by fungi (*17*) are immunogenic to all land plants (*18*–*21*), but a common principle of chitin perception and signaling is lacking (*5*, *6*, *22*). In legumes, *Lj*CERK6 or *Mt*CERK1 and *Lj*LYS13, *Lj*LYS14, or *Mt*LYR4 (*Mt*, *Medicago truncatula*, henceforth *Medicago*; *Lj*, *Lotus japonicus*, henceforth *Lotus*) are required for chitin immunity, and both receptors of *Medicago* bind CO8 (*6*, *21*). Moreover, CO4 to CO8 activated components of the pathway (*6*, *23*) induced by lipochitooligosaccharides (LCOs) produced by symbionts, and chitin elicitor receptor kinase (CERK) was found to be important for symbiosis with arbuscular mycorrhiza (AM) fungi, suggesting a role for chitin and/or chitin perception in both immunity and AM symbiosis (*6*, *24*). These variations indicate that, despite its early emergence (*25*), the mechanism for chitin perception and signaling appears to have diversified over the course of plant evolution (*22*).

Symbiotic nitrogen-fixing bacteria produce structurally well-defined LCOs [nodulation (Nod) factors] that are recognized by legumes with high sensitivity (10^{-12} M) (*26*). This interaction is fully dependent on binding of distinctly decorated Nod factors to LysM receptors that control nodule organogenesis, intracellular infection, and nitrogen fixation (*1*, *27*–*29*). In pea, soybean, and model legumes, a receptor with an active kinase (NFR1 and LYK3 in *Lotus* and *Medicago*, respectively) and one with a pseudokinase (NFR5 and NFP in *Lotus* and *Medicago*, respectively) are required for Nod factor signaling, and both NFR1 and NFR5 were found to be capable of binding Nod factors (*30*). Perception of Nod factors or chitin and activation of downstream signaling leading to root nodulation or immunity operate in parallel in legume epidermal root cells (*21*, *31*).

We found that receptors recognizing Nod factors and chitin have a very similar structure but contain two diverging motifs in the LysM1 domain that are necessary for discriminating between immunity and symbiotic functions, which can be further modulated by interactions at intracellular domains. These motifs define the ligand-binding sites, and in Nod factor receptors an adjacent motif contributes to diversity in legume-rhizobia compatibility. We show how this knowledge can be used to alter the binding specificities in known LysM receptors and to engineer specific Nod factor recognition and signaling into a chitin receptor.

[1]Department of Molecular Biology and Genetics, Aarhus University, 8000 Aarhus C, Denmark. [2]Sainsbury Laboratory, University of Cambridge, Cambridge CB2 1LR, UK. [3]Department of Chemistry, University of Copenhagen, 1871 Frederiksberg, Denmark. [4]Université Grenoble Alpes, CNRS, CERMAV, 38000 Grenoble, France. [5]Department of Microbiology and Immunology, University of Otago, Dunedin 9054, New Zealand.
*These authors contributed equally to this work.
†Present address: Frick Chemistry Laboratory, Department of Chemistry, Princeton University, Princeton NJ 08544, USA.
‡Present address: Institut de Recherche en Infectiologie de Montpellier, UMR 9004-CNRS, University of Montpellier, 34293 Montpellier, France.
§These authors contributed equally to this work.
¶Corresponding author. Email: kra@mbg.au.dk (K.R.A.); radutoiu@mbg.au.dk (S.R.)

LysM ectodomains are critical for nodulation and immunity

To understand how Nod factor or chitin perception and signaling are established by LysM receptors, we evaluated the contribution of corresponding domains (Fig. 1A and fig. S1) in *Lotus* NFR1 and CERK6 receptors. First, we investigated the contribution of the ectodomain, the transmembrane and juxtamembrane (TJ), and the kinase for signaling after *Mesorhizobium loti* (*M. loti*) inoculation or CO8 treatment. Intact NFR1 (**1** in Fig. 1, B and C) and all chimeras with the ectodomain of NFR1 (**2**, **3**, and **4** in Fig. 1B) induced nodule formation on *nfr1-1* (*nfr1*) mutants but were not able to restore reactive oxygen species (ROS) production in *cerk6-1* (*cerk6*) mutants after CO8 treatment (**9**, **10**, **11**, and **12** in Fig. 1D). Chimeras enabled nodulation of *nfr1* with different efficiencies. Chimera containing the kinase of CERK6 (**3**) was less efficient than **1** or **2**, whereas exchanging both TJ and kinase with CERK6 in **4** had a significant effect on nodulation. Only 2 out of the 33 plants expressing **4** formed nodules (Fig. 1B), indicating that combining elements present in the kinase and TJ regions of CERK6 had a negative impact on nodulation. All nodules were infected by *M. loti* bacteria (Fig. 1C and fig. S2), and we detected induction of the symbiotic marker p*Nin*-GUS only in the nodulated roots (fig. S2). None of the chimeras containing CERK6 ectodomain (**5**, **6**, **7**, or **8**) triggered nodulation of *nfr1*. Analyses of the CO8-induced immune response indicated that CERK6 (**13** in Fig. 1D) and chimera **14** enabled ROS production in *cerk6* (Fig. 1D). In contrast, chimeras containing CERK6 ectodomain and the NFR1 kinase (**15** and **16**) were unable to trigger ROS in *cerk6*. This result indicates that NFR1 and CERK6 kinases differ in their capacity to activate immunity. Expression in tobacco leaf cells of yellow fluorescent protein–tagged receptors with the same domain structures present in receptors **4** and **12**, **5** and **13**, or **7** and **15** localized at the plasma membrane, mirroring the synthesis and expression observed for NFR1 (**1** and **9**) or CERK6 (**5** and **13**) (fig. S3). However, we cannot rule out effects on folding, stability, or expression levels for the chimeric receptors found to be nonfunctional throughout our in planta assays. Previous studies based on overexpression of chimeric receptors between *Lotus* and *Arabidopsis* LysM proteins pinpointed the crucial role of NFR1 ectodomains in symbiosis (*32*, *33*). Our results, based on native expression of chimeric receptors derived from paralogous proteins, show that ectodomains of NFR1 and CERK6 contain major determinants for ligand perception and signaling specificity that can be further modulated by their intracellular regions. Similar modulation of specificity in the final signaling output by the intracellular domains has

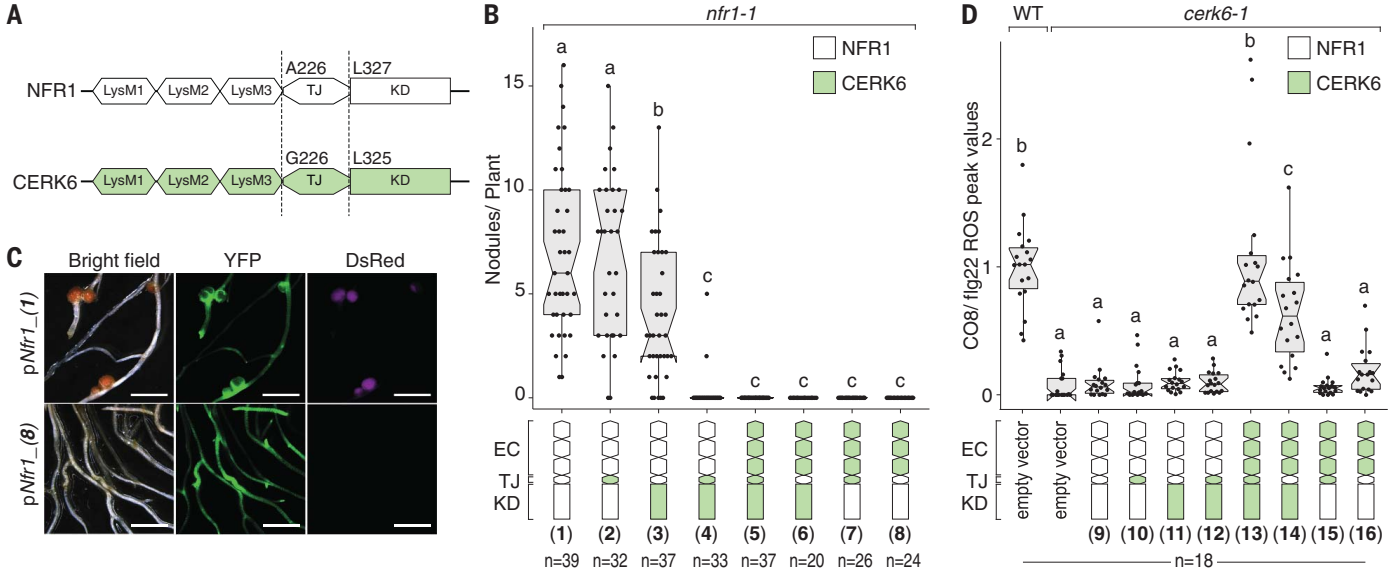


Fig. 1. Chimeric receptors identify domains important for chitin and Nod factor signaling. (**A**) Schematics of NFR1 and CERK6. Segments represent the three LysM domains (LysM1, LysM2, and LysM3) constituting the ectodomain (EC), the transmembrane and juxtamembrane (TJ) domain, and the kinase domain (KD). Dashed vertical lines and amino acids specify boundaries for chimera design. Single-letter abbreviations for the amino acid residues used throughout the figures are as follows: A, Ala; C, Cys; D, Asp; E, Glu; F, Phe; G, Gly; H, His; I, Ile; K, Lys; L, Leu; M, Met; N, Asn; P, Pro; Q, Gln; R, Arg; S, Ser; T, Thr; V, Val; W, Trp; and Y, Tyr. (**B**) Nodules formed on *nfr1* expressing the indicated chimeras. (**C**) Phenotype of *nfr1* roots expressing chimeras **1** and **8**. Scale bars, 5 mm. YFP, yellow fluorescent protein. (**D**) Reactive oxygen species (ROS) production observed for wild type (WT) and *cerk6* expressing the indicated constructs. In (B) and (D), lowercase letters indicate significant differences between samples [analysis of variance (ANOVA), Tukey, $P < 0.05$], and *n* indicates the number of plants (B) or samples (D) analyzed.

been observed with leucine-rich repeat receptor kinases (*34*).

Nod factor and chitin selectivity are determined by the LysM1 domain

To determine which LysM domain in NFR1 and CERK6 harbors ligand specificity determinants, we tested functionality of chimeric receptors where combinations of the three LysM domains originating from the two receptors were coupled either to NFR1 or CERK6 TJ and kinases (Fig. 2A). We found that recognition of *M. loti* and CO8 was dependent on the origin of the LysM1 domain. All chimeras containing the NFR1 LysM1 (**17**, **18**, and **19**) restored nodulation (Fig. 2B) and infection of *nfr1* (fig. S4), while chimeras with CERK6 LysM1 (**20**, **21**, and **22**) did not (Fig. 2B and fig. S4). Reciprocal results were obtained for CO8-induced ROS in *cerk6*, where roots expressing constructs with LysM1 of CERK6 (**28**, **29**, and **30**) produced ROS, while those with LysM1 of NFR1 (**25**, **26**, and **27**) were nonfunctional in immunity (Fig. 2C). Results from expression of **18** and **19** revealed a lower efficiency of nodulation compared with that of **1** or **17**, indicating a negative impact of CERK6 LysM2 on nodulation. Besides this modest influence, the origin of LysM2 and LysM3 had no major impact on nodulation or ROS production. Previous structural studies of *At*CERK1 (*At*, *Arabidopsis thaliana*, henceforth *Arabidopsis*) ectodomain identified a chitin-binding site in LysM2 (*35*). Our study of *Lotus* receptors attributes functional specificity to LysM1. We therefore assayed which of the putative LysM1 or LysM2 binding sites could be perturbed without functional consequences for NFR1 or CERK6. The structure of CERK6 and the chitin-bound structure of *At*CERK1 were used to identify conserved amino acids in LysM1 and LysM2 that, when mutated to a bulky residue, could disrupt the possible binding pocket (Fig. 2D) (*35*). Functional analyses of receptors with substitutions in LysM1 (NFR1-I78W and CERK6-V79W, **23** and **31**, respectively) or LysM2 (NFR1-I140W and CERK6-I141W, **24** and **32**, respectively) revealed that only mutations affecting LysM1 impaired the ability of receptors to induce symbiosis or immunity (Fig. 2, B and C, and figs. S3 and S4). These results explain previous observations where mutants in LysM1 of pea *Sym37* (*36*) and *Medicago Lyk3* were found to be defective in symbiosis (*37*). Together, these results provide evidence for the major role of the LysM1 domain in determining the selectivity for Nod factor and chitin perception.

Two regions in LysM1 are required for specific signaling

To dissect which elements in LysM1 are important for NFR1 and CERK6 functions, we identified four structural regions with substantial sequence differences (Fig. 2E, I to IV) and tested their requirement for Nod factor and CO8 recognition (Fig. 2, F and G). We found that regions I and III can be swapped between NFR1 and CERK6 with no detrimental consequence on nodulation (**33** and **35** in Fig. 2F) or ROS production (**37** and **39** in Fig. 2G). In contrast, regions II and IV were both necessary for receptor functions in planta (**34**, **36**, **38**, and **40** in Fig. 2, F and G, and fig. S4). Expression in tobacco revealed that CERK6 chimeras with regions II and IV from NFR1 are produced and localized at the plasma membrane (fig. S3), indicating that our structure-aided strategy for exchanging regions between paralogous receptors preserved the structure and stability of the proteins. Next, we investigated whether the corresponding regions in LysM1 of orthologous receptors NFR1 and LYK3 (Fig. 3, A and B) are required for recognition of Nod factors varying in their decorations at the reducing and nonreducing ends (Fig. 3C). For this, we first investigated the capacity of LYK3 to complement *nfr1*, and of NFR1 to complement *lyk3* (Fig. 3, D and E, and fig. S1). The absence of nodulation in these assays (**41** in Fig. 3D and **46** in Fig. 3E) supports the role of these receptors in symbiont recognition (*38*, *39*). Moreover, in both legumes, the receptor ectodomains were found to be necessary for symbiotic signaling (**42** and **43** in Fig. 3D, **48** and **49** in Fig. 3E, and fig. S5). Embedding regions II and IV of LYK3 into NFR1 (**1**) or into chimera **42** abolished their capacity to induce nodulation in *nfr1* by *M. loti* (**44** and **45** in Fig. 3D). Parallel experiments in *Medicago*, where II and IV of NFR1 were embedded into LYK3 (**47**) or chimera **49**, revealed a similar lack of nodulation in *lyk3* by *Sinorhizobium meliloti* (*S. meliloti*) (**50** and **51** in Fig. 3E and fig. S5). Together,

these results from in planta experiments provide support for the presence of molecular determinants for Nod factor signaling specificity in the LysM1 of NFR1 and LYK3.

In parallel, we recombinantly expressed the ectodomains of NFR1, LYK3, and CERK6 in insect cells and tested their capacity to bind *M. loti* and *S. meliloti* Nod factors using biolayer interferometry (fig. S6). This testing revealed that LYK3 binds its cognate *S. meliloti* Nod factor with a dissociation constant (K_d) of 27.4 ± 0.4 μM and showed an approximately sixfold reduction in binding (K_d = 173.2 ± 0.9 μM) to the noncognate Nod factor from *M. loti* (Fig. 3F). In contrast, and less expectedly, NFR1 binds both cognate and noncognate Nod factors with similar affinity, K_d = 38.7 ± 0.4 μM and K_d = 22.1 ± 0.2 μM, respectively (Fig. 3G). CERK6 and likewise NFR1 with regions II and IV from CERK6 (fig. S6) showed no binding to *M. loti* (Fig. 3H) or *S. meliloti* (fig. S6) Nod factor. Together, these results from in planta and in vitro binding assays demonstrate the crucial role of regions II and IV in LysM1 of this class of LysM receptors with active kinases for recognition of chitinous ligands.

LYK3 reveals structural differences in the LysM1 binding site

Our detailed investigations of ectodomain regions were aided by the available crystal structure of CERK6 (*21*). For the Nod factor

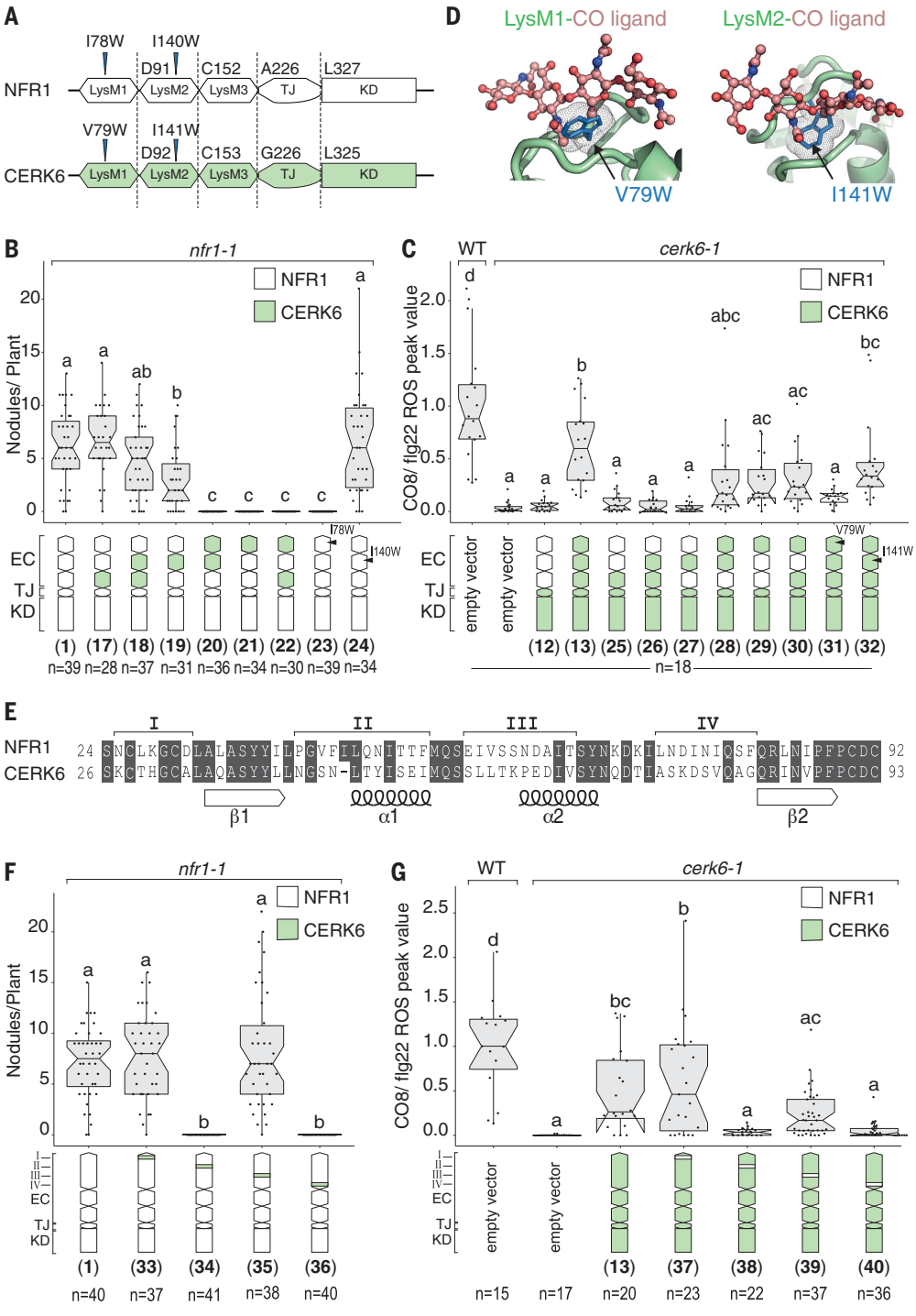


Fig. 2. Two regions in LysM1 domains of NFR1 and CERK6 are required for chitin and Nod factor signaling. (**A**) Schematics of NFR1 and CERK6. Segments represent the EC LysM domains, TJ domains, and KD. Vertical dashed lines and amino acids specify boundaries for chimera design or mutations. (**B** and **F**) Nodules formed on *nfr1* expressing the indicated chimeras. (**C** and **G**) ROS production observed for WT and *cerk6* expressing the indicated chimeras. In (B), (C), (F), and (G), lowercase letters indicate significant differences (ANOVA, Tukey, $P < 0.05$), and *n* indicates the number of plants [(B) and (F)] or samples [(C) and (G)] analyzed. (**D**) Model of the predicted chitin-binding groove in LysM1 and LysM2 of CERK6. Arrows indicate the location of the tryptophan (Trp, W) that was tested in chimeras **31** and **32**. (**E**) Alignment of the LysM1 from NFR1 and CERK6. Identical amino acids are shaded in gray. Regions I, II, III, and IV, beta strands (β1 and β2), and alpha helices (α1 and α2) based on the CERK6 structure are indicated.

receptors, no structural information was available, limiting the understanding of how these proteins distinguish different chitinous ligands at the molecular level. We crystallized the ectodomain of LYK3 and determined the structure at an atomic resolution of 1.5 Å (table S1). The structure revealed a classical fold of three LysM domains in a clover-leaf arrangement stabilized by three disulfide bridges (Fig. 4A). Comparison of LYK3 and CERK6 showed that the overall fold was conserved and the two structures align well with an RMSD (root mean square difference) of 0.5 Å (181 Cα atoms aligned) (Fig. 4B). The main structural differences were observed in the LysM1 domain. In particular, region IV revealed a different conformation in LYK3 compared with CERK6 (Fig. 4, C and D). Mapping both regions II and IV onto the LYK3 structure showed that these constitute the major part of a putative ligand-binding site containing the functionally important residues L77 from SYM37 (*36*) and the NFR1-I78 in **23** (Figs. 2B and 4E). Together, these observations further support the conclusion that these regions of LysM1 define a ligand-binding site within the NFR1-type receptor ectodomains.

Contrasting motifs characterize chitin and Nod factor binding sites

The identification of regions in LysM1, necessary and structurally positioned for the recognition of chitinous ligands, prompted us to investigate whether these represent general features in Nod factor and chitin receptors from legume species.

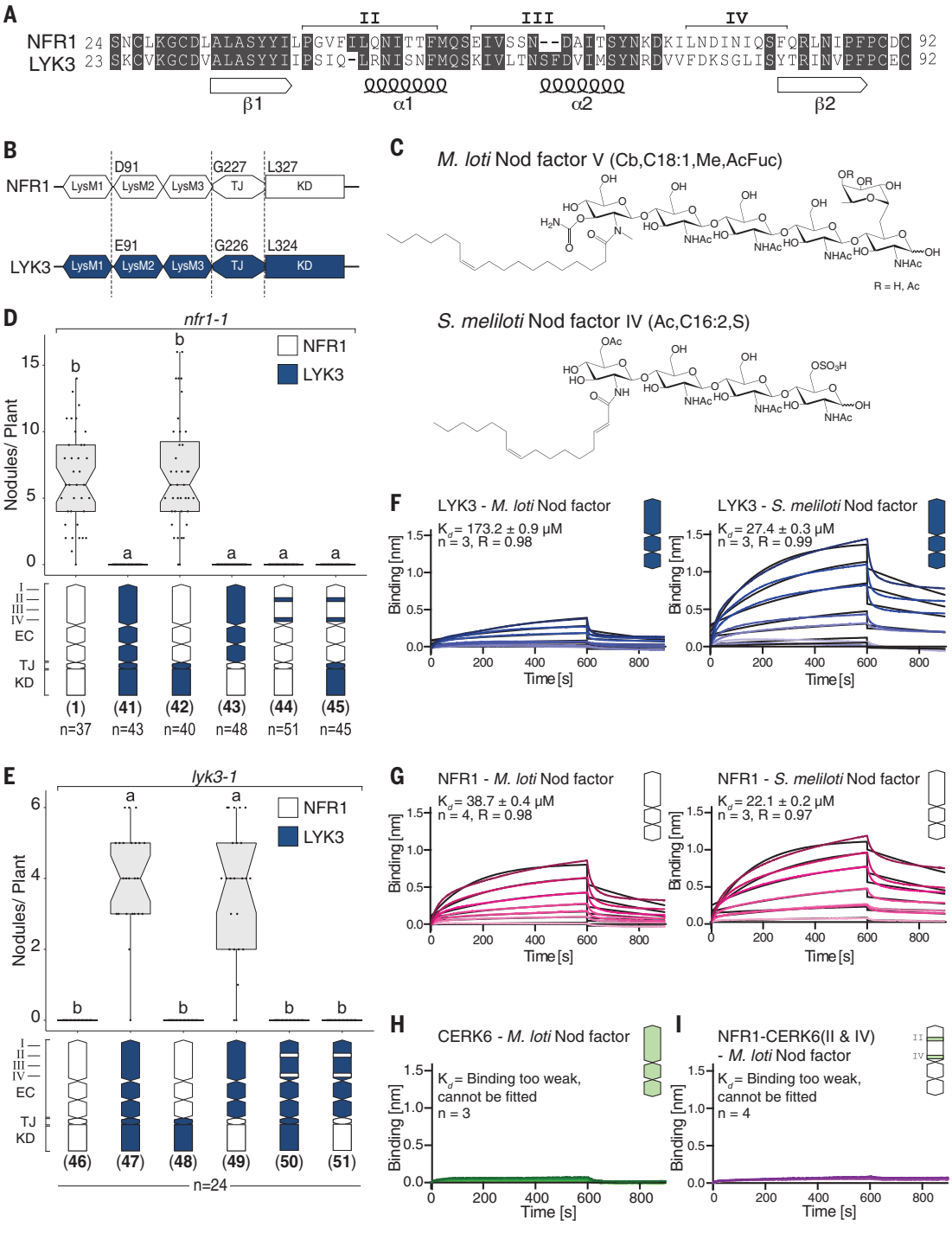


Fig. 3. Two regions in LysM1 domains of NFR1 and LYK3 are required for specificity of Nod factor signaling. (**A**) Alignment of the LysM1 domains of NFR1 and LYK3. Identical amino acids are shaded in gray. Regions II, III, and IV, beta strands (β1 and β2), and alpha helices (α1 and α2) based on the LYK3 structure are indicated. (**B**) Schematic showing NFR1 and LYK3. Vertical dashed lines and amino acids specify boundaries for chimera design. Segments represent the EC LysM domains, TJ domains, and KD. (**C**) Chemical structures of *M. loti* and *S. meliloti* Nod factors. (**D**) Nodules formed on *nfr1* expressing the indicated chimeras. (**E**) Nodules formed on *lyk3* expressing the indicated chimeras. In (D) and (E), lowercase letters indicate significant differences (ANOVA, Tukey, $P < 0.05$), and *n* indicates the number of plants analyzed. Binding of Nod factors to LYK3 (**F**) or NFR1 (**G**) ectodomains. Binding of *M. loti* Nod factor to CERK6 (**H**) or chimeric NFR1 with regions II and IV from CERK6 (**I**). In (F) to (I), binding of depicted (LYK3, CERK6, and NFR1) ectodomains (dilution series: 100, 50, 25, 12.5, 6.25, 3.13, and 1.56 µM) to immobilized Nod factors. n, number of replicates using independent protein preparations; R, the global fit *R* squared.

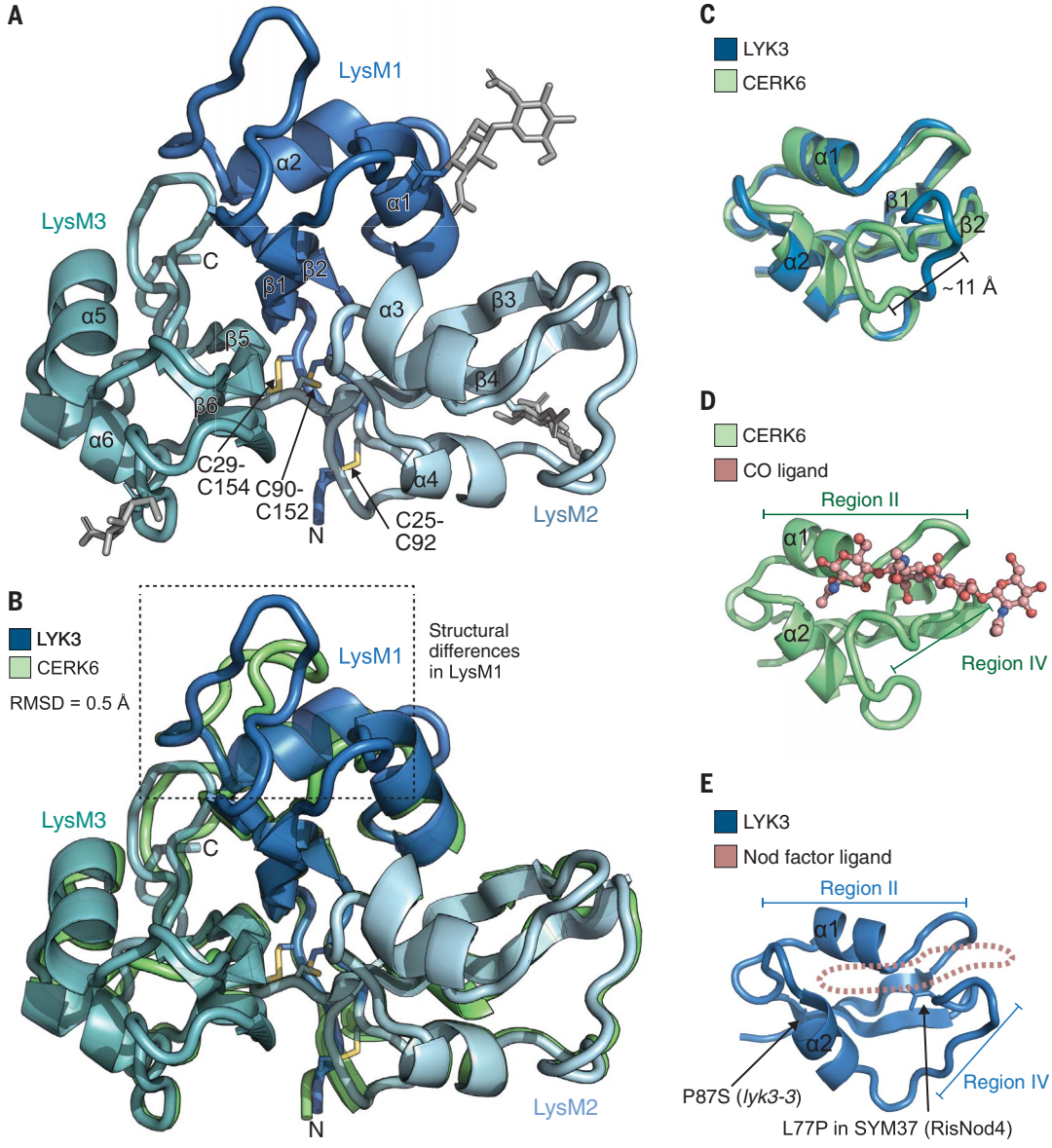


Fig. 4. Crystal structure of LYK3 reveals differences in Nod factor versus a chitin-binding site. (**A**) Cartoon representation of the crystal structure of LYK3 ectodomain with LysM1, LysM2, and LysM3 colored as indicated. Glycosylations are in gray, the three conserved disulfide bridges in yellow. (**B**) Structural superposition of LYK3 with CERK6 [Protein Data Bank (PDB) ID 5LS2] (*21*) in green. (**C**) Close-up of LysM1 showing the structural differences between LYK3 and CERK6. C, carboxyl terminus; N, amino terminus. Superposition of chitotetraose from the *At*CERK1 crystal structure (PDB ID 4EBZ) (*35*) onto LysM1 from CERK6 (**D**) or LYK3 (**E**) with the identified regions II and IV highlighting the ligand-binding site. No steric clashes are observed for CERK6 to the superpositioned ligand. Location of P87S (Pro^{87}→Ser) mutation in *lyk3* and L77P mutation in RisNod4 mutant is shown.

We reasoned that residues responsible for Nod factor recognition will be diverse between legumes recognizing variable and species-defined decorations of Nod factors. Conversely, we hypothesized that the chitin receptors will be conserved in the corresponding regions, giving the invariable structure of this ligand. Alignments and modeling of the entire ectodomains revealed a high surface conservation across the core LysM2 and LysM3 domains (fig. S7). Most differences between species were found to be present in LysM1 of NFR receptors (fig. S7A). Further dissection revealed that residues 40 to 46 and 75 to 81 (amino acid numbers in LYK3) embedded in regions II and IV were the most variable parts in LysM1 of NFRs (Fig. 5A and fig. S7, A and B). In contrast, the corresponding regions in CERKs were found to be highly conserved (Fig. 5B and fig. S7, C and D). Superposition of a chitin oligomer onto the structure of CERK6 LysM1 domain and prediction of the ligand interaction properties on the basis of *At*CERK1-chitin binding (*35*) identified six residues in both regions II (GSNLTY) and IV (KDSVQA) that are structurally positioned to enable contact with the chitin molecule (Fig. 5B). These residues are highly conserved among legume CERKs and could represent CO-binding motifs (Fig. 5B).

Engineering receptors for specific Nod factor recognition

Identification of the two variable regions in NFRs (Fig. 5, A and B) raised the question of whether Nod factor selectivity can be reprogrammed by using these molecular fingerprints. To answer this question, we modified the non-signaling receptors containing LYK3 ectodomain (**41** and **43**) (Fig. 3D) by exchanging regions II and IV with corresponding regions from NFR1 and tested for *M. loti* recognition. Parallel experiments were performed in *Medicago lyk3*, where regions II and IV of NFR1 in **46** and **48** (Fig. 3E) were exchanged with LYK3 residues. The engineered chimeras enabled nodulation of *nfr1* (**52** and **53** in Fig. 5C and fig. S5) but not of *lyk3* (**54** and **55** in Fig. 5D and fig. S5). As in NFR1-CERK6 chimeras (**2**, **3**, and **4**), we found that the efficiency of signaling from the engineered ectodomain is modulated by the cognate intracellular regions (**52** and **53**), possibly by fine-tuning interaction with species-defined downstream signaling components. This indicates that symbiosis with *M. loti* in *Lotus* can be gained by engineering the LysM1 of LYK3, but a similar strategy does not suffice in *Medicago*. To locate additional elements that contribute to *S. meliloti* recognition, we inspected the 23 sequences from

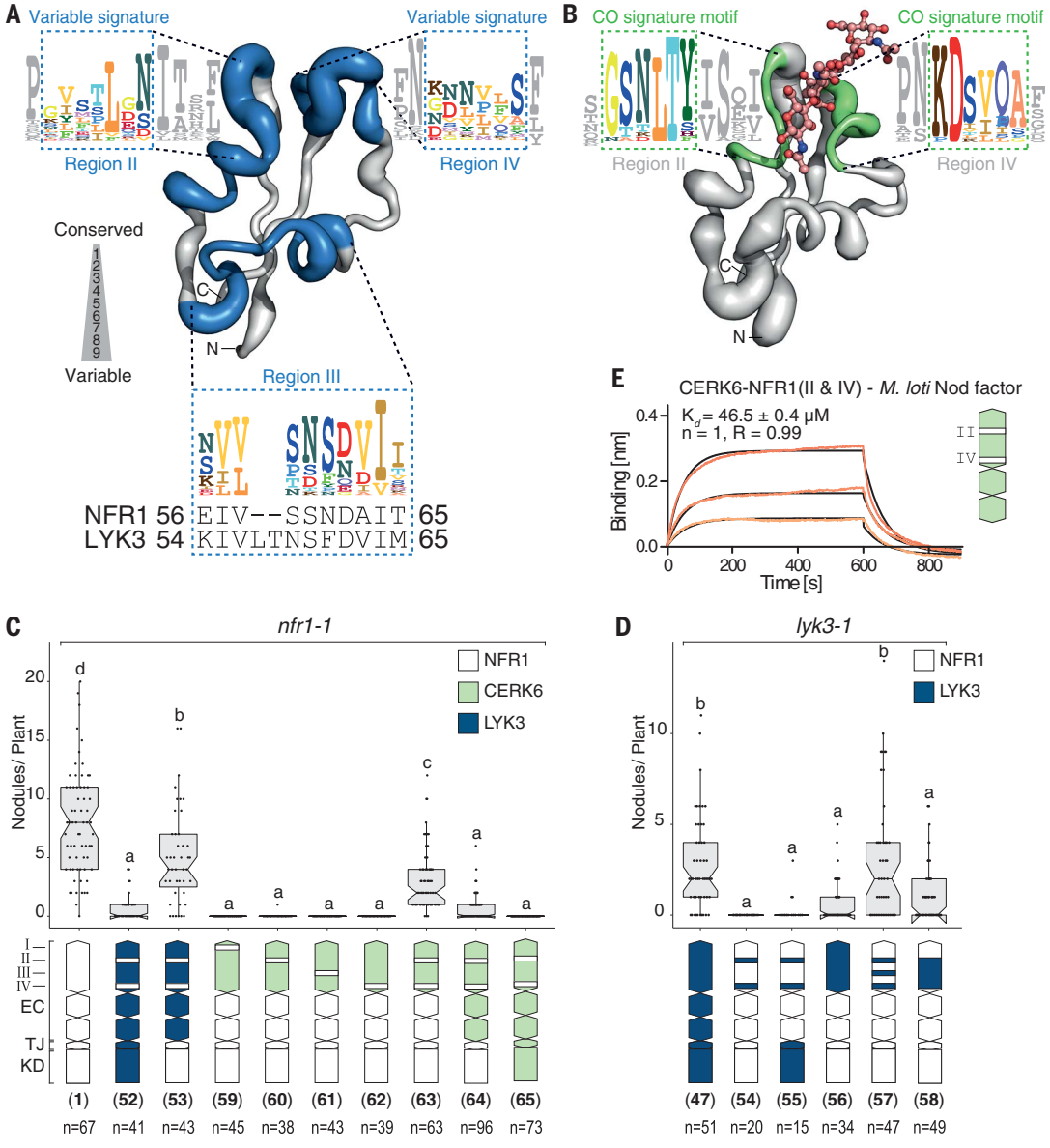


Fig. 5. Engineering of CERK6, NFR1, and LYK3 for specific Nod factor recognition. (**A**) Modeling conservation of NFR-type receptors onto the structure of LYK3 LysM1. Regions II, III, and IV are highlighted in blue. (**B**) Modeling conservation of CERK-type receptors onto the structure of CERK6 LysM1. Regions II and IV are highlighted in green. In (A) and (B), the thickness of the cartoon representation signifies conservation. The alignment logos of regions II, III, and IV are shown in boxes. (**C**) Nodules formed on *nfr1* expressing the indicated chimeras. (**D**) Nodules formed on *lyk3* expressing the indicated chimeras. In (C) and (D), lowercase letters indicate significant differences (ANOVA, Tukey, $P < 0.05$), and *n* indicates the number of plants analyzed. (**E**) Binding of the ectodomain of CERK6 (green) with regions II and IV from NFR1 (white) (dilution series: 12.5, 6.25, and 3.13 µM) to immobilized *M. loti* Nod factor.

legume receptors (fig. S7) and observed that region III in NFR-type receptors (residues 54 to 65 in LYK3) also contained considerable variation among legumes (fig. S7, A and B). This region is spatially close to the proposed binding site (Fig. 5A). We explored the role of this region for recognition of *S. meliloti* by testing additional NFR1-LYK3 chimeras (**56**, **57**, and **58**) (Fig. 5D) and found that addition of LYK3 region III enabled *S. meliloti* recognition (Fig. 5D and fig. S5), which indicates that regions close to the Nod factor binding site are important for engineering specificity into these receptors.

Reprogramming CERK6 receptor to recognize Nod factors and mediate nodulation

Initiation of nodulation by Nod factor–producing rhizobia is restricted to leguminous plants and *Parasponia* species (*40*), while chitin recognition is ubiquitous among plants. Given our results of engineering LYK3 and NFR1 (Fig. 5, C and D), we sought to determine whether recognition of *M. loti* Nod factor can be further extended by engineering CERK6. Systematic replacement of regions I, II, III, or IV in receptor **21** (Fig. 2A), containing LysM1 domain of CERK6, with corresponding NFR1 was insufficient for engineering perception of *M. loti* Nod factor (**59**, **60**, **61**, and **62** in Fig. 5C and fig. S5), indicating that a more complex engineering approach is required. However, a cooperative involvement of NFR1 regions II and IV was found when testing receptor **63** that enabled nodulation of *nfr1* (Fig. 5C and fig. S5). The overall nodulation induced by **63** was lower compared with NFR1 (**1**), but the frequency of complementation was high (60 out of 63 transformed plants formed nodules), showing that **63** is an efficient Nod factor receptor. Embedding NFR1 regions II and IV in chimera **8** (Fig. 1A) with the entire CERK6 ectodomain resulted in few nodules per plant and low nodulation efficiency (35 out of 95 transformed plants) (**64** in Fig. 5C and fig. S5), whereas similar engineering of the full-length CERK6 (**5** in Fig. 1A) was not sufficient to allow nodulation in *nfr1* (**65** in Fig. 5C and fig. S5). This gradual reduction in the efficiency of nodulation may occur as a result of the observed negative impact of CERK6 LysM2 (**18** and **19** in Fig. 2B) and CERK6 TJ and kinase (**4** in Fig. 1B) on nodulation. To resolve whether these findings from in planta were a result of changes in Nod factor binding properties of CERK6 (Fig. 3H), we tested the ectodomain of **64** for

in vitro binding to *M. loti* Nod factor. Unlike CERK6, this chimeric ectodomain had the capacity to bind *M. loti* Nod factor (Fig. 5E) with an apparent K_d of 46.5 μM, similar to NFR1 ectodomain (Fig. 3G), demonstrating that regions II and IV from NFR1 are sufficient for engineering *M. loti* recognition in CERK6 ectodomain.

In this work, we investigated the molecular mechanism behind recognition of immunogenic and symbiotic chitin-based glycans by LysM receptors that have an active kinase. Comparative structural and functional studies resolved the role of regions II and IV in LysM1 for creating a structurally defined binding pocket that discriminates between CO8 and Nod factor ligands, while additional layers of signaling ability are enabled by the intracellular regions (Figs. 1, B and D, and 5, C and D). Two motifs with a high degree of conservation were identified in regions II and IV of legume CERKs (Fig. 5B), likely reflecting their ability to recognize and bind the structurally invariable chitin ligand (Fig. 5B and fig. S7, C and D). In contrast, Nod factor receptors show sequence degeneration in corresponding motifs (Fig. 5A), reflecting the diversity in legume-rhizobia compatibility and Nod factor structures (Fig. 5A and fig. S7, A and B). LYK3 and NFR1 vary in their signaling flexibility. Regions II and IV from NFR1 are sufficient to enable recognition of *M. loti* by LYK3 in *Lotus* (Fig. 5C), while regions II, III, and IV from LYK3 are necessary to enable efficient recognition of *S. meliloti* by NFR1 in *Medicago* (Fig. 5D). Region III is variable between legume species (Fig. 5A and fig. S7, A and B), and we envision that this region could be required for establishing species-specific interactions with the ligand-bound or unbound co-receptor of the NFR5 and NFP class. We demonstrate that LysM receptors with an active kinase have programmable capacity for ligand perception, which enables rational engineering of selective signaling. Our findings therefore provide a solid basis for addressing future challenges such as engineering highly sensitive receptor complexes that could enable hosts outside of the nodulation clade to perceive symbiotic signals from nitrogen-fixing rhizobia.

REFERENCES AND NOTES

1. J. Dénarié, J. Cullimore, *Cell* **74**, 951–954 (1993).
2. K. Tsukada *et al.*, *Physiol. Plant.* **116**, 373–382 (2002).
3. A. A. Gust *et al.*, *J. Biol. Chem.* **282**, 32338–32348 (2007).
4. J. Wan *et al.*, *Plant Physiol.* **160**, 396–406 (2012).
5. Y. Cao *et al.*, *eLife* **3**, e03766 (2014).
6. F. Feng *et al.*, *Nat. Commun.* **10**, 5047 (2019).
7. E. B. Madsen *et al.*, *Plant J.* **65**, 404–417 (2011).
8. H. Kaku *et al.*, *Proc. Natl. Acad. Sci. U.S.A.* **103**, 11086–11091 (2006).
9. Y. Kawaharada *et al.*, *Nature* **523**, 308–312 (2015).
10. S. Radutoiu *et al.*, *Nature* **425**, 585–592 (2003).
11. J. Wan *et al.*, *Plant Cell* **20**, 471–481 (2008).
12. R. Willmann *et al.*, *Proc. Natl. Acad. Sci. U.S.A.* **108**, 19824–19829 (2011).
13. E. B. Madsen *et al.*, *Nature* **425**, 637–640 (2003).
14. L. Buendia, A. Girardin, T. Wang, L. Cottret, B. Lefebvre, *Front Plant Sci* **9**, 1531 (2018).
15. X. C. Zhang, S. B. Cannon, G. Stacey, *BMC Evol. Biol.* **9**, 183 (2009).
16. G. V. Lohmann *et al.*, *Mol. Plant Microbe Interact.* **23**, 510–521 (2010).
17. A. Sánchez-Vallet, J. R. Mesters, B. P. Thomma, *FEMS Microbiol. Rev.* **39**, 171–183 (2015).
18. G. Felix, M. Regenass, T. Boller, *Plant J.* **4**, 307–316 (1993).
19. P. Vander, K. M. Vårum, A. Domard, N. Eddine El Gueddari, B. M. Moerschbacher, *Plant Physiol.* **118**, 1353–1359 (1998).
20. B. Zhang, K. Ramonell, S. Somerville, G. Stacey, *Mol. Plant Microbe Interact.* **15**, 963–970 (2002).
21. Z. Bozsoki *et al.*, *Proc. Natl. Acad. Sci. U.S.A.* **114**, E8118–E8127 (2017).
22. T. Shinya *et al.*, *Plant Cell Physiol.* **53**, 1696–1706 (2012).
23. A. Genre *et al.*, *New Phytol.* **198**, 190–202 (2013).
24. G. Carotenuto *et al.*, *New Phytol.* **214**, 1440–1446 (2017).
25. S. Bressendorff *et al.*, *Plant Cell* **28**, 1328–1342 (2016).
26. G. E. Oldroyd, R. M. Mitra, R. J. Wais, S. R. Long, *Plant J.* **28**, 191–199 (2001).
27. D. W. Ehrhardt, R. Wais, S. R. Long, *Cell* **85**, 673–681 (1996).
28. J. A. Downie, S. A. Walker, *Curr. Opin. Plant Biol.* **2**, 483–489 (1999).
29. S. Radutoiu *et al.*, *EMBO J.* **26**, 3923–3935 (2007).
30. A. Broghammer *et al.*, *Proc. Natl. Acad. Sci. U.S.A.* **109**, 13859–13864 (2012).
31. Y. Kawaharada *et al.*, *Nat. Commun.* **8**, 14534 (2017).
32. T. Nakagawa *et al.*, *Plant J.* **65**, 169–180 (2011).
33. W. Wang, Z. P. Xie, C. Staehelin, *Plant J.* **78**, 56–69 (2014).
34. U. Hohmann *et al.*, bioRxiv 2020.02.18.954479 [Preprint]. 19 February 2020. https://doi.org/10.1101/2020.02.18.954479.
35. T. Liu *et al.*, *Science* **336**, 1160–1164 (2012).
36. V. Zhukov *et al.*, *Mol. Plant Microbe Interact.* **21**, 1600–1608 (2008).
37. P. Smit *et al.*, *Plant Physiol.* **145**, 183–191 (2007).
38. P. Lerouge *et al.*, *Nature* **344**, 781–784 (1990).
39. P. Rodpothong *et al.*, *Mol. Plant Microbe Interact.* **22**, 1546–1554 (2009).
40. M. J. Trinick, *Nature* **244**, 459–460 (1973).

ACKNOWLEDGMENTS

The authors thank J. Keller and P.-M. Delaux for providing access to genomic sequences before publication; S. Thirup for input at the start of the project; F. Pedersen for plant care; and L. H. Madsen, E. Soumpourou, and M. Downes for assistance with gene cloning. **Funding:** This work was supported by the Bill and Melinda Gates Foundation and the UK government's Department for International Development (DFID) through the Engineering Nitrogen Symbiosis for Africa project (ENSA; OPP11772165) and the Danish National Research Foundation grant DNRF79. S.F. received technical support from ICMG (FR 2607) mass spectrometry and NMR platforms and partial financial support from Labex ARCANE and CBH-EUR-GS (ANR-17-EURE-0003), Glyco@Alps (ANR-15-IDEX-02), and PolyNat Carnot Institut (ANR-16-CARN-0025-01).

Author contributions: Z.B., gene cloning and in planta functional analyses; K.G., purification and affinity studies of LYK3 and NFR1 ectodomains and crystallization of LYK3; S.B.H., purification of NFR1, CERK6, and CERK6-NFR1 ectodomains and affinity studies; D.L., C.Kr., F.F., and M.K., gene cloning and in planta functional analyses; N.d.J., gene cloning and plant transformation; M.V., protein purification; M.B.T., E.E., and C.Kr., biotin tagging of Nod factors and CO8; S.F., CO8 synthesis; J.T.S., purification of Nod factors. K.J.J., M.B., G.O., and J.S. conceived the experiments. K.R.A. and S.R. conceived the experiments, analyzed data, and coordinated studies. K.R.A. and S.R. wrote the manuscript with input from K.G., S.B.H., D.L., C.Kr., G.O., and J.S. **Competing interests:** Some findings in this manuscript have been submitted in patent applications. Z.B., K.G., S.B.H., J.S., K.R.A., and S.R. are inventors on patent application 62/718,186 submitted by Aarhus University, which covers LysM receptors ("Genetically altered LysM receptors with altered agonist specificity and affinity"). S.R., K.R.A., D.L., C.Kr., and J.S. are inventors on patent application 63/027,151 submitted by Aarhus University, which covers LysM receptor motifs. **Data and materials availability:** All data are available in the main text or the supplementary materials. Crystallographic coordinates and structure factors are available from PDB under ID 6XWE. Gene constructs used in this study for functional and biochemical assays are available from S.R. and K.R.A. under a material agreement with Aarhus University, Denmark.

SUPPLEMENTARY MATERIALS

science.sciencemag.org/content/369/6504/663/suppl/DC1
Materials and Methods
Figs. S1 to S7
Table S1
References (*41*–*52*)
MDAR Reproducibility Checklist

View/request a protocol for this paper from *Bio-protocol*.

18 February 2020; accepted 12 June 2020
10.1126/science.abb3377

REPORT

NANOMATERIALS

Chemical vapor deposition of layered two-dimensional $MoSi_2N_4$ materials

Yi-Lun Hong[1,2]*, Zhibo Liu[1]*, Lei Wang[1,2]*, Tianya Zhou[1,2], Wei Ma[1,2], Chuan Xu[1], Shun Feng[1,3], Long Chen[1], Mao-Lin Chen[1,2], Dong-Ming Sun[1,2], Xing-Qiu Chen[1,2], Hui-Ming Cheng[1,2,4,5], Wencai Ren[1,2]†

Identifying two-dimensional layered materials in the monolayer limit has led to discoveries of numerous new phenomena and unusual properties. We introduced elemental silicon during chemical vapor deposition growth of nonlayered molybdenum nitride to passivate its surface, which enabled the growth of centimeter-scale monolayer films of $MoSi_2N_4$. This monolayer was built up by septuple atomic layers of N-Si-N-Mo-N-Si-N, which can be viewed as a MoN_2 layer sandwiched between two Si-N bilayers. This material exhibited semiconducting behavior (bandgap ~1.94 electron volts), high strength (~66 gigapascals), and excellent ambient stability. Density functional theory calculations predict a large family of such monolayer structured two-dimensional layered materials, including semiconductors, metals, and magnetic half-metals.

Two-dimensional (2D) materials have attracted increasing interest because of the properties and various applications that emerge in the monolayer limit (*1*). Transition metal carbides and nitrides (TMCs and TMNs) are a large family of nonlayered materials that combine the properties of ceramics and metals (*2*, *3*). The MAX phases (where M is an early transition metal, A is an A-group element such as Al or Si, and X is carbon, nitrogen, or both) are the basis for monolayer MXenes, which have been synthesized by selectively etching the A-element layer (*4*–*7*). Such materials have both a hydrophilic surface and high electrical conductivity, and hold much promise for applications including energy storage, electromagnetic interference shielding, composites, sensors, and catalysis (*5*–*7*). However, chemical etching can only produce surface-terminated defective flakes with hexagonal structure and a specific formula of $M_{n+1}X_nT_x$ (where T_x stands for hydroxyl, oxygen, or fluorine), which are not stable in the presence of ambient oxygen and water and display mechanical properties inferior to their theoretical value (*6*, *8*).

A recently developed chemical vapor deposition (CVD) method has enabled the growth of high-quality pristine nonlayered 2D TMC and TMN crystals with diverse structures

[1]Shenyang National Laboratory for Materials Science, Institute of Metal Research, Chinese Academy of Sciences, Shenyang 110016, P. R. China. [2]School of Materials Science and Engineering, University of Science and Technology of China, Shenyang 110016, P. R. China. [3]School of Physical Science and Technology, ShanghaiTech University, Shanghai 200031, P. R. China. [4]Shenzhen Geim Graphene Center, Tsinghua-Berkeley Shenzhen Institute, Tsinghua University, Shenzhen 518055, P. R. China. [5]Advanced Technology Institute, University of Surrey, Guildford, Surrey GU2 7XH, UK.
*These authors contributed equally to this work.
†Corresponding author. Email: wcren@imr.ac.cn

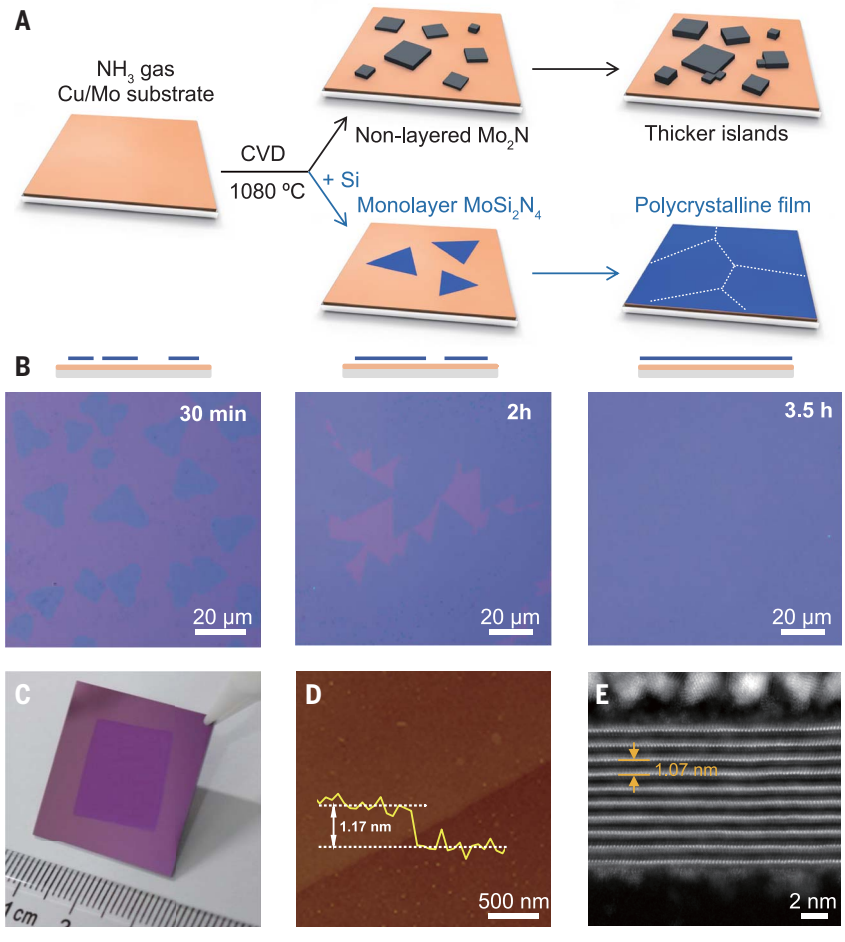


Fig. 1. CVD growth of $MoSi_2N_4$. (**A**) Schematic of two CVD growth processes, showing that layered $MoSi_2N_4$ is formed by simply adding Si during the growth of nonlayered 2D Mo_2N. (**B**) Optical images of $MoSi_2N_4$ grown by CVD for 30 min, 2 hours, and 3.5 hours, illustrating the formation process of a monolayer $MoSi_2N_4$ film (schematic shown at top). The samples were transferred onto SiO_2/Si substrates. (**C**) Photograph of a CVD-grown 15 mm × 15 mm $MoSi_2N_4$ film transferred onto a SiO_2/Si substrate. (**D**) A typical AFM image of $MoSi_2N_4$ film, showing thickness of ~1.17 nm. (**E**) Cross-sectional HAADF-STEM image of a thick $MoSi_2N_4$ domain, showing a layered structure with an interlayer spacing of ~1.07 nm.

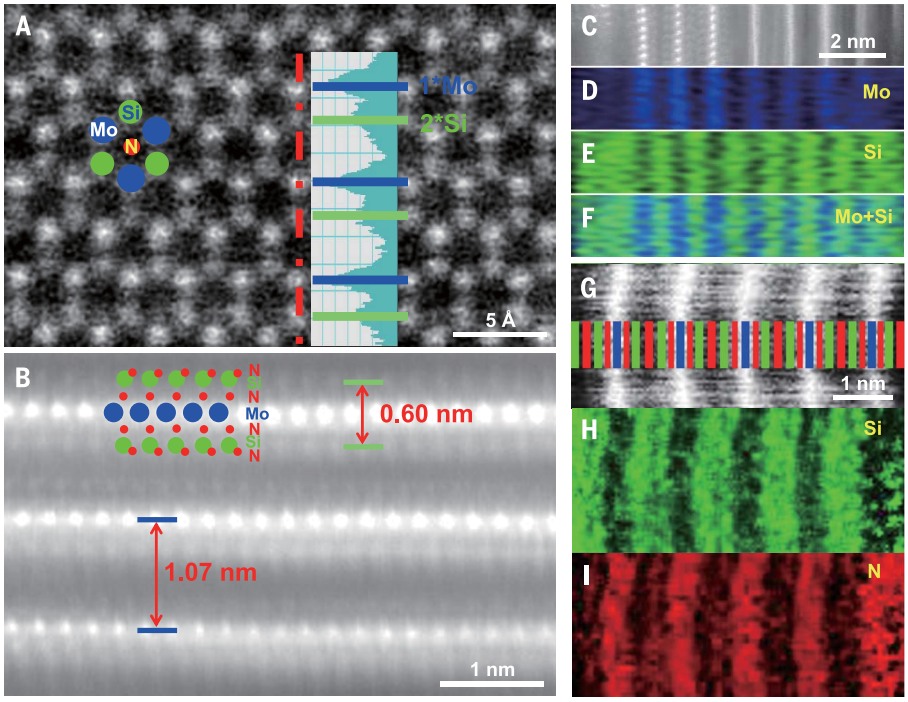


Fig. 2. Structural characterizations of $MoSi_2N_4$. (**A**) Plan-view HAADF-STEM image of monolayer $MoSi_2N_4$. Inset is the intensity profile along the red dash-dot line, indicating that the bright dots are Mo atoms and the less bright dots are Si atoms. The image intensity is proportional to $Z^{1.7}$ (where Z is atomic number). (**B**) Cross-sectional high-magnification HAADF-STEM image of multilayer $MoSi_2N_4$, showing a layered structure and Mo and Si atoms in each layer. The N atoms are marked according to the calculated structure. (**C** to **F**) Cross-sectional HAADF-STEM image (C) of a multilayer $MoSi_2N_4$, the corresponding high-resolution EDS mappings of Mo (D) and Si (E) elements, and mixed EDS mapping of Mo and Si elements (F). (**G** to **I**) Cross-sectional HAADF-STEM image (G) of a multilayer $MoSi_2N_4$, clearly showing the Mo layer, and the corresponding high-resolution EELS mapping of Si (H) and N (I) elements. The colored lines in (G) represent the positions of different elements (blue, Mo; green, Si; red, N).

(*9*, *10*), such as orthorhombic Mo_2C, hexagonal WC, cubic TaC, and hexagonal TaN. However, these nonlayered materials tend to grow as islands rather than layers because of surface energy constraints (*11*), and only nonuniform 2D crystals a few nanometers in thickness with lateral size up to ~100 μm have been achieved (*9*, *10*).

Layer growth tends to occur when the deposited material has a smaller surface energy than the growth substrate (*11*). Passivating the sites of high surface energy to promote layer growth is the key to uniform growth of TMC or TMN films down to the monolayer limit. We show that introducing Si can passivate the surface dangling bonds of nonlayered 2D molybdenum nitride and enable the growth of centimeter-scale monolayer films of a 2D van der Waals (vdW) layered material, $MoSi_2N_4$, which can be viewed as a MoN_2 layer sandwiched by two Si-N bilayers. It is a semiconductor (bandgap ~1.94 eV) with high strength (~66 GPa) and remarkable stability.

We grew 2D molybdenum nitride and $MoSi_2N_4$ by CVD (*9*) with a Cu/Mo bilayer as the substrate and NH_3 gas as the nitrogen source (see supplementary materials). As shown in Fig. 1A and fig. S1, without the addition of Si, only micrometer-scale nonlayered 2D Mo_2N domains (~10 nm thick) were obtained. However, the growth changed markedly when elemental Si was introduced (Fig. 1A; see also supplementary materials and figs. S2 to S7). Triangular domains with uniform thickness (at the same optical contrast) were formed initially and then expanded and merged as growth time extended, until finally a centimeter-scale uniform polycrystalline film was obtained (Fig. 1, B and C, and fig. S8). The thickness of the domains, ~1.17 nm as determined by atomic force microscopy (AFM) (Fig. 1D), remained unchanged during the entire growth process (Fig. 1B and fig. S5), and no additional layers formed after extending the growth time for another 30 min (fig. S6). The thickness and coverage of the domains as a function of growth time (fig. S7) showed a surface growth behavior similar to the growth of graphene on Cu (*12*). Moreover, this surface growth process was very robust. The thickness was independent of growth temperature and the thickness of Cu foils in a broad growth window, although the growth rate could be increased by increasing the growth temperature or reducing the thickness of Cu foil (fig. S9).

After we introduced additional NH_3 gas, thick domains formed on the surface of the monolayer (Fig. 1E and fig. S10). Steps with a uniform height of ~1.10 nm were occasionally observed in some samples (fig. S10A), and the cross section of the thick domain showed a layered structure with an interlayer spacing of ~1.07 nm (Fig. 1E). Typically, adding an element during the growth of a 2D material leads to doping but does not change the basic crystal structure of the matrix (*13*, *14*). In sharp contrast, our results indicate that adding elemental Si during the growth of nonlayered molybdenum nitride created a new layered compound rather than simple doping. Note that the interlayer spacing value is consistent with the thickness of the film, indicating that the film is a monolayer. The vdW layered structure free of dangling bonds enabled layer growth, rather than the island growth mode that was usually observed for the growth of nonlayered materials such as TMCs (*9*) and Mo_2N described above.

Advanced transmission electron microscopy (TEM) was used to identify the crystal structure of this new layered 2D material. Energy-dispersive x-ray spectroscopy (EDS), electron energy-loss spectroscopy (EELS), and x-ray photoelectron spectroscopy (XPS) measurements showed that the material contained Mo, Si, and N with an atomic ratio of ~1:2:4 (figs. S11 and S12). The triangular shape and electron diffraction pattern of single-crystal monolayer domains indicated that the crystal inherited the hexagonal symmetry and lattice parameter (~2.94 Å) of δ_1-MoN (*15*) (fig. S11). A honeycomb structure constructed by alternating Mo and Si atoms was observed by in-plane atomic-level high-angle annular dark field scanning TEM (HAADF-STEM) imaging (Fig. 2A).

Cross-sectional HAADF-STEM images showed that each single-layer block consisted of one layer of heavy atoms sandwiched by two layers of light atoms with a distance of ~0.60 nm (Fig. 2B). Atomic-scale EDS mapping confirmed the sandwich structure with a Si-Mo-Si configuration (Fig. 2, C to F). Note that the atomic positions of Si and Mo were analogous to 2H-MoS_2 (*16*); that is, Mo atoms were located in the center of trigonal prisms constructed by Si atoms. Further atomic-scale EELS mapping showed that the N atomic layers were located between Mo and Si atomic layers and

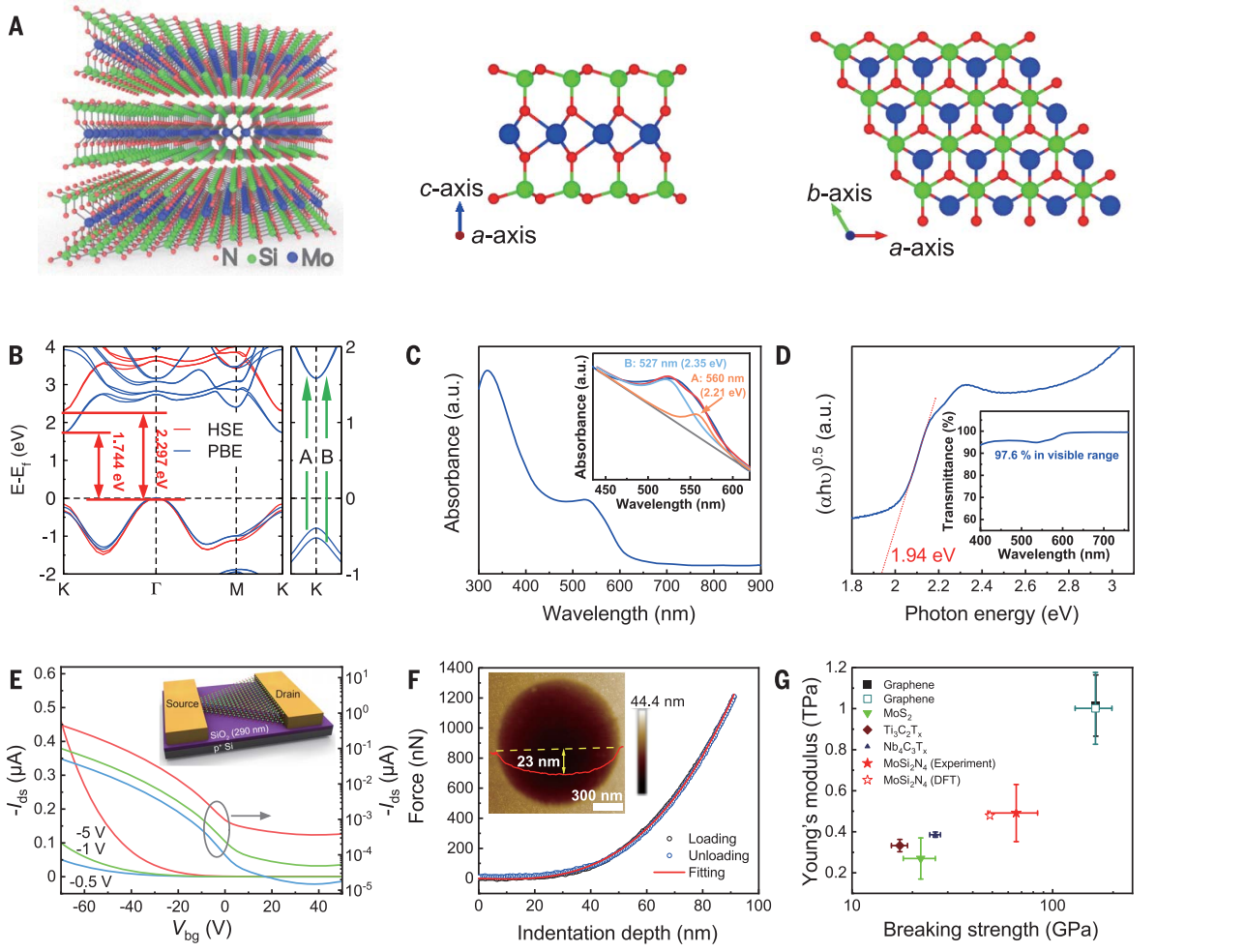


Fig. 3. Atomic structure, band structure, and optical, electrical, and mechanical properties of $MoSi_2N_4$. (**A**) The atomic model of $MoSi_2N_4$ with three layers (left) and the detailed cross-sectional (center) and in-plane (right) crystal structure of the monolayer. (**B**) Electronic band structure of monolayer $MoSi_2N_4$ calculated with PBE (blue lines) and HSE (red lines), respectively. Green arrows indicate two direct excitonic transitions at the *K* point, with the energy splitting originating from VB spin-orbit coupling. (**C**) Optical absorption spectrum of a monolayer $MoSi_2N_4$ film in the visible range. The inset shows that the peak at 500 to 600 nm can be fitted into two subpeaks, A (560 nm, 2.21 eV) and B (527 nm, 2.35 eV), corresponding to the two direct excitonic transitions in (B). (**D**) Tauc plot of a monolayer $MoSi_2N_4$ film. The inset shows the optical transmittance in the visible range. (**E**) Transfer characteristics of a monolayer $MoSi_2N_4$ BG-FET in linear scale (left axis, lower curves) and log scale (right axis, upper curves) measured at 77 K. Channel length, 30 μm. Inset: 3D schematic of a $MoSi_2N_4$-based BG-FET on a Si substrate with 290-nm SiO_2. (**F**) A typical force-displacement curve of a single-crystal $MoSi_2N_4$ monolayer in AFM nanoindentation. The black, blue, and red lines are the loading, unloading, and fitting curves, respectively. Inset: AFM image of a suspended $MoSi_2N_4$ monolayer before indentation test; the height profile (red line) along the yellow dashed line shows an indentation of ~23 nm in the hole. (**G**) Comparison of Young's modulus and breaking strength of monolayer $MoSi_2N_4$ with those of monolayer graphene, MoS_2, and MXenes reported in the literature (table S3). All the strength values were derived according to the linear elastic model. The DFT-calculated modulus and strength of monolayer $MoSi_2N_4$ (open star) and the modulus and strength of monolayer graphene that we measured (open square) are also included.

also on top of Si atomic layers (Fig. 2, G to I). We used short colored lines to assign element positions in EELS mapping (Fig. 2G). Each layer of this 2D material was built up by septuple layers of N-Si-N-Mo-N-Si-N. This structure was consistent with the XPS analyses, which showed the presence of Mo-N and Si-N bonds (fig. S12).

Imaging the exact positions of N atoms by TEM is challenging because of the small scattering cross section (*17*). We performed density functional theory (DFT) calculations, which revealed that the structure with the lowest energy has N atoms surrounding the Si atom, forming a polyhedral linkage between Si-N tetrahedra (the basic structural unit of Si_3N_4) and Mo-N trigonal prisms (the basic structural unit of hexagonal MoN) (Fig. 3A, fig. S13, and table S1). This structure confirms that a vdW layered 2D material formed as a stoichiometric compound with formula $MoSi_2N_4$, and its monolayer can be viewed as a MoN_2 layer sandwiched by two Si-N bilayers (Fig. 3A). Note that all of the theoretical crystallographic parameters of this structure are consistent with the experimental values. Further phonon and ab initio molecular dynamics calculations show that this structure is dynamically and thermodynamically stable (fig. S13). Moreover, the calculated Raman spectrum and the bonding states are in good agreement with the experimental ones (figs. S12 to S14). From the structural point of view, such vdW layered $MoSi_2N_4$ was grown by passivating the surface dangling bonds of MoN_2 layer with Si-N tetrahedra when introducing elemental Si. The very sharp Raman peaks, the single valence state of Mo species, and the strict stoichiometric ratio suggest the

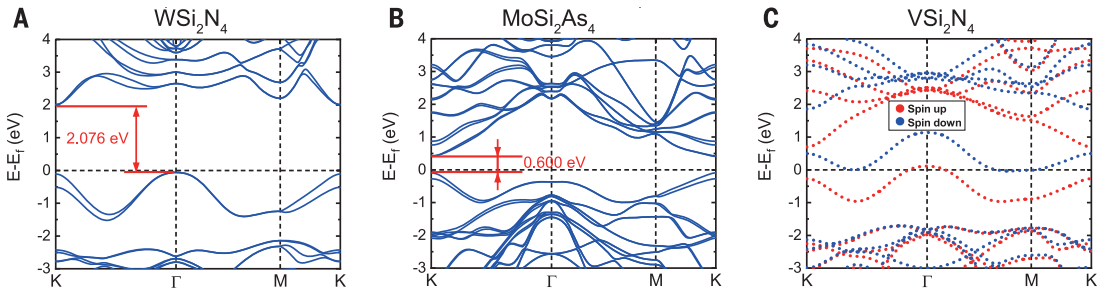


Fig. 4. DFT predictions of the MA_2Z_4 family. (**A** to **C**) Electronic band structure of (A) monolayer WSi_2N_4, (B) $MoSi_2As_4$, and (C) VSi_2N_4 calculated with PBE. In (C), the blue and red curves correspond to the spin-up and spin-down channels of the electronic band structure of the ferromagnetic ordering configuration, respectively.

high crystal quality of the as-grown $MoSi_2N_4$ (figs. S11, S12, and S14).

We calculated the electronic band structure of monolayer $MoSi_2N_4$ with conventional DFT using a Perdew-Burke-Ernzerhof (PBE) functional as well as with the more accurate hybrid DFT using a Heyd-Scuseria-Ernzerhof (HSE) functional. Both calculations show that monolayer $MoSi_2N_4$ is a semiconductor with an indirect bandgap (E_g) of 1.744 eV (PBE) or 2.297 eV (HSE) (Fig. 3B). Moreover, the bandgap slightly decreases with an increased number of layers (figs. S15 and S16). On the basis of deformation potential theory (*18*), we also calculated the intrinsic carrier mobility μ_{2D} of monolayer $MoSi_2N_4$. Table S2 shows that the intrinsic electron and hole mobilities of monolayer $MoSi_2N_4$ at K point in the Brillouin zone are ~270 $cm^2\ V^{-1}\ s^{-1}$ and ~1200 $cm^2\ V^{-1}\ s^{-1}$, respectively; these values are greater than those of monolayer MoS_2 by factors of 4 to 6 (*19*). The main contribution to the carrier mobility in $MoSi_2N_4$ is the elastic modulus, which is ~4 times that of MoS_2 (table S2).

We studied the optical properties of monolayer $MoSi_2N_4$ film transferred onto a sapphire substrate to measure its bandgap. The optical absorption spectrum (Fig. 3C) showed a strong peak at ~320 nm and a broad peak at 500 to 600 nm, which we fit with two subpeaks, A and B, corresponding to two direct excitonic transitions (Fig. 3B). This energy splitting arises from valence band (VB) splitting at the K point in the 2D Brillouin zone, which originates from VB spin-orbit coupling. The measured A and B excitonic transitions (2.21 eV and 2.35 eV, respectively) have an energy difference of ~140 meV, which is in good agreement with the values predicted with PBE and HSE (129 meV and 172 meV, respectively). Interestingly, the Raman signals of monolayer $MoSi_2N_4$ are resonantly enhanced with the excitons (fig. S17).

The indirect E_g was then evaluated by Tauc plot [$(\alpha h\nu)^n$ versus $h\nu$] analysis (*20*), where α is the absorption coefficient and $h\nu$ is the photon energy (h, Planck constant; ν, frequency). Here, n was set to 0.5 because of the indirect bandgap of monolayer $MoSi_2N_4$. Thus, the estimated indirect E_g was 1.94 eV (Fig. 3D), which is near the DFT-predicted value (Fig. 3B). Because of the semiconducting nature, ~1.07-nm-thick monolayer $MoSi_2N_4$ shows a high optical transmittance with an average of 97.5 ± 0.2% in the visible range (inset of Fig. 3D), comparable to that of 0.335-nm-thick monolayer graphene (97.7%) (*21*).

We also fabricated back-gated field-effect transistors (BG-FETs; Fig. 3E, inset) with monolayer $MoSi_2N_4$ single-crystal domains transferred onto SiO_2/Si substrates to evaluate their electrical transport properties. The devices show typical p-type semiconductor behavior at room temperature in air (fig. S18) and at 77 K in vacuum (Fig. 3E), with an on/off ratio of ~4000 at 77 K. $MoSi_2N_4$ had good ohmic contact with electrodes in both cases (fig. S19). Measurements on dozens of $MoSi_2N_4$ samples showed similar transport properties. However, the measured electrical property was inferior to the theoretical data; this may have been caused by the defects and Cu residues (fig. S20) introduced during transfer and/or by an unoptimized device structure.

We measured the mechanical properties of monolayer $MoSi_2N_4$ by using AFM nanoindentation as reported previously (*22*). To do this, we transferred the single-crystal $MoSi_2N_4$ domains onto a SiO_2/Si substrate with an array of holes (diameter ~1.2 μm) to create suspended membranes (Fig. 3F, inset). We also measured the mechanical properties of monolayer graphene to confirm the reliability of our method (fig. S21). Figure 3F shows a typical force-displacement curve obtained by using an AFM with a diamond tip of radius 11.07 nm. The identical loading and unloading curves demonstrated the elastic behavior of the membrane. The breaking strength was derived from the linear elastic model (*22*). On the basis of the thickness of monolayer $MoSi_2N_4$ (1.07 nm), the extracted Young's modulus and breaking strength were 491.4 ± 139.1 GPa and 65.8 ± 18.3 GPa, respectively (Fig. 3G and fig. S22). These values are nearly consistent with the DFT-calculated ones (~479 GPa and ~49 GPa; Fig. 3G and fig. S23) and much higher than those for monolayer $Ti_3C_2T_x$ MXene (333 GPa and 17 GPa) (*8*), $Nb_4C_3T_x$ MXene (386 GPa and 26 GPa) (*23*), and MoS_2 (270 GPa and 22 GPa) (*24*) that were obtained with the same model (Fig. 3G and table S3).

The monolayer $MoSi_2N_4$ showed no appreciable change after immersion in HCl aqueous solution for 24 hours (fig. S24). During preparation of TEM samples, the monolayer $MoSi_2N_4$ was subjected to a further annealing in air for 10 hours after transfer, and the obtained samples were robust without obvious defects being generated under 80-kV electron microscopy (Fig. 2). Moreover, no structural change was observed under ambient conditions for 6 months, in non-degassed deionized water for 1 week, and in 80°C non-degassed deionized water for 8 hours (fig. S25), nor after annealing at 250°C in Ar for 3 hours (figs. S26 and S27). Therefore, the stability of monolayer $MoSi_2N_4$ is sufficient for handling, storage, and processing without a protective environment. Its stability was much better than that of most reported monolayer semiconductors. For instance, black phosphorene can be easily etched away under exposure to air moisture (*25*), and the surface of MoS_2 starts oxidizing in moist air below 100°C (*26*).

DFT calculations showed that many transition metal elements of groups IVB, VB, and VIB, elements of group IVA, and elements of group VA could potentially replace the corresponding elements in $MoSi_2N_4$, which would create a broad class of 2D vdW layered materials that have the same stoichiometric ratio and crystal structure as $MoSi_2N_4$. These materials have a general formula of MA_2Z_4, where M represents an early transition metal (Mo, W, V, Nb, Ta, Ti, Zr, Hf, or Cr), A is Si or Ge, and Z stands for N, P, or As (fig. S28). Table S4 lists 12 kinds of monolayer MA_2Z_4 materials that are predicted to be dynamically stable (fig. S29). The diversity of the elements in MA_2Z_4 enables wide tunability of their gap and magnetic properties (Fig. 4, A to C, and table S4), which is essential for applications in electronics, optoelectronics, and spintronics. For example, monolayer WSi_2N_4 has a wider bandgap than monolayer $MoSi_2N_4$ (Fig. 4A), whereas monolayer $MoSi_2As_4$ has a narrow direct bandgap in the near-infrared range (Fig. 4B) and monolayer VSi_2N_4 is a half-metallic magnetic material (Fig. 4C). Such materials provide possibilities for the investigation of many exciting properties and applications that are absent in existing layered materials, and the CVD method presented

here paves the way for synthesizing such materials, especially for their 2D and monolayer forms. For instance, 2D vdW layered WSi_2N_4 has also been synthesized by CVD (figs. S30 and S31).

REFERENCES AND NOTES

1. A. K. Geim, K. S. Novoselov, *Nat. Mater.* **6**, 183–191 (2007).
2. V. L. E. Toth, *Transition Metal Carbides and Nitrides* (Academic Press, 1971).
3. S. T. Oyama, *The Chemistry of Transition Metal Carbides and Nitrides* (Springer, 1996).
4. M. Naguib *et al*., *Adv. Mater.* **23**, 4248–4253 (2011).
5. M. Naguib, V. N. Mochalin, M. W. Barsoum, Y. Gogotsi, *Adv. Mater.* **26**, 992–1005 (2014).
6. B. Anasori, M. R. Lukatskaya, Y. Gogotsi, *Nat. Rev. Mater.* **2**, 16098 (2017).
7. B. Anasori, Y. Gogotsi, *2D Metal Carbides and Nitrides (MXenes): Structure, Properties and Applications* (Springer, 2019).
8. A. Lipatov *et al*., *Sci. Adv.* **4**, eaat0491 (2018).
9. C. Xu *et al*., *Nat. Mater.* **14**, 1135–1141 (2015).
10. Z. Wang *et al*., *Adv. Mater.* **29**, 1700364 (2017).
11. J. A. Venables, G. D. T. Spiller, M. Hanbücken, *Rep. Prog. Phys.* **47**, 399–459 (1984).
12. X. Li *et al*., *Science* **324**, 1312–1314 (2009).
13. L. Lin *et al*., *Sci. Adv.* **5**, eaaw8337 (2019).
14. J. Gao *et al*., *Adv. Mater.* **28**, 9735–9743 (2016).
15. A. Y. Ganin, L. Kienle, G. V. Vajenine, *J. Solid State Chem.* **179**, 2339–2348 (2006).
16. Q. H. Wang, K. Kalantar-Zadeh, A. Kis, J. N. Coleman, M. S. Strano, *Nat. Nanotechnol.* **7**, 699–712 (2012).
17. C. L. Jia, M. Lentzen, K. Urban, *Science* **299**, 870–873 (2003).
18. J. Bardeen, W. Shockley, *Phys. Rev.* **80**, 72–80 (1950).
19. Y. Cai, G. Zhang, Y.-W. Zhang, *J. Am. Chem. Soc.* **136**, 6269–6275 (2014).
20. L. Najafi *et al*., *ACS Nano* **12**, 10736–10754 (2018).
21. R. R. Nair *et al*., *Science* **320**, 1308 (2008).
22. C. Lee, X. Wei, J. W. Kysar, J. Hone, *Science* **321**, 385–388 (2008).
23. A. Lipatov *et al*., *Adv. Electron. Mater.* **6**, 1901382 (2020).
24. S. Bertolazzi, J. Brivio, A. Kis, *ACS Nano* **5**, 9703–9709 (2011).
25. A. Castellanos-Gomez *et al*., *2D Mater.* **1**, 025001 (2014).
26. A. K. Geim, I. V. Grigorieva, *Nature* **499**, 419–425 (2013).

ACKNOWLEDGMENTS

We thank B. Wu for help with TEM technical support, Y. Yang for help with optical property measurements and analysis, and X. Wang for help with Raman measurements with the 488-nm laser. **Funding:** Supported by the National Natural Science Foundation of China (nos. 51325205, 51725103, 51290273, 51521091, and 51671193), the Key Research Program of Frontier Sciences of the Chinese Academy of Sciences (no. ZDBS-LY-JSC027), the Strategic Priority Research Program of the Chinese Academy of Sciences (no. XDB30000000), the National Key R&D Program of the Ministry of Science and Technology of China (no. 2016YFA0200101), LiaoNing Revitalization Talents Program (no. XLYC1808013), the Program for Guangdong Introducing Innovative and Entrepreneurial Teams, and the Development and Reform Commission of Shenzhen Municipality for the development of the "Low-Dimensional Materials and Devices" discipline. **Author contributions:** W.R. conceived and supervised the project; W.R. and Y.-L.H. designed the experiments; Y.-L.H. performed growth experiments, optical, AFM, Raman, XPS, and optical property measurements and stability tests; Z.L. performed TEM characterizations; L.W. and X.-Q.C. carried out theoretical calculations and analyzed the theoretical data; T.Z. and L.C. helped with growth experiments; C.X. helped with growth experiments and mechanical property measurements; W.M. performed mechanical property measurements; S.F. and M.-L.C. fabricated devices and performed transport measurements under the supervision of D.-M.S.; Y.-L.H., Z.L., W.M., S.F., D.-M.S., and W.R. analyzed the experimental data; Y.-L.H., Z.L., X.-Q.C., and W.R. wrote the manuscript with input from all authors; and H.-M.C. advised the project and commented on the manuscript. **Competing interests:** W.R., Y.-L.H., Z.L., L.W., T.Z., W.M., C.X., X.-Q.C., and H.-M.C. are listed as co-inventors on a pending Chinese patent application related to this work filed by Institute of Metal Research, Chinese Academy of Sciences (no. 202010446362.9). All other authors declare that they have no competing interests. **Data and materials availability:** All data needed to evaluate the conclusions in the paper are present in the paper and/or the supplementary materials. Additional data related to this paper are available from the corresponding author upon request.

SUPPLEMENTARY MATERIALS

science.sciencemag.org/content/369/6504/670/suppl/DC1
Materials and Methods
Figs. S1 to S31
Tables S1 to S4
References (*27*–*50*)

12 March 2020; accepted 9 June 2020
10.1126/science.abb7023

FRAMEWORK MATERIALS

Sequencing of metals in multivariate metal-organic frameworks

Zhe Ji[1,2,3,4], Tong Li[5]*, Omar M. Yaghi[1,2,3,4,6]*

We mapped the metal sequences within crystals of metal-oxide rods in multivariate metal-organic framework–74 containing mixed combinations of cobalt (Co), cadmium (Cd), lead (Pb), and manganese (Mn). Atom probe tomography of these crystals revealed the presence of heterogeneous spatial sequences of metal ions that we describe, depending on the metal and synthesis temperature used, as random (Co, Cd, 120°C), short duplicates (Co, Cd, 85°C), long duplicates (Co, Pb, 85°C), and insertions (Co, Mn, 85°C). Three crystals were examined for each sequence type, and the molar fraction of Co among all 12 samples was observed to vary from 0.4 to 0.9, without changing the sequence type. Compared with metal oxides, metal-organic frameworks have high tolerance for coexistence of different metal sizes in their rods and therefore assume various metal sequences.

Multivariate metal-organic frameworks (MOFs), in which either multiple organic functionalities (*1*) or metal ions (*2*) (variate units) are incorporated into their backbone, are capable of highly selective separations (*3*–*6*) and catalysis (*7*–*12*), exceeding in performance their less functionalized "simple" counterparts. Although the identity and ratio of the variate units can be readily quantified for these MOFs, determining their spatial arrangements remains a challenge. On the conceptual level, the sequences that the variate units may have in a MOF is likened to that of nucleotides in DNA (*13*). The arrangements of the variate units in MOFs introduce, as do the nucleotides in DNA, what we consider "heterogeneity within order" (*14*). The heterogeneity describes the changing spatial arrangements of the variate units, which are covalently bound to an otherwise ordered, translationally symmetric backbone.

We focused on mixed metals in infinite metal-oxide rods [known as secondary building units (SBUs)] (*15*) because such rods are well represented in MOFs (*16*), most especially those exhibiting unusual properties such as carbon capture (*17*–*19*) and water harvesting (*20*, *21*). Because these rods are atomically defined, they can be considered as thin fragments of metal oxides for which the arrangements of mixed metals have been examined (*22*–*25*). We sought to apply similar techniques to mixed-metal rod MOFs and recognized the potential for finding varying distributions of metals. In this study involving MOFs of this kind, the metals are known to be arranged along the rod in a "chain" configuration. Their spatial arrangement may follow many different scenarios, among which we consider four categories: random (uniform distribution), short and long duplicates (metals of the same kind adjacent to each other, and their number is defined as duplicate size), and insertions (a metal inserted in the duplicates of another metal type) (Fig. 1). The duplicates and insertions show recognizable regularity relative to that of the random category. We viewed each one of these as a metal sequence running along the rod, and therefore it was reasonable to expect that such sequences may form the basis for tunable gas adsorption and separation, effective polarization of incoming guest molecules, and highly selective catalysis along a cascade of heterometals.

The heterogeneity in DNA is characterized by means of sequencing using enzymes, but for MOFs, the conventional characterization methods, such as x-ray crystallography and nuclear magnetic resonance, are not as helpful because they measure statistical averages over bulk samples. Previously, attempts have been made to decipher heterogeneity of variate units in multivariate MOFs by using these techniques (*7*, *26*, *27*); however, molecular-level sequencing and obtaining real-space information remain an outstanding challenge. Because heterogeneity in variate units in MOFs manifests itself on the molecular level, it further complicates analysis by use of electron (*28*) and fluorescent microscopy imaging techniques (*29*). Fundamentally, there has been no method to distinguish MOF crystals of the same compound that are synthesized with the same composition of metals, in which the metals may very well adopt different sequence types. In general, the lack of capability to characterize mixed-metal MOFs has impeded their study and the development of more complex systems. In this contribution, we show how atom probe tomography (APT) (Fig. 1) can provide useful information in characterizing mixed-metal rod MOFs.

We chose the well-known structure of MOF-74 (*15*) to perform our APT studies. This structure is composed of metal-oxide rod SBUs joined by organic linkers to form a honeycomb pattern of rods and pores propagating along the crystallographic *c* axis (Fig. 1, along the *z* direction). It crystallizes into hexagonal-prism–shaped single crystals, and the metal-oxide rods run parallel to the long dimension of these crystals (Fig. 2A). A binary combination of cobalt (Co), cadmium (Cd), lead (Pb), and manganese (Mn) ions were used to synthesize the mixed-metal MOF-74 crystals. These metals were chosen because they have distinctive isotopes, an aspect critical to their successful identification in the APT measurements. The use of different metal combinations has the potential to cause variation in the type of metal sequence achieved within the MOF. The size difference of the mixed metals and its impact on bond lengths and angles exemplify chemical effects that introduce biasing into metal sequences. Another chemical effect explored in this study is the temperature of synthesis, by which the competition between mixing enthalpy (lattice matching) and configurational entropy (the number of ways metals may arrange themselves in a lattice) comes into play. The consequence of this biasing is that for a binary mixture of metals, one would expect sequences that deviate from randomness.

Accordingly, crystals of MOF-74 were synthesized in which the metal combination and synthesis temperature were varied: Co,Cd-MOF-74 (120°C), Co,Cd-MOF-74 (85°C), Co, Pb-MOF-74 (85°C), and Co,Mn-MOF-74 (85°C) (supplementary text S1.1). For each of these combinations and synthetic conditions, three crystals were measured in parallel by means of APT for a grand total of 12 crystals, where the molar fraction of Co (χ_{Co}) within each crystal ranged from 0.4 to 0.9 (table S1). The statistical average of metal molar fractions over all the crystals in a bulk sample was provided by inductively coupled plasma-atomic emission spectroscopy (ICP-AES) measurements and found to be 0.6 to 0.9 (table S2). The structure of the obtained MOF-74 crystals was confirmed with powder x-ray diffraction (fig. S1). The crystal size and morphology were measured and confirmed with scanning electron microscopy (SEM) (fig. S2). The two metal types in the mixed-metal MOF crystals were observed by means of energy-dispersive x-ray spectroscopy mapping and found to be distributed evenly on a mesoscopic level throughout the whole MOF crystals (fig. S3).

A higher resolution of the metal distributions in the crystals was achieved with APT, which combines field ion microscopy with

[1]Department of Chemistry, University of California, Berkeley, Berkeley, CA 94720, USA. [2]Materials Sciences Division, Lawrence Berkeley National Laboratory, Berkeley, CA 94720, USA. [3]Kavli Energy NanoSciences Institute at Berkeley, Berkeley, CA 94720, USA. [4]Berkeley Global Science Institute, Berkeley, CA 94720, USA. [5]Institute for Materials, Ruhr-Universität Bochum, Universitätsstraße 150, 44801 Bochum, Germany. [6]University of California, Berkeley–King Abdulaziz City for Science and Technology (KACST) Joint Center of Excellence for Nanomaterials for Clean Energy Applications, KACST, Riyadh 11442, Saudi Arabia.
*Corresponding author. Email: tong.li@ruhr-uni-bochum.de (T.L.); yaghi@berkeley.edu (O.M.Y.)

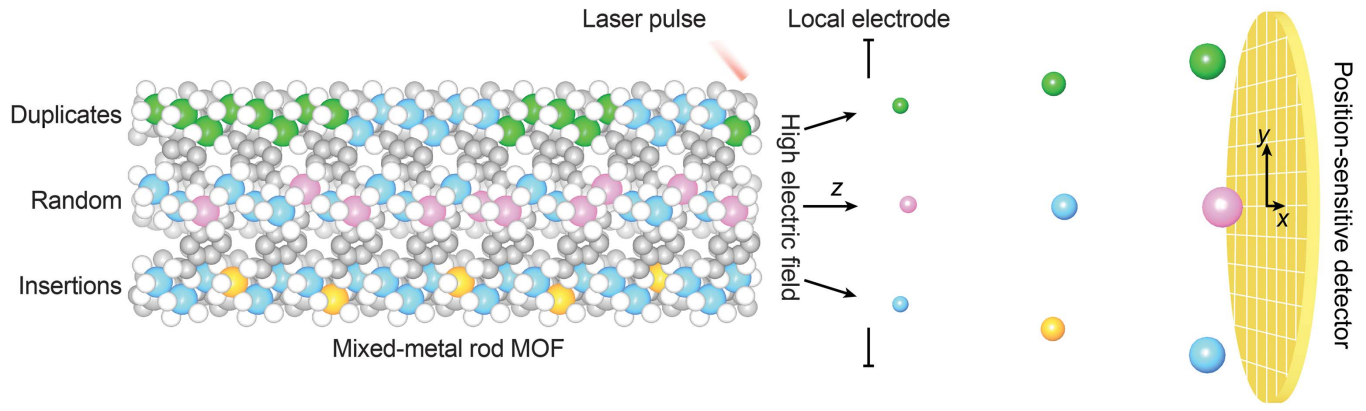


Fig. 1. Experimental approach. Shown is the use of APT technique to determine the type of metal sequences that exist in mixed-metal MOFs containing metal-oxide rods as building units linked by organics. Separating the sample and the position-sensitive detector is a local electrode for modulating the electric field. Metals of different kinds are shown in blue, green, pink, and orange, respectively. Carbon (C) and oxygen (O) atoms are colored in gray and white, respectively. The sizes of the atoms are arbitrarily adjusted for better illustration of metal sequence.

mass spectrometry (*30*) and has been used for mapping elemental distributions in alloys (*31*–*33*) and metal-oxide minerals (*22*–*25*). Triggered by laser pulsing, ions in the sample are sequentially evaporated from the surface by field effect and projected onto a position-sensitive detector, with their mass-to-charge ratio recorded with time-of-flight mass spectrometry (Fig. 1). Accordingly, both the chemical identity and geometrical position of these ions are determined and thereby used to construct a three-dimensional (3D) map for structural study of the sample.

In this work, we show that we can use APT to map the metal sequences within the 12 crystals in real space and that the analysis of these sequences gives four types of metal sequence, depending on the specific metal combination and the synthesis temperature: random (Co, Cd, 120°C), short duplicates of two to four metals (Co, Cd, 85°C), long duplicates of greater than four metals (Co, Pb, 85°C), and insertions of a single metal into duplicates of another metal (Co, Mn, 85°C). Our analysis distinguished different sequences by using reconstituted metal chains (with ~84% accuracy) based on the experimental 3D map obtained from APT. Because APT has not before been used in the analysis of MOFs, we outline the basic methodology and the challenges that we had to overcome to obtain meaningful information for metal sequences in mixed-metal MOFs by using APT.

An important goal for the APT analysis was to distinguish different types of metal sequence in the mixed-metal rod MOF. Pairwise multicomponent short-range order (PM-SRO) has been used to describe how the observed arrangements of metals in alloys differ from the uniformity implied by their nominal stoichiometry (*34*, *35*). It is this parameter that we aimed to determine so as to help in identifying sequence types. The PM-SRO parameter is defined as

$$\alpha_m^{AB} = \frac{p_m^{AB} - \chi_B}{\delta^{AB} - \chi_B}$$

where p_m^{AB} is the observed frequency of finding a B-type atom at the position m from an origin placed on an A-type atom, and χ_B represents the molar fraction of B in the mixture. δ^{AB} equals 1 if $A = B$ and 0 if $A \neq B$. In our study, the latter case was not considered because we always compared the same metal across the sequence for determining their duplicate size; thus, in our analysis $A = B$ always. A positive value of α^{AB} indicates the tendency toward segregation of A and B, whereas a negative one suggests intermingling (mixing) of these atoms. It would be zero if the distribution of A and B were randomly uniform.

In contrast to bulk metals and metal oxides, the analysis space in our rod MOFs is reduced to one dimension, and m can only take on integer values, representing the distance between metal pairs on a chain (supplementary text S2.1, fig. S4, and table S3). To use the PM-SRO parameter α, the span of m that keeps $\alpha > 0$ was examined and treated as the duplicate size predominating the metal sequence because it is expected to have a high probability for finding metals of the same type within a distance shorter than the duplicate size. We define sequence types as long duplicates, short duplicates, insertions, or random when they have excessive duplicates (compared with randomness) in size >4, between 2 and 4, 1, or 0, respectively. This definition has the advantage of having an unbiased PM-SRO parameter α when only a subset of metals from a sample are detected, as is typically the case for APT measurements. Even though in our experiments the detection efficiency is 52%, it will not bias the measurement of α, as evidenced by measuring the effect of random data removal on simulated sequences (supplementary text S2.2 and figs. S5 to S8). Through our APT experiments, the 52% detection efficiency still yielded more than 5000 metal ions identified from each MOF-74 crystal, a data size sufficient to provide an accuracy of α within ± 0.03 for a 95% confidence level, as calculated with the Johnson-Klotz Markov chain method (*36*) (supplementary text S2.3 and table S4). The unbiased and accurate measurement of α allows for robust identification of metal sequence types.

We also analyzed the distribution of duplicate sizes by directly counting duplicates in metal sequences, which provided further guidance on assigning sequence types (supplementary text S2.4). Unlike the PM-SRO parameter, duplicate size distribution is susceptible to data loss (figs. S5 to S8). Because of the 52% detection efficiency, the obtained duplicate size distribution underestimates the level of deviation from randomness; the real sequence type of metals in the crystals deviates more from randomness than what the distribution of duplicate size tells us. Therefore, the distribution of duplicate size should be used with caution and be combined with analysis of the PM-SRO parameter.

In mapping metals by using APT, one must be cognizant of spatial resolutions of ~0.2 nm for depth (z axis, the vertical direction) and 0.5 to 1 nm for lateral (xy plane) (Fig. 1). The lower resolution of the latter is caused by trajectory aberrations and local magnification effects (*37*), blurring out the in-plane position of atoms from their true lattice sites (*23*). Nevertheless, the depth resolution along z is sufficiently high to distinguish atoms emanating from different depths (*38*). In this study, we took advantage of the high depth resolution by aligning the rod

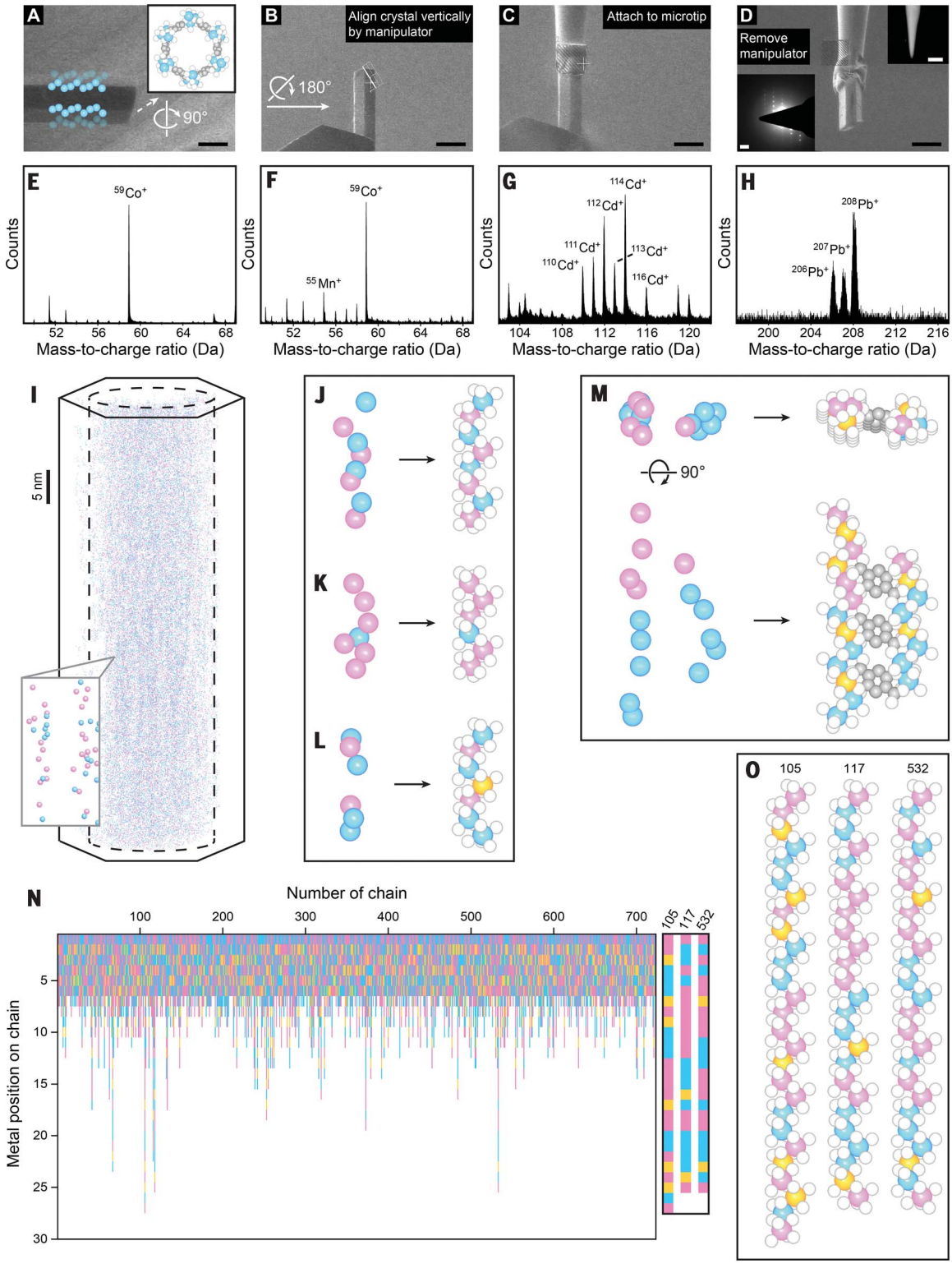


Fig. 2. APT measurement and sequencing of metals in a Co,Cd-MOF-74 single crystal. (**A** to **D**) The APT sample preparation procedure was recorded by a snapshot mode in a dual-beam focused ion beam/SEM. A single crystal of Co,Cd-MOF-74 was (A) attached to a nanomanipulator, (B) aligned vertically, (C) welded to a Si microtip, (D) detached from the nanomanipulator, and last [(D), top right inset], sharpened into a tip shape. Six of the metal-oxide rods in the MOF crystal, enclosing a hexagonal pore, are drawn [(A), inset] and arbitrarily enlarged to overlay on the crystal for better illustration of its long dimension, which is parallel to the rods. [(D), bottom-left inset] The selected-area electron diffraction pattern obtained from the APT tip is indexed in fig. S9 according to the crystal structure of MOF-74. Scale bars, 2 μm; (D), top right inset, 0.4 μm; and (D), bottom left inset, 2 nm^{-1}. (**E** to **H**) The mass spectra of MOF-74 samples identified (E) $^{59}Co^+$, (F) $^{55}Mn^+$, (G) Cd^+, and (H) Pb^+ isotopes, and other species (figs. S11 to S24). (**I**) 3D-APT reconstruction shows all the metals detected (56,605 in total) from a single crystal of Co,Cd-MOF-74 in a 3D space of 20 by 20 by 70 nm. A zoomed-in region where there are metal chains is shown. (**J** to **L**) Metal chains extracted from the raw data were reconstituted into metal-oxide rod SBUs, yielding (J) a good match, (K) a redundant metal, and (L) a missing metal. (**M**) The neighboring metal chains were reconstituted into rods that are connected by organic linkers. (**N**) The sequence of 723 metal chains is presented in a bitmap, where the color of squares represents the identity of metals located in the chain. Among these metal sequences, those of the 105th, 117th, and 532nd metal chains are displayed with magnification. (**O**) The metal-oxide rods reconstituted from the 105th, 117th, and 532nd metal chains. Color code: Co, blue; Cd, pink; missing metals, orange; O, white; and C, gray. The sizes of atoms follow the same condition as in Fig. 1.

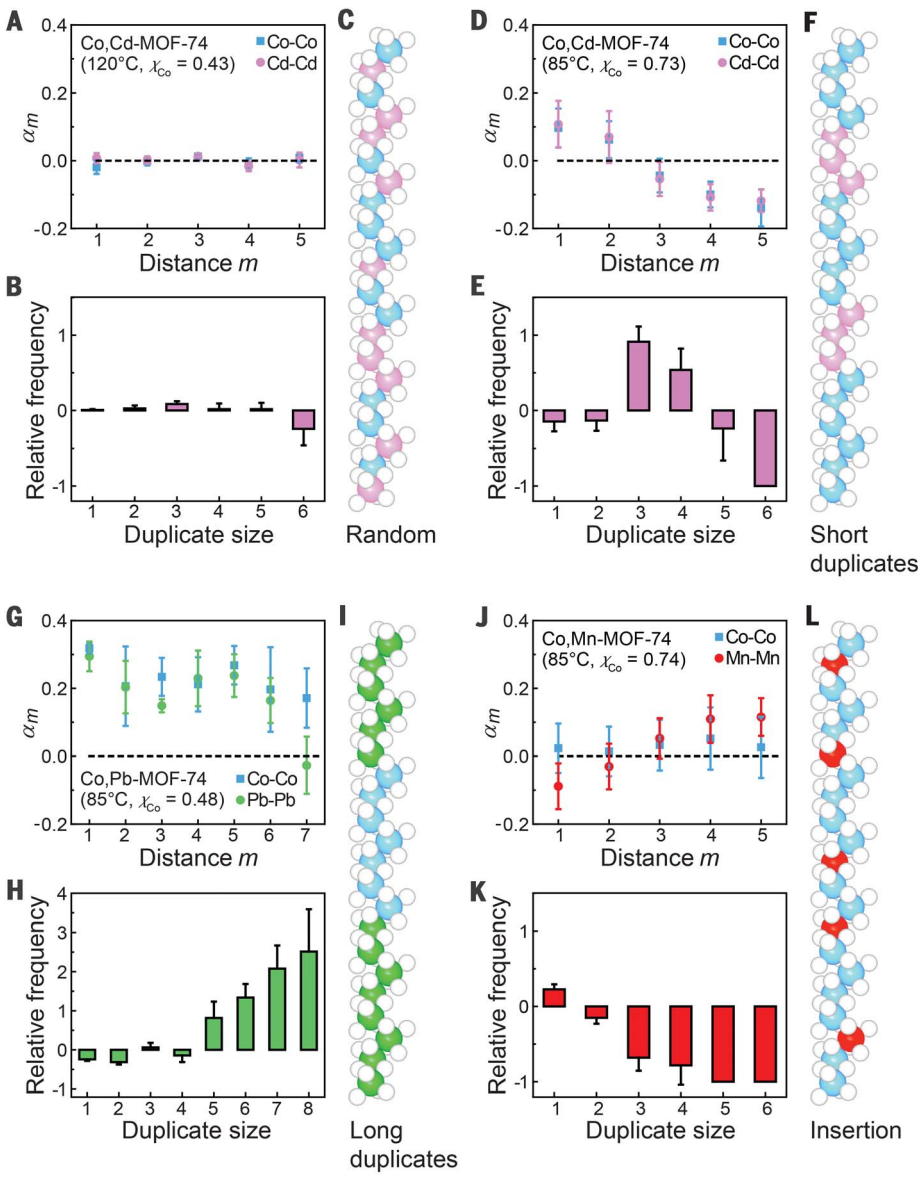


Fig. 3. Statistical analysis of metal arrangements in multivariate MOF-74. (**A**) The PM-SRO parameter α plotted against the distance *m* between metal pairs in Co,Cd-MOF-74 (120°C). (**B**) The histogram of duplicate sizes in this MOF crystal. Relative frequency is calculated by normalizing the difference between the number of duplicates observed and that simulated according to uniform distribution. (**C**) The structure model of metal-oxide rod SBUs in a random sequence for Co,Cd-MOF-74 (120°C). (**D** to **F**) The α plot, duplicate size histogram, and structural model for Co,Cd-MOF-74 (85°C). (**G** to **I**) The α plot, duplicate size histogram, and structural model for Co,Pb-MOF-74 (85°C). (**J** to **L**) The α plot, duplicate size histogram, and structural model for Co, Mn-MOF-74 (85°C). Error bars were calculated according to five independent runs of data processing, and the uncertainty was derived from the stochastic nature of the *k*-means clustering algorithm. Some error bars are not shown because these duplicate sizes are consistently not found (relative frequency remained −1 without variability). Color code: Co, blue; Cd, pink; Pb, green; Mn, red; and O, white.

SBUs of the MOF along the longest dimension of the hexagonal-prism crystal perpendicular to the detection plane (Fig. 2, A to D, and supplementary text S3.1). As such, the chain of metals in the metal-oxide rod SBUs are subject to metal sequence "reading" along the measurement *z* axis. The final MOF specimen was sharpened by using a dual-beam focused ion beam into a tip (diameter of <100 nm) (Fig. 2D, top right inset) suitable for APT measurements, without loss of crystallinity, as confirmed by means of electron diffraction (Fig. 2D, bottom left inset, and fig. S9).

We performed APT on all 12 crystals (supplementary text S3 and fig. S10). All the constituent metals were identified from mass spectra because their isotopes have mass-to-charge ratios distinctive from that of the complex fragments generated from the organic linker during the APT experiment (Fig. 2, E to H; figs. S11 to S24; and table S5). We choose here as an illustrative example Co,Cd-MOF-74 (120°C), where the position and the chemical identity of 56,605 metals were collected and mapped (Fig. 2I). A prerequisite for the reconstitution of rod SBUs is that the lateral-position inaccuracy of APT not be too large to turn data into complete randomness, and thus chains of metal can still be discernable from their 3D map. An aspect that works in our favor is the choice of a rod MOF as an object for this study. The separation of the metal rods through organics works against the unfavorable contributions of the lateral resolution because the overlap in detecting metals on different rods is reduced.

To assess whether the distribution of metals statistically displays a linear trend, we evaluated their clustering tendency along different directions. For a metal chain propagating along the *z* direction, its projection onto the *xy* plane displays a cluster where the metals appear on top of each other (eclipsed). By contrast, its projections onto the *xz* or the *yz* plane would assume a linear configuration, with higher position variance than that of a cluster. To distinguish this anisotropy for our sample, the 3D map containing the identity of the metals as well as their positions was flattened into each of the three Cartesian planes (supplementary text S4.1 and S4.2). These data were input into a *k*-means clustering algorithm for partitioning metals into clusters on the basis of their in-plane proximity. This gave the variance in metal positions within a cluster, which was found to be lower in the *xy* plane (as expected owing to the metals being eclipsed), compared with those in the *xz* and *yz* plane, all of which are lower than that of a randomly uniform distribution (fig. S25). The tendency

that metals are preferentially clustered along the z axis and therefore arranged in a linear pattern in this direction allowed the reconstitution of the rod SBUs in the crystal of Co, Cd-MOF-74 (120°C).

The reconstitution of metal chains was done by developing an algorithm specifically designed to assign the metals from the 3D map into chains (supplementary text S4.3, figs. S26 and S27, and table S6). The metals belonging to the same cluster partitioned by the k-means algorithm on the xy plane will constitute a chain if their vertical distances match the crystallographic vertical distance of 2.25 Å between two neighboring metals in the structure of MOF-74. On the basis of this distance criterion, metals falling within ±50% (considering the depth resolution of APT measurements) were assumed to be neighbors, assigned to the same metal chain, and reconstituted together into a metal-oxide rod (Fig. 2J). However, if within this range more than one metal was found, the one closest to the crystallographic position was chosen to minimize the chance of mistaking it with an off-position metal that actually belongs to a neighboring chain (Fig. 2K). If no metal satisfied this distance criterion, a missing ion was assumed to be in that position and arbitrarily placed to accommodate the 52% detection efficiency (Fig. 2L). This allowed for the continuous search for the next metal in the chain. The search for metals belonging to a chain terminated when two missing metals were found in a row. Then, the metal assignment for the next chain was initiated until the entire 3D map of metal was exhausted. If two separate metal chains were spaced by the size of a phenylene ring (5.6 Å), they were reconstituted into neighboring rod SBUs connected by organic linkers (Fig. 2M and supplementary text S4.4). All the metal chains thus extracted from the 3D map are shown in Fig. 2N. Among the 723 chains examined in this single crystal, the longest one (the 105th) was found to be 27 metals in length and has 9 Co, 12 Cd, and 6 missing metals (Fig. 2O). Even though the detection efficiency was 52%, the reason that the number of missing metals appears low has to do with our choice of long chains of relatively fewer missing metals to proceed to the next sequence analysis (supplementary text S4.5). This helped in increasing the accuracy of metal-chain reconstitution.

We used the developed chain-searching algorithm to confirm the proper alignment of MOF crystals during sample preparation. The alignment of MOFs during sample preparation (Fig. 2, A to D) might not be 100% accurate, causing the inaccuracy in chain searching. The orientation of chains along the z direction was corroborated by intentionally rotating the 3D map along the x or y axis to examine whether this operation yields fewer number of chains (supplementary text S4.7). When this was done for the crystal of Co,Cd-MOF-74 (120°C), we found that it was aligned as we expected (fig. S28 and table S7). These results indicate that the metal-oxide rods were aligned along the z axis (misalignment angle < 5°) and were structurally preserved despite some lateral deviation during the measurements.

To evaluate the impact of trajectory aberration on the accuracy of assigning metals in chains, we applied the same algorithm presented above to a virtual 3D map of metals that was simulated by adding a Gaussian noise (*23*) to their lateral crystallographic positions (supplementary text S4.8). The positional deviation resulting from the added noise was chosen to match the simulated data with the experimental ones in terms of the within-cluster metal-position variance obtained from the k-means algorithm (figs. S29 and S30). By tracking the number of metals that were correctly assigned into chains, the accuracy was estimated to be ~81% (table S8). When only metal chains with few missing atoms and a small variation in lateral position (constituent metals are more eclipsed) were used for metal rod reconstitution, the accuracy can be further enhanced to ~84%. Whereas a lower accuracy will turn regularity into randomness, this accuracy was found sufficient to allow us to observe recognizable deviation from randomness in metal sequences.

To determine the sequence type of our samples, the PM-SRO parameter α was calculated for the obtained reconstituted chains. Its value was found to remain near zero at different distances for Co,Cd-MOF-74 (120°C) (Fig. 3A), corresponding to the existence of a random sequence of metals (Fig. 3C). Consistently, the histogram of duplicate sizes within this sequence obtained through direct counting was in good agreement with those of the sequences simulated through uniform distribution (Fig. 3B).

A crystal of the same metal combination but synthesized at a lower temperature (85°C) showed duplicates for both Co and Cd (Fig. 3F), evidenced by the enhanced frequency of finding metals of the same type within a distance of 2 and in a lower frequency beyond this distance (Fig. 3D). This result indicates the dominance of duplicates in the size of 3, which was corroborated by the duplicate size histogram (Fig. 3E). These types of sequence were found to be consistent among crystals made under the same synthetic conditions (fig. S31), although their molar fraction of metals varies.

The physical nature behind the observed metal arrangements in multivariate MOF-74

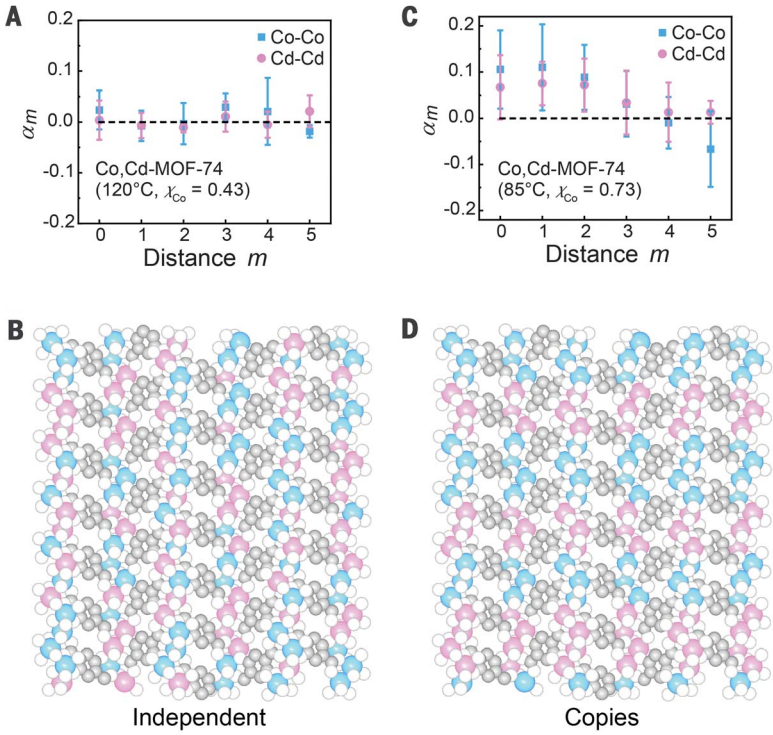


Fig. 4. The metal arrangement across neighboring metal-oxide rods. (**A**) The PM-SRO parameter α for describing the distribution of metal pairs on the neighboring rods in Co,Cd-MOF-74 (120°C). (**B**) The structure model of Co,Cd-MOF-74 (120°C), illustrating the independent type of metal arrangement across rods. (**C**) The PM-SRO parameter for Co,Cd-MOF-74 (85°C). (**D**) The structure model of Co,Cd-MOF-74 (85°C), displaying sequence copies across rods. Color code: Co, blue; Cd, pink; O, white; and C, gray.

is rationalized by an energy diagram (supplementary text S5.2 and fig. S32). Fundamentally, the distinct metal sequences represent intermediate states in the continuum between complete phase separation and ordered alternation in a single phase. A random sequence maximizes the configurational entropy (*39*), which could be translated into the minimum free energy under the assumption that the enthalpy change involved in the permutation of components is negligible. This assumption does not hold true, for example, when metals of varying sizes are mixed into an alloy. The Hume-Rothery Rule requires that the atomic radius of the metals in solid-solution alloys must differ by no more than 15% (*40*). The requirement of similar ion radii has also been observed for metal oxides, with the difference being up to 25% (*41*–*43*). Otherwise, the generated lattice mismatch causes substantial strain, and the resultant energy cost drives the system to deviate from the entropic maximum. Within metal-oxide rods in MOF-74, the partial replacement of Co (0.65 Å in radius for +2 ions) by the larger Cd (0.95 Å) induces distorted metal-O bonds (*44*), and consequently, a duplicate sequence is favored to minimize the energy penalty. When we performed synthesis at a higher temperature, the contribution of configuration entropy became more dominant, thus making the entropy well steeper (fig. S32). Therefore, the combination of Co and Cd—which grows into short duplicates at low synthesis temperature—at a higher temperature falls into the regime of random sequences.

Although duplicate sizes as large as 5 and 6 were mostly absent from Co,Cd-MOF-74 (85°C), these long duplicates and even longer ones were indeed highly populated in Co,Pb-MOF-74 (85°C), where instead shorter duplicates were unfavorable (Fig. 3, H and I). This is evidenced by the values of the PM-SRO parameter, where we found that they remained positive in distant regions (Fig. 3G). When the larger Pb (1.19 Å) was used instead of Cd in their combination with Co, metal mixing involved more substantial size mismatch and therefore yielded longer duplicate sizes, as expected. The size difference of 83% between Co and Pb in MOF-74 far exceeds the 25% limit observed for solid-solution metal oxides, without entering the phase separation stage. This crystal having equal amounts of metals and the observation of long duplicates rather than random are evidence of the importance of chemical effects in biasing sequences and the power of APT in illuminating how metals are mixed in multimetallic MOFs.

Last, insertion sequences (Fig. 3L) were found for Co,Mn-MOF-74 (85°C), where one metal prefers to insert into duplicates of the other, thus leading to a decrease in the segregation of the inserting metal (Fig. 3K) and a corresponding increase in PM-SRO parameters for longer distances (Fig. 3J). The insertion sequence indicates a possible attractive interaction between Co and Mn, which have similar sizes (0.65 and 0.67 Å, respectively). For Co,Pb-MOF-74 and Co,Mn-MOF-74, we halved the analyzed crystals and found that there was no disparity in sequence type between their respective segments (fig. S33).

We further extended our method to the analysis of sequences of neighboring chains (Fig. 4). Other than the metal sequences within the metal-oxide rods, there are in general three different ways to spatially arrange these sequences: copies (the same metal sequences in neighboring rods that are aligned with respect to each other), inverse (the metal type in one sequence is displaced by another metal type in neighboring rods), and independent (no correlation between the sequences on neighboring rods) (fig. S34). To decipher the metal arrangements across neighboring rods, we performed the same PM-SRO analysis on the obtained sequences except for the origin used for defining position, which we placed on the rod neighboring the one under evaluation (supplementary text S2.1). A distance of zero means that the two metals are aligned at the same height on neighboring rods. According to the interchain PM-SRO parameters, Co,Cd-MOF-74 (120°C) displayed an independent metal arrangement between rods (Fig. 4, A and B). However, in Co,Cd-MOF-74 (85°C), short duplicates of the same type were found to be aligned between neighboring rods, constituting a copy arrangement (Fig. 4, C and D).

REFERENCES AND NOTES

1. H. Deng *et al.*, *Science* **327**, 846–850 (2010).
2. L. J. Wang *et al.*, *Inorg. Chem.* **53**, 5881–5883 (2014).
3. O. M. Yaghi, M. J. Kalmutzki, C. S. Diercks, *Introduction to Reticular Chemistry: Metal-Organic Frameworks and Covalent Organic Frameworks* (Wiley-VCH, 2019).
4. Z. Dong, Y. Sun, J. Chu, X. Zhang, H. Deng, *J. Am. Chem. Soc.* **139**, 14209–14216 (2017).
5. Y. B. Zhang *et al.*, *J. Am. Chem. Soc.* **137**, 2641–2650 (2015).
6. T. Li *et al.*, *Microporous Mesoporous Mater.* **272**, 101–108 (2018).
7. Q. Liu, H. Cong, H. Deng, *J. Am. Chem. Soc.* **138**, 13822–13825 (2016).
8. A. M. Fracaroli *et al.*, *J. Am. Chem. Soc.* **138**, 8352–8355 (2016).
9. Q. Xia *et al.*, *J. Am. Chem. Soc.* **139**, 8259–8266 (2017).
10. L. M. Aguirre-Díaz *et al.*, *J. Am. Chem. Soc.* **137**, 6132–6135 (2015).
11. L. Wang *et al.*, *ACS Appl. Mater. Interfaces* **8**, 16736–16743 (2016).
12. S. Lin *et al.*, *Science* **349**, 1208–1213 (2015).
13. T. M. Osborn Popp, O. M. Yaghi, *Acc. Chem. Res.* **50**, 532–534 (2017).
14. H. Furukawa, U. Müller, O. M. Yaghi, *Angew. Chem. Int. Ed.* **54**, 3417–3430 (2015).
15. N. L. Rosi *et al.*, *J. Am. Chem. Soc.* **127**, 1504–1518 (2005).
16. A. Schoedel, M. Li, D. Li, M. O'Keeffe, O. M. Yaghi, *Chem. Rev.* **116**, 12466–12535 (2016).
17. S. R. Caskey, A. G. Wong-Foy, A. J. Matzger, *J. Am. Chem. Soc.* **130**, 10870–10871 (2008).
18. P. D. C. Dietzel *et al.*, *Chem. Commun.* **41**, 5125–5127 (2008).
19. D. Britt, H. Furukawa, B. Wang, T. G. Glover, O. M. Yaghi, *Proc. Natl. Acad. Sci. U.S.A.* **106**, 20637–20640 (2009).
20. F. Fathieh *et al.*, *Sci. Adv.* **4**, eaat3198 (2018).
21. N. Hanikel *et al.*, *ACS Cent. Sci.* **5**, 1699–1706 (2019).
22. B. Scherrer *et al.*, *Chem. Mater.* **32**, 1031–1040 (2020).
23. J. E. Schmidt, L. Peng, J. D. Poplawsky, B. M. Weckhuysen, *Angew. Chem. Int. Ed.* **57**, 10422–10435 (2018).
24. D. E. Perea *et al.*, *Nat. Commun.* **6**, 7589 (2015).
25. A. Devaraj *et al.*, *Nat. Commun.* **6**, 8014 (2015).
26. X. Kong *et al.*, *Science* **341**, 882–885 (2013).
27. C. Castillo-Blas *et al.*, *Sci. Adv.* **3**, e1700773 (2017).
28. Y. Zhu *et al.*, *Nat. Mater.* **16**, 532–536 (2017).
29. W. Schrimpf *et al.*, *Nat. Commun.* **9**, 1647 (2018).
30. B. Gault, M. P. Moody, J. M. Cairney, S. P. Ringer, *Atom Probe Microscopy*, vol. 160, Springer Series in Material Science (Springer, 2012).
31. Y.-S. Chen *et al.*, *Science* **355**, 1196–1199 (2017).
32. M. Kuzmina, M. Herbig, D. Ponge, S. Sandlöbes, D. Raabe, *Science* **349**, 1080–1083 (2015).
33. Y.-S. Chen *et al.*, *Science* **367**, 171–175 (2020).
34. D. de Fontaine, *J. Appl. Cryst.* **4**, 15–19 (1971).
35. A. V. Ceguerra *et al.*, *Acta Crystallogr. A* **68**, 547–560 (2012).
36. C. A. Johnson, J. H. Klotz, *Technometrics* **16**, 483–493 (1974).
37. F. Vurpillot, A. Bostel, D. Blavette, *Appl. Phys. Lett.* **76**, 3127–3129 (2000).
38. B. Gault, M. P. Moody, J. M. Cairney, S. P. Ringer, *Mater. Today* **15**, 378–386 (2012).
39. D. A. Porter, K. E. Easterling, M. Y. A. Sherif, *Phase Transformation in Metals and Alloys* (CRC Press, ed. 3, 2009).
40. W. B. Pearson, *A Handbook of Lattice Spacings and Structures of Metals and Alloys*, *International Series of Monographs on Metal Physics and Physical Metallurgy*, vol. 4 (Pergamon, 1958).
41. A. Urban, A. Abdellahi, S. Dacek, N. Artrith, G. Ceder, *Phys. Rev. Lett.* **119**, 176402 (2017).
42. X.-W. Zhang, Q. Wang, B.-L. Gu, *J. Am. Ceram. Soc.* **74**, 2846–2850 (1991).
43. L. Zhang *et al.*, *J. Power Sources* **185**, 534–541 (2008).
44. J. D. Howe *et al.*, *J. Phys. Chem. C* **121**, 627–635 (2017).

ACKNOWLEDGMENTS

We thank A. Kostka [Zentrumfür Grenzflächendominierte Höchstleistungswerkstoffe (ZGH)] for the TEM experiment; Y. Wei (Stanford University) for the assistance of data processing; and B. Rungtaweevoranit, H. Lyu, and C. S. Diercks (members of the Yaghi Laboratory) for SEM measurements and helpful discussions. T.L. acknowledges ZGH at Ruhr University Bochum for the access to infrastructure (FEI Helios G4 CX FIB/SEM and Cameca LEAP 5000 XR). We thank G. Prieto (ITQ Institute of Chemical Technology), F. Schüth (Max-Planck-Institut für Kohlenforschung), B. Gault [Max-Planck-Institut für Eisenforschung GmbH (MPIE)], and D. Raabe (MPIE) for initiating the collaboration and providing infrastructures for preliminary trials. **Funding:** This research was supported by King Abdulaziz City for Science and Technology (Center of Excellence for Nanomaterials and Clean Energy Applications). **Author contributions:** O.M.Y., Z.J., and T.L. designed the project. Z.J. synthesized MOF crystals. T.L. performed APT measurements. Z.J. and T.L. analyzed the APT data. Z.J., T.L., and O.M.Y. prepared the manuscript. **Competing interests:** None declared. **Data and materials availability:** All data needed to evaluate the conclusion in the paper are present in the paper or the supplementary materials. Code written for the chain searching algorithm is available at https://github.com/sequencingMOF/metalchain.

SUPPLEMENTARY MATERIALS

science.sciencemag.org/content/369/6504/674/suppl/DC1
Materials and Methods
Supplementary Text
Figs. S1 to S34
Tables S1 to S8
References (*45*, *46*)

9 September 2019; resubmitted 9 March 2020
Accepted 17 June 2020
10.1126/science.aaz4304

FERROELECTRICS

Emergent helical texture of electric dipoles

Dmitry D. Khalyavin[1]*, Roger D. Johnson[2,3], Fabio Orlandi[1], Paolo G. Radaelli[3], Pascal Manuel[1], Alexei A. Belik[4]

Long-range ordering of magnetic dipoles in bulk materials gives rise to a broad range of magnetic structures, from simple collinear ferromagnets and antiferromagnets, to complex magnetic helicoidal textures stabilized by competing exchange interactions. In contrast, dipolar order in dielectric crystals is typically limited to parallel (ferroelectric) and antiparallel (antiferroelectric) collinear alignments of electric dipoles. Here, we report an observation of incommensurate helical ordering of electric dipoles by light hole doping of the quadruple perovskite $BiMn_7O_{12}$. In analogy with magnetism, the electric dipole helicoidal texture is stabilized by competing instabilities. Specifically, orbital ordering and lone electron pair stereochemical activity compete, giving rise to phase transitions from a nonchiral cubic structure to an incommensurate electric dipole and orbital helix via an intermediate density wave.

The long-range ordering of magnetic and/or electric dipoles is a canonical cause of phase transitions in crystalline materials and is associated with a variety of functional properties. Despite the fundamentally different nature of the interactions between magnetic and electric dipoles, there are many similarities between the two types of phase transition, as first mentioned by Valasek (*1*) in 1922. In particular, many materials display parallel dipole alignments (as in ferromagnets and ferroelectrics) or antiparallel dipole alignments (as in antiferromagnets and antiferroelectrics). First predicted theoretically by Néel in 1948 (*2*), antiferromagnetic spin ordering was experimentally confirmed in MnO one year later using the newly established neutron diffraction technique (*3*), a discovery that led to rapid experimental and theoretical developments (*4*). Antiferroelectricity was first proposed in $PbZrO_3$ by Sawaguchi, Maniwa, and Hoshino in 1951 (*5*) on the basis of the antiparallel displacements of Pb established by x-ray diffraction. Although by far the most common, collinear ferro-dipolar and antiferro-dipolar orderings (as well as their simple combinations such as ferri-structures and canted structures) are not the only possibilities. In the late 1950s and early 1960s, Koehler *et al.* (*6*, *7*) and Yoshimori (*8*) discovered the first examples of noncollinear helical magnetic ordering in Ho and other rare earth metals, as well as in rutile MnO_2.

Nowadays, many exotic orderings of magnetic dipoles are known, where spins gradually rotate creating complex patterns whose period is often incommensurate with the crystal structure. Such spin textures, characterized by additional macroscopic quantities such as chirality and polarity, play a central role in the physics of multiferroic materials, frustrated magnetism, skyrmions, and magnetic domain walls. By analogy, one could expect that helical ordering should also occur in materials containing electric dipoles. However, such electric dipole textures have been challenging to observe experimentally in a bulk material. Here, we report an example of incommensurate helical ordering of electric dipoles in the lightly doped quadruple perovskite $BiCu_xMn_{7-x}O_{12}$. In addition to completing the analogy between ordering of magnetic and electric dipoles, our discovery demonstrates that many principles of noncollinear magnetism can be adopted to understand the properties of dielectric materials.

The parent compound $BiMn_7O_{12}$ is a so-called quadruple perovskite with Mn^{3+} on both A and B perovskite sites, $[BiMn^{3+}{}_3]_A[Mn^{3+}{}_4]_BO_{12}$. It combines two well-known electronic instabilities, leading to a complex structural behavior (*9*): the stereochemical activity of Bi^{3+} caused by the $6s^2$ lone-pair electrons, and the Jahn-Teller (JT) instability caused by the degenerate e_g electronic states of octahedrally coordinated Mn^{3+}. The former promotes off-centric cation displacements and the formation of local electric dipoles (*10*) and is thus responsible for the ferroelectric properties of many Bi-containing perovskite oxides (*11*–*13*). The latter often results in a structural phase transition characterized by a coherent, spontaneous distortion of polyhedra coordinating Mn^{3+}, for instance, as in the case of $LaMnO_3$ (*14*). At high temperatures, $BiMn_7O_{12}$ adopts a cubic nonferroelectric structure with space group (SG) *Im-3*, whereas upon cooling it undergoes three distinct structural transitions at temperatures T_{JT} ~ 608 K, T_C ~ 460 K, and T_S ~ 290 K. The highest-temperature transition at T_{JT} (to SG *I*2/*m*) is driven by cooperative JT distortions, leading to a B-site orbital pattern identical to the prototype manganite $LaMnO_3$ (*14*). At the Curie temperature T_C, $BiMn_7O_{12}$ becomes ferroelectric owing to ferro-dipolar ordering of the Bi lone pairs, whereas the crystallographic transition at T_S is between the higher-temperature (SG *Im*) and ground-state (SG *P*1) ferroelectric phases. This transition can be interpreted as an electric dipole reorientation at which the electric polarization (initially confined within the *ac* plane) rotates to a general direction (*15*). Throughout both ferroelectric phases, the $LaMnO_3$-type orbital order remains largely unchanged.

As is the case for other manganites (*16*, *17*), a small amount of hole doping achieved, for example, by the replacement of A-site Mn^{3+} with Cu^{2+}, is expected to tune both instabilities because it affects both the JT ordering [doped holes are localized on B sites (*18*, *19*) such that Mn^{3+} tends toward non-JT-active Mn^{4+}] and the immediate coordination of Bi^{3+}. Similar to the undoped compound, $BiCu_{0.1}Mn_{6.9}O_{12}$ is cubic at high temperatures [structural parameters for this phase as well as for the phases discussed below are summarized in tables S1 to S5 and figs. S1 to S8 (*20*)] and undergoes a JT-order phase transition to the nonpolar monoclinic structure with SG *I*2/*m* at a slightly lower T_{JT} of ~560 K (Fig. 1A and fig. S3) accompanied by the same $LaMnO_3$-type orbital order.

The nature of the two lower-temperature phase transitions in $BiCu_{0.1}Mn_{6.9}O_{12}$ is notably different than in $BiMn_7O_{12}$ (Fig. 1A and figs. S4 to S6). The Curie and structural transitions are replaced by transitions to two incommensurately modulated phases at T_{I1} ~ 435 K and T_{I2} ~ 390 K, both of which are described below. The transitions are strongly first-order and are associated with large thermal hysteresis (fig. S9). In both modulated phases, the incommensurate satellite reflections observed in the diffraction patterns (Fig. 1B and figs. S4 and S5) are very strong. These sudden structural changes at such low doping strongly suggest that the modulation can be associated with reconstruction of the primary electronic instabilities, namely, ferroelectric dipole ordering and/or orbital polarization.

Crystallographic analysis performed at T = 427 K (below T_{I1}) revealed that the structure is metrically triclinic with the incommensurate modulation vector $\boldsymbol{k}_{HT}$ = (−0.0037(8), 0.026(1), 0.1233(8))—approximately parallel to the body diagonal of the pseudocubic cell. Structural refinements performed in the *R*-1(αβγ)0 superspace group (SSG) established that the Bi cations predominantly shift along the *a* axis (former cubic $[0\text{-}11]_C$ direction) (Fig. 2A) and adopt the largest modulation amplitude of all atomic species. The large displacements of Bi confirm that the modulation is related to the ordering of lone electron pairs, which in the parent material, $BiMn_7O_{12}$, induces ferroelectricity by adopting parallel ordering. In contrast, in the triclinic

[1]ISIS Facility, Rutherford Appleton Laboratory, Harwell Campus, Didcot OX11 0QX, UK. [2]Department of Physics and Astronomy, University College London, London WC1E 6BT, UK. [3]Department of Physics, University of Oxford, Oxford OX1 3PU, UK. [4]International Center for Materials Nanoarchitectonics (WPI-MANA), National Institute for Materials Science (NIMS), Namiki 1-1, Tsukuba, Ibaraki 305-0044, Japan.
*Corresponding author. Email: dmitry.khalyavin@stfc.ac.uk

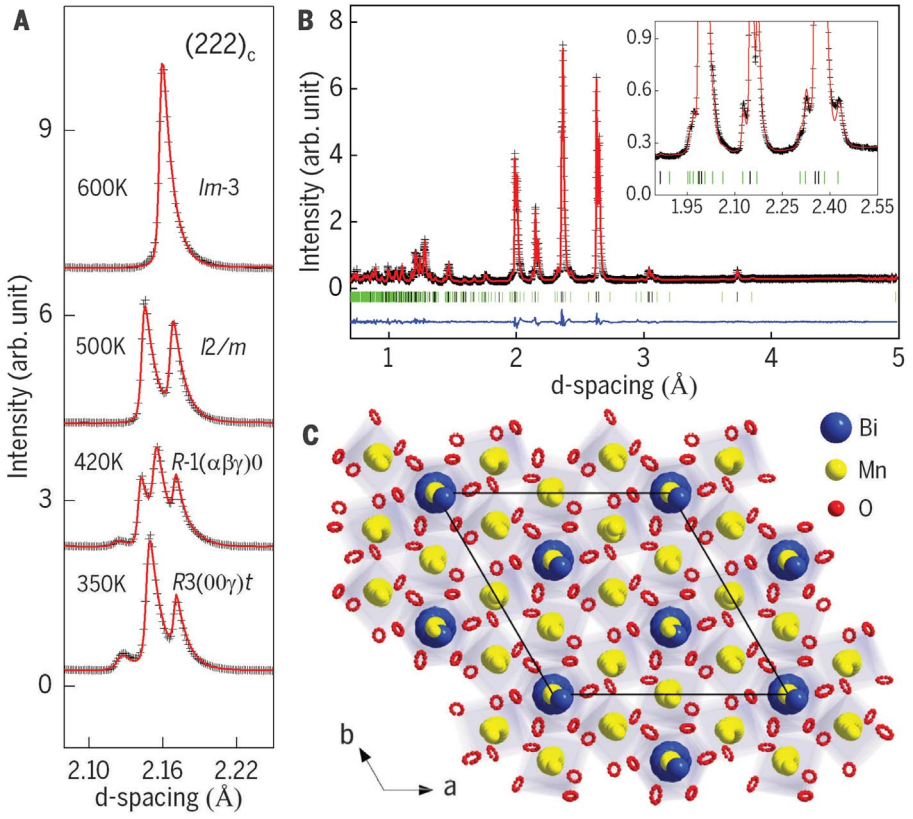


Fig. 1. Crystal structure refinement. (**A**) Thermal evolution of $(222)_C$ fundamental reflection measured by neutron diffraction in the different phases of $BiCu_{0.1}Mn_{6.9}O_{12}$. arb. unit, arbitrary unit. (**B**) Rietveld refinement of the neutron diffraction data collected at room temperature in the modulated helical phase. Cross symbols and solid red line represent experimental and calculated intensities, respectively, and the blue line below is the difference between them. The black tick marks indicate positions of the fundamental peaks, and the green tick marks indicate positions of the satellites. The corresponding structural parameters are listed in table S4. The inset shows a region where the strongest satellite reflections are observed in the modulated helical phase. (**C**) View along the *c* axis of the crystal structure of $BiCu_{0.1}Mn_{6.9}O_{12}$ in the modulated helical phase, demonstrating chiral atomic displacements. For simplicity, all sites occupied by transition metals are labeled as Mn and colored yellow. In the studied material, ~3% of the A-site Mn is substituted with Cu.

phase of $BiCu_{0.1}Mn_{6.9}O_{12}$, the Bi displacements are aligned on a fixed axis, but their amplitude is modulated giving zero net ferroelectric polarization. This electric dipole ordering strongly resembles the incommensurate structure of magnetic moments in a spin density wave (SDW), which is a feature of many magnetic systems with frustrated exchange interactions. Our triclinic dipole density wave (DDW) structure is stable only in a narrow temperature range below the phase transition—another point of similarity with SDWs in insulators, where this type of magnetic ordering is almost always entropically stabilized.

The low-temperature phase of $BiCu_{0.1}Mn_{6.9}O_{12}$, below T_{12} ~ 390 K and down to the ground state, is metrically trigonal and heavily modulated along the *c* axis; $\boldsymbol{k}_{LT} = (0,0,\gamma)$ with $\gamma = 0.1046(5)$ at $T = 380$ K. This modulation vector is on the Λ line of symmetry and is oriented exactly along the body diagonal of the pseudocubic cell [$\boldsymbol{k}_{LT} = (2/3\gamma,2/3\gamma,2/3\gamma)$ in the *Im*-3 setting]. A systematic test of all isotropy subgroups of *Im*-3 associated with this type of modulation (*21*–*23*) revealed that only the noncentrosymmetric SSG $R3(00\gamma)t$ can provide an excellent refinement quality for both neutron (Fig. 1B) and x-ray (fig. S5) diffraction patterns. The obtained crystal structure comprises a distinct pattern of modulated distortions (Fig. 1C). The largest refined atomic displacements are, once again, associated with Bi and lie in the *ab* plane of the trigonal cell, and all have the same amplitude of 0.41(1) Å at $T = 300$ K. This value is extremely large: It exceeds the ferroelectric displacements of the cations in the undoped $BiMn_7O_{12}$ (~0.37 Å) (*9*, *24*) and $BiFeO_3$ (~0.40 Å) (*25*).

In the lower-temperature phase of $BiCu_{0.1}Mn_{6.9}O_{12}$ ($T < 390$ K), the displacement vectors rotate perpendicular to the modulation wave vector propagating along the *c* axis (Figs. 1C and 2, B and C) and are therefore the structural analog of a magnetic incommensurate proper helix. Thus, in this phase, the lone electron pairs of Bi^{3+} cations are ordered into a helical structure, making $BiCu_{0.1}Mn_{6.9}O_{12}$ a textbook example of a helical texture of electric dipoles. In general, the order parameter of a structural or magnetic helical phase can be defined as a mixed product $\sigma_s = \boldsymbol{k}_{LT}\cdot[\boldsymbol{r}_i \times \boldsymbol{r}_j]$ or $\sigma_m = \boldsymbol{k}_m\cdot[\boldsymbol{S}_i \times \boldsymbol{S}_j]$, where $\boldsymbol{r}_i$ and $\boldsymbol{r}_j$ ($\boldsymbol{S}_i$ and $\boldsymbol{S}_j$) are atomic displacements (spins) in adjacent unit cells along the propagation vector $\boldsymbol{k}_{LT}$ ($\boldsymbol{k}_m$) (Fig. 2, B and C). In both cases, this quantity is a time-reversal-even pseudoscalar, which in the present case measures the modulus and sign of the structural chirality (or helicity). Once again, the parallel with the magnetic counterparts is particularly apparent in the sequence of phase transitions we have observed in $BiCu_{0.1}Mn_{6.9}O_{12}$ (paraelectric–DDW–helical), which is completely analogous to that of frustrated magnets such as the prototypical type-II multiferroic $TbMnO_3$ (paramagnetic–SDW–cycloidal) (*26*, *27*).

One notable implication is that the $BiCu_xMn_{7-x}O_{12}$ series provides a distinctive example of emergent structural chirality acting as a macroscopic order parameter (ferrochirality). In most type-II multiferroics, including the prototypes $TbMnO_3$ (*26*–*28*) and $CaMn_7O_{12}$ (*29*, *30*), spin (vector) chirality appears below a magnetic phase transition and is coupled to improper ferroelectricity through a suitable free-energy invariant. In $TbMnO_3$, this invariant describes a direct coupling between vector spin chirality and the electric polarization and is allowed only in the weakly ferroelectric cycloidal phase, not in the high-temperature, nonpolar SDW phase (*27*, *28*). Unlike the case of $TbMnO_3$, where the magnetic chirality and electric polarization are directly coupled, multiferroicity in $CaMn_7O_{12}$ requires the presence of an additional axial structural distortion $\boldsymbol{A}$ (known as ferro-axiality) (*29*–*31*) to form the free-energy invariant $\sigma_m\boldsymbol{AP}$ (where $\boldsymbol{P}$ is the electric polarization). The above analysis leads us to the prediction that improper (weak) ferroelectricity should also be induced in $BiCu_{0.1}Mn_{6.9}O_{12}$ by precisely the same mechanism, as the free-energy invariant $\sigma_s\boldsymbol{AP}$ (with the spin chirality σ_m being replaced by the structural chirality σ_s) is allowed in the low-temperature $R3(00\gamma)t$ phase of $BiCu_{0.1}Mn_{6.9}O_{12}$.

We tested this prediction by performing ferroelectric polarization–electric field (*P*-*E*) hysteresis loop measurements (fig. S10) at the temperature of liquid nitrogen (77 K). It is

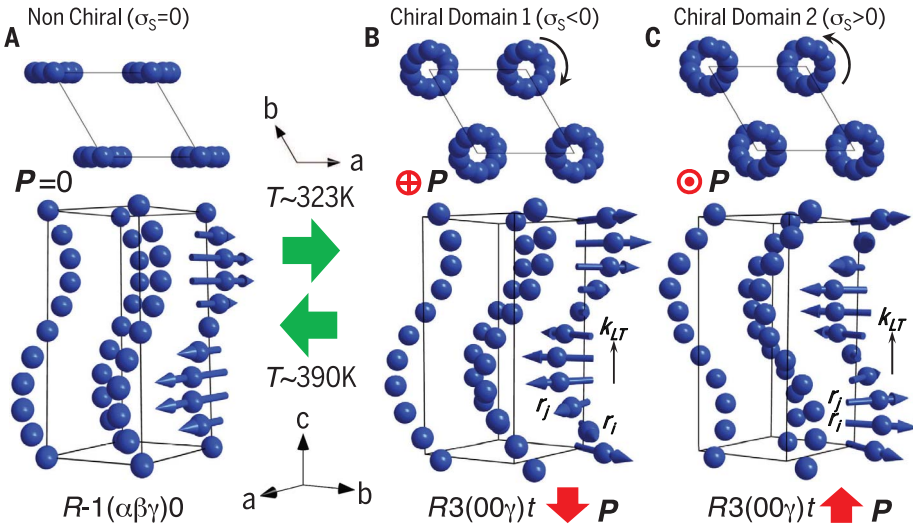


Fig. 2. Modulated atomic displacements. Schematic representation of the displacements of Bi in the (**A**) high-temperature nonchiral and (**B** and **C**) low-temperature chiral modulated phases of $BiCu_{0.1}Mn_{6.9}O_{12}$. Atoms related by *R*-centering are omitted for clarity. The black lines indicate an approximately commensurate supercell. The displacement directions are shown by arrows whose length is proportional to the magnitude of the displacement. In the chiral phase, two domains with opposite chirality, and hence opposite direction of the weak macroscopic polarization ***P***, are shown.

well known that standard *P-E* measurements can be compromised by factors unrelated to the intrinsic polarization switching, such as leakage currents (*32*). We therefore used the so-called positive-up-negative-down (PUND) method, which has been developed to distinguish true, intrinsic ferroelectric switching from artificial responses due to current leakage (*33*). The resultant *P-E* loop is consistent with the phenomenological prediction of weak improper ferroelectric polarization in the helical phase, with $|\boldsymbol{P}|$ being 4000 times smaller than the value of polarization estimated for the parent compound $BiMn_7O_{12}$ (*24*). ***P*** should, by symmetry, be directed along the *c* axis, although this could not be established for our polycrystalline samples. We note that the coexistence of ferroelectric and chiral orders is also known in smectic phases of liquid crystals with chiral molecules (*34*). These substances, however, are noncrystalline, with only directional order of anisotropically shaped molecules, giving substantially different underlying physics and materials properties.

In multiferroics, it has been shown that magnetic domains with different spin chirality can be controlled by external electric fields (*35*). By analogy, we predict that the structural chirality domains in $BiCu_{0.1}Mn_{6.9}O_{12}$ should also be controllable by an electric field, given that the polarization takes opposite directions in these domains (Fig. 2, B and C). If this controllability were to be confirmed by single-crystal or epitaxial thin films measurements, $BiCu_{0.1}Mn_{6.9}O_{12}$ would prove an unusual system in which structural chirality could be permanently switched by a static electric field. This effect would be essentially different from the electrogyration effect, in which the induced chirality has no associated hysteresis. Importantly, this functionality could be amenable to a variety of perspective applications based on materials properties associated with structural chirality (*36*, *37*), such as optical activity (a rotation of the polarization of linearly polarized light) and circular dichroism (differential absorption of left- and right-handed polarized light), particularly because the chiral phase in $BiCu_xMn_{7-x}O_{12}$ is stable up to temperatures well above room temperature.

One final question concerns the nature of orbital ordering in $BiCu_{0.1}Mn_{6.9}O_{12}$ and its relation to structural chirality. This can be established by inspecting the oxygen octahedra coordinating the B-site Mn ions in the different phases, given that differential occupancy of the e_g electronic orbitals produces unequal B-O distances within the BO_6 octahedra. The orbital state of Mn can be quantified using the mixing angle formalism proposed by Goodenough (*38*). The mixing angle θ defines an admixture between $3z^2$-r^2 and x^2-y^2 orbital states within an orbital plane, through the relation $\tan\theta = \sqrt{3}(d_{B\text{-}Oy} - d_{B\text{-}Oz})/(2d_{B\text{-}Ox} - d_{B\text{-}Oy} - d_{B\text{-}Oz})$, where $d_{B\text{-}O}$ are B-O bond lengths along *x*, *y*, or *z* direction of the local Cartesian coordinate system, as shown in Fig. 3, A to C, and E (in our analysis, we use oxygen-oxygen distances, $d_{O\text{-}O} = 2\langle d_{B\text{-}O}\rangle$, to reduce the experimental uncertainty).

As previously stated, the monoclinic phase just below T_{JT} adopts the $LaMnO_3$-type planar orbital ordering characterized by a commensurate pattern of BO_6 octahedral distortions, which gives close to fully polarized orbital states for all manganese ions (Fig. 3A). By comparison, in the triclinic DDW and the trigonal helical phases, the incommensurate atomic displacements modulate the BO_6 octahedral distortions giving rise to an incommensurate modulation of the orbital occupancy [i.e., an orbital density wave (ODW)]. The closely related quadruple perovskite $CaMn_7O_{12}$ also displays an ODW, with the orbital occupancy gradually changing between $3x^2$-r^2 and $3y^2$-r^2 along the modulation direction (*30*). In the triclinic modulated structure of $BiCu_{0.1}Mn_{6.9}O_{12}$, three out of the four symmetry-distinct Mn B-sites (Mn4, Mn5, and Mn6) display a $CaMn_7O_{12}$-type ODW (albeit in different directions) (Fig. 3B and fig. S4), whereas the Mn7 site maintains the fully polarized, unmodulated orbital state inherited from the higher-temperature monoclinic phase.

The ODW in the trigonal helical phase involves two symmetry-independent Mn B-sites, Mn2 and Mn3 (Fig. 3C and fig. S6). The latter is located on a threefold axis of symmetry, and the mixing angle θ for this site takes all values between 0° and 360° through the period of the modulation (Fig. 3, D and E). Therefore, the orbital state of the Mn3 continuously rotates in the orbital plane either clockwise or counterclockwise, following the rotation of the Bi displacements and giving rise to a chiral ODW (Fig. 3, E and F). The orbital occupancies on the Mn2 sites, which can be considered as triangular motifs interrelated by threefold symmetry, are also modulated and alternate between $3z^2$-r^2 and z^2-x^2 states (and the equivalent states obtained by threefold rotation). The phase of the modulation is not uniform on the triangle of sites, as it is in $CaMn_7O_{12}$, but instead differs by $\pm 2\pi/3$, also making the global Mn2 ODW chiral.

Thus, the orbital ordering in the hole-doped manganite $BiCu_{0.1}Mn_{6.9}O_{12}$ gradually evolves from the monoclinic $LaMnO_3$-type, commensurate phase with nearly fully polarized orbital states but disordered Bi displacements, to the incommensurate trigonal phase with chiral ODW and helical (chiral) Bi dipole displacements. The evolution takes place via an intermediate incommensurate triclinic phase combining the nonchiral Bi DDW and the nonchiral Mn ODW. This remarkable structural behavior can be interpreted as a competition between the two primary electronic instabilities, one related to the lone electron pair of Bi^{3+} and the other to the degeneracy of e_g electronic states of the octahedrally coordinated B-site Mn^{3+}—both requiring different types of structural distortions. The role of competition again underscores the analogy with magnetism, where the noncollinear spin textures appear as a result of competing exchange interactions. The apparent

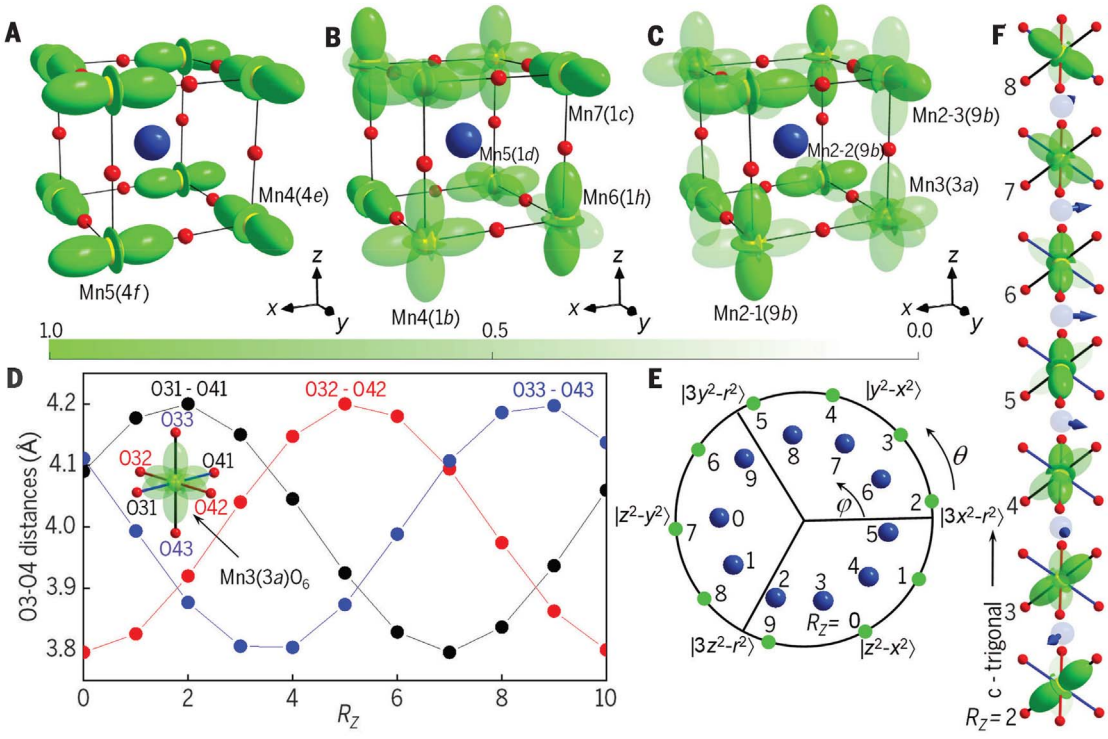


Fig. 3. Orbital ordering. Schematic representation of the B-site orbital patterns in the (**A**) monoclinic, (**B**) triclinic, and (**C**) trigonal phases of $BiCu_{0.1}Mn_{6.9}O_{12}$. For clarity, the patterns are shown relative to the familiar pseudocubic perovskite unit cell, whose edges are co-aligned with the Cartesian coordinate system (x, y, z) used to define the orbital states. In the triclinic (B) and trigonal (C) phases, the orbital ordering is incommensurate, and the orbital state of B-site Mn gradually changes upon propagation through the crystal. The probability of electronic occupancy for different orbitals, averaged over the modulation period, is represented by an "orbital density" (degree of transparency). In the triclinic structure, the orbital polarization changes between $|3x^2\text{-}r^2\rangle$ and $|3z^2\text{-}r^2\rangle$ for Mn4, $|3x^2\text{-}r^2\rangle$ and $|3y^2\text{-}r^2\rangle$ for Mn5, and $|3z^2\text{-}r^2\rangle$ and $|z^2\text{-}y^2\rangle$ for Mn6—a pattern that, on each site, is strongly reminiscent of $CaMn_7O_{12}$ (*30*). The Mn7 site adopts an unmodulated fully polarized $|3y^2\text{-}r^2\rangle$ state (see fig. S4 for more details). In the trigonal structure, the orbital occupancy of the Mn3 site changes between all three polarized states $|3x^2\text{-}r^2\rangle$, $|3y^2\text{-}r^2\rangle$, and $|3z^2\text{-}r^2\rangle$, making the orbital density wave chiral. The orbital polarization of the Mn2 sites in this structure changes between $|3z^2\text{-}r^2\rangle$ and $|z^2\text{-}x^2\rangle$ for Mn2-1, $|3x^2\text{-}r^2\rangle$ and $|y^2\text{-}x^2\rangle$ for Mn2-2, and $|3y^2\text{-}r^2\rangle$ and $|z^2\text{-}y^2\rangle$ for Mn2-3. In addition, the phase of the orbital modulation differs by $\pm 2/3\pi$ on these three symmetry-related sites (see fig. S5 for more details). (**D**) Oxygen-oxygen bond distances, used to characterize the anisotropy of the $Mn3O_6$ octahedra, as a function of the lattice translation $\boldsymbol{R}_Z$ along c axis in the trigonal phase. (**E**) Orbital states of the Mn3 site, defined by the mixing angle θ ($\tan\theta = \sqrt{3}[d_{032\text{-}042} - d_{033\text{-}043}]/[2d_{031\text{-}041} - d_{032\text{-}042} - d_{033\text{-}043}]$) (green circles), and the displacement of Bi in the ab plane, defined by angle φ (angle between the Bi displacement and projection of the x axis on the ab plane) (blue circles) for different values of the lattice translation $\boldsymbol{R}_Z$. To reduce the experimental uncertainty, we exploit the relation $d_{O\text{-}O} = 2\langle d_{B\text{-}O}\rangle$ for B-O bonds on either side of a given B site. (**F**) Chiral orbital density wave localized on the Mn3 site (transparency represents the probability of electronic occupation, with lower transparency corresponding to higher probability), and modulated displacements of Bi in the trigonal phase.

similarity between noncollinear electric and magnetic dipole orderings demonstrates that the formation of chiral incommensurate structures is a universal mechanism that allows a coexistence of competing degrees of freedom.

An immediate implication of the presently observed chiral electric dipole and orbital textures lies in our understanding of ferroelectric domain walls, whereby a growing number of experiments have shown that the ordering phenomenon in ferroelectric domain walls is far more complicated than previously believed (*39*–*42*). In this sense, the $BiCu_xMn_{7-x}O_{12}$ helical dipole phase can be thought of as the extended version of a ferroelectric Bloch domain boundary. In addition, by analogy with magnetism, more complex but closely related chiral objects such as electric skyrmions are likely to be feasible as well. The magnetic skyrmion lattice is often described as a multi-k phase represented by the superposition of three helical spin textures and induced from a single-k state by an external magnetic field (*43*). Electric skyrmions can be expected to also be stabilized by external stimuli or found in the domain boundaries of the $BiCu_xMn_{7-x}O_{12}$ helical phase where three single-k states merge together. Crucially, the formation of chiral electric dipole textures has previously been discussed only in the context of complex artificial nanostructures (*44*–*46*) or domain walls (*39*–*42*), with specific electrostatic boundary conditions or a delicate balance between electrostatic, elastic, and lattice-mismatch strain energies. Our work demonstrates a distinct approach to stabilizing these textures via competing electronic instabilities that is equally efficient for both bulk and low-dimensional structures. This perspective opens an additional dimensionality in the design of materials and suggests architectures for heterostructures, photonic crystals, and superlattices that combine traditional ingredients with components that comprise layers of chiral electric and orbital textures.

REFERENCES AND NOTES

1. J. Valasek, *Phys. Rev.* **19**, 478–491 (1922).
2. L. Néel, *Ann. Phys. (Paris)* **12**, 137–198 (1948).
3. C. G. Shull, J. S. Smart, *Phys. Rev.* **76**, 1256–1257 (1949).
4. C. Kittel, *Phys. Rev.* **82**, 729–732 (1951).
5. E. Sawaguchi, H. Maniwa, S. Hoshino, *Phys. Rev.* **83**, 1078 (1951).
6. W. C. Koehler, *J. Appl. Phys.* **32**, S20–S21 (1961).
7. W. C. Koehler, J. W. Cable, M. K. Wilkinson, E. O. Wollan, *Phys. Rev.* **151**, 414–424 (1966).
8. A. Yoshimori, *J. Phys. Soc. Jpn.* **14**, 807–821 (1959).
9. A. A. Belik *et al.*, *Inorg. Chem.* **56**, 12272–12281 (2017).
10. R. Seshadri, N. A. Hill, *Chem. Mater.* **13**, 2892–2899 (2001).
11. J. B. Neaton, C. Ederer, U. V. Waghmare, N. A. Spaldin, K. M. Rabe, *Phys. Rev. B* **71**, 014113 (2005).
12. A. A. Belik *et al.*, *Chem. Mater.* **18**, 798–803 (2006).
13. M. R. Suchomel *et al.*, *Chem. Mater.* **18**, 4987–4989 (2006).
14. J. Rodríguez-Carvajal *et al.*, *Phys. Rev. B* **57**, R3189–R3192 (1998).
15. W. A. Sławiński, H. Okamoto, H. Fjellvåg, *Acta Crystallogr. B* **73**, 313–320 (2017).
16. M. B. Salamon, M. Jaime, *Rev. Mod. Phys.* **73**, 583–628 (2001).
17. Y. Tokura, *Rep. Prog. Phys.* **69**, 797–851 (2006).

18. R. D. Johnson *et al*., *Phys. Rev. Lett.* **120**, 257202 (2018).
19. A. A. Belik, Y. Matsushita, D. D. Khalyavin, *Angew. Chem. Int. Ed.* **56**, 10423–10427 (2017).
20. See supplementary materials.
21. H. T. Stokes, D. M. Hatch, B. J. Campbell, ISOTROPY Software Suite; https://iso.byu.edu.
22. B. J. Campbell, H. T. Stokes, D. E. Tanner, D. M. Hatch, *J. Appl. Crystallogr.* **39**, 607–614 (2006).
23. V. Petricek, M. Dusek, L. Palatinus, *Z. Kristallogr. Cryst. Mater.* **229**, 345–352 (2014).
24. F. Mezzadri *et al*., *Phys. Rev. B* **79**, 100106 (2009).
25. A. Palewicz, I. Sosnowska, R. Przeniosło, A. W. Hewat, *Acta Phys. Pol. A* **117**, 296–301 (2010).
26. T. Kimura *et al*., *Nature* **426**, 55–58 (2003).
27. M. Kenzelmann *et al*., *Phys. Rev. Lett.* **95**, 087206 (2005).
28. M. Mostovoy, *Phys. Rev. Lett.* **96**, 067601 (2006).
29. R. D. Johnson *et al*., *Phys. Rev. Lett.* **108**, 067201 (2012).
30. N. J. Perks, R. D. Johnson, C. Martin, L. C. Chapon, P. G. Radaelli, *Nat. Commun.* **3**, 1277 (2012).
31. R. D. Johnson *et al*., *Phys. Rev. Lett.* **107**, 137205 (2011).
32. J. F. Scott, *J. Phys. Condens. Matter* **20**, 021001 (2008).
33. K. M. Rabe, M. Dawber, C. Lichtensteiger, C. H. Ahn, J.-M. Triscone, in *Physics of Ferroelectrics: A Modern Perspective*, K. M. Rabe, C. H. Ahn, J.-M. Triscone, Eds., vol. 105 of *Topics in Applied Physics* (Springer, 2007), pp. 1–30.
34. R. B. Meyer, L. Liebert, L. Strzelecki, P. Keller, *J. Physique Lett.* **36**, 69–71 (1975).
35. A. J. Hearmon *et al*., *Phys. Rev. Lett.* **108**, 237201 (2012).
36. P. Lodahl *et al*., *Nature* **541**, 473–480 (2017).
37. J. B. Pendry, *Science* **306**, 1353–1355 (2004).
38. J. B. Goodenough, *Magnetism and the Chemical Bond* (Interscience Publishers, John Wiley and Sons, 1963).
39. G. Catalan, J. Seidel, R. Ramesh, J. F. Scott, *Rev. Mod. Phys.* **84**, 119–156 (2012).
40. C. L. Jia, K. W. Urban, M. Alexe, D. Hesse, I. Vrejoiu, *Science* **331**, 1420–1423 (2011).
41. S. Cherifi-Hertel *et al*., *Nat. Commun.* **8**, 15768 (2017).
42. J.-Y. Chauleau *et al*., *Nat. Mater.* **19**, 386–390 (2020).
43. R. Takagi *et al*., *Sci. Adv.* **4**, eaau3402 (2018).
44. I. I. Naumov, L. Bellaiche, H. Fu, *Nature* **432**, 737–740 (2004).
45. A. K. Yadav *et al*., *Nature* **530**, 198–201 (2016).
46. S. Das *et al*., *Nature* **568**, 368–372 (2019).
47. D. D. Khalyavin *et al*., Experimental data for emergent helical texture of electric dipoles, Version 1, Zenodo (2020); https://doi.org/10.5281/zenodo.3749292.

ACKNOWLEDGMENTS

We thank Y. Katsuya, M. Tanaka, and Y. Matsushita of NIMS for their help with synchrotron x-ray and SEM data collections. The synchrotron radiation experiments were performed at SPring-8 with the approval of the NIMS Synchrotron X-ray Station (proposal numbers: 2016B4504 and 2017A4503). The authors also acknowledge the Science and Technology Facility Council for the provision of neutron beam time on the WISH instrument (RB1810030). **Funding:** R.D.J. acknowledges support from a Royal Society University Research Fellowship. A.A.B. acknowledges partial support from grant JPJ004596 (ATLA, Japan). **Author contributions:** D.D.K. and F.O. performed interpretation and refinement of the neutron and x-ray diffraction data collected by P.M. and A.A.B. at different facilities. R.D.J. and P.G.R. suggested the symmetry principles of coupling between structural chirality and macroscopic polarization and performed (*P-E*) measurements. A.A.B. developed the concept, carried out the materials synthesis, characterization, and physical property measurements. All authors contributed to the preparation of the manuscript and to discussion of the results. **Competing interests:** The authors declare no competing interests. **Data and materials availability:** The experimental data used in this study are available at Zenodo (*47*).

SUPPLEMENTARY MATERIALS

science.sciencemag.org/content/369/6504/680/suppl/DC1
Materials and Methods
Figs. S1 to S10
Tables S1 to S5
References (*48*–*50*)

17 July 2019; accepted 12 June 2020
10.1126/science.aay7356

FLUID MECHANICS

A new wrinkle on liquid sheets: Turning the mechanism of viscous bubble collapse upside down

Alexandros T. Oratis[1], John W. M. Bush[2], Howard A. Stone[3], James C. Bird[1]*

Viscous bubbles are prevalent in both natural and industrial settings. Their rupture and collapse may be accompanied by features typically associated with elastic sheets, including the development of radial wrinkles. Previous investigators concluded that the film weight is responsible for both the film collapse and wrinkling instability. Conversely, we show here experimentally that gravity plays a negligible role: The same collapse and wrinkling arise independently of the bubble's orientation. We found that surface tension drives the collapse and initiates a dynamic buckling instability. Because the film weight is irrelevant, our results suggest that wrinkling may likewise accompany the breakup of relatively small-scale, curved viscous and viscoelastic films, including those in the respiratory tract responsible for aerosol production from exhalation events.

Wrinkling of thin sheets appears in a variety of settings across a wide range of length scales, including those in neutrophil phagocytosis (*1*), in the development of the epithelial tissue responsible for fingerprints (*2*), and in subduction zones in plate tectonics (*3*). Generally speaking, sheets wrinkle because they require less energy to buckle than to compress when they are subjected to compressive stresses (*4*). Most recent studies have focused on understanding the bending deformations that occur when a thin elastic sheet is stretched (*5*, *6*), poked (*7*, *8*), or wrapped around a curved object (*9*, *10*); however, viscous liquids can also buckle (*11*–*13*). A visually prominent example is the "parachute instability" that develops spontaneously when a bubble rising in a viscous liquid reaches the surface and ruptures (Fig. 1). Bubbles collect at the surface of viscous liquids during processes including glass manufacturing, spray painting (*14*), vitrification of radioactive waste (*15*), and volcanic eruptions (*16*). Having surfaced, the bubble consists of a thin liquid film in the form of a spherical cap that is supported by the gas trapped inside it (Fig. 1A). When the bubble ruptures, the liquid film develops a growing hole that allows the trapped gas to escape. Without the support of this gas, the forces on the liquid film are unbalanced, causing bubble collapse and the development of radial wrinkles around the bubble periphery. Previous investigations have concluded that the wrinkles develop as a consequence of the weight of the collapsing thin film and the geometric constraint imposed by the opening hole (*17*, *18*). We demonstrate here that the wrinkling instability relies on neither gravity nor the presence of the hole.

The development of wrinkles from a collapsing bubble with radius R = 1 cm on a silicone oil bath with viscosity $\mu \approx 10^6$ cP is illustrated in Fig. 1B. The wrinkles emerged in an isolated annular region near the bubble's edge, when the bubble height Z reached a distance of approximately $Z/R \approx 0.6$ from the bath's surface. Before hole formation, the equilibrium shape of a bubble at the air–liquid interface is established by the balance between the pressure excess inside the bubble, ΔP, and a combination of gravitational and capillary forces (*19*). Because the bubble radius in this example is much larger than the capillary length $(\gamma/\rho g)^{1/2} \approx 1$ mm, where γ is the surface tension, ρ the liquid density, and g the acceleration due to gravity, the bubble extends substantially beyond the bath surface and forms a hemisphere. Gravity drives drainage in the thin hemispherical film, causing the bubble walls to thicken toward the base (*17*). Puncturing the film generates a hole and prompts the film retraction from the point of rupture, driven by surface tension and the local curvature of the hole's rim (*20*–*22*). In addition, puncturing the film equilibrates the pressure across the interface, causing $\Delta P \rightarrow 0$. The presence of the hole thus leaves the capillary and gravitational forces acting on the film unbalanced, ultimately causing the bubble collapse. Considering a surface element dA on the spherical cap, the gravitational force acting on the film thickness h scales as $F_g \sim \rho h g dA$, whereas the capillary force pulling the film inward scales as $F_c \sim (4\gamma/R)dA$ (Fig. 1A). For a centimeter-sized bubble with a characteristic thickness of $h \approx 10$ μm, capillary forces (F_c) dominate gravitational forces (F_g) by a factor of $F_c/F_g \sim 4\gamma/(\rho g R h) \approx 80$. This scaling argument indicates that the collapse process is dominated by surface tension rather than gravity.

To test this hypothesis, we conducted an identical experiment after turning the bubble upside down (Fig. 1C). The approach is possible because the liquid is sufficiently viscous that the experiments can be conducted before the silicone oil flows out of the inverted container. We first prepared the bubble right-side up, and then we rapidly rotated the sample and ruptured the bubble within seconds. When inverted, the bubble film (thickness $h \approx 2.4$ μm) maintained its shape and thickened at the

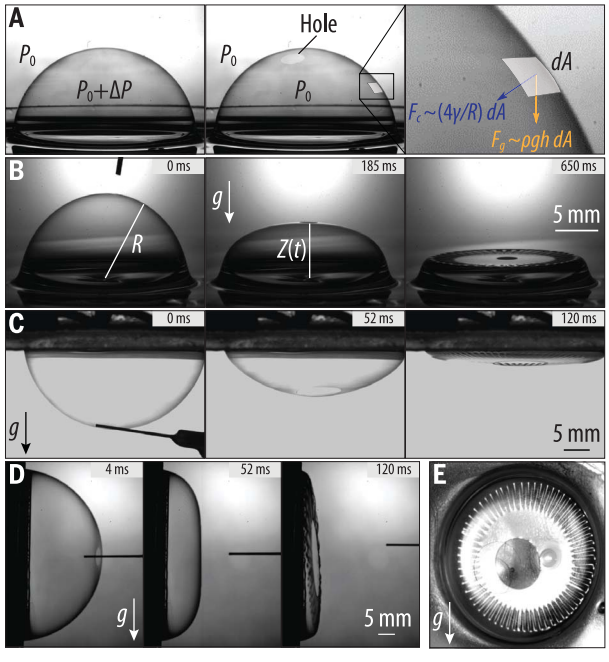


Fig. 1. Collapse of a viscous bubble film upon rupture. (**A**) If a hole develops in the surface of a bubble resting on a liquid surface, then the pressurized air escapes, leaving the gravitational and surface tension forces unbalanced. (**B**) An air bubble with radius R = 1 cm at the surface of a viscous silicone oil bath collapses and its height $Z(t)$ decreases after rupture. As the bubble collapses, wrinkles appear along its periphery. (**C**) When the bubble is rapidly turned upside down and ruptured, it collapses in a similar fashion. (**D** and **E**) Rotating the sample such that its base is parallel to the direction of gravity g results in a similar collapse (D) and wrinkles still appear (E).

[1]Department of Mechanical Engineering, Boston University, Boston, MA 02215, USA. [2]Department of Applied Mathematics, Massachusetts Institute of Technology, Cambridge, MA 02139, USA. [3]Department of Mechanical and Aerospace Engineering, Princeton University, Princeton, NJ 08544, USA.
*Corresponding author. Email: jbird@bu.edu

apex at a rate of ~10 nm/s; therefore, the film geometry does not vary appreciably during either the rotation or inversion (*23*). If gravity and viscosity were the dominant forces, then the inverted bubble would elongate downward, as previously demonstrated in simulations (*24*). Instead, the inverted bubble retracted upward against the force of gravity, and wrinkles formed again during the final stages of bubble collapse (Fig. 1C). The direction of motion clearly demonstrates that gravity does not drive the collapse; however, it does not rule out the possibility that it is involved in the wrinkles. By repeating the experiment with the bubble on its side (Fig. 1D), we found that wrinkles still appeared (Fig. 1E). We thus conclude that gravity plays a negligible role during bubble collapse and wrinkling instability.

To understand the extent to which surface tension drives bubble collapse, we measured the maximum distance of the bubble film $Z(t)$ from the bath surface. From the evolution of the bubble height with time, we can extract a collapse speed $V = dZ/dt$ that will dictate the characteristic time scale of collapse. If surface tension drives the collapse, then it would be expected that the speed would depend on the competing capillary and viscous forces. Indeed, balancing the capillary force γR with the viscous force $\mu h_0 V$ yields a characteristic velocity $V \sim \gamma R/\mu h_0$, where h_0 is the initial film thickness at the apex (*23*). Therefore, we expect the evolution of the bubble height Z and the associated collapse speed V to depend on both the viscosity and thickness of the film. We tested this conjecture through systematic experiments in which we used silicone oils with viscosities of 100, 800, and 3000 Pa • s and also varied the thickness of the film at rupture. Once punctured, the bubble collapsed, decelerating as it reached the bath surface (Fig. 2A). From the high-speed images, we calculated a representative velocity V at the onset of wrinkling by averaging the downward speed dZ/dt over the range $0.6 < Z/R < 1$ (*23*). Increasing the viscosity of the silicone oil slowed down the collapse. As expected, the data collapse when the normalized height Z/R is plotted against the dimensionless time Vt/R (Fig. 2A, inset).

To gain further insight, we determined the rupture thickness at the bubble apex, h_0, by combining optical techniques with the gravitational drainage theory of Debrégeas *et al.* (*17*). Under a monochromatic light, concentric interference fringes could be seen to emanate from the bubble's apex (Fig. 2B, inset). The circles are evidence of axisymmetric drainage, and the rate at which they appear can be measured with thin-film interferometry to estimate the thickness at the apex (*23*). Thinner bubbles collapsed faster (Fig. 2B), as expected from the predicted scaling $V \sim \gamma R/\mu h_0$ (solid line). We acknowledge sizable deviations of the experimental data from this simple scaling, especially for the 100 Pa • s silicone oil bubbles. Nevertheless, the overall trends support the hypothesis that the bubble collapse is driven by surface tension, in which case the characteristic time scale $R/V \sim \mu h_0/\gamma$ becomes independent of the bubble radius.

The model of da Silveira *et al.* (*18*) suggests that gravity and viscosity lead to wrinkling in such a way that the number of wrinkles scales as $n \sim (\rho g R_H^3 \tau_c/\mu h^2)^{1/2}$, with R_H being the radius of the hole and τ_c the time it takes for the film to collapse. The radius of the hole grows rapidly at early times but slows down sufficiently to be adequately modeled as a constant during the instability. This model thus claims that the number of wrinkles depends strongly on the size of the hole, with no wrinkles predicted if $R_H = 0$. To investigate the role of the hole in the development of wrinkles, we performed experiments by drilling a small opening at the bottom of the petri dish in which the silicone oil was placed. We inserted a narrow tube into the opening, injected air to create the bubble, and then sealed the opening with a valve. Once the bubble had reached the surface to create a hemispherical dome, we opened the valve to allow the pressurized air inside the bubble to escape. When the air escaped, $\Delta P \rightarrow 0$, causing the capillary force from the curved surface to be unbalanced and the bubble to collapse (Fig. 3A). Wrinkles again appeared at the final stages of the collapse, indicating that the hole plays a role in wrinkling only by eliminating the pressure difference across the bubble surface (Fig. 3B). We thus need to revisit the wrinkling dynamics to deduce a consistent physical picture for the wrinkling mechanism.

We propose a mechanism in which the wrinkles result when the crushing dynamics of the spherical film lead to a hoop compression that overcomes the smoothing effects of surface tension. Here, the capillary-driven collapse induces a radial velocity in a cylindrical reference frame that scales as $V_r \sim V \sim \gamma R/\mu h_0$ (Fig. 3A). This radial velocity leads to compression rates $\dot{\varepsilon}_{rr}$ and $\dot{\varepsilon}_{\theta\theta}$ in the radial and azimuthal directions, respectively, for the r,θ coordinate system defined in Fig. 3C. For a Newtonian fluid, this compression generates both a radial stress $\bar{\sigma}_{rr}$ and hoop stress $\bar{\sigma}_{\theta\theta}$, which can be related to the rate of radial compression through a Trouton model (*25*), yielding $\bar{\sigma}_{rr} \sim \bar{\sigma}_{\theta\theta} \sim 4\mu h V_r/R$ for a film with thickness h. Here, the overbar denotes that the 3D stress has been integrated over the thickness, leading to a 2D stress with dimensions of force per length. It follows from our scaling for V_r that $\bar{\sigma}_{rr} \sim \bar{\sigma}_{\theta\theta} \sim \gamma h/h_0$ when spatial variation in V_r is neglected. Thus, we expect the crushing kinematics to generate larger compressive stresses at an outer annulus (Fig. 3A, red ring) than at the center because of the larger local film thickness. Regardless of the source of these compressive stresses, surface tension imparts a tensile stress to the liquid sheet that acts to minimize the surface area (Fig. 3D). We believe that the competition of these tensile and compressive stresses is responsible for the location of the wrinkling pattern at a distance L from the center (Fig. 3B). Because the thickness profile is unknown, it is not possible to make a quantitative deduction of the stress field, as would be needed to predict the exact position of the wrinkling pattern. The sheet should remain smooth if surface tension exceeds the compressive stresses throughout the sheet. However, the presence of wrinkles indicates that at a sufficient distance from the center, the

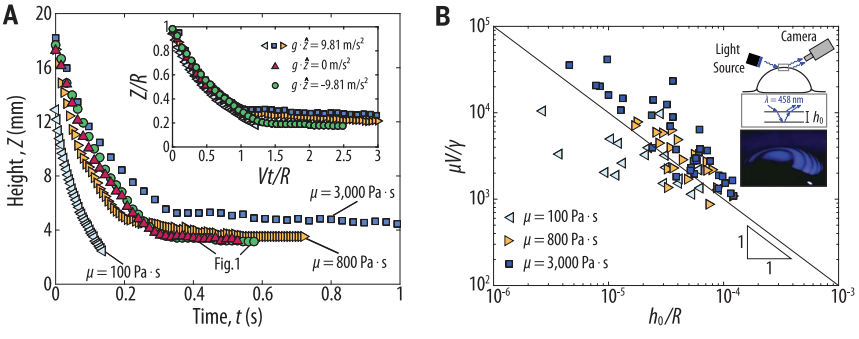


Fig. 2. Effect of bubble film thickness and viscosity on collapse dynamics. (**A**) Measured bubble heights Z versus time t for each orientation and viscosity μ. Inset: The normalized bubble heights Z/R fall onto the same curve when plotted against the dimensionless time Vt/R, highlighting the strong dependence of the collapse speed V on viscosity but not on gravity. (**B**) The collapse speed V is inversely proportional to the measured film thickness h_0, consistent with the notion that surface tension γ drives the collapse. In particular, the experimental results (symbols) suggest that $\mu V/\gamma = 0.1(h_0/R)^{-1}$ (solid line). Here, h_0 is the thickness at the bubble apex, which is estimated using thin-film interferometry (inset).

compressive stresses dominate those acting to keep the sheet smooth. This behavior is analogous to 1D viscous sheets buckling when the rate of compression is faster than the smoothing effect of surface tension (*11*, *13*). To sidestep the theoretical challenges posed by the thickness variation, we approximate the wrinkled region as an annulus of constant thickness h.

To model the development of the wrinkles, we deduced a dynamic version of the first Föppl–von Kármán equation (*23*, *26*, *27*), which describes the normal force balance along the sheet's center line $\zeta(r, \theta, t)$ as follows (Fig. 3D):

$$\rho h\frac{\partial^2\zeta}{\partial t^2}+\frac{\mu h^3}{3}\nabla^4\left(\frac{\partial\zeta}{\partial t}\right)-\bar{\sigma}_{rr}\frac{\partial^2\zeta}{\partial r^2}-\frac{1}{r^2}\bar{\sigma}_{\theta\theta}\left(\frac{\partial^2\zeta}{\partial\theta^2}+r\frac{\partial\zeta}{\partial r}\right)=2\gamma\nabla^2\zeta \quad (1)$$

where ∇^4 is the biharmonic operator and ∇^2 the Laplacian. Motivated by the observation of multiple radial wrinkles, we sought solutions of the form $\zeta(r, \theta, t) = f(r)\exp(\omega t + in\theta)$. Here, $f(r)$ determines the radial variation of the wrinkle amplitude, ω is the wrinkle growth rate, and n the number of wrinkles. In terms of these parameters, Eq. 1 becomes:

$$\left[\rho h\omega^2 f\right]+\left[\frac{\omega\mu h^3}{3}\left\{\frac{1}{r}\frac{d}{dr}\left(r\frac{d}{dr}\right)-\left(\frac{n^2}{r^2}\right)\right\}^2 f\right]-\left[(\bar{\sigma}_{rr}+2\gamma)\frac{d^2f}{dr^2}+(\bar{\sigma}_{\theta\theta}+2\gamma)\left(\frac{1}{r}\frac{d}{dr}-\frac{n^2}{r^2}\right)f\right]=0 \quad (2)$$

The three square-bracketed terms in Eq. 2 correspond, respectively, to inertia, bending, and compression. Given the high viscosity of the film, one might be tempted to neglect inertial effects. However, the rate of wrinkle development, ω^{-1}, is ~10 ms (Fig. 3E), sufficiently short for the inertial term to become non-negligible. Indeed, for a typical thickness $h \approx 10$ μm, we found the ratio of the inertial and radial compression terms to be of order $\rho h R^2\omega^2/\gamma \sim 1$, justifying the inclusion of inertia in Eq. 1.

When considering axisymmetric film effects, the radial stress $\bar{\sigma}_{rr}$ can have a pronounced role in wrinkling caused by the release of azimuthal stress $\bar{\sigma}_{\theta\theta}$ as the wrinkles develop (*6*). As the dominant stress changes from azimuthal to radial, the dependence on n in the dominant terms of Eq. 2 also changes. Scaling relationships for the growth rate ω and the number of wrinkles n can be obtained from a dominant balance. Specifically, the inertial term scales as $\rho h\omega^2$, the azimuthal bending as $\omega n^4\mu h^3/R^4$, and the radial stress component as γ/R^2. The simultaneous balance of these three dominant terms yields a growth rate $\omega^{-1} \sim \sqrt{\rho h R^2/\gamma}$ and the number of wrinkles $n \sim (2\gamma R^2/\omega\mu h^3)^{1/4}$, or equivalently:

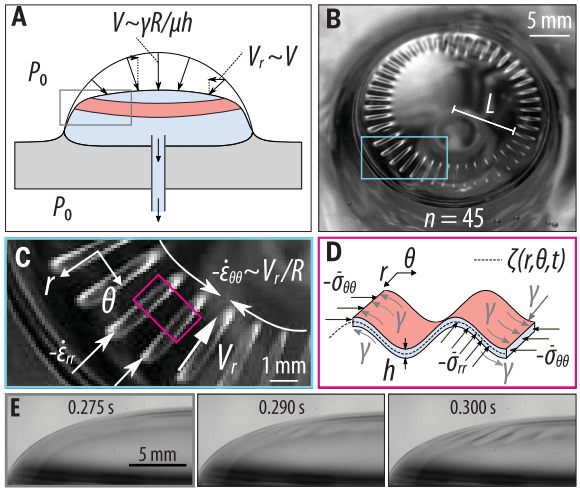


Fig. 3. Mechanism for bubble collapse without rupture. (**A**) Schematic illustrating the experimental setup used to collapse the bubble without rupture. As the bubble collapses, the viscous film obtains a radial velocity V_r proportional to the collapse speed V. (**B**) Wrinkles can still appear without the presence of the hole at a radial distance L from the center. (**C**) Near the periphery of the bubble, the radial and azimuthal compression rates, $\dot{\varepsilon}_{rr}$ and $\dot{\varepsilon}_{\theta\theta}$, respectively, can be related to the radial velocity V_r. (**D**) The azimuthal rate of compression leads to compressive stresses $\bar{\sigma}_{rr}$ and $\bar{\sigma}_{\theta\theta}$, which tend to bend the sheet's centerline $\zeta(r, \theta, t)$ despite being opposed by surface tension γ, which acts to smooth the surface. (**E**) As the bubble collapses, the wrinkles grow and develop within ~25 ms.

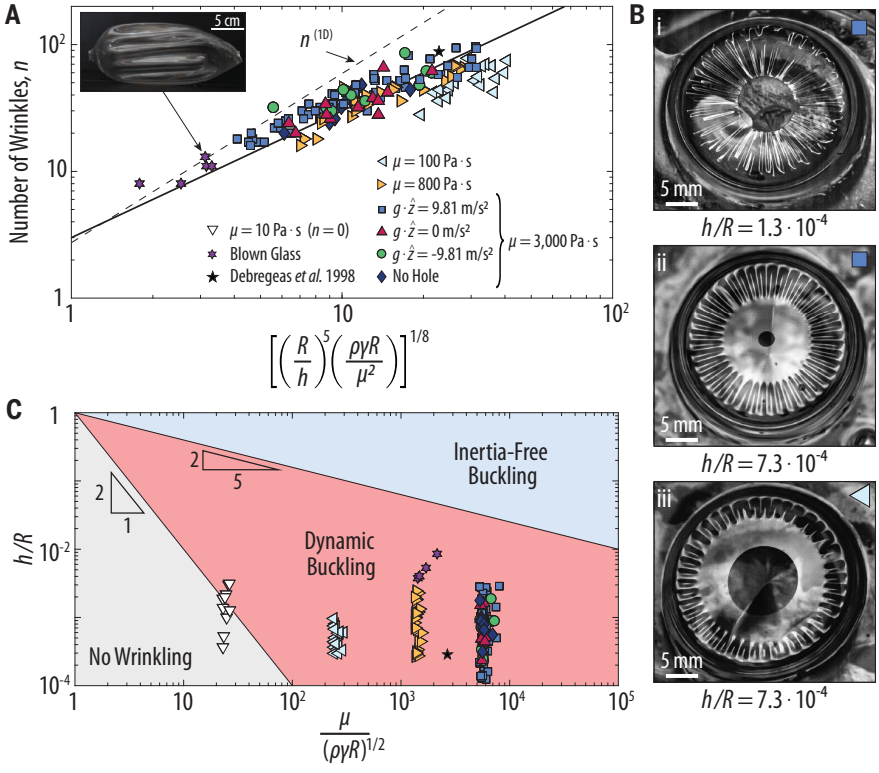


Fig. 4. Comparison of data and model predictions. (**A**) Number of wrinkles n observed on bubbles of various orientations and viscosities is in satisfactory agreement with the scaling of Eq. 3. Wrinkles on blown glass (inset) are also consistent with this trend, although the 1D hoop model (dashed line) is expected to be more appropriate for this nearly cylindrical geometry. (**B**) Top-view images of wrinkled films for: (**i**) viscosity μ = 3000 Pa • s and aspect ratio h/R = 1.3 • 10^{-4}, (**ii**) μ = 3000 Pa • s and h/R = 7.3 • 10^{-4}, and (**iii**) μ = 100 Pa • s and h/R = 7.3 • 10^{-4}. The radial extent of the wrinkles for the thinnest films is limited by the size of the hole, whereas the location L of wrinkles generally increases as the film viscosity decreases. (**C**) Our analysis predicts that inertia is negligible only when $\mu/\sqrt{\rho\gamma R} \gtrsim (R/h)^{5/2}$ (blue region). Because all available data (symbols) are outside of this regime, we incorporated inertial effects into our model. The analysis predicts that there is insufficient growth time for wrinkles to develop when $\mu/\sqrt{\rho\gamma R} \lesssim (R/h)^2$ (gray region), consistent with no wrinkles being observed at the lowest film viscosity (white triangles). Here, the thickness h is computed using the collapse speed V through the relation $h = \gamma R/\mu V$.

$$n \sim \left[\left(\frac{R}{h}\right)^5 \left(\frac{\rho\gamma R}{\mu^2}\right)\right]^{1/8} \quad (3)$$

To test the scaling of Eq. 3 for the number of wrinkles, we conducted systematic experiments in which we varied the bubble viscosity and orientation while keeping the bubble size confined to the range $0.8 < R < 2$ cm. We also repeated the experiments that involved evacuation rather than puncture of the bubble. We estimated the wrinkled film thickness h using the collapse time $R/V \equiv \mu h/\gamma$, which yields a result that is approximately an order of magnitude larger than the apex thickness h_0 (Fig. 2C). Furthermore, we performed additional experiments with thicker structures by extracting blown molten glass from a furnace and allowing the trapped air to escape through the glass-blowing pipe (*23*). As the air escaped, the blown glass collapsed and adopted a wrinkled shape with thickness $h \approx 200$ μm (Fig. 4A, inset).

The experimental results for the number of wrinkles are illustrated in Fig. 4A. Depending on the initial radius, thickness, and viscosity, the number of wrinkles can range between eight and 96. The experimental results (data points) are in fair agreement with our theoretical prediction (solid line) from Eq. 3. A limitation of our model applies to the data with the thinnest films. For these bubbles, the collapse was so abrupt that the wrinkling pattern lost its symmetry and the wrinkles spanned the entirety of the bubble (Fig. 4Bi). In addition, one should be cautious when interpreting the data for the 100 Pa • s bubble films given the discrepancy evident in Fig. 2B. This discrepancy may stem in part from variations in the thickness profile, which may explain the larger hole size and wrinkle location L observed at this lower viscosity (Fig. 4, Bii and Biii). Note that our analysis is based on the assumption that the wrinkle location L is proportional to the bubble radius and does not account for any dependence of L on film thickness or viscosity.

Our model assumes that the wrinkles develop on an axisymmetric portion of a spherical shell, which may be less appropriate for the blown glass. Specifically, because the molten glass was constantly rotated as it was worked into a thin film, the molten glass bubble (Fig. 4A, inset) assumed the form of a cylindrical shell with roughly hemispherical caps before collapse, and a wrinkled cylinder thereafter. For this case, in solving Eq. 2, we considered a hoop with radius R, where the amplitude f is approximately constant. This approach yields the 1D dynamic buckling dispersion relation $\rho h\omega^2 + \omega\mu h^3 n^4/3R^4 - \bar{\sigma}_{\theta\theta} n^2/R^2 = 0$ (*23*). Linear stability analysis revealed that the most unstable wrinkling pattern is then associated with a growth rate $\omega^{(1D)} \sim (\gamma^2/\rho\mu h^4)^{1/3}$ and a number of wrinkles $n^{(1D)} \sim [(R/h)^5(\rho\gamma R/\mu^2)]^{1/6}$, results analogous to those of Howell (*26*). Although the number of experiments performed with blown glass was insufficient to draw a definitive conclusion, we expect the 1D scaling (Fig. 4A, dotted line) to be more appropriate for this nearly cylindrical geometry. The 2D disk scaling of Eq. 3 is more convincing for all of the data involving the spherical cap bubble geometry.

A prediction of our model is that wrinkling will not occur for all conditions. In both the 1D and 2D scaling, inertia played a critical role in determining the number of wrinkles. Indeed, in both cases, inertia was relevant when $n > 1$, or equivalently $h/R < (\mu/\sqrt{\rho\gamma R})^{-2/5}$, a criterion satisfied by all of our data (Fig. 4C). For the 1D model, had inertia been neglected, the resulting buckled profile would be the equivalent of Euler buckling for a straight beam (*23*). Inertia also appears to dominate the instability growth rate ω: We found no evidence that the viscosity influenced this growth rate time, consistent with our model (*23*). For wrinkles to develop, the time scale for them to grow, $\sqrt{\rho h R^2/\gamma}$, must be less than that of collapse, $\mu h/\gamma$. We thus predict that no wrinkling will occur when $h/R < (\mu/\sqrt{\rho\gamma R})^{-2}$. To test this hypothesis, we ruptured bubbles formed from a silicone oil with viscosity $\mu = 10$ Pa • s (Fig. 4C, white triangles) and indeed found that they did not support any wrinkles.

We have demonstrated that surface tension rather than gravity drives the collapse of viscous surface bubbles after rupture and is likewise responsible for the parachute instability. The capillary-driven collapse initiates a dynamic buckling instability prescribed by the simultaneous interplay of inertia, compression, and viscous bending of the retracting film. Our results suggest that analogous wrinkling is likely to arise on relatively small, curved films, where the effects of gravity are entirely negligible. Equation 1, governing the number of wrinkles, is the viscous counterpart of the elastic Föppl–von Kármán equations used to study the deformation of elastic plates and shells. Our system thus presents an example of viscous sheets exhibiting elastic-like instabilities when rapidly compressed. On the basis of the similar roles played by viscosity and elasticity in these two systems, we can foresee extending our model to systems involving viscoelastic films, in which viscoelastic, capillary, and inertial effects all contribute to the dynamics. For instance, the exhalation of potentially pathogen-bearing aerosols has been linked to the breakup of thin bubble films in the viscoelastic fluid lining of the respiratory tract (*28*, *29*). Our deduction that surface tension alone may prompt buckling during viscous film rupture and retraction suggests the possibility of these films folding and entrapping air, thereby enriching the aerosolization process.

REFERENCES AND NOTES

1. M. B. Hallett, S. Dewitt, *Trends Cell Biol.* **17**, 209–214 (2007).
2. M. Kücken, A. C. Newell, *EPL* **68**, 141–146 (2004).
3. L. Mahadevan, R. Bendick, H. Liang, *Tectonics* **29**, n/a (2010).
4. D. P. Holmes, *Curr. Opin. Colloid Interface Sci.* **40**, 118–137 (2019).
5. J. Huang *et al*., *Science* **317**, 650–653 (2007).
6. B. Davidovitch, R. D. Schroll, D. Vella, M. Adda-Bedia, E. A. Cerda, *Proc. Natl. Acad. Sci. U.S.A.* **108**, 18227–18232 (2011).
7. D. Vella, A. Ajdari, A. Vaziri, A. Boudaoud, *Phys. Rev. Lett.* **107**, 174301 (2011).
8. D. Vella, J. Huang, N. Menon, T. P. Russell, B. Davidovitch, *Phys. Rev. Lett.* **114**, 014301 (2015).
9. H. King, R. D. Schroll, B. Davidovitch, N. Menon, *Proc. Natl. Acad. Sci. U.S.A.* **109**, 9716–9720 (2012).
10. J. Hure, B. Roman, J. Bico, *Phys. Rev. Lett.* **109**, 054302 (2012).
11. G. I. Taylor, in *Proceedings of the Twelfth International Congress of Applied Mechanics, Stanford, 1968* (Springer, 1969), pp. 382–388.
12. J. Teichman, L. Mahadevan, *J. Fluid Mech.* **478**, 71–80 (2003).
13. M. Le Merrer, D. Quéré, C. Clanet, *Phys. Rev. Lett.* **109**, 064502 (2012).
14. M. Kadoura, N. Saranjam, S. Chandra, H. Fan, *Prog. Org. Coat.* **99**, 452–462 (2016).
15. R. Pokorny *et al*., *J. Am. Ceram. Soc.* **98**, 3112–3118 (2015).
16. H. M. Gonnermann, M. Manga, *Annu. Rev. Fluid Mech.* **39**, 321–356 (2007).
17. G. Debrégeas, P.-G. de Gennes, F. Brochart-Wyart, *Science* **279**, 1704–1707 (1998).
18. R. da Silveira, S. Chaıeb, L. Mahadevan, *Science* **287**, 1468–1471 (2000).
19. Y. Toba, *J. Oceanogr. Soc. Jpn* **15**, 121–130 (1959).
20. F. Culick, *J. Appl. Phys.* **31**, 1128–1129 (1960).
21. G. Debrégeas, P. Martin, F. Brochard-Wyart, *Phys. Rev. Lett.* **75**, 3886–3889 (1995).
22. N. Savva, J. W. M. Bush, *J. Fluid Mech.* **626**, 211–240 (2009).
23. See the supplementary materials.
24. N. M. Ribe, *J. Fluid Mech.* **457**, 255–283 (2002).
25. F. T. Trouton, *Proc. R. Soc. London A Contain. Pap. Math. Phys. Character* **77**, 426–440 (1906).
26. P. D. Howell, *Eur. J. Appl. Math.* **7**, 321–343 (1996).
27. S. Bhattacharya, R. V. Craster, M. R. Flynn, *Phys. Fluids* **25**, 043102 (2013).
28. G. R. Johnson, L. Morawska, *J. Aerosol Med. Pulm. Drug Deliv.* **22**, 229–237 (2009).
29. J. B. Grotberg, *Phys. Fluids* **23**, 21301 (2011).

ACKNOWLEDGMENTS

We thank P. Houk for blowing the ultrathin glass bubbles and the referees who urged us to consider a 2D model, which we believe led to a substantially improved manuscript. **Funding:** This work was supported by National Science Foundation grant nos. 1004678 and 1351466 and Office of Naval Research grant no. N00014-16-1-3000. **Author contributions:** A.T.O., J.W.M.B., H.A.S., and J.C.B. designed the study. A.T.O. and J.C.B. conducted the experiments and acquired the data. A.T.O., J.W.M.B., H.A.S., and J.C.B. interpreted the data and proposed mechanical models. A.T.O., J.W.M.B., H.A.S., and J.C.B. contributed equally to the final version of the manuscript. **Competing interests:** The authors declare no competing interests. **Data and materials availability:** All data are available in the main text or the supplementary materials.

SUPPLEMENTARY MATERIALS

science.sciencemag.org/content/369/6504/685/suppl/DC1
Materials and Methods
Figs. S1 to S10
Table S1
References (*30*–*37*)
Movies S1 to S8
Experimental Data Files

12 November 2019; accepted 25 June 2020
10.1126/science.aba0593

METALLURGY

How hair deforms steel

Gianluca Roscioli[1], Seyedeh Mohadeseh Taheri-Mousavi[1,2], Cemal Cem Tasan[1]*

Steels for sharp edges or tools typically have martensitic microstructures, high carbide contents, and various coatings to exhibit high hardness and wear resistance. Yet they become practically unusable upon cutting much softer materials such as human hair, cheese, or potatoes. Despite this being an everyday observation, the underlying physical micromechanisms are poorly understood because of the structural complexity of the interacting materials and the complex boundary conditions of their co-deformation. To unravel this complexity, we carried out interrupted tests and in situ electron microscopy cutting experiments with two micromechanical testing setups. We investigated the findings analytically and numerically, revealing that the spatial variation of lath martensite structure plays the key role leading to a mixed-mode II-III cracking phenomenon before appreciable wear.

Humankind has optimized materials and processes to produce sharp edges for millennia, to be used as utensils (*1*), swords (*2*), blades (*3*), and other tools. Cutting processes today are routinely used in various industries, including medicine (*4*), manufacturing (*5*), food processing (*6*), and home appliances (*7*). Although each application creates specific engineering requirements, the overall material design aim is typically the same: achieving high sharpness and hardness. A typical metallic material used for blades in straight razors, for example, is a carbide-rich lath martensitic stainless steel, honed to a wedge geometry (*8*) with an angle of 17° and a tip radius of 40 nm to obtain the desired sharpness (*9*) (Fig. 1A). This material is coated with even harder materials (*10*) such as diamond-like carbon (*7*) and a final polytetrafluoroethylene layer to reduce friction (*11*, *12*). Even then, as commonly experienced by razor blade users, the hard lath martensitic steel progressively loses its functionality upon cutting hair, a material that is softer by more than one order of magnitude (hardness scale in Fig. 1A). Such material performance degradations are common in other cutting operations as well (*5*, *13*, *14*), creating operational and environmental consequences (*15*). Kitchen knives, for example, get dull (*16*, *17*) upon cutting soft materials such as cheese (*18*) or potatoes (*19*). As commonly practiced, resharpening resets the cutting capabilities of dull knives (*20*, *21*), creating the general conception that wear mechanisms are responsible for the performance degradation of sharp metallic edges, including martensitic steel razor blades (*22*).

Although wear does occur during haircutting (*5*, *23*, *24*), the failure mechanisms are more complex for two reasons. First, the two interacting materials have hierarchical microstructures with anisotropic and size-dependent mechanical responses (*25*, *26*) (Fig. 1A). Lath martensitic steels have a hierarchy (*27*) of prior-austenite, packet, block, subblock, and lath boundaries (*28*–*30*) (Fig. 1A) and a high density of heterogeneously distributed dislocations (*31*, *32*). Interstitial carbon is trapped in solid solution during quenching, but tempering or autotempering can lead carbon to decorate dislocations (*25*, *33*) or precipitate as carbides (*34*). All these structural features provide ferrous martensite with high hardness but a nonuniform micromechanical response (*35*–*37*). Similarly, human hair is a highly anisotropic composite with a noncircular cross section and an average diameter ranging between 80 and 200 μm. The outer layer is the ~170-MPa hard cuticle (*38*) that forms a shell with cells arranged like shingles on a roof (Fig. 1A). The middle layer, the cortex, is three times softer and composed of a hierarchy of fibrils elongated along the hair direction. The medulla is the hollow inner layer and has little mechanical contribution to the cutting response (*39*). Because hair is hygroscopic, in the presence of moisture its cell structure is altered to accommodate water molecules, lowering both elastic modulus and yield strength (*26*, *39*). Both the blade and the hair are anisotropic and exhibit size-dependent mechanical behavior. This generates a mechanical response that depends on the stress state and on the volume that contributes to deformation.

Second, the boundary conditions of their co-deformation can vary dynamically, even during a single cutting operation (Fig. 1B). During shaving, each single hair can be represented as a flexible cantilever, quasi-fixed at the end toward the skin and completely free at the other. In this configuration, the hair is free to bend when the blade approaches it and penetrates in it during the cut, influencing the mode of deformation (Fig. 1B). The hair is predominantly experiencing mode I opening. Depending on whether the hair is bending or not (Fig. 1B), the stress is applied (i) on both surfaces of the crack (straight indentation, $\gamma = 0°$) or (ii) only on one of the two surfaces. This results in a pure mode II stress on the blade in the former case or a mixed-mode II-III stress in the latter one. The geometry of the cutting problem further necessitates that, at different stages of cutting, different volumes of the two materials interact and contribute to the deformation process.

These complexities call for systematic experiments to investigate the interaction of the two materials. To this end, we investigated martensitic stainless steel blades (Fig. 1A) typical of commercial safety razors (fig. S1). Scanning electron microscope (SEM) and electron backscatter diffraction (EBSD) analyses revealed their lath martensitic matrix (Fig. 1A) with heterogeneously distributed carbides (Fig. 1A, inset). The honing process causes deformation of the microstructure within ~5 μm of the tip (*8*), as highlighted in the EBSD image quality (fig. S2F), kernel average misorientation (fig. S2D), and grain boundary maps (fig. S2E). We measured hardness values within 70 μm from the tip using an in situ SEM picoindenter and conducted nanoindentation experiments in the bulk material, revealing an average hardness value of 8.7 ± 0.7 (SD) GPa. This statistical variation can arise because of the presence of carbides, retained austenite, and martensite substructure heterogeneity (*25*, *27*–*32*, *40*). Edge effects prevented confirmation of a hardness increase near the tip implied by the deformed zone.

To measure blade wear evolution in real shaving conditions, we performed interrupted tests on disposable razor cartridges (sample 1 in fig. S1) by tracking different regions using SEM analyses after different stages of use (fig. S3 and movie S1). We quantified the average blade wear rate along the sharp edge using image analysis, although contamination-induced charging limits the accuracy of this method (fig. S3E). The level of wear was low: 12 nm^3/nm after 5 shaves and 13 nm^3/nm after 10 shaves. However, these interrupted tests revealed the occurrence of chips along the sharp edge (Fig. 1C). Although sharp at the macroscale, the edges of razor blades are asperous at the microscale, even in the unused condition (Fig. 1C-1). We observed that microcrack nucleation takes place from these asperities during haircutting (Fig. 1C-2). Only a small fraction of the asperities proceed to form microcracks, and these are not necessarily the largest asperities present along the edge. These microcracks initially propagate orthogonally to the edge (Fig. 1C-2) before deviating their direction to form the final chip geometry (Fig. 1C-3). The deformation marks (Fig. 1C-2) show that the portion of the sharp edge that belongs to the chip being

[1]Department of Materials Science and Engineering, Massachusetts Institute of Technology, 77 Massachusetts Avenue, Cambridge, MA 02139, USA. [2]Department of Mechanical Engineering, Massachusetts Institute of Technology, 77 Massachusetts Avenue, Cambridge, MA 02139, USA.
*Corresponding author. Email: tasan@mit.edu

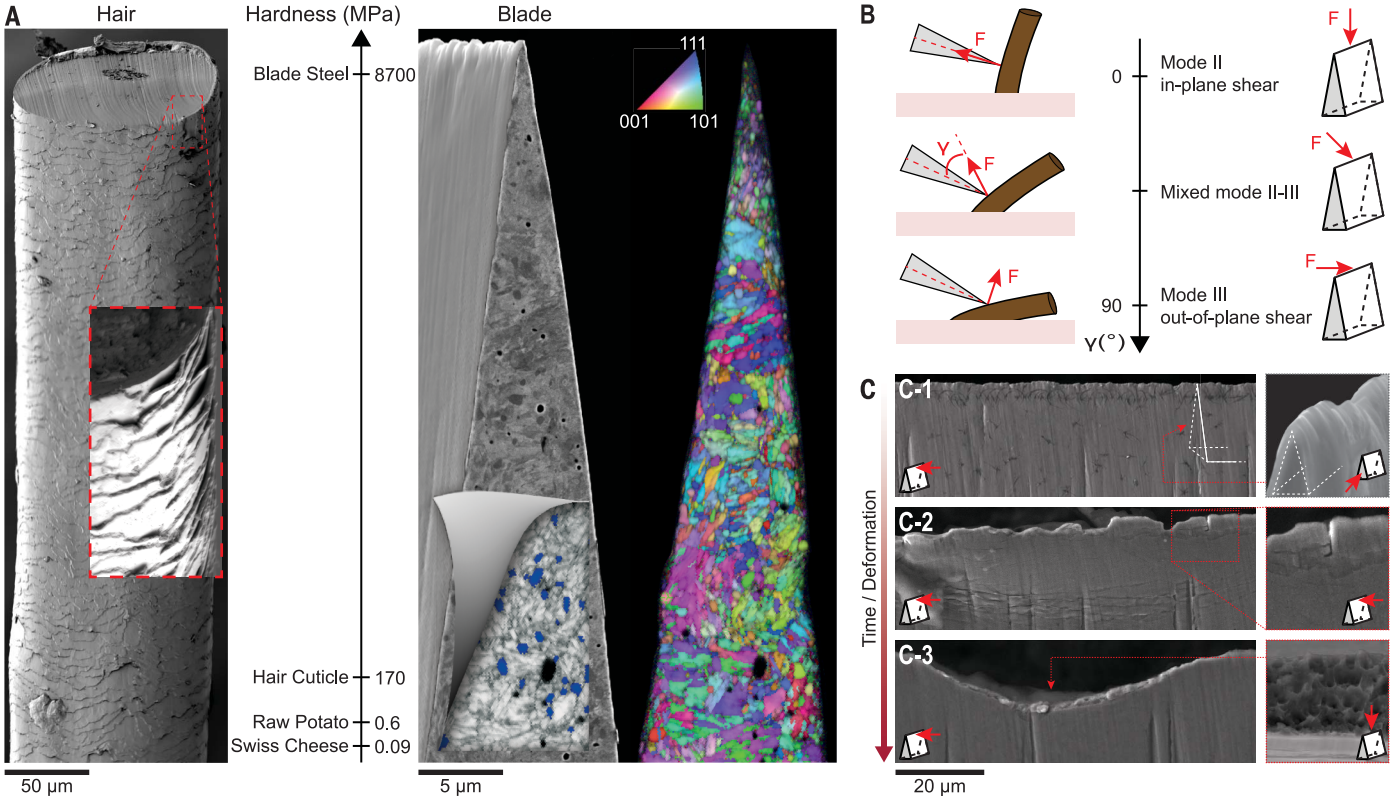


Fig. 1. Materials and mechanics of the shaving process. (**A**) Human hair and martensitic steel blades both have complex hierarchical structures. The former is a layered anisotropic material; meanwhile, the latter has a fine lath martensitic matrix structure (EBSD–Inverse Pole Figure map) with heterogeneously distributed carbides (highlighted in blue in the inset). As shown by the scale, the difference in the hardness of these two materials is substantial (~50 times). (**B**) Stress state on the blade during haircutting depends on the force angle γ, so that any configuration between pure in-plane and out-of-plane shear is possible. (**C**) Deformation sequence of a blade from unused conditions (C-1) to initial crack nucleation at the sharp edge and localized bending (C-2) to final ductile failure (C-3).

created rigidly bends out of plane as the microcrack changes direction. The presence of dimples on the resulting fracture surface reveals that the martensitic structure exhibits ductile deformation before fracture (Fig. 1C-3). The hard coatings, by contrast, exhibited brittle fracture features resulting from the bending of the substrate (fig. S4).

To better understand the development of this failure process before the activation of other failure modes (fatigue, corrosion, and wear), we carried out 25 in situ SEM tests using a microdeformation stage with customized clamps that can hold a blade on one side and single or multiple hair(s) on the other [Fig. 2, fig. S5, and movies S2 to S4, (*38*)]. Running in situ SEM tests enables expedited investigation of the underlying damage mechanisms, because the dry cutting conditions in the SEM should increase the haircutting force. Even then, we did not observe blade deformation or chipping for straight orthogonal cuts, in which there is no out-of-plane force component. By contrast, creating a more realistic condition by tilting the blade 21° to the cutting direction (Fig. 2B) led to an out-of-plane force component and, in turn, to plastic deformation and chipping in several cases (Fig. 2C and movie S2). Tests using hairs of different diameters allowed us to conclude that the size of the chips is not dominated by the diameter of the hair or the number of hairs sequentially cut, nor by the cutting angle alone. The same portion of a sharp edge can cut several hairs with different cutting angles γ (Fig. 1B), leading to no visible deformation, until the blade suddenly fails (fig. S6 and movie S3). We also discovered that the chips most commonly appear in correspondence to the edges of the hair. For example, one single hair can produce two chips in the blade, each of them starting from one edge of the hair (Fig. 2C). In addition, we observed that the chips generally extended beyond the ~5-µm highly deformed region near the tip of the blade (Fig. 1C), suggesting that the observed phenomenon is not dominated by honing-induced effects. Last, the comparison of the SEM images from the dry in situ experiments (Fig. 2C) and from the wet interrupted tests (Fig. 1C) reveals identical failure mechanism in both cases (except the increased failure rate in the former), confirming the validity of the expedited in situ approach.

We used three-dimensional parametric finite element simulations to identify the role of asperities and the direction of the applied load on deformation and chipping (Fig. 3, A to C). We modeled the martensitic steel as a homogeneous isotropic elasto-plastic material with a yield strength of ~1690 MPa and flow behavior as determined by our tensile tests (fig. S7). We added notches with a size determined by our SEM analyses (e.g., Fig. 1C-1) to replicate an extreme condition of the asperities along the sharp edge and simulated the cutting stress on the blade as an evenly distributed surface traction acting only on one side [Fig. 3A, (*38*)], with a magnitude of 50 MPa. To determine this value, we measured the force to cut a single hair by carrying out dedicated in situ SEM single-hair cutting-force measurements using a picoindenter, with tip and sample holder modified to host the blade on one side and a single hair on the other (Fig. 2, D to F). Representative results are shown in Fig. 2F and in movie S4, revealing a maximum value of ~0.2 N independent of hair diameter or cross-sectional shape (fig. S8).

Our first simulations focused on identifying the location of the highest stress intensity

notch, as a function of the direction of the applied stress. As seen in Fig. 3B, a straight indentation of the hair (surface traction of 0°) produces stress intensification at the notches in contact with the hair, but the values are not high enough to promote plastic deformation. Cutting the hair at an angle, instead, produces higher stress values in the region of the blade contacted by the hair, with a maximum stress at the notch in contact with the edge of the hair. Our analysis of the von Mises stresses as a function of the surface traction angle (Fig. 3C) showed that (i) the stress at the tip of the notches does not change substantially if the surface traction direction is contained in the blade cross section (for cutting angles below 8.5°); (ii) the stress at the tip of the notches in contact with the hair increases with the cutting angle for angles above this value; (iii) meanwhile, it decreases for notches not in contact with the hair; and (iv) the highest stress intensification occurs at the notch in contact with the edge of the hair. Our simulation results are consistent with the in situ SEM haircutting experiments (Fig. 2C), in which the chips preferentially nucleated at positions in contact with the edge of the hair.

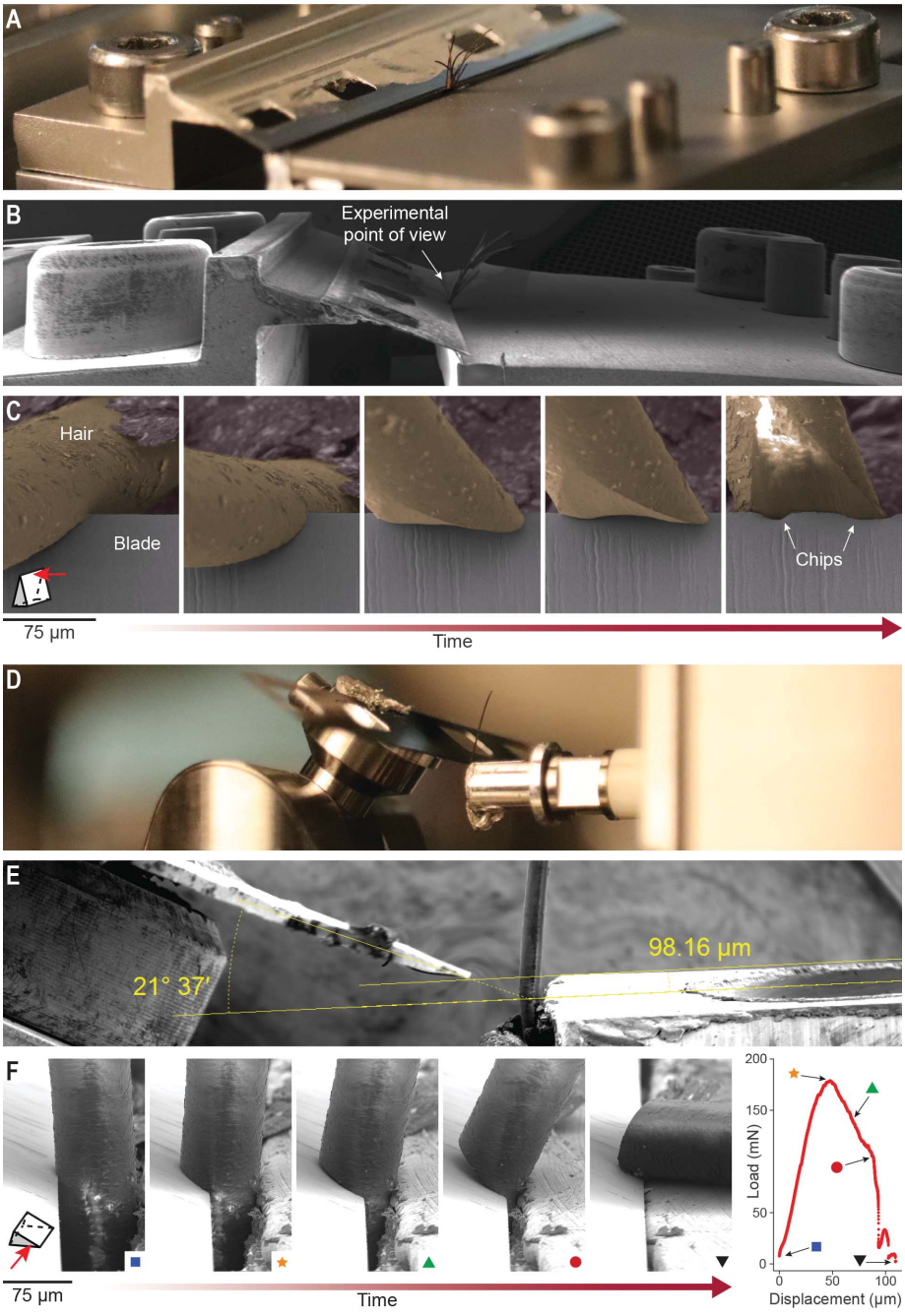


Fig. 2. Two sets of in situ SEM haircutting experiments. (**A** to **C**) Multihair cutting experiments to identify the underlying damage mechanisms. (A) and (B) show optical and SEM images of the experimental setup used to cut multiple hairs in situ; meanwhile, (C) provides a representative example of the results through a sequence of images (colored from movie S2) in which a single hair produces two chips in the blade. The waviness of the honing marks on the blade is an imaging artifact due to the blade advancing in a vertical direction during imaging. (**D** to **F**) Single-hair in situ SEM cutting-force measurements. (D) and (E) show optical and SEM images of the experimental setup; meanwhile, (E) provides a representative result through a sequence of experimental images corresponding to points highlighted in the load-displacement plot.

We observed microcracking and chipping at lower angles than those suggested in the simulations (fig. S6 and movie S3). To explain this, we hypothesized a process that links the heterogeneity of the lath martensitic structure to an increase in microcracking sensitivity (Fig. 3, D to H). We adapted an analytical model to calculate the energy release rate of an interfacial lateral crack in a thin, bimaterial, semi-infinite plate with constant thickness to our mixed-mode II-III problem, with the crack potentially propagating along the interface between the two materials [Fig. 3D, (*38*)]. We applied a 50-MPa stress while varying the direction of the load between pure mode II and pure mode III and considered materials with identical Poisson's ratio (0.3) but different Young's moduli. The small modulus variations we introduced follow the values we obtained from the continuous-stiffness-measurement mode nanoindentation experiments on the lath martensitic steel (fig. S9). The energy release rate increases when moving from pure mode II to pure mode III (Fig. 3D). Changing the Young's moduli of the two materials while keeping their average constant produces an upward shift of the energy release rate curve: A larger difference between the two moduli creates a greater shift (Fig. 3D). This corresponds to a higher probability of crack propagation for two dissimilar materials than for a homogeneous one with a similar average property.

We conducted another set of three-dimensional parametric simulations to analyze the energy release rate at the tip of a single notch in a blade, considering its wedge geometry with increasing thickness ahead of the notch and different crack propagation directions [Fig. 3, E to H; (*38*)]. We used a single or two different materials on the opposite sides of the notch. The energy release rate for a crack propagating along the original crack direction (θ = 0°) increases as the mode III component of the stress increases (Fig. 3F). The energy release rate also varies with the crack propagation direction (Fig. 3G). The critical direction, corresponding to the maximum energy release rate, depends on both loading direction and material combination (Fig. 3H). When the load is applied on a compliant

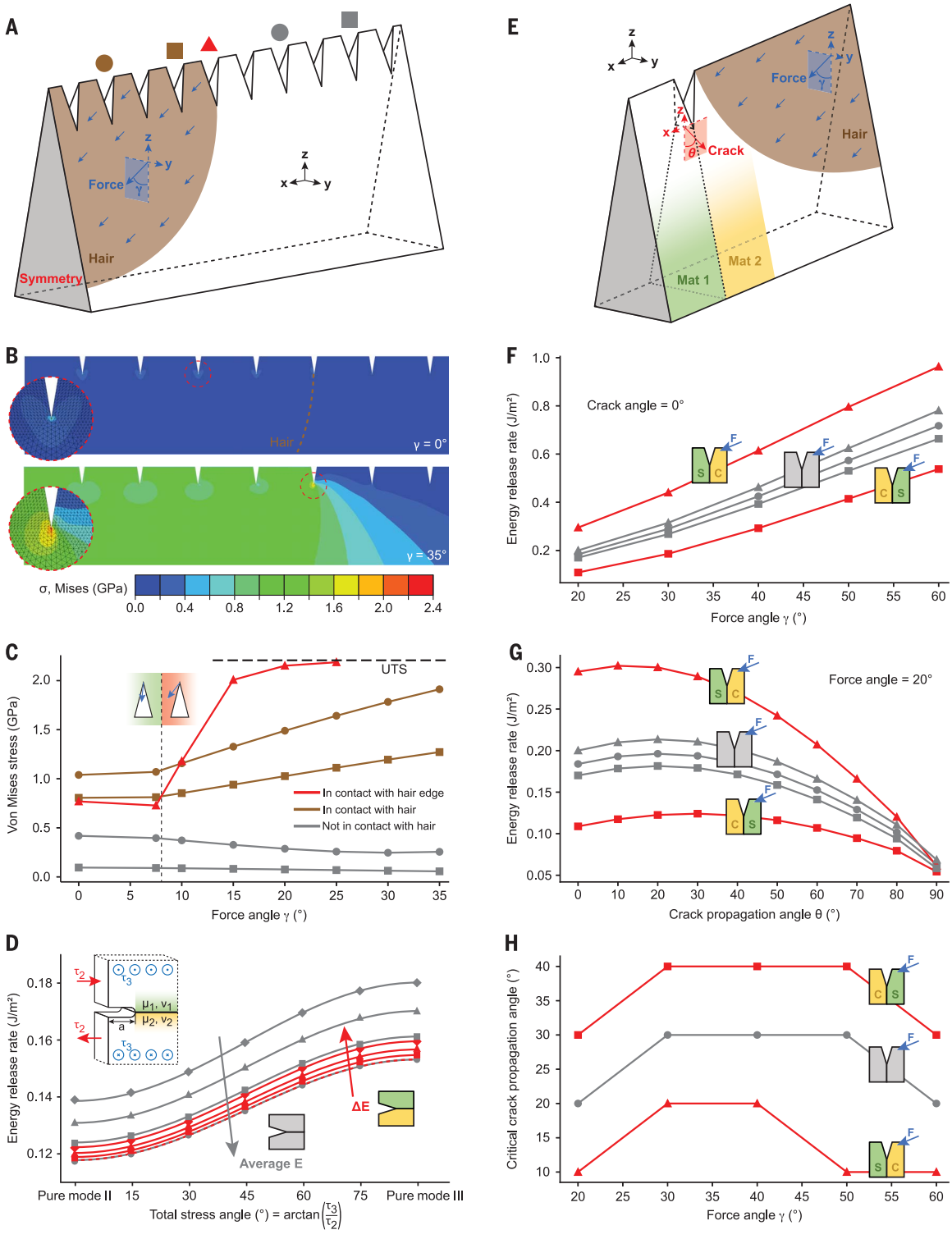


Fig. 3. Notch with critical stress intensification during haircutting, and energy release rate dependence on material heterogeneity and force angle. (**A**) Simulation model to identify the position of the notch with critical stress intensification as a function of the angle of the force imparted by the hair. The first four notches from the left are in contact with the hair, the fifth notch is in contact with the hair edge [brown dashed line in (B)], and the other notches are not in contact with the hair. (**B**) Von Mises stress distribution along the midplane of the blade resulting from a straight indentation (top) and a force oriented at 35° (bottom). (**C**) Plots of the von Mises stress evolution at the tip of selected notches as a function of the force angle γ, using the color code and marker shapes reported in (A). UTS, ultimate tensile strength. (**D**) Results of the analytical model (model in the inset) for a thin, bimaterial, semi-infinite plate with constant thickness and a lateral notch at the interface. E, Young's modulus. (**E** to **H**) Model (E) and results (F to H) of finite element simulations to determine energy release rate dependence on material (Mat) heterogeneity and force angle γ for a crack propagating from the notch with critical stress intensification (near the edge of the hair) along different possible crack propagation angles θ. In (D) and (F to H), gray and red curves represent homogeneous and heterogeneous materials, respectively. C, compliant (modulus of 170 GPa); F, force; S, stiff (modulus of 200 GPa).

material next to a stiff one (C and S in the schematic, respectively) with an interfacial notch, the crack is more likely to propagate than in the reversed configuration. The critical crack propagation angle in this situation is also smaller (Fig. 3G). Furthermore, the microcracks nucleated at the sharp edge propagate at an angle with respect to the blade axis (*z* axis in Fig. 3E), deviating toward the region of application of the load. This propagation path is determined both by the asymmetric mode II component of the force, which promotes crack kinking out of its original plane (*41*, *42*), and by the geometry of the blade, with a thickness increasing along

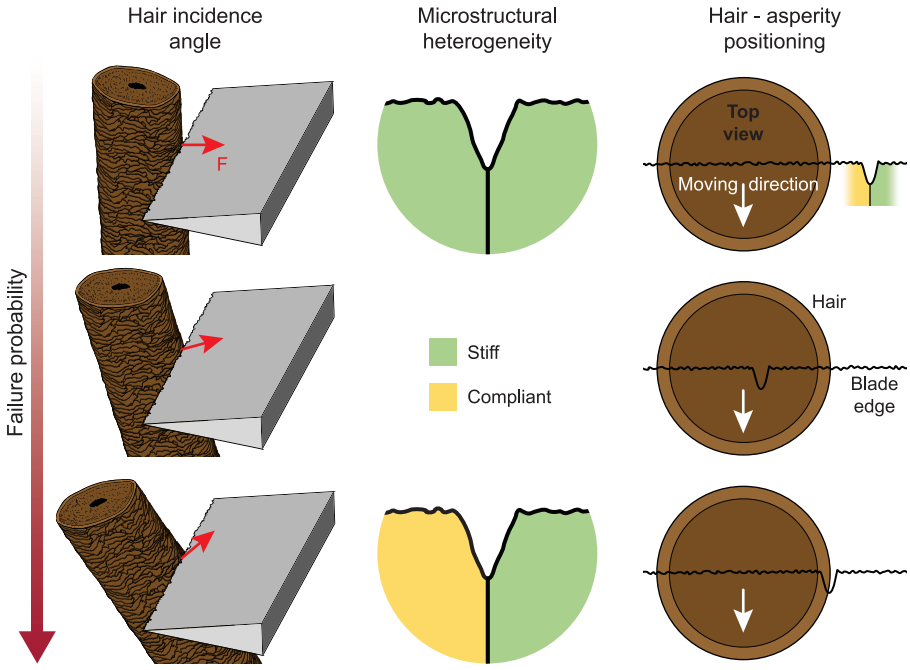


Fig. 4. Critical factors for lath martensite failure upon cutting hair. The three factors affecting razor blade chipping are shown from left to right: (i) hair incidence angle, (ii) heterogeneity present in the microstructure and at the asperities along the sharp edge, and (iii) relative position between an asperity and the edge of the hair when it is halfway through the cut. Failure probability depends on whether these conditions are simultaneously met.

the blade axis. Assuming that the surface energy of the material is constant, the energy penalty for the crack to stay along this axis is higher than it would be to propagate in a direction of constant (or less increasing) thickness, as staying along this axis would produce a larger surface per unit length of propagation. For the same reason, the crack will ultimately turn backward toward the sharp edge, forming a chip.

To confirm the mechanistic effects of microstructural heterogeneity predicted by our analytical and numerical results, we conducted in situ SEM haircutting experiments with focused ion beam half-milled blades, which enable visualization of the microstructure during deformation (fig. S10). The milling creates contrast between the martensitic matrix and the carbides, allowing us to unravel damage mechanisms. In this experiment, we observed that the microcracks typically nucleated (i) at martensite-carbide boundaries that neighbor an asperity (fig. S10B, left) and (ii) when the hair was in contact with the more compliant constituent. The microcracks then propagated at an angle, causing decohesion at multiple carbide-matrix boundaries or carbide cracking (fig. S10B, right), as well as microplasticity in martensitic regions in between.

With our experimental, analytical, and numerical results, we have shown that haircutting can induce damage nucleation, growth, and coalescence (in the form of chipping) in lath martensitic steel and that these occur before other proposed failure modes due to wear effects (*5*, *14*, *16*, *17*, *43*, *44*) or brittleness of the hard coatings (*5*, *24*, *43*, *45*). This failure process requires the concurrence of (i) sufficient levels of hair bending to create stresses with a considerable mode III component; (ii) processing-induced asperities on the blade edge with microstructural constituents of sufficiently different properties on either side; and (iii) positioning of the hair such that the outermost circumferential point is aligned with such an asperity (to produce the highest stress intensification) and in contact with the side containing the more compliant constituent (Fig. 4). Because these conditions are simultaneously met only in rare cases, hair-induced chipping is not common, and typical commercial blades fail only after multiple uses. The presence of multiple criteria also demonstrates why stand-alone postmortem or in situ analyses cannot reveal the full nature of this complex fracture process.

Current design philosophy for cutting tool materials follows the Archard law, which linearly correlates the average hardness of an annealed metal to its wear resistance. The failure recipe identified above suggests [along with wedge angle increase, which would be at the expense of the sharpness (*9*, *46*)] reconsideration of the microstructure design guidelines toward the reduction of asperities and microcracking tendencies, both of which arise as a result of structural heterogeneity. In case of fine lath martensite, several microstructural constituents of contrasting mechanical behavior can be larger than the blade tip radius (~40 nm) (Fig. 1A) (*25*, *27*–*32*, *35*). This creates spatial variation of mechanical properties along the sharp edge, with different constituents at different positions. This heterogeneity can be beneficial because a microcrack is less likely to propagate in a heterogeneous structure than in a homogeneous one as long as the hair being cut gets in contact with a stiff constituent neighboring a compliant constituent (Fig. 3F). However, this ideal scenario is impossible to guarantee during the haircutting process, and the opposite scenario favoring microcrack propagation is equally likely. Consequently, additional microcracks will form from carbide cracking or carbide-matrix decohesion, further opening as microvoids (*47*, *48*), coalescing, and eventually resulting in ductile failure (Fig. 1C-*3*). The heterogeneity in the blade also lowers the minimum force angle for a crack to propagate in the material. Given a critical value for the energy release rate, independent of the loading direction (*41*), a heterogeneous configuration at an asperity reaches this critical value for smaller force angles than a homogeneous one (Fig. 3F). The chip shape and size variations we observed are also linked to the heterogeneity of the material being cut (Fig. 3H). Both depend on the initial critical crack propagation angle for which the energy release rate is maximum. A large critical angle will lead to short, shallow chips, whereas a small critical angle will lead to longer and deeper chips. Asperity formation during processing is also linked to microstructure heterogeneity. For example, for the lath martensitic steel we tested, honing causes strain localization and carbide knockoff, resulting in a rough edge at the microscale. All of these insights suggest the design of hard but more homogeneous microstructures for cutting tools. This can be realized by creating even finer structures at sharp edges, for instance, by further refining martensitic structure, by creating other nanostructured alloys to benefit from size effects, or even by avoiding crystallinity altogether (*49*–*51*). The ability to produce more efficient and longer-lasting sharp edges would also have a favorable environmental impact by lengthening material lifetime, motivating further investigations.

REFERENCES AND NOTES

1. E. H. Cline, *The Oxford Handbook of the Bronze Age Aegean* (Oxford Univ. Press, 2012); www.oxfordhandbooks.com/view/10.1093/oxfordhb/9780199873609.001.0001/oxfordhb-9780199873609.
2. D. Sapiro, B. Webler, *JOM* **68**, 3180–3185 (2016).
3. J. D. Verhoeven, *Sci. Am.* **284**, 74–79 (2001).
4. D. Black, R. Marks, A. Caunt, *Bioeng. Skin* **1**, 111–123 (1985).

5. D. Petersen, R. Link, K. Budinski, *J. Test. Eval.* **25**, 226 (1997).
6. R. W. McGorry, P. C. Dowd, P. G. Dempsey, *Appl. Ergon.* **36**, 71–77 (2005).
7. G. E. Gregory, R. C. Hamby, *Surf. Eng.* **16**, 373–378 (2000).
8. W. I. Nissen, R. M. Atwater, Methods and apparatus for sharpening razor blades or similar cutting tools, U.S. Patent 3,461,616A (1966); https://patents.google.com/patent/US3461616.
9. C. T. McCarthy, M. Hussey, M. D. Gilchrist, *Eng. Fract. Mech.* **74**, 2205–2224 (2007).
10. R. L. Moore, *Thin Solid Films* **270**, 331–334 (1995).
11. C. J. Clipstone, S. Hahn, N. Sonnenberg, C. White, A. Zhuk, Razor blade technology, U.S. Patent 6,684,513B1 (2004); https://patents.google.com/patent/US6684513.
12. O. H. Claus *et al*., Razor blades, U.S. 9,079,321B2 (2015).
13. C. Arcona, T. A. Dow, *J. Mater. Sci.* **31**, 1327–1334 (1996).
14. G. Keturakis, V. Lisauskas, *Mater. Sci. Medzg.* **16**, 205–209 (2010).
15. U.S. Environmental Protection Agency (EPA), "Environmental Consumer's Handbook" (EPA, 1990); https://nepis.epa.gov/Exe/ZyPDF.cgi/2000URC7.PDF?Dockey=2000URC7.PDF.
16. J. Marsot, L. Claudon, M. Jacqmin, *Appl. Ergon.* **38**, 83–89 (2007).
17. S. Schuldt, G. Arnold, J. Kowalewski, Y. Schneider, H. Rohm, *J. Food Eng.* **188**, 13–20 (2016).
18. N. Vásquez *et al*., *J. Food Eng.* **219**, 8–15 (2018).
19. N. Özkan, H. Xin, X. D. Chen, *J. Food Sci.* **67**, 1814–1820 (2002).
20. O. Hallén, *Nature* **173**, 958 (1954).
21. J. Karltun, K. Vogel, M. Bergstrand, J. Eklund, *Appl. Ergon.* **56**, 92–100 (2016).
22. Q. Zhu, J. Li, J. Zhang, C. Shi, *J. Mater. Eng. Perform.* **28**, 4511–4521 (2019).
23. T. Tamaoki, A. Okada, K. Uemura, Y. Uno, *J. Japan Soc. Precis. Eng.* **79**, 950–954 (2013).
24. M. I. Mendelson, in *Ceramic Engineering and Science Proceedings*, vol. 22 (Loyola Marymount University, 2001), pp. 293–300.
25. L. Morsdorf, C. C. Tasan, D. Ponge, D. Raabe, *Acta Mater.* **95**, 366–377 (2015).
26. S. M. Thozhur, A. D. Crocombe, P. A. Smith, K. Cowley, N. Mullier, *J. Mater. Sci.* **41**, 1109–1121 (2006).
27. L. Qi, A. G. Khachaturyan, J. W. Morris Jr., *Acta Mater.* **76**, 23–39 (2014).
28. C. C. Kinney, K. R. Pytlewski, A. G. Khachaturyan, J. W. Morris Jr., *Acta Mater.* **69**, 372–385 (2014).
29. S. Morito, H. Saito, T. Ogawa, T. Furuhara, T. Maki, *ISIJ Int.* **45**, 91–94 (2005).
30. S. Morito, H. Tanaka, R. Konishi, T. Furuhara, T. Maki, *Acta Mater.* **51**, 1789–1799 (2003).
31. S. Morito, X. Huang, T. Furuhara, T. Maki, N. Hansen, *Acta Mater.* **54**, 5323–5331 (2006).
32. T. Ohmura, A. M. Minor, E. A. Stach, J. W. Morris, *J. Mater. Res.* **19**, 3626–3632 (2004).
33. C. Lerchbacher, S. Zinner, H. Leitner, *Micron* **43**, 818–826 (2012).
34. J. Zhang, L. Morsdorf, C. C. Tasan, *Mater. Charact.* **111**, 137–146 (2016).
35. L. Morsdorf *et al*., *Acta Mater.* **121**, 202–214 (2016).
36. A. Shibata, T. Nagoshi, M. Sone, S. Morito, Y. Higo, *Mater. Sci. Eng. A* **527**, 7538–7544 (2010).
37. T. Ohmura, K. Tsuzaki, S. Matsuoka, *Scr. Mater.* **45**, 889–894 (2001).
38. Materials and methods are available as supplementary materials.
39. B. Bhushan, C. LaTorre, in *Nanotribology and Nanomechanics*, B. Bhushan, Ed. (Springer, ed. 2, 2008), pp. 1325–1485.
40. J. W. Morris Jr., C. Kinney, K. Pytlewski, Y. Adachi, *Sci. Technol. Adv. Mater.* **14**, 014208 (2013).
41. J. Chang, J. Xu, Y. Mutoh, *Eng. Fract. Mech.* **73**, 1249–1263 (2006).
42. M. R. Ayatollahi, B. Saboori, *Eng. Fract. Mech.* **144**, 32–45 (2015).
43. K. G. Budinski, *Surface Engineering for Wear Resistance* (Prentice Hall, 2007).
44. C. T. McCarthy, M. Hussey, M. D. Gilchrist, *Key Eng. Mater.* **293–294**, 769–776 (2005).
45. Z. Su *et al*., *IOP Conf. Ser. Mater. Sci. Eng.* **472**, 12054 (2019).
46. C. T. McCarthy, A. N. Annaidh, M. D. Gilchrist, *Eng. Fract. Mech.* **77**, 437–451 (2010).
47. C. McVeigh, F. Vernerey, W. K. Liu, B. Moran, G. Olson, *J. Mech. Phys. Solids* **55**, 225–244 (2007).
48. S. C. O'Keeffe *et al*., *Acta Mater.* **82**, 503–510 (2015).
49. J. S.-C. Jang *et al*., *Intermetallics* **65**, 56–60 (2015).
50. J. P. Chu *et al*., *Sci. Rep.* **9**, 15558 (2019).
51. J. Yi, W. H. Wang, J. J. Lewandowski, *Adv. Eng. Mater.* **17**, 620–625 (2015).

ACKNOWLEDGMENTS

The authors gratefully acknowledge contributions of M. E. Wagner, A. Mijailovic, and all the members of the Tasan Group at Massachusetts Institute of Technology for their support and thoughtful discussions. **Funding:** The research is partially supported by several seed grants at MIT, which are gratefully acknowledged. **Author contributions:** C.C.T. designed the research and supervised the team. G.R. was the lead scientist of the study, designing and carrying out both experiments and simulations and analyzing the data. S.M.T.-M. provided guidance on the application of the analytical model and supervised the design of simulations. All authors contributed to the discussion of the results and the writing of the manuscript. **Competing interests:** The authors declare no competing interests. **Data and materials availability:** Main data of the research are provided in the paper and the supplementary materials. Auxiliary data are fully available upon request.

SUPPLEMENTARY MATERIALS

science.sciencemag.org/content/369/6504/689/suppl/DC1
Materials and Methods
Figs. S1 to S10
Movies S1 to S5
References (*52*–*61*)

17 January 2020; accepted 15 June 2020
10.1126/science.aba9490

SOLAR PHYSICS

Global maps of the magnetic field in the solar corona

Zihao Yang[1], Christian Bethge[2,3], Hui Tian[1,4]*, Steven Tomczyk[3]*, Richard Morton[5], Giulio Del Zanna[6], Scott W. McIntosh[3], Bidya Binay Karak[7], Sarah Gibson[3], Tanmoy Samanta[8,9], Jiansen He[1], Yajie Chen[1,10], Linghua Wang[1]

Understanding many physical processes in the solar atmosphere requires determination of the magnetic field in each atmospheric layer. However, direct measurements of the magnetic field in the Sun's corona are difficult to obtain. Using observations with the Coronal Multi-channel Polarimeter, we have determined the spatial distribution of the plasma density in the corona and the phase speed of the prevailing transverse magnetohydrodynamic waves within the plasma. We combined these measurements to map the plane-of-sky component of the global coronal magnetic field. The derived field strengths in the corona, from 1.05 to 1.35 solar radii, are mostly 1 to 4 gauss. Our results demonstrate the capability of imaging spectroscopy in coronal magnetic field diagnostics.

The solar atmosphere is shaped by its magnetic field. Because of magnetic coupling between the various atmospheric layers, understanding many physical processes in the solar atmosphere requires information on the magnetic field of the whole atmosphere. However, only limited measurements are available for the magnetic field in the upper solar atmosphere, especially in the outermost atmospheric layer, the corona (*1*).

Information on the magnetic field at the solar surface is usually obtained through the Zeeman effect, the splitting of spectral lines in the presence of a magnetic field. However, it is difficult to use this method to measure the coronal magnetic field, mainly because of the negligible line splitting induced by the much weaker magnetic field in the corona. A few attempts have been made to measure the coronal magnetic field using the Zeeman effect, but only in small regions where a strong field is present (*2*, *3*). Spectro-polarimetric measurements can also determine the local coronal magnetic field in some cool loop–like structures or prominences (e.g., *4*, *5*). Coronal magnetic field strengths can be inferred from observations of waves and oscillations, although most previous studies only provided an estimate of the average field strengths in individual oscillating structures (e.g., *6*–*9*). Observations of shocks driven by solar eruptions can also be used to infer coronal magnetic field strengths along the shock paths (e.g., *10*, *11*) but such shocks are only occasionally observed. Radio observations have also been used to estimate the coronal magnetic field but only in localized regions (e.g., *12*, *13*); this method often requires accurate identification of the radio-emission mechanisms, which are not always clear. Because of the observational difficulties with each of these methods, no routine measurements of the global coronal magnetic field are available.

We used the Coronal Multi-channel Polarimeter (CoMP) (*14*) to observe the corona outside the whole disk of the Sun on 14 October 2016. The CoMP data included spectral profiles of the Fe XIII lines at 1074.7 and 1079.8 nm in the corona from 1.05 to 1.35 solar radii (*15*). We fitted each line profile with a gaussian function to obtain the line intensity and Doppler velocity at each pixel within the CoMP field of view (FOV) (*16*). Figure 1, B and C, shows the intensity images of these two lines averaged over the period of 19:24 to 20:17 UT. For comparison, Fig. 1A shows a simultaneous coronal image in the Fe XII 19.3-nm channel of the Atmospheric Imaging Assembly (AIA) (*17*) on the Solar Dynamics Observatory (SDO) spacecraft. The intensity ratio of the two Fe XIII lines (Fig. 1D) is sensitive to the electron density, allowing us to derive (*15*) a global map of the coronal electron density (Fig. 1E). The measured electron number density is mostly in the range of $10^{7.5}$ to $10^{8.5}$ cm^{-3}. The associated uncertainties, which arise from both the statistical measurement uncertainties and the systematic uncertainties in the atomic physics parameters used to calculate the relationship between electron density and line ratio (*15*), were mostly 10 to 25% (Fig. 1F). Assuming a standard coronal elemental abundance and electrical neutrality, the corresponding total mass density (ρ) was calculated as $\rho = 1.2 N_e m_P$, where m_P is the mass of a proton (*18*).

Previous CoMP observations have found propagating periodic disturbances in the Doppler velocity of Fe XIII 1074.7 nm, indicating the ubiquitous presence of transverse magnetohydrodynamic (MHD) waves in the corona (e.g., *19*-*22*). A wave-tracking technique has previously been developed to track the propagation of the Doppler velocity perturbation and to calculate the phase speed of the transverse wave along its propagation path (*20*). Similarly pervasive velocity fluctuations also appear in our dataset (movie S1). We applied a modified version of the wave-tracking technique (*15*) to the Doppler velocity image sequence of Fe XIII 1074.7 nm during the time period of 20:39 to 21:26 UT and calculated the wave phase speed and measurement uncertainty (*15*) at each pixel within the FOV (Fig. 2). The phase speed mostly fell in the range of 300 to 700 km s^{-1}, and the associated uncertainty was generally smaller than 40 km s^{-1}.

We identified the observed transverse MHD waves as kink waves, which have an Alfvénic nature (e.g., *8*, *23*-*26*). The phase speed (kink speed), c_k, can be expressed as follows (*27*):

$$c_k^2 = \frac{B_i^2 + B_o^2}{\mu_0(\rho_i + \rho_o)} \quad (1)$$

where μ_0 is the magnetic permeability of a vacuum, B is the magnetic field strength, ρ is the mass density, and the subscripts i and o indicate physical parameters inside and outside the wave-guiding magnetic field structures (flux tubes), respectively. In the coronal plasma environment, the pressure balance across flux tubes is dominated by the magnetic pressure, so $B_i \sim B_o$ [see, e.g., (*20*), (*21*), and (*26*)]. Because individual flux tubes are likely unresolved at the spatial resolution of CoMP (~7000 km), we used the density averaged inside and outside flux tubes (ρ) within each spatial pixel and estimated the magnetic field strength using the following equation (*21*, *26*, *28*):

$$c_k = \frac{B}{\sqrt{\mu_0 \rho}} \quad (2)$$

Our measurements are based on spectral profiles that result from an integration of the spectral line emissivity (the released energy per unit time per unit volume during an electron transition from a higher energy level to a lower one, increasing with density) along the line of sight (LOS). The derived density, phase speed, and magnetic field strength are therefore all weighted by the emissivity along the LOS. Because the density generally decreases with distance from the solar limb, LOS weighting favors magnetic structures in the vicinity of the plane of sky (POS), i.e., the plane passing through the center of the Sun and perpendicular to the LOS. We expect the phase speed measured from the data to correspond to the kink speed projected onto the POS. If we further approximate the

[1]School of Earth and Space Sciences, Peking University, Beijing 100871, People's Republic of China. [2]Universities Space Research Association, Huntsville, AL 35805, USA. [3]High Altitude Observatory, National Center for Atmospheric Research, Boulder, CO 80307, USA. [4]Key Laboratory of Solar Activity, National Astronomical Observatories, Chinese Academy of Sciences, Beijing 100012, People's Republic of China. [5]Department of Mathematics, Physics and Electrical Engineering, Northumbria University, Newcastle Upon Tyne NE1 8ST, UK. [6]Department of Applied Mathematics and Theoretical Physics, Centre for Mathematical Sciences, University of Cambridge, Cambridge CB3 0WA, UK. [7]Department of Physics, Indian Institute of Technology (Banaras Hindu University), Varanasi 221005, India. [8]Department of Physics and Astronomy, George Mason University, Fairfax, VA 22030, USA. [9]Johns Hopkins University Applied Physics Laboratory, Laurel, MD 20723, USA. [10]Max Planck Institute for Solar System Research, 37077 Göttingen, Germany.
*Corresponding author. Email: huitian@pku.edu.cn (H.T.); tomczyk@ucar.edu (S.T.)

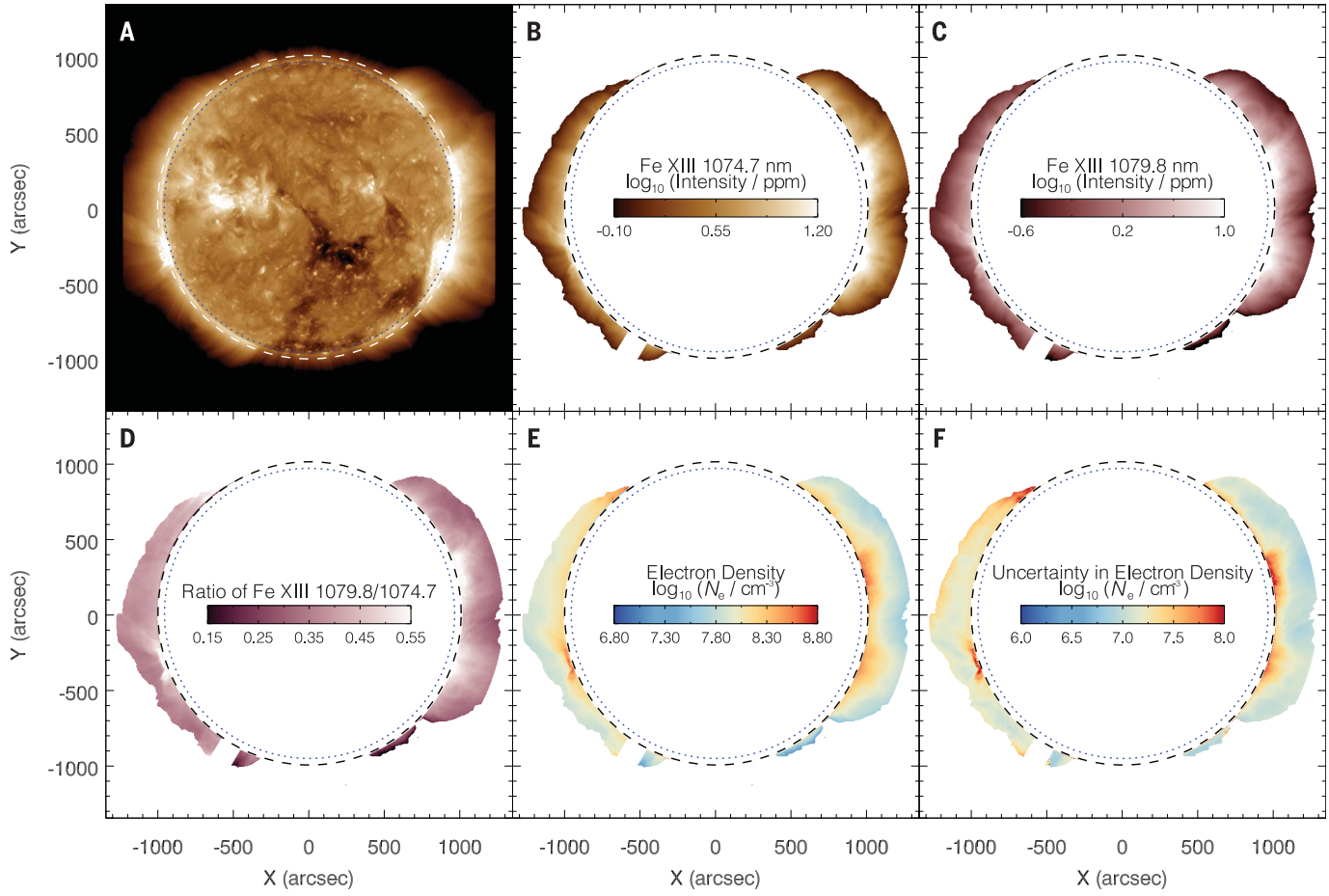


Fig. 1. Images of the solar corona and density diagnostic results. (**A**) AIA 19.3-nm intensity image taken at 19:25:55 UT on 14 October 2016. (**B** and **C**) CoMP Fe XIII 1074.7-nm and 1079.8-nm peak intensity images averaged over the time period of 19:24 to 20:17 UT on 14 October 2016 expressed as parts per million (ppm) of the solar disk intensity and plotted on a logarithmic color scale. (**D**) Map of the 1079.8-nm/1074.7-nm intensity ratio. (**E** and **F**) Maps of the derived electron density and associated uncertainty. In all panels, the dotted circle marks the edge of the solar disk (limb) and the dashed circle indicates the inner boundary of the CoMP FOV. The *x* and *y* coordinates are positions in the east–west and south–north directions, respectively, measured from the center of the solar disk.

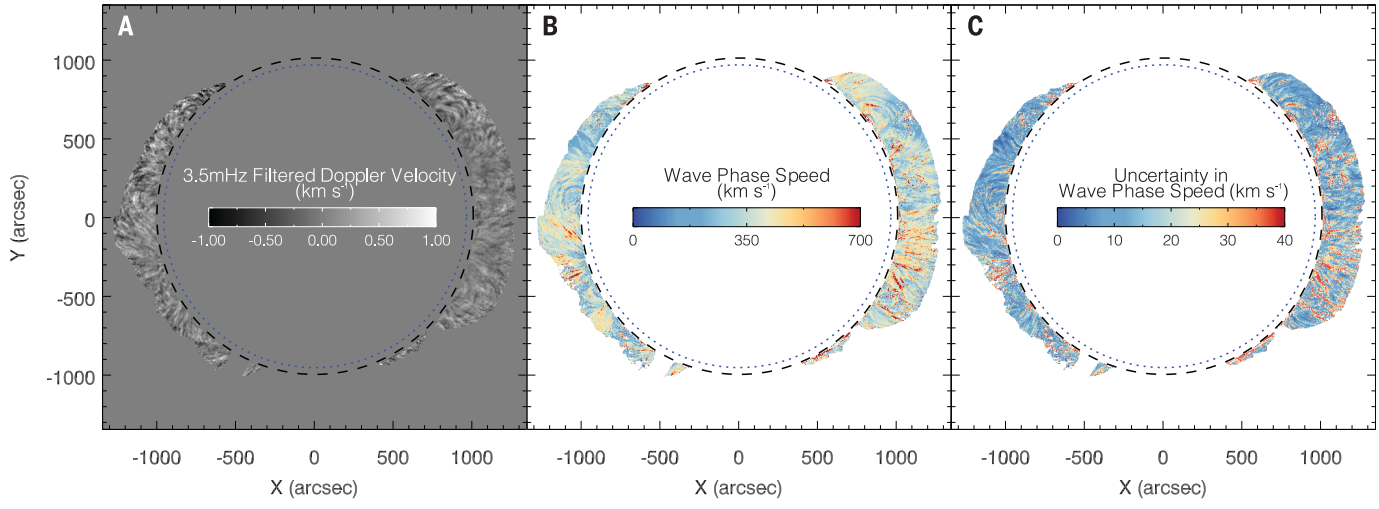


Fig. 2. Doppler velocity and wave-tracking results. (**A**) Map of the Doppler velocity of the Fe XIII 1074.7-nm line at 20:39:09 UT. A 3.5-mHz gaussian filter has been applied to the Doppler shift image sequence (*15*). Movie S1 shows an animated version of this panel. (**B** and **C**) Maps of the derived wave phase speed and associated uncertainty. The circles are as in Fig. 1.

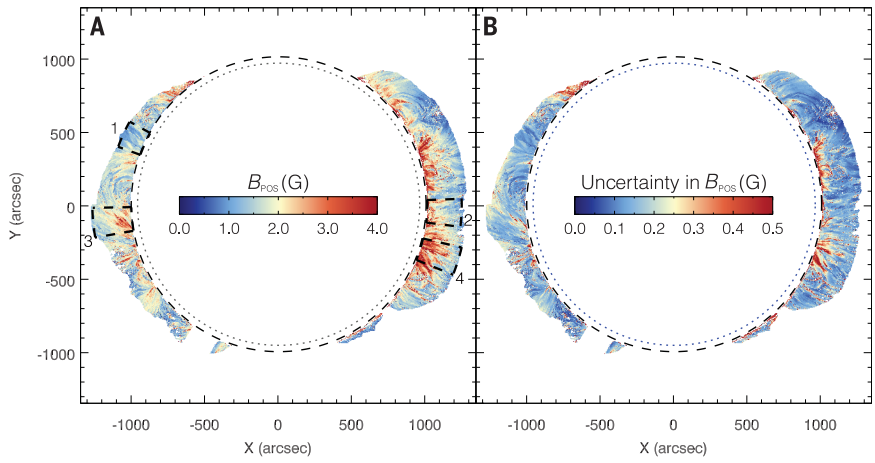


Fig. 3. Maps of the coronal magnetic field derived from observations. (**A**) Map of B_{POS}. The four numbered black annulus sectors indicate the regions used for Fig. 4, C to F. (**B**) Map of the associated uncertainty. The circles are as in Fig. 1.

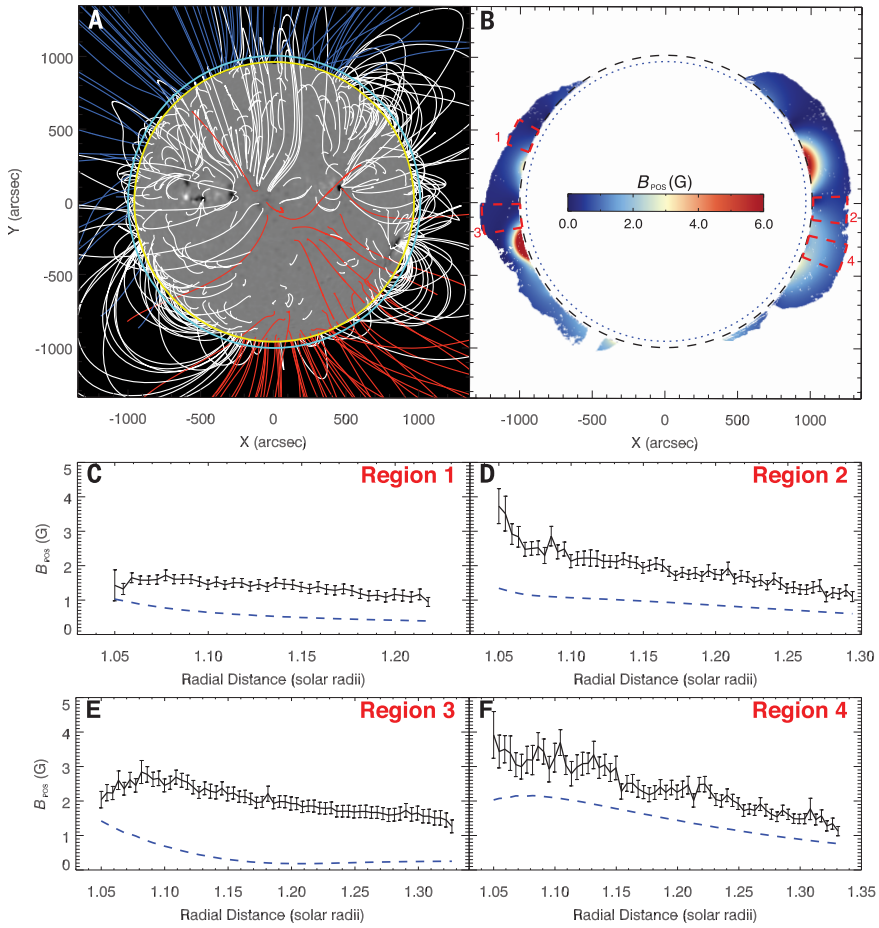


Fig. 4. Comparison between the coronal magnetic field derived from observations and that extrapolated using the PFSS model. (**A**) PFSS model field lines overlain on a photospheric synoptic magnetogram (*15*) reconstructed using HMI observations from the SDO. The magnetogram and model field lines sampled at 18:03:28 UT have been rotated and are shown from the Earth's viewpoint at 20:39:09 UT. The yellow and cyan circles mark the solar limb and the inner boundary of the CoMP FOV, respectively. The white lines are closed field lines, and the red and blue lines represent open field lines with opposite polarities. (**B**) Same as Fig. 3A but showing the map of B_{POS} generated from the PFSS model. (**C** to **F**) Average magnetic field strengths as a function of radial distance from the solar center for the four sectors marked in (B) and in Fig. 3A. The black solid lines with error bars are B_{POS} derived from the observations and associated uncertainties, and the blue dashed lines show B_{POS} calculated from the PFSS model.

average density in the vicinity of the POS with the derived density, we can obtain the POS component of the coronal magnetic field strength (B_{POS}) using Eq. 2. Forward simulations of propagating Alfvénic waves have shown that this is an appropriate approximation (*28*).

Our derived global coronal magnetic field map and its uncertainty are shown in Fig. 3. Comparing Fig. 3A with the intensity images in Fig. 1, A to C, shows that the magnetic field is higher in regions with stronger coronal emission. Typical values of B_{POS} in the FOV are 1 to 4 gauss, similar to the magnetic field strengths in smaller coronal regions inferred using other methods (*3*, *10*, *11*). The uncertainties in B_{POS}, which we calculated by propagating the uncertainties in the measured density and phase speed (*15*), are shown in Fig. 3B and are generally smaller than 15%. There could be an additional uncertainty caused by our use of the POS emissivity instead of the LOS-integrated emissivity in the calculation of the theoretical relationship between line ratio and electron density. Because the electron density distribution along the LOS is unknown, we estimated the impact of this assumption using a model of homogeneous density distribution with spherical symmetry (*15*). The density estimated with our line ratio method was lower than the local density in the POS (from the density model) by ~30%. Following Eq. 2, this corresponds to a possible additional uncertainty of ~12% on the measured B_{POS}.

In the absence of routine measurements of the coronal magnetic field, the potential field source surface (PFSS) model (*15*, *29*) is often adopted to extrapolate the observed magnetic field on the solar surface to the corona. For comparison with our method, we also used the PFSS model to reconstruct the three-dimensional coronal magnetic field structures from observations of the Helioseismic and Magnetic Imager (HMI) (*30*) on SDO (Fig. 4A) and obtain a map of B_{POS} from the model (*15*) (Fig. 4B). A comparison between the map of B_{POS} extrapolated using the PFSS model and that estimated from our data shows similar distributions of coronal magnetic field on the global scale but differences at scales smaller than ~200 arcsec. At many locations, the radial variation of B_{POS} has a discrepancy between CoMP measurements and PFSS results (Fig. 4, C to F). Some of these differences may arise because the magnitude of B_{POS} from the PFSS model is plotted for a POS slice. The B_{POS} derived from our CoMP data represents a measurement weighted by the emissivity along the LOS and is the POS component of the magnetic field strength averaged inside and outside flux tubes. We nevertheless compared the two B_{POS} maps because the LOS weighting favors magnetic structures in the vicinity of the POS. Differences between the two B_{POS} maps could also be related to the assumptions used in the PFSS model (*15*).

Our method for measuring the coronal magnetic field requires a continuous observation of 1 to 2 hours under good conditions, including ~1 hour to observe the transverse waves and additional time for density diagnostics. This implicitly assumes that the coronal structures do not evolve during the observing period. We expect this to be valid in the absence of eruptive events. The technique may not be applied to regions affected by solar eruptions, where signatures of transverse waves are often masked by the rapidly changing magnetic field environment.

Subject to these assumptions and limitations, our results demonstrate that imaging spectroscopy can be used to determine the coronal magnetic field. In principle, this technique could be applied to continuous observations from CoMP-like instruments to produce routine global coronal magnetic field maps.

REFERENCES AND NOTES

1. T. Wiegelmann, J. K. Thalmann, S. K. Solanki, *Astron. Astrophys. Rev.* **22**, 78 (2014).
2. H. Lin, M. J. Penn, S. Tomczyk, *Astrophys. J.* **541**, L83–L86 (2000).
3. H. Lin, J. R. Kuhn, R. Coulter, *Astrophys. J.* **613**, L177–L180 (2004).
4. D. Kuridze *et al*., *Astrophys. J.* **874**, 126 (2019).
5. B. Schmieder *et al*., *Astron. Astrophys.* **569**, A85 (2014).
6. W. Liu *et al*., *Astrophys. J.* **736**, L13 (2011).
7. V. M. Nakariakov, L. Ofman, *Astron. Astrophys.* **372**, L53–L56 (2001).
8. H. Tian *et al*., *Astrophys. J.* **759**, 144 (2012).
9. Y. Chen *et al*., *Astrophys. J.* **728**, 147 (2011).
10. N. Gopalswamy, N. Nitta, S. Akiyama, P. Mäkelä, S. Yashiro, *Astrophys. J.* **744**, 72 (2012).
11. A. Kumari, R. Ramesh, C. Kathiravan, T. J. Wang, N. Gopalswamy, *Astrophys. J.* **881**, 24 (2019).
12. G. D. Fleishman *et al*., *Science* **367**, 278–280 (2020).
13. S. Mancuso, M. V. Garzelli, *Astron. Astrophys.* **560**, L1 (2013).
14. S. Tomczyk *et al*., *Sol. Phys.* **247**, 411–428 (2008).
15. Materials and methods are available as supplementary materials.
16. H. Tian *et al*., *Sol. Phys.* **288**, 637–650 (2013).
17. J. R. Lemen *et al*., *Sol. Phys.* **275**, 17–40 (2012).
18. E. Priest, *Solar Magnetohydrodynamics* (Springer, 1982).
19. S. Tomczyk *et al*., *Science* **317**, 1192–1196 (2007).
20. S. Tomczyk, S. W. McIntosh, *Astrophys. J.* **697**, 1384–1391 (2009).
21. R. J. Morton, S. Tomczyk, R. Pinto, *Nat. Commun.* **6**, 7813 (2015).
22. R. J. Morton, M. J. Weberg, J. A. McLaughlin, *Nat. Astron.* **3**, 223–229 (2019).
23. B. De Pontieu *et al*., *Science* **318**, 1574–1577 (2007).
24. M. Goossens, J. Terradas, J. Andries, I. Arregui, J. L. Ballester, *Astron. Astrophys.* **503**, 213–223 (2009).
25. S. W. McIntosh *et al*., *Nature* **475**, 477–480 (2011).
26. D. M. Long, G. Valori, D. Pérez-Suárez, R. J. Morton, A. M. Vásquez, *Astron. Astrophys.* **603**, A101 (2017).
27. P. M. Edwin, B. Roberts, *Sol. Phys.* **88**, 179–191 (1983).
28. N. Magyar, T. Van Doorsselaere, *Astrophys. J.* **856**, 144 (2018).
29. K. H. Schatten, J. M. Wilcox, N. F. Ness, *Sol. Phys.* **6**, 442–455 (1969).
30. P. H. Scherrer *et al*., *Sol. Phys.* **275**, 207–227 (2012).
31. Source codes for: Z. Yang, C. Bethge, H. Tian, S. Tomczyk, R. Morton, G. Del Zanna, S. W. McIntosh, B. B. Karak, S. Gibson, T. Samanta, J. He, Y. Chen, L. Wang, Global maps of the magnetic field in the solar corona, Zenodo (2020); https://doi.org/10.5281/zenodo.3884044.

ACKNOWLEDGMENTS

We thank the SDO team for providing the AIA and HMI data, M. Galloy for running the CoMP data-processing pipeline, and M. DeRosa for helpful discussion about PFSS. This material is based on work supported by the National Center for Atmospheric Research, which is a major facility sponsored by the National Science Foundation under cooperative agreement no. 1852977. The AIA and HMI are instruments on SDO, a mission of NASA's Living With a Star Program. **Funding:** This work was supported by NSFC grants 11825301, 11790304(11790300), 41421003, 41774183, 41861134033, and 41874200; the Strategic Priority Research Program of CAS (grant no. XDA17040507), the Max Planck Partner Group program, STFC (UK) through consolidated grants to the atomic astrophysics group at DAMTP at the University of Cambridge (ST/P000665/1 and ST/T000481/1); and the Department of Science and Technology (SERB/DST) through the Ramanujan Fellowship (project no. SB/S2/RJN-017/2018). **Author contributions:** H.T. led the project. S.T. developed the CoMP instrument, designed the observing sequences, and processed the raw data. Z.Y. analyzed the data and generated the figures and movies under H.T.'s guidance. H.T. and Z.Y. wrote the manuscript. C.B improved the CoMP data-processing pipeline and led the first stage of data analysis. R.M. contributed to the magnetic field determination. G.D.Z. contributed to the density estimation. S.T. and S.W.M. developed the wave-tracking method, with contributions from R.M. and B.B.K. S.G. developed the software for the calculation of POS magnetic field from the PFSS model. Y.C. assisted with the PFSS calculation. T.S., J.H., and L.W. advised on the data analysis and contributed to the interpretation of the observations. All authors have discussed the results and commented on the manuscript. **Competing interests:** The authors declare no competing interests. **Data and materials availability:** The CoMP data can be obtained at http://download.hao.ucar.edu/d5/mlso/pub/comp-continuum-correction/; we used the files that begin with 20161014. The AIA data are available at the Joint Science Operations Center (JSOC) http://jsoc.stanford.edu/AIA/AIA_lev1.html; we used the AIA 193 Å image taken at 19:25:55 UT on 14 October 2016. The HMI synoptic photospheric magnetogram and results of our PFSS model are available in hierarchical data format at https://www.lmsal.com/solarsoft/archive/ssw/pfss_links_v2/Bfield_20161014_180328.h5. Source codes for the wave tracking and density diagnostic are available at Zenodo (*31*).

SUPPLEMENTARY MATERIALS

science.sciencemag.org/content/369/6504/694/suppl/DC1
Materials and Methods
Supplementary Text
Figs. S1 to S4
References (*32*–*54*)
Movie S1

24 February 2020; accepted 10 June 2020
10.1126/science.abb4462

PLANT SCIENCE

Cell-cell adhesion in plant grafting is facilitated by β-1,4-glucanases

Michitaka Notaguchi[1,2,3,4]*, Ken-ichi Kurotani[1], Yoshikatsu Sato[3,5], Ryo Tabata[2], Yaichi Kawakatsu[2], Koji Okayasu[2], Yu Sawai[2,4], Ryo Okada[2], Masashi Asahina[6], Yasunori Ichihashi[7,8], Ken Shirasu[7,9], Takamasa Suzuki[10], Masaki Niwa[2,4], Tetsuya Higashiyama[3,5,9]

Plant grafting is conducted for fruit and vegetable propagation, whereby a piece of living tissue is attached to another through cell-cell adhesion. However, graft compatibility limits combinations to closely related species, and the mechanism is poorly understood. We found that *Nicotiana* is capable of graft adhesion with a diverse range of angiosperms. Comparative transcriptomic analyses on graft combinations indicated that a subclade of β-1,4-glucanases secreted into the extracellular region facilitates cell wall reconstruction near the graft interface. Grafting was promoted by overexpression of the β-1,4-glucanase. Using *Nicotiana* stem as an interscion, we produced tomato fruits on rootstocks from other plant families. These findings demonstrate that the process of cell-cell adhesion is a potential target to enhance plant grafting techniques.

Plant grafting has been applied to improve crop traits for thousands of years (*1*). Wound healing allows growth of two or more segments of connected plant tissue to grow as a single plant (*2*–*4*). Grafting has been used to propagate fruit trees and vegetables. With grafting, root (stock) characteristics, such as disease resistance and tolerance of unfavorable soil conditions, can support growth of favored fruit and vegetable characteristics from the shoot (scion) (*1*, *5*). Grafting is also used to study systemic signaling in plants and long-distance vascular transport (*6*–*9*). Although grafting is most successful between members of the same family (*2*–*4*, *6*), several interfamily graft combinations have been reported (*10*–*14*): A *Nicotiana benthamiana* scion (*Nb*, Solanaceae) can be grafted onto an *Arabidopsis thaliana* stock (*At*, Brassicaceae) (*15*), although the *Nb* scion grows slowly (fig. S1 and movie S1).

Here, we studied interfamily graft combinations. We observed that *Nicotiana* shows grafting potential with phylogenetically distant plant species: Interfamily grafts survived for more than 1 month (Fig. 1 and tables S1 and S2). With *Chrysanthemum morifolium* (*Cm*, Asteraceae), we conducted *Cm*/*Cm* homografts (scion/stock notation) and interfamily grafts with *Glycine max* (*Gm*, soybean, Fabaceae) and *Nb*. *Cm*/*Cm* homografts established and the *Cm* scions produced flowers, whereas the *Gm*/*Cm* interfamily grafts did not establish and the *Gm* scions died (Fig. 1, A and B). By contrast, in *Nb*/*Cm* interfamily grafts, the *Nb* scions established and grew (Fig. 1C). The *Nb* scion grew for more than 3 months until setting seeds. *Nicotiana* interfamily grafting was also successful with *Nb* as the stock (fig. S1C).

In transverse sections of the graft junctions, a necrotic layer was visible at the graft boundary in unsuccessful *Gm*/*Cm* interfamily grafts but developed only weakly in successful *Cm*/*Cm* homografts and *Nb*/*Cm* interfamily grafts 2 weeks after grafting (Fig. 1, D to F). Necrotic layer formation is an indicator of incompatibility in cell-cell adhesion in grafting (*12*–*14*). Thus, *Nb*/*Cm* grafts showed interfamily cell-cell adhesion. Unsuccessful interfamily *Gm*/*Cm* grafts had folded cell wall remnants caused by graft injury (Fig. 1G), whereas successful *Nb*/*At* interfamily grafts formed a thin cell wall at the graft interface (Fig. 1, H to K, and fig. S2). Thus, *Nb* can accomplish cell-cell adhesion in interfamily combinations.

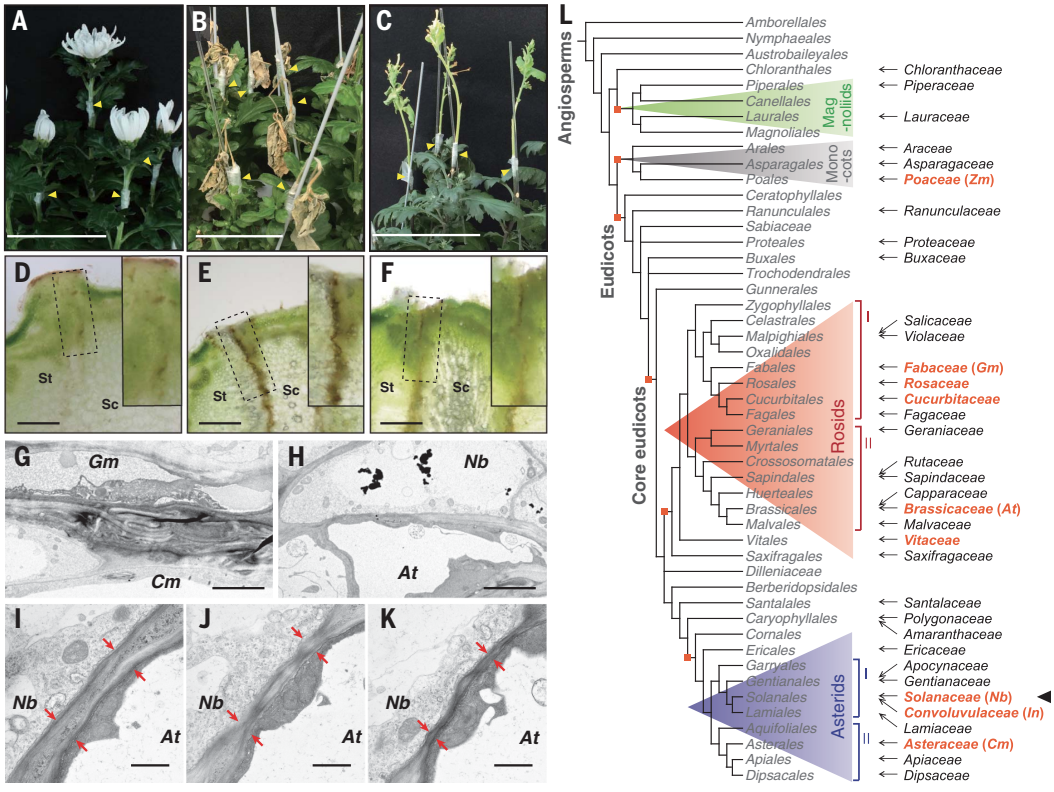


Fig. 1. *Nicotiana* interfamily grafting establishes through cell-cell adhesion. (**A** to **C**) Interfamily grafts, shown at 4 weeks after grafting between the *Cm*, *Gm*, and *Nb* scions, respectively, and the *Cm* stock. Yellow arrowheads denote graft junctions. Scale bars, 10 cm. (**D** to **F**) Transverse sections made at graft junctions shown in (A) to (C). Dashed rectangles indicate the position of insets. St, stocks; Sc, scions. Scale bars, 1 mm. (**G** and **H**) Transmission electron microscopy (TEM) images near the junction of the *Gm*/*Cm* (G) and *Nb*/*At* (H) interfamily grafts. Scale bars, 5 μm. (**I** to **K**) TEM images of serial sections of a cell-cell boundary at the graft interface of a *Nb*/*At* interfamily graft at 14 DAG. Arrows highlight the thickness of the cell wall between two cells. Scale bars, 1 μm. (**L**) Phylogenetic trees showing plant families for which *Nicotiana* plants (arrowhead) have preserved grafting beyond the family (arrows). Plant families including major crops are indicated in red. Abbreviations for plants used in transcriptome analysis are indicated in parentheses.

We then examined the range of angiosperms with which *Nicotiana* can establish grafts. We conducted grafting experiments using plants of seven *Nicotiana* species and an interfamily partner from 84 species in 42 families, chosen from among 416 angiosperm families (*16*). *Nicotiana* species, used as either scion or stock, supported interfamily grafting with 73 species from 38 families, including two species of magnoliids, five species of monocots, and 65 species of eudicots, including various vegetable, flower, and fruit tree crops (Fig. 1L, fig. S3, and tables S1 and S2). Thus, *Nicotiana* plants can graft to a range of angiosperms.

To examine the cellular mechanism of *Nicotiana* interfamily grafting, we analyzed transcriptomes at graft junctions from *Nb*/*At* interfamily grafts from 2 hours to 28 days after grafting (DAG) (Fig. 2). The transcriptome changed within 2 hours after grafting, and the state shifted further over time after grafting (Fig. 2, A and B). Genes associated with grafting (*17*, *18*) (table S3) whose expression was up-regulated in response to *Nb*/*At* interfamily grafting included genes associated with auxin action, wound repair, and cambium and vascular development (Fig. 2B). Their expression was comparable to, or higher than, that observed in *Nb*/*Nb* homografts (Fig. 2C). Transcriptomic changes at the graft junction were consistent with morphological changes in the *Nicotiana* interfamily grafts: Proliferation and xylem bridge formation were observed in the grafted region, but the xylem bundle was thin (fig. S4, A to E). Dye tracer experiments using toluidine blue, an apoplastic tracer, and carboxyfluorescein, a symplasmic tracer, showed establishment of both apoplastic and symplasmic transport at 3 DAG or later (fig. S4, F to H). Transport of mRNAs (*15*) and green fluorescent proteins across the heterograft junction was also detected (fig. S4, I and J) but was less than that for homografts. Hence, the viability of the *Nb* scions was preserved by parenchymatous tissue formation at the graft interface.

To elucidate the molecular events of graft formation, we identified 189 genes as early–up-regulated in the *Nb* scion of *Nb*/*At* interfamily grafts (Fig. 2D and table S3). Top Gene Ontology (GO) terms for these genes were

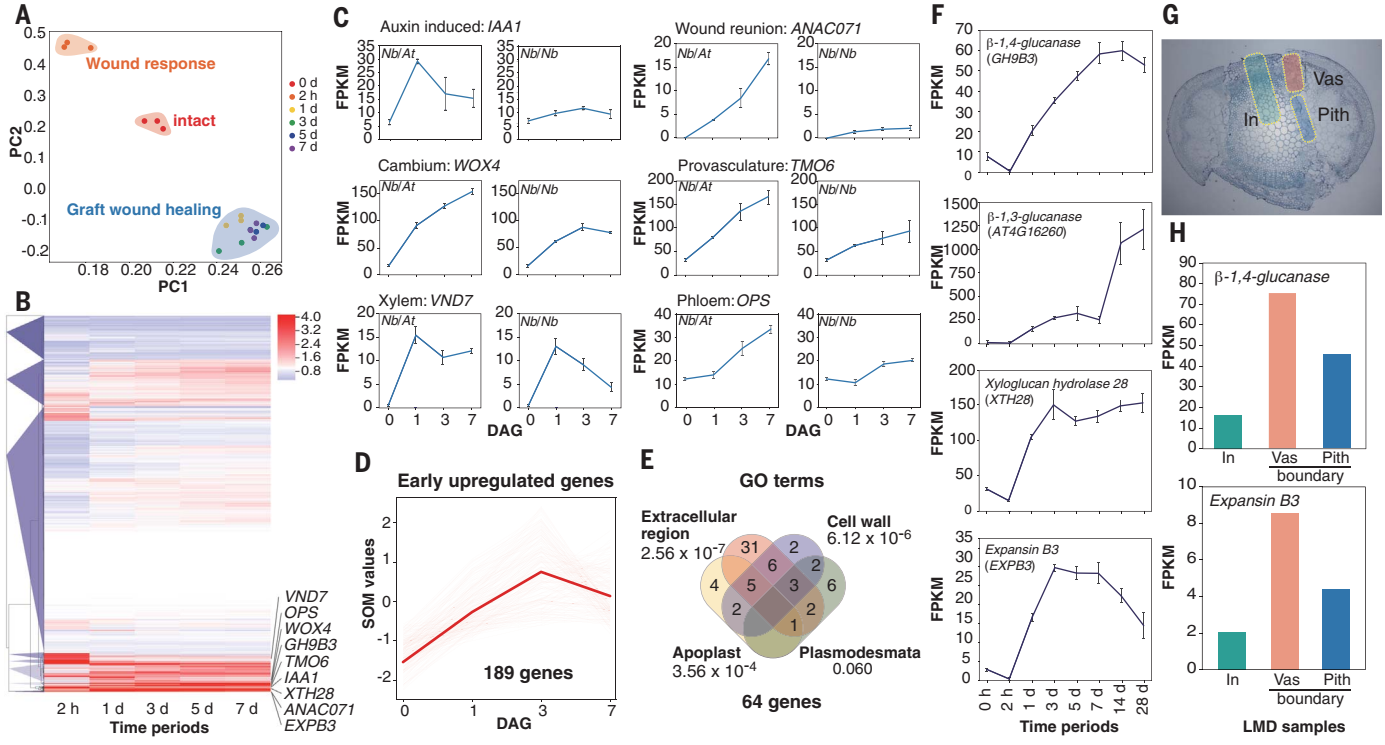


Fig. 2. Transcriptomic analysis reveals conventional graft-associated gene expression in *Nicotiana* interfamily grafting. (**A**) Principal components analysis of the transcriptome of the *Nb* intact stem and the scion of the *Nb*/*At* interfamily grafts at five time points (three biological replicates per time point). PC, principal component. (**B**) Hierarchical clustering with Euclidean distance and Ward's minimum variance method over ratio of RNA sequencing (RNA-seq) data from five time points after *Nb*/*At* grafting against intact plants. Genes for which association to grafting has been reported in previous studies are named. (**C**) Expression of genes associated with auxin action, wound reunion, and cambium, provasculature, xylem, and phloem development in *Nb*/*At* and *Nb*/*Nb* grafts. Table S3 provides details. FPKM, fragments per kilobase of transcript per million fragments mapped. (**D**) Extraction of early up-regulated genes for heterograft formation. See supplementary materials for extraction criteria. Profiles of 189 candidate genes are plotted against self-organizing map (SOM) values. Bold red line indicates the average of 189 genes. (**E**) GO enrichment analysis of 189 genes. Each numerical value represents the *P* value of GO analysis. (**F**) Expression profiles of representative genes after grafting. (**G**) Laser microdissection of *Nb*/*At* heterograft tissue was performed for the RNA-seq analysis. In, middle inside area of *Nb* scion tissue; Vas, cambial area of the graft boundary; Pith, pith area of the graft boundary. (**H**) Laser microdissection (LMD) RNA-seq of two of the genes shown in (F). Error bars in (C) and (F) denote SD.

[1]Bioscience and Biotechnology Center, Nagoya University, Furo-cho, Chikusa-ku, Nagoya 464-8601, Japan. [2]Graduate School of Bioagricultural Sciences, Nagoya University, Furo-cho, Chikusa-ku, Nagoya 464-8601, Japan. [3]Institute of Transformative Bio-Molecules, Nagoya University, Furo-cho, Chikusa-ku, Nagoya 464-8601, Japan. [4]GRA&GREEN Inc., Incubation Facility, Nagoya University, Furo-cho, Chikusa-ku, Nagoya 464-8601, Japan. [5]Graduate School of Science, Nagoya University, Furo-cho, Chikusa-ku, Nagoya 464-8601, Japan. [6]Department of Biosciences, Teikyo University, Utsunomiya, Tochigi 320-8551, Japan. [7]Center for Sustainable Resource Science, RIKEN, Tsurumi, Yokohama, Kanagawa 230-0045, Japan. [8]RIKEN BioResource Research Center, Tsukuba, Ibaraki 305-0074, Japan. [9]Graduate School of Science, University of Tokyo, Yayoi, Bunkyo-ku, Tokyo 113-8657, Japan. [10]College of Bioscience and Biotechnology, Chubu University, Matsumoto-cho, Kasugai 487-8501, Japan.
***Corresponding author. Email: notaguchi.michitaka@b.mbox.nagoya-u.ac.jp**

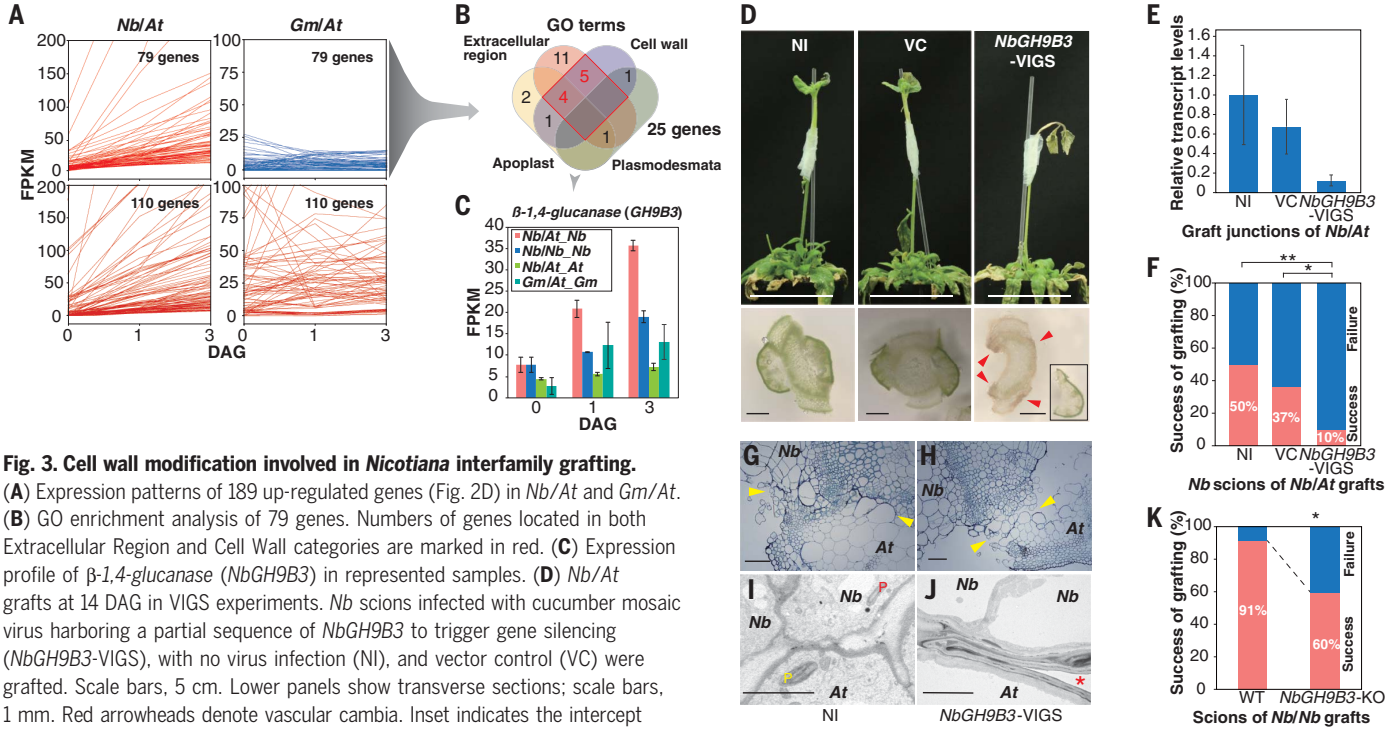


Fig. 3. Cell wall modification involved in *Nicotiana* interfamily grafting. (**A**) Expression patterns of 189 up-regulated genes (Fig. 2D) in *Nb/At* and *Gm/At*. (**B**) GO enrichment analysis of 79 genes. Numbers of genes located in both Extracellular Region and Cell Wall categories are marked in red. (**C**) Expression profile of β-*1,4-glucanase* (*NbGH9B3*) in represented samples. (**D**) *Nb/At* grafts at 14 DAG in VIGS experiments. *Nb* scions infected with cucumber mosaic virus harboring a partial sequence of *NbGH9B3* to trigger gene silencing (*NbGH9B3*-VIGS), with no virus infection (NI), and vector control (VC) were grafted. Scale bars, 5 cm. Lower panels show transverse sections; scale bars, 1 mm. Red arrowheads denote vascular cambia. Inset indicates the intercept of *At* tissues separated. (**E**) Suppression of *NbGH9B3* expression by VIGS was verified by quantitative reverse transcription polymerase chain reaction. (**F**) Effect of the *NbGH9B3*-VIGS on graft establishment. Differences between the sample groups were tested with Fisher exact tests with α set at $*P < 0.05$ or $**P < 0.01$, $n = 30$. (**G** to **J**) Transverse sections of grafted stem sample. [(G) and (H)] Optical microscope images. Yellow arrowheads indicate the boundary of *Nb* and *At*. Scale bars, 100 μm. [(I) and (J)] TEM images. Yellow P and red P indicate the plastids of *At* and *Nb*, respectively. Asterisk indicates a gap formed between *Nb* and *At* cells. Scale bars, 5 μm. (**K**) Effect of CRISPR knockout (KO) of *NbGH9B3* on graft establishment. Means were compared by Fisher exact test ($*P < 0.05$), $n = 45$ to 47. Error bars in (C) and (E) denote SD.

Extracellular Region, Cell Wall, and Apoplast (Fig. 2E and supplementary materials), implicating cell wall modification in *Nicotiana* interfamily grafting. Genes encoding cell wall modification/reconstruction enzymes, including β-1,4-glucanase, β-1,3-glucanase, xyloglucan hydrolase, and expansin, were up-regulated at 1 to 28 DAG (Fig. 2F). Laser microdissection samples of *Nb/At* interfamily graft junctions confirmed enhanced expression of a number of these genes in the cells that proliferated from the cambial or pith region of the graft boundary (Fig. 2, G and H). Transcriptomic studies of intrafamily grafting (*19*–*21*) and wounding response (*22*) also showed expression changes for genes associated with cell wall dynamics. Thus, *Nicotiana* activates cell wall reconstruction in both intrafamily and interfamily grafting.

By comparing interfamily grafting transcriptomes, we identified genes that were up-regulated in *Nb* scions of *Nb/At* interfamily grafts but not in soybean (*Gm*) scions of *Gm/At* interfamily grafts. We selected genes from *Gm* that showed the highest homology to each of the up-regulated *Nb* genes. Of 189 genes up-regulated in *Nb* scions (Fig. 2D), only 110 homologous genes in *Gm* scions were up-regulated (Fig. 3A and supplementary materials). We further analyzed the 79 homologous genes up-regulated in *Nb* but not *Gm* scions. Genes associated with Extracellular Region and Cell Wall were overrepresented in the 79 genes (Fig. 3B) (in comparison with Fig. 2E, the number of genes associated with Extracellular Region and Cell Wall was 9 out of 14, whereas the number of genes associated with the other GO terms was 16 out of 50). This result suggested that successful *Nicotiana* interfamily grafting requires cell wall reconstruction.

One gene expressed at *Nb* interfamily grafts was *NbGH9B3* (named on the basis of similarity to *At* genes), which encodes β-1,4-glucanase of the glycosyl hydrolase 9B (GH9B) family. The expression of *NbGH9B3* was up-regulated at 1 DAG and increased further at 3 DAG, but not significantly for that of the *Gm* homolog in *Gm/At* interfamily grafts (Fig. 3C). β-1,4-glucanases of the GH9B family function in cellulose digestion and cell wall relaxation or construction during plant growth processes such as root elongation (*23*, *24*). We hypothesized that *NbGH9B3* facilitates adhesion of facing cells at the graft boundary and further analyzed *NbGH9B3* function in grafting.

We applied virus-induced gene silencing (VIGS) to examine the function of *NbGH9B3* in *Nb/At* interfamily grafting (Fig. 3, D to F). Silencing of *NbGH9B3* caused failure of *Nb/At* interfamily grafting 2 weeks after grafting: The *Nb* scion was easily detached from the *At* stocks, and *Nb* tissues formed a necrotic layer on the graft surface (Fig. 3D). The amount of *NbGH9B3* expression reflected the success of grafting (Fig. 3, E and F). Folded cell walls, characteristic of failed grafts, were frequently observed at the graft interface of *Nb* scions in which *NbGH9B3* was down-regulated by VIGS, but not in noninfected controls (Fig. 3, G to J). We generated a knockout line of *NbGH9B3* (*NbGH9B3*-KO) using CRISPR/Cas9 editing (see supplementary materials). The percentage success of interfamily grafting onto *At* stocks was 91% for wild-type *Nb* scions and 60% for *NbGH9B3*-KO scions (Fig. 3K). Thus the β-1, 4-glucanase encoded by *NbGH9B3* facilitates graft establishment in *Nicotiana* interfamily grafting.

We next examined whether β-1,4-glucanase also functions in intrafamily grafting for other genera (Fig. 4, A and B), including soybean (*Gm*), morning glory (*In*), maize (*Zm*), and *Arabidopsis* (*At*). At *Gm*, *In*, and *At* homografts, one *GH9* family gene was up-regulated within 7 DAG; all belonged to the *GH9B3* clade (Fig. 4, A and B, and Fig. S5). For *Gm* and *In* scions grafted onto *At* stocks (Fig. 4B), *GH9B3* gene expression increased by 1 DAG and remained unchanged afterward. Thus, up-regulation of *GH9B3* gene expression during graft adhesion was conserved among these plants. *Zm*

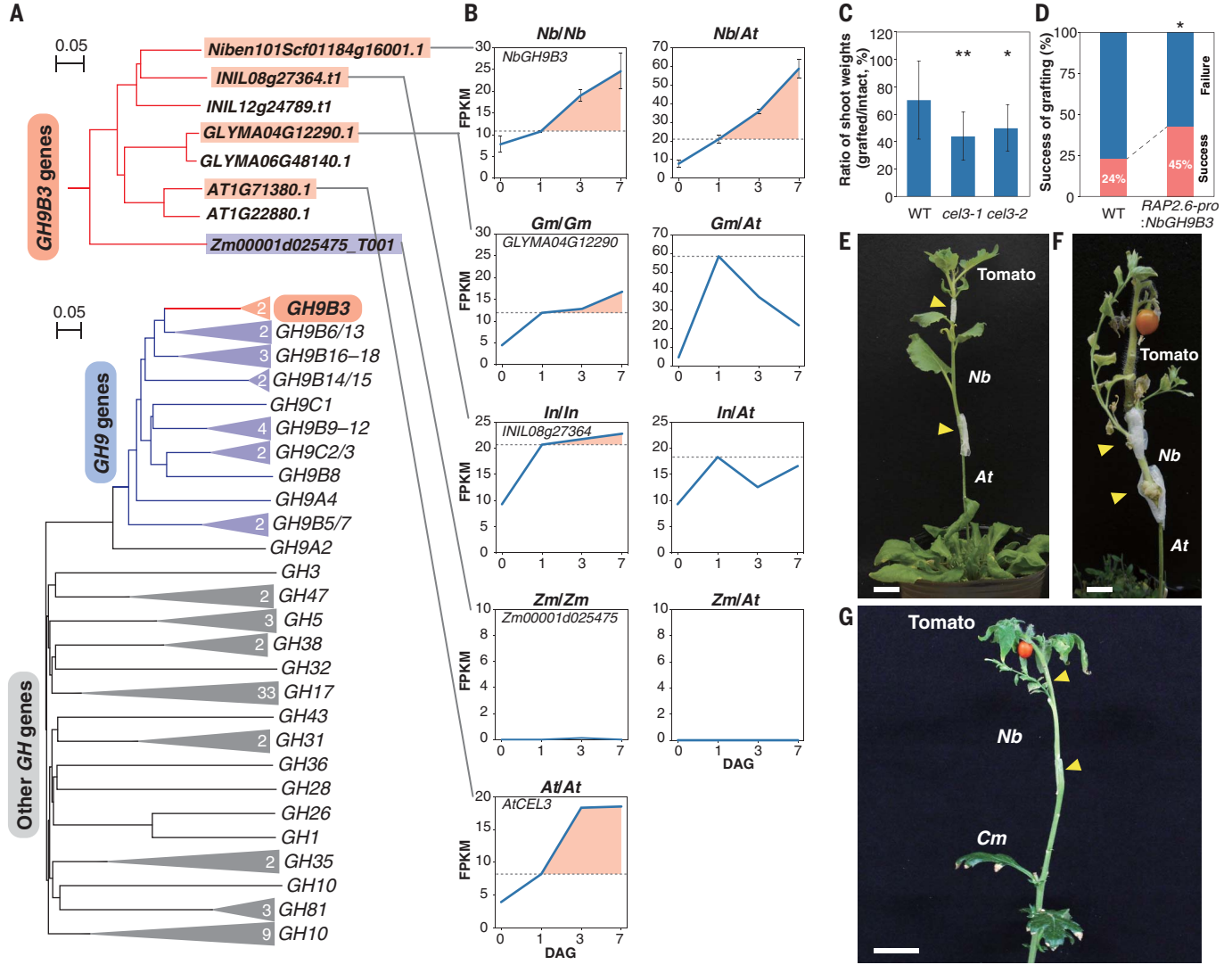


Fig. 4. Glycosyl hydrolase 9B3 is essential for graft wound healing in plants. (**A**) Phylogeny of plant glycosyl hydrolase gene family including the *GH9B3* clade. Top: Tree for the *GH9B3* clade genes. Bottom: Tree for all *GH* clades. Numbers of *At* genes included in each clade are shown in triangles (see supplementary materials). (**B**) *GH9B3* clade genes located in the same clade as *Niben101Scf01184 g16001* show a common expression pattern. (**C**) Increase in shoot fresh weight after grafting in two lines of mutants for *AtCEL3*. *P < 0.05, **P < 0.01 (Student t test); n = 14 to 19. (**D**) An *At* overexpression line of *NbGH9B3* using a RAP2.6 wound-inducible promoter (*NbGH9B3*-OX) increased percentage success of grafting relative to wild-type grafting (n = 64 and 102). Viability of the scion was determined at 14 DAG; the effect of overexpression was evaluated by Fisher exact test (*P < 0.05). (**E** to **G**) Grafts of tomato scion onto *At* [at 21 DAG (E) and 4 months after grafting (F)] or *Cm* [3 months after grafting (G)] using a *Nb* interscion. Yellow arrowheads indicate grafting points. Scale bars, 1 cm [(E) and (F)], 5 cm (G). Error bars in (B) and (C) denote SD.

homografts failed, as monocot species lack cambial activity in the stem (*25*). In *Zm* grafts, an orthologous gene was not up-regulated in either homografts or interfamily grafts.

To study *GH9B3* genes in grafting in other plant genera, we performed seedling micrografting in *Arabidopsis* using wild-type and two T-DNA insertion mutant lines for *CELLULASE3* (*AtCEL3*), a *GH9B3* clade gene that was up-regulated in *At* homografts (Fig. 4C). No significant difference in percentage success was observed between wild-type and *cel3-1* or *cel3-2* mutant homografts. However, shoot growth after grafting was decreased in grafts of both mutant lines relative to that of the wild type (Fig. 4C). Thus, GH9B3 is not required for establishment of the graft connection in *At* but does contribute to shoot growth after grafting (Fig. 3, F and K). To examine the effect of GH9B3 overexpression on grafting, we generated transgenic lines of *Arabidopsis* that overexpressed *NbGH9B3* under the control of a wound-induced *RAP2.6* promoter (*NbGH9B3*-OX) (*26*). The percentage success of micrografting using the *NbGH9B3*-OX line was significantly higher than that of wild-type grafting (Fig. 4D). Thus, GH9B3 functions in graft formation in *Arabidopsis* as well as in *Nicotiana*.

Our results show that *Nicotiana* plants use a mechanism for interfamily grafting that is generally activated only for intrafamily grafting. To exploit this capability, we examined whether *Nicotiana* could act as an intermediate in the grafting of different plant families. We grafted a tomato scion onto *At* or *Cm* stocks using a *Nicotiana* interscion. The *Nicotiana* interscion formed an intrafamily graft with the tomato scion and an interfamily graft with the *Cm* or *At* stocks. The tomato scions were successfully stabilized and produced fruit 3 to 4 months after grafting (Fig. 4, E to G, and fig. S6A). We also achieved other interfamily grafts in which the scion, interscion, and stock all belonged to different plant families (table S4 and fig. S6B).

Successful grafting requires wound response, cell regeneration, cell proliferation, cell-cell adhesion, and cell differentiation (*6*–*9*). *Nicotiana* shows graft compatibility with diverse plant species through the function of a conserved clade of extracellular-localized β-1,4-glucanases, the GH9B3 family, which probably target cellulose in cell walls (*23*, *27*). How the GH9B3 enzymes promote cell-cell adhesion is a key question for future research. Enhanced plant grafting techniques may increase the variety of root systems available to aid crop production with minimal destruction of ecosystems.

REFERENCES AND NOTES

1. K. Mudge, J. Janick, S. Scofield, E. E. Goldschmidt, *Hortic. Rev.* **35**, 437–493 (2009).
2. H. T. Hartmann, D. E. Kester, *Plant Propagation: Principles and Practices* (Prentice-Hall, ed. 3, 1975), pp. 314–427.
3. P. K. Andrews, C. S. Marquez, *Hortic. Rev.* **15**, 183–231 (1993).
4. C. W. Melnyk, *Regeneration* **4**, 3–14 (2016).
5. J. M. Lee, M. Oda, *Hortic. Rev.* **28**, 61–124 (2003).
6. E. E. Goldschmidt, *Front. Plant Sci.* **5**, 727 (2014).
7. J. Wang, L. Jiang, R. Wu, *New Phytol.* **214**, 56–65 (2017).
8. H. Tsutsui, M. Notaguchi, *Plant Cell Physiol.* **58**, 1291–1301 (2017).
9. B. S. Gaut, A. J. Miller, D. K. Seymour, *Annu. Rev. Genet.* **53**, 195–215 (2019).
10. S. V. Simon, *Jb. Wiss. Bot.* **72**, 137–160 (1930).
11. L. G. Nickell, *Science* **108**, 389 (1948).
12. R. Moore, D. B. Walker, *Am. J. Bot.* **68**, 831–842 (1981).
13. R. Kollmann, C. Glockmann, *Protoplasma* **124**, 224–235 (1985).
14. M. A. Flaishman, K. Loginovsky, S. Golobowich, S. Lev-Yadun, *J. Plant Growth Regul.* **27**, 231–239 (2008).
15. M. Notaguchi, T. Higashiyama, T. Suzuki, *Plant Cell Physiol.* **56**, 311–321 (2015).
16. Angiosperm Phylogeny Group, *Bot. J. Linn. Soc.* **181**, 1–20 (2016).
17. K. Matsuoka *et al*., *Plant Cell Physiol.* **57**, 2620–2631 (2016).
18. C. W. Melnyk *et al*., *Proc. Natl. Acad. Sci. U.S.A.* **115**, E2447–E2456 (2018).
19. S. J. Cookson *et al*., *J. Exp. Bot.* **64**, 2997–3008 (2013).
20. Y. Ren *et al*., *Plant Physiol. Biochem.* **129**, 368–380 (2018).
21. L. Xie, C. Dong, Q. Shang, *BMC Plant Biol.* **19**, 373 (2019).
22. Y. H. Cheong *et al*., *Plant Physiol.* **129**, 661–677 (2002).
23. D. J. Cosgrove, *Nat. Rev. Mol. Cell Biol.* **6**, 850–861 (2005).
24. D. R. Lewis *et al*., *Plant Cell* **25**, 3329–3346 (2013).
25. D. Roodt, Z. Li, Y. Van de Peer, E. Mizrachi, *Genome Biol. Evol.* **11**, 1986–1996 (2019).
26. K. Matsuoka *et al*., *Plant Mol. Biol.* **96**, 531–542 (2018).
27. B. R. Urbanowicz *et al*., *Plant Physiol.* **144**, 1693–1696 (2007).

ACKNOWLEDGMENTS

We thank D. Kurihara, T. Araki, K. Shiratake, S. Otagaki, S. Ishiguro, and Japan Tobacco Inc. for plant materials; C. Masuta for the VIGS vectors; A. Iwase for the *RAP2.6* plasmid vector; T. Shinagawa, H. Fukada, A. Ishiwata, R. Masuda, Y. Hakamada, M. Hattori, M. Matsumoto, I. Yoshikawa, A. Yagi, A. Shibata, and A. Furuta for technical assistance; and T. Akagi, Y. Hattori, and K. Toyokura for discussions. **Funding:** Supported by grants from the Japan Society for the Promotion of Science Grants-in-Aid for Scientific Research (18KT0040, 18H03950, and 19H05361 to M.No.; JP16H06280 and 19H05364 to Y.Sat.; 15H05959 and 17H06172 to K.S.), the Canon Foundation (R17-0070), the Project of the NARO Bio-oriented Technology Research Advancement Institution (Research Program on Development of Innovative Technology 28001A and 28001AB) to M.No., and the Japan Science and Technology Agency (ERATO JPMJER1004 to T.H.; START15657559 and PREST015665754 to M.No.). **Author contributions:** M.No., K.-i.K., Y.Sat., and M.Ni. conceived of the research and designed experiments; M.No. and K.O. performed grafting experiments; M.No. and Y.Saw. analyzed tissue sections; M.No. collected microscopic data with Y.Sat.'s support; R.T. performed VIGS experiments; Y.K. performed micrografting experiments; M.A. collected LMD samples; K.-i.K., R.O., and Y.I. generated RNA-seq libraries; T.S. performed sequencing; K.-i.K. analyzed transcriptome data; M.No., M.Ni., K.S., and T.H. supervised the experiments; and M.No., K.K., and M.Ni. wrote the paper. **Competing interests:** Nagoya University has filed for patents regarding the following topics: "Interfamily grafting technique using *Nicotiana*," inventor M.No. (patent publication nos. WO 2016/06018 and JP 2014-212889); "Grafting facilitation technique using cellulase," inventors M.No., K.K., R.T., and Y.K. (patent application nos. JP 2019-052727 and JP 2020-042379). T.H. is an adviser for GRA&GREEN Inc. **Data and materials availability:** RNA-seq data are available from the DNA Data Bank of Japan (www.ddbj.nig.ac.jp/) under accession number DRA009936. All other data are available in the main text or the supplementary materials. M.N. will handle requests for materials. All plasmid vectors and transgenic plants generated in this study are available from M.N. under a material agreement with Nagoya University.

SUPPLEMENTARY MATERIALS

science.sciencemag.org/content/369/6504/698/suppl/DC1
Materials and Methods
Figs. S1 to S6
Tables S1 to S5
References (*28*–*37*)
Movie S1
MDAR Reproducibility Checklist

View/request a protocol for this paper from *Bio-protocol*.

21 April 2020; accepted 12 June 2020
10.1126/science.abc3710

CORONAVIRUS

Unexpected air pollution with marked emission reductions during the COVID-19 outbreak in China

Tianhao Le[1]*, Yuan Wang[1]*†, Lang Liu[2,3]*, Jiani Yang[1], Yuk L. Yung[1], Guohui Li[2,3], John H. Seinfeld[4]

The absence of motor vehicle traffic and suspended manufacturing during the coronavirus disease 2019 (COVID-19) pandemic in China enabled assessment of the efficiency of air pollution mitigation. Up to 90% reduction of certain emissions during the city-lockdown period can be identified from satellite and ground-based observations. Unexpectedly, extreme particulate matter levels simultaneously occurred in northern China. Our synergistic observation analyses and model simulations show that anomalously high humidity promoted aerosol heterogeneous chemistry, along with stagnant airflow and uninterrupted emissions from power plants and petrochemical facilities, contributing to severe haze formation. Also, because of nonlinear production chemistry and titration of ozone in winter, reduced nitrogen oxides resulted in ozone enhancement in urban areas, further increasing the atmospheric oxidizing capacity and facilitating secondary aerosol formation.

The abrupt outbreak of the coronavirus disease 2019 (COVID-19) pandemic produced previously unseen societal impacts in China. To curb the virus spread among humans, a preventive lockdown was first implemented on 23 January in Wuhan, Hubei. Other major cities and counties in China subsequently followed suit, and the entire nation's lockdown lasted for at least 3 weeks (varying in different regions). During the lockdown period, emissions from the traffic sector were markedly reduced. Such a shutdown serves as a natural experiment to evaluate air-quality responses to a marked emissions reduction and to assess the interplay between emission, atmospheric chemistry, and meteorological conditions. In this work, we synthesize multiple-year satellite-retrieved atmospheric compositions, national ground-station measurements of major pollutants, meteorology from reanalysis data, and a suite of state-of-the-art online atmospheric chemistry model simulations to assess the atmospheric influence of the COVID-19 outbreak in China and to reveal its implications for air pollution control strategies.

China has continued to battle particulate haze pollution (*1*). Long-term regulatory plans targeting energy and industrial emissions have been implemented (*2*), and nationwide improvement of fine particulate matter (PM) levels has been reported (*3*). Nonetheless, the key chemical and physical processes responsible for severe haze formation in China remain elusive, including exacerbated ozone levels (*4*, *5*), pathways of secondary aerosol formation (*6*, *7*), and emissions-meteorology interactions (*8*). Certain societal events in China with short-term stringent emission controls have been studied as natural experiments, such as the "Olympic Blue" during the 2008 Beijing Summer Olympic Games (*9*) and the "APEC Blue" during the 2014 Asia-Pacific Economic Cooperation (APEC) Economic Leaders' Meetings in Beijing (*10*, *11*). Emission controls during these two events resulted in a 40 to 60% reduction in SO_2, NO_2, nonmethane volatile organic compounds (VOCs), and PM.

The primary focus period during the COVID-19 lockdown in China was from 23 January to 13 February 2020 (hereafter referred to as the 2020-CLD period). This period encompassed a 7-day national holiday traditionally celebrating the Lunar New Year, during which previous studies have noted the reduction in anthropogenic emissions (*12*). NO_2 is key in atmospheric chemistry and serves as an important precursor for both ozone production and secondary aerosol formation (*6*, *13*). Changes in NO_2 during the lockdown period can be assessed by comparing spaceborne NO_2 measurements in the same time periods over different years. The TROPOspheric Monitoring Instrument (TROPOMI) on board the Copernicus Sentinel-5 Precursor satellite has provided key trace gas measurements of high accuracy since 2018. TROPOMI data show a quite low amount of column-integrated NO_2 during the 2020-CLD, with a mean value of 1.72 mg m^{-2}, and general uniformity throughout the whole country (Fig. 1A). By contrast, in the same period in 2019, hotspots of NO_2 were evident over eastern China, where the regional mean NO_2 abundance was four to five times higher than that in other regions of China (Fig. 1B). Regional means over eastern China experienced a reduction of 5.70 mg m^{-2} in NO_2, corresponding to a −71.9% fractional change (Fig. 1C). At the peak of the disease outbreak, Wuhan experienced a 93% fractional reduction in NO_2. Such a short-term human-induced reduction in NO_2 has been previously unseen, well exceeding the previous 2014 APEC Blue,

[1]Division of Geological and Planetary Sciences, California Institute of Technology, Pasadena, CA, USA. [2]State Key Laboratory of Loess and Quaternary Geology, Institute of Earth Environment, Chinese Academy of Sciences, Xi'an, Shaanxi, China. [3]Key Lab of Aerosol Chemistry and Physics, Institute of Earth Environment, Chinese Academy of Sciences, Xi'an, Shaanxi, China. [4]Divisions of Chemistry and Chemical Engineering and Engineering and Applied Science, California Institute of Technology, Pasadena, CA, USA.
*These authors contributed equally to this work.
†Corresponding author. Email: yuan.wang@caltech.edu

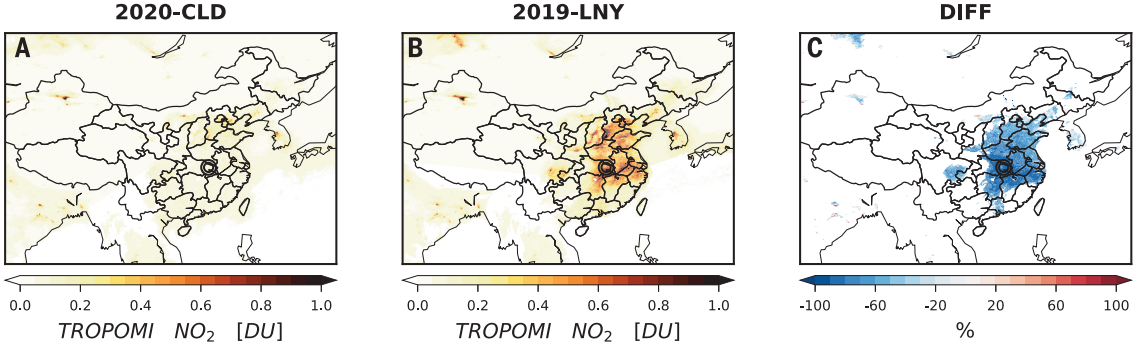


Fig. 1. Spaceborne measurements of NO_2 from TROPOMI. (**A**) Column-integrated NO_2 averaged over the 2020-CLD period for 3 weeks during 23 January to 13 February 2020. (**B**) Column-integrated NO_2 averaged over the reference period in 2019. To account for the annual holiday, the 2019 reference period we choose is the same as that in 2020-CLD in the Chinese lunar calendar, including the Chinese Lunar New Year (2019-LNY). TROPOMI NO_2 is available only starting from June 2018. (**C**) The fractional changes (DIFF) between (A) and (B), calculated only for the regions with NO_2 in 2019-LNY greater than 0.2 Dobson units (DU). The symbols in the maps indicate the location of Wuhan, the city most affected by COVID-19. 1 DU = 0.4462 mmol m^{-2}.

with the largest NO_2 reduction of ~40% (*10*). Compared with a 5-year climatology (2015 to 2019) based on the NASA Aura Ozone Monitoring Instrument, the NO_2 reductions mainly occurred over the North China plain (fig. S1).

In addition to spaceborne retrievals, we explore surface measurements of fine-mode aerosols and trace gas species over the entire region of eastern China (fig. S2). We calculate separately the climatological means of the past 5 years (2015 to 2019) during the same 3-week period as the 2020-CLD, including the Lunar New Year (hereafter referred to as CLIM-LNY) and the same 3-week period in the Georgian calendar (CLIM). The difference between CLIM-LNY and CLIM is attributed mainly to the holiday effect. In Wuhan, surface concentrations of NO_2 and SO_2 were the lowest compared with the 3-week means before the 2020-CLD as well as the climatological means over the past 5 years. $PM_{2.5}$ (PM with aerodynamic diameter less than 2.5 μm) was reduced by 23.2 μg m^{-3} (–32.4%) and 37.4 μg m^{-3} (–43.5%) as compared with CLIM-LNY and CLIM, respectively (Fig. 2A). In contrast to the changes to the $PM_{2.5}$, the surface ozone mixing ratio showed an enhancement of +5.0 parts per billion (ppb) (+25.1%) in Wuhan during the 2020-CLD as compared with CLIM-LNY. Ozone chemistry is highly nonlinear, and in the winter in urban areas in China, its production is in a NO_x-saturated regime (NO_x = NO + NO_2) because of the relative lack of HO_x radicals (*13*). Besides, reduction of fresh NO emissions alleviates ozone titration (*13*, *14*). Thus, a reduction of NO_x leads to an increase in ozone. Previous studies also attributed the anticorrelation between $PM_{2.5}$ and ozone to the aerosol radiative effect on the photochemistry of ozone formation (*4*, *15*), as well as the aerosol sink for ozone precursors (*5*). Changes in gaseous and particulate levels in the major cities of southern China, Guangzhou (Fig. 2C) and Shanghai (Fig. 2D), resemble those of Wuhan during the city lockdown.

In contrast to southern and central China, $PM_{2.5}$ in northern China during the outbreak period increased substantially (Fig. 2B). During the 3 weeks of 2020-CLD, several severe haze events occurred in Beijing with the maximum daily $PM_{2.5}$ level of 273.8 μg m^{-3}. The 2020-CLD mean surface $PM_{2.5}$ in Beijing increased by 16.3 μg m^{-3} (+23.4%) and 30.6 μg m^{-3} (+55.1%) in comparison with CLIM-LNY and CLIM, respectively (Fig. 2B). Nonetheless, NO_2 and SO_2 remained the lowest among the past 6 years, similar to that of the southern cities. Response of ozone concentration in Beijing followed a similar trend as that of $PM_{2.5}$, reaching a peak during the 2020-CLD. Daytime relationships between NO_2 and ozone concentrations in the winter of northern China show remarkable ozone titration during daytime, particularly with increasing $PM_{2.5}$, which further attenuates the incoming solar radiation, but the titration effect becomes considerably alleviated during the city lockdown (fig. S3). Nationwide, 1515 state monitoring stations show clear hotspots of surface $PM_{2.5}$ over northern China during the 2020-CLD (Fig. 2E), although the national mean of the 2020-CLD $PM_{2.5}$ was 52.1 μg m^{-3}, which falls in the 1σ range of variation of national climatology, 54.7 ± 6.1 μg m^{-3}. Satellite-observed aerosol optical depth (AOD) based on the Moderate Resolution Imaging Spectroradiometer corroborates the persistent haze over northern China. Significantly high levels of AOD (>0.8)

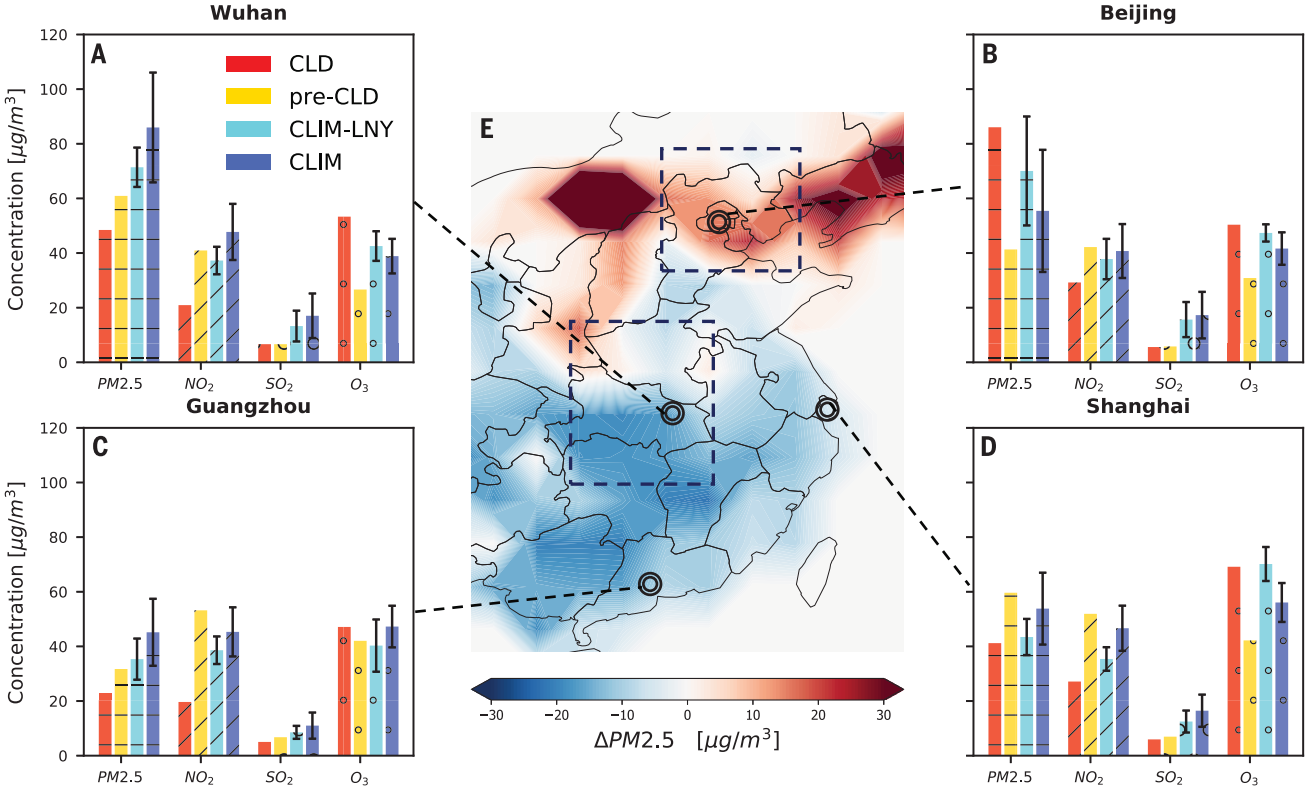


Fig. 2. Ground-based station observation of $PM_{2.5}$, NO_2, SO_2, and ozone in eastern China, including four megacities. (**A**) Wuhan. (**B**) Beijing. (**C**) Guangzhou. (**D**) Shanghai. The figure compares the 3-week averages during the city lockdown period (CLD), the 3-week averages before 2020-CLD (pre-CLD), the 5-year climatology for 2015 to 2019 during the same period of 2020-CLD in the Chinese lunar calendar that covers the Lunar New Year (CLIM-LNY), and the 5-year climatology for 2015 to 2019 during the same period with 2020-CLD in the Gregorian calendar (CLIM). Error bars indicate SDs over multiple years. (**E**) Map of surface $PM_{2.5}$ changes in 2020-CLD compared with CLIM-LNY based on the 1515 state monitoring stations (fig. S2). The low-resolution patterns in the north and west are caused by the sparsity of stations. Two boxes indicate the BTH and central China regions. For ozone, 1 μg m^{-3} is ~0.47 ppb under a standard condition.

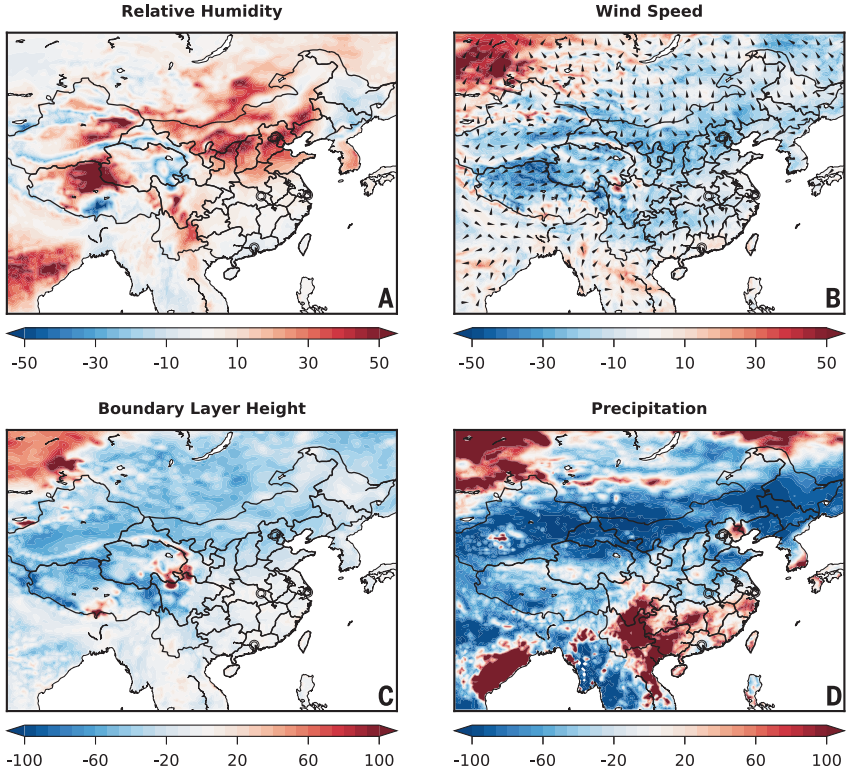


Fig. 3. Fractional changes (%) in meteorological conditions between the 2020-CLD and CLIM-LNY during 2015 to 2019 based on the ERA5 reanalysis data. (**A**) Relative humidity of 1000 hPa, (**B**) 10-m wind speed (contours) and wind direction (vectors), (**C**) boundary-layer height, and (**D**) daily precipitation. Symbols in the maps indicate the location of the four major cities in Fig. 2.

were present over the North China plain but did not occur in any previous year since 2015 (fig. S4), leading to 40 to 100% increases in AOD during the city lockdown.

Possible factors that explain enhanced $PM_{2.5}$ and ozone levels in the face of declining precursor gas emissions include the complex chemistry of secondary aerosols and ozone (*7*, *13*) as well as the meteorological influence (*8*). Changes in relative humidity (RH), near-surface wind speed and direction, planetary boundary layer (PBL) height, and precipitation between the 2020-CLD and CLIM-LNY are shown in Fig. 3, based on fifth-generation European Centre for Medium-Range Weather Forecasts (ECMWF) global atmospheric reanalysis (ERA5). In northern China, which is climatologically dry during the winter, a larger than usual amount of moisture accumulated near the surface during the city lockdown, with a 3-week mean RH of 55.2% and a maximum of 100%. Compared with the climatology, RH increased by 30 to 50% (Fig. 3A), facilitating multiphase reactions for aerosol formation and growth (*16*). Wind conditions were also favorable for haze formation; in Beijing, the mean wind speed decreased by 20%, and winds that normally originate from the polluted industrial regions in Hebei Province switched to southerly (Fig. 3B). Consistent with the increase in RH and the decrease in wind speed, PBL height in northern China generally declined during the city lockdown, inducing a stable boundary layer and stagnant air (Fig. 3C). As a result, both ozone and $PM_{2.5}$ increased in Beijing. During the same period, as precipitation occurred mainly over southern China, no anomalous washout occurred in northern China, conducive for haze development during the city lockdown. Also, as positive feedback to the meteorological variations (*17*), aerosols can reduce PBL height and stabilize the lower atmosphere through their radiative effects (*18*) and suppress light precipitation through their microphysical effects (*19*).

To reveal the physical and chemical mechanisms of the unexpected $PM_{2.5}$ and ozone enhancement in northern China during the COVID-19 outbreak, we have conducted atmospheric chemistry and transport simulations using the Weather Research and Forecast model online coupled with full gaseous and aerosol chemistry (WRF-Chem). The unusual particulate levels during the 2020-CLD in the Beijing-Tianjin-Hebei area (BTH) are well reproduced in our baseline simulations, in terms of consistent peak values of ~200 $\mu g\ m^{-3}$, well-simulated temporal evolution over the 3 weeks, and small mean bias (MB) of ~2.6 $\mu g\ m^{-3}$ (Fig. 4A). Surface ozone concentrations and diurnal cycles are comparable with ground-based observations (Fig. 4B), as with other precursor trace gases, including SO_2, NO_2, and CO (fig. S5). Predicted aerosol chemical composition shows that organic aerosol (OA), nitrate, and sulfate are predominant species in BTH (fig. S6). When severe haze forms with a stable boundary layer and high humidity, inorganic fractions markedly increase with reduced OA, consistent with previous observations in the same area (*20*).

A series of model sensitivity simulations was conducted using altered emission rates, different meteorological conditions, and different sophistication of chemical schemes. An 80% NO_x emission reduction from all sectors in the model, consistent with the observed NO_2 reduction during the city-lockdown period, induces a 13.0% reduction in nitrate aerosol but 26.3% and 15.1% increases in sulfate and secondary OA (SOA), respectively (Fig. 4C). The latter increases can be attributed to the enhanced atmospheric oxidizing capacity after the 42.9% ozone increase (Fig. 4D). The net $PM_{2.5}$ change by NO_x reduction is not evident because of the cancellation of changes in different aerosol components. The meteorological influence on $PM_{2.5}$ and ozone is assessed by comparing a pair of simulations with the meteorological conditions from this year and a multiyear climatology during the same period. It shows that, because of the adverse ventilation conditions and anomalously high humidity during the city-lockdown period, all aerosol species are increased, with the largest fractional change of 63.5% for sulfate (Fig. 4C). Total $PM_{2.5}$ is increased by 31.3% accordingly. Moreover, heterogeneous chemistry processes (materials and methods) contribute positively to the aerosol formation and haze development during the city-lockdown period, because of the concurrent high humidity and aerosol water. Our model assessment shows a 12.0% increase in $PM_{2.5}$ contributed from heterogeneous chemistry in northern China. Comparisons among the simulations altering emissions, chemistry, and meteorology reveal that the previously unseen NO_x reduction during the COVID-19 outbreak does not significantly reduce aerosol formation, because of the nonlinear ozone and aerosol chemistry. In addition, meteorological variations are crucial in the haze formation in northern China by trapping pollutants in the urban area and inducing more efficient aerosol formation from heterogeneous chemistry. Because high humidity and atmospheric stability were absent over central China, including Wuhan, a gradual decline of $PM_{2.5}$ during the lockdown period can be seen in both ground-based observations and model simulations (fig. S7). An increasing trend of ozone can also be identified in the temporal evolution. Aerosol chemical compositions generally are

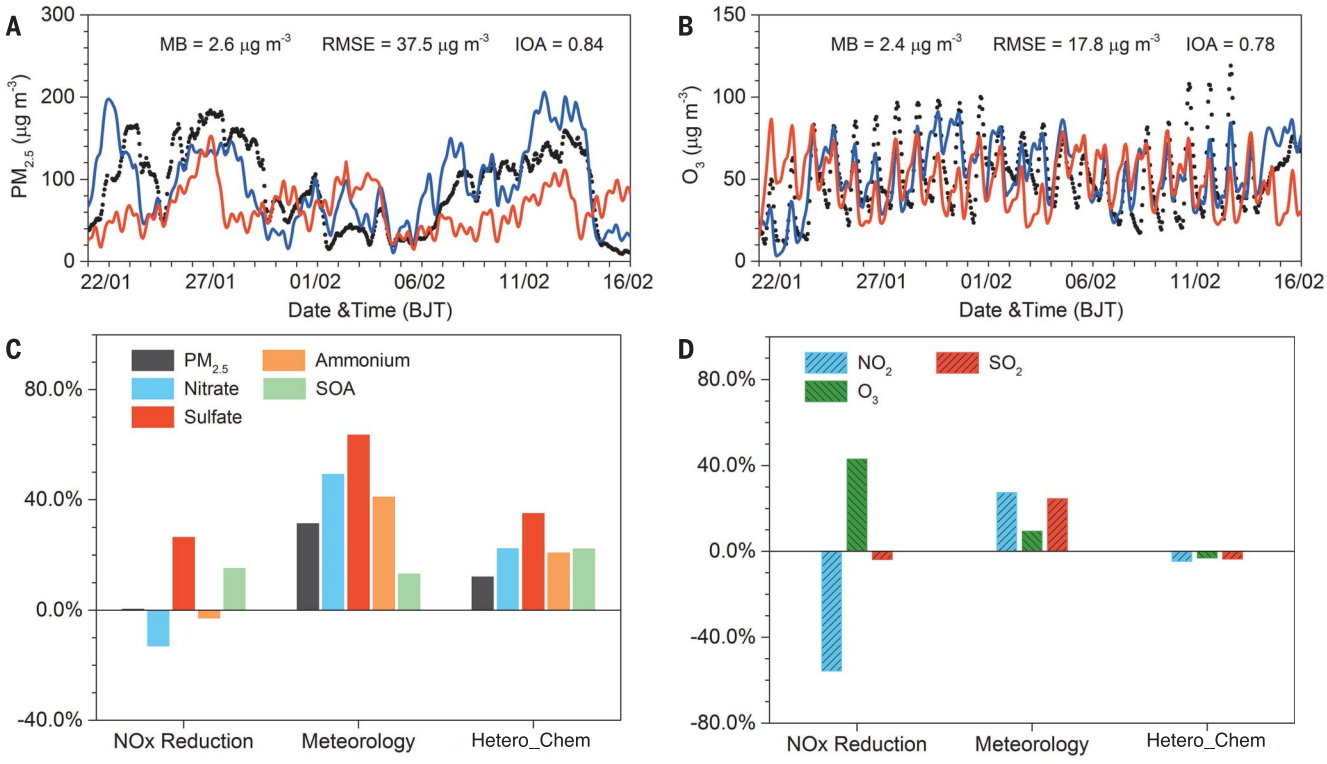


Fig. 4. WRF-Chem simulated aerosol species and precursor gases during the COVID-19 city lockdown period in the BTH region and their sensitivity to the altered emissions, meteorological conditions, and chemical pathways. (**A**) Time evolution of surface $PM_{2.5}$ concentrations in the ground-based observations (black dots), the baseline simulation (blue line), and the sensitivity simulation with the climatological (2015 to 2019) meteorological conditions (red line) (table S3). BJT, Beijing time; IOA, index of agreement; RMSE, root mean square error. (**B**) Same with (A) but for ozone. (**C**) Simulated fractional changes in different aerosol species in response to changes in NO_x emissions, meteorological conditions, and the representation of heterogeneous chemistry. (**D**) Same with (C) but for gaseous pollutants including NO_2, SO_2, and O_3.

maintained, with OA accounting for 36 to 40% of total aerosol mass and sulfate-nitrate-ammonium for another 40% (fig. S6).

The COVID-19 outbreak led to previously unseen anthropogenic emission reductions from traffic and manufacturing sectors and the consequent city lockdowns. Hence, it offered an opportunity to assess the interplay between emissions, chemistry, and meteorology. Our synergistic analyses of the spatiotemporal distributions of PM and precursor gases, meteorological fields, and simulated PM formation pathways reveal a surprising PM exacerbation due to the unfavorable meteorological conditions, invigorated heterogeneous chemistry, and enhanced secondary aerosol formation with the elevated ozone oxidation capacity by NO_x reduction. In particular, our work provides unambiguous evidence that reduction in aerosol precursor emissions was compromised by multiphase chemistry promoted by increased humidity. The role of multiphase chemistry in haze formation is presently uncertain, and the findings in this study call for future research in this area.

Reductions in NO_x and SO_2 from traffic and manufacturing sectors have long been considered as the normal protocol in implementing regulatory policies. Our work shows that such a protocol achieves only limited effects on PM and ozone levels, without simultaneous emission controls from power plants and heavy industry, such as petrochemical facilities. Therefore, we suggest a more comprehensive regulation of precursor gases from all possible sectors when developing an emission control strategy. For example, our model sensitivity experiments show a 20% reduction in ozone and 5% reduction in $PM_{2.5}$ by implementing 30% reductions of VOCs from all possible emission sources (fig. S8). As opposed to the previous Olympic Blue and APEC Blue shutdowns, an unexpected increase in PM levels in northern China occurred in a 3-week period during the COVID-19 pandemic. The decisive role of meteorology in this unexpected haze formation in northern China during this episode underscores the importance of taking meteorological factors into account when short-term stringent emission controls are planned.

As the COVID-19 pandemic is still ongoing, the unexpected PM elevation has potentially profound implications for the airborne transmission of virus (*21*). An emerging study shows plausible virus transmission through aerosols in populous areas (*22*). Meanwhile, exposure to high levels of PM can cause adverse effects on the respiratory and cardiovascular systems and possibly increase the fatality rate of COVID-19. Therefore, future work is urgently needed to establish the causal relationship between aerosol pollution and COVID-19.

REFERENCES AND NOTES

1. Z. An *et al.*, *Proc. Natl. Acad. Sci. U.S.A.* **116**, 8657–8666 (2019).
2. B. Zhao *et al.*, *Proc. Natl. Acad. Sci. U.S.A.* **115**, 12401–12406 (2018).
3. Q. Zhang *et al.*, *Proc. Natl. Acad. Sci. U.S.A.* **116**, 24463–24469 (2019).
4. G. Li *et al.*, *Atmos. Chem. Phys.* **17**, 2759–2774 (2017).
5. K. Li *et al.*, *Proc. Natl. Acad. Sci. U.S.A.* **116**, 422–427 (2019).
6. G. Wang *et al.*, *Proc. Natl. Acad. Sci. U.S.A.* **113**, 13630–13635 (2016).
7. F. Zhang *et al.*, *Proc. Natl. Acad. Sci. U.S.A.* **117**, 3960–3966 (2020).
8. L. Mao *et al.*, *Natl. Sci. Rev.* **6**, 515–523 (2019).
9. S. Wang *et al.*, *Environ. Sci. Technol.* **44**, 2490–2496 (2010).
10. K. Huang, X. Zhang, Y. Lin, *Atmos. Res.* **164–165**, 65–75 (2015).
11. R. Meng *et al.*, *Remote Sens.* **7**, 15224–15243 (2015).
12. D.-Y. Gong *et al.*, *J. Geophys. Res. Atmos.* **119**, 6306–6324 (2014).
13. J. H. Seinfeld, S. N. Pandis, *Atmospheric Chemistry and Physics: From Air Pollution to Climate Change* (Wiley, 2016).
14. M. Levy *et al.*, *Atmos. Environ.* **94**, 231–240 (2014).
15. J. Wu *et al.*, *Proc. Natl. Acad. Sci. U.S.A.* **117**, 9755–9761 (2020).
16. X. Tie *et al.*, *Sci. Rep.* **7**, 15760 (2017).
17. Z. Li *et al.*, *J. Geophys. Res. Atmos.* **124**, 13026–13054 (2019).
18. Y. Wang, A. Khalizov, M. Levy, R. Zhang, *Atmos. Environ.* **81**, 713–715 (2013).

19. Y. Wang, P.-L. Ma, J. H. Jiang, H. Su, P. J. Rasch, *J. Geophys. Res. Atmos.* **121**, 5878–5887 (2016).
20. S. Guo *et al*., *Proc. Natl. Acad. Sci. U.S.A.* **117**, 3427–3432 (2020).
21. R. Zhang, Y. Li, A. L. Zhang, Y. Wang, M. J. Molina, *Proc. Natl. Acad. Sci. U.S.A.* **117**, 14857–14863 (2020).
22. Y. Liu *et al*., *Nature* **582**, 557–560 (2020).

ACKNOWLEDGMENTS

We are grateful to C. Liu and A. Lyapustin for helpful discussions on the satellite products and Y. Wang and Y. Huang for chemistry analysis. **Funding:** Y.W. and Y.L.Y. acknowledge the support of the Jet Propulsion Laboratory, California Institute of Technology, under contract with NASA. Additional support was provided by the NSF (grant AGS-1700727). G.L. and L.L. acknowledge the National Key R&D Plan (grant 2017YFC0210000) and the Strategic Priority Research Program of the Chinese Academy of Sciences (grant XDB40030203). **Author contributions:** Y.W. conceived and designed the research. T.L., Y.W., and Y.L.Y. performed the data analyses and produced the figures. L.L., Y.W., and G.L. performed and analyzed the WRF-Chem simulations. J.Y. and L.L. obtained the ground-based pollution data. Y.W. and J.H.S. wrote the paper. All authors contributed to the scientific discussions and preparation of the manuscript. **Competing interests:** The authors declare no competing interests. **Data and materials availability:** All data are available in the manuscript or the supplementary materials. This work is licensed under a Creative Commons Attribution 4.0 International (CC BY 4.0) license, which permits unrestricted use, distribution, and reproduction in any medium, provided the original work is properly cited. To view a copy of this license, visit https://creativecommons.org/licenses/by/4.0/. This license does not apply to figures/photos/artwork or other content included in the article that is credited to a third party; obtain authorization from the rights holder before using such material.

SUPPLEMENTARY MATERIALS

science.sciencemag.org/content/369/6504/702/suppl/DC1
Materials and Methods
Figs. S1 to S9
Tables S1 to S3
References (*23*–*41*)

16 March 2020; accepted 9 June 2020
Published online 17 June 2020
10.1126/science.abb7431

CORONAVIRUS

Type III interferons disrupt the lung epithelial barrier upon viral recognition

Achille Broggi[1]*, Sreya Ghosh[1]*, Benedetta Sposito[1,2]*, Roberto Spreafico[3]†, Fabio Balzarini[1,2], Antonino Lo Cascio[1,2], Nicola Clementi[4], Maria De Santis[5], Nicasio Mancini[4,6], Francesca Granucci[2,7], Ivan Zanoni[1,2,8]‡

Viral infections of the lower respiratory tract are a leading cause of mortality. Mounting evidence indicates that most severe cases are characterized by aberrant immune responses and do not depend on viral burden. In this study, we assessed how type III interferons (IFN-λ) contribute to the pathogenesis induced by RNA viruses. We report that IFN-λ is present in the lower, but not upper, airways of patients with coronavirus disease 2019 (COVID-19). In mice, we demonstrate that IFN-λ produced by lung dendritic cells in response to a synthetic viral RNA induces barrier damage, causing susceptibility to lethal bacterial superinfections. These findings provide a strong rationale for rethinking the pathophysiological role of IFN-λ and its possible use in clinical practice against endemic viruses, such as influenza virus as well as the emerging severe acute respiratory syndrome coronavirus 2 (SARS-CoV-2) infection.

The ability to resolve viral infections of the lung is dependent on the actions of interferons (IFNs) and inflammatory cytokines, yet their relative contributions to host defense and return to homeostasis remain undefined. In particular, type III IFNs (IFN-λ) have attracted much attention, as they operate primarily at mucosal surfaces (*1*). Recent work established that, unlike other IFNs, IFN-λ signaling induces antiviral activities while simultaneously limiting the tissue-damaging functions of neutrophils (*2*–*4*). When considered in the context of respiratory viral infections in which inflammation appears to be the primary driver of life-threatening symptoms, including the recently emerged severe acute respiratory syndrome coronavirus 2 (SARS-CoV-2) (*5*), the ability of IFN-λ to limit immunopathology but maintain antiviral activity is noteworthy. Discussions on the possible use of IFN-λ against SARS-CoV-2 have begun (*6*), and clinical trials have been initiated. However, despite this interest in the use of IFN-λ to treat viral infections, the long-term effects of IFN-λ on lung physiology remain largely overlooked. For example, during viral infections of the lung, immunopathology may predispose the host to opportunistic bacterial infections, and IFN-λ impairs bacterial control during superinfections (*7*, *8*). It remains unresolved whether this is due to the anti-inflammatory activity of IFN-λ, which reduces host resistance, or to the capacity of IFN-λ to alter lung physiology upon a viral encounter. Indeed, superinfections represent the first cause of lethality upon influenza virus infection (*9*) and correlate with severity in coronavirus disease 2019 (COVID-19) patients (*10*).

Mouse models of SARS, Middle East respiratory syndrome (MERS) (*11*, *12*), and influenza (*1*, *13*) are characterized by a robust induction of type I and III IFNs. However, the involvement of these cytokines in COVID-19 is controversial (*14*, *15*). To directly evaluate the capacity of SARS-CoV-2 to induce IFNs, we tested nasooropharyngeal swabs of COVID-19 patients and healthy controls, as well as the bronchoalveolar lavage fluid (BALF) of SARS-CoV-2–positive patients with severe COVID-19. Levels of IFN mRNAs in the upper airways of COVID-19 patients were not significantly different from levels in healthy controls. By contrast, BALF of patients with severe disease presented elevated levels of both inflammatory cytokines as well as type I and III IFNs (Fig. 1, A to E).

To evaluate the contribution of IFN-λ to the immunopathology driven by RNA respiratory viruses uncoupled from its effect on viral replication, we devised an experimental system in which pattern recognition receptors (PRRs) involved in viral sensing were stimulated with their cognate ligands. RNA viruses are sensed via either endosomal Toll-like receptor (TLR) 3 and TLR7 or cytoplasmic retinoic acid–inducible gene I (RIG-I) and melanoma differentiation-associated protein 5 (MDA5) (*16*). We intratracheally instilled the TLR7 ligand, R848, or the synthetic analog of double-stranded RNA, polyinosine:polycytidylic acid [poly (I:C)], that stimulates both TLR3 and the RIG-I–MDA5 pathway in vivo (*17*). PRRs were stimulated over the course of 6 days to elicit prolonged innate immune activation in the lung. Both ligands induced hypothermia (Fig. 1F) and weight loss (fig. S1A), but only poly (I:C) compromised barrier function (Fig. 1G and fig. S1B). IFN mRNAs were strongly up-regulated by poly (I:C) but not R848 (Fig. 1, H and I). By contrast, R848 treatment induced the up-regulation of proinflammatory cytokines (i.e., *Il1b*), but this did not correlate with barrier function decrease (Fig. 1, G to J, and fig. S1B).

Alterations in the epithelial barrier predispose mice to lethal bacterial superinfections (*18*). We therefore infected mice treated with either R848 or poly (I:C) with *Staphylococcus aureus*. Mice treated with poly (I:C) died upon *S. aureus* infection (Fig. 1K) and had higher bacterial burdens (Fig. 1L), more intense hypothermia, and greater barrier damage (fig. S2, A and B). *S. aureus* infection did not alter the pattern of cytokine expression compared to that in mice treated with viral ligands only (fig. S2, C to E). Upon poly (I:C) administration, IFN-β and IFN-λ transcript and protein levels were rapidly up-regulated and plateaued (fig. S3, A to D), whereas *S. aureus* bacterial burden increased with consecutive injections of poly (I:C) (fig. S3E). IFN-stimulated genes, but not proinflammatory cytokines, were also sustained over time (fig. S3, F to I). These data suggest that chronic exposure to IFNs aggravates bacterial superinfections. Because the protein levels of IFN-λ were very high compared with those of IFN-β (fig. S3, C and D), we assessed whether IFN-λ was sufficient to exacerbate bacterial superinfections. We administered exogenous IFN-λ either alone, or with R848, which induces inflammation but not IFN production (Fig. 1, H to J). The administration of IFN-λ with R848, but not IFN-λ alone, was sufficient to induce sensitivity to *S. aureus* infection (Fig. 1, M and N, and fig. S3J). Thus, in an inflamed lung, IFN-λ is sufficient to aggravate superinfections.

In contrast to wild-type (WT) mice, mice deficient in IFN-λ receptor 1 (*Ifnlr1*) expression were protected from poly (I:C)–induced morbidity and barrier damage (Fig. 2, A and B, and fig. S4, A and B). *Ifnlr1*$^{-/-}$ mice were also resistant to superinfection with *S. aureus* (Fig. 2, C to F). By contrast, the absence of *Ifnlr1* did not affect mRNA or protein levels of IFNs or proinflammatory cytokines (fig. S4, C to H). We next generated reciprocal bone marrow chimeras in which either the hematopoietic or the stromal compartments were defective for IFN-λ signaling. Absence of *Ifnlr1* in the stromal compartment, but not in hematopoietic cells, phenocopied complete *Ifnlr1* deficiency (Fig. 2, G and H, and fig. S5). Furthermore, there was no difference in myeloid immune cell recruitment in *Ifnlr1*$^{-/-}$ compared to WT mice (fig. S6, A to D), and depletion of neutrophils did not affect bacterial burden (fig. S6E). Thus, IFN-λ signaling in epithelial cells is necessary and

[1]Harvard Medical School, Boston Children's Hospital, Division of Immunology, Boston, MA, USA. [2]Department of Biotechnology and Biosciences, University of Milano-Bicocca, Milan, Italy. [3]Institute for Quantitative and Computational Biosciences, University of California, Los Angeles, CA, USA. [4]Laboratory of Medical Microbiology and Virology, Vita-Salute San Raffaele University, Milan, Italy. [5]Department of Rheumatology and Clinical Immunology, Humanitas Clinical and Research Center - IRCCS, Rozzano, Italy. [6]IRCCS San Raffaele Hospital, Milan, Italy. [7]National Institute of Molecular Genetics (INGM) "Romeo ed Enrica Invernizzi," Milan, Italy. [8]Harvard Medical School, Boston Children's Hospital, Division of Gastroenterology, Boston, MA, USA.
*These authors contributed equally to this work.
†Present address: Vir Biotechnology, San Francisco, CA, USA.
‡Corresponding author. Email: ivan.zanoni@childrens.harvard.edu

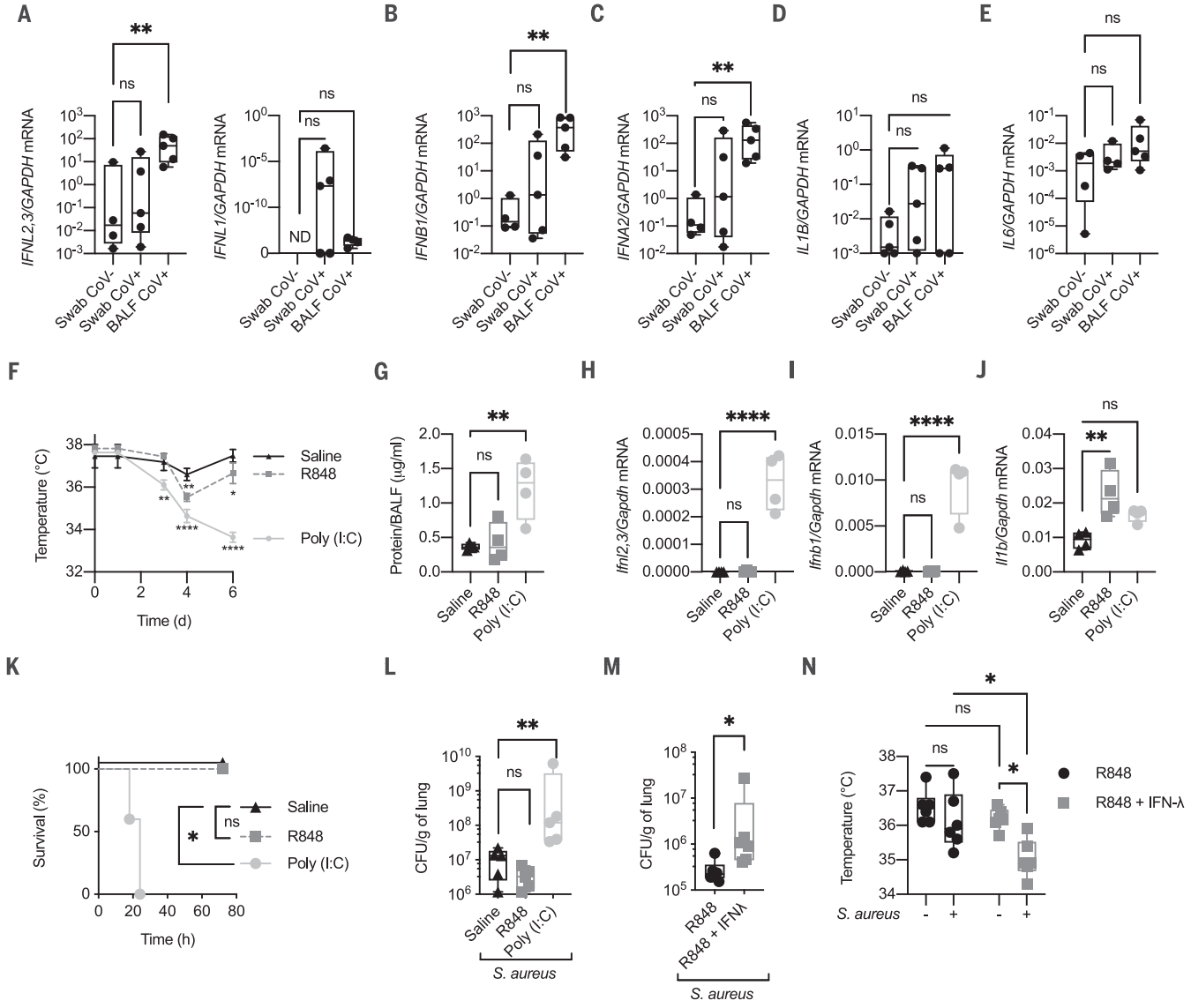


Fig. 1. Morbidity correlates with the high expression of type I IFN and IFN-λ in the lung of COVID-19 patient BALF and of poly (I:C)–treated mice. (**A** to **E**) *IFNL2,3*, *IFNL1* (A), *IFNB* (B), *IFNA2* (C), *IL1B* (D), and *IL6* (E) mRNA expression was evaluated in naso-oropharyngeal swabs from SARS-CoV-2–positive (Swab CoV$^+$) and –negative (Swab CoV$^-$) participants and from the BALF of intensive care unit (ICU)–hospitalized SARS-CoV-2–positive patients (BALF CoV$^+$) (five participants per group). GAPDH, glyceraldehyde phosphate dehydrogenase; ND, not detectable. (**F** to **J**) Mice were intratracheally (i.t.) administered 2.5 mg of poly (I:C) per kilogram of body weight, 2.5 mg of R848 per kilogram of body weight, or saline daily for 6 days. (F) Body temperatures of the treated mice measured over time. (G) Amount of total protein in the BALF measured after 6 days of poly (I:C) treatment. (H to J) *Ifnl2,3* (H), *Ifnb1* (I), and *Il1b* (J) mRNA expression was assessed in total lung lysate harvested 6 days after treatment. (**K** and **L**) Mice treated as in (F) to (J) were infected at day 6 with 5×10^7 colony-forming units (CFU) of *S. aureus* administered i.t. and were monitored for survival (K). Bacterial loads in the lungs of the treated mice normalized to lung weight were assessed 12 hours postinfection (hpi) (L). Mice were i.t. administered R848 (2.5 mg/kg) or a combination of R848 and IFN-λ (50 µg/kg) daily for 6 days and were then infected as in (K). Lung bacterial burdens (**M**) and body temperatures (**N**) before and after *S. aureus* infection are shown [(G) to (J), (L) to (N)]. Each symbol represents one mouse. The median and range are represented. (F) Means ± SDs of five mice per group are represented. (G to J) Four, (L and M) five, and (N) six mice per group are represented, and median and range are shown. (K) Survival plot of five mice per group. (F to N) Representative data of three independent experiments. Statistics: ns, not significant ($P > 0.05$); *$P < 0.05$; **$P < 0.01$; ****$P < 0.0001$. Two-way analysis of variance (ANOVA) [(F) and (N)], one-way ANOVA [(G) to (J), (L)], or two-tailed *t* test (M) was performed. Logarithmic values were fitted when evaluating bacterial load [(L) and (M)]. Log-rank (Mantel-Cox) test, corrected for multiple comparisons, was performed to evaluate survival (K).

sufficient to induce susceptibility to a secondary infection.

A targeted transcriptomic analysis on lung epithelial cells from mice treated with poly (I:C) revealed a potent down-regulation of the IFN signature in *Ifnlr1*$^{-/-}$ compared with WT mice (Fig. 3, A and B, fig. S7, and data S1). This finding confirmed the predominant role of IFN-λ as opposed to type I IFNs during prolonged viral sensing in the lung. Consistent with the observed defect in barrier function, genes associated with apoptosis and the activation of the p53 pathway were enriched in WT compared to *Ifnlr1*$^{-/-}$ epithelial cells (Fig. 3B). By contrast, pathways involved in positive regulation of the cell cycle were enriched in *Ifnlr1*$^{-/-}$ cells (Fig. 3C). Accordingly, epithelial cells in *Ifnlr1*$^{-/-}$ mice, as well as in stromal *Ifnlr1*$^{-/-}$ chimeras, proliferated more

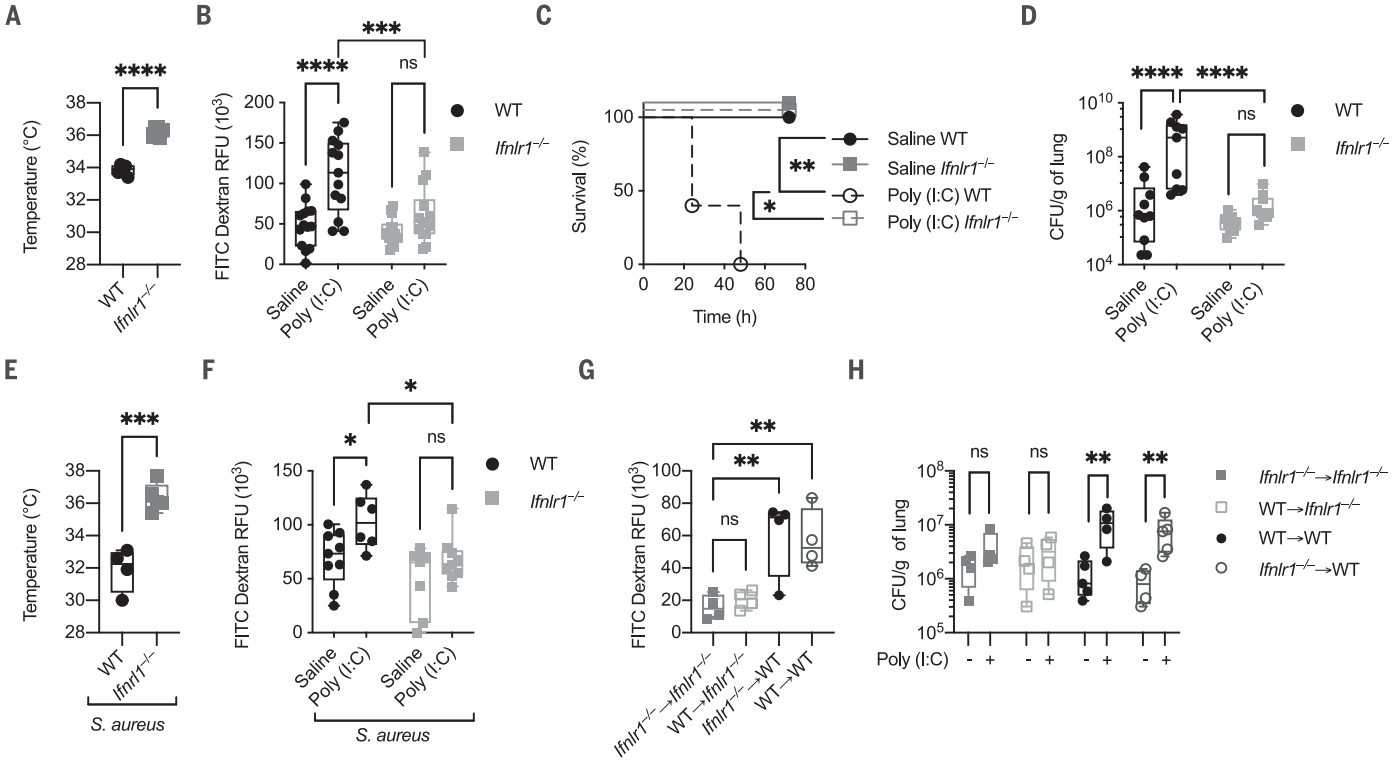


Fig. 2. IFN-λ is necessary to increase susceptibility to bacterial infection induced by antiviral immunity. (**A** and **B**) WT and *Ifnlr1*$^{-/-}$ mice were i.t. treated with 2.5 mg/kg poly (I:C) or saline daily for 6 days. (A) Body temperatures of poly (I:C)–treated WT and *Ifnlr1*$^{-/-}$ mice were recorded on day 6. (B) On day 6, mice were i.t. treated with fluorescein isothiocyanate (FITC)–dextran (10 μg per mouse). Barrier permeability was measured as relative fluorescent units (RFU) of FITC-dextran leaked in plasma 1 hour after injection. (**C** to **F**) WT and *Ifnlr1*$^{-/-}$ mice i.t. treated with 2.5 mg/kg poly (I:C) or saline for 6 days were i.t. infected with 5×10^7 CFU of *S. aureus* and monitored for survival (C). Lung bacterial burdens normalized by lung weight (D), body temperature (E), and barrier permeability (F) [as in (B)] were assessed 12 hpi. (**G** and **H**) Lethally irradiated WT or *Ifnlr1*$^{-/-}$ recipients were reconstituted with donor bone marrow (*Ifnlr1*$^{-/-}$ or WT) for 6 weeks and were then treated as in (C) to (F). Resulting chimeric mice were defective for IFN-λ signaling in either the hematopoietic compartment (*Ifnlr1*$^{-/-}$ → WT) or in the stromal compartment (WT → *Ifnlr1*$^{-/-}$). *Ifnlr1*$^{-/-}$ → *Ifnlr1*$^{-/-}$ and WT → WT chimeras were used as controls. (G) Barrier permeability [as in (B)] and (H) lung bacterial burdens were evaluated 12 hpi. Each symbol represents one mouse. The median and range are represented. (C) Survival plot of five mice per group. (A to H) Representative data of three independent experiments. (A, E, G, and H) Four, (B) 14, and (D and F) 10 mice per group; median and range are represented. Statistics: ns, not significant ($P > 0.05$); *$P < 0.05$; **$P < 0.01$; ***$P < 0.001$; ****$P < 0.0001$. Two-way ANOVA [(B), (D), (F), (H)], one-way ANOVA (G), or two-tailed *t* test [(A) and (E)] was performed. Logarithmic values were fitted when evaluating bacterial load [(D) and (H)]. Log-rank (Mantel-Cox) test, corrected for multiple comparisons, was performed to evaluate survival (C).

efficiently after poly (I:C) administration, in the presence or absence of *S. aureus* (Fig. 3, D to G). The most down-regulated gene in *Ifnlr1*$^{-/-}$ epithelial cells compared with WT cells was the E3 ubiquitin-protein ligase makorin-1 (*Mkrn1*) (Fig. 3A and data S1). The protein encoded by this gene induces p21 degradation and favors apoptosis via p53 under oxidative stress conditions and after DNA damage (hallmarks of severe viral infections) (*19*). Indeed, *Ifnlr1*$^{-/-}$ epithelial cells showed elevated levels of p21 (Fig. 3, H and I). Thus, the ability of IFN-λ to reduce tissue tolerance stems from its capacity to inhibit tissue repair by directly influencing epithelial cell proliferation and viability.

We next investigated the cellular source and molecular pathways that drive IFN-λ production. Upon poly (I:C) administration, lung-resident dendritic cells (DCs) expressed the highest levels of IFN-λ transcript, during both the early and late phases after poly (I:C) administration (Fig. 4A and fig. S8A). By contrast, epithelial cells, alveolar macrophages, and monocytes expressed type I IFNs and proinflammatory cytokines but no IFN-λ transcripts (fig. S8, A to C). Depletion of CD11c$^+$ DCs was sufficient to abolish the production of IFN-λ but not type I IFNs (Fig. 4, B and C, and fig. S8, D and E). Alveolar macrophages were not depleted upon diphtheria toxin administration (fig. S8F) and did not produce IFN-λ in response to poly (I:C) (Fig. 4A). By using in vitro–generated DCs, we found that IFN-λ was induced only when the TLR3 pathway was activated (Fig. 4D and fig. S9, A and B). Consistent with in vivo data, TLR7 stimulation in vitro induced only the up-regulation of proinflammatory cytokines (Fig. 4D and fig. S9, A and B). Ex vivo analysis showed that conventional DC1 (cDC1) are the major producer of IFN-λ (fig. S10). Activation of RIG-I and MDA5 via intracellular delivery of poly (I:C) (Fig. 4D and fig. S9, A and B) and of triphosphate hairpin RNA (3p-hpRNA; fig. S11, A to E) induced high levels of type I IFNs, but not type III IFNs, in a mitochondrial antiviral signaling protein (MAVS)–dependent manner. Blockade of endosomal acidification via chloroquine treatment confirmed the importance of TLR3 for IFN-λ induction (fig. S12, A and B). WT mice or mice that do not respond to TLR3 stimulation [Toll-like receptor adaptor molecule 1 deficient (*Ticam1*$^{-/-}$)] were treated in vivo with poly (I:C). Only DCs sorted from *Ticam1*$^{-/-}$ mice did not express IFN-λ mRNA, although they still expressed type I IFN mRNA (Fig. 4, E and F). Furthermore, *Ticam1*$^{-/-}$ mice were protected against *S. aureus* superinfections (Fig. 4G). *Ticam1*$^{-/-}$ mice also showed lower levels of IFN-λ mRNA (but not type I IFN

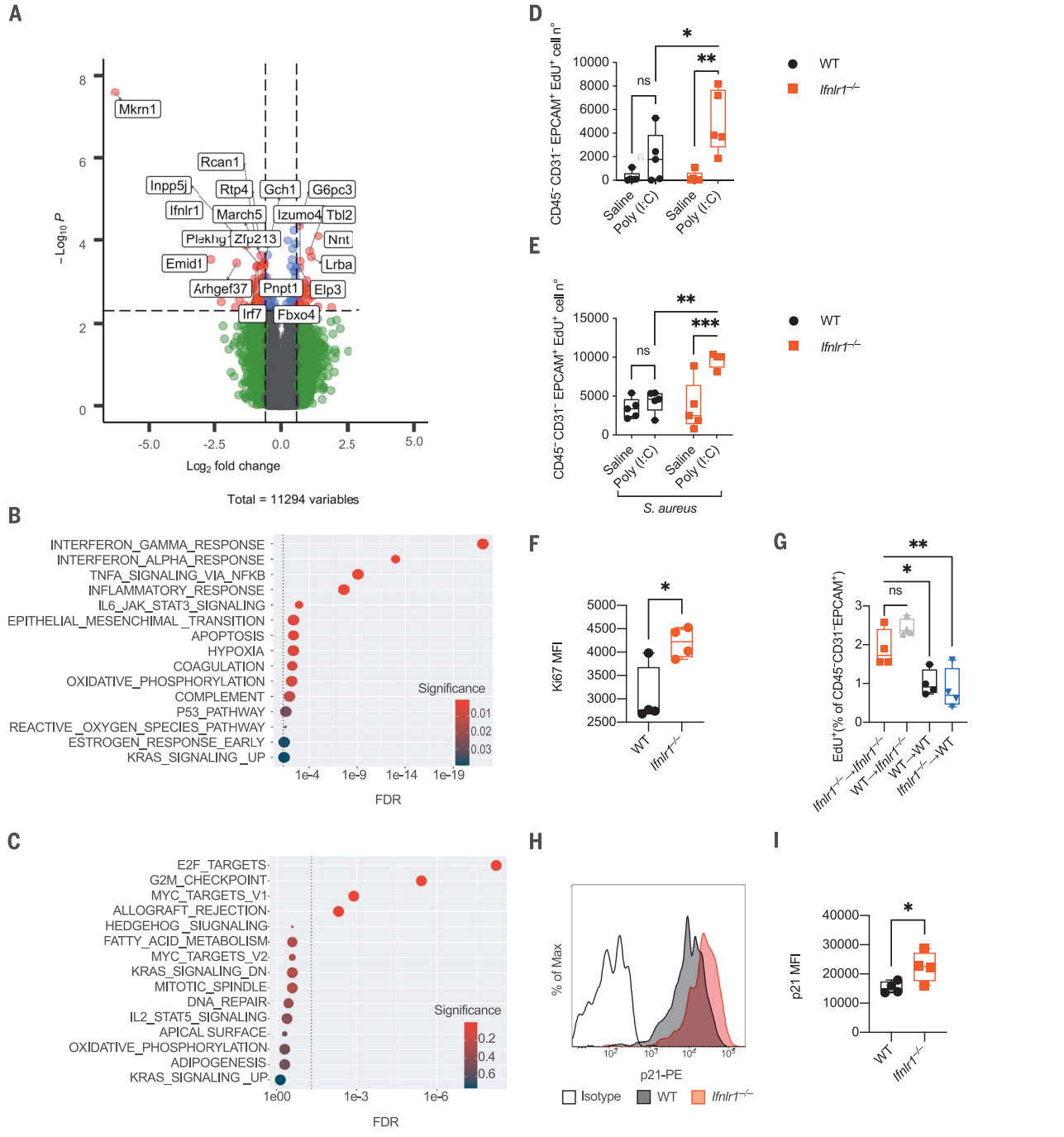


Fig. 3. IFN-λ signaling directly inhibits lung epithelia proliferation and impairs repair upon viral recognition. (**A** to **C**) Targeted transcriptome sequencing was performed on lung epithelial cells isolated on day 6 from WT and *Ifnlr1*$^{-/-}$ mice i.t. treated with 2.5 mg/kg poly (I:C) daily for 6 days. (A) Volcano plot of differentially expressed genes (DEGs) between WT and *Ifnlr1*$^{-/-}$. DEGs ($P < 0.005$) with a fold change >1.5 (or <−1.5) are indicated in red; DEGs with a fold change <1.5 (or >−1.5) are in blue. Nonsignificant DEGs ($P > 0.005$) and genes not differentially expressed are indicated in green and gray, respectively. (B and C) Dot plot visualization of gene set enrichment analysis for pathways enriched in (B) WT epithelial cells compared to *Ifnlr1*$^{-/-}$ and (C) *Ifnlr1*$^{-/-}$ epithelial cells compared to WT. The color of the dots represents the adjusted *P* value (significance) for each enriched pathway; dot size represents the gene set size. FDR, false discovery rate. (**D** and **E**) Epithelial cell proliferation was assessed as 5-ethynyl-2′-deoxyuridine (EdU) incorporation in (D) lung epithelial cells (CD45^{-}CD31^{-}EPCAM^{+}) in WT and *Ifnlr1*$^{-/-}$ mice treated as in (A) to (C) or (E) treated as in (A) to (C) and i.t. infected on day 6 with 5×10^7 CFU *S. aureus* for 12 hours. (**F**) Mean fluorescence intensity (MFI) of Ki67 in CD45^{-}CD31^{-}EPCAM^{+} cells of WT and *Ifnlr1*$^{-/-}$ mice treated as in (A) to (C). (**G**) EdU incorporation in lung epithelial cells of WT or *Ifnlr1*$^{-/-}$ chimeric mice reconstituted with *Ifnlr1*$^{-/-}$ or WT bone marrow treated as in (E). (**H** and **I**) p21 levels in lung epithelial cells (CD45^{-}CD31^{-}EPCAM^{+}) from WT and *Ifnlr1*$^{-/-}$ mice treated as in (A) to (C). Representative histogram (H) and MFI (I) are depicted. (A to C) Four mice per genotype. (D and E) Five and (F to I) four mice per group; median and range are represented. (D to I) Representative data of three independent experiments. Statistics: ns, not significant ($P > 0.05$); *$P < 0.05$; **$P < 0.01$; ***$P < 0.001$. (D and E) Two-way ANOVA, (G) one-way ANOVA, and (F and I) and two-tailed *t* tests were performed.

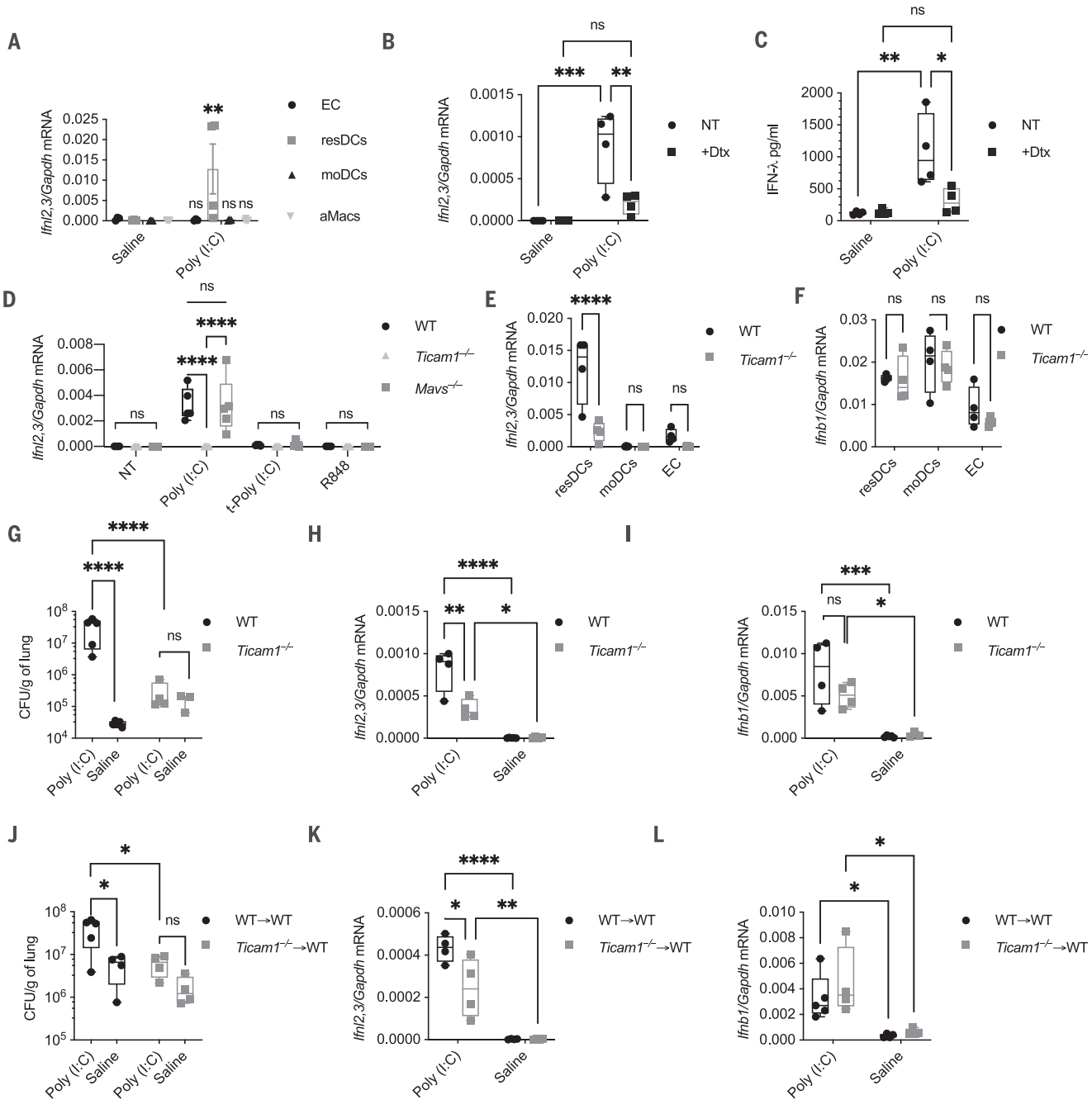


Fig. 4. Lung-resident DCs produce IFN-λ downstream of TLR3 upon viral recognition. (**A**) *Ifnl2,3* relative mRNA expression in lung epithelial cells (EC), resident DCs (resDCs), monocyte-derived DCs (moDCs), and alveolar macrophages (aMacs) sorted from WT mice i.t. treated with 2.5 mg/kg poly (I:C) or saline daily for 6 days measured on day 6. (**B** and **C**) CD11c-DTR mice were injected with diphtheria toxin (DTx) to deplete the $CD11c^+$ cells in vivo. Relative *Ifnl2,3* mRNA (B) and IFN-λ protein levels (C) from lung homogenates were evaluated on day 6. NT, no toxin. (**D**) DCs differentiated from bone marrow cells in the presence of FMS-like tyrosine kinase 3 ligand (Flt3l) for 9 days from WT, *Ticam1*$^{-/-}$, or *Mavs*$^{-/-}$ mice were treated with 50 μg/ml poly (I:C), 1 μg transfected poly (I:C) per 10^6 cells, or 50 μg/ml R848 for 3 hours. Relative *Ifnl2,3* mRNA expression was evaluated by quantitative polymerase chain reaction. (**E** and **F**) *Ifnl2,3* (E) and *Ifnb1* (F) relative mRNA expression in lung EC, resDCs, and moDCs sorted from WT and *Ticam1*$^{-/-}$ mice treated as in (A) was measured on day 6. (**G** to **I**) WT and *Ticam1*$^{-/-}$ mice were treated with poly (I:C) as in (A) and subsequently i.t. infected with 5×10^7 CFU of *S. aureus* on day 6 for 12 hours. Lung bacterial burden normalized by lung weight (G), *Ifnl2,3* (H), and *Ifnb1* (I) relative mRNA expression were evaluated. (**J** to **L**) WT chimeric mice reconstituted with *Ticam1*$^{-/-}$ bone marrow (*Ticam1*$^{-/-}$ → WT) or WT bone marrow (WT → WT) were treated as in (G) to (I). Lung bacterial burden normalized by lung weight (J) and *Ifnl2,3* (K) and *Ifnb1* (L) relative mRNA expression 12 hpi were evaluated. Representative data of three independent experiments are shown. Statistics: ns, not significant ($P > 0.05$); *$P < 0.05$; **$P < 0.01$; ***$P < 0.001$; ***$P < 0.001$ (two-way ANOVA). Four mice per group; median and range are depicted [(A) to (C), (E) to (L)]. Means ± SEMs of four mice [(A) to (C), (E), and (F)] and of three independent experiments (D) are depicted.

mRNA) than WT mice (Fig. 4, H and I). Similar results were obtained when only hematopoietic cells were deficient in *Ticam1* (Fig. 4, J to L).

The immune system evolved to protect against pathogens, but doing so often threatens host fitness and can cause immunopathologies (*20*). In COVID-19, SARS, MERS, and flu, severe symptoms and death occur late, and after the peak in viral load, indicating a central role for the immune system in driving the pathology (*21*–*24*). In our system, we isolated the effect of immune activation from resistance to lung viral infections and demonstrated that sustained IFN-λ is produced by DCs via TLR3. TLR3 detects replication intermediates from dying cells (*25*) and thus is insensitive to viral immune evasion. Correspondingly, IFN-λ acts on lung epithelial cells and compromises lung barrier function, predisposing the host to lethal secondary bacterial infections.

Previous findings suggested that IFN-λ protects against viral infections (*26*) and increases the barrier functions of gut epithelial cells and endothelial cells (*27*–*29*). These discrepancies may have arisen because, in those studies, the particular cell types targeted by IFN-λ were different. Furthermore, our data support the hypothesis that the detrimental activities of IFN-λ occur only upon chronic exposure and in the presence of tissue damage. Early administration of IFN-λ in a mouse model of COVID-19 could instead confer protection (*30*). Our data enjoin clinicians to carefully analyze the duration of IFN-λ administration and to consider the severity of disease when IFN-λ is used as a therapeutic agent against lung viral infections.

REFERENCES AND NOTES

1. A. Broggi, F. Granucci, I. Zanoni, *J. Exp. Med.* **217**, e20190295 (2020).
2. A. Broggi, Y. Tan, F. Granucci, I. Zanoni, *Nat. Immunol.* **18**, 1084–1093 (2017).
3. I. E. Galani *et al.*, *Immunity* **46**, 875–890.e6 (2017).
4. K. Blazek *et al.*, *J. Exp. Med.* **212**, 845–853 (2015).
5. M. Merad, J. C. Martin, *Nat. Rev. Immunol.* **20**, 355–362 (2020).
6. L. Prokunina-Olsson *et al.*, *J. Exp. Med.* **217**, e20200653 (2020).
7. H. E. Rich *et al.*, *Infect. Immun.* **87**, e00114-19 (2019).
8. P. J. Planet *et al.*, *mBio* **7**, e01939-15 (2016).
9. J. A. McCullers, *Nat. Rev. Microbiol.* **12**, 252–262 (2014).
10. G. Zhang *et al.*, *J. Clin. Virol.* **127**, 104364 (2020).
11. R. Channappanavar *et al.*, *J. Clin. Invest.* **129**, 3625–3639 (2019).
12. M. B. Frieman *et al.*, *PLOS Pathog.* **6**, e1000849 (2010).
13. J. Major *et al.*, *Science* **369**, 712–717 (2020).
14. D. Blanco-Melo *et al.*, *Cell* **181**, 1036–1045.e9 (2020).
15. Z. Zhou *et al.*, *Cell Host Microbe* **27**, 883–890.e2 (2020).
16. A. Iwasaki, P. S. Pillai, *Nat. Rev. Immunol.* **14**, 315–328 (2014).
17. H. Kato *et al.*, *Nature* **441**, 101–105 (2006).
18. A. M. Jamieson *et al.*, *Science* **340**, 1230–1234 (2013).
19. E. W. Lee *et al.*, *EMBO J.* **28**, 2100–2113 (2009).
20. R. Medzhitov, D. S. Schneider, M. P. Soares, *Science* **335**, 936–941 (2012).
21. J. S. Peiris *et al.*, *Lancet* **361**, 1767–1772 (2003).
22. Z. A. Memish, S. Perlman, M. D. Van Kerkhove, A. Zumla, *Lancet* **395**, 1063–1077 (2020).
23. R. Wölfel *et al.*, *Nature* **581**, 465–469 (2020).
24. C. K. Lee *et al.*, *Emerg. Infect. Dis.* **17**, 287–291 (2011).
25. O. Schulz *et al.*, *Nature* **433**, 887–892 (2005).
26. L. Ye, D. Schnepf, P. Staeheli, *Nat. Rev. Immunol.* **19**, 614–625 (2019).
27. C. Odendall, A. A. Voak, J. C. Kagan, *J. Immunol.* **199**, 3270–3279 (2017).
28. H. M. Lazear *et al.*, *Sci. Transl. Med.* **7**, 284ra59 (2015).
29. F. Douam *et al.*, *mBio* **8**, e00819-17 (2017).
30. K. H. Dinnon III *et al.*, bioRxiv 081497 [Preprint]. 7 May 2020). https://doi.org/10.1101/2020.05.06.081497.

ACKNOWLEDGMENTS

We thank J. C. Kagan for discussion, help, and support. **Funding:** I.Z. is supported by NIH grants 1R01AI121066 and 1R01DK115217 and NIAID-DAIT-NIHAI201700100. A.B. is supported by CCFA RFA 549868. F.G. is supported by AIRC (IG 2019Id.23512), Fondazione Regionale per la Ricerca Biomedica, FRRB (IANG-CRC - CP2_12/2018), and Ministero della Salute, Ricerca Finalizzata (RF-2018-12367072). **Author contributions:** A.B., S.G., and B.S. designed and performed experiments and analyzed the results; A.B. wrote the paper; R.S. analyzed the sequencing data; F.B. and A.L.C. performed experiments; N.C., M.D.S., and N.M. performed human experiments and analyzed the results; F.G. contributed to the design of the experiments; and I.Z. conceived the project, designed the experiments, supervised the study, and wrote the paper. **Competing interests:** The authors declare no conflicts of interest. **Data and materials availability:** All data are available in the manuscript or the supplementary materials. Use of *Ifnlr1*$^{-/-}$ mice and polyethylene glycol–conjugated IFN-λ2 was performed under a material transfer agreement with Bristol-Myers Squibb. This work is licensed under a Creative Commons Attribution 4.0 International (CC BY 4.0) license, which permits unrestricted use, distribution, and reproduction in any medium, provided the original work is properly cited. To view a copy of this license, visit https://creativecommons.org/licenses/by/4.0/. This license does not apply to figures/photos/artwork or other content included in the article that is credited to a third party; obtain authorization from the rights holder before using such material.

SUPPLEMENTARY MATERIALS

science.sciencemag.org/content/369/6504/706/suppl/DC1
Materials and Methods
Figs. S1 to S13
Tables S1 to S3
MDAR Reproducibility Checklist
Data S1

View/request a protocol for this paper from *Bio-protocol*.

21 April 2020; accepted 8 June 2020
Published online 11 June 2020
10.1126/science.abc3545

CORONAVIRUS

Type I and III interferons disrupt lung epithelial repair during recovery from viral infection

Jack Major[1], Stefania Crotta[1], Miriam Llorian[2], Teresa M. McCabe[1]*, Hans Henrik Gad[3], Simon L. Priestnall[4,5], Rune Hartmann[3], Andreas Wack[1]†

Excessive cytokine signaling frequently exacerbates lung tissue damage during respiratory viral infection. Type I (IFN-α and IFN-β) and III (IFN-λ) interferons are host-produced antiviral cytokines. Prolonged IFN-α and IFN-β responses can lead to harmful proinflammatory effects, whereas IFN-λ mainly signals in epithelia, thereby inducing localized antiviral immunity. In this work, we show that IFN signaling interferes with lung repair during influenza recovery in mice, with IFN-λ driving these effects most potently. IFN-induced protein p53 directly reduces epithelial proliferation and differentiation, which increases disease severity and susceptibility to bacterial superinfections. Thus, excessive or prolonged IFN production aggravates viral infection by impairing lung epithelial regeneration. Timing and duration are therefore critical parameters of endogenous IFN action and should be considered carefully for IFN therapeutic strategies against viral infections such as influenza and coronavirus disease 2019 (COVID-19).

During infection with respiratory viruses, disease severity is linked to lung epithelial destruction, owing to both cytopathic viral effects and immune-mediated damage. Epithelial loss contributes to acute respiratory distress syndrome, pneumonia, and increased susceptibility to bacterial superinfections. Thus, the restoration of damaged epithelial tissues is paramount to maintain lung function and barrier protection.

Interferons (IFNs) are key to the antiviral host defense. IFN-α and IFN-β (IFN-α/β) and IFN-λ are induced upon viral recognition, and they trigger transcription of IFN-stimulated genes with antiviral functions in infected and bystander cells. Because of widespread expression of the type I IFN receptor (IFNAR) in immune cells, IFN-α/β responses can result in immunopathology during viral infections, including influenza virus and severe acute respiratory syndrome–coronavirus 1 (SARS-CoV-1) (*1*–*4*). The IFN-λ receptor (IFNLR) is mainly expressed at epithelial barriers, and IFN-λ responses are therefore often characterized by their ability to confer localized antiviral protection at the site of infection without driving damaging proinflammatory responses like those associated with IFN-α/β. In addition to antiviral and proinflammatory activity, IFNs exert antiproliferative and proapoptotic functions (*5*). Despite a growing understanding of immunopathology in respiratory viral infection, it is unknown how IFN responses affect lung epithelial repair.

Influenza virus infection in C57BL/6 (B6) wild-type (WT) mice resulted in weight loss accompanied by substantial immune cell infiltration and lung damage (fig. S1, A to D). Recovery from infection coincided with the onset of epithelial regeneration (fig. S1, B to D). To further investigate the dynamics of lung repair after influenza virus infection, epithelial cell proliferation was analyzed by flow cytometry using the proliferation marker Ki67 (see gating strategy in fig. S2). During steady-state conditions, type II alveolar epithelial (AT2) cells ($EpCam^{+}MHCII^{+}CD49f^{lo}$) (*6*–*8*) showed a low rate of turnover (Fig. 1A). However, after influenza virus–induced lung damage, AT2 cells underwent rapid proliferation starting at days 5 to 7 after infection, which correlated with mouse recovery and weight gain (Fig. 1A and fig. S1B).

To compare the dynamics of epithelial recovery with IFN production, we analyzed IFN subtypes (IFN-α, IFN-β, and IFN-λ) in bronchoalveolar lavage fluid (BALF) throughout infection. IFNs were produced rapidly, peaking 2 days after infection (Fig. 1B). The magnitude of IFN-λ production was significantly greater than that of IFN-α/β, both in duration and in length of peak production. Notably, only IFN-λ was detected 7 to 8 days after infection, coinciding with the onset of epithelial recovery (Fig. 1, A and B). Thus, after influenza virus infection, signaling triggered by IFNs—particularly by IFN-λ—overlaps with the onset of lung repair.

To compare the effects of equipotent amounts of IFN-α, IFN-β, and IFN-λ on lung repair, mice were treated during recovery from influenza virus infection (7 to 10 days after infection; figs. S3A and S4). To study the effects of IFN treatment specifically on epithelial cells, we generated irradiation bone marrow (BM) chimeras in which WT recipients were given $Ifnar1^{-/-}$ BM cells ($Ifnar1^{-/-}$ → WT BM chimeric), thereby restricting IFNAR expression to the stromal compartment.

In chimeric mice, both IFN-α and IFN-β treatments significantly reduced the proliferation of AT2 cells on day 11 after influenza virus infection (Fig. 1C). Similarly, IFN-λ treatment reduced AT2 cell proliferation in WT mice (Fig. 1D). Reductions in proliferation were independent of changes in viral burden (fig. S3, B and C). The IFN-λ–mediated reduction in AT2 cell proliferation did not require IFN-λ signaling in neutrophils (*9*–*11*), as neutrophil depletion in WT mice using an anti-Ly6G monoclonal antibody had no effect (fig. S3, D and E). A caveat to bear in mind when using inbred mouse strains for influenza virus infection is their lack of a functional Mx1 protein, a crucial IFN-inducible influenza virus restriction factor in both mice and humans (*12*). We therefore infected mice expressing functional Mx1 alleles (B6-Mx1) with the influenza virus strain hvPR8-ΔNS1 for a more–clinically relevant influenza model. IFN-λ treatment significantly reduced epithelial proliferation in the presence of functional Mx1 as well (Fig. 1E).

We next used $Ifnar1^{-/-}$ and $Ifnlr1^{-/-}$ mice to determine the role of endogenous IFNs during lung repair. AT2 cells were analyzed on day 8 after influenza virus infection, the time when IFN signaling and epithelial cell proliferation overlapped (Fig. 1, A and B). Both $Ifnar1^{-/-}$ and $Ifnlr1^{-/-}$ mice had improved AT2 cell proliferation compared with WT controls (Fig. 1, F and G). This was dependent on IFN signaling specifically through the epithelium, because receptor deficiency in the stromal compartment alone was sufficient to increase lung epithelial cell proliferation (Fig. 1H). Improved proliferation was independent of major changes in viral burden (fig. S5A). Viral control in individual IFN receptor–knockout mice was likely unaffected owing to redundancy between type I and III IFN antiviral responses in epithelial cells (*13*, *14*). Despite type I and III IFN redundancy in viral control (fig. S5A), the lack of redundancy in antiproliferative IFN responses—with both $Ifnar1^{-/-}$ and $Ifnlr1^{-/-}$ mice displaying enhanced epithelial proliferation (Fig. 1, F to H)—led us to further interrogate the phenotype. IFNAR signaling has been previously shown to be important for the production of IFN-λ during influenza virus infection (*15*, *16*). Consistent with these findings, we observed a significant reduction in IFN-λ (and in IFN-α/β) production in $Ifnar1^{-/-}$ mice compared with WT; yet, we saw little change in IFN-α/β levels in $Ifnlr1^{-/-}$ mice (fig. S5B). Thus, the improved epithelial proliferation in $Ifnar1^{-/-}$ mice may result from reduced IFN-λ. IFN production defects in

[1]Immunoregulation Laboratory, The Francis Crick Institute, London, UK. [2]Bioinformatics and Biostatistics, The Francis Crick Institute, London, UK. [3]Department of Molecular Biology and Genetics, Aarhus University, Aarhus, Denmark. [4]Department of Pathobiology and Population Sciences, The Royal Veterinary College, Hatfield, UK. [5]Experimental Histopathology Science Technology Platform, The Francis Crick Institute, London, UK.
*Present address: Adaptive Immunity Research Unit, GlaxoSmithKline, Stevenage, UK.
†Corresponding author. Email: andreas.wack@crick.ac.uk

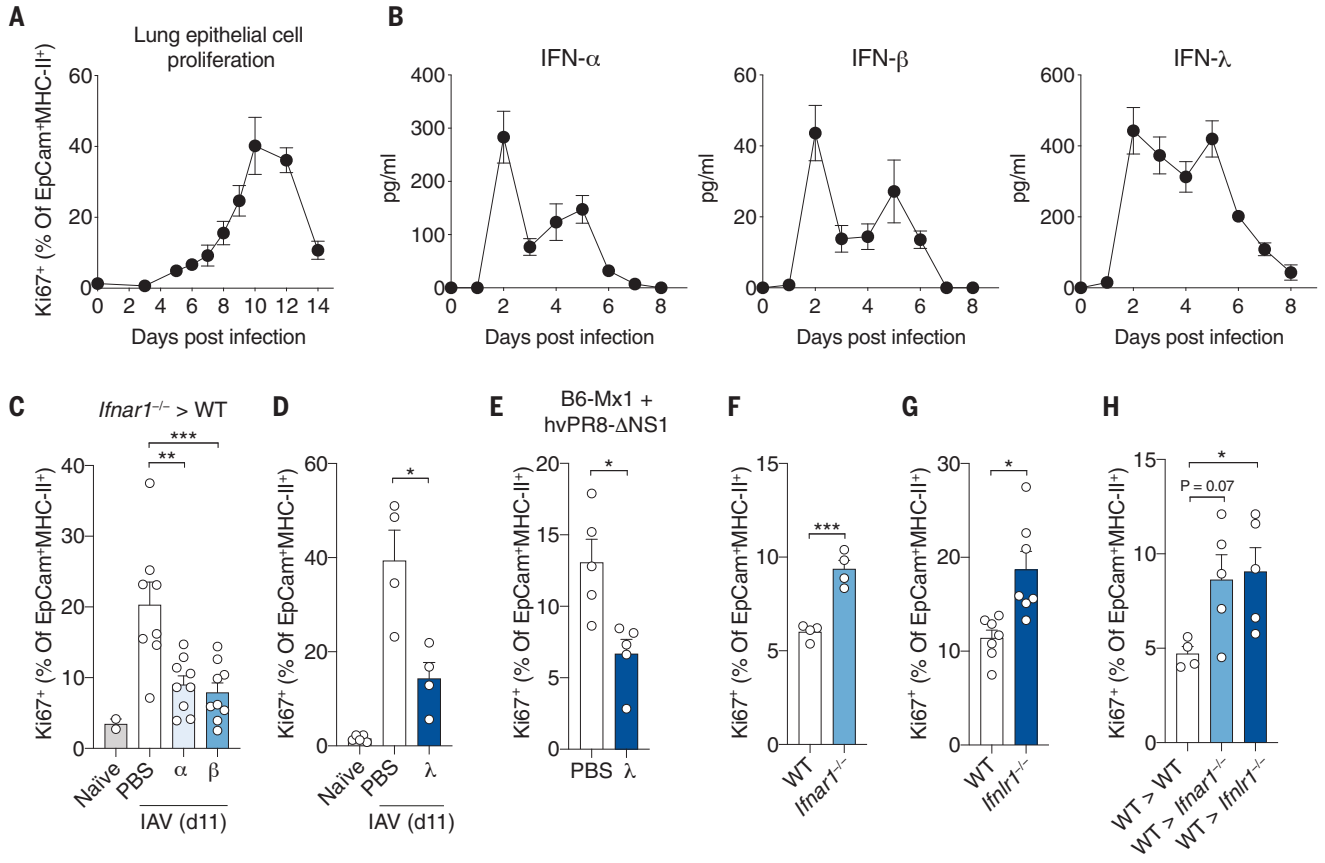


Fig. 1. Type I and III IFNs reduce epithelial cell proliferation during lung repair. (**A** and **B**) Mice were infected intranasally with 10^4 $TCID_{50}$ X31 (H3N2) influenza virus in 30 μl. (A) Proliferating ($Ki67^+$) AT2 cells ($EpCam^+MHCII^+CD49f^{lo}$) were measured by flow cytometry (n = 5 mice). (B) Type I and III IFN levels were detected in BALF (n = 4) on indicated days after infection. (**C** and **D**) X31-infected mice were administered IFNs every 24 hours (on days 7 to 10 after infection). Proliferating ($Ki67^+$) AT2 cells ($EpCam^+MHCII^+CD49f^{lo}$) were measured by flow cytometry on day 11 after infection. (C) Lethally irradiated WT mice were injected with $Ifnar1^{-/-}$ BM cells. After reconstitution, influenza virus–infected chimeric mice were treated with phosphate-buffered saline (PBS) control (n = 8), IFN-α (n = 9), or IFN-β (n = 9). Naïve controls were uninfected, untreated BM chimeric mice (n = 2). (D) Infected WT mice were treated with IFN-λ (n = 4) or PBS control (n = 4). Naïve controls were uninfected, untreated WT mice (n = 5). IAV, influenza A virus. (**E**) B6-Mx1 mice were infected with 2.5×10^3 $TCID_{50}$ hvPR8-ΔNS1 (H1N1) and treated with IFN-λ (n = 4) or PBS control (n = 4). IFN treatment and lung analysis were performed as for (C) and (D). (**F** to **H**) Lungs from X31-infected WT mice (n = 4 to 7), $Ifnar1^{-/-}$ mice (n = 4) (F), $Ifnlr1^{-/-}$ mice (n = 7) (G), and BM chimeric mice (n = 4 to 5) (H) were harvested; and proliferating ($Ki67^+$) AT2 cells were measured by flow cytometry on day 8 after infection. All data are representative of at least two independent experiments. Data are shown as means ± SEM, and statistical significance was assessed by one-way analysis of variance (ANOVA) with Dunnett's posttest [(C), (D), and (H)] or unpaired two-tailed Student's t test [(E) to (G)]. $P > 0.05$; $^*P \le 0.05$; $^{**}P \le 0.01$; $^{***}P \le 0.001$.

$Ifnar1^{-/-}$ mice are linked to reduced steady-state priming in the absence of tonic IFNAR activation in immune cells (*17*). To circumvent this, we administered an anti-IFNAR monoclonal antibody (MAR1-5A3) only from the onset of influenza virus infection. Anti-IFNAR treatment maintained steady-state priming required for IFN-λ production (fig. S5C), despite blocking IFN-α/β signaling through IFNAR (fig. S5D). Notably, anti-IFNAR treatment from day 0 or day 3 after infection had no effect on lung epithelial cell proliferation (fig. S5E). Thus, in murine influenza virus infection, endogenous IFN-λ responses are most effective in disrupting epithelial regeneration during influenza recovery through direct effects on epithelial cells.

To understand mechanistically how IFNs exert the observed antiproliferative effects, we set up primary murine airway epithelial cell (AEC) cultures. AECs undergo rapid proliferation and differentiation upon exposure to an air-liquid interface (ALI), which recapitulates lung repair processes observed in vivo (*18*, *19*). IFNs used for in vitro assays were titrated on AEC cultures to compare IFN subtypes at equivalent biological potencies (fig. S6). All three IFN subtypes significantly impaired the growth of AEC cultures, with IFN-β and IFN-λ having the most significant effects (Fig. 2, A to E, and fig. S7A). Similar effects were observed when primary human AEC cultures were treated with equivalent doses of IFN subtypes (Fig. 2C). Growth inhibitory effects were dependent on the presence of the respective IFN receptor (fig. S7B). IFN-β or IFN-λ treatment increased the frequency of apoptotic or necrotic cells (defined as annexin V^+ and TO-PRO-3^+) (fig. S7, C and D); however, the growth inhibitory effects of IFNs were only observed in actively dividing cultures (fig. S7, E to G). Thus, the increase in apoptosis observed may occur as a result of failed progression through the cell cycle after IFN treatment, as has been seen previously (*20*).

We next examined the effects of IFNs on AEC differentiation. After acute damage, populations of basal cells and $Scgb1a1^+$ secretory cells give rise to secretory and multiciliated cell subtypes (*21*). To study the effects of IFNs on AEC

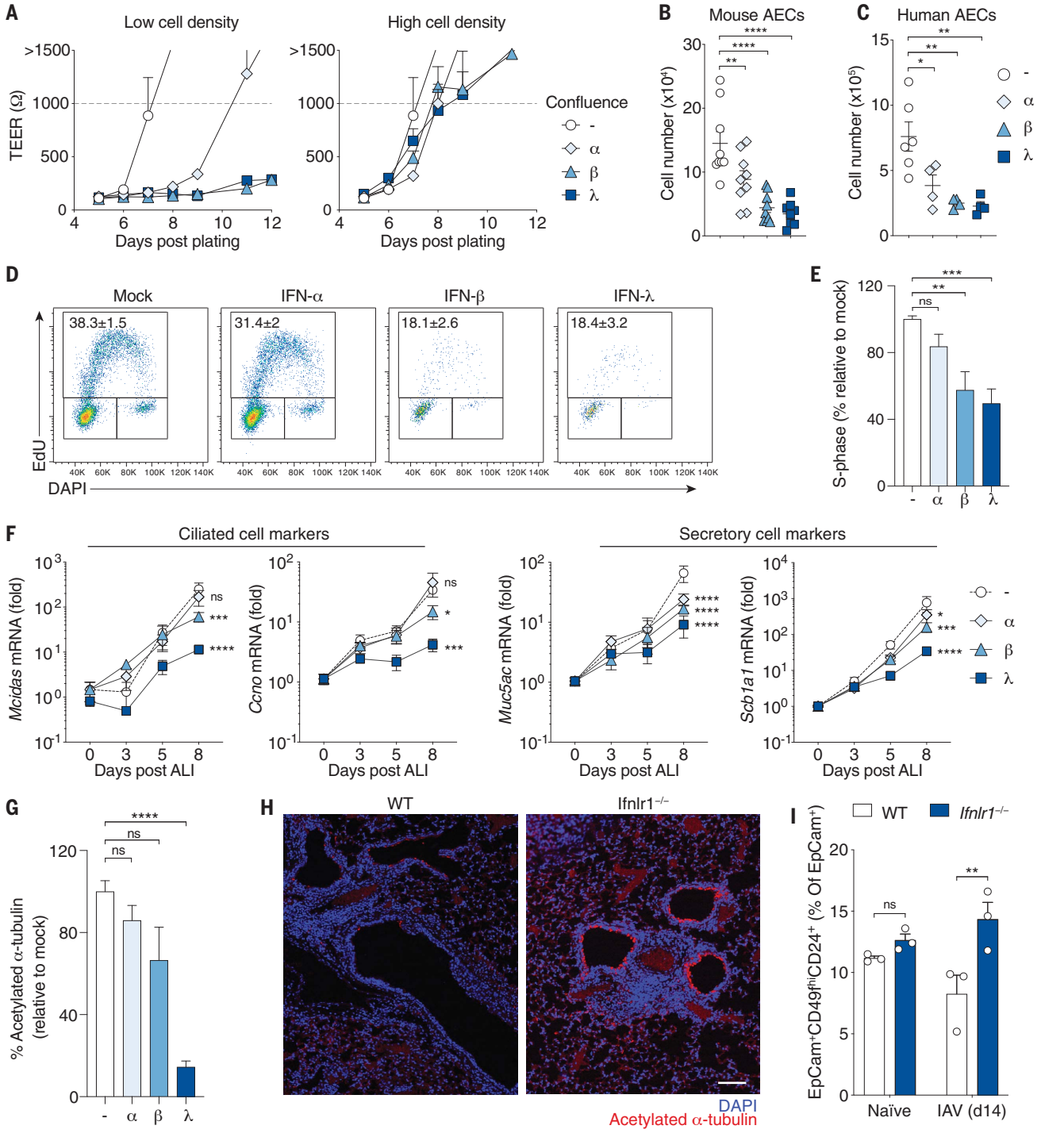


Fig. 2. IFN signaling blocks AEC growth and differentiation. (**A**) Murine AECs were seeded at a low density (500 cells per transwell) or high density (10^4 cells per transwell) in the presence of equivalent doses of IFN-α, IFN-β, IFN-λ, or media control, and then grown for 12 days (n = 3 transwells for all conditions). Confluence was determined by measuring transepithelial electrical resistance (TEER) (>1000 ohm = confluent cultures). (**B**, **D**, and **E**) Proliferating murine AEC cultures (2 days before exposure to an ALI) were treated for 5 days with IFNs (2 days before ALI to day 3 after ALI), and effects on growth were determined by cell number (n = 9) (B) and incorporation of the thymidine analog EdU to measure proliferation (n = 9) [(D) and (E)]. DAPI, 4′,6-diamidino-2-phenylindole; EdU, 5-ethynyl-2′-deoxyuridine. (**C**) Primary human AEC cultures were treated with IFNs for 5 days and cells were counted (n = 4 to 6). (**F** and **G**) Murine AECs were grown to confluence, then exposed to an ALI for 2 days. IFNs were then administrated for 6 days during ALI exposure (n = 6 for all conditions). Differentiation was determined by mRNA expression of the indicated genes (F) and the level of acetylated α-tubulin staining in cultures (G). (**H** and **I**) WT and *Ifnlr1*$^{-/-}$ mice were infected with influenza virus, and lungs were analyzed by immunofluorescence (DAPI or acetylated α-tubulin) on day 10 after infection (n = 4 mice) (H), and flow cytometry (EpCam$^+$CD49f^{hi}CD24$^+$) on day 14 after infection (n = 3) (I). All data are representative of at least three independent experiments. Data are shown as means ± SEM, and statistical significance was assessed by one-way [(B), (C), (E), and (G)] or two-way [(F) and (I)] ANOVA with Dunnett's posttest. Scale bar represents 100 μm (H). ns, not significant; $P > 0.05$; *$P \le 0.05$; **$P \le 0.01$; ***$P \le 0.001$; ****$P \le 0.0001$.

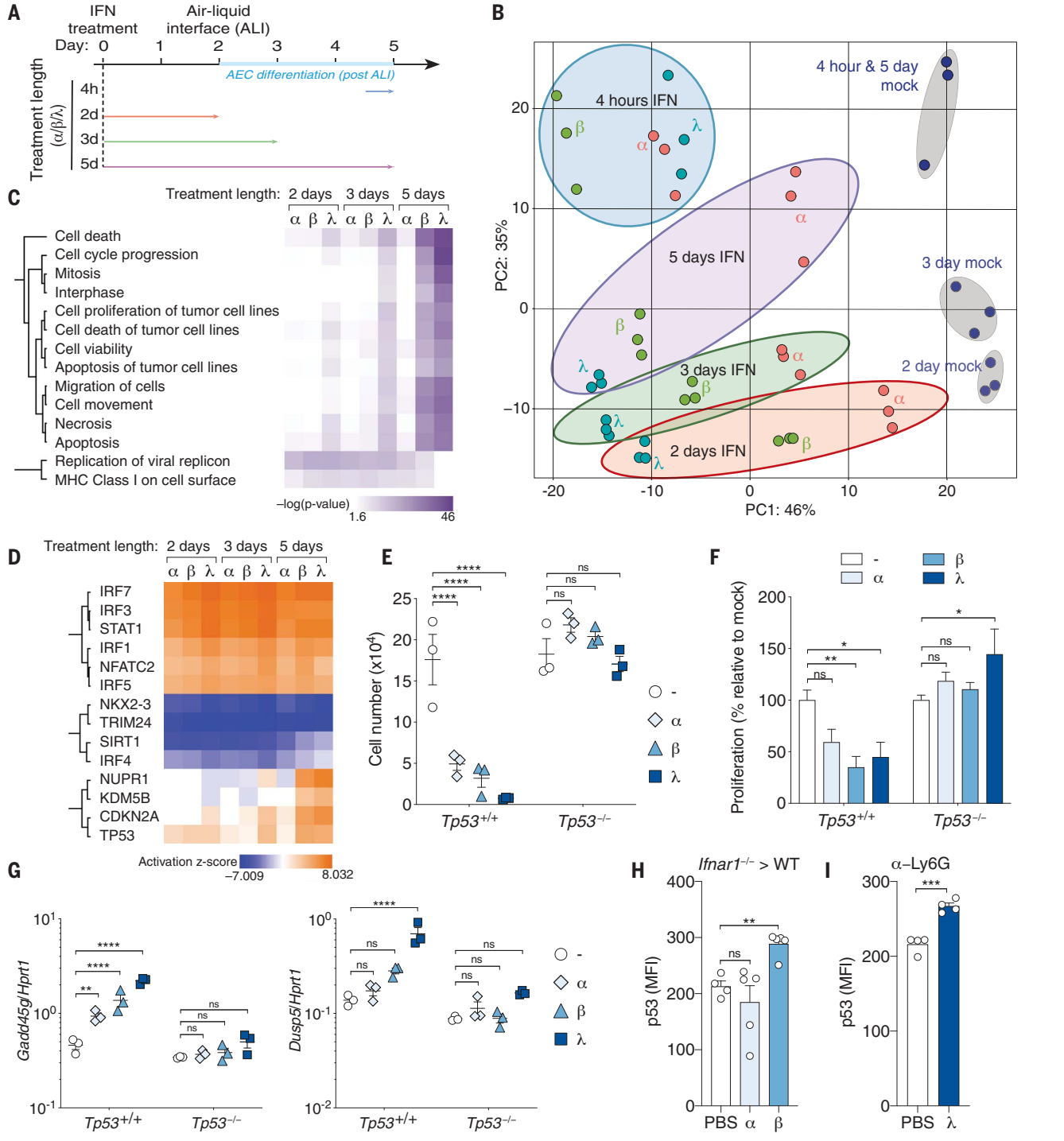


Fig. 3. Type I and III IFNs activate antiproliferative and cell death pathways in AECs via induction of p53. (**A**) Schematic diagram for IFN treatment of murine AECs for RNA-sequencing analysis. (**B**) PCA plot of RNA-sequencing data from AECs after IFN treatment and from untreated controls. (**C**) Heatmap for significant differences in canonical pathways for nine pairwise comparisons between indicated IFN treatment and the respective mock, at each time point (fold change >1.5, one-way ANOVA with Benjamini-Hochberg correction, $P < 0.05$). Gene expression was compared using ingenuity pathway comparison analysis. MHC, major histocompatibility complex. (**D**) Predicted upstream transcriptional regulators of differentially expressed genes (ingenuity pathway analysis). (**E** to **G**) WT and *p53*$^{-/-}$ murine AECs were treated with IFN subtypes for 5 days and measured for growth by cell number (E), CFSE (carboxyfluorescein diacetate succinimidyl ester) dilution (F), and mRNA expression of indicated genes (G) ($n = 3$ transwells for all conditions). (**H** and **I**) *Ifnar1*$^{-/-}$ → WT BM chimeric mice ($n = 4$ to 5 mice) (H) and α-Ly6G treated mice ($n = 4$) (I) infected with influenza virus (X31), and treated with IFN every 24 hours consecutively for 4 days (days 7 to 10 after infection), before EpCam^{+}MHCII^{+}CD49f^{lo} AT2 cells were analyzed for p53 mean fluorescence intensity (MFI) on day 11 after infection by flow cytometry. All data are representative of at least two independent experiments [(E) to (I)]. Data are shown as means ± SEM, and statistical significance was assessed by two-way [(E) to (G)] or one-way (H) ANOVA with Dunnett's posttest or by unpaired two-tailed Student's *t* test (I). ns, not significant; $P > 0.05$; *$P \leq 0.05$; **$P \leq 0.01$; ***$P \leq 0.001$; ****$P \leq 0.0001$.

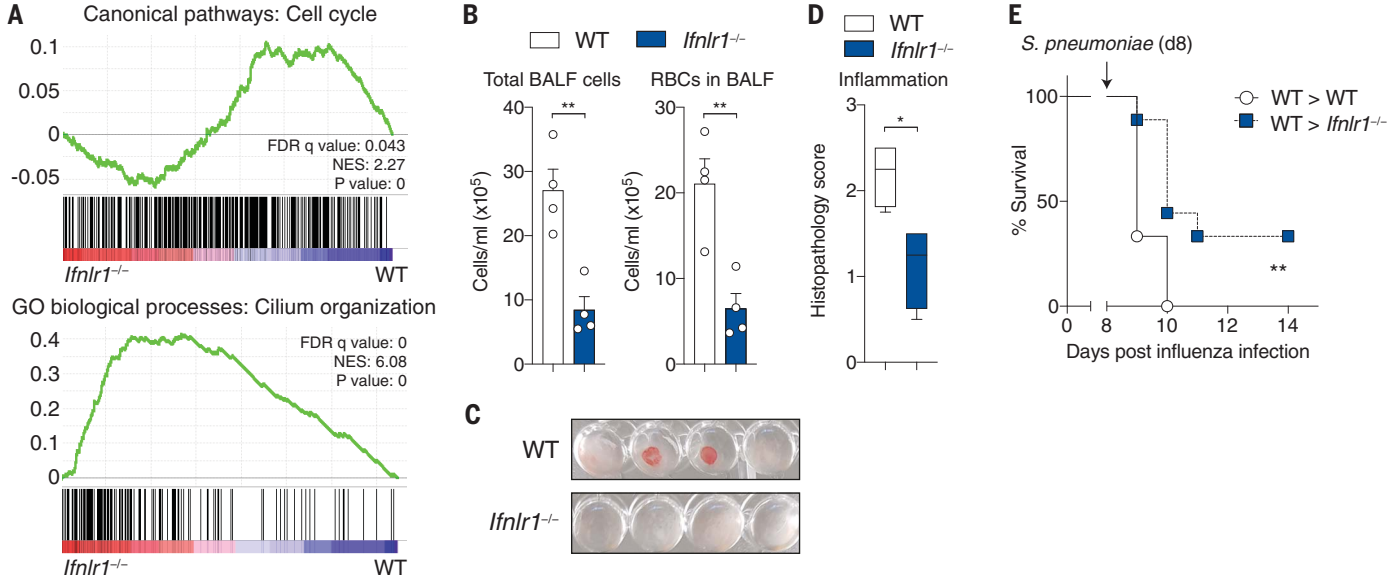


Fig. 4. *Ifnlr1*$^{-/-}$ mice have improved lung repair, reduced damage, and improved epithelial barrier function. WT and *Ifnlr1*$^{-/-}$ mice were infected with 10^4 $TCID_{50}$ X31 influenza virus (X31). (**A**) GSEA plots of RNA-sequencing datasets from WT or *Ifnlr1*$^{-/-}$ bulk lung epithelial cells (EpCam$^+$) on day 8 after infection. FDR, false discovery rate; NES, normalized enrichment score; GO, gene ontology. (**B** and **C**) Total cell and red blood cell (RBC) (TER-119$^+$) number in BALF on day 8 after infection (n = 4 mice for both WT and *Ifnlr1*$^{-/-}$). (**D**) Histopathological analysis of hematoxylin and eosin (H&E) lung sections on day 9 after infection (n = 4 for both WT and *Ifnlr1*$^{-/-}$). (**E**) Lethally irradiated WT and *Ifnlr1*$^{-/-}$ mice were injected with WT BM cells. After reconstitution, chimeric mice were challenged with 2×10^5 colony-forming units TIGR4 in 30 µl on day 8 (d8) after influenza virus infection (n = 8 WT; n = 9 *Ifnlr1*$^{-/-}$). All data are representative of at least two independent experiments [(B) to (E)]. Data are shown as means ± SEM, and statistical significance was assessed by unpaired two-tailed Student's t test (B), Mann-Whitney U test (D), or log-rank (Mantel-Cox) test (E). *$P \le 0.05$; **$P \le 0.01$.

differentiation, we initiated IFN treatment late during the course of AEC growth, during air exposure when AEC differentiation is induced (fig. S8A). IFN-β and IFN-λ treatment significantly reduced the expression of genes pertaining to multiciliated (*Mcidas* and *Ccno*) and secretory (*Muc5AC* and *Scb1a1*) cell differentiation (Fig. 2F). Expression of the basal cell marker *Krt5* remained unchanged or was increased by IFN-λ treatment, which suggests maintenance of stemness (fig. S8B). We also found reduced numbers of multiciliated cells in AEC cultures (acetylated α-tubulin$^+$) after IFN-λ treatment, but we did not observe this with IFN-α or IFN-β treatment (Fig. 2G and fig. S8C). In vivo, *Ifnlr1*$^{-/-}$ mice displayed increased multiciliated cells in repairing conducting airways on day 10 after influenza virus infection (Fig. 2H). Using flow cytometry, we quantified this increase in the frequency of differentiated AECs (EpCam^{hi}CD49f^{hi}CD24$^+$) composed of multiciliated, goblet, and club cells (Fig. 2I and fig. S2) (*22*). Thus, IFN-λ signaling reduces the capacity for basal cell differentiation during recovery from influenza virus infection.

To understand how IFNs mediate antiproliferative effects, we performed RNA sequencing on IFN-treated AEC cultures (Fig. 3A). Principal components analysis (PCA) clustered 4-hour IFN-treated samples together regardless of subtype (Fig. 3B), which confirmed equal subtype dosage on the basis of previous titrations (fig. S9A). Five days of IFN-β or IFN-λ treatment clustered AECs together separately from untreated controls on both PC1 and PC2 (Fig. 3B). Gene ontology analysis confirmed that genes contributing to this variance are involved in IFN signaling and epithelial cell development (supplementary text and fig. S9B). Ingenuity pathway analysis revealed induction of pathways regulating cell cycle and cell death after prolonged IFN treatment, most significantly induced by IFN-λ across all time points (Fig. 3C). Predicted upstream transcriptional regulators identified typical regulators of IFN function—including STAT (signal transducer and activator of transcription) and IRF (IFN regulatory factor) proteins—in addition to cell cycle regulators (Fig. 3D). We identified the tumor suppressor protein p53 as a top candidate regulating IFN-inducible antiproliferative effects. p53 has previously been shown to directly regulate IFN-α/β antitumor responses (*23*). Gene set enrichment analysis (GSEA) identified IFN-mediated induction of the p53 pathway (fig. S9C), and we identified induction of p53-regulated downstream targets in expression data (fig. S9D). To confirm the role of p53, we utilized *Tp53*$^{-/-}$ AEC cultures. IFN-mediated reduction in AEC growth, differentiation, and induction of antiproliferative downstream p53 target genes *Gadd45g* and *Dusp5* (*24*, *25*) was p53-dependent, with no changes observed in *Tp53*$^{-/-}$ AECs (Fig. 3, E to G, and fig. S9E). We next examined whether IFNs regulate p53 activity in epithelial cells during lung repair in vivo. To study IFN effects specifically in the lung epithelium, we once again generated *Ifnar1*$^{-/-}$ → WT BM chimeric mice for IFN-α or IFN-β treatment, and we depleted neutrophils in WT mice with anti-Ly6G for IFN-λ treatment (fig. S3A). IFN-β and IFN-λ, but not IFN-α, significantly up-regulated p53 expression in repairing lung epithelial cells (Fig. 3, H and I). Thus, IFN-β and IFN-λ mediate antiproliferative effects in AECs via the induction of p53.

Our data support a key role for IFN signaling, particularly IFN-λ, in the reduction of epithelial proliferation and differentiation during lung repair. We therefore tested whether IFNs alter the state or barrier function of lung epithelia. RNA sequencing of sorted lung epithelial cells (EpCam$^+$CD31$^-$CD45$^-$) from influenza virus–infected WT or *Ifnlr1*$^{-/-}$ mice confirmed an up-regulation of pathways pertaining to proliferation and multiciliogenesis in *Ifnlr1*$^{-/-}$ mice (Fig. 4A). Improved repair correlated with reduced lung damage, with a reduction in both the total number of cells and the number of red blood cells in the BALF of *Ifnlr1*$^{-/-}$ mice at day 8 after infection (Fig. 4, B and C, and fig. S10A). Additionally, *Ifnlr1*$^{-/-}$ mice had fewer immune

cells infiltrating lung tissue (Fig. 4D). In humans, influenza virus–induced epithelial damage increases susceptibility to infection by opportunistic bacterial pathogens, including *Streptococcus pneumoniae* (*26*). To measure the effects of IFN-λ on lung barrier function, we challenged influenza virus–infected mice with *S. pneumoniae*. Both full-IFNLR-knockout mice and mice lacking IFNLR in the stromal compartment (WT → *Ifnlr1*$^{-/-}$) had improved survival after bacterial superinfection (Fig. 4E and fig. S10B). Thus, IFN-λ signaling reduces the capacity for epithelial repair, which results in prolonged lung damage, compromised barrier function, and increased susceptibility to bacterial superinfection.

In this work, we describe a mechanism by which type I and III IFN signaling aggravates lung pathology during respiratory viral infection. Although all three IFN subtypes reduced lung proliferation after treatment during influenza recovery, only endogenous IFN-λ compromised repair. This is likely because of increased IFN-λ production during infection combined with greater induction of antiproliferative pathways. A recent study has shown that IFN-λ produced by dendritic cells inhibits lung epithelial repair after viral recognition (*27*). Influenza virus–infected macaques have been found to have an elevated IFN signature late during infection in bronchial tissue (*28*). Additionally, COVID-19 patients have displayed strong induction of IFN and p53 signaling in collected BALF samples (*29*). Analysis of lung tissue and BALF from respiratory virus–infected patients experiencing severe disease will provide insight into the mechanisms regulating disease pathogenesis. IFN-λ treatment early during influenza virus infection is protective in mice, offering antiviral protection without the proinflammatory responses associated with IFN-α/β (*30*, *31*). By studying specific effects in the respiratory epithelium, we identified a mechanism by which IFN exacerbates respiratory virus disease, independent of immunomodulation. Our data indicate the need for effective regulation of host IFN responses and the importance of timing and duration when considering IFNs as therapeutic strategies to treat respiratory virus infections. Optimal protection could be achieved by strong induction of IFN-stimulated genes early during infection to curb viral replication followed by timely down-regulation of IFN responses, thereby enabling efficient lung epithelial repair.

REFERENCES AND NOTES

1. J. R. Teijaro *et al*., *Science* **340**, 207–211 (2013).
2. S. Davidson, S. Crotta, T. M. McCabe, A. Wack, *Nat. Commun.* **5**, 3864 (2014).
3. R. Channappanavar *et al*., *Cell Host Microbe* **19**, 181–193 (2016).
4. E. B. Wilson *et al*., *Science* **340**, 202–207 (2013).
5. B. S. Parker, J. Rautela, P. J. Hertzog, *Nat. Rev. Cancer* **16**, 131–144 (2016).
6. K. Hasegawa *et al*., *Respir. Res.* **18**, 150 (2017).
7. A. N. Nabhan, D. G. Brownfield, P. B. Harbury, M. A. Krasnow, T. J. Desai, *Science* **359**, 1118–1123 (2018).
8. W. J. Zacharias *et al*., *Nature* **555**, 251–255 (2018).
9. K. Blazek *et al*., *J. Exp. Med.* **212**, 845–853 (2015).
10. A. Broggi, Y. Tan, F. Granucci, I. Zanoni, *Nat. Immunol.* **18**, 1084–1093 (2017).
11. V. Espinosa *et al*., *Sci. Immunol.* **2**, eaan5357 (2017).
12. O. Haller, P. Staeheli, M. Schwemmle, G. Kochs, *Trends Microbiol.* **23**, 154–163 (2015).
13. M. Mordstein *et al*., *PLOS Pathog.* **4**, e1000151 (2008).
14. S. Crotta *et al*., *PLOS Pathog.* **9**, e1003773 (2013).
15. P. Österlund *et al*., *J. Virol.* **79**, 9608–9617 (2005).
16. N. A. Jewell *et al*., *J. Virol.* **84**, 11515–11522 (2010).
17. D. J. Gough, N. L. Messina, C. J. P. Clarke, R. W. Johnstone, D. E. Levy, *Immunity* **36**, 166–174 (2012).
18. Y. You, E. J. Richer, T. Huang, S. L. Brody, *Am. J. Physiol. Lung Cell. Mol. Physiol.* **283**, L1315–L1321 (2002).
19. J. A. Zepp, E. E. Morrisey, *Nat. Rev. Mol. Cell Biol.* **20**, 551–566 (2019).
20. P. S. Subramaniam, P. E. Cruz, A. C. Hobeika, H. M. Johnson, *Oncogene* **16**, 1885–1890 (1998).
21. B. L. M. Hogan *et al*., *Cell Stem Cell* **15**, 123–138 (2014).
22. J. Quantius *et al*., *PLOS Pathog.* **12**, e1005544 (2016).
23. A. Takaoka *et al*., *Nature* **424**, 516–523 (2003).
24. M. L. Smith *et al*., *Science* **266**, 1376–1380 (1994).
25. K. Ueda, H. Arakawa, Y. Nakamura, *Oncogene* **22**, 5586–5591 (2003).
26. J. A. McCullers, *Nat. Rev. Microbiol.* **12**, 252–262 (2014).
27. A. Broggi *et al*., *Science* **369**, 706–712 (2020).
28. D. Kobasa *et al*., *Nature* **445**, 319–323 (2007).
29. Z. Zhou *et al*., *Cell Host Microbe* **27**, 883–890 (2020).
30. S. Davidson *et al*., *EMBO Mol. Med.* **8**, 1099–1112 (2016).
31. I. E. Galani *et al*., *Immunity* **46**, 875–890.e6 (2017).

ACKNOWLEDGMENTS

We are grateful to A. Suarez-Bonnet for histopathology scoring of lung H&E sections and to A. O'Garra, G. Stockinger, P. Staeheli, and D. Schnepf for critically reading the manuscript. We thank T. Matambanadzo for assistance performing animal procedures. We thank the Francis Crick Institute's sequencing, histopathology, flow cytometry, and animal facilities for their excellent support. **Funding:** J.M., S.C., M.L., T.M.M., S.L.P., and A.W. were supported by the Francis Crick Institute, which receives its core funding from Cancer Research UK (FC001206), the UK Medical Research Council (FC001206), and the Wellcome Trust (FC001206). R.H. and H.H.G. were supported by the Independent Research Fund Denmark, Medical Sciences (research grant agreement 11-107588) and by the Novo Nordisk Foundation (grant agreement NNF19OC0058287). **Author contributions:** Conception: A.W., S.C., and J.M.; research design and experimentation: J.M., S.C., and T.M.M.; data analysis: J.M., S.C., S.L.P., and M.L.; production and provision of key reagents: H.H.G. and R.H.; writing and editing of the manuscript: J.M., A.W., and S.C. All authors read and approved the final manuscript. **Competing interests:** The authors declare no competing interests. **Data and materials availability:** Gene expression data are deposited and available under the Gene Expression Omnibus (GEO) accession code GSE148712. All other data supporting the findings of this study are available within the paper or in the supplementary materials. This work is licensed under a Creative Commons Attribution 4.0 International (CC BY 4.0) license, which permits unrestricted use, distribution, and reproduction in any medium, provided the original work is properly cited. To view a copy of this license, visit https://creativecommons.org/licenses/by/4.0/. This license does not apply to figures/photos/artwork or other content included in the article that is credited to a third party; obtain authorization from the rights holder before using such material.

SUPPLEMENTARY MATERIALS

science.sciencemag.org/content/369/6504/712/suppl/DC1
Materials and Methods
Supplementary Text
Figs. S1 to S10
Table S1
References (*32*–*38*)
MDAR Reproducibility Checklist
Data S1 to S3

View/request a protocol for this paper from *Bio-protocol*.

21 April 2020; accepted 8 June 2020
Published online 11 June 2020
10.1126/science.abc2061

CORONAVIRUS

Impaired type I interferon activity and inflammatory responses in severe COVID-19 patients

Jérôme Hadjadj[1,2]*, Nader Yatim[2,3]*, Laura Barnabei[1], Aurélien Corneau[4], Jeremy Boussier[3], Nikaïa Smith[3], Hélène Péré[5,6], Bruno Charbit[7], Vincent Bondet[3], Camille Chenevier-Gobeaux[8], Paul Breillat[2], Nicolas Carlier[9], Rémy Gauzit[10], Caroline Morbieu[2], Frédéric Pène[11,12], Nathalie Marin[12], Nicolas Roche[9,11], Tali-Anne Szwebel[2], Sarah H. Merkling[13], Jean-Marc Treluyer[14,15], David Veyer[6,16], Luc Mouthon[2,11], Catherine Blanc[4], Pierre-Louis Tharaux[5], Flore Rozenberg[11,17], Alain Fischer[1,18,19], Darragh Duffy[3,7]†, Frédéric Rieux-Laucat[1]†, Solen Kernéis[10,20,21]†, Benjamin Terrier[2,5]†‡

Coronavirus disease 2019 (COVID-19) is characterized by distinct patterns of disease progression that suggest diverse host immune responses. We performed an integrated immune analysis on a cohort of 50 COVID-19 patients with various disease severity. A distinct phenotype was observed in severe and critical patients, consisting of a highly impaired interferon (IFN) type I response (characterized by no IFN-β and low IFN-α production and activity), which was associated with a persistent blood viral load and an exacerbated inflammatory response. Inflammation was partially driven by the transcriptional factor nuclear factor–κB and characterized by increased tumor necrosis factor–α and interleukin-6 production and signaling. These data suggest that type I IFN deficiency in the blood could be a hallmark of severe COVID-19 and provide a rationale for combined therapeutic approaches.

Early clinical descriptions of the first severe acute respiratory syndrome coronavirus 2 (SARS-CoV-2)–caused coronavirus disease 2019 (COVID-19) cases at the end of 2019 rapidly highlighted distinct patterns of disease progression (*1*). Although most patients experience mild to moderate disease, 5 to 10% progress to severe or critical disease, including pneumonia and acute respiratory failure (*2*, *3*). On the basis of data from patients with laboratory-confirmed COVID-19 from mainland China, admission to intensive care unit (ICU), invasive mechanical ventilation, or death occurred in 6.1% of cases (*1*), and the death rate from recent current French data was 0.70% (*3*). This proportion of critical cases is higher than that estimated for seasonal influenza (*4*). Additionally, relatively high rates of respiratory failure were reported in young adults (aged 50 years and lower) with previously mild comorbidities (such as hypertension, diabetes mellitus, or overweight) (*5*). Severe cases can occur early in the disease course, but clinical observations typically describe a two-step disease progression, starting with a mild-to-moderate presentation followed by a secondary respiratory worsening 9 to 12 days after the first onset of symptoms (*2*, *6*, *7*). Respiratory deterioration is concomitant with extension of ground-glass lung opacities on chest computed tomography (CT) scans, lymphocytopenia, high prothrombin time, and increased D-dimer levels (*2*). This biphasic evolution marked by a substantial increase of acute phase reactants in the blood suggests a dysregulated inflammatory host response, resulting in an imbalance between pro- and anti-inflammatory mediators. This leads to the subsequent recruitment and accumulation of leukocytes in tissues, causing acute respiratory distress syndrome (ARDS) (*8*). However, little is known about the immunological features and the molecular mechanisms involved in COVID-19 severity.

To test the hypothesis of a virally driven hyperinflammation leading to severe disease, we used an integrative approach based on clinical and biological data, in-depth phenotypical analysis of immune cells, standardized whole-blood transcriptomic analysis, and cytokine measurements on a group of 50 COVID-19 patients with variable severity from mild to critical.

COVID-19 patients (n = 50) and healthy controls (n = 18) were included. Patients' characteristics are detailed in the supplementary materials and depicted in table S1 and fig. S1. Patients were analyzed after a median duration of 10 days (interquartile range, 9 to 11 days) after disease onset. On admission, the degree of severity of COVID-19 was categorized as mild to moderate (n = 15 patients), severe (n = 17 patients), and critical (n = 18 patients).

As reported in previous studies (*1*, *2*, *8*), lymphocytopenia correlates with disease severity (Fig. 1A). To further characterize this, we used mass cytometry and performed visualization of t-distributed stochastic neighbor embedding (viSNE) (*9*) to compare cell population densities according to disease severity (Fig. 1B). viSNE representation and differentiated cell counts showed a decrease in the density of natural killer (NK) cells and $CD3^+$ T cells, including all T cell subsets, that was more pronounced for $CD8^+$ T cells. This phenotype was more prominent in severe and critical patients, contrasting with an increase in the density of B cells and monocytes (Fig. 1, C to F). No major imbalance in $CD4^+$ and $CD8^+$ T cell naïve/memory subsets was observed (fig. S2). Data on T cell polarization and other minor T cell subsets are shown in fig. S3. Plasmablasts were enriched in all infected patients (Fig. 1F), as supported by the increase in genes associated with B cell activation and plasmablast differentiation—such as *IL4R*, *TNFSF13B*, and *XBP1* (fig. S4)—but without any significant increase of serum immunoglobulin concentrations (fig. S5).

We then assessed the functional status of specific T cell subsets and NK cells using markers of activation [CD25, CD38, and human lymphocyte antigen (HLA)–DR] and exhaustion [programmed cell death 1 (PD-1) and Tim-3] (fig. S6A). The $CD4^+$ and $CD8^+$ T cell populations were characterized by an increase in $CD38^+$ HLA-DR^+–activated T cells in all infected patients, with an expression of PD-1 moderately increasing with disease severity (Fig. 1G and fig. S6B). A similar increase in activated NK cells was found in all infected patients, especially critical patients, and NK cells displayed a significant increase in Tim-3 expression (Fig. 1G). Furthermore, expression of exhaustion-related genes—such as *BATF*, *IRF4*, and *CD274*—significantly increased with disease severity (fig. S6C). High annexin-V expression (by means of flow cytometry) and up-regulation of apoptosis-related genes in the blood from severe and

[1]Université de Paris, Imagine Institute Laboratory of Immunogenetics of Pediatric Autoimmune Diseases, INSERM UMR 1163, F-75015 Paris, France. [2]Department of Internal Medicine, National Reference Center for Rare Systemic Autoimmune Diseases, AP-HP, APHP-CUP, Hôpital Cochin, F-75014 Paris, France. [3]Institut Pasteur, Laboratory of Dendritic Cell Immunobiology, INSERM U1223, Department of Immunology, F-75015 Paris, France. [4]Sorbonne Université, UMS037, PASS, Plateforme de cytométrie de la Pitié-Salpêtrière CyPS, F-75013 Paris, France. [5]Université de Paris, INSERM, U970, PARCC, F-75015 Paris, France. [6]Service de Microbiologie, AP-HP, APHP-CUP, Hôpital Européen Georges Pompidou, F-75015 Paris, France. [7]Institut Pasteur, Cytometry and Biomarkers UTechS, CRT, F-75015 Paris, France. [8]Department of Automated Diagnostic Biology, Hôpital Cochin, APHP, APHP-CUP, F-75014 Paris, France. [9]Department of Pulmonology, Hôpital Cochin, AP-HP, APHP-CUP, F-75014 Paris, France. [10]Equipe Mobile d'Infectiologie, Hôpital Cochin, AP-HP, APHP-CUP, F-75014 Paris, France. [11]Université de Paris, Institut Cochin, INSERM U1016, CNRS UMR8104, F-75006 Paris, France. [12]Service de Médecine Intensive et Réanimation, Hôpital Cochin, AP-HP, APHP-CUP, F-75014 Paris, France. [13]Institut Pasteur, Insect-Virus Interactions Unit, UMR 2000, CNRS, Paris, France. [14]Université de Paris, Pharmacologie et Evaluation des Thérapeutiques Chez l'Enfant et la Femme Enceinte EA7323, F-75006 Paris, France. [15]Recherche Clinique et Pharmacologie, AP-HP, APHP-CUP, Hôpitaux Cochin Necker, F-75014 Paris, France. [16]Université de Paris and Sorbonne Université, INSERM, Centre de Recherche des Cordeliers, Functional Genomics of Solid Tumors (FunGeST), F-75006 Paris, France. [17]Service de Virologie, Hôpital Cochin, AP-HP, APHP-CUP, F-75014 Paris, France. [18]Department of Paediatric Immuno-Haematology and Rheumatology, AP-HP, APHP.CUP, Hôpital Necker, F-75015 Paris, France. [19]Collège de France, Paris, France. [20]Université de Paris, INSERM, IAME, F-75006 Paris, France. [21]Institut Pasteur, Epidemiology and Modelling of Antibiotic Evasion (EMAE), F-75015 Paris, France.

*These authors contributed equally to this work. †These authors contributed equally to this work.

‡Corresponding author. Email: benjamin.terrier@aphp.fr

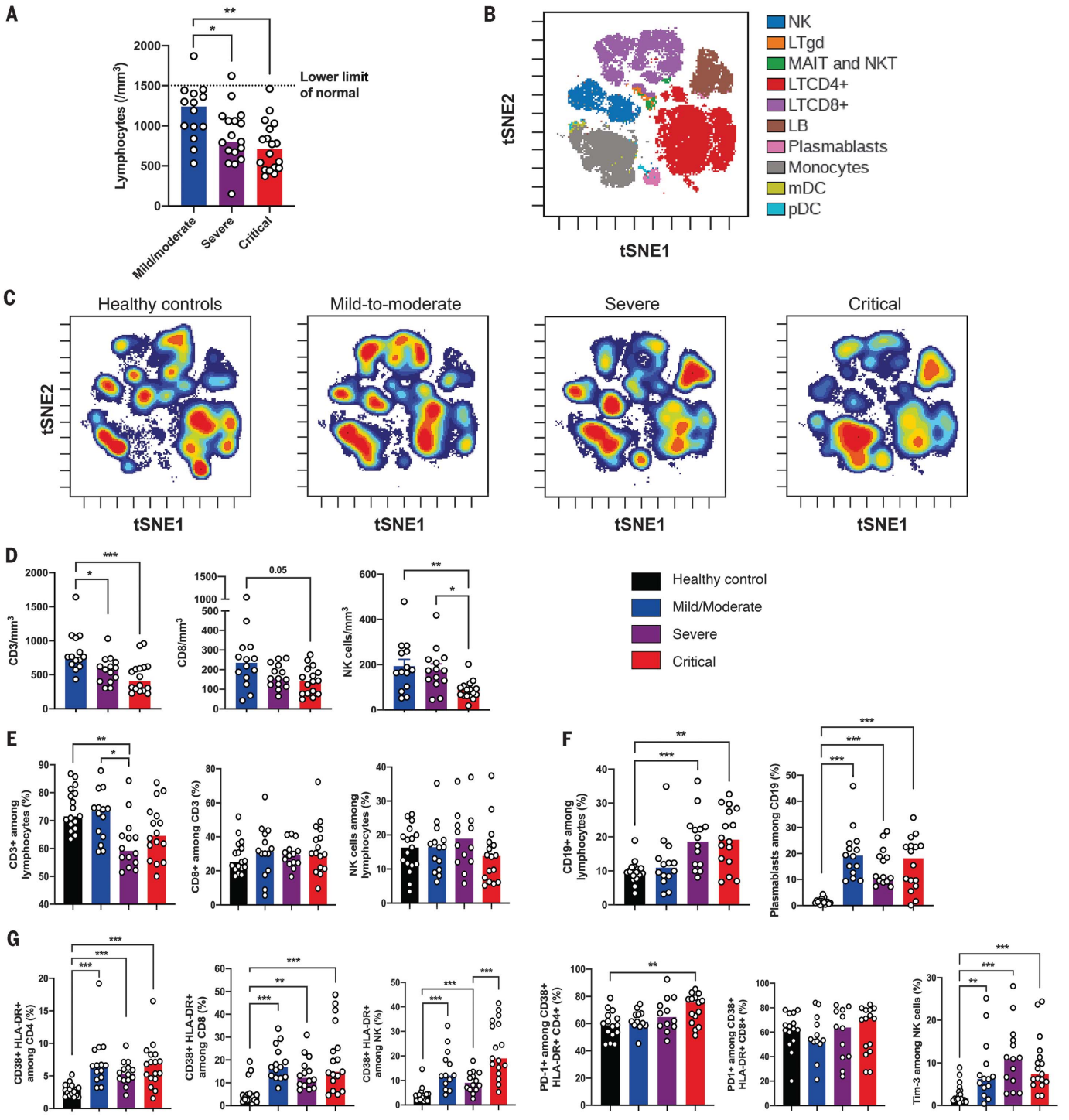


Fig. 1. Phenotyping of peripheral blood leukocytes in patients with SARS-CoV-2 infection. (**A**) Lymphocyte counts in whole blood from COVID-19 patients were analyzed between days 8 and 12 after onset of first symptoms, according to disease severity. (**B**) viSNE map of blood leukocytes after exclusion of granulocytes, stained with 30 markers and measured with mass cytometry. Cells are automatically separated into spatially distinct subsets according to the combination of markers that they express. LTgd, γδ T cell; MAIT, mucosal-associated invariant T cell; LB, B lymphocyte. (**C**) viSNE map colored according to cell density across disease severity (classified as healthy controls, mild to moderate, severe, and critical). Red indicates the highest density of cells. (**D**) Absolute number of $CD3^+$ T cells, $CD8^+$ T cells, and $CD3^-CD56^+$ NK cells in peripheral blood from COVID-19 patients, according to disease severity. (**E** and **F**) Proportions (frequencies) of lymphocyte subsets from COVID-19 patients. (E) Proportions of $CD3^+$ T cells among lymphocytes, $CD8^+$ T cells among $CD3^+$ T cells, and NK cells among lymphocytes. (F) Proportions of $CD19^+$ B cells among lymphocytes and CD38hi CD27hi plasmablasts among $CD19^+$ B cells. (**G**) Analysis of the functional status of specific T cell subsets and NK cells based on the expression of activation (CD38, HLA-DR) and exhaustion (PD-1, Tim-3) markers. In (D) to (G), data indicate median. Each dot represents a single patient. *P* values were determined with the Kruskal-Wallis test, followed by Dunn's post-test for multiple group comparisons with median reported; $*P < 0.05$; $**P < 0.01$; $***P < 0.001$.

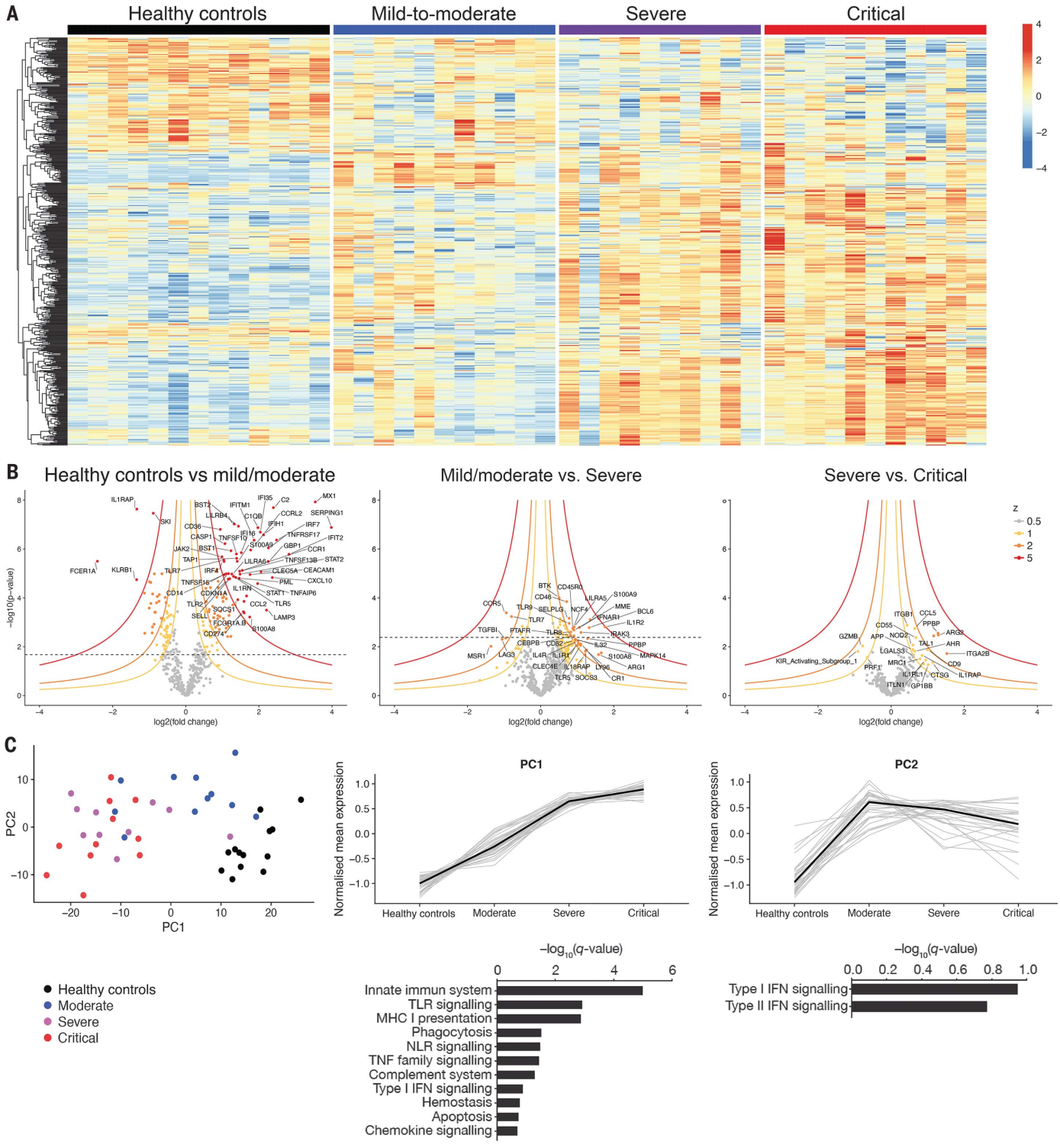


Fig. 2. Immunological transcriptional signature of SARS-CoV-2 infection. RNA extracted from patient whole blood and RNA counts of 574 genes were determined by means of direct probe hybridization, using the Nanostring nCounter Human Immunology_v2 kit. (**A**) Heatmap representation of all genes, ordered by hierarchical clustering. Healthy controls (n = 13 patients), mild to moderate (n = 11 patients), severe (n = 10 patients), and critical (n = 11 patients). Up-regulated genes are shown in red, and down-regulated genes are shown in blue. (**B**) Volcano plots depicting log10 (P value) and log2 (fold change), as well as z value for each group comparison (supplementary materials, materials and methods). Gene expression comparisons allowed the identification of significantly differentially expressed genes between severity grades (heathy controls versus mild to moderate, 216 genes; mild to moderate versus severe, 43 genes; severe versus critical, 0 genes). (**C**) (Left) PCA of the transcriptional data. (Middle and right) Kinetic plots showing mean normalized values for each gene and severity grade, where each gray line corresponds to one gene. Median values over genes for each severity grade are plotted in black. Gene set enrichment analysis of pathways enriched in PC1 and PC2 are depicted under corresponding kinetic plot.

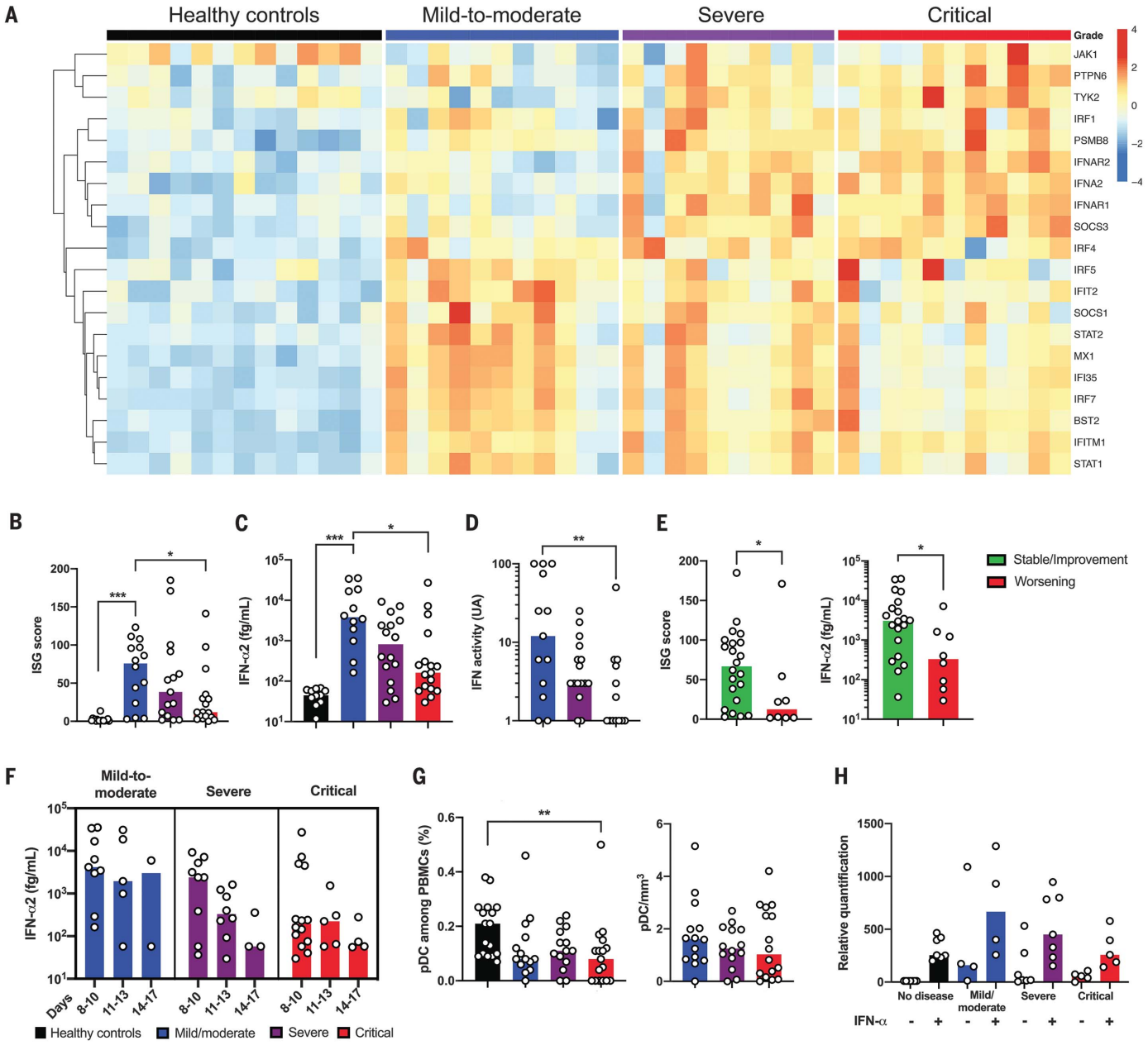


Fig. 3. Impaired type I IFN response in patients with severe SARS-CoV-2 infection. (**A**) Heatmap showing expression of type I IFN-related genes by using the reverse transcription- and PCR-free Nanostring nCounter technology in patients with mild-to-moderate (n = 11), severe (n = 10), and critical (n = 11) SARS-CoV2 infection, and healthy controls (n = 13). Up-regulated genes are shown in red, and down-regulated genes are shown in blue. (**B**) ISG score based on expression of six genes (*IFI44L*, *IFI27*, *RSAD2*, *SIGLEC1*, *IFIT1*, and *IS15*) measured with quantitative RT-PCR in whole blood cells from mild to moderate (n = 14), severe (n = 15), and critical (n = 17) patients and healthy controls (n = 18). (**C**) IFN-α2 (fg/ml) concentration evaluated by use of Simoa and (**D**) IFN activity in plasma according to clinical severity. (**E**) Mild to moderate (n = 14) and severe patients (n = 16) were separated in two groups depending on the clinical outcome, namely critical worsening requiring mechanical ventilation (to denote severe status). (Left) ISG score and (right) IFN-α2 plasma concentration are shown. (**F**) Time-dependent IFN-α2 concentrations are shown according to severity group. (**G**) Quantification of plasmacytoid dendritic cells (pDCs) as a percentage of PBMCs and as cells/milliliter according to severity group. (**H**) ISG score before and after stimulation of whole blood cells by IFN-α (10^3UI/ml for 3 hours). (**I**) Viral loads in nasal swabs estimated by means of RT-PCR and expressed in cycle threshold (Ct) and blood viral load evaluated by means of digital PCR. In (B) and (E), ISG score results represent the fold-increased expression compared with the mean of unstimulated controls and are normalized to *GAPDH* (glyceraldehyde phosphate dehydrogenase). In (B) to (I), data indicate median. Each dot represents a single patient. P values were determined with the Kruskal-Wallis test, followed by Dunn's post-test for multiple group comparisons and the Mann-Whitney test for two group comparisons with median reported; *P < 0.05; **P < 0.01; ***P < 0.001.

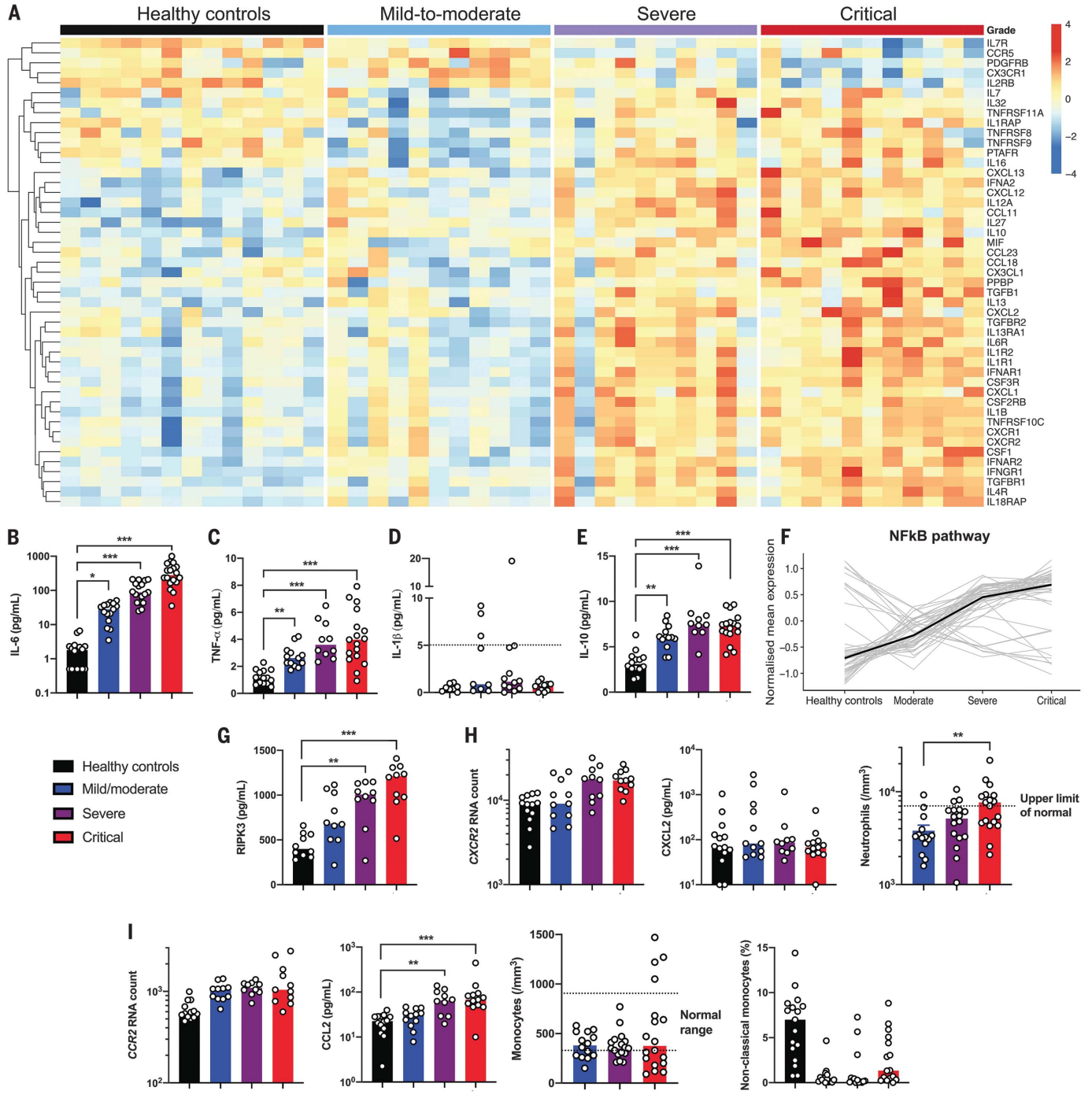


Fig. 4. Immune profiling in patients with severe and critical SARS-CoV-2 infection. (**A**) Heatmap showing the expression of cytokines and chemokines that are significantly different in severe and critical patients, ordered by hierarchical clustering. Included are healthy controls (n = 13) and mild to moderate (n = 11), severe (n = 10), and critical (n = 11) patients. Up-regulated genes are shown in red, and down-regulated genes are shown in blue. (**B**) IL-6, (**C**) TNF-α, (**D**) IL-1β, and (**E**) IL-10 proteins were quantified in the plasma of patients by using Simoa technology or a clinical-grade ELISA assay (supplementary materials, materials and methods). Each group includes n = 10 to 18 patients. The dashed line indicates the limit of detection (LOD). (**F**) Kinetic plots showing mean normalized value for each gene and severity grade. Each gray line corresponds to one gene belonging to the NF-κB pathway. Median values over genes for each severity grade are plotted in black. (**G**) Plasma quantification of RIPK-3. Each group included n = 10 patients. (**H**) Absolute RNA count for (left) *CXCR2*, (middle) CXCL2 protein plasma concentration measured with Luminex technology, and (right) blood neutrophil count depending on severity group. The dashed line indicates the upper normal limit. Each group includes n = 10 to 13 patients. (**I**) Absolute RNA count for (left) *CCR2*; (middle left) CCL2 protein plasma concentration measured by Luminex technology; and (middle right) blood monocyte count depending on severity group. The dashed lines depict the normal range. (Right) The percentage of nonclassical monocytes, depending on severity grade. Each group shows n = 10 to 18 patients. RNA data are extracted from the Nanostring nCounter analysis (supplementary materials, materials and methods). In (B) to (I), data indicate median. Each dot represents a single patient. P values were determined with the Kruskal-Wallis test, followed by Dunn's post-test for multiple group comparisons with median reported; $^{*}P < 0.05$; $^{**}P < 0.01$; $^{***}P < 0.001$.

critical patients supported the notion that lymphocytopenia could be partly explained by exacerbated T cell apoptosis (fig. S7).

To investigate the immunological transcriptional signatures that characterize disease severity, we quantified the expression of immune-related genes in peripheral white blood cells (Fig. 2A). We identified differentially expressed genes as a function of severity grades (Fig. 2B). Unsupervised principal components analysis (PCA) separated patients with high disease severity on principal component 1 (PC1), driven by inflammatory and innate immune response encoding genes (gene set enrichment analysis enrichment score with q value < 0.2) (Fig. 2C). PC2, which was enriched in genes encoding proteins involved in both type I and type II interferon (IFN) responses, distinguished mild to moderate patients from the other groups. Collectively, these data suggested a severity grade–dependent increase in activation of innate and inflammatory pathways; by contrast, the IFN response was high in mild to moderate patients, whereas it was reduced in more severe patients.

Type I IFNs are essential for antiviral immunity (*10*). Multiplex gene expression analysis showed an up-regulation of genes involved in type I IFN signaling (such as *IFNAR1*, *JAK1*, and *TYK2*) contrasting with a striking down-regulation of IFN-stimulated genes (ISGs) (such as *MX1*, *IFITM1*, and *IFIT2*) in critical SARS-CoV-2 patients (Fig. 3A). Accordingly, a validated ISG score, based on the mean of expression of six ISGs defining a type I IFN signature (*11*), was significantly reduced in critical patients compared with patients that had mild to moderate infection (Fig. 3B and fig. S8A). *IFN*-β mRNA was undetectable in all infected patients (fig. S8B) as well as IFN-β protein (fig. S8C). Consistent with ISG scores, plasma levels of IFN-α2 protein measured with Simoa digital enzyme-linked immunosorbent assay (ELISA) (*12*) were significantly lower in critical than in mild to moderate patients (Fig. 3C) and correlated with ISG [coefficient of determination (R^2) = 0.30; P < 0.0001] (fig. S8D). This result apparently contrasted with the increased detection of *IFNA2* mRNA in most severe patients, albeit at levels just above the limit of detection (fig. S8E). To assess the global type I IFN activity, we used an in vitro cytopathic assay (*13*). IFN activity in serum was significantly lower in severe or critical patients as compared with mild to moderate patients (Fig. 3D). ISG score and plasma levels of IFN-α2 from blood collected before respiratory failure requiring mechanical ventilation revealed that the low type I IFN response preceded clinical deterioration to critical status (Fig. 3E). Furthermore, low plasma levels of IFN-α2 was significantly associated with an increased risk of evolution to critical status [odds ratio (OR) 12; 95% confidence interval (CI) 1.21 to 118; P = 0.03]. Analysis in patients for whom multiple time points were available showed distinct patterns of IFN-α production with sustained high response in mild to moderate patients, high but short response in severe patients, and low or no response in critical patients (Fig. 3F). The proportion of plasmacytoid dendritic cells, the main source of IFN-α (*14*), was reduced in infected patients compared with healthy controls, possibly because of migration to sites of infection (*15*), but without any difference between groups (Fig. 3G). We next evaluated the response of whole blood cells to IFN-α stimulation (*11*) and observed a comparable increase in ISG score upon IFN-α stimulation between groups of any severity and controls (Fig. 3H), suggesting that the potential for response to type I IFN was not affected in COVID-19 patients. As a possible consequence of impaired IFN-α production, we used ultrasensitive droplet–based digital polymerase chain reaction (ddPCR) and found an increased plasma viral load in severe and critical patients, which is a possible surrogate marker of uncontrolled lung infection, whereas viral load in nasal swabs by using classical reverse transcription (RT)–PCR was comparable between groups (Fig. 3I). Overall, these data suggest that infected patients had no detectable circulating IFN-β and that an impaired IFN-α production characterized the most severe COVID-19 cases.

Severe COVID-19 was reported to be associated with hypercytokinaemia (*8*, *16*). Cytokine- and chemokine-related genes were found to be increasingly expressed as a function of disease severity in the study cohort (Fig. 4A and fig. S9A). Cytokine whole blood RNA levels did not always correlate with protein plasma levels. Interleukin-6 (IL-6), a key player of the exacerbated inflammatory response in COVID-19 (*17*), was not detected in peripheral blood at the transcriptional level (fig. S9B), contrasting with high amounts of IL-6 protein (Fig. 4B). Expression of IL-6–induced genes—such as *IL6R*, *SOCS3*, and *STAT3*—was significantly increased (fig. S9B), reflecting the activation of the IL-6 signaling pathway. Tumor necrosis factor–α (TNF-α), a key driver of inflammation, was only moderately up-regulated at the transcriptional level (fig. S9C), whereas circulating TNF-α was significantly increased (Fig. 4C). Accordingly, TNF pathway–related genes were also up-regulated, including *TNFSF10* (fig. S9, D and E), which supports TNF-α having an important role in the induction of inflammation. The discrepancy between RNA quantification and protein measurement suggests that cellular sources of TNF-α and IL-6 may be the injured lungs and/or endothelial cells. Conversely, whereas *IL1B* transcripts were significantly up-regulated (fig. S9F), the active form of IL-1β protein was low (Fig. 4D), which suggests that pro–IL-1β was poorly cleaved and secreted but does not exclude a local production in the lung (*15*). Circulating IL-1α also was not detected (fig. S9F). These findings contrasted with the detection of high amounts of circulating IL-1 receptor antagonist (IL-1RA) and up-regulation of *IL1R1* transcripts, indicating an active antagonism of IL-1 in critically ill patients (fig. S9F). We also detected *IL10* transcripts and IL-10 protein in both severe or critical patients (Fig. 4E and fig. S9G). IFN-γ was increased in mild to moderate patients, and at a lesser extent in severe patients, but not in critical patients. By contrast, no increase in IL-17A amounts was detected in all infected patients' groups (fig. S10).

We next explored the expression of transcription factors that may drive this exacerbated inflammation and found that genes specifically up-regulated in severe or critical patients mainly belonged to the NF-κB pathway (Fig. 4F and fig. S11, A and B). Among several triggering pathways, aberrant NF-κB activation can result from excessive innate immune sensor activation by pathogen-associated molecular patterns (PAMPs) (such as viral RNA) and/or damage-associated molecular patterns (DAMPs) (for example, released by necrotic cells and tissue damage). Lactate dehydrogenase (LDH), a marker of necrosis and cellular injury, correlated with disease severity (fig. S1C), and receptor-interacting protein kinase–3 (RIPK-3), a key kinase involved in programmed necrosis and inflammatory cell death, was also significantly increased in severe or critical patients (Fig. 4G) and correlated with LDH (R^2 = 0.47; P < 0.0001).

The exacerbated inflammatory response has been associated with a massive influx of innate immune cells—namely, neutrophils and monocytes—which may aggravate lung injury and precipitate ARDS (*15*). We therefore analyzed expression of chemokines and chemokine receptors involved in the trafficking of innate immune cells (Fig. 4A). Although the neutrophil chemokine CXCL2 was detected in the serum but with no difference between groups, its receptor *CXCR2* was significantly up-regulated in severe and critical patients (Fig. 4H). Consistently, severe disease was accompanied with higher neutrophilia (Fig. 4H). The inflammatory response pattern remained increased even after normalization of transcriptional data with neutrophil counts (fig. S12). Monocyte chemotactic factor chemokine (C-C motif) ligand 2 (CCL2) was increased in the blood of infected patients as well as the transcripts of its receptor *CCR2*; this was associated with low counts of circulating inflammatory monocytes (Fig. 4I), suggesting a role for the CCL2/CCR2 axis in the monocyte chemoattraction into the inflamed lungs. These observations are in accordance with published studies in bronchoalveolar fluids from COVID-19 patients, describing the key role of monocytes (*15*). Overall, these results support a framework

in which an ongoing inflammatory cascade, in the setting of impaired type I IFN production and high viral load, may be fueled by both PAMPs and DAMPs.

In this study, we identified an impaired type I IFN response in severe and critical COVID-19 patients, accompanied by high blood viral load and an excessive NF-κB–driven inflammatory response associated with increased TNF-α and IL-6. Innate immune sensors, such as Toll-like receptors (TLRs) and retinoic acid inducible gene I (RIG-I)–like receptors, play a key role in controlling RNA virus by sensing viral replication and alerting the immune system through the expression of a diverse set of antiviral genes (*18*). Type I IFNs—which include IFN-α, -β and -ω—are hence rapidly induced and orchestrate a coordinated antiviral program via the Janus kinase (JAK)–signal transducers and activators of transcription (STAT) signaling pathway and expression of ISGs (*19*). We observed that SARS-CoV-2 infection was characterized by an absence of circulating IFN-β in COVID-19 patients with all disease-severity grades. In addition, most severe COVID-19 patients displayed impaired IFN-α production that was associated with lower viral clearance. This low type I IFN signature was similar to that observed in young children with severe, but not mild, respiratory syncytial virus infection (*20*) but was remarkably different from the transcriptional response induced by other respiratory viruses such as human parainfluenza virus 3 or influenza A virus, both characterized by a stronger type I IFN response in in vitro experiments (*21*). Although our study was not designed for longitudinal analyses, we observed that low IFN-α plasma levels preceded clinical deterioration and transfer to ICU and that distinct patterns of circulating IFN-α characterized each disease grade. Formal longitudinal studies will be necessary to dissect type I IFN dynamics during SARS-CoV-2 infection. It will be important to assess in severe and critical COVID-19 patients whether this reduced type I IFN production is present at the onset of infection, whether the production is delayed, or whether IFN production is exhausted after an initial peak. Recent data confirmed in cellular and animal models that SARS-CoV-2 inhibited type I and III induction (*21*). These results suggest that SARS-CoV-2 has developed efficient mechanisms to shut down host IFN production.

Conversely, on the host side, several hypotheses may be proposed to explain variability in type I IFN responses to infection. Comorbidities are risk factors for severe COVID-19 that could negatively affect IFN production and in contrast exacerbate inflammatory responses (*22*, *23*). Genetic susceptibility can be also suspected because monogenic disorders in children (*24*) or susceptibility variants in adults (*25*), each involving the type I IFN pathway, have been associated with life-threatening influenza infections. Identification of patients with insufficient IFN production but preserved cellular response to type I IFN could define a high-risk population who might benefit from IFN-α or -β treatment. Benefit and risk as well as the best time window for efficacy of IFN administration nevertheless require to be weighed. Alternatively, IFN-λ (type III IFN) could be tested, as recently proposed (*26*), because the receptor is localized on epithelial cells, which may avoid potential adverse effects caused by type I IFN.

Viral replication within the lungs in conjunction with an increased influx of innate immune cells mediates tissue damage and may fuel an auto-amplification inflammatory loop, including targetable production of IL-6 (*27*) and TNF-α (*28*), potentially driven by NF-κB. Our study provides a case for the inhibition of the TNF-α axis; TNF-α is highly expressed in alveolar macrophages, and anti–TNF-α does not block immune responses in animal models of viral infection (*28*).

Our study has some limitations. First, the study was designed as a cross-sectional analysis, although sequential time points were available for some patients. Second, data provided are mainly derived from the blood and do not allow the assessment of immune responses within the lung. In this respect, data from Bost *et al.* describe a reduced type I IFN signature in bronchoalveolar lavage macrophages from severe COVID-19 patients, supporting the validity of our analysis (*29*).

On the basis of our study, we propose that type I IFN deficiency is a hallmark of severe COVID-19 and infer that severe COVID-19 patients might be potentially relieved from the IFN deficiency through IFN administration and from exacerbated inflammation through adapted antiinflammatory therapies that target IL-6 or TNF-α—a hypothesis worth cautious testing.

REFERENCES AND NOTES

1. W.-J. Guan *et al.*, *N. Engl. J. Med.* **382**, 1708–1720 (2020).
2. C. Huang *et al.*, *Lancet* **395**, 497–506 (2020).
3. H. Salje *et al.*, *Science* eabc3517 (2020).
4. E. J. Chow, J. D. Doyle, T. M. Uyeki, *Crit. Care* **23**, 214 (2019).
5. C. Wu *et al.*, *JAMA Intern. Med.* 10.1001/jamainternmed.2020.0994 (2020).
6. Q. Li *et al.*, *N. Engl. J. Med.* **382**, 1199–1207 (2020).
7. G. Grasselli *et al.*, *JAMA* **323**, 1574 (2020).
8. P. Mehta *et al.*, *Lancet* **395**, 1033–1034 (2020).
9. A. D. Amir *et al.*, *Nat. Biotechnol.* **31**, 545–552 (2013).
10. U. Müller *et al.*, *Science* **264**, 1918–1921 (1994).
11. N. Jeremiah *et al.*, *J. Clin. Invest.* **124**, 5516–5520 (2014).
12. M. P. Rodero *et al.*, *J. Exp. Med.* **214**, 1547–1555 (2017).
13. P. Lebon, G. Ponsot, J. Aicardi, F. Goutières, M. Arthuis, *Biomedicine* **31**, 267–271 (1979).
14. B. Reizis, *Immunity* **50**, 37–50 (2019).
15. Z. Zhou *et al.*, Overly exuberant innate immune response to SARS-CoV-2 infection. (2020); available at http://dx.doi.org/10.2139/ssrn.3551623.
16. S. F. Pedersen, Y.-C. Ho, *J. Clin. Invest.* **130**, 2202–2205 (2020).
17. G. Chen *et al.*, *J. Clin. Invest.* **130**, 2620–2629 (2020).
18. J. Rehwinkel, M. U. Gack, *Nat. Rev. Immunol.* (2020).
19. S.-Y. Liu, D. J. Sanchez, R. Aliyari, S. Lu, G. Cheng, *Proc. Natl. Acad. Sci. U.S.A.* **109**, 4239–4244 (2012).
20. S. Heinonen *et al.*, *Sci. Transl. Med.* **12**, eaaw0268 (2020).
21. D. Blanco-Melo *et al.*, *Cell* **181**, 1036–1045.e9 (2020).
22. E. Terán-Cabanillas, J. Hernández, *Inflammation* **40**, 58–67 (2017).
23. E. Galkina, K. Ley, *Annu. Rev. Immunol.* **27**, 165–197 (2009).
24. M. J. Ciancanelli *et al.*, *Science* **348**, 448–453 (2015).
25. S. Clohisey, J. K. Baillie, *Crit. Care* **23**, 303 (2019).
26. L. Prokunina-Olsson *et al.*, *J. Exp. Med.* **217**, e20200653 (2020).
27. M. Roumier, R. Paule, M. Groh, A. Vallee, F. Ackermann, medRxiv, 2020.04.20.20061861 [Preprint] 22 April 2020. https://doi.org/10.1101/2020.04.20.20061861.
28. M. Feldmann *et al.*, *Lancet* **395**, 1407–1409 (2020).
29. P. Bost *et al.*, *Cell* **181**, 1475–1488.e12 (2020).

ACKNOWLEDGMENTS

We acknowledge all health care workers involved in the diagnosis and treatment of patients in Cochin Hospital, especially C. Azoulay, L. Beaudeau, E. Canoui, P. Cohen, A. Contejean, B. Dunogué, D. Journois, P. Legendre, J. Marey, and A. Régent. We thank Y. Gaudin for his advices on viral mechanism. We thank all the patients, supporters, and our families for their confidence in our work. **Funding:** This study was supported by the Fonds IMMUNOV, for Innovation in Immunopathology. The study was also supported by the Institut National de la Santé et de la Recherche Médicale (INSERM) and the Institut Pasteur, by a government grant managed by the Agence National de la Recherche as part of the "Investment for the Future" program (ANR-10-IAHU-01 and the Laboratoire d'Excellence "Milieu Intérieur", grant ANR-10-LABX-69-01), by a grant from the Agence National de la Recherche (ANR-flash Covid19 "AIROCovid" to FRL and "CoVarImm" to DD), and by the FAST Foundation (French Friends of Sheba Tel Hashomer Hospital). J.H. is a recipient of an Institut Imagine M.D.-Ph.D. fellowship program supported by the Fondation Bettencourt Schueller. L.B. is supported by the EUR G.E.N.E. (reference ANR-17-EURE-0013) program of the Université de Paris IdEx ANR-18-IDEX-0001 funded by the French Government through its "Investments for the Future" program. **Author contributions:** J.H., N.Y., D.D., F.R.-L., S.K., and B.T. conceived and designed the study, had full access to all of the data in the study, and take responsibility for the integrity of the data and the accuracy of the data analysis. J.H., N.Y., A.F., D.D., F.R.-L., S.K., and B.T. drafted the paper. J.H., N.Y., L.B., A.C., J.B., N.S., D.D., F.R.-L., S.K., and B.T. performed the analysis, and all authors critically revised the manuscript for important intellectual content and gave final approval for the version to be published. All authors agree to be accountable for all aspects of the work in ensuring that questions related to the accuracy or integrity of any part of the work are appropriately investigated and resolved. **Competing interests:** We declare no competing interests. **Data and materials availability:** All data are available in the main text or the supplementary materials. This work is licensed under a Creative Commons Attribution 4.0 International (CC BY 4.0) license, which permits unrestricted use, distribution, and reproduction in any medium, provided the original work is properly cited. To view a copy of this license, visit https://creativecommons.org/licenses/by/4.0. This license does not apply to figures/photos/artwork or other content included in the article that is credited to a third party; obtain authorization from the rights holder before using such material.

SUPPLEMENTARY MATERIALS

science.sciencemag.org/content/369/6504/718/suppl/DC1
Materials and Methods
Supplementary Text
Figs. S1 to S12
Tables S1 and S2
References (*30*–*33*)

View/request a protocol for this paper from *Bio-protocol*.

3 May 2020; accepted 7 July 2020
Published online 13 July 2020
10.1126/science.abc6027

ORGANIC CHEMISTRY

A short de novo synthesis of nucleoside analogs

Michael Meanwell[1], Steven M. Silverman[2], Johannes Lehmann[1], Bharanishashank Adluri[1], Yang Wang[1], Ryan Cohen[2], Louis-Charles Campeau[2], Robert Britton[1]*

Nucleoside analogs are commonly used in the treatment of cancer and viral infections. Their syntheses benefit from decades of research but are often protracted, unamenable to diversification, and reliant on a limited pool of chiral carbohydrate starting materials. We present a process for rapidly constructing nucleoside analogs from simple achiral materials. Using only proline catalysis, heteroaryl-substituted acetaldehydes are fluorinated and then directly engaged in enantioselective aldol reactions in a one-pot reaction. A subsequent intramolecular fluoride displacement reaction provides a functionalized nucleoside analog. The versatility of this process is highlighted in multigram syntheses of D- or L-nucleoside analogs, locked nucleic acids, iminonucleosides, and C2′- and C4′-modified nucleoside analogs. This de novo synthesis creates opportunities for the preparation of diversity libraries and will support efforts in both drug discovery and development.

As fundamental biomolecules, nucleosides play key roles in diverse cellular processes, ranging from cell signaling to metabolism (*1*). Not surprisingly, synthetic nucleoside analogs (NAs), which are designed to mimic their natural counterparts, are widely exploited in medicinal chemistry (*2*–*6*) and used as tool compounds in chemical biology. NAs have been in use for more than half a century for the treatment of cancer (*2*, *5*), and they represent the largest class of small molecule antivirals (e.g., **1** to **3**, Fig. 1) (*3*, *4*). Mechanistically, after in vivo phosphorylation, NAs operate as toxic antimetabolites (*4*) and can inhibit enzymes that are crucial to cancer cell growth or viral replication (e.g., DNA or RNA polymerases, ribonucleotide reductases, or nucleoside phosphorylases) (*2*, *4*). Recently, NAs have also demonstrated promise as epigenetic modulators, and NA inhibitors of DNA methyltransferase have been approved for cancer therapy (*4*).

The discovery and development of anticancer and antiviral NAs builds on several decades of medicinal chemistry (*5*, *7*, *8*). In the early 1980s, C2′ fluorination was found to improve metabolic stability and influence furanose conformation [PSI-6206 (*9*): **1**] (*3*, *7*, *10*). Methylation at C2′ and modifications to C3′ and C4′ functionalization (e.g., methyl, azido, and alkynyl) can also influence furanose conformation and attenuate reactivity of the C3′ and C5′ alcohols toward chain extension (MK-8591: **2**) (*8*, *11*). Modified nucleobases can often improve NA potency or drug-like properties, and five-membered ring heterocycles [e.g., ribavirin (**3**)] (*12*) have been shown to mimic structurally related intermediates that are involved in de novo purine nucleotide biosynthesis (*13*). In recent years, there has also been increased interest in unnaturally configured NAs (*14*, *15*). For example, the β-L-NA lamivudine (3TC) has found widespread use in the treatment of HIV-1 and AIDS, and several α-D-thymidine analogs have demonstrated promise as antimalarials (*16*).

Despite intense efforts, NA synthesis still presents many challenges (*17*). First, NAs are often synthesized from naturally occurring carbohydrates, which limits patterns of substitution and furanose stereochemistry. Second, the addition of nucleobases to activated ribose derivatives (the Vorbrüggen reaction) often fails or proceeds with poor diastereoselectivity with C2′- or C4′-modified NAs (*18*, *19*). Third, modifications at C2′ often require multistep protecting group manipulations, and efficient strategies for producing C4′-modified NAs do not exist. In fact, a recent summit of key opinion leaders highlighted the synthesis of noncanonical nucleosides as an "emerging area of high potential impact" (*20*). Although efforts to develop de novo NA syntheses have aimed to address these challenges, the resulting processes are often lengthy and target specific, as highlighted by the 16-step process required to produce the C4′-modified NA MK-8591 (**2**) (*19*). As a notable example of de novo NA synthesis, MacMillan and colleagues have reported the synthesis of C2′-modified NAs, including the core of sofosbuvir (**1**), using a sequence that involved a Mukaiyama aldol coupling between a ketene acetal (**5**) and an α-oxyaldehyde (**6**) (*21*). In this work, we disclose a straightforward NA synthesis that involves a one-pot, proline-catalyzed α-fluorination and aldol reaction (αFAR) of heteroaryl-substituted acetaldehydes **9** followed by reduction or organometallic addition and annulative fluoride displacement (AFD). This concise (two- to three-step) process addresses several major and longstanding challenges in NA synthesis by enabling direct access to C3′- and C5′-protected NAs **10** (and hence C2′-modified NAs), providing flexibility in nucleobase substitution, and offering a direct route to C4′-modified NAs. We expect this strategy will become a powerful tool that will enable and inspire drug synthesis.

In a proposed prebiotic synthesis of DNA (*22*), couplings between nucleobase-type enamines **11** (Fig. 2A) and glyceraldehyde form a nucleobase iminium ion **12** before the furanose in a ribose-last approach. Our experiences in ribose synthesis from chlorohydrins (*23*) have suggested that N and Cl hemiaminals are too unstable to serve as precursors to related nucleobase iminium ions. Thus, as a synthetic equivalent to **12**, we proposed the fluorinated acyclic NA **13** on the basis of the broad utility of glycosyl fluorides as sugar donors. Control over both relative and absolute stereochemistry in **13** may be possible through an organocatalytic aldol reaction of a dihydroxyacetone derivative (e.g., **8**) (*24*) and the α-fluoroaldehyde **14** (*25*–*27*). This approach to NAs would require (i) harnessing the reactivity of notoriously unstable α-fluoroaldehydes (*28*) coupled with the additional challenge of a nucleobase connected via an N and F hemiaminal (e.g., **14**) and (ii) developing an AFD reaction to form the ribose ring in the last step.

To explore this process, we investigated the α-fluorination (*27*) of α-pyrazolyl aldehyde **15** (Fig. 2B) and found that a combination of L-proline and *N*-fluorobenzenesulfonimide (NFSI) in dimethylformamide (DMF) (*29*) provided an α-fluorohydrate (table S1) as the sole product. Although we were unable to dehydrate this material, direct addition of dioxanone **8** in acetonitrile (MeCN) afforded the fluorohydrins **16a** and **16b** in good yield and enantioselectivity (Fig. 2B, entry 2; see table S1 for full optimization details). Fluorohydrins **16a** and **16b** were formed as an ~1.4:1 mixture of epimers at the pseudo-anomeric carbon (indicated with an asterisk in Fig. 2B) that do not interconvert during the reaction or isolation. This result is consistent with a slow epimerization of α-pyrazolyl-α-fluoroaldehydes that precludes a dynamic kinetic resolution (*23*) or indicates that the transition structures for the proline catalyzed aldol reaction between dioxanone **8** and (*R*)- or (*S*)-α-pyrazolyl-α-fluoroaldehydes are energetically similar. Nevertheless, we anticipated that the cyclization event would proceed through the formation of a transient azacarbenium cation (*30*), which would render the fluoromethine configuration inconsequential. Toward cyclization (AFD), reduction of the fluorohydrins **16a** and **16b** provided a mixture of 1,3-*syn* diols, and subsequent reaction with the fluorophilic Lewis acid $Sc(OTf)_3$ afforded the NA **17** as a single β-anomer (entry 4). Alternatively, treatment of the diols **18a** and **18b** with base (NaOH) resulted in the formation of a mixture of α- and

[1]Department of Chemistry, Simon Fraser University, Burnaby, BC V5A 1S6, Canada. [2]Department of Process Research and Development, Merck & Co., Inc., Rahway, NJ 07065, USA.
*Corresponding author. Email: rbritton@sfu.ca

β-anomeric NAs that varied in composition depending on reaction conditions (entries 5 and 6). Using an excess of NaOH (entry 6), the β-anomer **17** was formed as the exclusive product in excellent yield. To examine the mechanism of cyclization, diols **18a** and **18b** were separated and their relative stereochemistry assigned by *J*-based configurational analysis and/or x-ray analysis (see supplementary materials). Subjecting the purified *syn*-fluorohydrin **18a** to NaOH (Fig. 2C) promoted a clean cyclization to the β-anomer **17** (an S_N2 process). Similarly, the *anti*-fluorohydrin **18b** cyclized to the α-anomer **19**, again through stereochemical inversion. Fortuitously, under these same basic reaction conditions, the α- anomer **19** epimerizes to afford the more stable and naturally configured β-anomer **17** (*14*, *31*). Thus, both fluorohydrin aldol products can be transformed together into a single naturally configured β-D-NA through this straightforward reaction sequence. It is notable that the enantiomeric purity of **17** (entry 6) represents an average of the enantiomeric purities of the epimeric fluorohydrins **16**.

To assess the general utility of this NA synthesis, we prepared a collection of acetaldehyde derivatives through the alkylation of several heterocycles with bromoacetaldehyde diethyl acetal (**20**) (Fig. 3A; see supplementary materials for details). Using either Selectfluor or NFSI as the electrophilic fluorinating agent (F^+), aldehydes **21** underwent proline-catalyzed αFAR with dioxanone **8** to provide fluorohydrins **22** functionalized with one of the heterocycles uracil, thymine, triazole, deazadenine, pyrazole, phthalimide, adenine, or 2,6-dichloropyrimidine. In the case of the adenine-containing fluorohydrin, the enantiomeric purity was lowered by competing (nonproline) catalysis in the αFAR. Each of the fluorohydrins was isolated as a mixture of epimers at the fluoromethine center that subsequently underwent a 1,3-*syn* selective carbonyl reduction and cyclization promoted by either base (Fig. 2B) or a Lewis acid (Fig. 2C), as indicated. We found that several heterocycles were compatible with this process and that uracil-, thymine-, or adenine-substituted acetaldehydes could be exploited in short (four-step total) de novo syntheses of the endogenous ribonucleosides uridine (U: **24**), 5-methyluridine (m^5U: **25**), and adenosine (A: **31**). Generally, the optimal Lewis acids for promoting AFD reactions were $InCl_3$ or $Sc(OTf)_3$, whereas pyrazole- and uracil-derived fluorohydrins cyclized using NaOH. With the exception of triazole **28**, trifluoromethyluracil **29**, and deazaadenines **32** and **33**, the NAs were produced as an approximate average of the enantiomeric purities of the precursor fluorohydrins **22**. Thus, most NAs examined undergo epimerization after AFD (*14*), which provides a straightforward means to convert mixtures of epimeric aldol products into naturally configured β-D-NAs. For the trifluoromethyl uracil **29** and deazaadenines **32** and **33**, αFAR products (e.g., **22**) were reduced, separated, and treated individually with $Sc(OTf)_3$ or $InCl_3$ (Fig. 3C). For trifluoromethyl uracil, only the *anti*-fluorohydrin underwent AFD to form **29**, which did not epimerize under the reaction conditions. With deazaadenine, both the *syn*-fluorohydrin and *anti*-fluorohydrin cyclized to provide the β- and α-anomers **32** and **33**, respectively, by direct fluoride displacement.

To evaluate the practical utility of these processes, several of the αFARs were demonstrated on a >10-g scale [e.g., **25**, **28**, **29**, **30**, and **32** (Fig. 3)] and proceeded without complication. C-linked NA **27** could be prepared using this reaction sequence (HetAr = 4,6-dichloropyrimidine), which further extends the utility of this strategy to an additional and important class of NAs (*32*). In this case, however, the major product of the aldol reaction cyclizes to an α-D-NA and then undergoes a second cyclization event to form the tricycle **27**. In addition to naturally configured NAs, this strategy can be adapted for the synthesis of enantiomeric (L-configured) NAs (Fig. 3E) by using D-proline in the αFAR. Thus, L-uridine (*ent*-**24**) and the L-configured NA *ent*-**28** were accessed in a straightforward manner. Crude reaction products were generally treated with aqueous acid to remove the acetonide protecting group, but eliminating

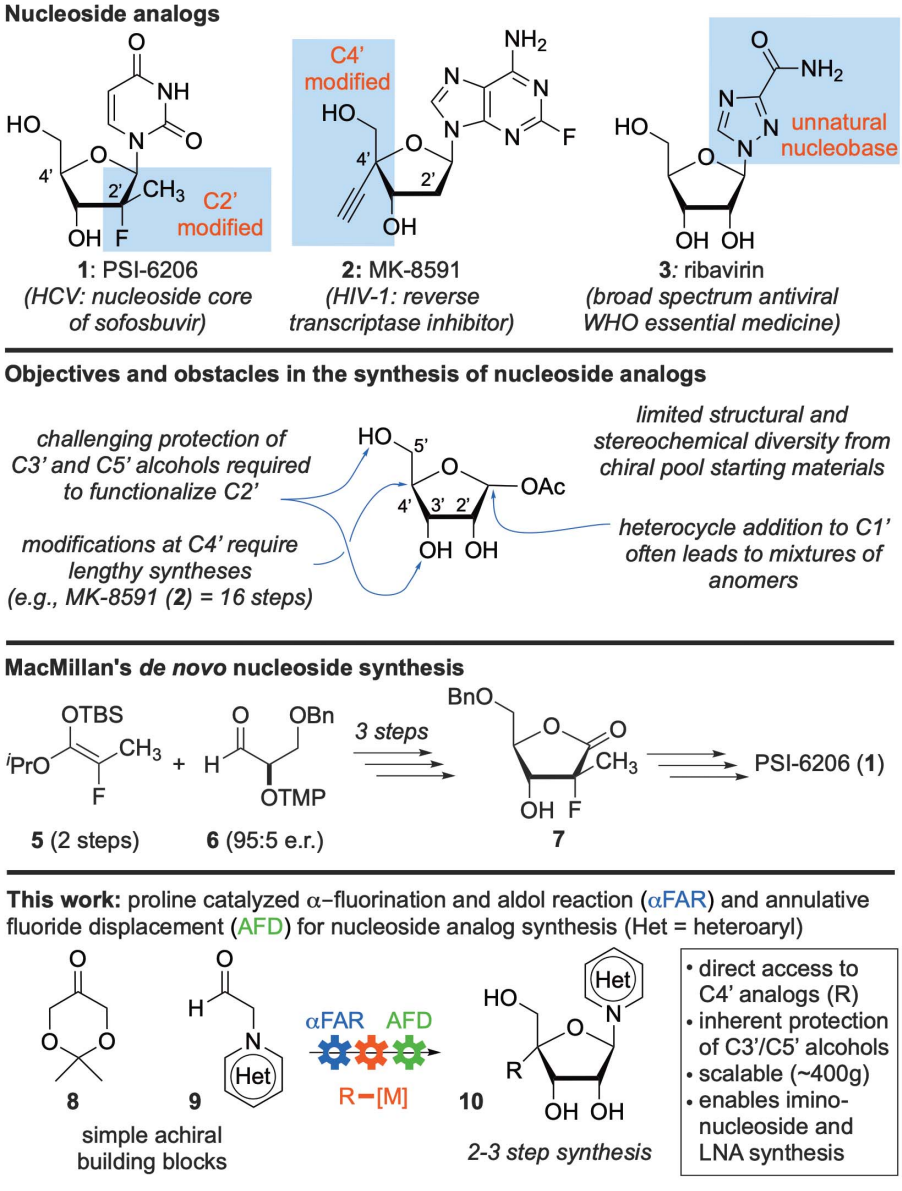
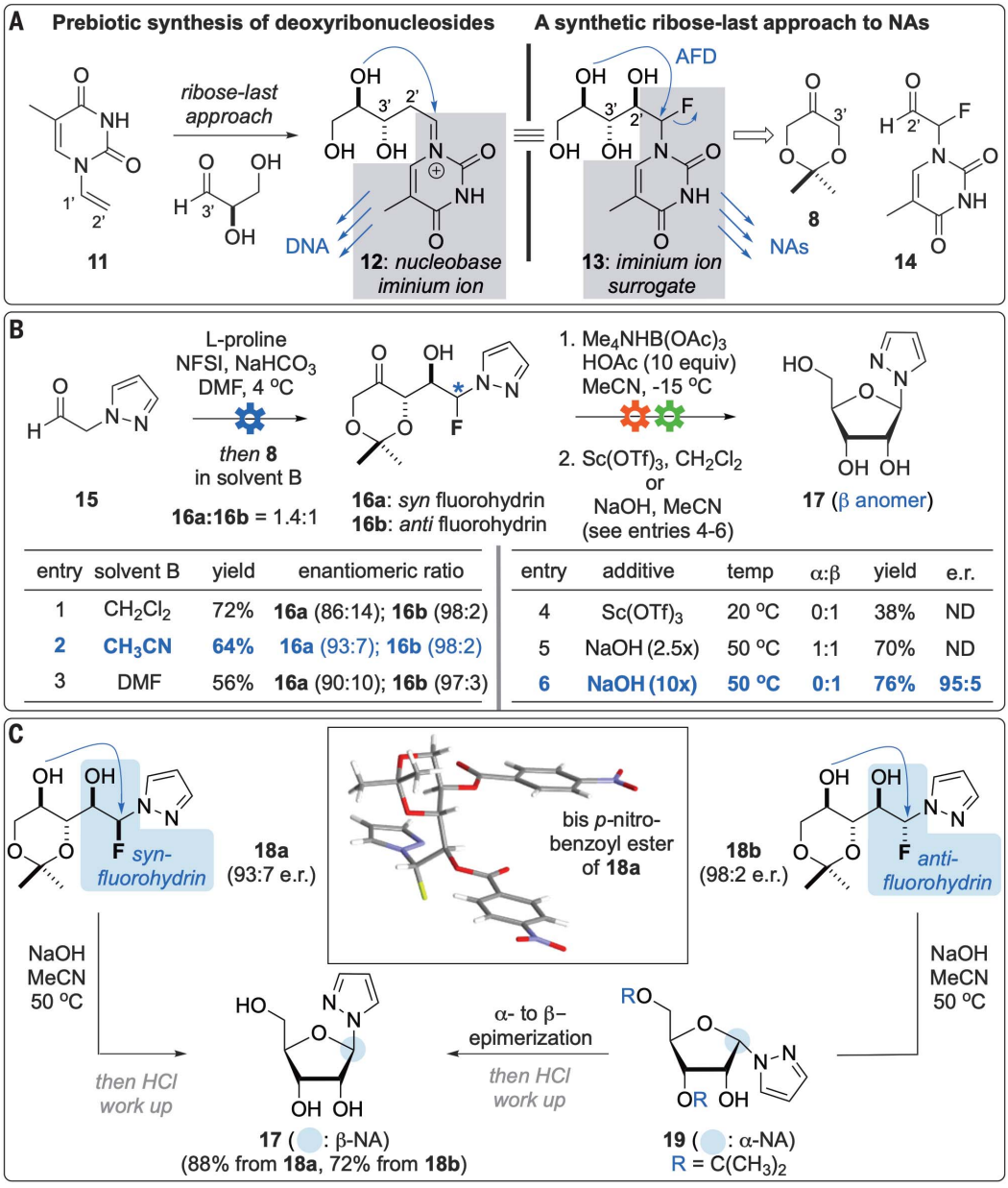


Fig. 1. Nucleoside analogs: objectives and obstacles. WHO, World Health Organization; e.r., enantiomeric ratio.

this step allowed us to isolate C3′- and C5′-protected NAs directly (e.g., **34** and **35**, Fig. 3D). To demonstrate that these acetonide-protected NAs can be further derivatized using standard protocols, several C2′-modified NAs were prepared, including C2′-oxo (**36**), C2′-deoxy (**37**), C2′-3° alcohol (**38**), and C2′-*epi* (**39**) (Fig. 3F).

Having ready access to a range of αFAR products, we anticipated that the addition of organometallic reagents (rather than hydride reduction) would lead directly to C4′-modified NAs. Toward this goal, we examined reactions of fluorohydrin **41** with a range of organometallic reagents under a variety of reaction conditions (see supplementary materials). Grignard reagents in CH_2Cl_2 proved to be most compatible, and executing the reactions at −78°C proved necessary because higher reaction temperatures promoted 1,2-hydride shift and fluoride displacement. These reactions generally gave mixtures of tertiary alcohols with a preference for addition to the *re* face (*24*), and when the crude reaction mixture was allowed to warm to room temperature, the intermediate magnesium alkoxide **42a** underwent AFD to provide the C4′-modified NA **43** directly. This short sequence enables access to enantiomerically enriched C4′-modified NAs in only three steps from simple achiral heterocycles and bromoacetaldehyde diethyl acetal. Alternatively, quenching the mixture of magnesium alkoxides **42a** and **42b** with ammonium chloride followed by a subsequent Lewis acid–promoted AFD using $InCl_3$ gave the anomeric α-D-NA **44**. In this case, the magnesium alkoxides **42a** and **42b** cyclize selectively using base or Lewis acid to afford access to α-L– and α-D–configured NAs, which are both unnaturally configured NAs of contemporary interest to medicinal chemists (*14*–*16*).

These results led us to examine the reaction of several additional Grignard reagents with aldol adducts containing triazole, deazaadenine, thymine, pyrazole, or trifluoromethyluracil functions (Fig. 4A). We found that diastereoselectivity depends on both the



entry	solvent B	yield	enantiomeric ratio
1	CH_2Cl_2	72%	**16a** (86:14); **16b** (98:2)
2	**CH_3CN**	**64%**	**16a** (93:7); **16b** (98:2)
3	DMF	56%	**16a** (90:10); **16b** (97:3)

entry	additive	temp	α:β	yield	e.r.
4	$Sc(OTf)_3$	20 °C	0:1	38%	ND
5	NaOH (2.5x)	50 °C	1:1	70%	ND
6	**NaOH (10x)**	**50 °C**	**0:1**	**76%**	**95:5**

Fig. 2. A short synthesis of the pyrazolyl NA 17. (**A**) Ribose-last approach in a proposed prebiotic synthesis of nucleosides inspired a synthetic strategy to NAs. (**B**) Proline-catalyzed αFAR, followed by reduction and AFD. (2.5x), 2.5 equivalence. (**C**) Mechanistic studies of the AFD process. NFSI, *N*-fluorobenzenesulfonimide; DMF, dimethylformamide; MeCN, acetonitrile; OTf, triflate; equiv, equivalence; ND, not determined.

solvent and the heterocycle, and reactions in tetrahydrofuran (THF) generally gave mixtures of tertiary alcohols of different composition from those generated in CH_2Cl_2. The addition of MeMgI to ketofluorohydrins substituted with triazole gave predominantly 1,3-*syn*-diols that cyclized to the naturally configured NA **48**. Thus, subtle differences in chelation structures involving the heterocycle and/or

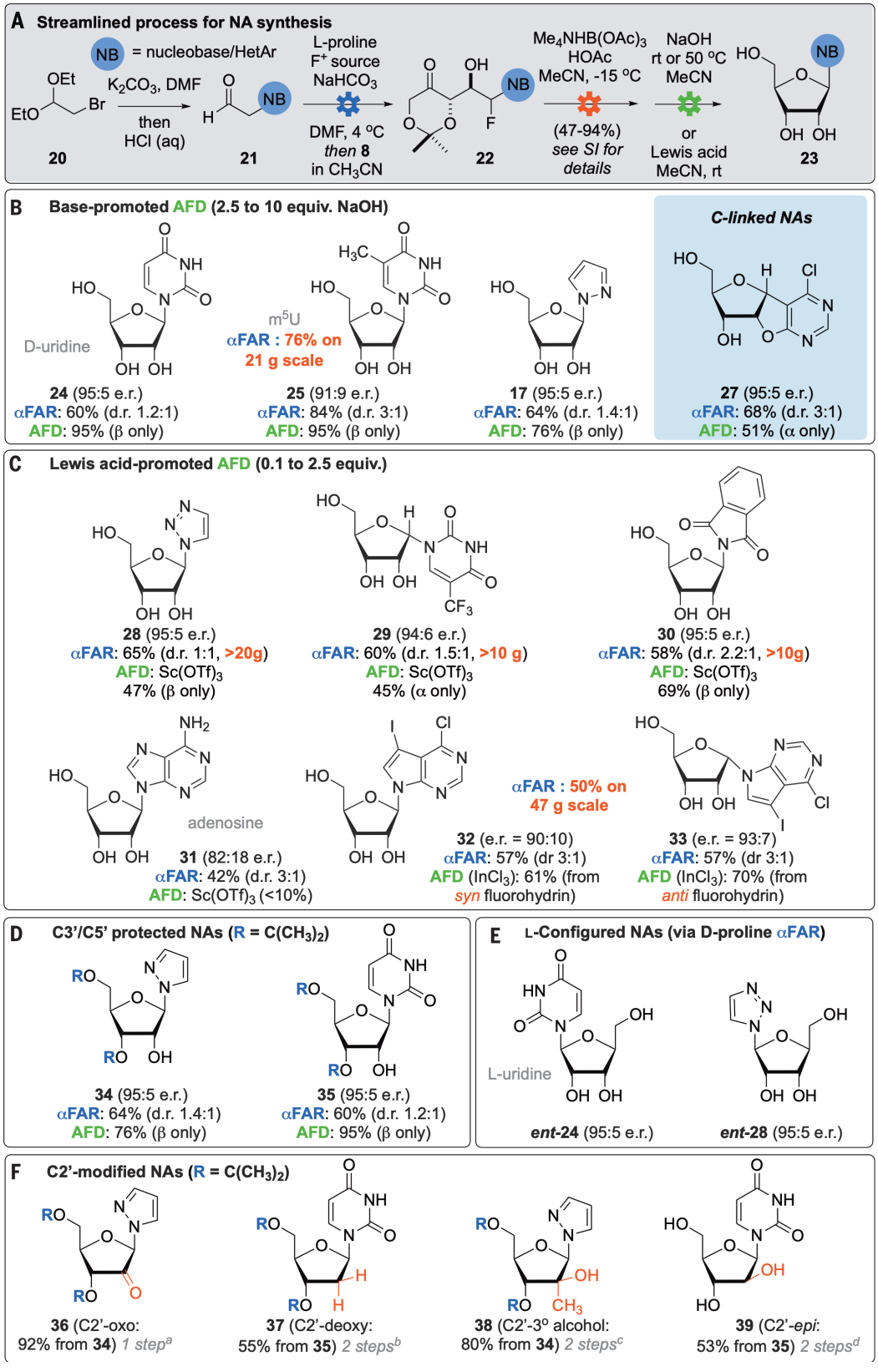


Fig. 3. Scope of nucleoside and NA synthesis. (**A**) A simple four-step reaction sequence converts readily available starting materials into enantioenriched and naturally configured β-D-NAs. (**B**) AFD to produce uracil, thymine, pyrazolyl, and 5-pyrimidinyl nucleosides; and NAs can be promoted by NaOH. (**C**) AFD to produce trifluoromethyl uracil, triazolyl, phthalimidyl, deazaadenine, and adenosine nucleosides; and NAs can be promoted by the Lewis acids $Sc(OTf)_3$ or $InCl_3$. (**D**) NAs protected at both the C3′ and C5′ alcohol functions are now readily available. (**E**) Using D-proline to catalyze the αFAR reaction, unnatural nucleosides (L-enantiomers) are now readily available. (**F**) Exploiting this convenient process, we prepared a small collection of C2′-modified NAs. [a]TEMPO, BAIB, CH_2Cl_2 (92% from **34**). [b]i) thiocarbonyldiimidazole, THF; ii) Bu_3SnH, azobisisobutyronitrile (55% over two steps from **35**). [c]i) TEMPO, BAIB, CH_2Cl_2; ii) MeMgBr, THF, −78°C (80% over two steps from **34**). [d]DAST, CH_2Cl_2 then HCl, methanol (MeOH) (53% from **35**). TEMPO, 2,2,6,6-Tetramethylpiperidin-1-yl)oxyl; BAIB, bis(acetoxy)iodobenzene; THF, tetrahydrofuran; DAST, diethylaminosulfur trifluoride; aq, aqueous; rt, room temperature; SI, supplementary materials; d.r., diastereomeric ratio.

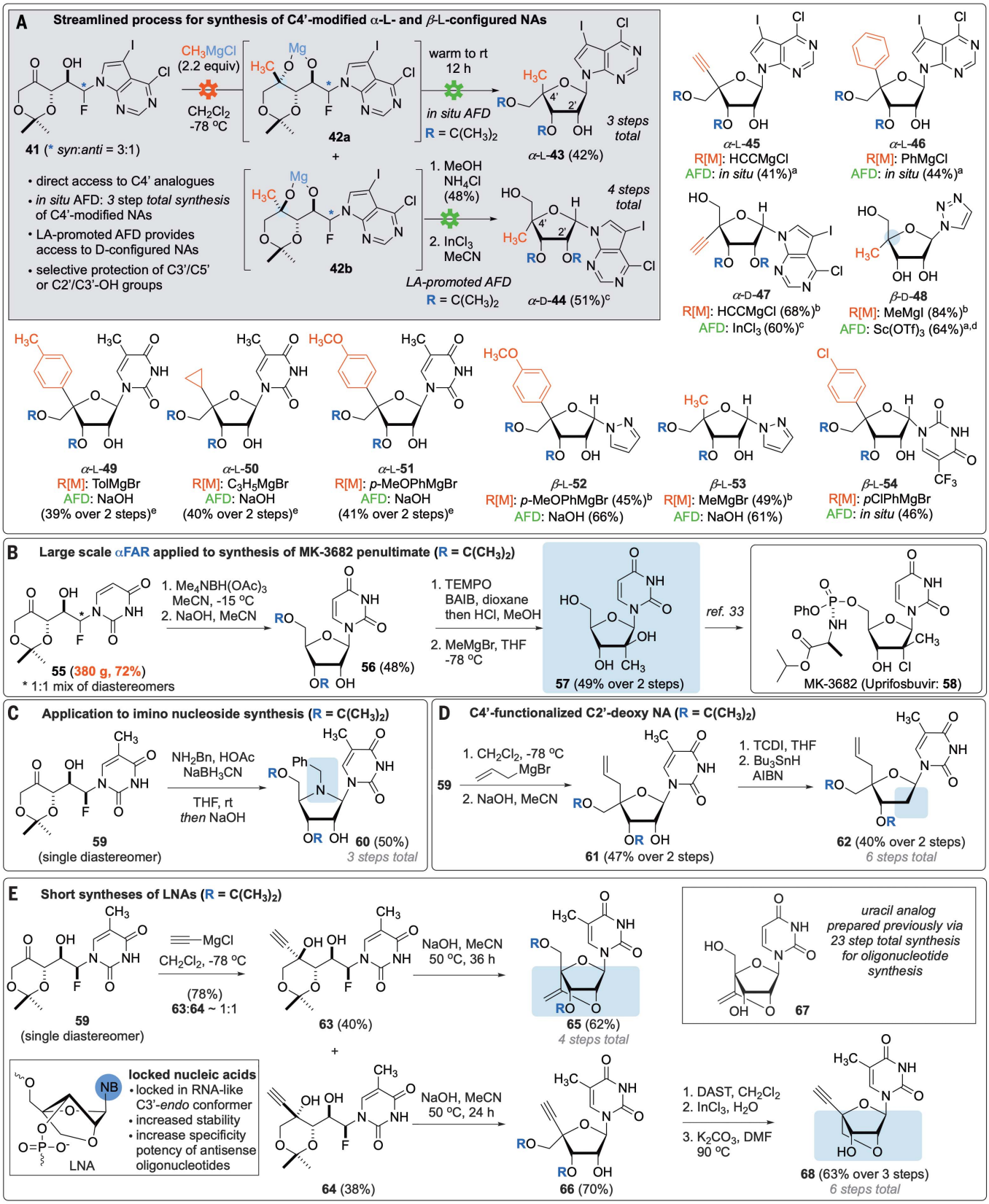


Fig. 4. Rapid synthesis of C4'-modified and other NAs. (**A** to **E**) Diversification and large-scale production of αFAR products provide access to C4'-modified NAs, iminonucleosides, and LNAs to support medicinal chemistry efforts. [a]Yield from keto-fluorohydrin aldol adduct. [b]Combined yield of diastereomers. [c]Product after heating of crude reaction mixture to 50°C with camphorsulfonic acid (CSA) and dimethoxyacetone. [d]Product after treatment of crude reaction mixture with aqueous HCl. [e]Starting from a single fluorohydrin **59**.

β-alkoxide function and organomagnesium reagents play a notable stereodetermining role in these 1,2-addition reactions. Controlling this aspect of the process to selectively access β-D–configured NAs will be the subject of future studies. In this study, a collection of deazaadenine-substituted NAs **43** to **47** were readily accessed as both α- and β-anomers. In general, and as noted in Fig. 3, base-promoted cyclizations resulted in C3′-OH– and C5′-OH–protected NAs (e.g., **49** to **54**), whereas Lewis acid–promoted cyclizations resulted in deprotection or protecting group migration (e.g., **44** and **47**). Densely functionalized L-configured C4′-modified NAs could be rapidly accessed from the corresponding ketofluorohydrin aldol adducts, including NAs substituted with methyl, cyclopropyl, aryl, and alkynyl groups (Fig. 4). From this study, it is clear that larger collections of C4′-modified NAs (e.g., focused screening libraries) are now readily available. It is worth highlighting that each of the C4′-methyl, cyclopropyl, *p*-methoxyphenyl, *p*-chlorophenyl, and alkynyl NAs **43** to **54** were prepared in only three or four steps total, which compares favorably to contemporary syntheses.

Considering the potential for this process to affect the large-scale production of NAs, we examined the synthesis of the D-uridine derivative **56** starting with 900 g of uracil. Without additional optimization, we were able to generate ~380 g of the aldol adduct **55** (Fig. 2B), which was converted into the protected uridine **56** in excellent yield. Oxidation of the C2′-OH function followed by deprotection and addition of MeMgBr in THF gave the tertiary alcohol **57**. This later compound is a previously reported intermediate in the large-scale production of MK-3682 (uprifosbuvir: **58**) (*33*), an HCV NS5B RNA polymerase inhibitor developed for the treatment of hepatitis C virus (HCV).

We also briefly assessed the utility of this process for accessing an unusual class of NAs known as iminonucleosides, wherein the furanose oxygen is replaced by a nitrogen atom. In a single example (Fig. 4C), we observed that reductive amination of the fluorohydrin aldol adduct **59** (isolated as a single diastereomer, as shown) using benzyl amine and followed by a basic work-up led directly to the β-D–configured iminonucleoside **60** in good yield. To further demonstrate the advantages of this strategy, we prepared a C4′-modified deoxy NA (Fig. 4D). In this case, C4′-allyl ribothymidine **61** was accessed through the addition of allylmagnesium bromide to the fluorohydrin **59** followed by base-promoted AFD. A Barton-McCombie deoxygenation then gave the C4′-allyl NA **62** in only six steps from thymine.

Finally, we aimed to exploit this facile C4′-functionalization strategy in the preparation of locked nucleic acids (LNAs) (*34*). These conformationally restricted NAs demonstrate improved stability, and their incorporation in antisense oligonucleotides can lead to substantial increases in specificity and potency. We evaluated the addition of alkynylmagnesium chloride to the thymine-containing aldol adduct **59** and found that the reaction gave two diastereomeric addition products **63** and **64**. The major product was transformed directly into the unusual LNA **65** by simply reacting with NaOH, which promoted both the AFD reaction and a subsequent cyclization between the free alcohol function and alkyne. This four-step total synthesis is comparable to the 23-step route reported for the analogous uracil LNA **67** (*35*). We were also able to generate the unusual alkyne-functionalized LNA **68**, an unreported scaffold in nucleoside chemistry, by simply effecting an AFD of the 1,2-addition product **64**. From here, formation of the 2,2′-anhydrothymidine followed by deprotection and treatment with base in warm DMF (*36*) gave the LNA **68**. This scaffold is primed for further diversification through standard click or Sonagashira coupling reactions.

The demonstration of several αFARs on scales >10 g and up to 400 g supports the use of this strategy in the process scale production of NAs. Several generations of medicinal chemistry and total synthesis have provided reliable templates for nucleoside and NA synthesis; however, this study provides opportunities that should influence the construction of diversity libraries and support future efforts in both drug discovery and development.

REFERENCES AND NOTES

1. G. M. Blackburn, M. J. Gait, D. Loakes, D. M. Williams, Eds., *Nucleic Acids in Chemistry and Biology* (Royal Society of Chemistry Publishing, 2006).
2. C. M. Galmarini, J. R. Mackey, C. Dumontet, *Lancet Oncol.* **3**, 415–424 (2002).
3. E. De Clercq, *Med. Res. Rev.* **33**, 1215–1248 (2013).
4. L. P. Jordheim, D. Durantel, F. Zoulim, C. Dumontet, *Nat. Rev. Drug Discov.* **12**, 447–464 (2013).
5. J. Shelton *et al.*, *Chem. Rev.* **116**, 14379–14455 (2016).
6. B. Ewald, D. Sampath, W. Plunkett, *Oncogene* **27**, 6522–6537 (2008).
7. K. L. Seley-Radtke, M. K. Yates, *Antiviral Res.* **154**, 66–86 (2018).
8. M. K. Yates, K. L. Seley-Radtke, *Antiviral Res.* **162**, 5–21 (2019).
9. H. Ma *et al.*, *J. Biol. Chem.* **282**, 29812–29820 (2007).
10. E. P. Gillis, K. J. Eastman, M. D. Hill, D. J. Donnelly, N. A. Meanwell, *J. Med. Chem.* **58**, 8315–8359 (2015).
11. H. Ohrui, *Chem. Rec.* **6**, 133–143 (2006).
12. J. T. Witkowski, R. K. Robins, R. W. Sidwell, L. N. Simon, *J. Med. Chem.* **15**, 1150–1154 (1972).
13. J. Zeidler, D. Baraniak, T. Ostrowski, *Eur. J. Med. Chem.* **97**, 409–418 (2015).
14. G. Ni *et al.*, *RSC Advances* **9**, 14302–14320 (2019).
15. G. Gumina, G. Y. Song, C. K. Chu, *FEMS Microbiol. Lett.* **202**, 9–15 (2001).
16. H. Cui *et al.*, *J. Med. Chem.* **55**, 10948–10957 (2012).
17. P. Merino, Ed., *Chemical Synthesis of Nucleoside Analogues* (Wiley, 2013).
18. M. Brodszki *et al.*, *Org. Process Res. Dev.* **15**, 1027–1032 (2011).
19. M. McLaughlin *et al.*, *Org. Lett.* **19**, 926–929 (2017).
20. K. R. Campos *et al.*, *Science* **363**, eaat0805 (2019).
21. M. Peifer, R. Berger, V. W. Shurtleff, J. C. Conrad, D. W. MacMillan, *J. Am. Chem. Soc.* **136**, 5900–5903 (2014).
22. J. S. Teichert, F. M. Kruse, O. Trapp, *Angew. Chem. Int. Ed.* **58**, 9944–9947 (2019).
23. M. Bergeron-Brlek, T. Teoh, R. Britton, *Org. Lett.* **15**, 3554–3557 (2013).
24. C. Grondal, D. Enders, *Adv. Synth. Catal.* **349**, 694–702 (2007).
25. W. Ren *et al.*, *Nat. Commun.* **9**, 3243 (2018).
26. A. Quintard, J. Rodriguez, *ACS Catal.* **7**, 5513–5517 (2017).
27. R. Britton, B. Kang, *Nat. Prod. Rep.* **30**, 227–236 (2013).
28. F. A. Davis, P. V. N. Kasu, G. Sundarababu, H. Qi, *J. Org. Chem.* **62**, 7546–7547 (1997).
29. D. D. Steiner, N. Mase, C. F. Barbas 3rd, *Angew. Chem. Int. Ed.* **44**, 3706–3710 (2005).
30. E. M. Sánchez-Fernández *et al.*, *Chem. Eur. J.* **18**, 8527–8539 (2012).
31. T. C. Britton, M. E. LeTourneau, Process for Anomerizing Nucleosides, U.S. Patent 5,420,266A (1995).
32. E. De Clercq, *J. Med. Chem.* **59**, 2301–2311 (2016).
33. A. M. Hyde, R. Calabria, R. Arvary, X. Wang, A. Klapars, *Org. Process Res. Dev.* **23**, 1860–1871 (2019).
34. M. A. Campbell, J. Wengel, *Chem. Soc. Rev.* **40**, 5680–5689 (2011).
35. P. P. Seth, E. E. Swayze, 6-Disubstituted or Unsaturated Bicyclic Nucleic Acid Analogs, U.S. Patent 8278283 B2 (2008).
36. T. Yamaguchi, M. Horiba, S. Obika, *Chem. Commun.* **51**, 9737–9740 (2015).

ACKNOWLEDGMENTS

The authors thank D. McKearney (Simon Fraser University) and J. A. Newman (Merck & Co., Inc.) for carrying out x-ray crystallographic analyses. **Funding:** R.B. acknowledges support from the Canadian Glycomics Network (Strategic Initiatives Grant, CD-46), the Natural Sciences and Engineering Research Council (NSERC) of Canada (Discovery Grant, RGPIN-2019-06468), and Merck & Co., Inc. M.M. was supported by an NSERC CGSD2 scholarship, and J.L. was supported by the Deutsche Forschungsgemeinschaft (DFG). **Author contributions:** M.M. and S.M.S. developed the methodology; M.M., S.M.S., J.L., B.A., and Y.W. performed the experiments; R.C. developed a protocol for assigning stereochemistry by nuclear magnetic resonance (NMR) spectroscopic and computational methods; L.-C.C. and R.B. were responsible for project administration; R.B. conceptualized the research; L.-C.C. and R.B. supervised the execution of experiments; and R.B. wrote the original draft. **Competing interests:** Simon Fraser University and Merck & Co., Inc. have filed a patent application describing the synthesis of nucleoside analogs via the process presented in this manuscript—U.S. provisional patent application no. 62/994,349. **Data and materials availability:** All data are available in the manuscript or the supplementary materials. X-ray structures are deposited at the Cambridge Crystallographic Data Centre under reference numbers 1955427, 2008890, and 1955420.

SUPPLEMENTARY MATERIALS

science.sciencemag.org/content/369/6504/725/suppl/DC1
Materials and Methods
Supplementary Text
Figs. S1 to S14
Tables S1 to S12
Liquid Chromatography Chromatograms
NMR Data
References (*37*–*52*)
MDAR Reproducibility Checklist

15 February 2020; accepted 5 June 2020
10.1126/science.abb3231

CORONAVIRUS

Broad neutralization of SARS-related viruses by human monoclonal antibodies

Anna Z. Wec[1], Daniel Wrapp[2], Andrew S. Herbert[3], Daniel P. Maurer[1], Denise Haslwanter[4], Mrunal Sakharkar[1], Rohit K. Jangra[4], M. Eugenia Dieterle[4], Asparouh Lilov[1], Deli Huang[5], Longping V. Tse[6], Nicole V. Johnson[2], Ching-Lin Hsieh[2], Nianshuang Wang[2], Juergen H. Nett[1], Elizabeth Champney[1], Irina Burnina[1], Michael Brown[1], Shu Lin[1], Melanie Sinclair[1], Carl Johnson[1], Sarat Pudi[1], Robert Bortz III[4], Ariel S. Wirchnianski[4], Ethan Laudermilch[4], Catalina Florez[4], J. Maximilian Fels[4], Cecilia M. O'Brien[3], Barney S. Graham[7], David Nemazee[5], Dennis R. Burton[5,8,9,10], Ralph S. Baric[6,11], James E. Voss[5], Kartik Chandran[4], John M. Dye[3], Jason S. McLellan[2], Laura M. Walker[1]*

Broadly protective vaccines against known and preemergent human coronaviruses (HCoVs) are urgently needed. To gain a deeper understanding of cross-neutralizing antibody responses, we mined the memory B cell repertoire of a convalescent severe acute respiratory syndrome (SARS) donor and identified 200 SARS coronavirus 2 (SARS-CoV-2) binding antibodies that target multiple conserved sites on the spike (S) protein. A large proportion of the non-neutralizing antibodies display high levels of somatic hypermutation and cross-react with circulating HCoVs, suggesting recall of preexisting memory B cells elicited by prior HCoV infections. Several antibodies potently cross-neutralize SARS-CoV, SARS-CoV-2, and the bat SARS-like virus WIV1 by blocking receptor attachment and inducing S1 shedding. These antibodies represent promising candidates for therapeutic intervention and reveal a target for the rational design of pan-sarbecovirus vaccines.

In December 2019, a novel pathogen emerged in the city of Wuhan in China's Hubei province, causing an outbreak of atypical pneumonia [a disease known as coronavirus disease 2019 (COVID-19)]. The infectious agent was characterized as a lineage B betacoronavirus, named severe acute respiratory syndrome coronavirus 2 (SARS-CoV-2) and shown to be closely related to SARS-CoV and several SARS-like bat CoVs (*1*). There are currently no approved vaccines or therapeutics available for the prevention or treatment of COVID-19.

CoV entry into host cells is mediated by the viral S glycoprotein, which forms trimeric spikes on the viral surface (*2*). Each monomer in the trimeric S assembly is a heterodimer of S1 and S2 subunits. The S1 subunit is composed of four domains: an N-terminal domain (NTD), a C-terminal domain (CTD), and subdomains I and II (*3*–*5*). The CTD of both SARS-CoV and SARS-CoV-2 functions as the receptor-binding domain (RBD) for the shared entry receptor, human angiotensin-converting enzyme 2 (hACE2) (*6*–*10*). The S2 subunit contains the fusion peptide, heptad repeats 1 and 2, and a transmembrane domain, all of which are required for fusion of the viral and host cell membranes.

The S glycoprotein of HCoVs is the primary target for neutralizing antibodies (nAbs) (*11*). SARS-CoV and SARS-CoV-2 share 76% amino acid identity in their S proteins, raising the possibility of conserved immunogenic surfaces on these antigens. Studies of convalescent sera and a limited number of monoclonal antibodies (mAbs) have revealed limited to no cross-neutralizing activity, demonstrating that conserved antigenic sites are rarely targeted by nAbs (*5*, *9*, *12*, *13*). However, the frequencies, specificities, and functional activities of cross-reactive antibodies induced by natural SARS-CoV and SARS-CoV-2 infection remain poorly defined.

We aimed to comprehensively profile the cross-reactive B cell response induced by SARS-CoV infection by cloning an extensive panel of SARS-CoV-2 S-reactive mAbs from the peripheral B cells of a convalescent donor (donor 84) who survived the 2003 SARS outbreak. To isolate cross-reactive antibodies, we obtained a blood sample from this donor about 3 years after infection and stained purified B cells with a panel of memory B cell (MBC) markers and a fluorescently labeled SARS-CoV-2 S protein. Flow cytometric analysis revealed that 0.14% of class-switched MBCs were SARS-CoV-2 S-reactive, which was about threefold greater than background staining observed with a SARS-CoV–naïve donor sample (Fig. 1A). Cognate antibody heavy- and light-chain pairs were amplified from 315 individual SARS-CoV-2–reactive B cells by single-cell reverse transcription polymerase chain reaction (RT-PCR) and subsequently cloned and expressed as full-length immunoglobulin Gs (IgGs) in an engineered strain of *Saccharomyces cerevisiae* (*14*). Of the 315 cloned antibodies, 200 bound to SARS-CoV-2 S in preliminary binding screens (Fig. 1B). Sequence analysis revealed that about half of the clones were members of expanded clonal lineages, whereas the other half were unique (Fig. 1C). Moreover, about 30% of isolated antibodies displayed convergent VH1-69/VK2-30 germline gene pairing (Fig. 1C). As expected, almost all the antibodies were somatically mutated, with members of clonally expanded lineages showing significantly higher levels of somatic hypermutation (SHM) compared with unique clones (Fig. 1D). Finally, consistent with the respiratory nature of SARS-CoV infection, index sorting analysis revealed that 33% of binding antibodies originated from IgA^+ MBCs and the remaining 66% from IgG^+ MBCs (Fig. 1E). We conclude that SARS-CoV infection elicited a high frequency of long-lived, cross-reactive MBCs in this donor.

We next measured the apparent binding affinities (K_D^{App}s) of the antibodies to prefusion-stabilized SARS-CoV and SARS-CoV-2 S proteins (*5*). Although most antibodies (153 out of 200) showed binding to both S proteins, a subset appeared to be SARS-CoV-2 S-specific (Fig. 2A). This result was unexpected given that the antibodies were isolated from a SARS-CoV–experienced donor and may relate to differences between the infecting SARS-CoV strain and the recombinant SARS-CoV S protein (Tor2) used for the binding studies. Alternatively, this result may be due to inherent differences in the stability or antigenicity of recombinant prefusion-stabilized SARS-CoV and SARS-CoV-2 S proteins. Indeed, about 30% of antibodies that failed to bind recombinant SARS-CoV S displayed reactivity with SARS-CoV S expressed on the surface of transfected cells, providing some evidence for differences in the antigenicity of recombinant and cell-expressed forms of S (fig. S1).

Paradoxically, most of the highly mutated and clonally expanded antibodies bound weakly (K_D^{Apps} > 10 nM) to both SARS-CoV and SARS-CoV-2 S (Fig. 2B). We sought to determine if these antibodies originated from preexisting MBCs induced by prior exposures to naturally circulating HCoVs, which share up to 32% S amino acid identity with SARS-CoV and SARS-CoV-2. Accordingly, we assessed binding of the antibodies to recombinant S proteins of naturally circulating human alphacoronaviruses (HCoV-NL63 and HCoV-229E) and betacoronaviruses (HCoV-OC43 and HCoV-HKU1).

[1]Adimab LLC, Lebanon, NH 03766, USA. [2]Department of Molecular Biosciences, The University of Texas at Austin, Austin, TX 78712, USA. [3]U.S. Army Medical Research Institute of Infectious Diseases, Frederick, MD 21702, USA. [4]Department of Microbiology and Immunology, Albert Einstein College of Medicine, New York, NY 10462, USA. [5]Department of Immunology and Microbiology, The Scripps Research Institute, La Jolla, CA 92037, USA. [6]Department of Epidemiology, The University of North Carolina at Chapel Hill, Chapel Hill, NC 27599, USA. [7]Vaccine Research Center, National Institute of Allergy and Infectious Diseases, National Institutes of Health, Bethesda, MD 20892, USA. [8]IAVI Neutralizing Antibody Center, The Scripps Research Institute, La Jolla, CA 92037, USA. [9]Consortium for HIV/AIDS Vaccine Development (CHAVD), The Scripps Research Institute, La Jolla, CA 92037, USA. [10]Ragon Institute of Massachusetts General Hospital, Massachusetts Institute of Technology, and Harvard, Cambridge, MA 02139, USA. [11]Departments of Microbiology and Immunology, The University of North Carolina at Chapel Hill, Chapel Hill, NC 27599, USA.
*Corresponding author. Email: laura.walker@adimab.com

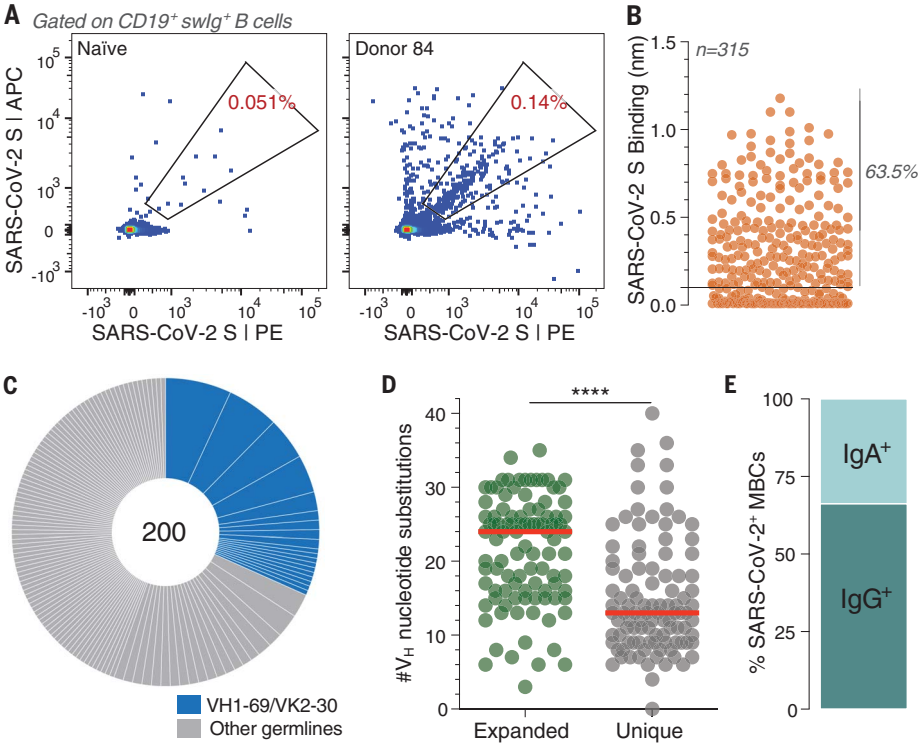


Fig. 1. Isolation of SARS-CoV-2 S-specific antibodies. (**A**) Frequency of SARS-CoV-2 S-reactive B cells in donor 84 and a SARS-CoV–naïve donor. Fluorescence-activated cell sorting plots are gated on $CD19^+CD20^+IgD^-IgM^-$ B cells. swIg, switched immunoglobulin. (**B**) Binding of 315 isolated antibodies to SARS-CoV-2 S, as determined by BLI. The dashed line indicates the threshold for designating binders (0.1 nm). (**C**) Clonal lineage analysis. Each lineage is represented as a segment proportional to the lineage size. The total number of antibodies is shown in the center of the pie. Clonal lineages were defined based on the following criteria: identical V_H and V_L germline genes, identical CDR H3 (third complementarity-determining region of the heavy chain) length, and CDR H3 amino acid identity ≥80%. (**D**) Somatic mutation load, expressed as the number of nucleotide substitutions in V_H, in unique antibodies and members of expanded clonal lineages. Red bars indicate medians. Statistical comparisons were made using the Mann-Whitney test (****$P < 0.0001$). (**E**) Proportion of SARS-CoV-2 S binders derived from IgG^+ and IgA^+ B cells, as determined by index sorting.

More than 80% of the low-affinity (K_D^{Apps} > 10 nM) SARS-CoV and SARS-CoV-2 cross-reactive antibodies reacted with one or more of the HCoV S proteins, suggesting that SARS-CoV infection may have boosted a preexisting MBC response induced by circulating HCoVs (Fig. 2B). Consistent with this hypothesis, the broadly cross-reactive antibodies showed significantly higher levels of SHM and clonal expansion compared with those that only recognized SARS-CoV and SARS-CoV-2 (Fig. 2, B to D). Furthermore, 72% of the broadly binding antibodies used VH1-69/VK2-30 germline gene pairing, suggesting germline-mediated recognition of a common antigenic site (Fig. 2B and fig. S2). Although we were unable to finely map the epitopes recognized by these antibodies, none of them bound to recombinant SARS-CoV-2 S1, suggesting that they likely target epitopes within the more conserved S2 subunit (fig. S3). Index sorting analysis revealed that the majority of the broadly cross-reactive antibodies were derived from IgA^+ MBCs, indicating a mucosal origin, whereas most of the SARS-CoV and SARS-CoV-2 cross-reactive antibodies originated from IgG^+ MBCs (Fig. 2E). Finally, all of the broad binders lacked polyreactivity, demonstrating that their cross-binding is not due to nonspecific cross-reactivity (fig. S4).

To investigate whether the above results were due to an original antigenic sin phenomenon, or rather simply due to avid binding of circulating HCoV-specific B cell receptors to the SARS-CoV-2 S tetramers used for cell sorting, we assessed whether similarly broadly binding antibodies were also present in SARS-CoV– and SARS-CoV-2–naïve donors that had been exposed to endemic HCoVs. We obtained peripheral blood mononuclear cell (PBMC) samples from three healthy adult donors with serological evidence of circulating HCoV exposure and no history of SARS-CoV or SARS-CoV-2 infection and stained the corresponding B cells with a fluorescently labeled SARS-CoV-2 S probe (fig. S5A). Flow cytometric analysis revealed that between 0.06 and 0.12% of total B cells in the three naïve donors displayed SARS-CoV-2 reactivity (fig. S5B). More than 350 SARS-CoV-2–reactive MBCs were sorted and amplified by single-cell RT-PCR, and 141 variable region of Ig heavy chain (V_H)–variable region of Ig light chain (V_L) pairs were cloned and expressed as full-length IgGs. Although a limited number of SARS-CoV-2 S binding antibodies (3 to 22) were isolated from all three naïve donors, they displayed significantly lower levels of SHM, clonal expansion, and K_D^{Apps} for both SARS-CoV and SARS-CoV-2 S compared with the cross-reactive antibodies identified from donor 84 (Fig. 2, F and G, and fig. S5C). Altogether, these results suggest that SARS-CoV infection likely led to the activation and expansion of preexisting cross-reactive MBCs induced by circulating HCoV exposure in this donor.

To map the antigenic sites recognized by the SARS-CoV and SARS-CoV-2 cross-reactive antibodies isolated from donor 84, we performed binding experiments using a panel of recombinant S protein subunits and individual domains. Because of the inherent technical challenges associated with measuring binding of low-affinity antibodies to monomeric proteins, we analyzed only the 64 high-affinity binders (K_D^{Apps} < 10 nM) to SARS-CoV-2 S (Fig. 2, A and B). We first evaluated binding to recombinant SARS-CoV-2 S1 and S2 subunits and observed that 75% of the antibodies recognized epitopes within S1, whereas the remaining 25% bound to epitopes within S2 (Fig. 3A). Two of the S2-directed antibodies also showed strong reactivity with OC43 S, suggesting recognition of a conserved antigenic site (fig. S6). We next evaluated the 49 S1-directed antibodies for reactivity with individual SARS-CoV-2 RBD and NTD proteins and found that 21 (43%) and 28 (57%) of the S1-specific antibodies recognized the RBD and NTD, respectively (Fig. 3A).

To further define the epitopes recognized by the 21 RBD-directed antibodies, we performed competitive binding studies with recombinant hACE2 and a previously described antibody, CR3022, that targets a conserved epitope that is distinct from the receptor binding site (Fig. 3B and fig. S7) (*15*). Six of the antibodies competed only with hACE2, three competed only with CR3022, four competed with both hACE2 and CR3022, and seven did not compete with hACE2 or CR3022 (Fig. 3B). Thus, these antibodies delineate at least four adjacent and potentially overlapping sites within the RBD. Most of the antibodies that competed with recombinant hACE2 binding to SARS-CoV-2 RBD in the biolayer interferometry (BLI) assay also interfered with binding of full-length SARS-CoV-2 S to endogenous ACE2 expressed on the surface of Vero E6 cells (Fig. 3C). The four antibodies (ADI-55951,

ADI-55993, ADI-56000, and ADI-56035) that showed stronger competition in the BLI assay displayed weak binding affinities for SARS-CoV-2 S (fig. S12), which likely explains their lower level of competition in the cell-surface assay. Thus, SARS-CoV infection elicited high-affinity cross-reactive antibodies to a range of antigenic sites within both the S1 and S2 subunits.

To evaluate the neutralization activities of the SARS-CoV-2 binding antibodies, we performed neutralization assays using both murine leukemia virus (MLV)– and vesicular stomatitis virus (VSV)–based pseudotype systems as well as authentic SARS-CoV-2. Because of the large number of antibodies, we first measured infection inhibition of authentic SARS-CoV-2 at a single concentration of purified IgG. Only 9 out of 200 antibodies displayed neutralizing activity at the 100 nM concentration tested, eight targeted the RBD, and the remaining one recognized the NTD (Fig. 3D). Similar results were observed in the VSV-based pseudovirus assay (fig. S8). Of the eight RBD-directed nAbs, four targeted epitopes overlapping with both the hACE2 and CR3022 epitopes and the other four recognized epitopes overlapping only the hACE2 epitope, suggesting the existence of two partially overlapping neutralizing epitopes within the RBD (Fig. 3B). Neutralization titration studies revealed that the median inhibitory concentrations (IC_{50}s) of the RBD-directed nAbs ranged from 0.05

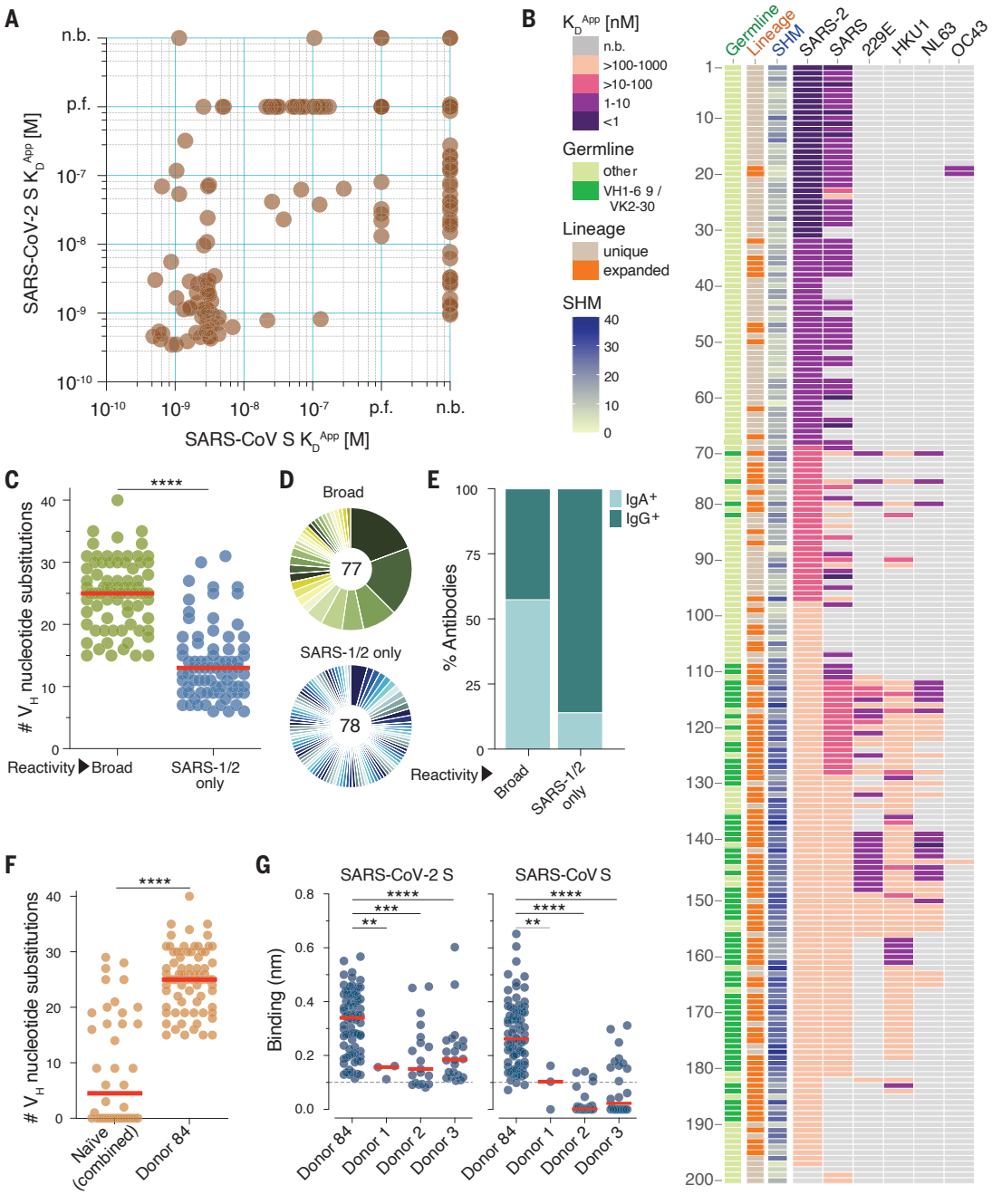


Fig. 2. Binding properties of SARS-CoV-2 S-specific antibodies. (**A**) Apparent binding affinities (K_D^{Apps}) of SARS-CoV-2 S-specific IgGs for prefusion-stabilized SARS-CoV and SARS-CoV-2 S proteins, as determined by BLI. Low-affinity clones for which binding curves could not be fit are designated as "poor fit" (p.f.) on the plot. n.b., nonbinder. (**B**) IgG K_D^{Apps} for SARS-CoV-2, SARS-CoV, 229E, HKU1, NL63, and OC43 S proteins. Germline gene usage, clonality, and SHM are presented in the three left-most columns. SHM load is represented as the number of nucleotide substitutions in V_H. (**C**) Load of somatic mutations in broadly cross-reactive and SARS-CoV– and SARS-CoV-2–specific antibodies. Red bars indicate medians. (**D**) Degree of clonal expansion in broadly cross-reactive and SARS-CoV– and SARS-CoV-2–specific antibodies. Each lineage is represented as a segment proportional to the lineage size. The total number of antibodies is shown in the center of the pie. (**E**) Proportion of broadly cross-reactive and SARS-CoV– and SARS-CoV-2–specific antibodies derived from IgG^+ and IgA^+ B cells, as determined by index sorting. (**F**) Load of somatic mutations in SARS-CoV-2 S-reactive antibodies isolated from three naïve donors and donor 84. Antibodies from healthy donors were combined for this analysis. (**G**) Binding activity of antibodies isolated from SARS-CoV-2 S-reactive B cells in donor 84 and three naïve donors to SARS-CoV and SARS-CoV-2 S proteins, as determined by BLI. Statistical comparisons were made using the Mann-Whitney test (**P < 0.01; ***P < 0.001; ****P < 0.0001).

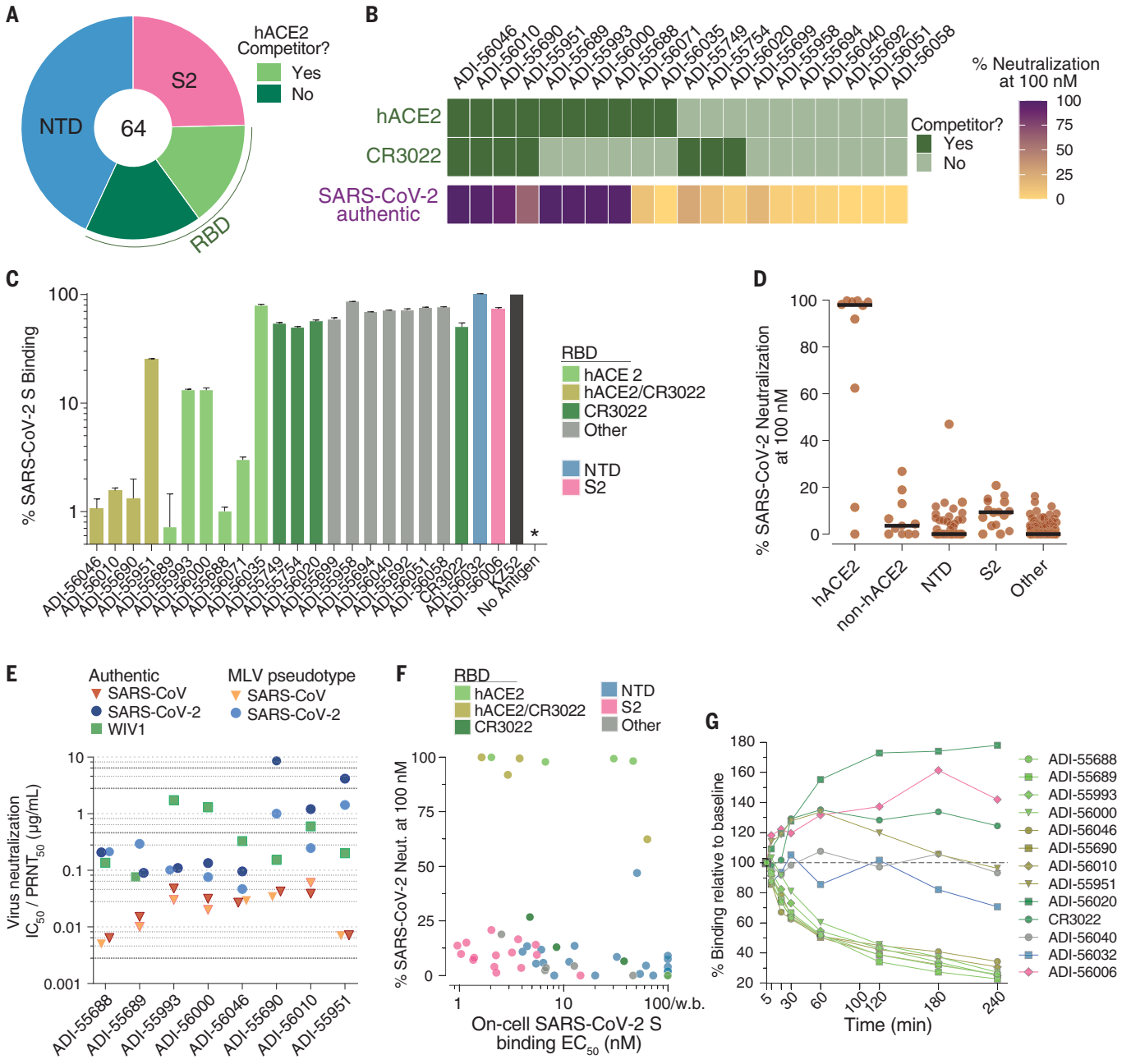


Fig. 3. Epitope mapping and neutralization screening. (**A**) Proportion of SARS-CoV-2 S-specific antibodies targeting each of the indicated antigenic sites. (**B**) Heat map showing the competitive binding profiles of the RBD-directed antibodies, as determined by BLI (top) and percent neutralization of authentic SARS-CoV-2 at a 100 nM concentration (bottom). (**C**) Antibody inhibition of SARS-CoV-2 S binding to endogenous ACE2 expressed on Vero E6 cells, as determined by flow cytometry. Antibodies were mixed with recombinant SARS-CoV-2 S bearing a Twin-Strep tag at a molar ratio of 10:1 before adding to Vero E6 cells. An anti-ebolavirus antibody (KZ52) was used as an isotype control. The "no antigen" control indicates secondary-only staining. The asterisk indicates that no detectable binding was observed. Bars are colored according to epitope specificity, as determined in the BLI competition assay. Data represent three technical replicates. (**D**) Percent authentic SARS-CoV-2 neutralization in the presence of 100 nM IgG. Antibodies are grouped according to epitope specificity. RBD-directed antibodies that compete or do not compete with ACE2 are designated as ACE2 and non-ACE2, respectively. (**E**) Antibody neutralization of SARS-CoV and SARS-CoV-2 MLV pseudovirus (strain n-CoV/USA_WA1/2020) using HeLa-ACE2 target cells, and neutralization of authentic SARS-CoV, SARS-CoV-2, and WIV1-CoV using Vero E6 target cells. Data represent two technical replicates. (**F**) Binding EC_{50}s for cell-surface SARS-CoV-2 S are plotted against the percent neutralization of authentic SARS-CoV-2 at 100 nM. Background binding was assessed using mock-transfected HEK-293 cells. Data points are colored according to epitope specificity. RBD-directed antibodies are further categorized based on their competition group: hACE2 indicates hACE2-only competitors; CR3022 indicates CR3022-only competitors; hACE2/CR3022 indicates antibodies that compete with hACE2 and CR3022; other indicates hACE2 and CR3022 noncompetitors. Antibodies with cell binding EC_{50}s >100 nM are designated as weak binders (w.b.) on the plot. (**G**) Antibody binding activity to cell-surface SARS-CoV-2 S over time, as determined by flow cytometry. IgGs were incubated with cells expressing WT SARS-CoV-2 over the indicated time intervals. Binding MFI was assessed at 240 min for all samples. CR3022 is included for comparison. Curves are colored by epitope specificity, as in (F). Data represent two technical replicates.

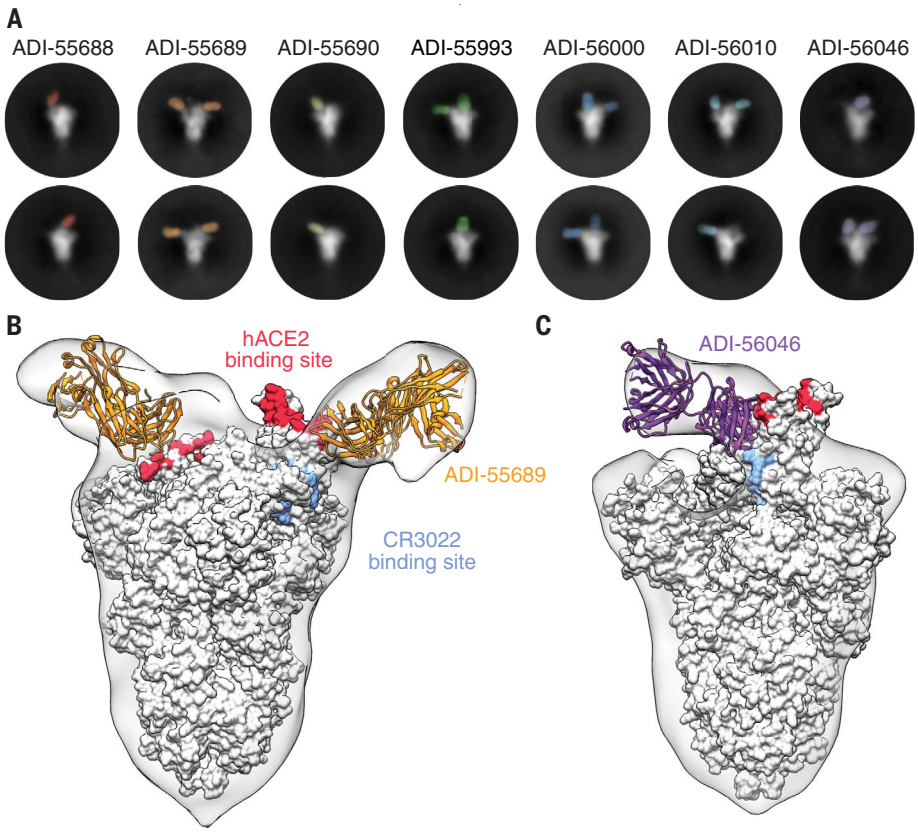


Fig. 4. Structures of cross-neutralizing antibodies bound to SARS-CoV-2 S. (**A**) Negative-stain EM 2D class averages of SARS-CoV-2 S bound by Fabs of indicated antibodies. The Fabs have been pseudocolored for ease of visualization. (**B** and **C**) 3D reconstructions of Fab:SARS-CoV-2 S complexes are shown in transparent surface representation (light gray) with the structure of the SARS-CoV-2 S trimer (white surface) and Fabs (ribbon) docked into the density. S-bound Fabs of ADI-55689 (B) and ADI-56046 (C) are colored in orange and purple, respectively. The hACE2 and CR3022 binding sites on S are shaded in red and light blue, respectively.

to 1.4 μg/ml against SARS-CoV-2 and 0.004 to 0.06 μg/ml against SARS-CoV in the MLV assay (Fig. 3E and fig. S9). Comparable neutralization IC_{50}s were observed in authentic SARS-CoV and SARS-CoV-2 neutralization assays (Fig. 3E and fig. S9). By contrast, the VSV–SARS-CoV-2 neutralization IC_{50}s were substantially lower (8- to 35-fold) than those observed for live SARS-CoV-2 (figs. S9 and S10). To assess the breadth of neutralization against representative preemergent SARS-like bat CoVs, we measured infection inhibition of authentic WIV1-CoV using a plaque reduction assay (*16*). All eight antibodies neutralized WIV1-CoV, with median plaque reduction neutralization titers ($PRNT_{50}$s) ranging from 0.076 to 1.7 μg/ml, demonstrating their breadth of activity (Fig. 3E and fig. S11). Crucially, none of the antibodies left an unneutralized viral fraction in any of the assays (figs. S9 and S11).

We observed little to no correlation between apparent binding affinity for wild-type (WT) SARS-CoV-2 cell surface S and neutralizing activity. For example, all of the S2-directed antibodies and a subset of NTD-directed antibodies bound with high avidity to both recombinant and cell surface S, but none were neutralizing (Fig. 3F). Surprisingly, even within the group of hACE2-blocking nAbs, we did not observe a strong correlation between binding to cell surface–S or recombinant-S and neutralization, suggesting that antibody potency is governed at least in part by factors beyond binding affinity (Fig. 3F and figs. S12 and S13). To determine whether the hACE2 competitor antibodies neutralized by inducing S1 shedding and premature S triggering (*17*), we incubated human embryonic kidney (HEK)–293 cells expressing WT SARS-CoV-2 S with saturating concentrations of antibody and measured the median fluorescence intensity (MFI) of antibody binding over time by flow cytometry. Indeed, all of the hACE2-blocking antibodies showed substantially decreased binding over time, consistent with induced S1 dissociation, whereas antibodies recognizing the NTD, S2 stem, and RBD epitopes outside of the hACE2 binding site displayed either no change or an increase in binding over time (Fig. 3G). We conclude that SARS-CoV infection induces high-affinity cross-reactive antibodies targeting multiple distinct antigenic sites on the S protein, but neutralizing activity is primarily restricted to RBD-directed antibodies that interfere with receptor binding and promote S1 dissociation.

To structurally characterize the epitopes recognized by the RBD-directed nAbs, we performed negative-stain electron microscopy (EM) to observe each of these Fabs bound to the SARS-CoV-2 S protein. Many of the two-dimensional (2D) class averages that we obtained displayed obvious heterogeneity in the number of Fabs that were bound to a single S trimer, which is likely due to dynamic inaccessibility of RBD epitopes and substoichiometric binding of S at the low protein concentrations used to prepare grids (Fig. 4A) (*5*, *18*). The 3D reconstructions of these complexes support the results of our biophysical competition assays and show that the RBD-directed nAbs recognize a single region on the solvent-exposed surface of the RBD with overlapping footprints. ADI-55689, which potently neutralizes and competes with hACE2, appears to bind at the edge of the hACE2 binding site, close to the more structurally conserved core domain of the RBD, without overlapping with the CR3022 epitope (Fig. 4B). ADI-56046, which exemplifies the group of antibodies that compete with both hACE2 and CR3022, binds slightly farther away from the flexible tip of the RBD, and thus its epitope spans both the hACE2 binding site and the CR3022 epitope (Fig. 4C). Our structural analysis suggests that all of the nAbs recognize a single patch on the surface of the RBD with overlapping footprints. These antibodies potently cross-neutralize SARS-CoV, SARS-CoV-2, and WIV1, suggesting that this antigenic surface exhibits extensive conservation among the SARS-like coronaviruses.

The potent cross-neutralizing antibodies described here bind to conserved epitopes overlapping the hACE2 binding site, thus illuminating this antigenic surface as a promising target for the rational design of pan-sarbecovirus vaccines. For example, the RBD epitope(s) defined by this class of antibodies could be presented on conformationally stable protein scaffolds to focus the antibody response on this site, as previously demonstrated for the motavizumab epitope on respiratory syncytial virus F (*19*). Furthermore, the nAbs themselves, alone or in combination, represent promising candidates for prophylaxis or therapy of SARS, COVID-19, and potentially future diseases caused by new emerging SARS-like viruses.

REFERENCES AND NOTES

1. F. Wu *et al.*, *Nature* **579**, 265–269 (2020).
2. F. Li, *Annu. Rev. Virol.* **3**, 237–261 (2016).
3. A. C. Walls *et al.*, *Nature* **531**, 114–117 (2016).
4. M. A. Tortorici, D. Veesler, *Adv. Virus Res.* **105**, 93–116 (2019).
5. D. Wrapp *et al.*, *Science* **367**, 1260–1263 (2020).
6. W. Song, M. Gui, X. Wang, Y. Xiang, *PLOS Pathog.* **14**, e1007236 (2018).

7. J. Lan *et al*., *Nature* **581**, 215–220 (2020).
8. M. Hoffmann *et al*., *Cell* **181**, 271–280.e8 (2020).
9. Q. Wang *et al*., *Cell* **181**, 894–904.e9 (2020).
10. F. Li, *J. Virol.* **89**, 1954–1964 (2015).
11. S. Jiang, C. Hillyer, L. Du, *Trends Immunol.* **41**, 355–359 (2020).
12. X. Ou *et al*., *Nat. Commun.* **11**, 1620 (2020).
13. H. Lv *et al*., *Cell Rep.* **31**, 107725 (2020).
14. M. S. Gilman *et al*., *Sci. Immunol.* **1**, eaaj1879 (2016).
15. M. Yuan *et al*., *Science* **368**, 630–633 (2020).
16. V. D. Menachery *et al*., *Proc. Natl. Acad. Sci. U.S.A.* **113**, 3048–3053 (2016).
17. A. C. Walls *et al*., *Cell* **176**, 1026–1039.e15 (2019).
18. J. Pallesen *et al*., *Proc. Natl. Acad. Sci. U.S.A.* **114**, E7348–E7357 (2017).
19. B. E. Correia *et al*., *Nature* **507**, 201–206 (2014).

ACKNOWLEDGMENTS

We thank E. Krauland and M. Vasquez for helpful comments on the manuscript. We also thank C. Kivler, C. O'Brien, and E. Platt for antibody expression and purification; M. Hagstroem, E. Worts, and A. Gearhart for antibody sequencing; and R. Niles and K. Canfield for providing mammalian culture support. We acknowledge the generous provision of PBMCs from a SARS survivor provided by I. Gordon, J. Ledgerwood, W. Kong, L. Wang, K. Corbett, and other members of the National Institute of Allergy and Infectious Diseases (NIAID) Vaccine Research Center. **Funding:** This work was funded in part by National Institutes of Health (NIH)–NIAID grants awarded to J.S.M. (R01-AI127521) and K.C. (U19 AI142777). D.Hu. and J.E.V. were supported by R01AI132317 and R01AI073148 (to D.N.). J.E.V. was also supported by the Bill and Melinda Gates Foundation (OPP 1183956 to J.E.V.). **Author contributions:** L.M.W., J.S.M., and A.Z.W. conceived and designed the study. A.Z.W., M.Sa., and D.P.M. performed ELISA and cell binding assays. J.S.M., N.W., and D.W. performed the structural studies. A.S.H., D.Ha., R.K.J., M.E.D., D.Hu., L.V.T., N.V.J., C.-L.H., R.B., A.S.W., E.L., C.F., J.M.F., and C.M.O. performed neutralization experiments. A.L., E.C., I.B., M.B., S.L., and M.Si. performed biolayer interferometry assays. J.H.N., C.J., and S.P. expressed and purified IgGs. B.S.G. provided convalescent PBMC samples. D.P.M., D.Hu., L.V.T., D.R.B., M.B., R.S.B., J.E.V., K.C., J.M.D., J.S.M., A.Z.W., D.W., A.S.H., and L.M.W. analyzed the data. L.M.W. and A.Z.W. wrote the paper, and all authors reviewed and edited the paper. **Competing interests:** A.Z.W., A.L., E.C., I.B., M.B., S.L., M.Sa., J.H.N., C.J., L.M.W., M.Si., D.P.M., and S.P. are employees of Adimab, LLC, and may hold shares in Adimab, LLC. L.M.W. and A.Z.W. are listed as inventors on pending patent applications describing the SARS-CoV-2 antibodies. D.R.B. is on the science advisory board of Adimab and holds shares in Adimab, LLC. **Data and materials availability:** Antibody sequences have been deposited in GenBank under accession codes MT565750 to MT566149. Standard material transfer agreements (MTAs) for scientific materials will be given to academic researchers through The Scripps Research Institute. Yeast-produced IgGs are available from the corresponding author under a MTA from Adimab. This work is licensed under a Creative Commons Attribution 4.0 International (CC BY 4.0) license, which permits unrestricted use, distribution, and reproduction in any medium, provided the original work is properly cited. To view a copy of this license, visit https://creativecommons.org/licenses/by/4.0/. This license does not apply to figures/photos/artwork or other content included in the article that is credited to a third party; obtain authorization from the rights holder before using such material.

SUPPLEMENTARY MATERIALS

science.sciencemag.org/content/369/6504/731/suppl/DC1
Materials and Methods
Figs. S1 to S13
References (*20*–*26*)
MDAR Reproducibility Checklist

View/request a protocol for this paper from *Bio-protocol*.

14 May 2020; accepted 11 June 2020
Published online 15 June 2020
10.1126/science.abc7424

The National Academies of SCIENCES ENGINEERING MEDICINE

USAID FROM THE AMERICAN PEOPLE

JEFFERSON SCIENCE FELLOWS PROGRAM
CALL FOR APPLICATIONS

Established by the Secretary of State in 2003, **Jefferson Science Fellows** program engages the American academic science, technology, engineering, and medical communities in U.S. foreign policy and international development.

Administered by the National Academies of Sciences, Engineering, and Medicine, this fellowship is open to tenured, or similarly ranked, faculty from U.S. institutions of higher learning who are U.S. citizens. After successfully obtaining a security clearance, selected Fellows spend one year on assignment at the U.S. Department of State or the U.S. Agency for International Development serving as advisers on issues of foreign policy and international development.

The deadline for applications is October 16, 2020 at 5 PM ET. To learn more about the program and to apply, **visit www.nas.edu/jsf**.

NIMS

ICYS Research Fellow at ICYS, NIMS, Japan

International Center for Young Scientists (ICYS) of National Institute for Materials Science (NIMS) invites applications for ICYS Research Fellow positions. ICYS will offer you the freedom to conduct independent and self-directed research in various area of materials science with full access to NIMS advanced research facilities.

Common language in ICYS is English. Clerical and technical support in English will be given by the ICYS staffs. An annual salary of approximately 5.35 million yen is guaranteed, which may be increased to the maximum of ~5.88 million yen depending on the performance of the Research Fellow*. In addition, research grant of 2 million yen per year will be provided to each Research Fellow. The initial contract term is two years, which may be extended for another year depending on one's performance.

All applicants must have obtained a PhD degree within the last ten years. Applicants should submit an **application form** including research proposal during the ICYS term, **CV Header, CV** with a list of publications and patents, **a list of DOI of journal publications, PDF files of three significant publications** to ICYS Recruitment Desk by **September 30, 2020 JST**. The format for the **application form** and **CV header** can be downloaded from **our website**. The selection will be made on the basis of originality and quality of the research proposal as well as the research achievements. Please visit our website for more details.

*Approximately 23% of annual salary will be deducted as social insurance premium, residence tax and income tax.

ICYS Recruitment Desk
National Institute for Materials Science
https://www.nims.go.jp/icys/recruitment/index.html

ScienceCareers
FROM THE JOURNAL SCIENCE AAAS

Confused about your next career move?

Download Free Career Advice Booklets!

ScienceCareers.org/booklets



DEPARTMENT OF PHARMACOLOGY AND PHYSIOLOGY CHAIR

DEPARTMENT CHAIR
Pharmacological and Physiological Science

Saint Louis University, a Catholic Jesuit institution dedicated to education, research, service and health care, has started a national search for the next **William Beaumont Professor and Chair of the Department of Pharmacological and Physiological Science**. The department encompasses multidisciplinary research particularly strong in the cardiovascular, endocrine and neuroscience areas and has an outstanding record in graduate education supported in part by an NIH-T32 training grant currently in its 30th year. The department seeks an individual with the vision and scientific stature to build and maintain robust basic and translational research programs, and continue the strong commitment to graduate and medical education. The successful applicant will have a Ph.D. and/or M.D. degree, a strong record of academic achievement, a solid level of extramural research funding and experience in both graduate student and medical student education. Interested candidates should submit a cover letter, curriculum vitae and a description of their leadership vision to Enrico Di Cera, M.D., Chair of the Search Committee (**enrico.dicera@health.slu.edu**).

*Saint Louis University is an equal opportunity/affirmative action employer. All qualified candidates will receive consideration for the position applied for without regard to race, color, religion, sex, age, national origin, disability, marital status, sexual orientation, military/veteran status, gender identity, or other non-merit factors. We welcome and encourage applications from minorities, women, protected veterans, and individuals with disabilities (including disabled veterans). If accommodations are needed for completing the application and/or with the interviewing process, please contact Human Resources at **314-977-5847**.*

By **Ruofan Yu**

Building bridges

I never thought I would miss the days when visa delays were my primary worry. But recently, my experience as a Chinese postdoc working in the United States has taken a darker turn. In February, I was forced to cut my family vacation in China short after hearing the U.S. government was about to issue a ban on travelers from China. Since then, I've been stunned how my people have suffered verbal and physical attacks, how my home country is being used as the name of a virus, and how my local Chinese consulate—which I've visited frequently—was ordered closed by the U.S. government. Last month, a graduate student I know was grilled on suspicion of espionage for 2 hours before boarding a plane to China. Imagining the fear he must have experienced, I was left in tears.

I moved from China to the United States 6 years ago to start my Ph.D. program. Having spent time in Canada before, I didn't face much of a language barrier or culture shock. My main source of stress was the visa approval process. On my first attempt, I received my visa in 5 days. But when I went to China to renew it last year—amid the turmoil of the trade war—the same process took an entire month. All things considered, I was quite lucky, as I know of others who have had to wait months—or even years. Some of my friends simply avoid going back home for the entire duration of their Ph.D. or postdoc years because they don't want to risk leaving the United States and not being able to get back on time.



"I felt better knowing that my academic community supports me."

Both countries have taken a progressively harder stance toward each other in recent years—and as U.S.-China tensions worsen, I am left wondering what will come next. In May, the U.S. government announced that Chinese STEM trainees who work on topics related to "military-civil fusion strategy" will no longer be allowed to enter the country. The announcement doesn't affect me directly—I study baking yeast—but it does make me worried for the future. Will all Chinese STEM trainees be looked at with suspicion from now on?

A few days after the May announcement, I received an email from my department chair, advising employees who are Chinese citizens not to leave the country until more was known about the policy. I appreciated the advice, but I wanted more empathy and emotion—some acknowledgment that my university administrators understood what I was going through. I was not alone: In chat groups and on social media, other Chinese trainees were sharing anger, frustration, and a yearning for support. But people outside our community seemed unaware.

So I wrote a letter sharing my thoughts and anxieties and sent it to my college's president. I mentioned it to other Chinese trainees, and I was impressed when some expressed interest in sending a second, co-signed letter; normally, Chinese trainees are reticent to voice concerns openly. I echoed the idea, and a few days later we sent a joint letter to school officials, including the president and the head of the graduate program.

We were pleasantly surprised when they responded promptly and organized virtual meetings to discuss our concerns. We received a lot of kind words and understanding, and a few days later, the institution issued public statements in support of all foreign trainees. The world did not change: The pandemic continued, and U.S.-China tensions did not go away. But I felt better knowing that my academic community supports me.

So I want to say this to my fellow foreign trainees: I understand that for a lot of us, it is hard to speak up and give voice to our feelings. It is scary to stand out as strangers in a foreign land, with limited rights and no family around. Nevertheless, it is important to share your concerns and ask for help. Send emails and letters. Speak up at town hall meetings. Open up to colleagues.

By sharing challenges and engaging in honest dialogue, we can educate the scientific community about the unique issues we face. Such conversations might not move the needle on foreign policy—but on a personal level, they can help build bridges and tear down walls. ■

Ruofan Yu is a postdoctoral researcher at the Baylor College of Medicine in Houston, Texas. Send your career story to SciCareerEditor@aaas.org.

ILLUSTRATION: ROBERT NEUBECKER

Published by AAAS